Synthesis and Investigation of Fluorinated Porous Organic Compounds

Inaugural-Dissertation

zur Erlangung des Doktorgrades
der Mathematisch-Naturwissenschaftlichen Fakultät
der Heinrich-Heine-Universität Düsseldorf

vorgelegt von

Tom Kunde
aus Berlin

Düsseldorf, Februar 2022

aus dem Institut für Organische Chemie und Makromolekulare Chemie I
der Heinrich-Heine-Universität Düsseldorf

Gedruckt mit der Genehmigung der
Mathematisch-Naturwissenschaftlichen Fakultät der
Heinrich-Heine-Universität Düsseldorf

Berichterstatter:

1. Dr. Bernd M. Schmidt

2. Prof. Dr. Thomas J. J. Müller

Tag der mündlichen Prüfung: 06.05.2022

Die vorliegende Arbeit wurde in der Zeit von April 2018 bis März 2022 am Institut für Organische Chemie und Makromolekulare Chemie I der Heinrich-Heine-Universität Düsseldorf unter der Anleitung von Dr. Bernd M. Schmidt angefertigt.

Publications by the author during the work on this thesis

1) T. Kunde, T. Pausch, P. A. Gunka, M. Krzyzanowski, A. Kasprzak and B. M. Schmidt, *Chem. Sci.*, DOI: 10.1039/D1SC06372C.
   T. Kunde, T. Pausch, A. Kasprzak and B. M. Schmidt conceived the project; T. Kunde, T. Pausch and B. M. Schmidt designed the experiments; T. Kunde and T. Pausch performed the majority of the experiments, analysed the data and wrote the manuscript with B. M. Schmidt.
2) T. Kunde‡, T. Pausch‡, G. J. Reiss and B. M. Schmidt, *Synlett*, 2022, **33**, 161–165.
   Highlighted on the Cover
   ‡ – both authors contributed equally. T. Kunde, T. Pausch and B. M. Schmidt conceived the project; T. Kunde and T. Pausch designed and performed the synthetic experiments, analyzed the data and wrote the manuscript with B. M. Schmidt.
3) T. Kunde‡, T. Pausch‡ and B. M. Schmidt, *Chem. Eur. J.*, 2021, **27**, 8457–8460.
   Highlighted on the Cover
   ‡ – both authors contributed equally. T. Kunde and T. Pausch designed and performed the synthetic experiments, analyzed the data and wrote the manuscript with B. M. Schmidt. T. Kunde designed the Cover graphic.
4) T. Kunde‡, T. Pausch‡ and B. M. Schmidt, *Eur. J. Org. Chem.*, 2021, **43**, 5844–5856.
   Highlighted on the Cover
   ‡ – both authors contributed equally. T. Kunde and T. Pausch wrote the manuscript with B. M. Schmidt. T. Kunde designed the Cover graphic.
5) T. Kunde, E. Nieland, H. V Schröder, C. A. Schalley and B. M. Schmidt, *Chem. Commun.*, 2020, **56**, 4761–4764.
   Highlighted on the Cover
   T. Kunde and B. M. Schmidt conceived the project and designed the experiments; T. Kunde and E. Nieland performed all experimental work and analyzed the data; T. Kunde and B. M. Schmidt wrote the manuscript. T. Kunde designed the Cover graphic.
6) T. Kunde and B. M. Schmidt, *Angew. Chem. Int. Ed.*, 2019, **58**, 666–668.
   (Highlight Article)
   T. Kunde and B. M. Schmidt wrote the manuscript.

Poster

T. Kunde, T. Pausch and B. M. Schmidt: “Fluorinated building blocks for porous organic compound self-assembly”, 15th International Symposium of Macrocyclic and Supramolecular Chemistry (ISMSC2021), online.

T. Kunde and B. M. Schmidt: “Synthesis and Application of Highly Fluorinated Supramolecular Imine Cages”, GDCh-Wissenschaftsforum, Aachen, Deutschland, 2019.

Danksagung

An dieser Stelle möchte ich mich bei allen Menschen bedanken, die mich auf meinem Weg während der Promotion unterstützt haben. Ohne euch wäre diese Arbeit so nicht möglich gewesen.

Zuallererst möchte ich mich sehr herzlich bei Dr. Bernd M. Schmidt für sein Vertrauen, die unzähligen Brainstorm-Sessions, die finanzielle Unterstützung für alle mehr oder weniger abgedrehten Cover-Entwürfe, seine unschätzbar wertvollen Ratschläge und seine Freundschaft bedanken. Ich kann mir nur schwer vorstellen, wie man sich fühlen muss am Beginn seiner Professoren-Laufbahn jemandem, den man kaum kennt, seine berufliche Zukunft in die Hände zu legen. Ich danke dir, dass ich derjenige sein durfte und das Glück hatte in einer Start-Up Atmosphäre promovieren zu dürfen. Für jede Idee hattest du immer ein offenes Ohr und einen guten Ratschlag. Ich werde nie vergessen, wie wir dort, wo ich die letzten vier Jahre verbracht habe, mit einem leeren Labor ohne Rotis und Glasgeräte gestartet sind. Was für eine wilde Fahrt!

Ich möchte Robin und Esther für die unzähligen schönen Momente außer- und innerhalb des Labors danken. Auch wenn ich euren Musikgeschmack nicht oft geteilt habe, muss ich sagen, dass ich den ein oder anderen Ohrwurm mit nach Hause genommen habe. Ich möchte euch außerdem für eure Ideen und euer Feedback danken, und mich gleichzeitig bei euch für meine schwankenden Launen entschuldigen. Vielen, vielen Dank, dass ihr mich ausgehalten habt und mir die besten Laborkolleg*innen wart.

Ein besonderer Dank gilt auch Tobi, der mit mir das Freud und Leid der fluorierten Materialien, erst als mein Masterand und dann als hoch geschätzter Kollege, geteilt hat. Durch deine unermüdliche Arbeit sind unsere gemeinsamen Publikationen zu einem Herzstück dieser Arbeit geworden und ich würde mit niemandem lieber gemeinsam über neue Ideen und Abbildung-Entwürfe sprechen, als mit dir.

Eine Arbeit diesen Umfangs wäre nicht ohne die Hilfe zahlreicher Handlanger*innen möglich gewesen. Aus diesem Grund möchte ich mich bei Jacob, Larissa, Esther, Hendrik, Tobi und Tim für die großartige Zusammenarbeit und Hilfe bedanken.

Einen essentiellen Teil zu dem Erfolg dieser Arbeit haben Mohanad Aian, Dr. Rainer Bürgel und Dr. Peter Tommes durch die Anfertigung der unzähligen NMR und Massenspektren beigetragen, wofür ich mich an dieser Stelle herzlich bedanken möchte.

Prof. Dr. Constantin Czekelius möchte ich für die Bereitstellung von Geräten und Chemikalien danken. Gerade beim Aufbau dieses Arbeitskreises waren diese “Stützräder“ wichtig um schnell auf die Beine zu kommen.

Dem Team von Prof. Dr. C. Lehmann am Max-Planck-Institut in Mülheim an der Ruhr möchte ich für das Messen meiner kristallinen Proben mittels Synchrotronstrahlung danken, ohne deren Hilfe die Strukturaufklärung einiger Verbindungen erfolglos geblieben wäre.
Weiterhin möchte ich auch Laura zur Horst und Prof. Dr. S. Höger (Universität Bonn) für die Aufreinigung meiner Proben mittels Gelpermeationschromatografie danken.
Einen großen Dank möchte ich auch an Flo, Dilcan, Dagmar, Luisa und Angelique richten. Danke, dass ich mit euch zusammen das Studium und wahnsinnig viele wunderschöne Momente erleben konnte. Egal wo uns das Schicksal auch hin verschlägt schaffen wir es trotzdem uns immer wieder zu treffen und ihr seid die besten Freunde, die ich mir wünschen könnte.
Meinen Eltern möchte ich für die Unterstützung auf meinem bisherigen Lebensweg danken, die mich bis zu dieser Promotion geleitet hat. Ohne eure Fürsorge und Liebe wäre ich nicht der, der ich heute bin.
Zu guter Letzt möchte ich der Frau danken, die einen der größten Anteile an dieser Arbeit hat. Sophie, ich danke dir für deine Liebe, deine Aufmunterungen, deine Kraft und vor allem für deine Aufopferung, dich um unsere Tochter zu kümmern, damit ich diese Arbeit beenden konnte. Egal, wie mein Tag lief, du hast es stets geschafft mir den Rückhalt zu geben, ohne den ich nicht soweit gekommen wäre.

Abstract

Fluorinated materials have long been known to exhibit properties that can be utilized for the generation of porous materials. Among the beneficial attributes of fluorinated framework materials are high thermal stability, great degrees of crystallinity, and enhanced H_2 and CO_2 gas uptakes. The use of fluorinated building blocks in the synthesis of porous organic cages (POCs) would allow for the material to be processed in solution, which enhances the usability of porous materials in even more fields of application.

In this work, the synthesis of fluorinated POCs (FPOCs) is investigated. By designing and synthesizing highly fluorinated building blocks and using them in cage syntheses that target different topologies, the utilization of these compounds is studied. The resulting cage molecules are investigated for their material properties, and it is evaluated whether the beneficial attributes of fluorinated framework materials could be reproduced. This leads to the discovery of FPOCs that differ greatly in their shapes and sizes. Throughout the study, several milestone structures are identified. Among these is a cage compound that exhibits an uptake of 19.0 wt% of CO_2, and also shows remarkable thermal stability and crystallinity. Furthermore, the importance of C–F$\cdots\pi_F$ interactions for the generation of cage molecules and for crystal packing is identified. These interactions are utilized in the synthesis of a decernary co-crystal, the synthesis of a large FPOC with a very rare geometry, and the synthesis of a flexible imine cage that has been said to be inaccessible to fluorinated compounds.

Overall, 23 fluorinated cage compounds are synthesized and investigated for their guest-encapsulating behavior, crystallinity, thermal stability, and gas uptake. The inverse distribution of electron density in fluorinated aromatic molecules, compared to non-fluorinated derivatives, is exploited for the use of FPOCs as sensor-like materials.

Ultimately, the knowledge about fluorinated porous materials is applied to the synthesis of a porous, supramolecular organic framework that is based on a highly fluorinated macrocycle.

This work exemplifies the great range of possibilities for the use of fluorinated building blocks in the generation of porous materials.

Zusammenfassung

Schon lange ist bekannt, dass fluorierte Materialien Eigenschaften aufweisen, die für die Herstellung poröser Materialien genutzt werden können. Zu diesen nützlichen Eigenschaften von fluorierten Gerüstmaterialien zählen unter anderem die hohe thermische Stabilität, der hohe Grad an Kristallinität und eine gesteigerte Aufnahme von H_2 und CO_2. Wäre es möglich, fluorierte Bausteine für die Synthese von porösen organischen Käfigstrukturen (POKs) einzusetzen, könnten die daraus hergestellten Materialien in Lösung verarbeitet werden. Das würde die Verfügbarkeit dieser Materialien auf noch mehr Anwendungsbereiche erweitern.

In dieser Arbeit wird die Synthese von fluorierten POKs (FPOKs) untersucht. Hochfluorierte Bausteine werden konstruiert, synthetisiert und für die Synthese von Käfigverbindungen eingesetzt, um die Eignung dieser Verbindungen für die Herstellung von POKs zu evaluieren. Die resultierenden Käfigverbindungen werden auf ihre Materialeigenschaften untersucht und es wird untersucht, ob die hervorragenden Eigenschaften der fluorierten Gerüstmaterialien reproduziert werden können. Dieser Ansatz führt zu der Entdeckung von FPOKs in verschiedenen Größen und Formen. Im Verlaufe dieser Arbeit werden verschiedene Meilenstein-Verbindungen identifiziert. Unter anderem wird eine Käfigverbindung behandelt, die in der Lage ist 19.0 wt% CO_2 aufzunehmen und darüber hinaus eine ausgezeichnete thermische Stabilität und Kristallinität besitzt.

Des Weiteren wird die Wichtigkeit von C–F$\cdots\pi_F$ Wechselwirkungen für die Herstellung von Käfigverbindungen und die Packungen innerhalb von Kristallstrukturen beleuchtet. Diese Wechselwirkungen können für die Synthese eines dezernären Co-Kristalls, die Synthese eines großen FPOKs mit einer seltenen Geometrie und darüber hinaus für die Synthese eines flexiblen Iminkäfigs, der für fluorierte Bausteine als unzugänglich galt, genutzt werden.

Insgesamt werden 23 fluorierte Käfigverbindungen synthetisiert, vorgestellt und deren Gast-Einschlusspotential, Kristallinität, thermische Stabilität sowie deren Gasaufnahme untersucht. Die inverse Elektronenverteilung von fluorierten aromatischen Strukturen im Vergleich zu nicht-fluorierten Aromaten wird für die Verwendung der FPOKs als sensorähnliche Anwendung ausgenutzt.

Im letzten Teil wird das gewonnene Wissen über fluorierte poröse Materialien of die Synthese einer porösen, supramolekularen, organischen Gerüstverbindung, basierend auf Makrozyklen, angewendet.

Diese Arbeit stellt beispielhaft die große Bandbreite an Möglichkeiten vor, die fluorierte Bausteine für die Erstellung von porösen Materialien besitzen.

Table of Contents

1. Introduction

1.1. General introduction

One of the main goals of every organic chemist's work is the formation of new bonds between atoms to generate new molecules. These novel structures then need to be analyzed to determine if their properties have changed and, if so, whether these new properties are beneficial for the concerned field of application. This approach to work has been the motor of scientific innovation across a broad range of life science fields (e.g. medicine, pharmaceuticals, agriculture) and material science fields (e.g. photovoltaics, energy storage applications, dyes, pigments, or elastomers) for many decades. The focus was mainly on predicting and engineering the structure-function relationship of individual molecules. With advancing analytical technologies and a rapidly increasing understanding of molecular interactions at the electronic level, the focus has shifted beyond individual molecules. This was the birth of a field we now address as "supramolecular chemistry," which is sometimes introduced as chemistry "beyond the covalent bond".[1]

The everyday work of a supramolecular chemist still includes the formation of new bonds between atoms to synthesize new compounds, but the purpose of their synthesis is the investigation of interactions with either molecules of the same sort or completely different molecules altogether. The understanding of phenomena like hydrogen bonds, π-π-stacking, van-der-Waals and dipole-dipole interactions led to new structure-function interpretations. How can one design and synthesize a molecule which then interacts in a specific way with another molecule, creating a larger "superstructure" in the process? The precise engineering of how the individual molecules interact in the resulting superstructure results in the generation of materials with unprecedentedly fine-tuned properties. Although the approach of synthesizing a molecule with the macroscopic properties already in mind has been exploited to some extent by polymer chemistry, the complexity and specificity that some applications demand require a more tailored solution.

Two of these applications are the storage and filtration of gases. With the ever growing need to store large amounts of H_2 in a stable form and a low volume for use in fuel cells and the need to store the climate-influencing CO_2, new materials have also emerged.[2] These materials show a high uptake of CO_2 and H_2 while also being able to release the gas under suitable conditions. To store gases inside a material, the structure needs to be large enough to contain void spaces, or "pores". The class of polymers of intrinsic microporosity (PIMs) proves that these molecules are large enough to contain voids by unfavorable packing of the molecule in the solid state.[3]

The "storage" of gases describes the process of either physi- or chemisorption of gas molecules onto the surface of pores inside a material. In PIMs, these pores are often created *via* sterically demanding substituents that circumvent effective packing in the solid state.[4] The result is a statistical formation of void spaces with almost no control over the respective pore shape, pore size, and pore surface area inside the material. Gas molecules can be stored inside, but they are poorly distributed and the desorption process is difficult. Furthermore, the aforementioned structure-function engineering remains very limited since no control can be exhibited regarding the pore geometries.

The separation of molecules was historically limited to exploiting different macroscopic properties, like melting or boiling points, and some microscopic properties, like differences in polarity. Only the advent of supramolecular chemistry allowed the separation of molecules by their molecular geometry, independent of macroscopic attributes. Like a cut-out board with different geometric forms, supramolecular structures can be synthesized to only be permeable to one specific molecule or to exclude it (Figure 1). To obtain this level of separation quality, the used material needs to be porous and be thoroughly controlled in terms of pore size and geometry.[5] This marks another problem that can only be addressed by supramolecular solutions.

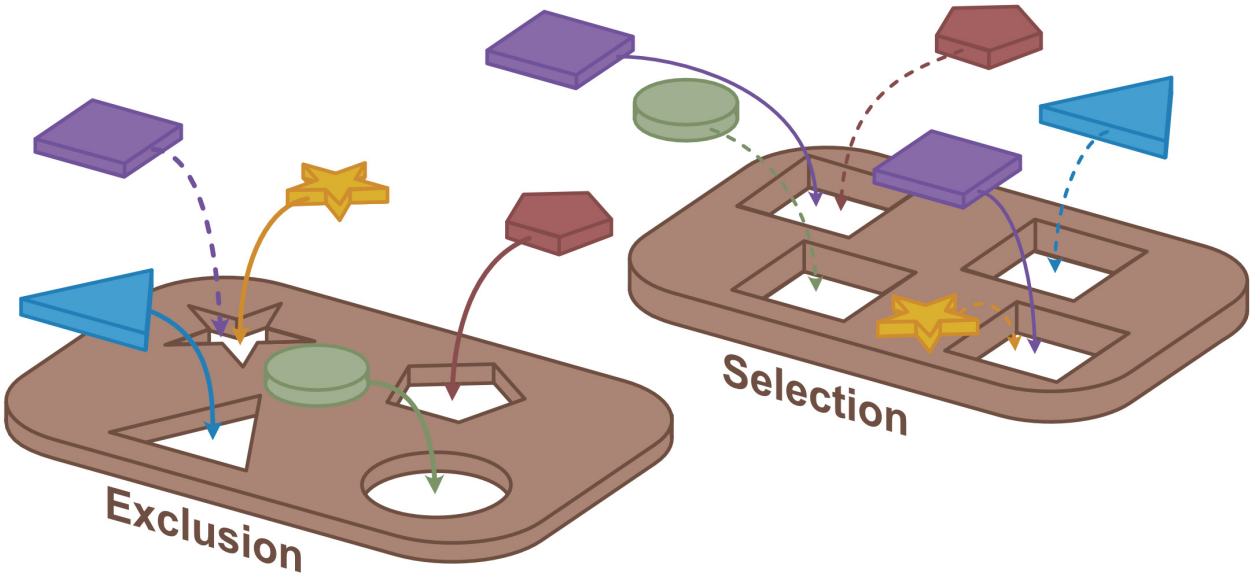

Figure 1: Model to explain the selection or exclusion of target molecules from the porous material's channels only by its geometric shape. Dashed arrows indicate the wrong shape of the molecule for fitting through the pores.

Material classes, which fulfill these criteria and have developed from microporous silica and zeolites, are regularly ordered structures in which one or more different organic and inorganic motifs repeat themselves inside a crystal lattice. If no metals are included and the individual molecules are seemingly endlessly connected through covalent bonds, the material is considered a *covalent organic framework* (COF).[6] When metal centers are connected to organic linkers through dative bonds and this binding motif is again endlessly repeated inside the crystal lattice, a *metal organic framework* (MOF) is obtained.[7] If two or more organic molecules of different geometries form a hollow superstructure with a distinct polyhedral shape *via* covalent bond formation (e.g. tetrahedron, octahedron), these molecules are called porous organic cages (POCs).[8] By precise tuning of the interactions between such POCs, the individual pores can be interconnected, forming a network of void spaces, analogous to COFs and MOFs.[9]

Framework materials like COFs and MOFs both exhibit the periodicity that is also encountered in crystals of pure compounds and salts. During the formation of these frameworks, the geometric prerequisites of the linker molecules allow the existence of large voids inside the unit cell. The endless repetition of these cells throughout the material results in the formation of two- or three-dimensional networks linked by covalent (COFs) or metal-dative (MOFs) interactions (Figure 2).These networks are filled with solvent molecules which have been trapped during the synthesis of said materials. Only the thorough thermal activation and application of a high vacuum enables the complete evaporation of solvent molecules. A hollow structure remains that can, if the pores are large enough, interact with gas molecules on the inner surface. Materials that are created in this way (e.g., NU-100 (MOF) and CALF-20 (MOF))[2] are among the best compounds for H_2 and CO_2 uptake and storage.

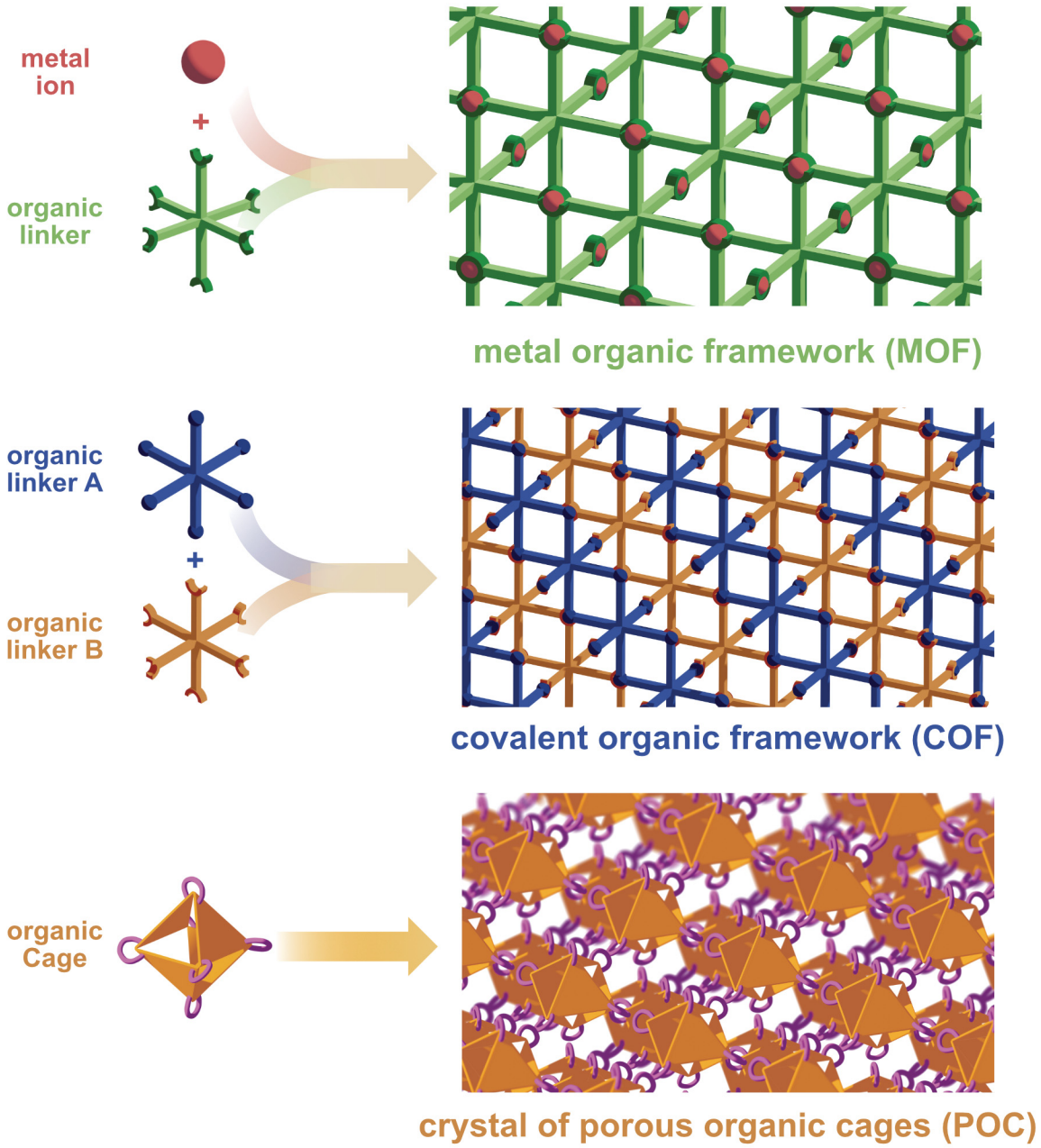

Figure 2: Overview of the different assembly modes for metal organic frameworks (MOFs, top), covalent organic frameworks (COFs, middle) and for a regular crystal lattice of porous organic cages (POCs, bottom).

The synthesis of POCs follows similar principles: two or more different organic molecules form a structure *via* dynamic covalent bond formation that, due to the geometric shape of the constituting linkers, allows the existence of voids. The main difference between framework materials is the connection *between* the different hollow unit cells. Whereas in frameworks the connection is very rigid and of a covalent nature, in POCs the adjacent unit cells remain individual molecules that interact *via* non-covalent, supramolecular forces. These weaker interactions allow the dissolving of POC materials in organic solvents or even water. These conclusions suggest a greater flexibility in the design of corresponding materials. Since the hollow unit remains intact, only the connection

between these units can be targeted precisely.

Furthermore, a dissolved POC enables access to each individual unit of the material lattice. This can be exploited to analyze the hollow molecules and further modify the individual structure post-synthesis to increase stability, influence the packing, or reshape the geometry of the hollow units. Although the weak connections between the cage molecules in POCs allow for greater flexibility and fine-tuning of the material properties, new challenges arise as well. The aforementioned evaporation of solvent molecules, trapped during synthesis, needs to be conducted using milder conditions due to the fragile nature of the non-covalent interconnections.

Several studies have been conducted on POCs employing different functionalities and the formation thereof. A class of POCs that has been underrepresented in these studies so far is the class of fluorinated POCs. Fluorine atoms have already been extensively used in the formation of MOFs and COFs and have contributed to the development of super-hydrophobic frameworks that exhibit high thermal stability while simultaneously possessing excellent H_2 and CO_2 storage capabilities.[10] Reports of POCs that incorporate fluorinated building blocks, however, are scarce and have encountered the aforementioned problem of an unfavorable crystal packing leading to decreased porosity.[11]

A thorough study on the topic of fluorinated porous organic cages (FPOCs) will be conducted in this work. First and foremost, the formation of smaller cages from highly reactive, fluorinated building blocks is studied (Sections 3.1 and 3.2) to improve the understanding of the kinetic and thermodynamic processes during the cage synthesis. These results are then applied to the targeted synthesis of a medium-sized tetragonal-shaped fluorinated POC (**FC1**), that exhibits high thermal stability, a high uptake of H_2 and CO_2 as well as high crystallinity (Section 3.3). The influence of the degree of fluorination on the properties of a known medium-sized cage is examined by stepwise substitution of non-fluorinated *vs.* fluorinated building blocks (Section 3.4). The resulting *hybrid POCs* are then analyzed regarding their thermal stability and crystallinity corresponding to their degree of fluorination. Larger fluorinated POCs were ultimately synthesized to increase the amount of suitable guest molecules and gases that can interact with the highly fluorinated pores of these large-pore materials (Section 3.5). These larger FPOCs are examined regarding their thermal stability, gas uptake and shape persistency. This work concludes with the successful transfer of the knowledge about FPOCs to two-dimensional pores and the class of fluorinated macrocycles (Section 3.6). A chiral, highly fluorinated macrocycle is synthesized, which forms one-dimensional stacks to create a porous tubular network.

1.2. Principles of supramolecular synthesis

The creation of an organic cage molecule always starts by assembling it from different building blocks. Molecules that constitute the cage by undergoing reversible (or irreversible in some cases) bond formation with each other need to be identified. The choice of which bond is best suited for the targeted cage must take accessibility, flexibility, and stability of the starting materials into account.

1.2.1. Irreversible bond formation

The groups of Vögtle and Cram were among the first to obtain "polycyclic cryptands", a name that was common for organic cage molecules around the 1980s and 90s.[12,13] At that time, such cavitands were synthesized using multiple steps and employing irreversible bond formations, in which the last step was usually the cyclization to the final product under high dilution conditions, e.g. *via* amide formation (Scheme 1, right). Another approach that the group of Vögtle was mainly focused on was the one-step synthesis of complex molecules from simple building blocks (Scheme 1, left). To facilitate the product formation, reactions were either conducted in very large amounts of solvent or with a very slow addition of one of the components to the reaction mixture, keeping the resulting concentration of starting materials low throughout the process.

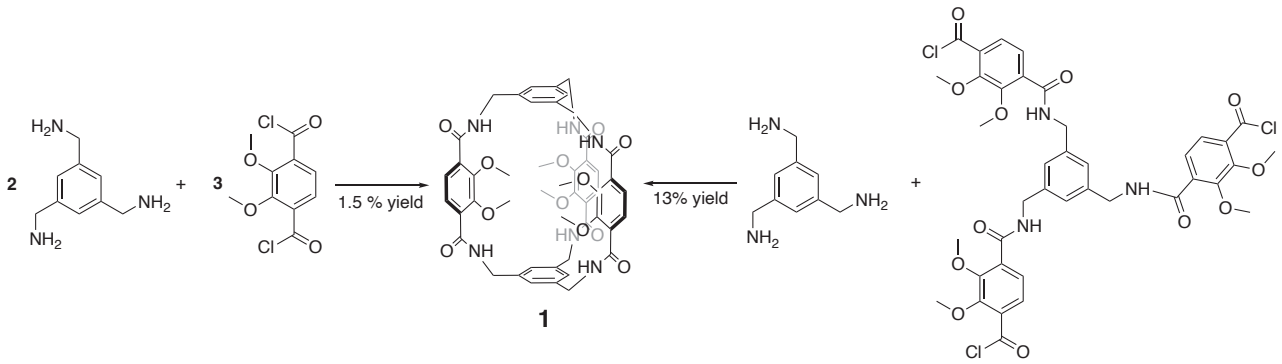

Scheme 1: Synthetic approaches of Vögtle to generate Cage **1** from the precursors (left) in a one-step synthesis and in a multi-step synthesis (right).[12]

The low yields of these syntheses require the tedious preparation of large quantities of starting materials and the repetition of the reaction numerous times. Although it is possible to facilitate the cyclization step by using sterical bias or hydrogen bonding motifs[14,15] the previous synthetic steps result in an overall very low yield when using a linear synthesis. This is exemplified in one case,

where the group of Vögtle employed a 7-step-synthesis with an overall yield of 2% to generate an organic cage that consists only of hydrocarbons (Scheme 2).[16]

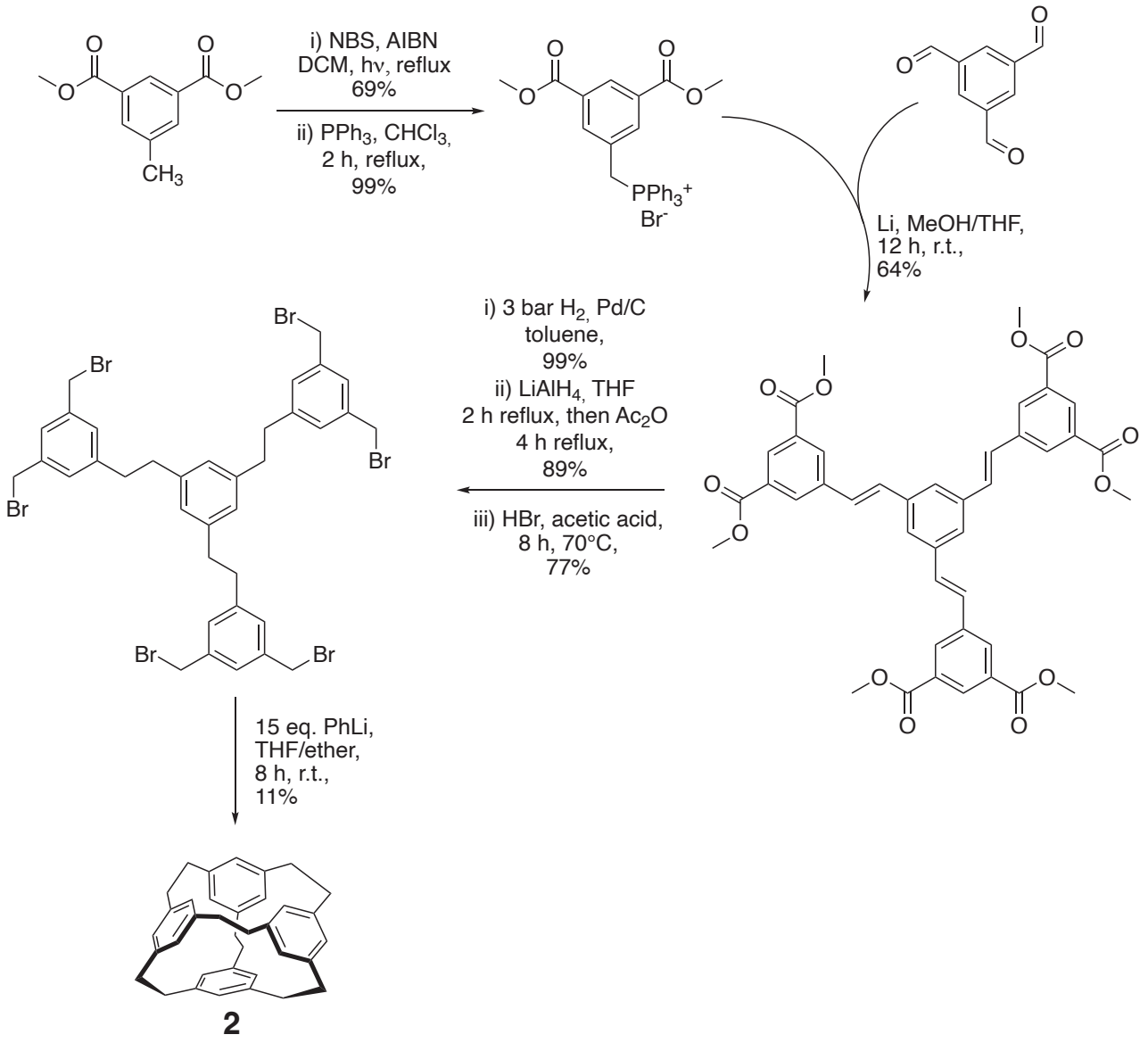

Scheme 2: Elaborate synthesis of a hydrocarbon cage by Vögtle *et al.* with an overall yield of 2%, symbolic of the difficulties encountered during the synthesis of very complex molecules.[13]

Template Effect

To circumvent the use of linear multi-step syntheses, another approach is needed. If very complex molecules (like **1** or **2**) could be obtained in a few steps from synthetically easily accessible molecules, the cage molecules would be easier to synthesize, analyze, and use in applications. When this approach is applied to the formation of amide cages using only high dilution conditions, the results are often very low yields and a very difficult isolation of the product (Scheme1). The group of Raymond, for example, could realize high-yielding syntheses of organic amide cages by

utilizing a strategy that had already been applied to the synthesis of molecular knots and macrocycles.[17] Raymond *et al.* were able to generate the, structurally very similar to **1**, cage **3**, in very high yields by using an iron(III) ion as a template (Scheme 3).

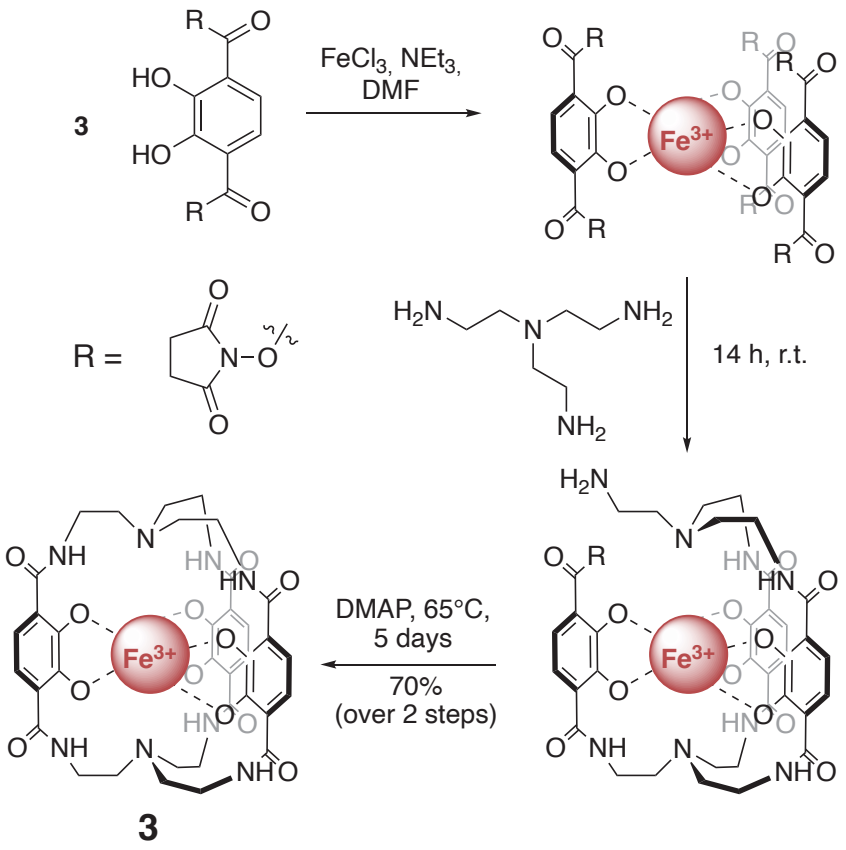

Scheme 3: Two-step, high-yielding synthesis of cage **3** starting from easily accessible building blocks.[17]

Using a template to geometrically preassemble parts of the complex structure of a cage molecule gives access to otherwise inaccessible compounds and reduces the possibility of unfavorable side reactions. The application of the templating effect necessitates the presence of suitable functional groups like diols or pyridines inside of the building blocks, which causes the reach of the method to be limited to very specific cases.[18,19]

1.2.2. Dynamic covalent bond formation

Since the multi-step synthesis and the one-step synthesis of complex molecular structures employing irreversible bond formation possess obvious disadvantages or limitations, the logical conclusion would be to investigate reversible bond formation reactions as a tool for successful cage construction. Reversible reactions that result in the formation of a covalent bond have been termed "dynamic" by Jean-Marie Lehn, when he first introduced the concept of dynamic combinatorial chemistry (DCC).[20] The key aspects of the abstracted field of dynamic covalent chemistry (DCvC) are that the starting materials for a dynamic system can interact in a reversible bond

formation reaction, which causes many different oligomeric and polymeric products to become accessible almost instantaneously after mixing. This species can then, at any time, be converted into each other (Scheme 4). This important aspect is the prerequisite for the system's ability to equilibrate to the thermodynamically most stable product over time.

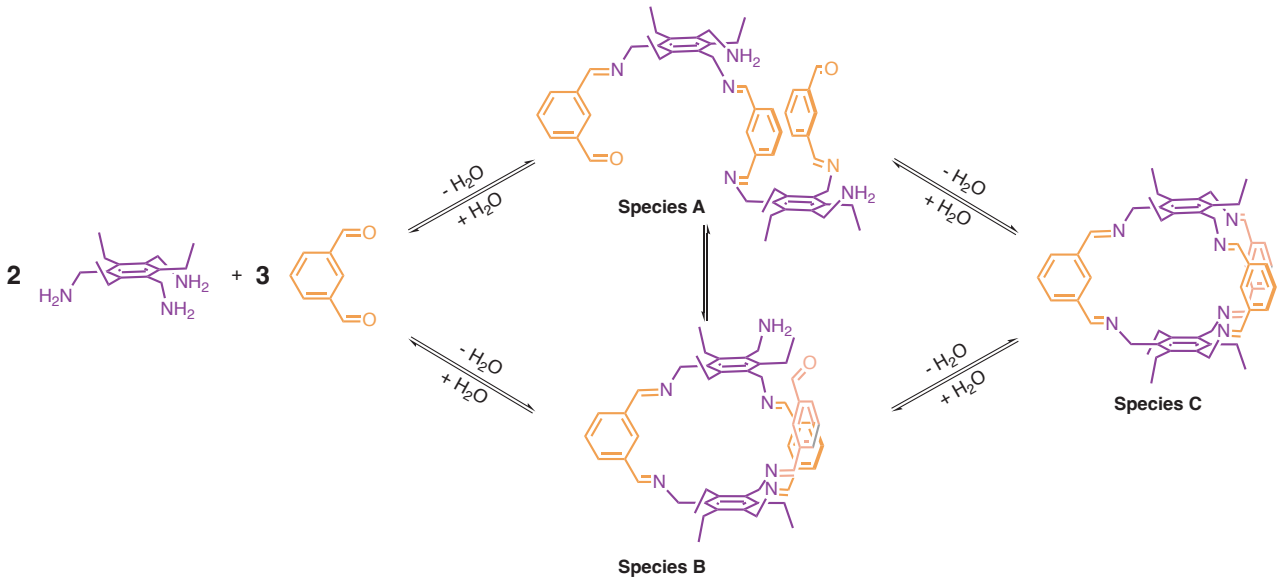

Scheme 4: Different states of a dynamic system created by the reversible imine bond formation between an amine (purple) and an aldehyde (orange).

A stable dynamic system consists of several species in which different numbers of building blocks are connected *via* covalent bonds and which are in equilibrium with each other. In most cases, the predominant species inside the system is determined by its thermodynamic stability under current conditions. In an ideal case, this allows for the vast exploration of different molecules with high complexity since many species on the systems' potential energy surface (PES) are accessible under the right reaction conditions. To influence the outcome of a dynamic bond formation reaction and to shift the equilibrium towards the desired organic cage product, parameters like reaction time, temperature, solvent, and stoichiometry of the starting materials are crucial.

Influences on the systems equilibrium

The first parameter that has a great impact on the dynamic system's outcome is the stoichiometry of the building blocks. Since most organic cage compounds are of a specific geometry, which can be divided into a number of repeating geometric elements, it is essential to combine these elements in the right ratio to circumvent the formation of oligomeric and polymeric species.

Since the assembly of complex cage structures often involves the reaction of ten or more functional groups with each other and is conducted under diluted conditions, reaction times are mostly in the span of days or even weeks.[21] The reaction times can be sped up by additives like Lewis- or Brønsted-Acids or hygroscopic compounds that either reduce the activation barrier or

further shift the equilibrium towards the condensation product. Thorough care must be taken when adding acid, though, as this can reduce the reaction time but also lower the activation barrier of previously inaccessible oligomeric or even polymeric species which are even lower in their total energy compared to the desired cage species, becoming the predominant species.[22] Raising the temperature has a similar effect to addition of acids: although reaction times can be reduced, other previously inaccessible species begin to emerge during the reaction. In many cases, when using building blocks bearing functional groups of low reactivity, higher temperatures (>70 °C) are needed to overcome the considerably large activation barrier.[23]

One of the most essential roles during the design of a successful organic cage synthesis is maybe played by the reaction solvent. The solvent needs to be carefully chosen, since it needs to solubilize all intermediate structures on the reaction pathway to the final cage compound and its interactions with the starting materials and the system's species can tip the scale in a delicate balancing across the PES towards the cage structure. Using protic/aprotic solvents e.g., can lead to drastically increased or decreased reactivities at the functional groups of the building blocks, but can also have a templating effect on intermediate structures essentially influencing further assembly steps during the equilibrium process of the system. This can lead to a drastically altered outcome, where completely unexpected cage geometries can emerge.[24] When chosen wisely though, the desired cage product can precipitate from the reaction solvent, facilitating an easy and straightforward purification process.

Geometry and Building Blocks

This leads to a closer examination of the shape of the discussed POCs. The majority of known POCs are well associated with a specific polyhedral geometric shape. This shape can, in turn, be broken into different repeating geometric elements. A cube, for example, can be divided into 8 vertices and 12 sides, whereas an octahedron can be broken down into 6 vertices and 8 faces. For a cage molecule to remain accessible to guests and essentially be classified as porous, its geometrically attributed shape needs to have either unoccupied face sites or no faces at all (Figure 3).

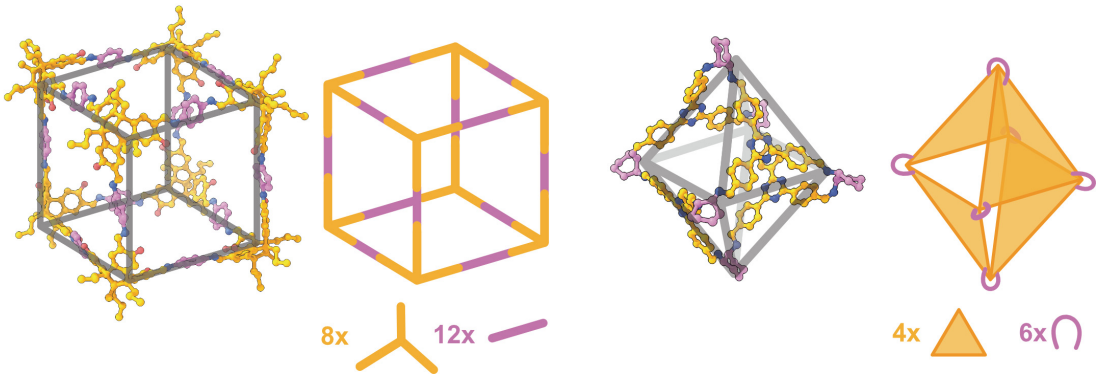

Figure 3: Cubic cage (left) and octahedral organic cage (right) exemplifying the geometric shapes of POCs.

When Mastalerz *et al.* were recently able to synthesize a cubic cage from eight tritopic aldehydes and twelve ditopic amines, they essentially created a molecular compound that perfectly resembles a cube but does not possess any faces at all.[25] The often encountered and prominently by Fujita *et al.* exploited motif of an octahedral cage geometry similarly shows very good agreement with a regular octahedron, but only half of the eight faces are occupied by tritopic building blocks.[26] In a purely organic example of this geometry by Yuan and Wang *et al.,* two adjacent faces are connected by ditopic amine structures, resulting in a facial arrangement where the faces opposite of the aldehyde linkers are vacant (open "cage windows").[27]

There are multiple geometries that are possible and have already been accessed during the synthesis of POCs. Independently of how different the sizes and shapes of these are, they all share the composition of two or three different building blocks.

The requirements for suitable building blocks are their topicality, rigidity, and geometric shape, or "bite angle". At least one of the two or more building blocks must possess three or more functional groups that are reacting in the DCvC reaction. If only two are present, the resulting macromolecule remains two-dimensional and cannot be classified as a cage molecule *per se*.[28] To inhibit the formation of long, polymeric structures during the equilibration of the dynamic system, the building blocks need to have a geometric bias towards the desired cage geometry encoded in their individual shapes. By cleverly exploiting steric repulsion or supramolecular interactions inside the building blocks, the supramolecular chemist can design molecules that lead very straightforwardly to the desired geometry, whereas other molecules with many degrees of freedom fail to generate a cage molecule at all.[29] When Mastalerz *et al*. tried to react 1,3,5-triformylbenzene (**TFB**) with different tritopic amines, they found that only when the rotation of the amine group around the adjacent C–C bond is limited, they were able to generate a cage product. They observed only insoluble polymeric structures when using the conformationally very flexible, unsubstituted 1,3,5-tris(aminomethyl)-benzene (Scheme 5, left). Suitable building blocks must therefore exhibit a certain degree of rigidity, but need to be simultaneously somewhat flexible as the binding angles inside the cage can sometimes differ drastically from the starting materials. This would lead to the introduction of serious strain in the cases of molecules that show no signs of flexibility at all.

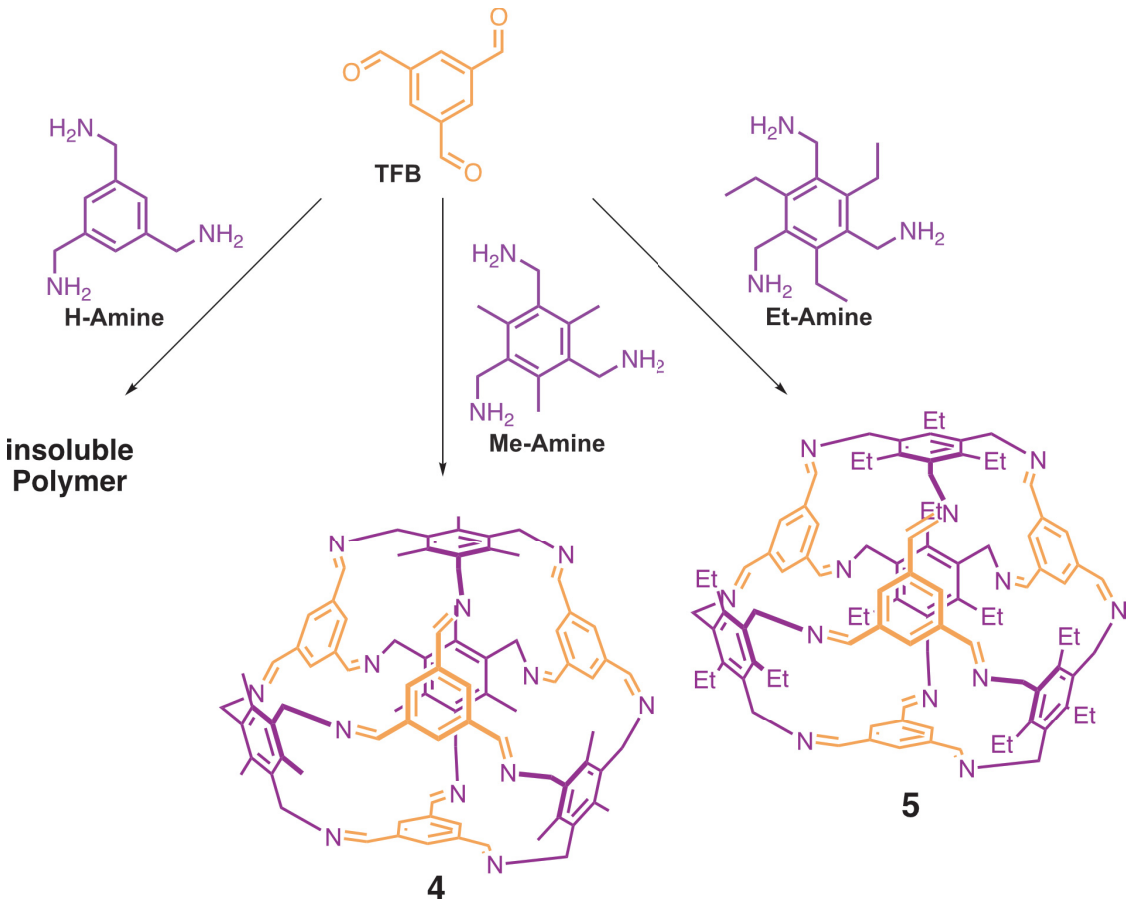

Scheme 5: Reaction of **TFB** with different tritopic amines, all employing different degrees of flexibility.

This somewhat abstract concept of flexibility can better be described by the so called “bite angle”. The group of Jelfs took a computational chemical look at the binding motifs that are most likely to generate a cage topology. They screened di-, tri- and tetratopic molecules with tested computational methods against 20 different geometrical shapes (12 of which have already been realized) and found which bite angles can be exploited for which geometry (Figure 4).

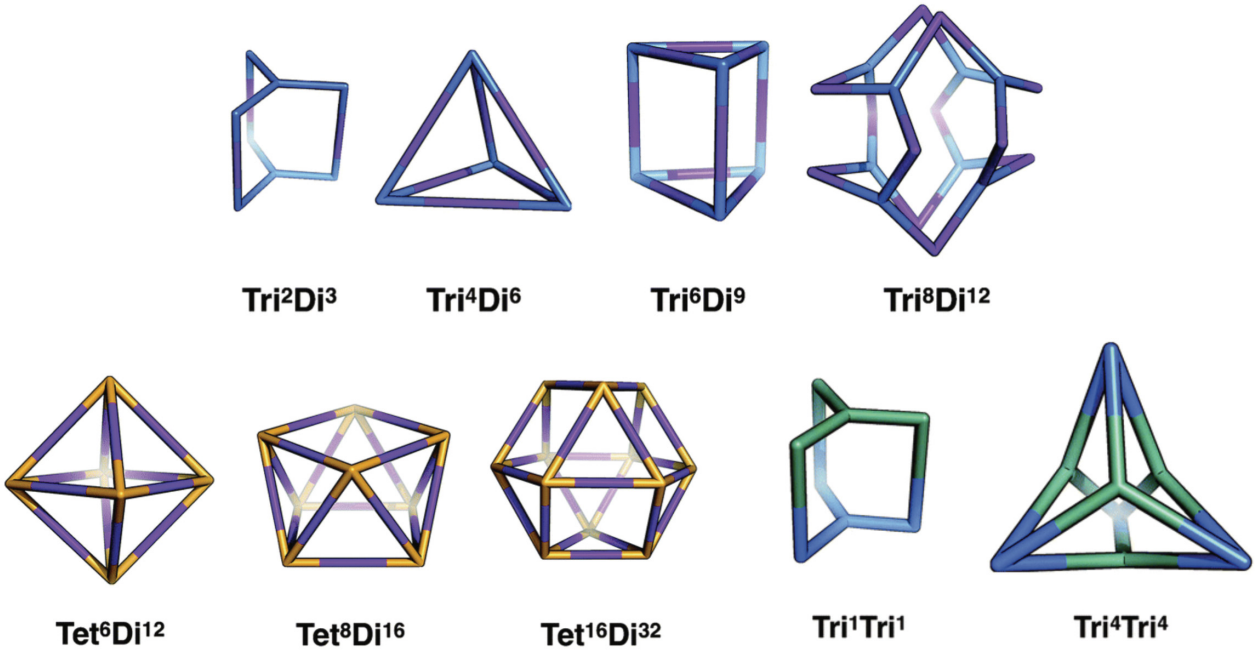

Figure 4: A selection of different cage topologies investigated by the group of Jelfs. This graphic was reproduced from Ref. [30] with permission from the Royal Society of Chemistry.[30]

Generally, there is a deviation of ≈ 10° around the perfect biting angle with which the desired geometry is still attainable. They also effortlessly introduced a nomenclature for the composition of cage molecules that will also be used throughout this manuscript.[30]

They proposed a combination of the topicality of the building blocks and their stoichiometry to enable an unequivocal identification of the cage geometry: $\mathbf{X^mY}$. **X** describes the topicality of the building block with the *most* functional groups and can be either **Di**, **Tri**, or **Tet**. The superscript **m** uses the number of building blocks **X** that are incorporated inside the described cage structure. Analogously, **Y** describes the topicality of the second building block, which can either be equal to or less than **X** (e.g. **Tri** or **Di** in the case of **X** being **Tri**), and **n** describes the number of building blocks of **Y** that are incorporated into the cage structure. As an example, the tetrahedral cage **5** would be accounted as a $\mathbf{Tri^4Tri^4}$ cage since both building blocks are tritopic and the cage is made up of four of each molecule.

1.2.3. Reversible bond types for cage synthesis

As previously discussed there is a multitude of bond types that have been employed in a successful cage synthesis (Scheme 6).

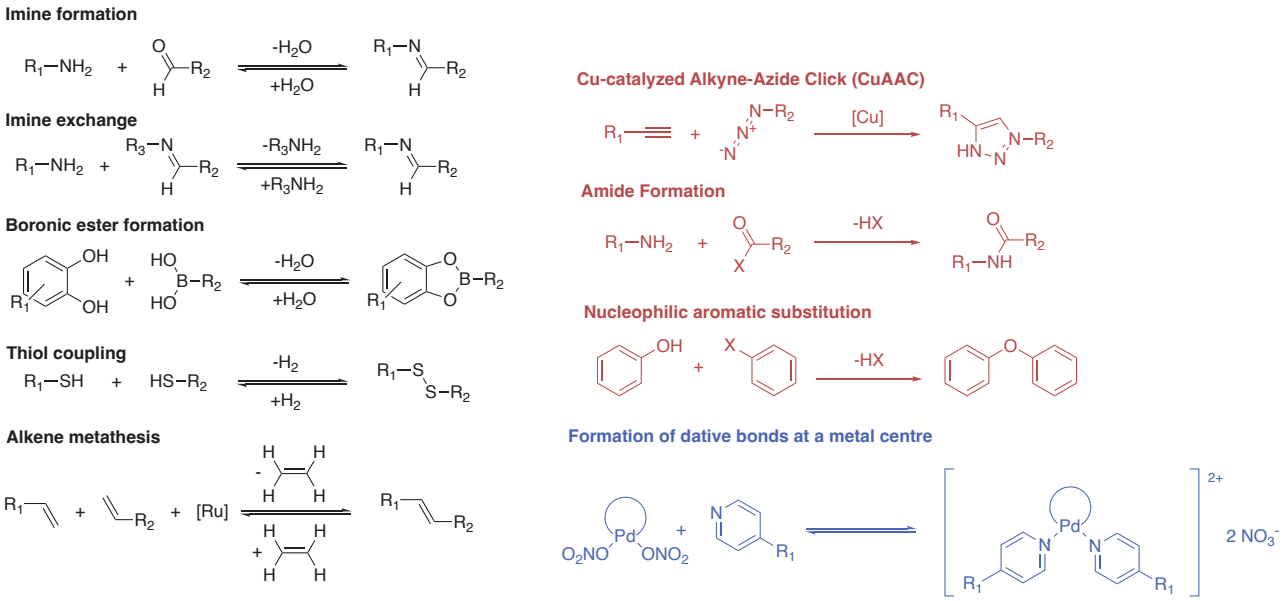

Scheme 6: Reversible (black, left), irreversible (red, right) and metal-coordinating (blue, right) bond formations used for the synthesis of organic cages.

Irreversible bond formations are subject to many limitations and disadvantages over reversible bond formations. Metal dative bonds often use expensive noble metals or the resulting cage compounds are difficult to isolate in their solid forms, thereby severely limiting the potential for a commercial material application. Hence, reversible bond formations offer the best combination of accessibility, stability, and complexity of the resulting dynamic systems. Their individual advantages and disadvantages will be discussed briefly in the following part.

Imine bond formation

The formation of an imine bond as a result of the condensation between an amine and an aldehyde is the most exploited reaction in the creation of dynamic systems and complex structures. It has been used during the synthesis of one of the first cage structures from DCvC[13,31] and is found throughout the synthesis of small, large, and complex POCs. There exist a wide variety of methods to introduce amine and aldehyde groups into a broad array of molecules, making this bond formation one of the most accessible. Furthermore, the imine group can easily be reduced to an amine group, "locking" the bond in an irreversible state. A method that has been identified by Lehn in his concept paper as highly important for the trapping of interesting structures from the dynamic library inside his systems.[20] Additionally, the imine bond is energetically very stable and therefore needs harsh conditions to be split either hetero- or homolytically. This largely applies to the absence of water, since the condensation between the amine and aldehyde can easily be reversed and the equilibrium shifted towards the starting materials. Interestingly, the group of Li has recently reported the synthesis of an imine cage from water, which cannot be degraded even when competitive amines are introduced into the aqueous

solution.[32] This only proves the wide applicability of imine-derived organic cages and makes the imine bond one of the most feasible bond types for a large area of applications.

Boronic ester bond formation

Similarly to the imine bond formation, a condensation takes place during the reaction of boronic acid and a diol to form a boronic ester bond. The participation of three functional groups in the formation of the bond, can be the foundation for interesting geometries but also introduces some limitations. Since one of the building blocks needs two hydroxy groups, the remaining sites for different functional groups are limited. Furthermore, boron possesses a very low electronegativity, making electron-deficient structures consistent of boronic ester bonds very susceptible to hydrolysis or even inaccessible.[33] Nevertheless has this bond type been used to generate impressively large and complex structures, like the large cubic **Tri^{8}Di^{12}** cage by the group of Beuerle (Scheme 7).[34]

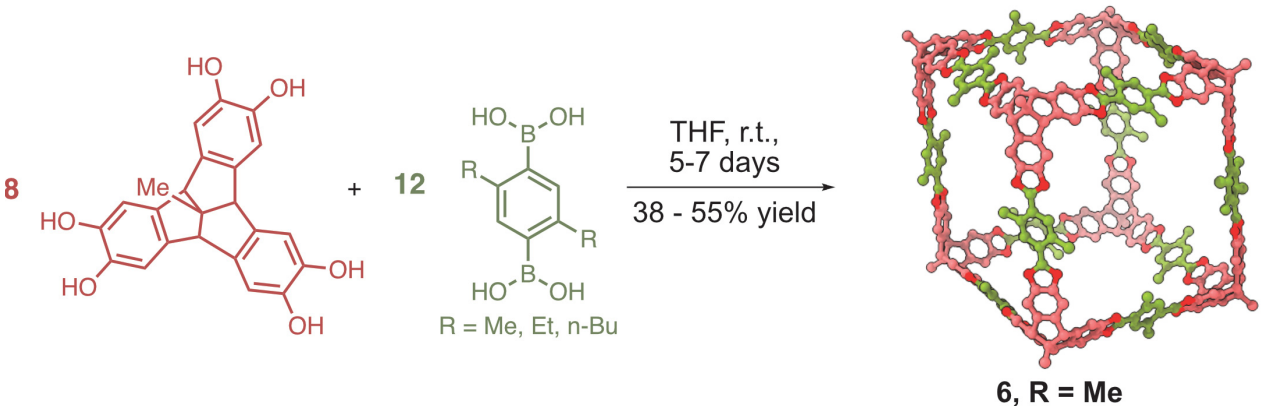

Scheme 7: Synthetic overview of a series of large cages employing boronic ester bond formation.[34]

The combination of imine bonds and boronic ester bonds has been used to overcome some of the stability issues while simultaneously employing the geometrical assembly possibilities unique to boronic esters.

Disulfide bond formation

Although disulfide formation from thiols has been extensively used in the synthesis of macrocycles and in other dynamic combinatorial library applications, the method has only rarely been used for the synthesis of cage structures. The group of Johnson could demonstrate that this approach can be used to create cages from only one kind of building blocks, since two thiols react with each other. With careful tuning of the reaction conditions, the group was able to isolate different cage geometries and macrocycles from the same building blocks.[19,35]

Alkene/Alkyne metathesis

The metathesis of terminal alkenes or alkynes is catalyzed by molybdenum or ruthenium, which has been widely used in the synthesis of macrocycles and other two-dimensional structures *via* DCvC.[36] The leap towards three-dimensional space was made possible by the aforementioned templating effect. The group of Shionoya, e.g., was able to use pyridyl units to coordinate the building blocks around Pd-centres so that terminal alkenes were in close proximity to each other. In the following metathesis step, they closed the structure, yielding a cage that can also be isolated without containing residual metal ions after thorough washing with ethylene diamine.[37] In the recent past, the group of Moore succeeded in the synthesis of a tetrahedral shaped cage by reacting four identical building blocks with each other using a precisely engineered molybdenum-catalyst (Scheme 8).[38]

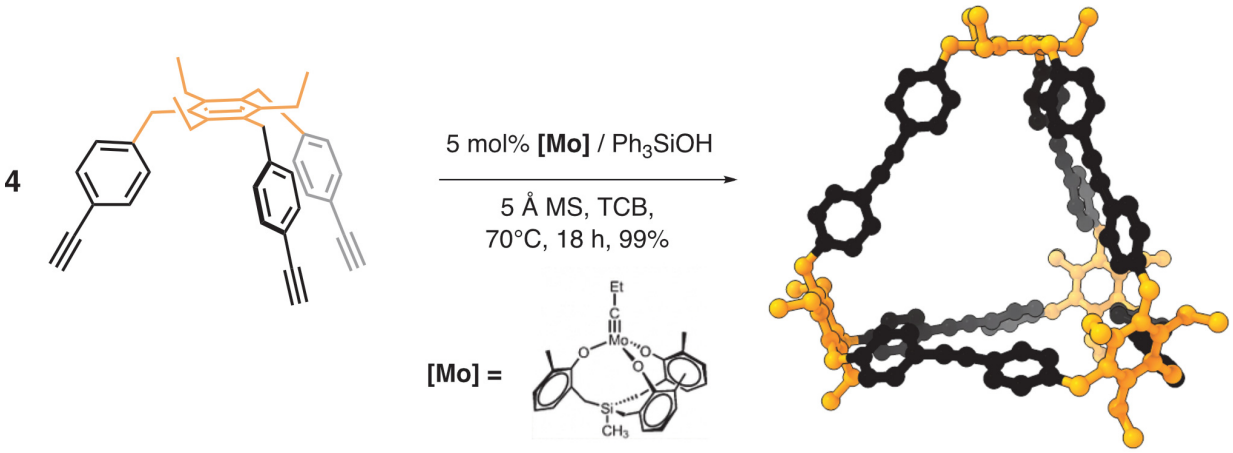

Scheme 8: Synthesis of a large tetrahedral cage from only one building block with almost quantitative yield.[38]

Although there are high-yielding examples in which alkyne metathesis was employed for the formation of POCs, this bond formation is still not very well understood in terms of its potential for the generation of three-dimensional structures.

To conclude the previous presentation of possible bond formation reactions suitable for the synthesis of novel POC structures, the most versatile and synthetically easiest method is the generation of imines. Since the major topic of this work is the synthesis and investigation of fluorinated POCs (FPOCs), it is only logical to choose a bond type that has proven to be robust in many applications, whose formation processes are well investigated and understood, and which offers the possibility to be trapped in an irreversible state *via* reduction to the corresponding amine bond. Therefore, the following parts of this work will mainly focus on imine-based POCs and other macromolecules.

1.3. From cages to materials

With the porous organic cage molecules in hand, the second important part of the supramolecular chemist's work begins: assembling them into a material. The main target for a POC-based material is to be porous. Several requirements emerge from this condition:

a) the individual POCs need to be assembled in a regular manner, most optimally as a crystalline solid
b) the cage windows inside this crystal must be connected (window-to-window packing) to create a porous network
c) the solvent used for material preparation (e.g. crystallization) must be evaporated completely
d) during the solvent evaporation, the POC's geometry and the material structure must remain intact
e) the individual POCs and the crystal lattice need to be stable towards chemical, mechanical and thermal stimuli

In framework materials like COFs and MOFs, the porosity originates from the voids that are created *during* the assembly of the material out of the individual linker molecules. Hence, a large, seemingly endless, *singular* molecular structure is created in the process. With cage-based porous materials, on the other hand, the constituent parts of the resulting material *already* contain voids inside their molecular structure. Thus, the structure of POC-containing materials consists of individual molecules that are connected through *supramolecular* bonds. For this kind of material to be porous, the individual voids must be connected into a network of pores.

1.3.1. Material assembly

By utilizing intermolecular interactions like hydrogen bonding, π-π-stacking or van-der-Waals interactions, the cage molecules can be assembled into a (semi)crystalline material. There are several ways to achieve the generation of a crystalline cage-based material inside of an organic chemistry lab. The most common methods include:

a) the evaporation of a solvent in which the corresponding cage is well soluble in (Figure 5a)
b) the combination of the starting materials inside of a solvent (mixture) in which the resulting cage molecule is only sparely soluble (b)

c) dissolving the cage in an appropriate solvent and the use of an anti-solvent in which the cage is insoluble or only sparely soluble to cause crystallization (Figure 5 c) and d))

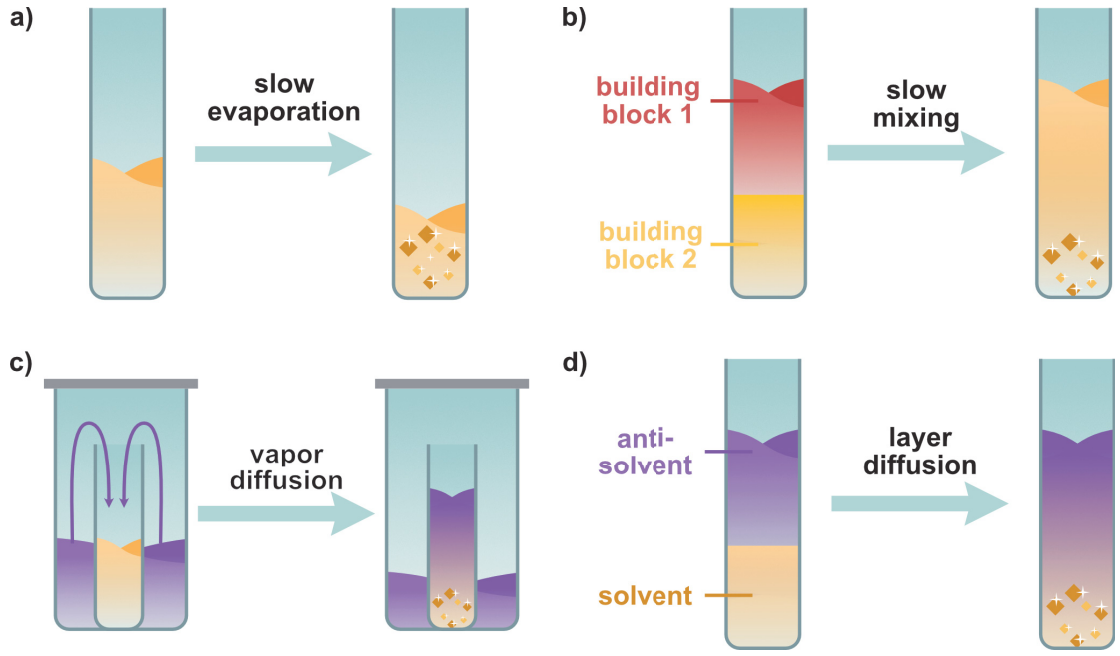

Figure 5: Methods used to generate crystalline cage-based materials; a) slow evaporation of solvent from a cage-containing solution yields crystalline material, b) the layering of solutions containing each of the starting materials above another and slow diffusion creates sparely soluble cage molecules which precipitate as a crystalline material, c) a volatile anti-solvent is evaporating inside a closed vessel, which leads to the diffusion into the cage-containing solution causing the precipitation of crystalline material from the resulting mixture, d) layering of an anti-solvent and the cage-containing solution above another results in the slow diffusion of the solvent molecules and a precipitation of crystalline material from the mixture.

The porosity of POCs, which is due to their innate containment of voids, can also be transferred to liquids since most of them are solution-processable. This leads to the generation of porous liquids in which certain gases or guests can be stored.[39] Another way of creating an ordered solid structure containing POCs is the casting on surfaces from solution.[40] The process, that is rarely encountered for framework materials, has for example, been used in the application of porous layers on the tip of a quartz crystal microbalance (QCM). The group of Waldvogel created an affinity system for the detection of aromatic molecules inside vapors.[41]

Crystallinity and Polymorphism

The generation of a crystalline material consisting of POCs is no guarantee of porosity either. Only when the individual pores of the cage molecules form a network does the material as a whole become porous.

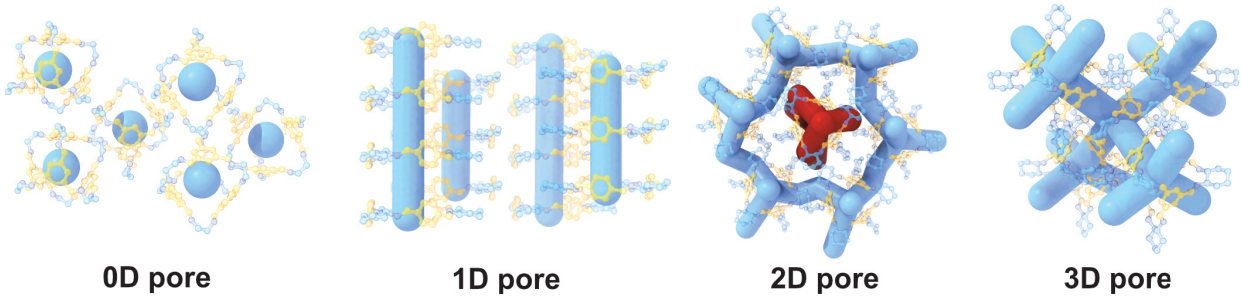

Figure 6: Distinction between porous materials with different dimensionality. This figure was reproduced with the authors permission from a previously published article.[9]

If the cages are crystallizing with a vertex facing the window of an adjacent cage molecule, no connection between the pores is established. The resulting material contains only isolated 0D pores and is therefore *not* porous (Figure 6, left).[42] When the individual void spaces of the cages are connected in a straight line, e.g. in the tubular stacking of macrocycles or in the work on tubular cages by Cooper *et al.*, the material contains one-dimensional pores.[43]

Two-dimensional pores are generated by either the thin-layer deposition of cages on a surface or by fine-tuning the crystallization conditions of a POC with three-dimensional connectivity to obtain porosity in only two dimensions.[44]

Three-dimensional pore networks are the most observed type in POC-based materials due to the pores of most cage molecules being able to geometrically connect in all three dimensions *via* open windows. The generated network of pores is in no way uniform in terms of diameter and/or structure. As a result of crystal packing, the windows are not always perfectly aligned, so the larger pores of the cage molecules are often interconnected by channels of smaller diameter. Different parameters have an influence on the overall crystal packing and can alter the dimensionality of the porous network of a cage molecule with three-dimensional connectivity.

Substituent effects on the crystal packing

In one of the field of POC materials' inaugural papers that greatly contributed to the increasing significance of POC-based materials, Cooper *et al.* investigated their **CCX** series of octahedral **Tri^{4}Di^6** imine cages that consist of six ditopic amines and four tritopic aldehydes. When they used less bulky substituents for the amines, e.g. 1,2-ethylene diamine, the crystal packing became unfavorable, resulting in a zero-dimensional material (**CC1**). Only the use of the rather bulky 1,2-*trans*-diaminocyclohexane (**DACH**) as the amine resulted in a considerably frustrated crystal packing, causing a very good alignment of the cage windows (**CC3**). This led to the generation of a three-dimensional pore network with a diameter of 5.8 Å for the cage windows and 7.2 Å for the cage itself.[45b] A follow-up investigation by the same group discovered that a minor switch in amines to the 1,2-*trans*-diaminocyclopentane resulted in a window-to-arene packing, which in turn led to the generation of one-dimensional, helical channels (Figure 7).[45a]

The cause of the porosity inside a material can be a network of intrinsic pores (inside the individual molecules) or extrinsic pores (between the molecules). By using sterically demanding substituents, it is possible to frustrate the crystal packing of a cage molecule to an extent where the extrinsic pores become utilizable. In another investigation into their **CCX** series, Cooper *et al.* used 1,2-diamino-1,2-diphenylethane as the amine for their **Tri^{4}Di^6** octahedral cage, which crystallized again in a window-to-arene packing. Due to the large extrinsic pores, generated by sterically frustrated packing, three of the cage's windows were connected to the extrinsic pores, which in turn formed a three-dimensional network.[11b]

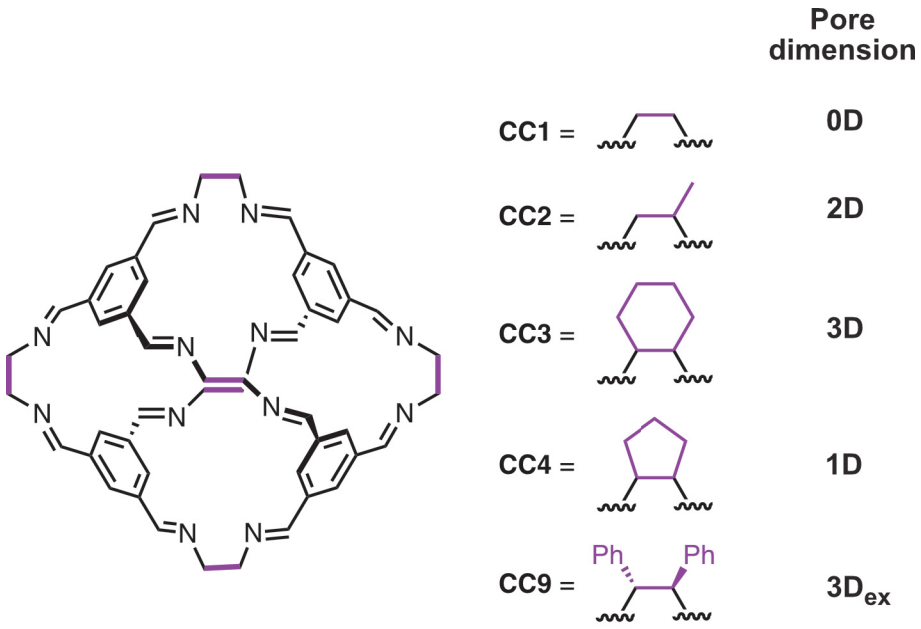

Figure 7: The series of **Tri^{4}Di^6** cages synthesized by Cooper *et al*. The different substituents on the amine cause a different packing inside the crystal lattice (see right, $3D_{ex}$ is for the connection of intrinsic with extrinsic pores).

On the other hand, if the substituents in the building blocks are too bulky, they can block the cage windows and thereby decrease the pore channel diameter. To a great extent, this could be observed in the aforementioned study of **Tri^{4}Tri^4** cages by the group of Mastalerz. Both the ethyl groups on 1,3,5,-triethyl-2,4,6-tris(aminomethyl)benzene (**Et-Amine**) and the ethyl groups on 1,3,5,-triethyl-2,4,6-triformylbenzene (**Et-Aldehyde**) were so large that they blocked all the cage windows, preventing even a nitrogen molecule from passing through. Reducing the bulkiness of the substituents at the aldehyde to a methyl group was not enough to unblock the cage's windows (**TCC2**, Figure 8). Only when they used **TFB** to create the cage **TCC3** (Figure 8) did the resulting material show porosity.[29]

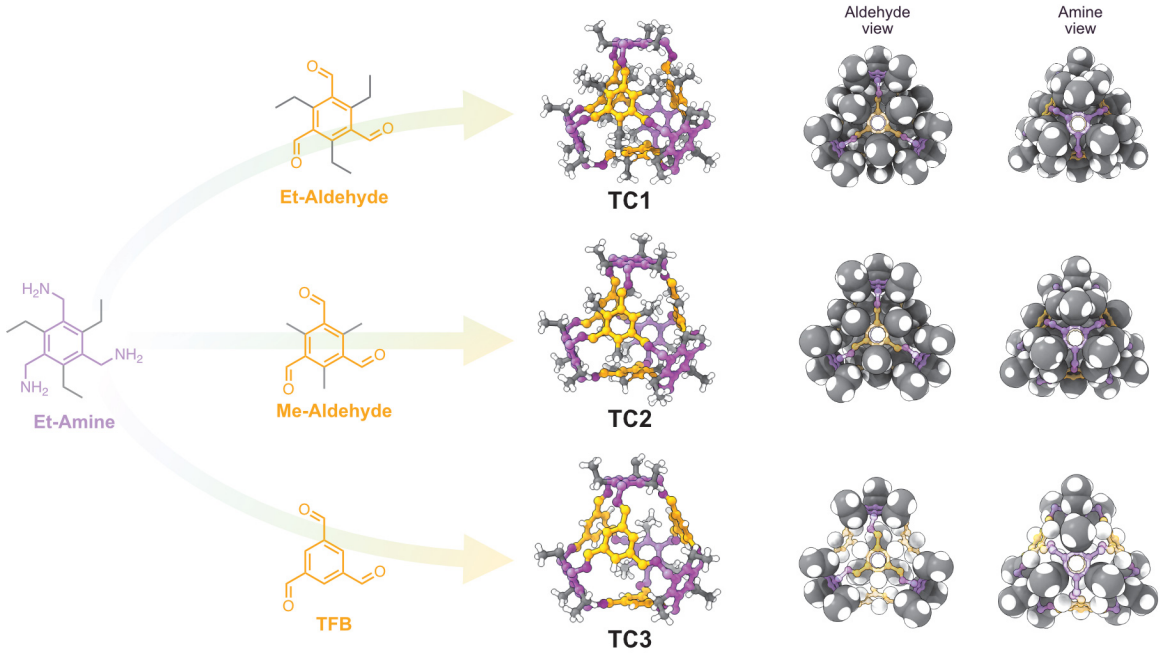

Figure 8: Synthesis of three **Tri^{4}Tri^4** cages with a tetrahedral geometry using differently substituted tritopic aldehydes. The substituents are depicted using a space-filling model, whereas the cage scaffolds are visualized as sticks for better understanding. This figure was reproduced with the author's permission from a previously published article.[9]

Solvent effects on the crystal packing

Not only are the substituents of the building blocks an important factor that influences crystal packing, but also the solvent used for the crystallization. As an example, the aforementioned **CC2** that crystallizes in a two-dimensional pore network can be crystallized as the new polymorph **CC2β** when using 1,4-dioxane as the crystallization solvent.[46] As previously described, mixtures of solvents often need to be used to facilitate crystallization of the porous material. Because the crystalline phase is solvent-dependent in some cases, either extensive solvent screening is required or a computational approach is considered. Computational studies on the formation of large molecules or materials often operate in an infinitely large vacuum, only rarely taking solvent effects into account due to the increasing complexity.[47] The group of Jelfs succeeded in the development of computational models that predict not only the structures of cages but also the most possible crystal structures. In one case, they were able to successfully predict the solvent effects on the crystal packing of a porous cage-based material.[48] Since the prediction of crystal packing for porous organic cages is still in its infancy, different solvents have to be screened and found using the principle of trial-and-error.[49]

Computational design of POC-based materials

Cooper *et al.* undertook a high-throughput synthesis of a range of cages varying in size and shape by combining Jelfs *et al.*'s cage structure prediction algorithms with the usage of a synthetic chemistry robot. They studied 78 potential cage molecules by modeling distinct di-, tri-, and tetratopic amines and aldehydes with their respective cage products. They made 31 cages in total, as expected. Two cage topologies deviated from the forecast, and the reaction products included an unusual catenated cage geometry.[50]

To summarize, computational methods are useful for discovering new cage structures and their crystal packing, but they are not yet capable of determining the effect of solvents on the formation of molecules and materials.

Another area in which a prediction can not be made reliably is the field of semicrystalline or amorphous porous cage based materials. Since porous materials that lack a certain degree of order, consist of crystalline subdomains and defects in their structure, a prediction about their porosity is difficult. The introduction of defects into a crystalline material can be beneficial, as it introduces the opportunity for the intrinsic pore network to be connected to the extrinsic network. When comparing the porosity of amorphous or semicrystalline POC-based materials with recrystallized samples, the group of Mastalerz discovered that defective, amorphous materials can in some cases exhibit increased porosity compared to the crystalline material.[51]

Ultimately the supramolecular chemist must still investigate a multitude of solvents and combinations thereof to generate a suitable crystalline material and its different polymorphic structures. The arbitrary synthesis of an amorphous or semicrystalline material can also be useful, since the introduction of defects is sometimes beneficial to a material's porosity.

1.3.2. Cage stability and solvent removal

Since the material's pores only become accessible to gases or other guests when they are empty, the solvent molecules that are trapped inside them during the crystallization and cage formation must be removed completely. This can be challenging because the cage windows must be large enough to release the trapped solvent molecules and, simultaneously, the cage should not collapse during the solvent removal. The process of solvent removal is also known as "activation" and is usually a combination of a dynamic vacuum and elevated temperatures to completely remove all solvent. Suitable activation conditions are mainly developed by analyzing the cage-based material using thermogravimetric analysis (TGA). If the material shows a minor percentual weight loss, but has a much higher onset decomposition temperature, this is a strong hint, that there is an evaporation of residual solvent happening during the first weight loss step. The temperature at which the solvent is evaporated is then usually combined with a dynamic vacuum,

to further facilitate the complete removal of solvent from the material. There are numerous cases in which the removal of the solvent resulted in the collapse of the cage structure. The cause of these collapses is the minimization in absolute energy of the cage molecules if the stabilizing interactions with the solvent molecules are removed. This is most often observed in two cases: a) if the cage structure is very large and has a resulting large pore diameter[52a] or b) if the cage is obtained in its *amine* form by reduction of the imine bonds.[52b,c] The reduction of imine to amine bonds in cages is common to increase their stability as a molecule and as a material towards hydrolysis. Unfortunately, this results in a higher conformational flexibility in the cage molecule which is then more prone to collapsing. The group of Cooper observed the same phenomenon during the reduction of their **Tri^{4}Di^6** imine cage **CC3** (Figure 9).

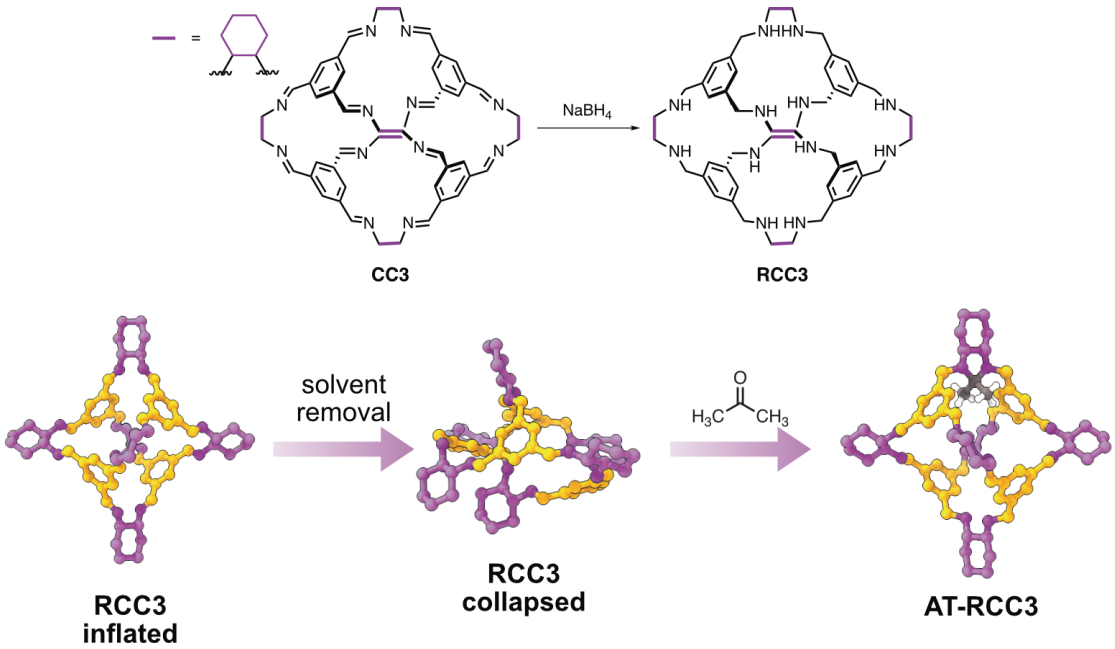

Figure 9: Reduction of **CC3** to the amine cage **RCC3** using sodium borohydride (top), crystal structures of the solvated (left) and acetone-tied cage **AT-RCC3** (right) and the calculated structure of desolvated, collapsed **RCC3** (middle, bottom). This figure was reproduced with the author's permission from a previously published article.[9]

The collapsed crystalline material did not exhibit porosity. Interestingly, when the group tried to crystallize **RCC3** from acetone, they obtained a structure in which two adjacent amines formed an aminal with an acetone molecule.[53] This "acetone-tied" cage **AT-RCC3** regained its former porosity and was also stable to acidic and alkaline hydrolysis conditions (Figure 9). Since the "tying" of two amines into an aminal inside a cage molecule is shape-dependent, alternative methods to stabilize the cage towards hydrolysis *and* collapsing are needed. Two methods were introduced by Mastalerz *et al.* when they investigated their **Tri^{4}Di^6** salicylbisimine cages (**Me-SC1** and **SC1**). Utilizing a twelvefold Pinnick oxidation on their **Me-SC1** cage, they obtained the porous amide cage **SC2**, which exhibited great stability over a broad pH range and is not directly

accessible from alternate building blocks.[54b] When reacting their **SC1** cage with phenylacetylene under Lewis-acid catalyzed conditions, they succeeded in the twelvefold Povarov cyclization, forming the quinoline cage **SC3** in a 25% yield.[54a] After activation, this cage was assembled into an amorphous material that retained great stability and porosity (Figure 10).

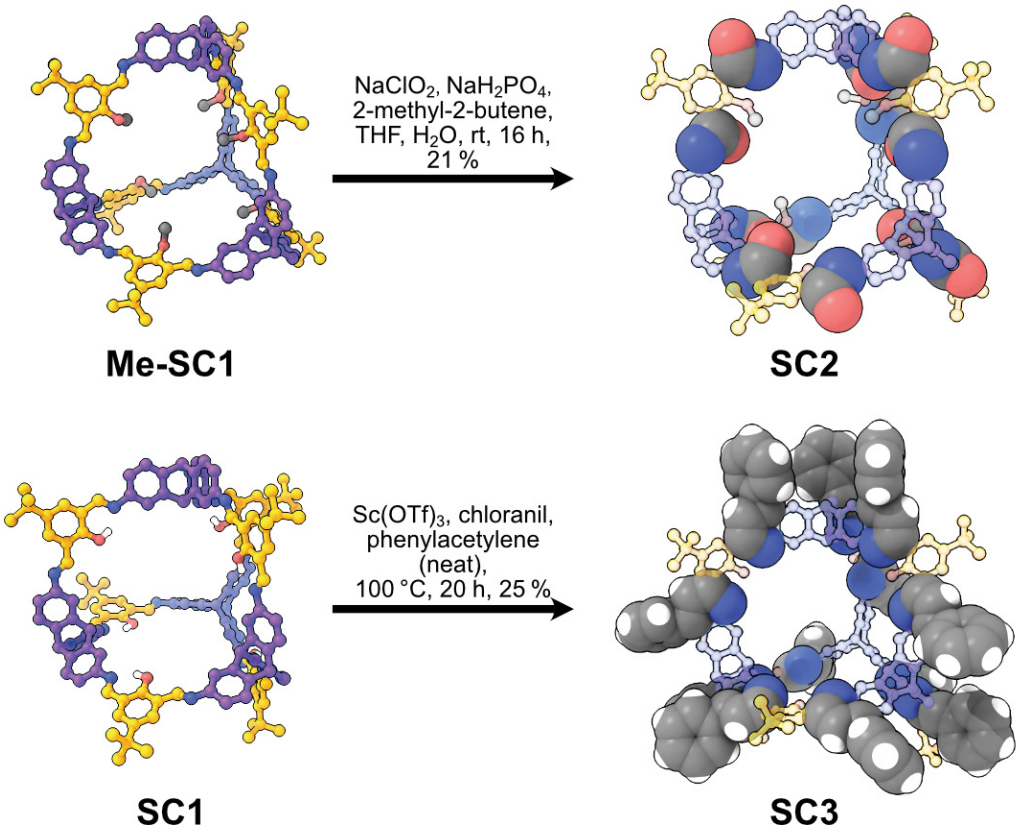

Figure 10: Twelvefold Pinnick oxidation of **Me-SC1**, yielding the porous amide cage **SC2** (top), **SC1** is reacted in a twelvefold Povarov cyclization forming the porous quinoline cage **SC3** in the process (bottom). This figure was reproduced with the author's permission from a previously published article.[9]

If the cage-based material could be activated without the collapse of the crystal structure or the individual cage molecule, it would now be finally ready to encapsulate guests or store gases. The investigation of the material's gas sorption behavior comes as the last step in a series of obstacles that needed to be overcome during the creation of a porous material, which are summarized in Figure 11. In this last part of the investigation of its properties, the porosity of the material needs to be quantified and its interaction with different gases examined.[55]

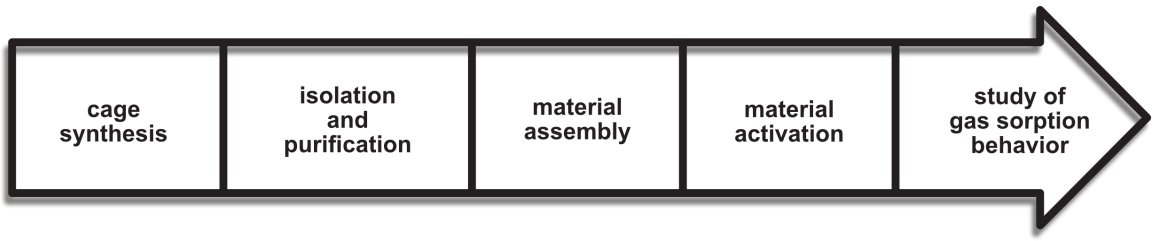

Figure 11: Summary of all steps necessary to generate a porous cage-based material.

The most common quantification method of porosity is the material's specific surface area. This quantifies the available surface area inside the material's pores. Different theoretical models for the physisorption of gas molecules on a surface exist. The most commonly used models are the Langmuir and Brunauer-Emmett-Teller (BET) sorption isotherms.[56,57] The main difference between both is the assumption of how many gas molecules are adsorbed *per* binding site. Whereas the Langmuir model assumes that only *one* molecule can be bound per adsorption site, the BET model does not limit the number of molecules per adsorption site. According to the BET model, there is a theoretical indefinite number of molecules that can be adsorbed onto the surface (Figure 12).

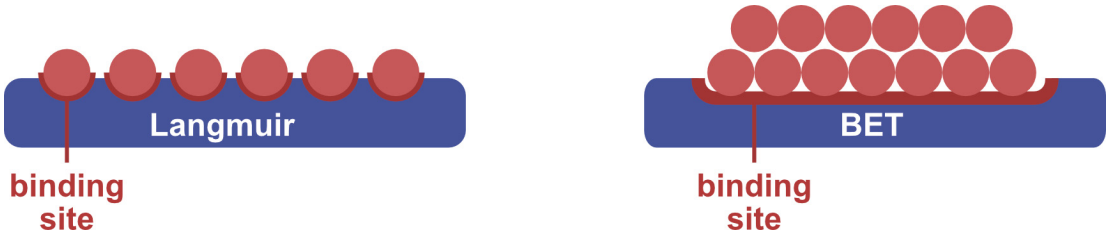

Figure 12: Langmuir's model of isothermal sorption of gas molecules onto a surface assumes a monolayer formation (left), whereas the BET theory assumes that an infinitely large number of molecules can populate each binding site (right).[56,57]

The BET model is rather an extension of the Langmuir approximation as it can easily be applied at a high concentration of the adsorbent species. This is closer to reality during the investigation of gas sorption behavior and is thus applied more often. In a typical BET surface area measurement, a dynamic vacuum is applied to the sample to ensure no binding site is occupied at the start of the measurement. Then the sample is preferably cooled down to the boiling point of the analytical gas (e.g. 77 K for nitrogen) to ensure that the gas molecules can be adsorbed on the surface *via* condensation with a sufficiently high concentration. After cooling, the analyte gas is introduced into the sample chamber in small doses with sufficient equilibration time between these steps. This is continued until saturation pressure p^0 is reached. With the total gas volume used to reach the saturation pressure, the adsorption coefficient K and the amount of gas molecules $q_{mono,max}$ used to

cover the sorbent surface with a monolayer can be derived, which yields the amount of gas adsorbed per mass of sorbent q (Equation 1).

$$q = q_{\mathrm{mono,max}} \cdot \frac{K \cdot \frac{p}{p^o}}{\left(1 - \frac{p}{p^o}\right) \cdot \left(1 + \frac{p}{p^o} \cdot (K - 1)\right)}$$

Equation 1: BET isothermal calculation of the amount of gas adsorbed per mass of sorbent (*q*), using the maximum amount of molecules needed to cover the surface in a monolayer (*qmono,max*), the adsorption coefficient (*K*), the pressure inside the sample chamber (*p*) and the saturation pressure (p^0).

Common gases that are used in the analysis of sorption behavior include N_2, H_2, CO_2 and CH_4. Depending on the field of application different gases like SF_6, SO_2 or NH_3 can also be investigated.[58] Due to the molecular shape of the analyte gases and its influence on the accessibility of the material's pores, monoatomic gases like Kr and Xe have also become commonly used analytes in gas sorption analysis. The amount of gas adsorbed per mass of sorbent is usually measured in either wt% or mmol g^{-1} and is specific to the analyte gas used. For better comparability the specific surface area SA_{BET} is used, which can be deducted from the BET measurement as well. This parameter directly describes the surface area of the pores inside the material regardless of the gas used. It is therefore used as the main parameter to compare the porosity of different materials prepared throughout the rest of this work.

1.3.3. Fluorinated materials

Two of the most important and investigated gases for adsorption are CO_2 and H_2. CO_2 is important since its rising emissions are one of the main causes of the climate change, the world is facing today. If a material was able to store large quantities of this gas, emissions could be temporarily reduced, causing a decrease in the accelerated heating of our world climate. The storage of H_2, on the other hand, is important because of the gas' potential in energy converting applications. Numerous techniques for the production of hydrogen are known, but for its storage, no well-established method has been found. There are many cases of accidents caused by explosions involving this highly flammable gas, so emerging energy technologies (e.g. fuel cells) are in dire need of a safe storage method.[59]

In the research area of MOFs and COFs, the introduction of fluorine atoms into some of the building blocks is known to have a beneficial effect not only on the thermal stability and crystallinity but also on the gas uptake of CO_2 and H_2.[60,61] The substitution of a hydrogen by a fluorine atom

does have a minute effect on the sterics but a profound effect on the electronic properties of a bond and, as a result, on the whole material.

Fluorinated MOFs

In their 2012 study, the group of Bannerjee compared the gas uptakes of CO_2 and H_2 between isostructural MOFs only differing in their number of fluorine atoms. They found that the introduction of fluorine atoms either increases the uptake of H_2 or keeps it approximately the same, but introduces greater stability. Interestingly, although the overall pore diameter is decreased by the introduction of fluorine, the uptake is kept constant or is increased. This is possibly due to the strong polarity of the C–F bonds inside the MOF structure, which can interact with the easily polarizable H_2 molecule or the already very polar CO_2 in a highly attractive fashion.[60c]

The introduction of fluorine atoms into MOFs is also accompanied by other benefits, as the group of Miljanic could report the synthesis of a fluorinated MOF (FMOF) with a high surface area of SA_{BET} = 2445 m^2 g^{-1}, which is considered extraordinarily high for FMOFs (Scheme 9). Furthermore, the material exhibited a remarkable uptake of ozone-depleting chlorofluorocarbons (CFCs) of up to 225 wt%.[60b]

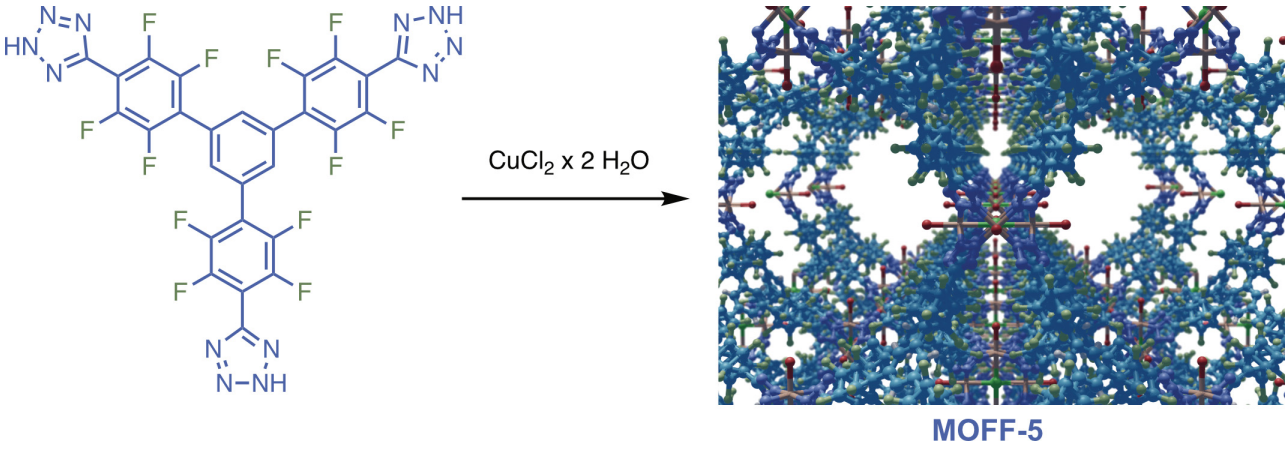

Scheme 9: Synthesis of the fluorinated MOF **MOFF-5** from a highly fluorinated building block.[60b]

Fluorinated COFs

A similar behavior was also reported for COFs. When investigating an isostructural series of COFs, the group of Wang reported that the fluorinated analogue not only had the highest CO_2-uptake of all three compounds investigated, but also exhibited an ideal adsorption solution theory (IAST) selectivity of CO_2/N_2 of 50:1.[61a] During a series of reports about partially fluorinated COFs it was discovered, that the introduction of fluorinated aromatic building blocks into the structure led to either a self-complementary stacking of fluorinated above non-fluorinated benzene rings or a favorable stacking of fluorinated benzene rings above another. This essentially locked the two-

dimensional layers of imine- or azine linked structures in place and greatly increased the porosity and crystallinity of the material (Figure 13).[61c-e]

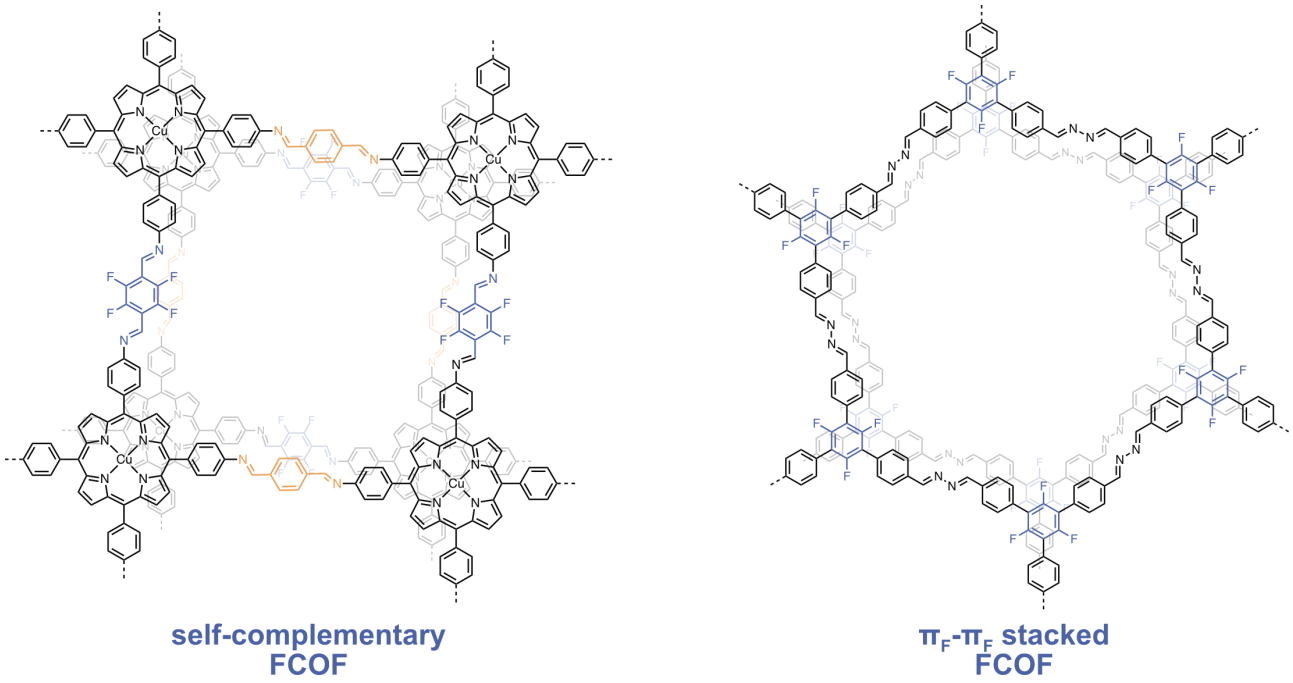

Figure 13: Fluorinated COFs exhibit higher crystallinity caused by different packing phenomena. Partially fluorinated building blocks can either stack above non-fluorinated analogues (left) or above other fluorinated aromatic rings (right).[61c-e]

A recent report of the Miljanic group identified a highly fluorinated covalent triazine framework (CTF) that exhibited a CO_2 uptake of 29 wt% at 273 K and 1 bar. That value ranks among the highest for the storage of CO_2 in a COF material ever reported.[61b]

Fluorinated porous molecular crystals

The same group could successfully transfer the benefits of fluorinated porous materials to a porous molecular crystal. This material is held together only by supramolecular interactions, marking a novelty for fluorinated porous materials. They identified a series of trigonal-shaped, linear compounds that crystallize in porous two-dimensional layers that are stacked above each other. Inside the layers, the predominant interactions are hydrogen bonds between acidic protons and nitrogen atoms of the pyrazole moieties (Figure 14). [62]This was the first example in which high porosity and thermal stability were observed in a purely organic, fluorinated material that does not contain any covalent bonds between its building blocks.

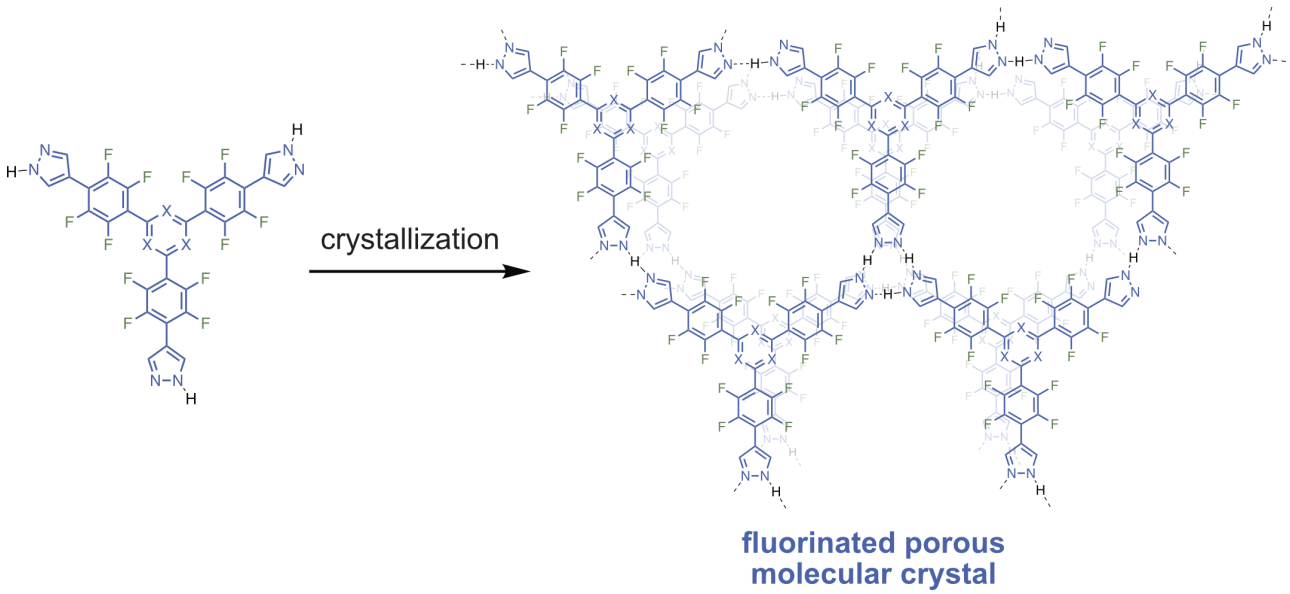

Figure 14: The fluorinated material discovered by Miljanic *et al.* employs the geometry of single molecule to create highly ordered, porous structures inside its molecular crystal.[62]

To date, there have only been a few attempts at transferring the beneficial effect of fluorine substitution on crystal packing, gas uptake, and thermal stability into the realm of POCs.

Fluorinated POCs

In the previously discussed study by Cooper *et al.*, in which they investigated the influence of the substituent's bulkiness on crystal packing, they also used (R,R)-1,2-bis(4-fluorophenyl)ethane-1,2-diamine in comparison to the non-fluorinated analogue to examine the influence of fluorine substitution. They found that the introduction did have a profound effect on the crystal packing, resulting in a loss of connection between the intrinsic pores of the cage and the extrinsic network. Compared to the non-fluorinated POCs, their fluorinated material possesses only half of the surface area of the optimal-packed hydrogenated material.[45a]

The group of Mastalerz also examined the influence of the degree of fluorination on the crystal packing of shape-persistent **Tri^{4}Di^6** boronic ester cages. By employing a triptycene motif in their diol building block, they were able to investigate how the introduction of fluorine atoms at different positions of the linear ditopic boronic acids influenced the cage forming reaction and the crystal packing inside the resulting material. When using the fluorinated analogues of the boronic acid, they were able to reduce the reaction time for the cage formation from 16 hours to 3–4 hours. This is a result of the electron-withdrawing nature of the fluorine atoms, leading to an increase in the electrophilicity of the boron center. They could obtain the single crystal structure of the non-fluorinated boron cage (**BC1**) and of the fluorinated isostructural boron cages (**BC2**, Figure 15). The main interactions inside the crystal packing of **BC2** were the π-π-interactions between neighboring triptycenes and the C–F···π contacts between the fluorine atoms and the triptycene motifs. This led to an unfavorable overall crystal packing concerning the porosity, as the gas

sorption studies revealed that **BC2** exhibited only a surface area of SA_{BET} = 60 m^2 g^{-1} (*vs.* 511 m^2 g^{-1} for **BC1**).[11a]

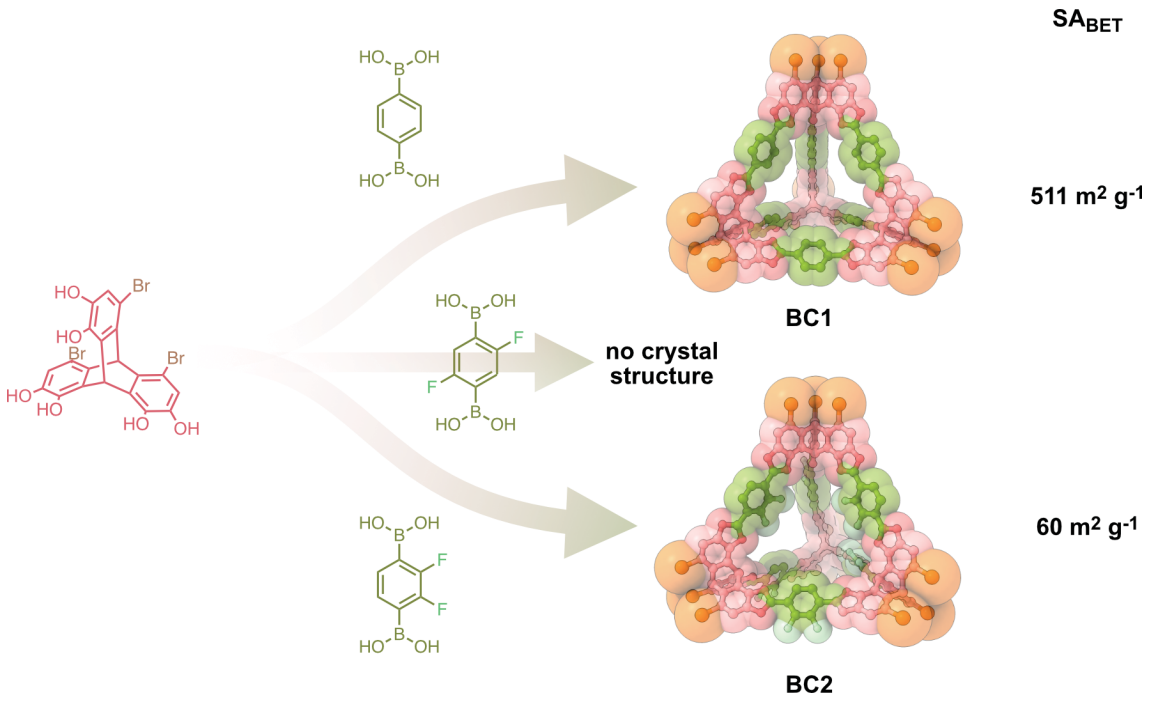

Figure 15: Crystal structure of two isostructural **Tri^{4}Di^6** boron cages and their respective apparent surface area. This figure was reproduced with the authors permission from a previously published article.[9]

These studies prove that little success has been made in the synthesis of fluorinated POCs that exhibit the same beneficial stability and gas uptake properties that their framework relatives are known for.

2. Motivation

In the preceding chapter, the main obstacles to the synthesis of porous organic cage molecules, their assembly into a porous material, and the importance of fluorinated porous materials were outlined. By using the currently available insights about the generation of POC-based materials as a foundation, this work aims to successfully transfer the benefits of fluorinated porous materials over to cage-incorporating compounds. The two previously reported studies about the influence of fluorine substitution on cage properties were only able to produce a material whose properties *suffered* from the introduction of fluorine into the compound structures.
The following strategy will be used in this work to overcome the initial setbacks encountered during the generation of porous fluorinated POCs:

i. identify and synthesize a small number of fluorinated building blocks that are encoded with a suitable geometry to ensure a beneficial cage/oligomer formation ratio
ii. generate different fluorinated small and large cage topologies using the previously prepared building blocks
iii. investigate the influence of fluorine introduction on the properties of a fluorinated POC-based material by creating a porous compound through suitable crystallization or amorphization techniques

This work will focus on the formation of fluorinated *imine* POCs. This is due to the easy access to fluorinated aldehydes by a formylation reaction of the hydrogen-containing precursors, but also to the enhanced reactivity of fluorinated aldehydes above their non-fluorine-containing derivatives. The increased reactivity allows for efficient imine formation, shifts the equilibrium further to the product side, and simultaneously reduces reaction times. Since fluorine is an electron-withdrawing substituent, it would decrease the nucleophilicity of an amine group. Therefore, the focus of the synthesis of fluorinated building blocks was mainly on the synthesis of aldehydes. Additionally, it has been shown by Mastalerz *et al.* that fluorinated boronic acids increase the electrophilicity of the boron atom to the point of increased solvolysis, creating instability in the resulting cage compound.[11a]
Five different amines were combined with seven different fluorinated aldehydes using a combinatorial approach (Figure 16). All building blocks chosen employ a bite angle that is indicative of a preferential cage formation over oligomers. Based on the distance between the aldehydes' formyl groups, the aldehydes were grouped into small (two molecules), medium (two molecules) and large (three molecules).

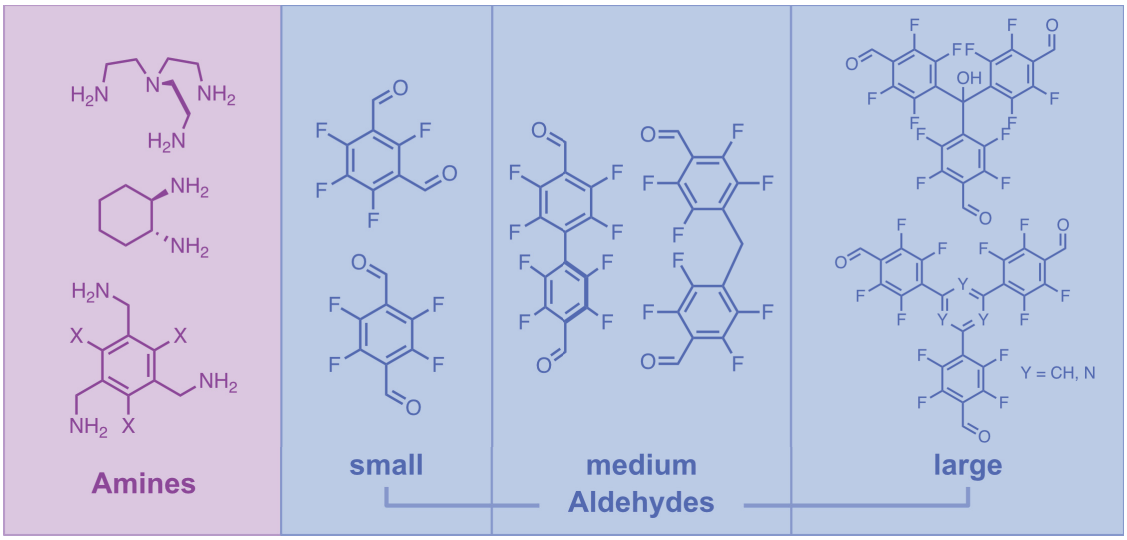

Figure 16: Schematic overview of the different building blocks synthesized in this work.

By combining the four tritopic amines (**Tri**) and one ditopic amine (**Di**) with three tritopic (**Tri**) and four ditopic (**Di**) fluorinated aldehydes, a total of 19 $\mathbf{Tri^{X}Di^{Y}}$ and 12 $\mathbf{Tri^{X}Tri^{Y}}$ cages became synthetically accessible. The resulting cages could also be classified into small, medium, and large cage compounds. Care must be taken to not draw the conclusion that small aldehydes result in the formation of small cages, though, as in a later part of this work, the generation of medium-sized cages from small aldehydes will be demonstrated. By theoretically having access to 31 different fluorinated cage molecules, this work aims to evaluate the suitability of fluorine substitution for the generation of porous cage molecules of different shapes and sizes.
This evaluation process can only be completed by either crystallizing or amorphizing the synthesized cage compounds into a material in which the individual pores are connected and form a multi-dimensional network. As a result, various preparation and crystallization techniques will be tested and discussed in the representative sections of this work, either during the cage synthesis or afterwards. The (semi)crystalline materials are investigated for their thermal stability, their crystallinity, and their gas sorption properties.
In addition to the analysis for the gas sorption properties of the POC-based materials, the possibility of guest uptake into the highly fluorinated pores of the cages in solution was to be examined.

The prepared FPOCs will not only be compared to isostructural or similarly structured non-fluorinated POCs, but the direct influence of fluoride substitution on crystal packing and thermal stability will also be investigated *via* an incremental substitution of non-fluorinated by fluorinated building blocks in a $\mathbf{Tri^{4}Di^{6}}$ cage (section 3.4). During the course of this work, the potential of the fluorine atom as a functional group for a novel post-synthetic method for the synthesis of an

irreversible, stable imine-related bond shall be investigated, to further strengthen the use of fluorinated molecules in supramolecular chemistry.

Finally, the possibility of applying the knowledge gained from FPOC syntheses and material creation to the field of other macromolecules, specifically macrocycles, will be investigated (section 3.6).

This work aims to generate a fundamental insight into the formation of fluorinated cages since the high reactivity of the fluorinated aldehydes could indicate differences from non-fluorinated analogues. It further explores the ability of fluorinated building blocks to be incorporated into porous cage structures of different topologies and sizes. The changes in properties observed when FPOCs are compared to non-fluorinated similar structured POCs will provide an answer to the question of whether FPOCs can have superior adsorption, crystallinity, and stability characteristics similar to FMOFs and FCOFs.

3. Results and Discussion

3.1. Small cages and post-synthetic functionalization

3.1.1. Introduction

As a starting point for the investigation of FPOCs, a rather simple system was targeted to understand the behavior of fluorinated building blocks during cage formation. Therefore, a **Tri^{2}Di^3** cage motif with a trigonal prismatic geometry was chosen as the first synthesis target (Scheme 10).

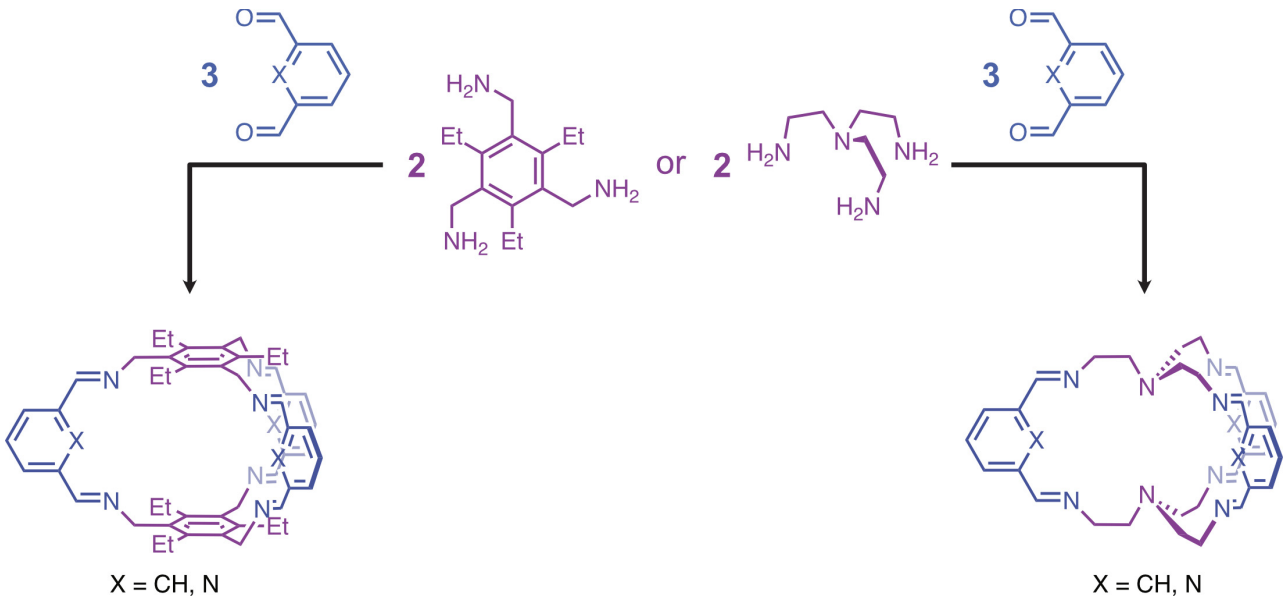

Scheme 10: Examples of **Tri^{2}Di^3** cages that have previously been studied.

Different amines have previously been employed to generate cages with a trigonal prismatic topology. By utilizing the aforementioned geometric bias, 1,3,5-tris(aminomethyl)benzenes with different substituents at the 2-, 4-, and 6-positions, in which all amine groups are oriented in the same direction, have been successfully used.[35,63,64] This is a result of the high energetic barrier regarding the rotation of the amine group around the C_1–C_{Ar} axis (Figure 17). The energetically most favorable dihedral angle between the amine bond and the aromatic plane is 90°, meaning the amine is oriented perpendicular to the aromatic ring. The high energetic barrier of 228 kcal mol^{-1} is due to a steric repulsion when the amine group is pointing directly at the adjacent ethyl substituent (at ≈ 30°). The most favorable overall conformation is therefore one in which the substituents are on the alternating sides of the aromatic plane and are "fixated" by the high rotational barrier.

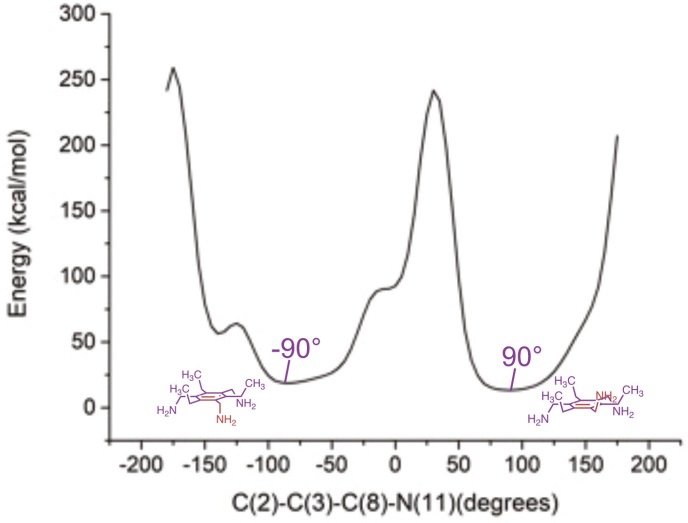

Figure 17: Energy plot of the rotation around the C_{sp2}–C_{sp3} bond of an aminomethyl substituent of 1,3,5-triethyl-2,4,6-tris(aminomethyl)benzene (MM2 calculation).

Tri^{2}Di^3 Cages that incorporate this amine have been synthesized by the groups of Cooper, Francesconi, and Mastalerz among others, and have been studied regarding their synthesis but have also been transformed into the corresponding amine cages. The resulting cages could easily be crystallized and were proven to be shape-persistent, making them an ideal target for investigation of the influence of fluorine substitution.

Another amine that has also previously been used for the generation of **Tri^{2}Di^3** cages is tris(2-aminoethyl)amine (TREN). Although there are no steric repulsions that cause a geometric orientation of all three amine groups towards the same direction, this is achieved by cooperative hydrogen bonding. A series of hydrogen bonds between the three outer amine groups are formed, which are in turn oriented towards the same side of the central nitrogen atom. This "fixation" of the amines is much weaker than for the previously discussed aromatic amine structures. As a result, the outcome of the imine condensation is difficult to control, and in combination with the rotationally more flexible bonds inside of the resulting cages, they are also less often shape-persistent.[65]

Taking previous research into account, the synthesis of novel fluorinated **Tri^{2}Di^3** cages was based on the use of 1,3,5-tris(aminomethyl)benzene as amines with different substituents in the 2-, 4-, and 6-positions and the use of small, aromatic fluorinated dialdehydes to study the formation of fluorinated organic cage molecules.

3.1.2. Synthesis

Synthesis of the building blocks

Three structurally different amines were chosen to investigate the formation of **Tri^{2}Di^3** cages (Figure 18).

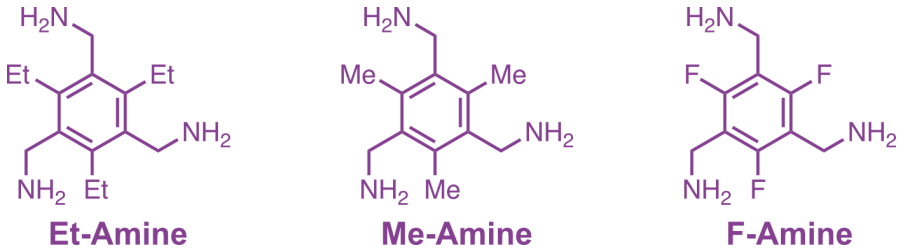

Figure 18: Amines used for the synthesis of fluorinated **Tri^{2}Di^3** cages.

Following an established literature procedure, 1,3,5-tris(aminomethyl)-2,4,6-triethylbenzene (**Et-Amine**) could be synthesized from benzene.[66] Benzene was reacted in a threefold Friedel-Crafts-alkylation with aluminum chloride and ethyl bromide to yield triethylbenzene **8**. This compound was then employed in a bromomethylation reaction using zinc bromide and paraformaldehyde in an HBr/AcOH mixture. The tris(bromomethyl)-benzene compound **9** was obtained in 75% yield. In a threefold pseudohalogen substitution, the bromine substituents were exchanged for azide groups, quantitatively yielding the triazide compound **10**. The triazide was reduced to the corresponding amine (**Et-Amine**) using a H_2 atmosphere and palladium on carbon in a 70% yield (Scheme 11).

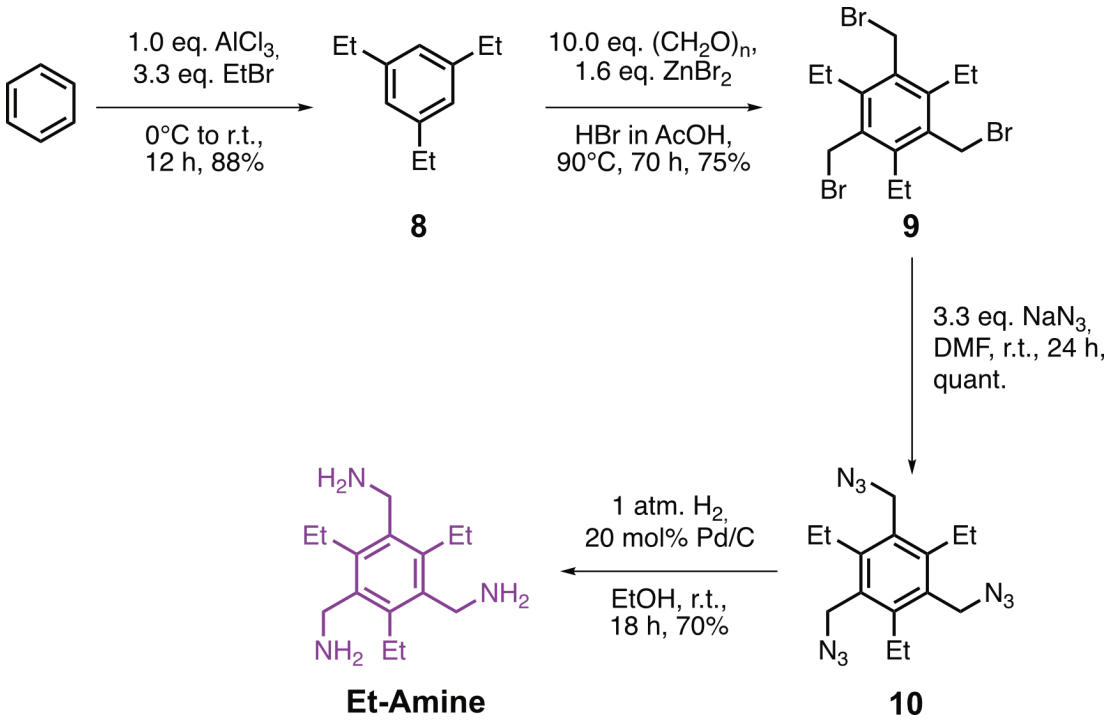

Scheme 11: Synthesis of **Et-Amine** starting from benzene.[66]

Using this four-step synthesis, the **Et-Amine** could be obtained on a multi-gram scale as a pale pink solid. To examine the influence of the substituents on the cage formation on the one hand and to prevent a blocking of the **Tri^{2}Di^3** cage's cavity by the bulky ethyl substituents on the other hand, an amine was synthesized in which the ethyl groups of **Et-Amine** were substituted by methyl groups. The synthesis of **Me-Amine** starts from mesitylene but follows the same general approach that was utilized in the synthesis of **Et-Amine**. The tris(bromomethyl) benzene compound **11** was synthesized in 95% yield using the same conditions as the synthesis of **9**. Analogously to the **Et-Amine** route, in a threefold pseudohalogen substitution, the bromo compound could be converted to triazide **12** quantitatively. The following reduction step gave a slightly lower yield of 55% for the **Me-Amine** compound (Scheme 12).

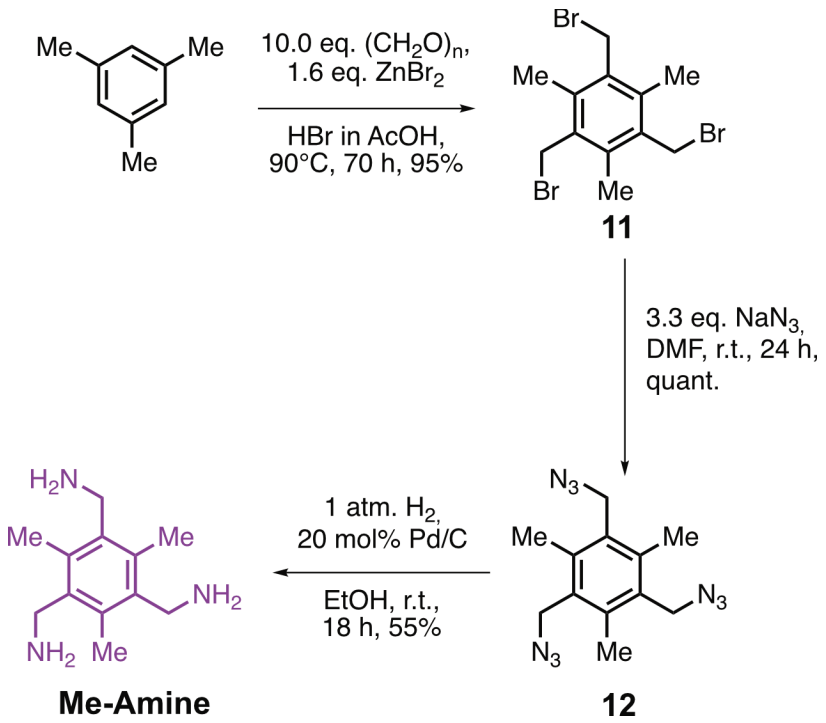

Scheme 12: Three step synthesis of the methyl-substituted aromatic amine **Me-Amine**.

The last amine in this trifecta of compounds utilizes the same structural motif but the methyl substituents have been exchanged for fluorine atoms. This amine is highly interesting for its use in the synthesis of organic cage compounds since the fluorine atoms are similar in their steric bulk to hydrogen atoms. As a result, the amine groups are able to rotate rather freely around the C_{Ar}–C_{sp3} bond. This raises the question of whether the pre-organization in this compound is enough to yield a cage compound or if other effects are influencing the cage formation. As a side effect, the

resulting cage would incorporate an even larger number of fluorine atoms, making it an interesting target for further gas or guest uptake studies.

To generate the fluorinated amine **F-Amine**, 1,3,5-trifluorobenzene was reacted in a threefold Friedel-Crafts alkylation by using aluminum chloride and chloromethyl methyl ether (MOM-Cl). This resulted in an 89% yield of the corresponding tris(chloromethyl) benzene compound **13**. Again, by substituting the chlorine atoms in a threefold pseudohalogen substitution, the triazide compound **14** was synthesized in a 75% yield. The final reduction proceeded very smoothly and gave the **F-Amine** in a high yield (Scheme 13).

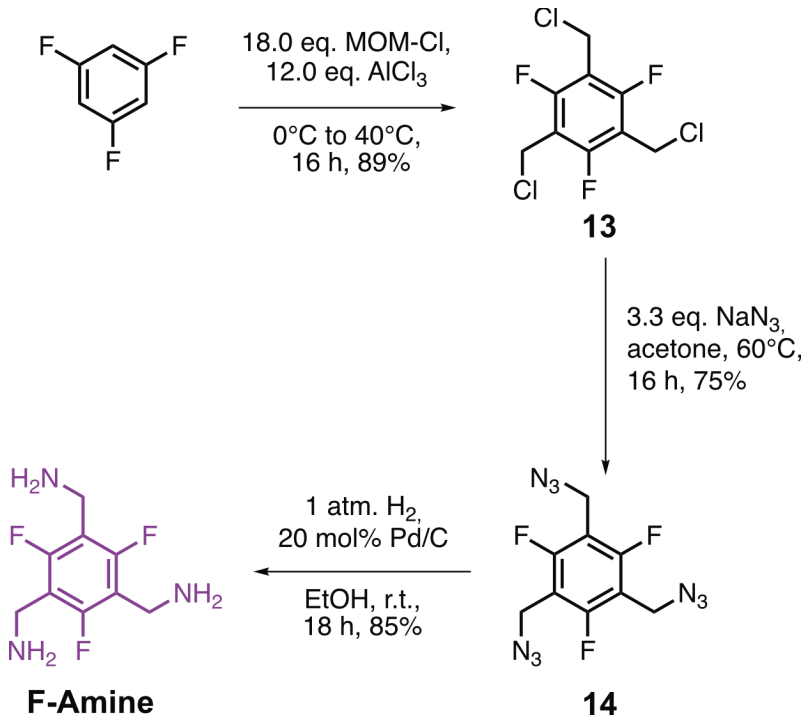

Scheme 13: Three step synthesis of the fluorinated Amine **F-Amine**.

The three different amines share the same aromatic core, but due to the different substituents, they are expected to behave differently during the imine condensation.

For the aldehydes, two tetrafluorinated benzene compounds were chosen in which only the positions of the formyl groups differed. The tetrafluoroisophthalaldehyde **15** could be synthesized *via* diisobutylaluminium hydride (DIBAL-H) mediated reduction of the corresponding dinitrile (Scheme 14), following a literature procedure.[67]

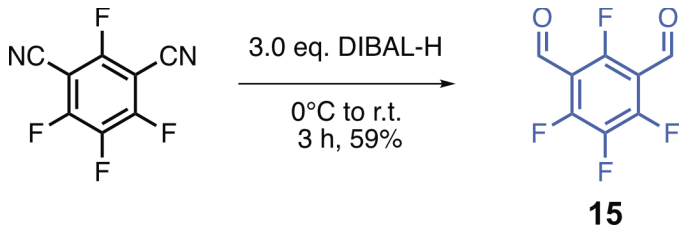

15

Scheme 14: Reduction of the dinitrile to the fluorinated dialdehyde **15**.

The corresponding *para*-substituted tetrafluoroterephthalaldehyde was commercially available.

Synthesis of fluorinated cages

With all the building blocks needed for the synthesis of the targeted **Tri^{2}Di^3** cages in hand, a screening for suitable synthesis conditions to obtain the pure cage products was conducted. All possible cage products are depicted in Figure 19.

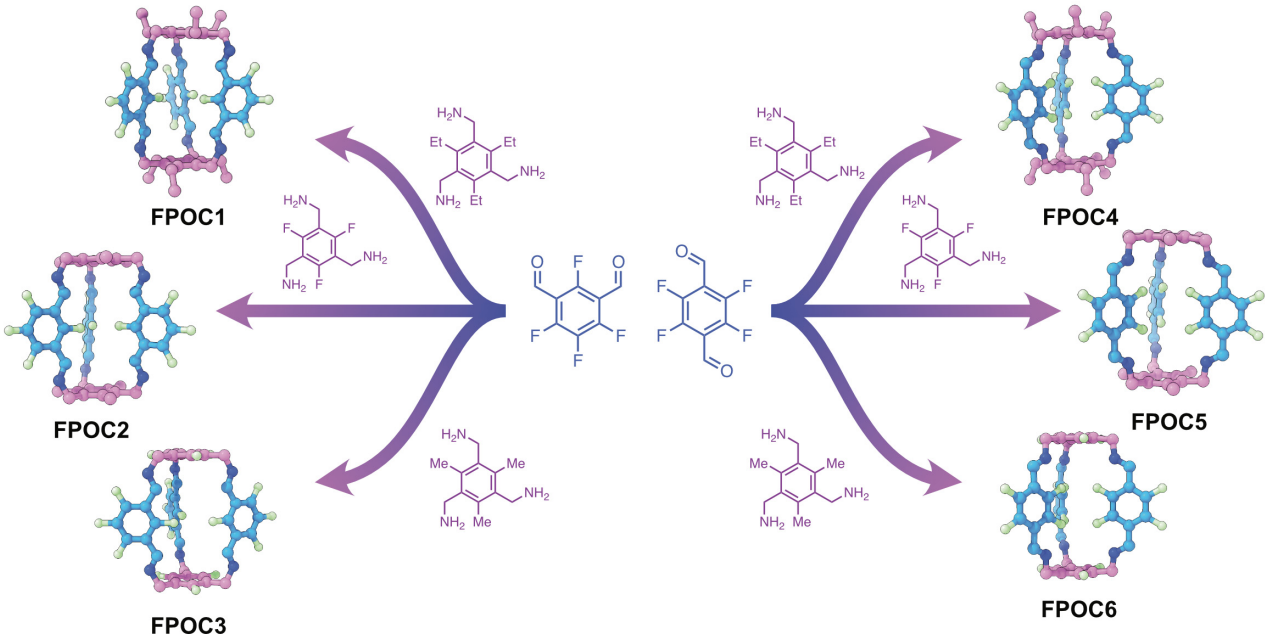

Figure 19: Universal force field-optimized (UFF) structures of all targeted **Tri^{2}Di^3** cages using fluorinated aldehydes and the three 1,3,5-tris(aminomethyl)benzene-based amines.

At first, the building blocks were stoichiometrically combined (1.0 eq. of amine and 1.5 eq. of aldehyde) in different solvents, and after three days, samples of the solution and, if a precipitate had formed, of an aliquot solution of precipitate were subjected to MALDI MS analysis. If the calculated mass of the singly charged molecular ion was found in either a solution or a precipitation sample, the solvent was considered suitable for cage formation.

Table 1: Solvents used in the solvent screening of **FPOC1**-**3**. A checkmark indicates successful cage formation, whereas a cross indicates the absence of any cage-related ion found in the MALDI MS spectra. (a - mass found in solution, b - mass found in precipitate)

solvent	FPOC1	FPOC2	FPOC3
chloroform	✓[a]	✓[a]	✗
dichloromethane	✓	✓	✗
THF	✗	✗	✗
acetone	✗	✗	✗
ethanol	✓[b]	✓[b]	✗
methanol	✓[b]	✓[b]	✓[b]
toluene	✗	✗	✗
benzene	✗	✗	✗

When using the *meta*-substituted aldehyde **15**, cage formations could be observed in chlorinated solvents like DCM and chloroform, but also in polar alcohols like methanol and ethanol (Table 1). In other investigated solvents, only signals that can be attributed to oligomeric structures could be observed in the MALDI MS. **FPOC3**, which contains the conformationally most flexible amine, did only form in methanol as a precipitate from the reaction mixture. In other solvents, only polymeric or oligomeric structures were observed. This is in good agreement with the low pre-organization exhibited by this amine and could explain that the successful formation as a precipitate is a result of the cage being a kinetic product that is removed from the reaction system.[20] Since the cages **FPOC1** and **FPOC2** did precipitate from solution and this resulted in an easy work-up and isolation of the products, methanol was chosen as the solvent for further optimization studies of these cages.

Interestingly, for **FPOC4-6,** no signal corresponding to the formation of a **Tri^{2}Di^3** cage could be observed in any solvent. In methanol and chloroform, there were clear indications that rather a **Tri^{4}Di^6** cage is formed in the reactions aiming to generate **FPOC4** and **FPOC5**, which will be discussed in Section 3.4. In the case of **FPOC6,** only signals contributing to oligomeric or polymeric species were observed.

During the solvent screening, it could be observed that after the complete addition of both building blocks to the reaction mixture, the solutions either turned pale yellow-greenish (chloroform) or became turbid (methanol) rather quickly. This indicates a fast formation of imine condensation products which can be attributed to the enhanced nucleophilicity in the formyl groups of **15** compared to non-fluorinated aldehydes. As a result, the reaction times in methanol were reduced to one day with no decrease in yields.

Cooper *et al.* reported in their high-throughput screening study that a different stoichiometric combination of the building blocks can increase the yield of the targeted cage. Therefore, the ratio of amine/aldehyde was changed to 1.0/1.2. This led to an almost quantitative yield for all three targeted **FPOC** structures.

The addition of acid in methanol led to the formation of an insoluble precipitate for all three cages and the absence of signals that could be contributed to cage species in the MALDI MS of redissolved aliquots. This can be explained by the lowering of the activation barrier towards insoluble oligomeric or polymeric structures that have lower total energy compared to the cage compounds, making these the thermodynamically favored products. Taking the results from the addition of acid into account, the precipitating cage structures **FPOC1**-**3** could be the kinetically favored products in methanol, which are eliminated from the systems' equilibrium.

The optimal synthesis conditions for the cage molecules **FPOC1**-**3** are the combination of 1.0 eq. of the amine with 1.2 eq. of the aldehyde at a concentration of 4 mmol L^{-1} (regarding the amine) in methanol for one day. This resulted in a precipitate that could be isolated from the solution, washed with fresh methanol, and then studied further.

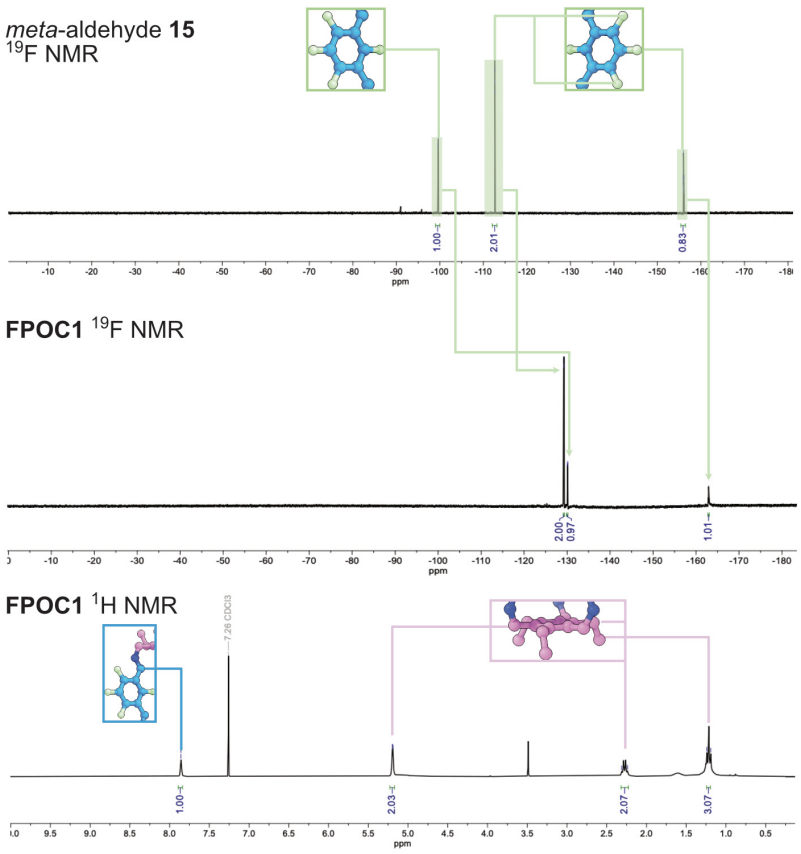

Figure 20: Stacked NMR-spectra of aldehyde **15** (top), ^{19}F NMR spectrum of **FPOC1** (middle) and ^{1}H NMR spectrum of **FPOC1** (bottom). Colored lines indicate the corresponding atom at which either the omitted hydrogens are attached or the fluorine atoms that correspond to the signals in the respective spectra.

In the ^{19}F-NMR spectra of the aldehyde and of **FPOC1,** a clear upfield shift can be observed for all fluorine atoms during the formation of the imine cage, indicating an increase in electron density (Figure 20). This effect is more pronounced for the fluorine atom that is located between the two reacting formyl groups. In the ^{1}H NMR spectrum, four signals can be assigned to the imine proton (7.9 ppm), the methylene protons adjacent to the former amine group (5.2 ppm) and the protons of the ethyl substituents (2.3 and 1.3 ppm) respectively. Compared to the ^{1}H NMR of **Et-Amine**, a clear downfield shift can be observed in the spectrum of **FPOC1** for all proton signals. This is most pronounced for the methylene protons adjacent to the amine group. In addition to the results of the ^{19}F NMR, this clearly indicates a transfer of electron density from the amine groups to the π-system of the fluorinated aromatic rings. The investigation of **FPOC2** and **FPOC3** *via* NMR analysis gave similar results.

3.1.3. Solid-state properties of small fluorinated cages

Crystal packing

After slow evaporation of a chloroform solution of **FPOC1**, crystals suitable for single-crystal X-ray diffraction analysis (SC–XRD) could be obtained. **FPOC1** crystallizes in the monoclinic space group *P2/n* and exhibits a highly ordered trigonal prismatic structure (Figure 21).

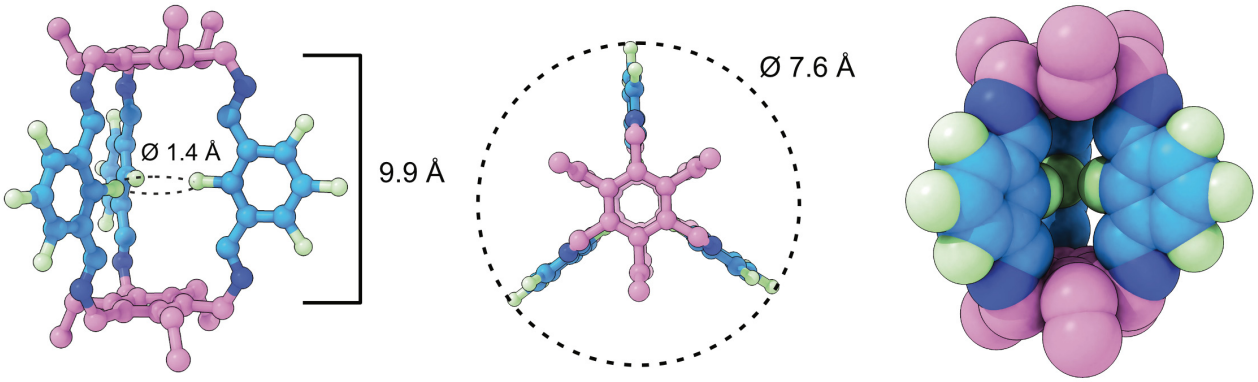

Figure 21: Crystal structure of **FPOC1** in side view (left), top view (middle) and depicted as space-filling model (right). R_1 = 0.05, wR_2 = 0.13 (crystal structure was obtained and refined by Dr. Bernd M. Schmidt).

The height of the prism is with ~10 Å comparable to other **Tri^{2}Di^3** cages that employ the same aldehyde connectivity.[35,63,64] The outer diameter of the cage is 7.6 when measured through the three outermost fluorine atoms, which is significantly larger than the outer diameter of cages that only incorporate hydrogenated aldehydes.These results are in good agreement with the DOSY NMR measurements (see Section 5.2). For **FPOC2**, a diffusion coefficient of D = 7.7 x 10^{-10} m^2 s^{-1} is measured, which, using the Stokes-Einstein equation, can be converted to a solvodynamic

radius of $r_S \approx 4.99$ Å.[68] The diameter of the inner pore between the three inward-pointing fluorine atoms is only 1.4 Å and therefore too small to generate an intrinsic pore.

During crystallization, three solvent molecules per unit cell are incorporated into the structure, essentially directing the crystal packing since no direct interaction between neighboring cage molecules can be observed (Figure 22). This results in a large two-dimensional extrinsic pore network, that is filled with chloroform molecules.

All attempts to crystallize **FPOC2** and **FPOC3** resulted in either the formation of an insoluble precipitate or the formation of a polymer-like foil.

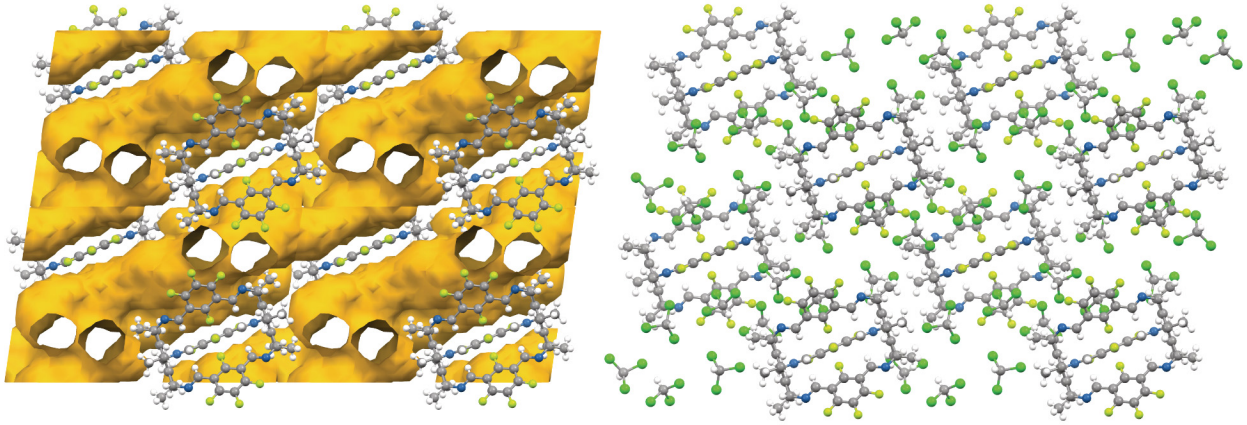

Figure 22: Crystal packing of **FPOC1** with the solvent molecules omitted (left) to showcase the large extrinsic pore network and the solvated crystal packing (right, (crystal structure was obtained and refined by Dr. Bernd M. Schmidt).

Thermal stability

To investigate the stability of the small fluorinated cages towards elevated temperatures, samples of all **Tri^{2}Di^3** cages were analyzed by thermogravimetric analysis (TGA). When comparing the different onset decomposition temperatures, all three cages decompose in the same temperature range between 330 and 350 °C. If comparing this to the acetone-tied **Tri^{4}Di^6** cage by Cooper *et al.*, which is similar in size but does not contain reversible imine bonds and is additionally stabilized by a rigid aminal between two of its amine groups (**AT-RCC3**), it becomes apparent that the fluorinated cages exhibit extraordinary thermal stability (Table 2).[53]

Table 2: Overview about onset decomposition temperatures of the small fluorinated **Tri^{2}Di^3** cages and the acetone-tied **Tri^{4}Di^6** cage **AT-RCC3**.

Sample name	Onset decomposition temperature (°C)
FPOC1	322
FPOC2	347
FPOC3	337
AT-RCC3	300

Gas sorption properties

Since the prepared materials exhibit high thermal stability, it was attempted to evaporate the volatile chloroform molecules from the crystal structure to obtain the previously discussed large extrinsic pore network. Although no crystal structure for **FPOC2** and **FPOC3** could be obtained, it was assumed that, due to the structurally closely related amines used, the other cages would possess a similar structure.

All attempts at evaporating the solvent from the materials completely led to the collapse of the extrinsic pores, indicated by the very low specific surface areas when using N_2 (Table 3).

Table 3: Apparent surface areas according to the BET-model measured using nitrogen as sorption gas.

Sample name	SA_{BET} (m^2g^{-1})
FPOC1	4
FPOC2	11
FPOC3	4

If the extrinsic pore network collapses, only the intrinsic pores remain, which are not porous to N_2 sorption (kinetic diameter of N_2 = 3.6) and are not connected to other pores.

During the analysis of the solid-state properties of the small, fluorinated cages, the obtained crystal structure of **FPOC1**, albeit not possessing an intrinsic pore, exhibited the potential to form an extrinsic pore network after successful activation. All three fluorinated cages possess extraordinarily high thermal stabilities; this even exceeds an amine cage that was additionally tied with a rigid bond to increase its stability (**AT-RCC3**). Following the extensive incorporation of solvent during the crystallization, which even dictated the crystal packing of the material, it was not possible to activate the material without a collapse of the extrinsic pore network, resulting in a complete loss of porosity.

In addition to the insights gained regarding the role of fluorine substitution on the solid-state properties of small **Tri^2Di^3** cages, the potential of fluorine substitution in solution-based applications of the cages was investigated.

3.1.4. Properties of small fluorinated cages in solution

To explore the space of solution-based supramolecular chemistry using **FPOC1-3,** the initial obstacle of their relatively low solubility in common organic solvents must be overcome. A well-known method to improve solubility is to reduce the imine cages to their corresponding amine compounds.[69]

By using an excess of sodium borohydride in methanol, all three **FPOC1-3** cages could be converted to the corresponding **RFPOC1-3** amine cages (Scheme 15). The resulting amine cages indeed exhibited increased solubility, making the recording of ^{13}C NMR spectra possible.

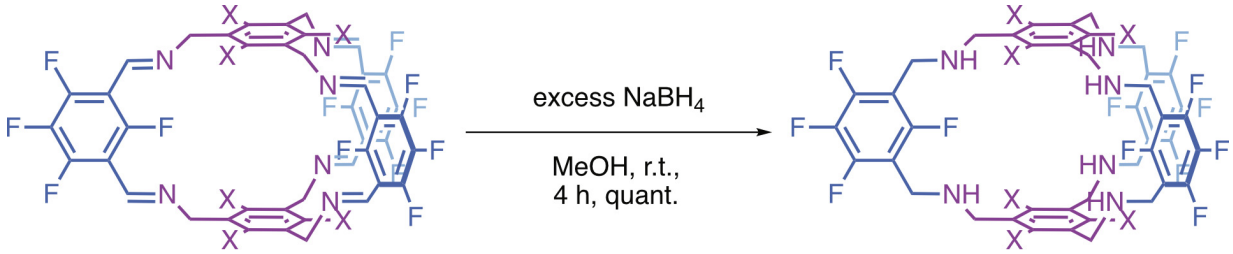

FPOC1, X = Et
FPOC2, X = Me
FPOC3, X = F

RFPOC1, X = Et
RFPOC2, X = Me
RFPOC3, X = F

Scheme 15: Reduction of the imine cages to the corresponding amine cages.

Using similarly structured cages, the group of Roelens was able to distinguish different glycolic molecules by the formation of host-guest complexes, in which their hexaaza compound acted as the host. The group of Felix could obtain crystal structures of their **Tri^{2}Di^3** amine cages from acidic solutions in which the cages acted as hosts for tetrahedral anions.[63] Investigating whether the amine cages **RFPOC1-3** could be used in a similar manner, the cages were dissolved in diluted acids, since Felix *et al*. pointed out that the complete protonation of their hexaaza compounds could already be achieved at a pH < 5.

Surprisingly, the cages **RFPOC1** and **RFPOC2** exhibited strong fluorescence upon dissolving in the diluted acids. Both amine cages exhibit a yellowish fluorescence when added to dilute aqueous hydrochloric acid, whereas the dissolving in diluted aqueous hydrobromic acid leads to a greenish fluorescence that appear to be lower in intensity when observed with the naked eye (Figure 23). To validate whether this effect is attributed to the protonated cage or the binding of anions, the amine cages were dissolved in diluted acetic acid, which did not exhibit fluorescence, and organic salts NBu_4Cl and NBu_4Br were added, keeping the concentration of protons roughly constant. The same fluorescence is exhibited as compared to the direct dissolving in the corresponding acids. Interestingly, when adding fluoride ions to an acidic solution of **FPOC1** or **FPOC2** containing Cl^- or

Br^- ions, the fluorescence is quenched. These phenomena could be explained by strong $\pi_F\cdots$anion interactions that result in either an aggregation induced emission (AIE) caused by the stacking of fluorinated aromatic rings of *adjacent* cage molecules under high concentrations (20 mmol L^{-1}) or by the interaction of one anion with two fluorinated aromatic rings of the *same* cage molecule, forming a charge-transfer complex in both scenarios.[70] When using fluoride ions, no fluorescence is observed. This could be explained by the anion binding so strongly that all other ions are exchanged. The smaller size of the F^- ion compared to Cl^- and Br^- could prevent aggregation or its high electronegativity prevents the formation of charge transfer interactions with the fluorinated aromatic structures.

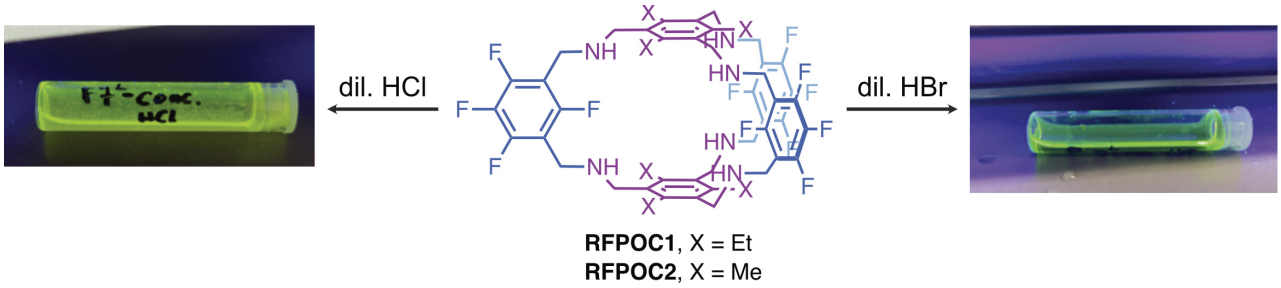

Figure 23: Pictures taken during the irradiation with UV light after dissolving samples of the amine cages **RFPOC1 and RFPOC2** in dilute acids.

To test the binding hypotheses, **RFPOC1** was dissolved in acetic acid (which exhibits no fluorescence) and one or ten equivalents of Cl^- ions were added by the addition of NBu_4Cl. The resulting mixtures were then subjected to ^{19}F NMR analysis using an internal standard. In Figure 24, a clear downfield shift after the addition of 10 equivalents of NBu_4Cl can be observed. This shift is most pronounced for the inward-pointing fluorine atoms (0.77 ppm). The signal shift at this atom can already be seen after the addition of one equivalent of chloride ions, indicating that no AIE is the cause of the fluorescence but rather a specific binding phenomenon between the ions and the individual cages.

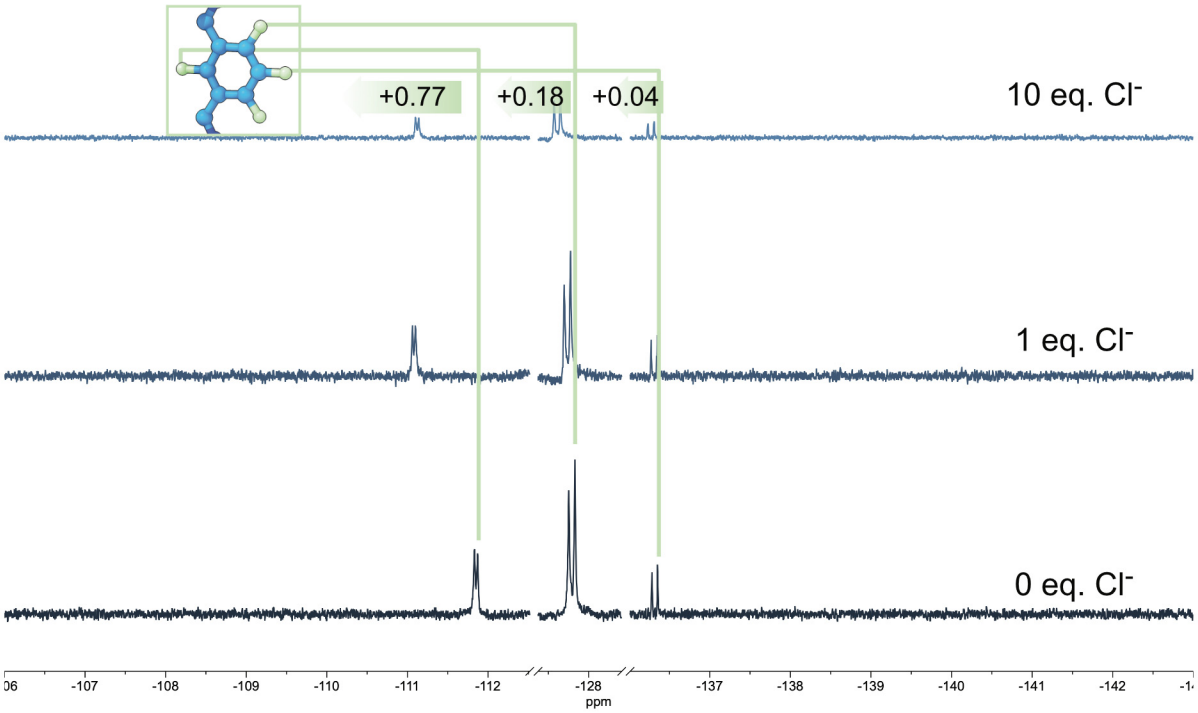

Figure 24: Stacked ^{19}F NMR spectra of **RFPOC1** in diluted acetic acid with different equivalents of NBu_4Cl added. The shifts depicted in the top spectrum are given in ppm. The colored lines indicate which fluorine atom can be attributed to which signal. Hexafluorobezene was used as an internal standard to assure the comparability of the obtained spectra.

A similar observation was made by Haley *et al*. in 2012 when they investigated a series of 2,6-bis(2-anilinoethynyl)pyridine scaffolds.[71] When a pentafluoropyridine substituent was used, one equivalent of chloride ions was enough to "turn on" an intense fluorescent state *via* extensive H-bonding, which "fixed" the chloride ion in place for charge transfer interactions. Since this phenomenon was only observed for the amine cage **RFPOC1**, a combination of H-bonding and charge transfer complexes seems plausible. Unfortunately, in the ^{1}H NMR spectra, only complex sets of signals were observed, which could not be certainly assigned to specific protons. These findings indicate that the small fluorinated **Tri^{2}Di^{3}** cages indeed possess the potential to be used in solvent-based sensing applications since they exhibit strong fluorescence and the initial titration experiments hint at a charge transfer complex formation that could be supported by hydrogen bonding. Further fluorescence measurements and titration experiments are necessary to confirm the exact nature of the binding. Further exploration of this method's scope could reveal insights about the role of fluorine substitution on anion sensing in solutions.

3.1.5. Post-synthetic functionalization

Reversible nucleophilic aromatic substitution

As the small, fluorinated **Tri^{2}Di^3** cages mark an entry point into the world of fluorinated imine cages, a possibility to further exploit the fluorine atoms as a unique functional group was investigated. In 2018, Swager and Ong demonstrated an interesting new dynamic covalent bond formation by showing that the nucleophilic aromatic substitution of highly fluorinated aromatics with thiols is a reversible process.[72] The imine cages **FPOC1-3** and the amine cages **RFPOC1-3** feature highly fluorinated aromatic panels that could be subjected to post-synthetic functionalization by nucleophilic aromatic substitution. Successful post-synthetic modifications to the abundantly present fluorine atoms could greatly increase the impact the fluorinated cage structure could have on the field of supramolecular chemistry, as this would create a durable platform for the exploration of novel structures.

When applying the considerably harsh conditions (alkaline, high temperatures, nucleophiles) used by Swager to the imine cages **FPOC1-3**, they readily decomposed (Scheme 16). A more robust, irreversible bond was needed. Therefore, the amine cages **RFPOC1-3** were investigated.

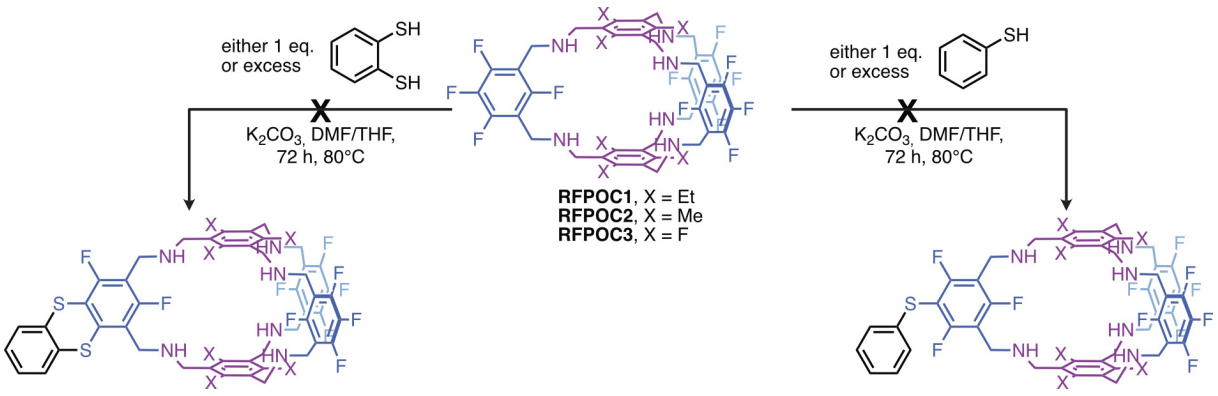

Scheme 16: Reactions of the amine cages with thiophenol (right) and benzene-1,2-dithiol (left). Both reactions failed to form the desired product.

Surprisingly, neither the reaction with thiophenol nor with benzene-1,2-dithiol resulted in the formation of a product, and only the starting materials could be recovered. Increasing the stoichiometry of the thiols from equimolar amounts to a twenty-fold excess had no effect on the reactions' outcome. The explanation for the failed reactions is very likely to be found in the electronic nature of the fluorinated aromatic rings inside the amine cages.

For the nucleophilic aromatic substitution to proceed smoothly and without the use of a catalyst, the aromatic ring must contain not only multiple fluorine substituents, but also electron-withdrawing substituents, such as nitro or nitrile groups.[73]

As previously discussed during the formation of **FPOC1** (see Section 3.1.2), the imine formation increases the electron density at the fluorinated benzene ring. The electron density is then further increased by the reduction of the imine to amine bonds. This is supported by the large upfield shift of all signals in the ^{19}F NMR when comparing the imine and amine cages (see Section 6.1). An upfield shift of the fluorine substituents' signals is a result of less electron density being localized at the fluorine core. This electron density can only be found in the delocalized electronic structure that is the aromatic ring.
Under the conditions that were reported by Swager and Ong and which are necessary to ensure reversibility in the bond formation, the imine cages were not stable enough and the amine cages proved to be simply not reactive enough.

Cyclization functionalizations

To harness the potential of the fluorine atoms as a functional group that is suitable for post-synthetic functionalization, a method that could utilize less activated electron-deficient arenes in a nucleophilic aromatic substitution was needed. In a 2010 study, Ohno *et al*. were able to employ monofluorinated arenes in a nucleophilic aromatic substitution, forming a six-membered ring in the process.[74] They reacted tetrahydropyrimidine-containing halogenated arenes with either carbon sulfide, isocyanates or isothiocyanates, forming a six-membered ring in high yields (Scheme 17).

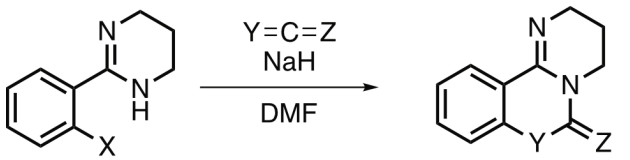

X = Br or F Y, Z = NR, S or O

Scheme 17: Reaction of halogenated arenes with carbon sulfide (Y = Z = S), isocyanates (Y = NR, Z = O) or isothiocyanates (Y = NR, Z = S) to form a new six-membered ring.[74]

During their studies, they found that the fluorinated derivatives outperformed the brominated derivatives in terms of reaction times and yields. When reacting with isocyanates or isothiocyanates, the newly introduced nitrogen atom bearing a substituent could either be located at the Y- or Z-position. This seemed to be directed by the bulkiness of the substituent. For smaller substituents, the nitrogen atom was always located at the Y-position, whereas the use of *tert*-butyl isothiocyanate led to the location of the nitrogen at the Z-position (Scheme 18).

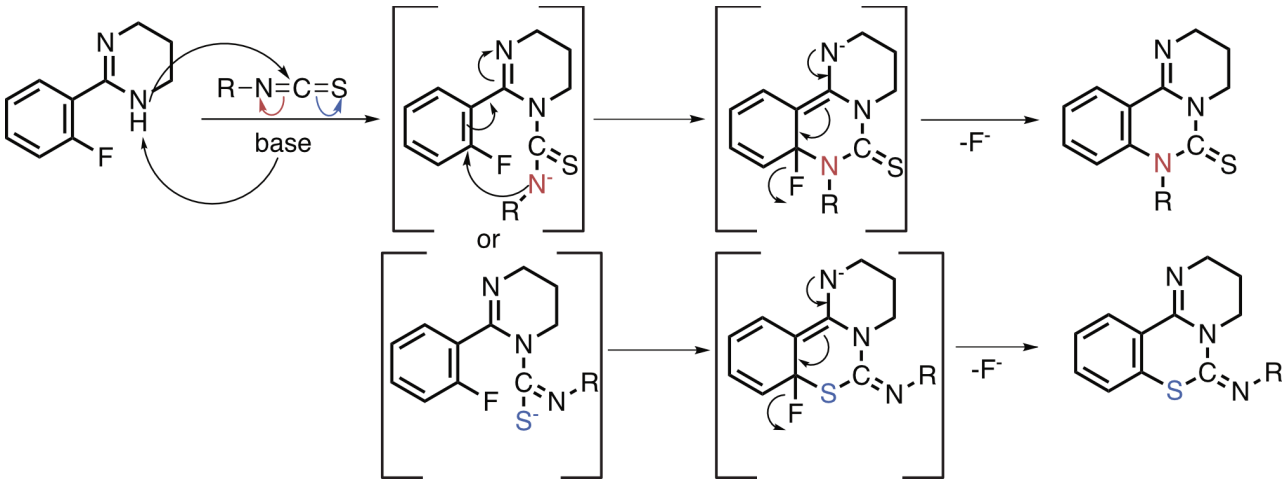

Scheme 18: Mechanism postulated by Ohno *et al*. for the nucleophilic aromatic substitution of non-activated arenes.[74]

The main driving force that made the nucleophilic aromatic substitution of even non-activated arenes possible was the cooperative effect of the tetrahydropyrimidine moiety during the reaction. The *–M* effect of the heterocycle could greatly enhance the reactivity and the formation of considerably stable intermediates.

Although no substituent that exhibits a *–M* effect is present in the amine cages **RFPOC1**-**3**, the greater number of electron-withdrawing substituents could be enough to facilitate a nucleophilic aromatic substitution.

Before testing the conditions used by Ohno *et al.* on the cage molecules, a suitable model compound was investigated (Scheme 19). The benzylamine-containing compound **18** was synthesized in three steps from 1,3,5-trifluorobenzene and could successfully be reacted with phenyl isothiocyanate to form the thiourea compound **19**.

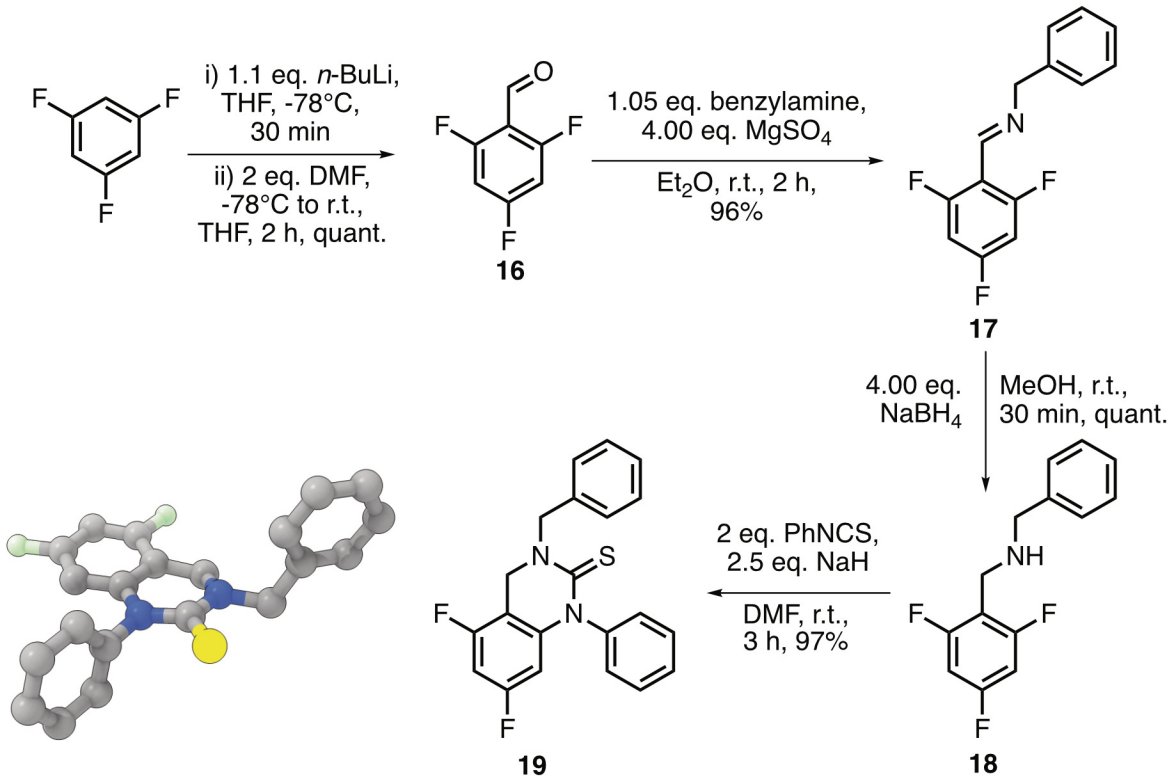

Scheme 19: Synthesis of model compound **18** and successful nucleophilic aromatic substitution to generate the thiourea compound **19**. Crystal structure of **19** (bottom left) confirming the thiourea motif in the compound (hydrogens omitted for clarity), space group *Pbca,* (crystal structure was obtained and refined by Dr. Bernd M. Schmidt).

Through the slow diffusion of cyclohexane into a chloroform solution of **19**, crystals suitable for SC–XRD analysis were obtained. The crystal structure confirms that indeed the thiourea compound is formed, which is in accordance with the observations made by Ohno *et al.*

When applying slightly modified reaction conditions to **FPOC1**, since the use of sodium hydride led to the substitution of fluorine atoms at elevated temperatures, instead of the clear formation of the mono-functionalized compound, a mixture of compounds could be observed (Figure 25). When subjecting the isolated sample to ESI HRMS analysis, two species could be identified in the product mixture: the mono-functionalized compound **20** ([**20**+H]$^+$ mass calculated: 1136.4841 m/z, found: 1136.4844 m/z) and the di-functionalized compound **21** ([**21**+2H]$^{2+}$ mass calculated: 626.2497 m/z, found: 626.2490 m/z). This is possibly due to the use of more than one equivalent of the isothiocyanate. When reducing the amount of PhNCS in the reaction, only an incomplete conversion to **20** in very low yields could be observed. The group of Ohno had previously hypothesized a cooperative mechanism in which two isothiocyanate molecules are needed to create a stabilized intermediate that can then further react towards the mono-functionalized product.[74]

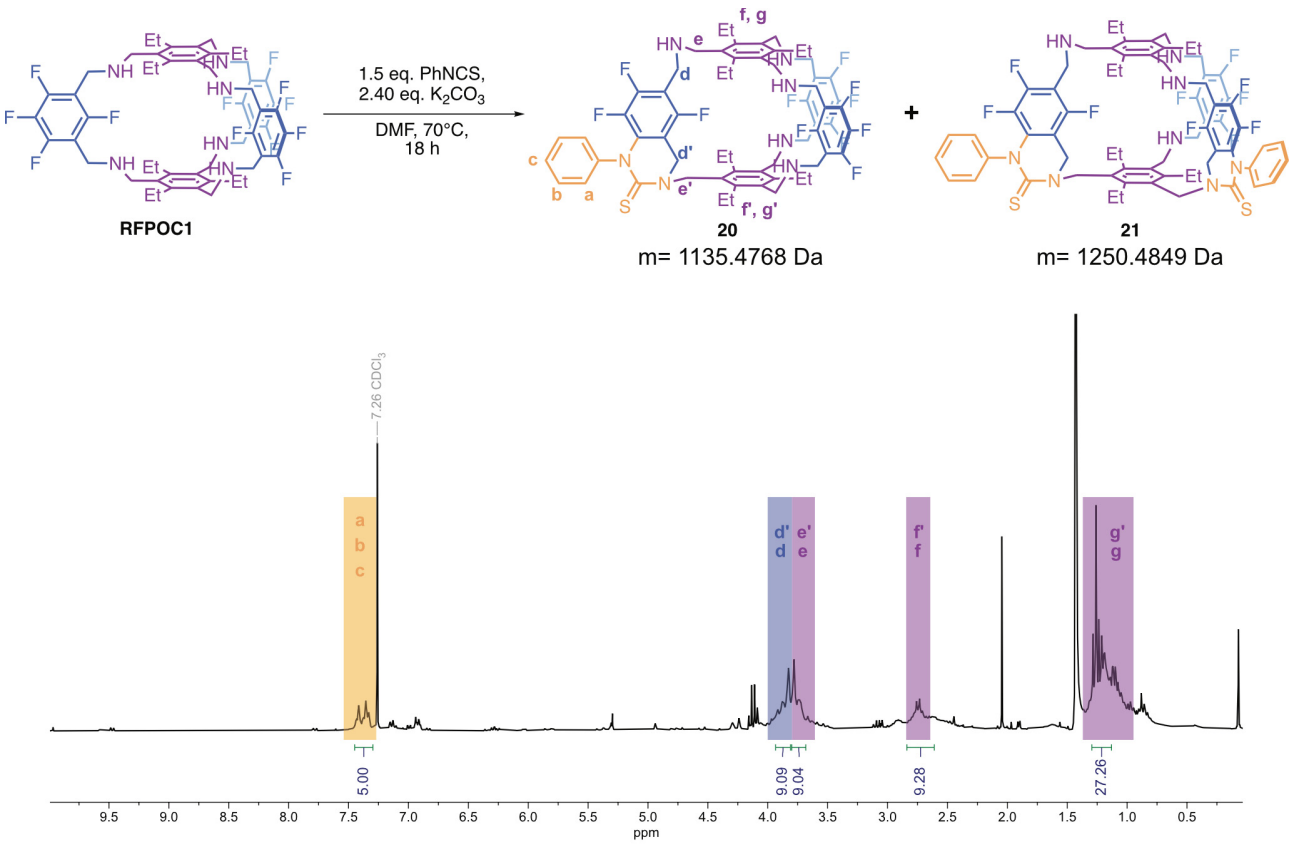

Figure 25: Synthesis conditions applied to the functionalization of **RFPOC1** resulting in the formation of mono-functionalized compound **20** and **21** (only one possible isomer is depicted for clarity). The ^{1}H NMR (bottom) indicates the formation of more than one product during the reaction.

The presence of more than one compound explains the broad signals observed in the ^{1}H NMR spectrum. Since the formation of more than one six-membered ring introduces the possibility of regioisomers, the presence of chemically distinct species is increased drastically. This results in many signals that are partly overlapping in their chemical shift.

The stabilization of a cage molecule with a post-synthetic modification reaction can only be achieved when all conformationally flexible or reversible bonds are modified in the process. Therefore, the reaction of **RFPOC1** with an excess of the isothiocyanate and potassium carbonate was repeated (Scheme 20).

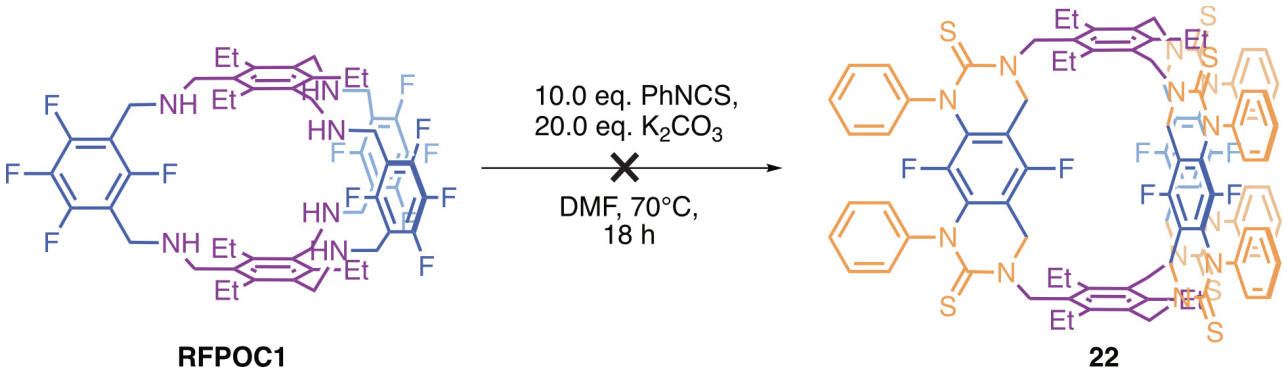

RFPOC1 **22**

Scheme 20: Using an excess of the isothiocyanate to yield the sixfold-functionalized compound **22** only resulted in the formation of unidentifiable structures.

Unfortunately, the use of 20 equivalents of PhNCS only resulted in the decomposition of the cage, accompanied by the formation of unidentifiable signals in the ^{1}H NMR spectrum. In the MALDI MS and ESI MS spectra, no signals that could be assigned to either **RFPOC1** nor any other functionalization products could be identified.

The successful functionalization of the model compound and the successful synthesis of the functionalized cage compounds **20** and **21**, prove that the use of fluorine substituents for novel post-synthetic modifications of cage compounds is indeed possible. However, further optimization is required to obtain the fully functionalized cage compound and then investigate its stability under different thermal and chemical conditions and study the crystal packing of the resulting material.

3.1.6. Summary

In this chapter, the successful synthesis of the three small **Tri^{2}Di^{3}** cages **FPOC1-3** and their building blocks was presented. The cages exhibited excellent thermal stability that even surpassed that of a stable acetone-tied cage, which is praised for its extraordinary stability. The crystal structure of these small cages revealed that due to the inward-pointing fluorine atoms, no intrinsic porosity is achieved. However, the incorporation of three chloroform molecules per cage molecule in the unit cell led to the generation of a large extrinsic pore network that is filled with solvent. Although all attempts to make this network available for gas sorption proved unsuccessful, the crystal packing provided an interesting insight into the possibilities of fluorinated materials.

To analyze the properties of the fluorinated cages in solution, **FPOC1-3** were transformed into the corresponding amine cages, **RFPOC1-3,** by reduction of their imine bonds. When dissolved in anion-containing, acidic, aqueous solutions, **RFPOC1** and **RFPOC2** exhibited strong fluorescence in the presence of chloride and bromide ions. Initial investigations nourished the hypothesis that a charge-transfer complex is created by attractive $\pi_F\cdots$anion interactions. Further work is required to

investigate the full potential of these small cages for sensing applications and to better understand the binding mode between the amine cages and the anions.

In an attempt to utilize the fluorine substituents of the cage molecules for the post-synthetic modification and stabilization, a model compound could be converted successfully into the cyclic thiourea compound **19**. With slightly altered reaction conditions, **RFPOC1** could be transformed into the mono-functionalized cage **20** and di-functionalized compound **21**. Although their synthesis was only possible as a mixture and their separation could not be achieved *via* standard column chromatography techniques, this proved that the post-synthetic modification technique can be used on fluorinated cages in the future. Additional studies are needed not only to generate a fully functionalized derivative of the cage, but also to control the regioselectivity.

3.2. Elongated imine cages

3.2.1. Introduction

As the previously synthesized fluorinated **Tri^{2}Di^3** cages **FPOC1-3** did not exhibit porosity due to the close proximity of the fluorine atoms inside the cavity, other building blocks needed to be investigated. To ensure the formation of a larger cavity inside the cage, two concepts were applied in the design of the new building blocks:

a) increase the distance between the functional groups to elongate the cavity
b) introduce a steric repulsion in the building blocks so that another geometry with a larger cavity is formed

At the time of writing, there were no reports about an amine that, similar to **Et-Amine** or TREN, exhibits a strong pre-organization, targets similar **Tri^{X}Di^Y** topologies, and has a larger distance between its functional groups. Therefore, the amines, **Et-Amine** and TREN, were chosen for the studies of larger cages. Leaving the amines constant results in the need for change in aldehyde building blocks to generate larger cages. Two aldehydes with a greater distance between their formyl groups were envisioned (Figure 26).

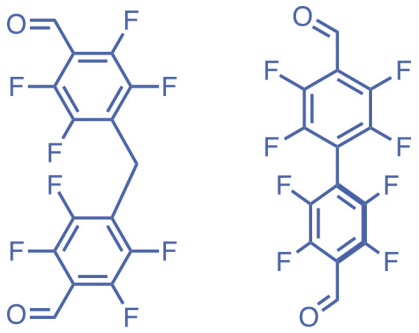

22 **23**

Figure 26: Two fluorinated aldehydes that were designed to increase the size of the cavity in newly formed cage molecules compared to **FPOC1-3**.

Inspiration for the design of compound **22** was drawn from the 2013 study of Mukherjee *et al*., in which they successfully synthesized a large **Tri^{2}Di^3** cage from the non-fluorinated analogue of **22** and **Me-Amine** in solution.[75] The fluorinated cage that would result from the reaction of **22** with **Et-Amine** should be large enough to possess a cavity in which the fluorine atoms are distanced far enough from each other for the material to exhibit intrinsic porosity.

The octafluorobiphenyl compound **23** exhibits a dihedral angle between its two aromatic rings that should make the building block bulky enough to render the formation of a **Tri^{2}Di^3** cage impossible, leading to a large **Tri^{4}Di^6** topology instead.

3.2.2. Synthesis

Synthesis of the building blocks

Both aldehydes could be obtained in a two-step synthesis, starting from pentafluoro-benzonitrile. The preparation of **22** proceeded after a modified literature procedure in which pentafluorobenzonitrile is reacted with methylmagnesium chloride in the first step to generate the dinitrile **24** in moderate yield (Scheme 21).[76]

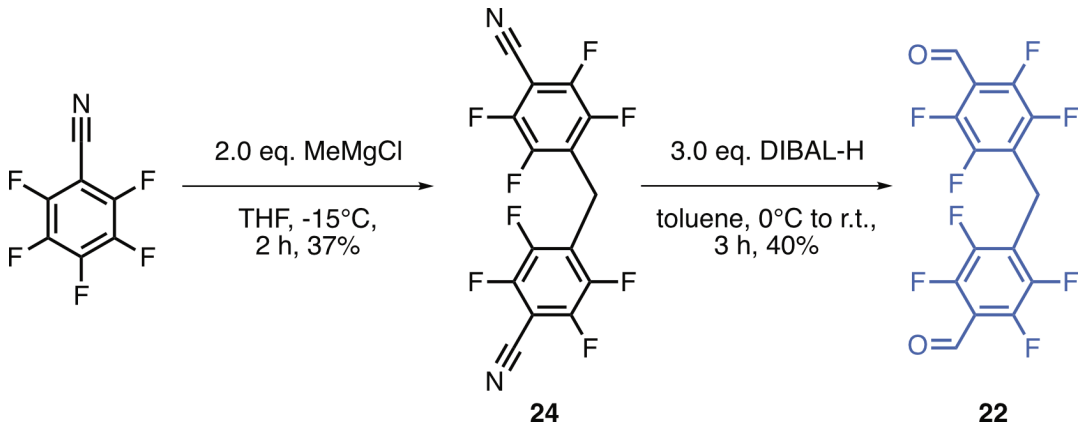

Scheme 21: Synthesis of the larger aldehyde **22** from pentafluoro-benzontrile in two steps.

In a second step, **24** is reduced to the corresponding aldehyde **22**, in a moderate yield by using an excess of DIBAL-H. Although the overall yield is considerably lower (15%), the short route still allows for the synthesis of a multi-gram scale of **22**.

For the synthesis of aldehyde **23**, pentafluorobenzonitrile is reacted with tris(N,N-diethylamino)phoshpin, to yield the dinitrile **25** in a homo-coupling reaction.[77] This dinitrile can then be reduced to the aldehyde **23** using DIBAL-H with moderate yields (Scheme 22).

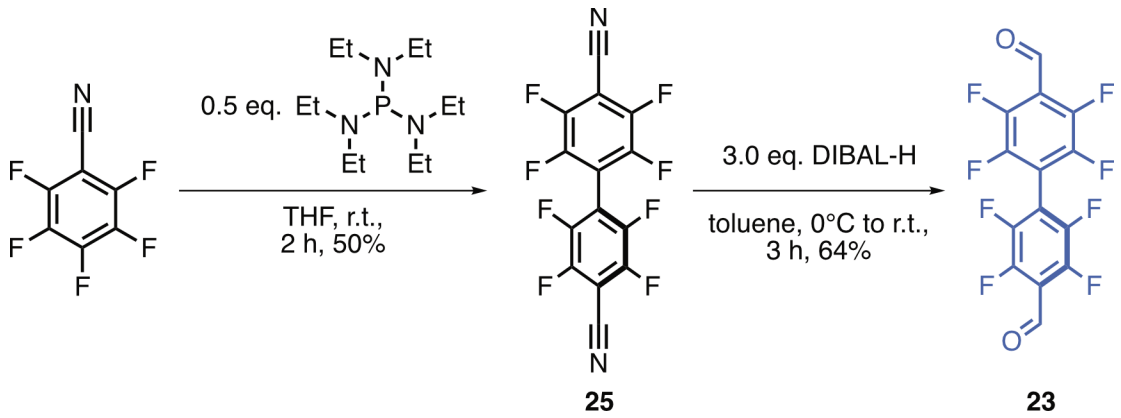

Scheme 22: Two-step synthesis of aldehyde **23** from pentafluorobenzonitrile.

With both aldehydes needed for the exploration of larger fluorinated cages in hand, the optimization of the cage formation conditions was investigated.

Cage formation studies

By combining the aldehyde **22**, in which two highly fluorinated aromatic rings are connected *via* a methylene bridge, with **Et-Amine** and TREN, the formation of large **Tri^{2}Di^3** cages, similar in structure to the cages by Mukherjee *et al*., was targeted. On the other hand, for the aldehyde **23**, the bite angle and the dihedral angle between the aromatic rings should be sufficient stimuli to steer the formation towards a **Tri^{4}Di^6** topology (Figure 27).

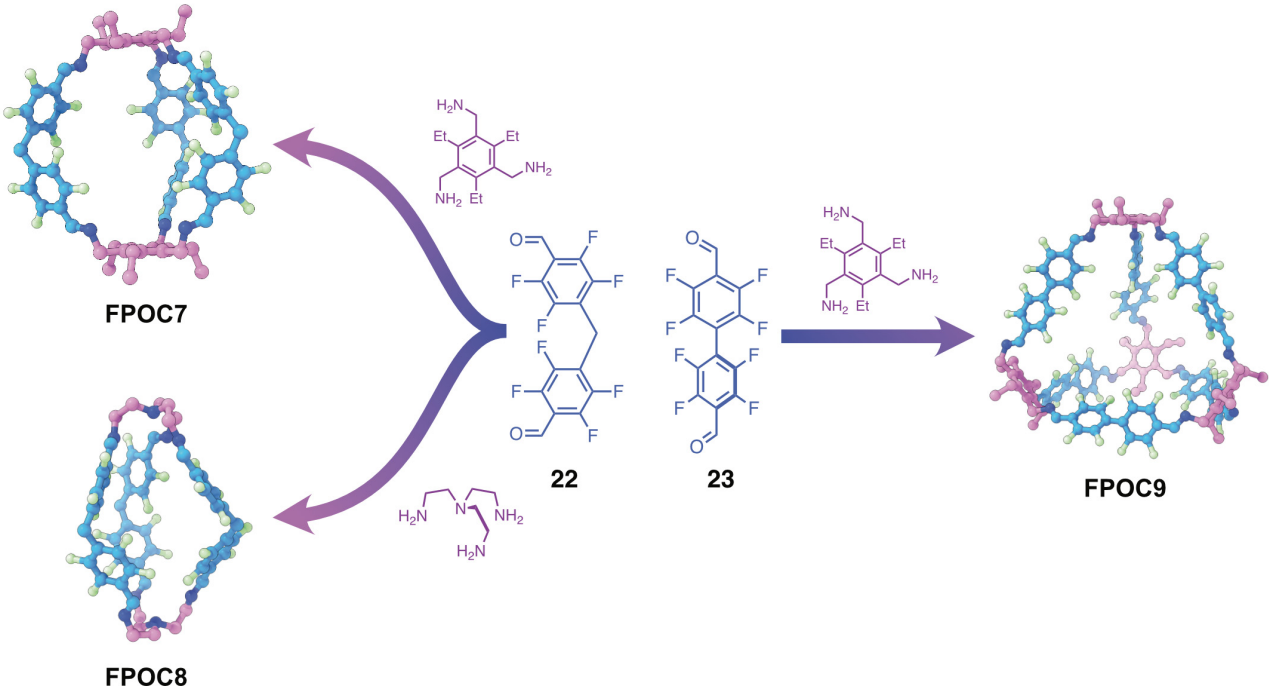

Figure 27: Calculated cage structures of the resulting cages from the combination of **Et-Amine** and TREN with the aldehydes **22** (left) and **23** (right) using UFF-8.

TREN has in the past failed to yield the large cage topology of **Tri^{4}Di^6**, possibly due to the conformational flexibility of its bonds, and therefore was not reacted with aldehyde **23**.

The combination of one equivalent of **Et-Amine** with 1.2 equivalents of **23** in methanol resulted in the formation of a yellow precipitate that could easily be filtered off. The solid was only very sparingly soluble, but could be dissolved in $CDCl_3$ to be investigated by NMR analysis (Figure 28). The considerably sharp signals can all be attributed to the formation of a cage species. Similar to the **Tri^{2}Di^3** cage species, the signal that can be assigned to the imine-adjacent proton can be observed at 7.87 ppm. The singlet at 5.15 ppm can be assigned to the methylene group that is adjacent to the nitrogen atom, whereas the quadruplet at 2.64 ppm and the triplet at 1.28 ppm can be assigned to the methylene and methyl groups of the ethyl substituent of the **Et-Amine** motif inside the cage.

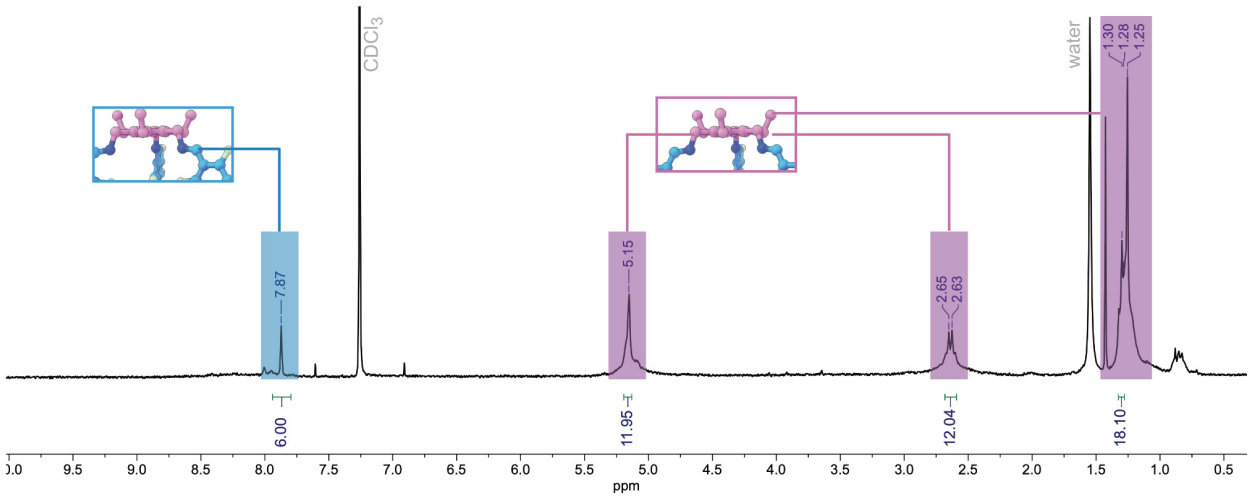

Figure 28: ^{1}H NMR spectrum of the precipitation product during the reaction of **Et-Amine** with aldehyde **23** for targeting **FPOC9**. Colored lines indicate the assignments of the signals to the corresponding protons in the structure.

Due to the low solubility of the condensation product in common NMR solvents, no DOSY spectrum of the compound could be obtained. To confirm the formation of the targeted **Tri^{4}Di^6** cage, a sample of the redissolved precipitate was subjected to ESI HRMS analysis.
Surprisingly, only signals that could be attributed to the **Tri^{2}Di^3** cage could be observed ([**FPOC9-Tri^{2}Di^3**+H]$^+$calculated = 1453.3630 m/z, found: 1453.3622 m/z). No signals that can be attributed to the formation of a **Tri^{4}Di^6** cage were observed in neither the remaining reaction mixture nor in the redissolved precipitation aliquot. Different concentrations and solvents were investigated to facilitate the formation of the targeted **Tri^{4}Di^6** topology, but they proved to yield only the **Tri^{2}Di^3** cage. All attempts to yield a crystalline material from the sparingly soluble precipitate only gave a

bright yellow, insoluble powder. When investigating the structure of the **Tri^{2}Di^3** in a universal force field calculation, which only considers bond lengths and angles, the hypothesis arose that the driving force in its formation could be the strong attractive interaction between a fluorine atom and the π_F–system in an adjacent octafluorobiphenyl motif (Figure 29).

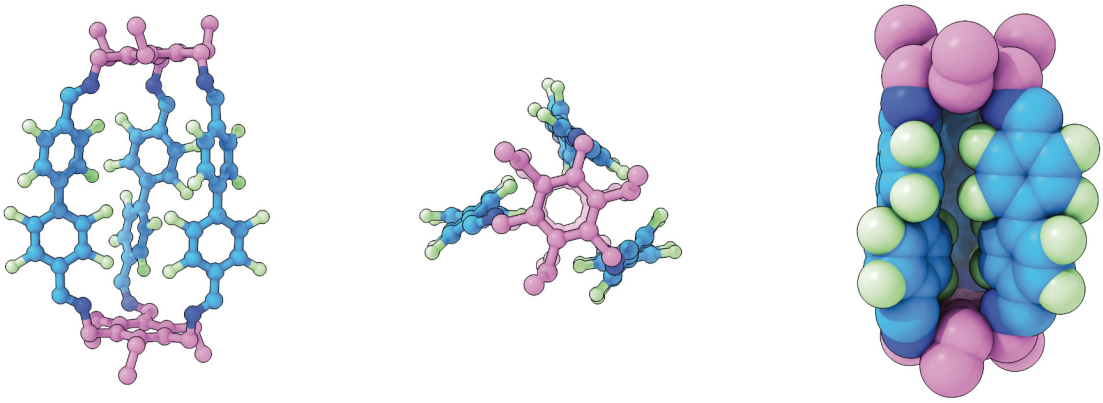

Figure 29: Calculated **Tri^{2}Di^3** structure of **FPOC9** using the universal force field method (UFF). Side view (left), top view (middle) and space-filling model (right).

In the space-filling model, the intriguing rotation dependency of all phenyl rings becomes apparent. No ring can rotate freely without either affecting another ring from the same biphenylic structure or an adjacent aromatic moiety. However, in the ^{19}F NMR, no discrimination between two sets of fluorine atoms can be made, which can only be explained by all six rings rotating in fast conjunction at room temperature (see Section 6.2).
The calculated structure of **FPOC9** does not show the possibility of the material to exhibit intrinsic porosity. Since the fluorinated biphenyls are so close to each other, no guest uptake in solution seems possible. In future studies, the amine form of this cage compound could be reinvestigated alongside the smaller **RFPOC1-3** cages for their potential as fluorescent sensors, as this cage could also partake in the development of $\pi_F\cdots$anion interactions. As the focus of this work is the influence of the fluorine atoms on the solid state properties of the resulting cage-based material and on the guest uptake in solution, **FPOC9** was not investigated further.

When combining one equivalent of **Et-Amine** with 1.2 equivalents of **22** in methanol, **FPOC7** precipitates almost quantitatively as a yellowish powder after 24 hours. The clean formation of the targeted **Tri^{2}Di^3** cage topology could be confirmed by NMR and MALDI MS analysis (Figure 30).

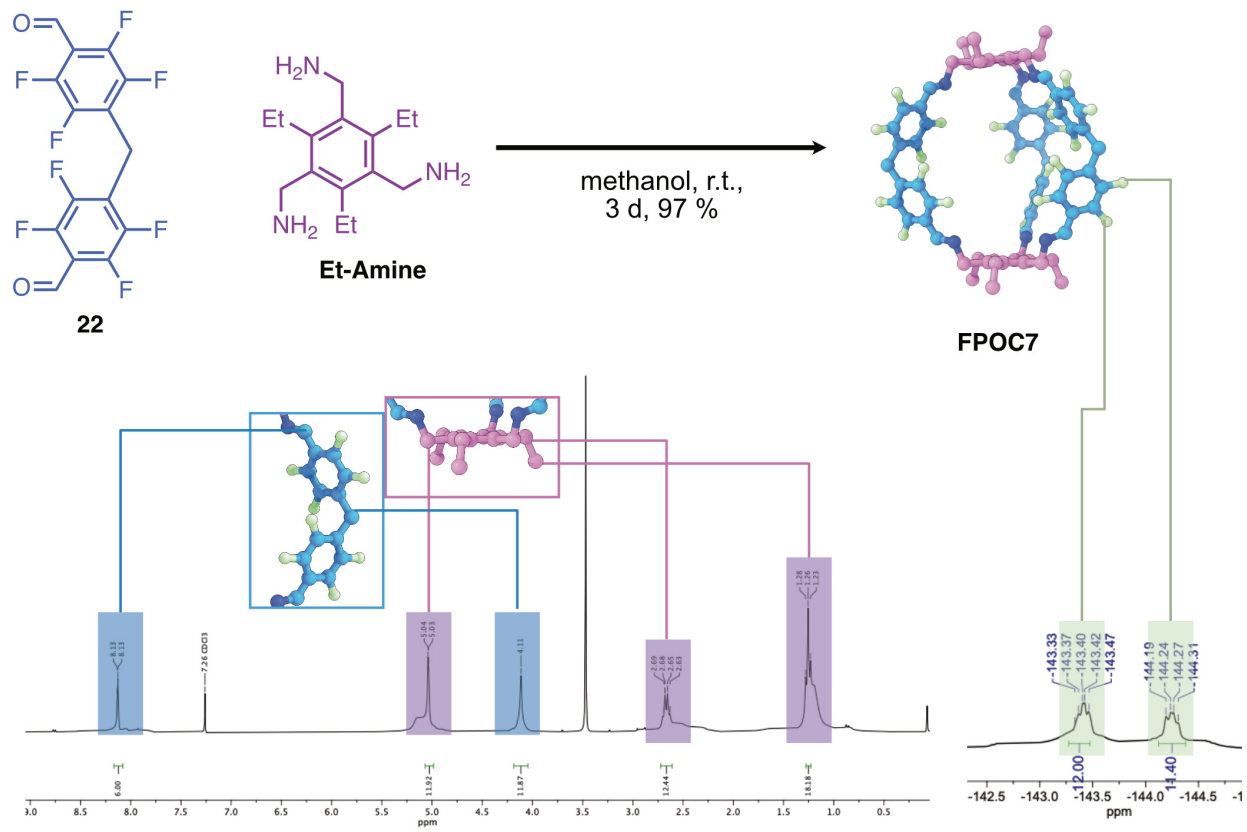

Figure 30: Synthetic scheme of the reaction yielding **FPOC7** (top). ^{1}H NMR spectrum (bottom left) and ^{19}F NMR spectrum (bottom right) of the redissolved precipitate from the reaction of **Et-Amine** with aldehyde **22**. The signals can be assigned to the clear formation of the targeted **Tri^{2}Di^{3}** cage **FPOC7**.

All attempts to generate a crystal of **FPOC7** suitable for SC–XRD were unsuccessful. Different conditions of layering the starting materials onto another and a broad variety of solvents were investigated. Although **FPOC7** is much more soluble than its smaller congeners, its comparatively low solubility still provides an obstacle to crystallization. Trying to activate the amorphous sample by heating the powder at 70 °C for 18 hours at 10^{-3} mbar resulted in a material that did not exhibit porosity. Gas sorption measurements were only able to reveal that the material possessed an apparent surface area of <5 m^2 g^{-1}.

When combining one equivalent of TREN with 1.5 equivalents of **22**, the reaction mixture turned deep yellow after a few hours (Scheme 23). After 24 hours, no precipitate had formed in the reaction vessel. MALDI MS of an aliquot confirmed the clean formation of **FPOC8** in solution.

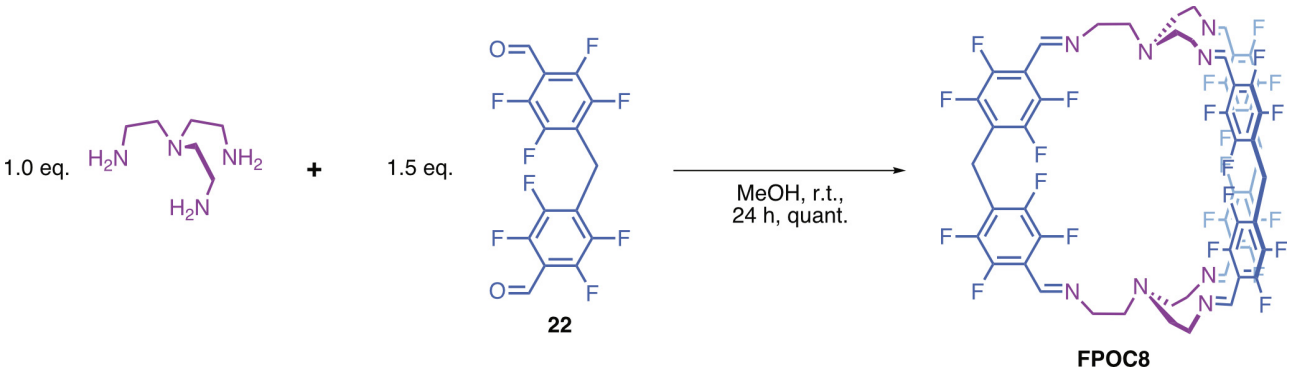

Scheme 23: Successful synthesis of highly fluorinated **Tri^{2}Di^3** cage **FPOC8** in methanol.

By the fast evaporation of methanol at room temperature, the **Tri^{2}Di^3** cage could be obtained quantitatively as a bright yellow solid. The solubility of **FPOC8** in DCM and chloroform proved to be excellent, allowing full characterization by NMR analysis (Figure 31), including the recording of a DOSY spectrum.

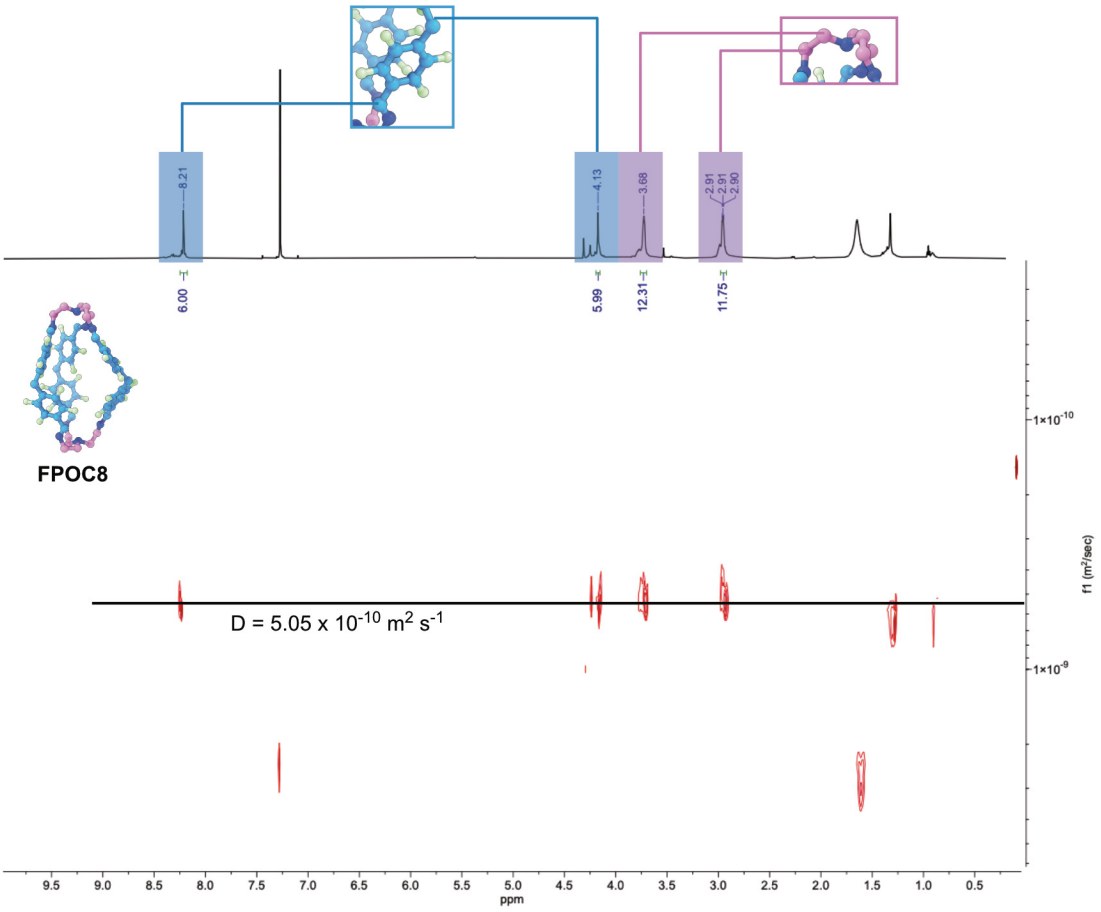

Figure 31: ^{1}H NMR (top) and DOSY NMR (bottom) indicating the successful formation of the **Tri^{2}Di^3** cage **FPOC8**.

With a diffusion coefficient of D = 5.05 x 10^{-10} m^2 s^{-1} this cage exhibits a hydrodynamic radius of ~7.67 Å. Since TREN-based cages do not feature shape-persistency, the solid state properties of **FPOC8** were not investigated. The apparent radius of the cage in solution offers the possibility for **FPOC8** to be used as a highly fluorinated host molecule.

3.2.3. Properties of the medium-sized cages in solution

Indicator-like behavior

Although the generation of a porous material from **FPOC7** could not be realized yet, an interesting discovery was made when an evaporating solution of **FPOC7** was standing in the fume hood next to an open ammonia solution: the former's yellow dispersion suddenly turned deep purple. The same change of color could be observed when grains of sodium hydride were added to a DCM solution of the cage. As the former aldehyde building block **22** features a methylene bridge between two highly fluorinated aromatic rings, the attached protons are quite acidic (signal at 4.2 ppm in Figure 30). When introduced to a base, the deprotonation of the methylene bridge causes a rapid change from yellow to the complementary deep purple color. The introduced negative charge at the methylene bridge results in the connection of the previously disconnected π-systems in the two fluorinated rings. The newly formed, vastly expanded π-system that stretches from one imine group to the other, is then able to absorb visual light of shorter wavelengths. This effect can already be observed in building block **22**. If a strong organic base like diazabicycloundecene (DBU) is reacted with **FPOC7** in solution, the mixture immediately turns deep purple (Figure 32).

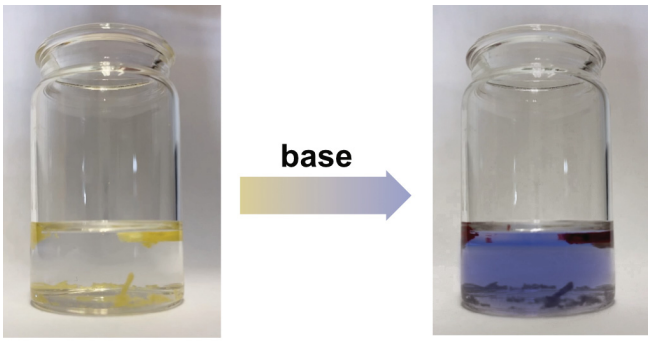

Figure 32: Addition of DBU to a dispersion of **FPOC7** in DCM, leads to a color change of the solution and also of the dispersed solid.

When adding acid to the deprotonated compound, this process can be reversed. Contact with an alkaline solution for an extended period of time causes the cage structure to decompose. Trying to solve this problem by transforming **FPOC7** into the amine cage **RFPOC7** using an excess of sodium borohydride in methanol leads to a readily decomposing cage. When using stoichiometric

amounts of the hydride source, only partially reduced cage compounds were obtained. In some cases, hydride sources like sodium borohydride can also act as bases, which could cause the deprotonated **FPOC7** to undergo side reactions in a reductive environment, ultimately leading to decomposition. As the color change from deprotonation is caused by the building block **22**, an investigation could also be feasible in **FPOC8**.

FPOC8 also exhibited a rapid color change from yellow to deep purple, even in its solid form. The color change is even more intense since the solubility of **FPOC8** far exceeds that of **FPOC7**. As the deprotonation of the methylene bridge in **FPOC8** proceeds very smoothly and surprisingly without signs of decomposition, a post-synthetic functionalization was investigated. When reacting **FPOC8** with one equivalent of DBU in DCM with ethyl bromide, the desired nucleophilic substitution of the bromine atom could not be observed. Signals in the MALDI MS indicated a decomposition of the cage and the reaction of **Et-Amine** with the bromide. Apparently, the reversible imine bond proved again to be the limiting factor for the chemical stability of the cage compound.

The transformation of the imine cage **FPOC8** to the amine cage **RFPOC8** with an excess of sodium borohydride in a mixture of methanol and chloroform could be conducted successfully (Scheme 24).

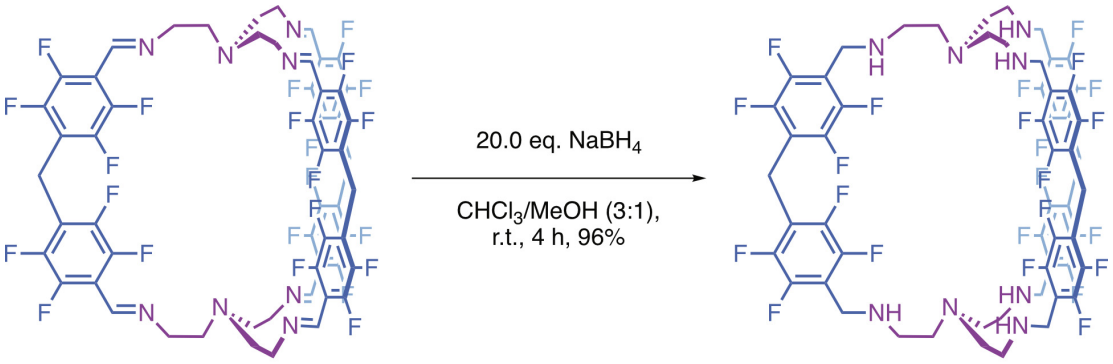

FPOC8 **RFPOC8**

Scheme 24: Reduction of the imine **Tri^{2}Di^3** cage to the amine cage using sodium borohydride, in very high yields.

Addition of base to a solution of **RFPOC8** leads to a color change from bright yellow to an intense orange color (Figure 33).

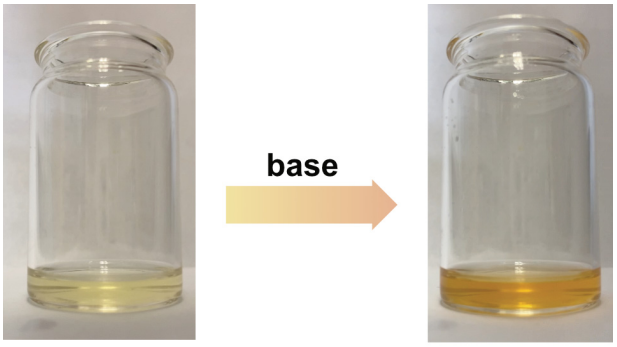

Figure 33: Addition of DBU to a solution of **RFPOC8** in DCM leads to a color change from bright yellow to intense orange.

Again, no decomposition of the cage was observed in the MALDI MS spectrum. There was no reaction when **RFPOC8** was reacted in the nucleophilic substitution with ethyl bromide. A possible explanation is the low nucleophilicity of the methylene carbon atom, since its free electron pair is largely delocalized across the newly formed π-system.

TREN-based amine cages, like **RFPOC8**, are known to be excellent cryptands for a variety of metal ions, but predominantly for copper ions.[78]

Guest uptake

When a DCM solution of **RFPOC8** was combined with two equivalents of a Cu(I)-complex, the yellow solution turned red immediately. By slow evaporation of the solvent mixture, single crystals suitable for SC–XRD could be obtained (Scheme 25).

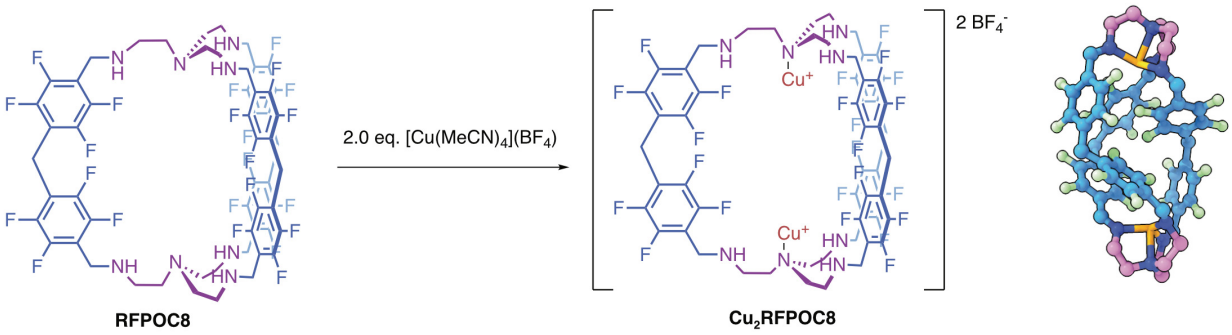

Scheme 25: Preparation of a dicopper complex using **RFPOC8** (left) and crystal structure of the complex from a crystal grown after slow evaporation of a DCM solution of the complex (right). Hydrogen atoms, counter ions, and solvent molecules were omitted for clarity (crystal structures were obtained and refined by Dr. Bernd M. Schmidt).

The crystal structure of the **RFPOC8**-based complex reveals the flexible nature of the amine cage. The height of 12.4 Å in **Cu_2RFPOC8** is in good agreement with the DOSY derived hydrodynamic radius for **RFPOC8** of 6.7 Å (D = 5.78 x 10^{-10} m^2 s^{-1}). In previous studies, the dicopper complexes of TREN cryptands could be used to bind anions or acids between the two copper centres.[78] The Cu···Cu distance of 10.0 Å should be enough to allow the hosting of guests inside the cage. Although the fluorinated linkers are twisted inside the crystal structure, the flexible amine bonds should facilitate an “opening” of the cage in solution for guest interactions.

A pollutant that has had recurrent appearances in the media is perfluorooctanoic acid (PFOA). If the dicopper cryptate **Cu_2RFPOC8** was able to bind or even scavenge PFOA from aqueous solutions, this could be used in the purification of waste water and subterranean water alike. For this purpose, one equivalent of PFOA was added to a chloroform solution of **Cu_2RFPOC8** to better study the interactions between host and guest, as the solubility of **Cu_2RFPOC8** in water is comparatively low (Figure 34).

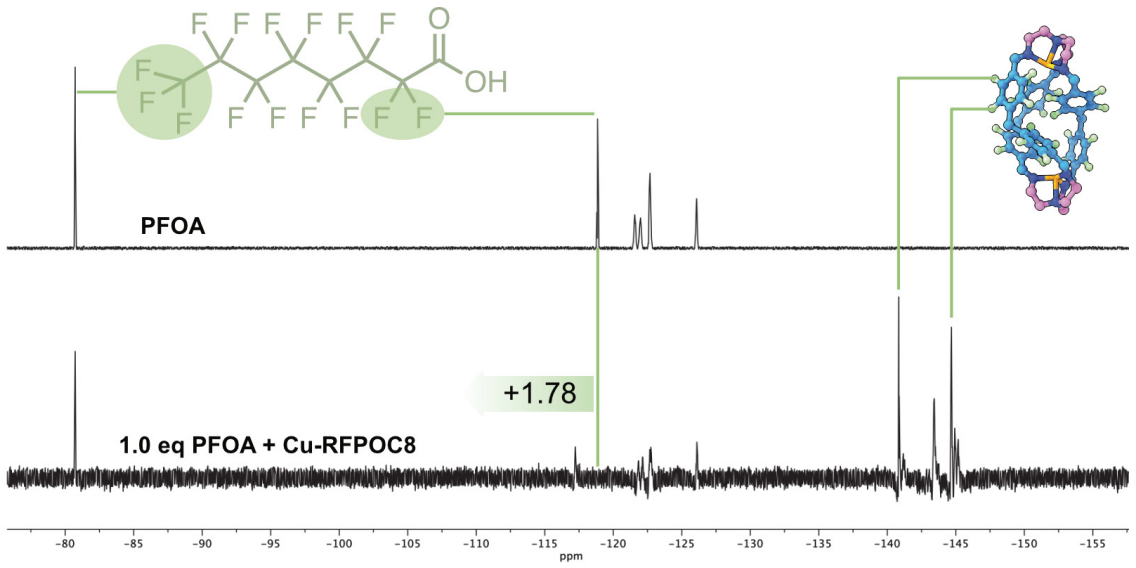

Figure 34: ^{19}F NMR spectra of PFOA (top) in $CDCl_3$ and one equivalent PFOA an **Cu_2RFPOC8** in $CDCl_3$ (bottom). The shift annotated in the bottom spectra is given in ppm. Hexafluorobenzene was used as an internal standard.

In the ^{19}F NMR spectra of the resulting mixture, a clear downfield shift of the fluorine signal that can be assigned to the CF_2 group adjacent to the carboxy group can be observed. This agrees well with the interaction of the carboxy group with the dicopper complex. In the case of a binding event at the copper center with the carboxy group, the electron density in the perfluorinated alkyl chain would ultimately be reduced. The further the CF_2 group is distanced from the carboxy group, the less pronounced the effect would be. Therefore, it is only logical for the CF_2 group adjacent to

the binding site to experience the largest chemical shift. The exact mode of interaction and the stoichiometry thereof remain the targets for further investigations.

3.2.4. Summary

Over the course of this section, the synthesis of three larger **Tri^{2}Di^3** imine cages on the basis of novel, highly fluorinated building blocks was presented. Due to steric bulk, **FPOC9** exhibited an unexpected **Tri^{2}Di^3** topology, although its fluorinated building blocks would indicate the formation of a **Tri^{4}Di^6** cage. The formation of the smaller geometry could be the result of attractive C–F$\cdots\pi_F$ interactions of neighboring biphenyl moieties. In the densely occupied cage compound, all six fluorinated rings rotate in fast conjunction since no separate signals could be observed in the NMR spectra. This is a surprising feature that could be the focus of future investigations regarding the application of fluorinated biphenyl moieties in molecular rotors.

In the investigation of the structurally closely related imine cages **FPOC7** and **FPOC8**, the change in the amine proved to have a dramatic effect on the solubility and stability of the cages. Whereas **FPOC7** is only slightly soluble and decomposes readily under alkaline conditions, **FPOC8** was extraordinarily soluble and showed no signs of decomposition in a DBU-containing chloroform solution. **FPOC8** could almost quantitatively be reduced to the amine cage **RFPOC8**. When subjected to alkaline conditions, **FPOC8** exhibited an intense change of color from yellow to deep purple. As the incorporated fluorinated aldehyde contains an acidic methylene bridge, its deprotonated form features a considerably large π-system that is "switched on" upon deprotonation. This effect was also observed in the amine cage **RFPOC8**, although the change in color is more subtle (yellow to orange).

When **RFPOC8** reacts with a Cu(I) salt, it forms a dicopper complex, **Cu_2RFPOC8**, that is deep red in color**.** The crystal structure reveals a Cu$\cdots$Cu distance of 10.0 Å that could be feasible for the binding of anionic and dicarboxylic guests in a highly fluorinated host. When the binding of the common pollutant PFOA was investigated *via* NMR analysis, the clear shift of the CF_2 group's signal adjacent to the carboxyl group hints at a binding event.

FPOC8 and **RFPOC8** responded to multiple stimuli with an intense change of color, and furthermore, the copper complex of **RFPOC8** showed signs of host activity. Therefore, this family of **Tri^{2}Di^3** cages remains an interesting target for further studies of the behavior of highly fluorinated cage compounds in solutions.

3.3. A medium sized fluorinated porous organic cage

3.3.1. Introduction

During the investigation of the small fluorinated **Tri^{2}Di^3** cages, the fluorinated amine **F-Amine** was able to yield cage **FPOC3**, but its formation was the least cleanest and its properties were the least favorable ones among the three isostructural cages. The fact that this imine cage was formed, albeit with the use of a highly conformationally flexible amine, led to the question of whether other cage geometries could be accessed as well. When Mastalerz *et al*. investigated a series of **Tri^{4}Tri^4** cages using different amines, they found that the pre-organization of the amine groups is crucial for successful cage formation.[29b] As the use of bulky ethyl substituents in the amine led to the blocking of the cage's windows, but the use of hydrogen atoms as substituents only produced polymeric, non-porous species, the investigation of **F-Amine** for the formation of a **Tri^{4}Tri^4** cage was intriguing. A fluorinated truncated tetrahedral cage would most likely feature a cavity that is large enough to host guest molecules or could be used for gas uptake, and simultaneously, the sterically less demanding fluorine atoms would ensure that the cage's windows remained accessible.[1]

3.3.2. Synthesis

The targeted **Tri^{4}Tri^4** cage would be synthesized from the reaction of triformylbenzene with **F-Amine.** Therefore, **TFB** was synthesized according to a literature procedure, from trimesic acid (Scheme 26).[29b]

[1] Large parts of this work have been published: T. Kunde, E. Nieland, H. V. Schröder, C. A. Schalley and B. M. Schmidt, *Chem. Commun.*, 2020, **56**, 4761–4764.

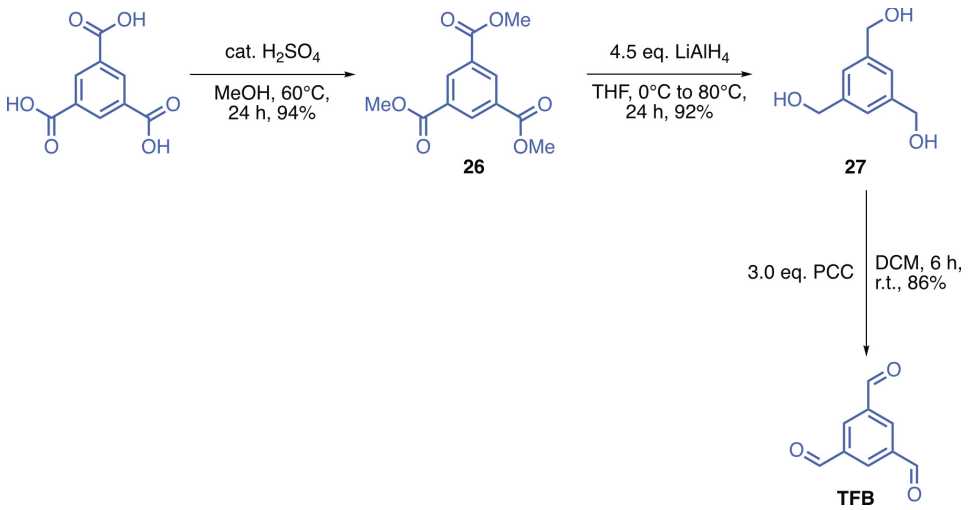

Scheme 26: Three step synthesis of 1,3,5-triformylbenzene (**TFB**) starting from trimesic acid.

When layering a DCM/methanol (3:1) solution of **TFB** and **F-Amine** above another for two days without stirring, the fluorinated **Tri^{4}Tri^4** cage **FC1** was obtained in 67% yield.

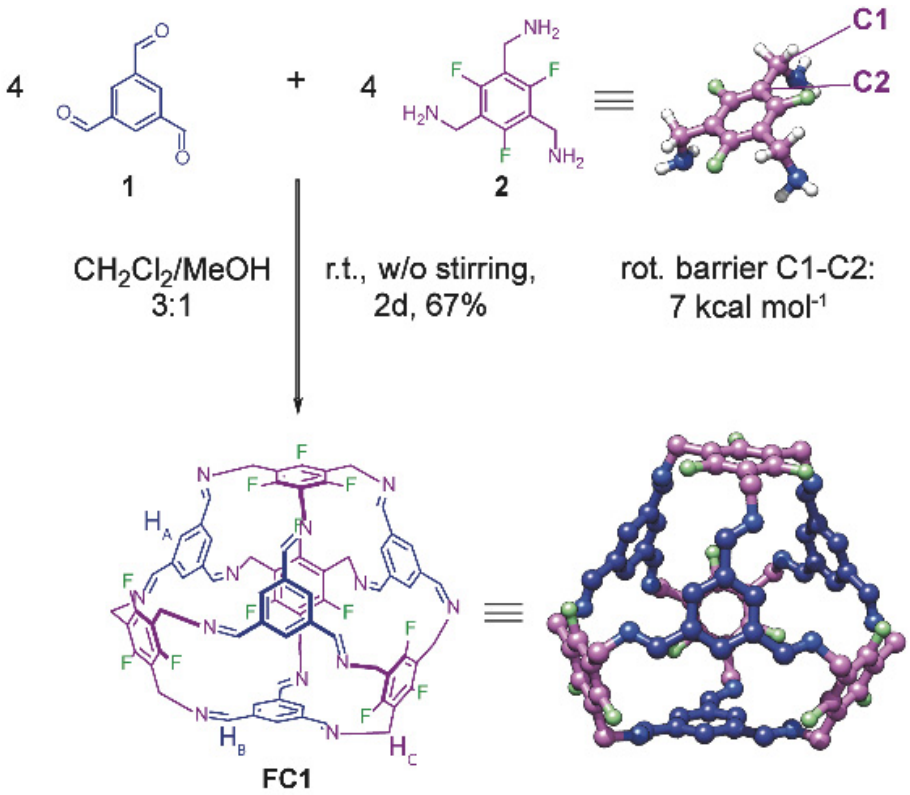

Scheme 27: Synthesis of **FC1** by combining equal amounts of **1** and **2** in DCM/methanol 3:1 at room temperature; the molecular structure of triamine **2**, as obtained from calculations using hybrid B3LYP 6-311++G(d,p) level of theory (calculations were conducted by Dr. Bernd M. Schmidt), showing the possible pre-organization by weak C–H···F contacts and the rotational barrier of the amines obtained from MM2 calculations; the calculated structure of the truncated tetrahedral cage **FC1** (M062X/def2-TZVP). The figure was reproduced from ref. [79] with permission from the Royal Society of Chemistry.

The cage is obtained as 1-2 cm long, colorless needles. **FC1** exhibits very low solubility in common organic solvents but proved soluble enough to be investigated by NMR analysis (Figure 35).

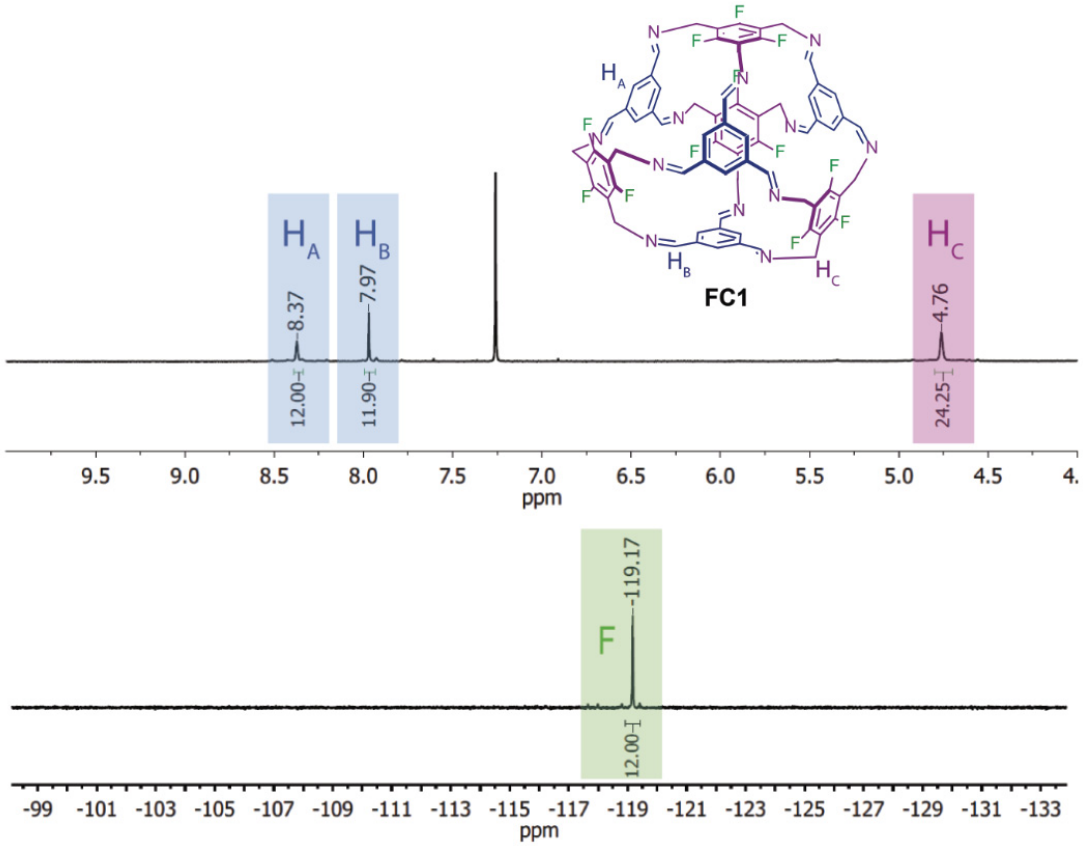

Figure 35: ^{1}H and ^{19}F NMR of the precipitated crystalline material, in $CDCl_3$ at 25 °C. The figure was reproduced from ref. [79] with permission from the Royal Society of Chemistry.

The ^{1}H NMR spectrum shows clear signals that can be assigned to the imine protons (8.37 ppm), to the protons at the benzene core (7.97 ppm) and to the methylene group at the **F-Amine** building block (4.76 ppm), proving the clean formation of **FC1**. In the ^{19}F NMR spectrum, only an intense singlet for the fluorine atoms can be observed.

MM2 calculations revealed the rotation barrier around the C1–C2 axis of **F-Amine** to be only 5.0 kcal mol^{-1}, which is tremendously lower than the high rotational barrier of 227.7 kcal mol^{-1} in **Et-Amine**. A possible explanation for the formation of **FC1** might be minute electronic effects rather than pure steroidal congestion. This proves that fluorine atoms have not only an important influence on the material properties, but can also have a dramatic impact on the cage formatiom.

3.3.3. Solid-state properties of FC1

Structure Investigation

The investigation of the as-synthesized material with scanning electron microscopy (SEM) reveals that **FC1** indeed crystallizes in centimeter-long block-shaped crystals that are 100–200 µm in diameter. Powder X-ray diffraction (PXRD) analysis also confirms the high crystallinity throughout the whole sample (Figure 36).

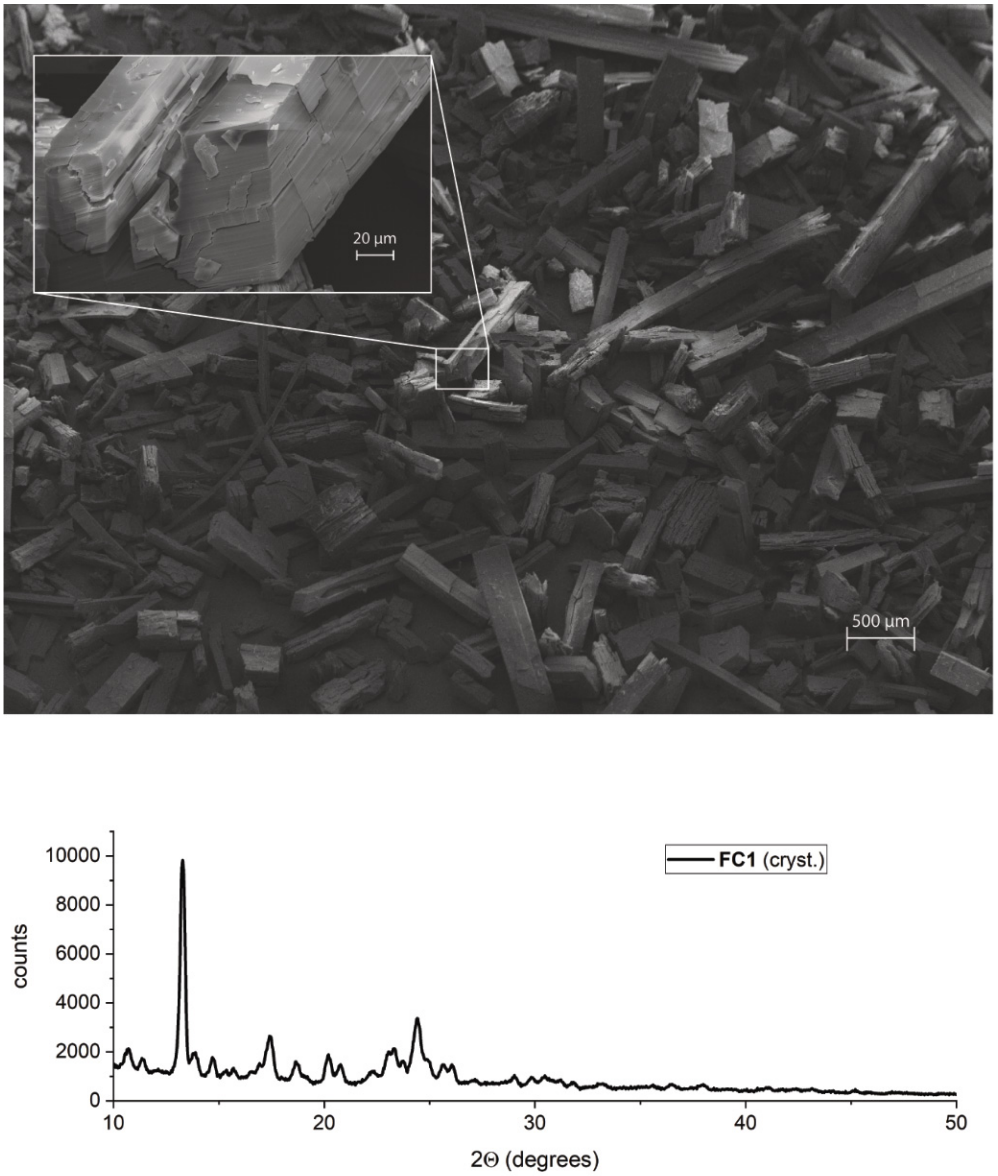

Figure 36: Scanning electron microscope (SEM) image of crystalline **FC1**, scanning voltage 12 kV (top); experimental powder X-ray diffraction (PXRD) pattern of crystalline **FC1** (bottom). The figure was reproduced from ref. [79] with permission from the Royal Society of Chemistry.

The crystalline material offers a solid foundation for the investigation of a porous fluorinated imine cage. When analyzing the calculated structure of **FC1** with pywindow, the cage featured a spherical cavity of 6.4 Å in diameter and windows that were unblocked and exhibited a diameter of 3.4 Å.[80] The window's diameter should be enough to make the intrinsic pore available for gases like N_2, H_2, and CO_2 (Figure 37).

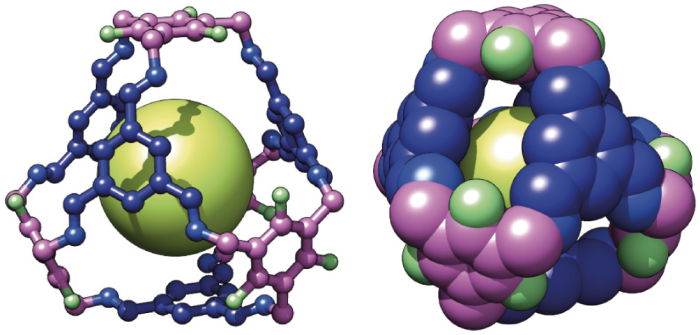

Figure 37: Calculated structure of **FC1** (M062X/def2-TZVP, ball-and-stick model left and space-filling model right, calculations were conducted by Dr. Bernd M. Schmidt) together with the calculated spherical pore (Volume of 158.2 $Å^3$, green) using pywindow. The figure was reproduced from ref. [79] with permission from the Royal Society of Chemistry.

Needle-shaped crystals suitable for SC–XRD analysis could be grown from a chloroform/methanol (3:1) mixture. The heavily solvated structure could be resolved at DESY's synchrotron diffraction beam line P11 at PETRA III with a 0.9 Å resolution by the team of Prof. Dr. C. Lehmann (Max-Planck-Institut for Kohlenforschung, Mühlheim an der Ruhr) and is shown in the appendix, agreeing very well with the calculated structure. The individual cage molecules form one-dimensional channels when looking along the crystallographic *a* axis. This is the result of a window-to-window packing inside the crystalline material. If the solvent molecules are deleted from the crystal structure, a large interconnected pore network can be identified (Figure 38).

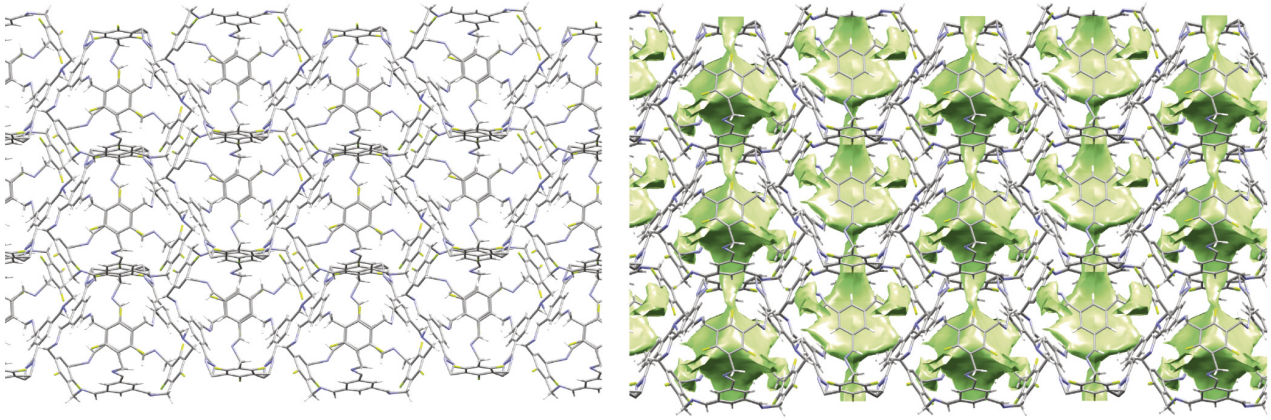

Figure 38: Crystal packing of **FC1** as obtained from the single-crystal structure, disordered solvent molecules within the pores were omitted for clarity (left); solvent accessible surface area without solvents for a molecular probe with 1.2 Å radius (green) within the crystal lattice (right, crystal structures were obtained by the group of Prof. C. Lehmann and refined by Dr. Bernd M. Schmidt). The figure was reproduced from ref. [79] with permission from the Royal Society of Chemistry.

To access the porous network that exists inside the crystalline material of **FC1**, the solvent must be evaporated while keeping the cages and the crystal lattice intact. The onset decomposition temperature of **FC1** is 373 °C, which is significantly higher than that of the non-fluorinated isostructural analogues (≈ 300 °C)**.** As the **Tri^{4}Tri^4** cage features excellent thermal stability, the cage was investigated regarding the uptake of gases.

Gas uptake

Needle-shaped crystals that were filtered off directly from the reaction mixture were dried and degassed for 16 hours at 80 °C and 10^{-3} mbar. Based on its nitrogen uptake, an apparent surface area of SA_{BET} = 536 m^2 g^{-1} could be derived from the BET isotherm, which very well agrees with a microporous type I model. It therefore marks the first fluorinated, shape-persistent POC that exhibits a surface area of >50 m^2 g^{-1} and is simultaneously the first **Tri^{4}Tri^4** imine cage, whose intrinsic pores are accessible to gases. Its surface area is similar to that of **CC2** (SA_{BET} = 533 m^2 g^{-1}) and **CC3** (SA_{BET} = 624 m^2 g^{-1}) which are one of the most versatile POCs created to date.[45b]

FC1 was further analyzed for its uptake of CO_2 and H_2 (Figure 39). The fluorinated POC is able to take up 19 wt% of CO_2 (4.2 mmol g^{-1}, 273 K and 1 bar) and 1.5 wt% of H_2 (7.5 mmol g^{-1}, 77 K and 1 bar).

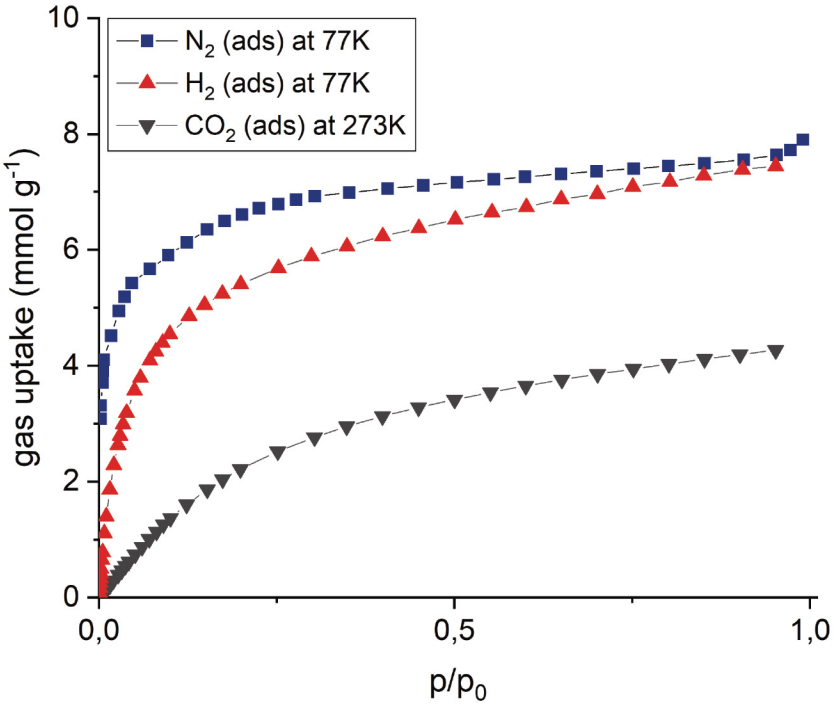

Figure 39: Gas adsorption isotherms for N_2 at 77 K (blue), H_2 at 77 K (red) and CO_2 at 273 K (grey).

Both values rank among the highest reported for similarly-sized POCs.[9] **CC3** (2.5 mmol g^{-1} CO_2 and 5.0 mmol g^{-1} H_2) is similar in size and also has comparable cage windows, but exhibits only ~66% of the CO_2 and H_2 uptake of **FC1**, albeit **CC3** exhibits a higher uptake of N_2. This phenomenon is in accordance with the reported increased CO_2-philicity upon the introduction of fluorine atoms in porous framework materials.[60] The very polar C–F bond can interact with the easily polarizable H_2 and CO_2, resulting in a strong binding event.

3.3.4. Gas- and solution phase properties

Analysis in the gas phase

When **FC1** was investigated *via* MALDI MS analysis, considerably intense signals for protonated dimers of **FC1** were observed. Recent reports of interlocked covalent organic cages motivated the investigation of the sample, regarding interlocked sparingly soluble species.[81] Using ESI MS/MS to prove the existence of interlocked species, collision-induced dissociation (CID) experiments were performed in the group of Prof. C. A. Schalley (FU Berlin) by Hendrik V. Schröder. The fragments that are generated by CID can then be analyzed *via* ion mobility mass spectrometry to rule out or confirm the existence of catenated species.[82] A sample solution of chloroform/acetonitrile (9:1) containing **FC1** was ionized by ESI. The signal $[2M+H]^+$, that corresponded to the

protonated dimer (m/z 2618), was isolated and subjected to CID with different collision voltages, using the monomolecular $[M+H]^+$ (m/z 1309) as a reference (Figure 40).

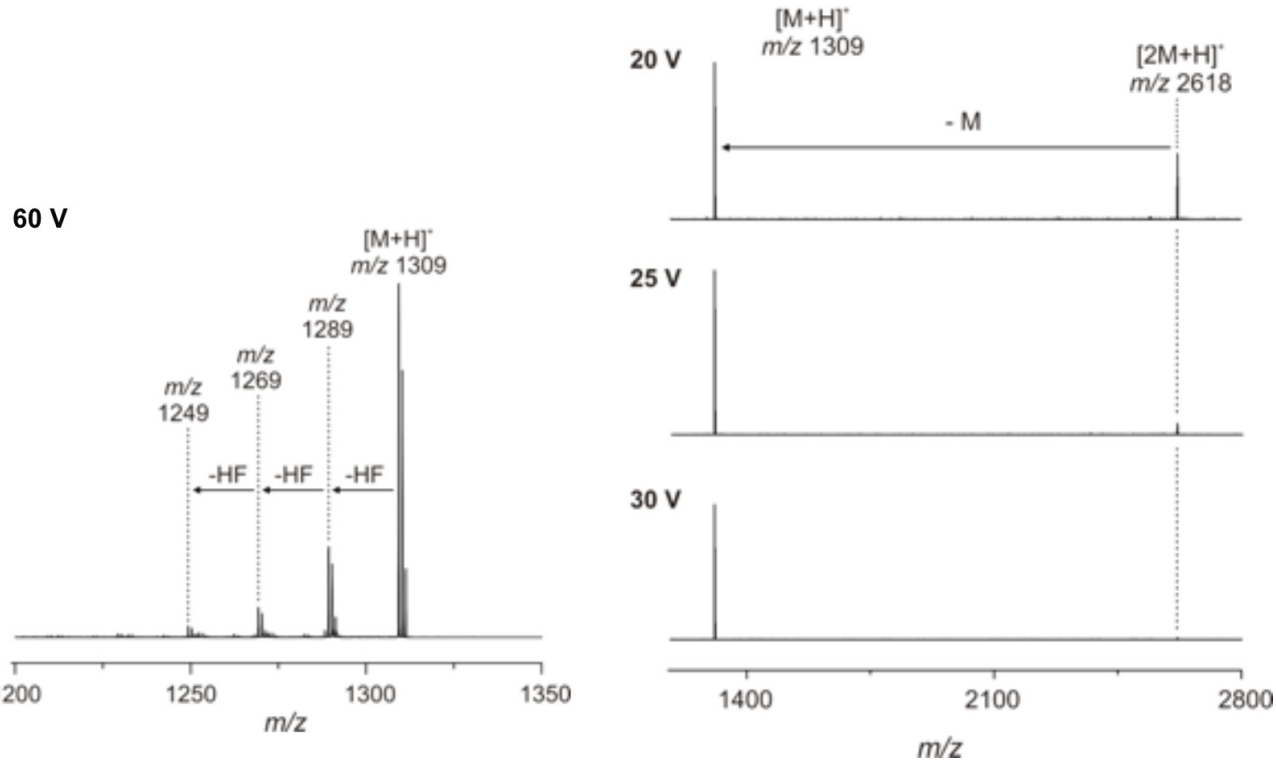

Figure 40: CID Experiment (collision voltage: 60 V) of the mass-selected signal *m/z* 1309 (left); CID experiments of the imine cage **FC1** with mass selected signals *m/z* 2618 at different collision voltages (conducted by Hendrik V. Schröder in the group of Prof. C. A. Schalley at FU Berlin). The figure was reproduced from ref. [79] with permission from the Royal Society of Chemistry.

The monomolecular ion shows no signs of decomposition until a collision voltage of 60 V, whereas the dimolecular ion is already converted into the monomolecular ion at 20 V. This is a clear sign against catenation and is therefore only indicative of a strong supramolecular interaction between adjacent cage molecules of **FC1**.

The 'janus-like' inner surface of the imine cage, with alternating electron-rich and electron-deficient aromatic rings, poses an interesting opportunity for the formation of host-guest complexes with aromatic molecules. A series of aromatic compounds were investigated for the formation of a host-guest complex with **FC1**. A solution of **FC1** was sonicated with an excess of each aromatic guest and was then subjected to ESI MS (Figure 41).

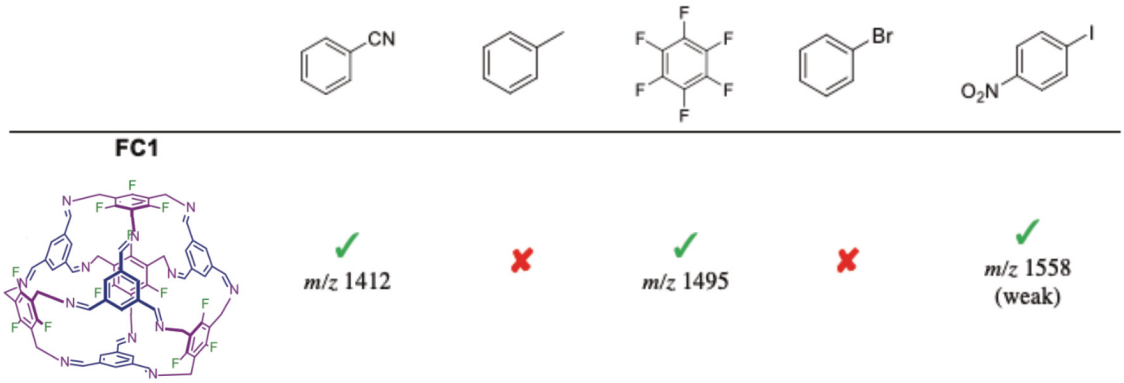

Figure 41: Overview of complexes that could be observed in the ESI-MS of **FC1** with different aromatic molecules (conducted by Hendrik V. Schröder in the group of Prof. C. A. Schalley at FU Berlin). The figure was reproduced from ref. [79] with permission from the Royal Society of Chemistry.

Only electron-deficient aromatic molecules formed complexes that survived the electronspray ionization process and could be detected. When the acetonitrile-complex ion was mass selected and subjected to CID, a decomposition could be detected at 20 V. Again, this is proof that the complex was not inclusive but rather formed through supramolecular binding on the exterior surface of **FC1**.

Properties in the solution phase

Since **FC1** was able to form strong supramolecular complexes on its surface in the gas phase, the investigation was extended to the solution phase. To render **FC1** soluble in common organic solvents, the imine bonds were reduced in refluxing methanol with an excess of sodium borohydride. The reaction required harsher conditions and the yield was considerably lower when compared to the ease of previous fluorinated imine cage reductions (Scheme28).

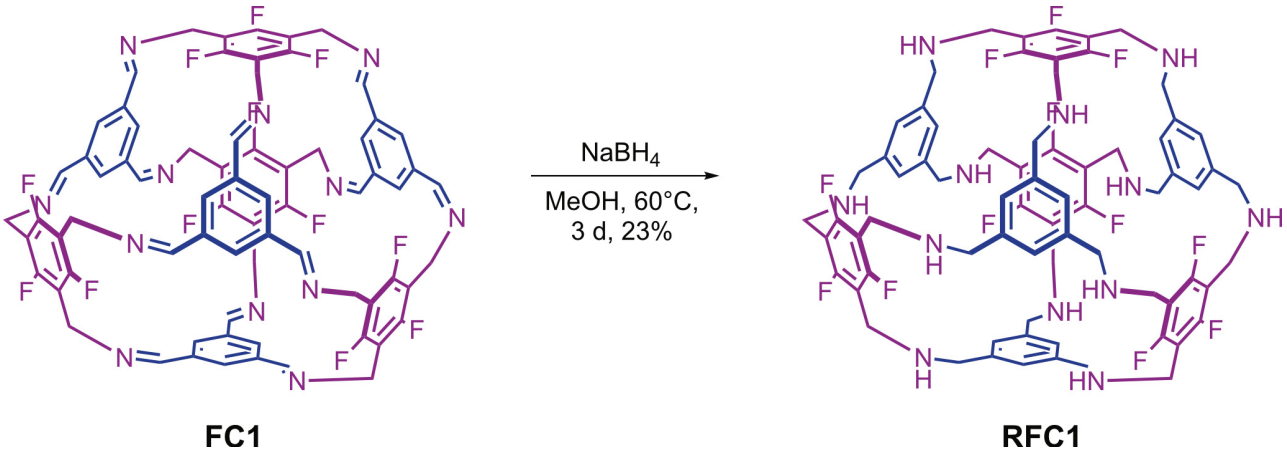

FC1 **RFC1**

Scheme 28: Reduction of the imine cage **FC1** to the amine cage **RFC1**.

RFC1 exhibited increased solubility in organic solvents and was again mixed with the aromatic compounds in a water/*iso*-propanol/formic acid (50:50:1) mixture and then subjected to ESI MS experiments. No signals for a complex formation could be observed. The very polar nature of the amine bonds could be an obstacle to the formation of unpolar π–π stackings between the cage and the aromatic compounds. Another explanation could be the collapse of the cavity inside **RFC1** that would eliminate the contact area for complex formation on both the inside and the outside.

3.3.5. Summary

In this chapter, the successful synthesis of the fluorinated **Tri^{4}Tri^4** imine cage **FC1**, which features a truncated tetrahedral geometry, was discussed. The fluorinated POC could be crystallized in good yields directly from the reaction mixture. Since **F-Amine** has a low rotational barrier of 5 kcal mol^{-1} around the binding axis of the amine group, this result is an important exception to the general rule that cage building blocks need to be pre-organized to form a cage compound in high yields.

When compared to the isostructural non-fluorinated **Tri^{4}Tri^4** imine cages, **FC1** exhibited increased crystallinity and thermal stability. Both features could be attributed to the introduction of fluorine atoms, as this is known to stabilize porous framework materials as well. As **FC1** is the only analogue of the **Tri^{4}Tri^4** cages in which the cage windows remain largely unblocked, the crystalline material should exhibit porosity when investigated by gas sorption measurements. This hypothesis was further strengthened when the crystal structure of **FC1** revealed the existence of a solvent-occupied large intrinsic pore network.

The material could be successfully activated and exhibits a moderately high surface area of SA_{BET} = 536 m^2 g^{-1} and one of the highest uptakes of CO_2 (4.2 mmol g^{-1}, 273 K and 1 bar) and H_2 (7.5 mmol g^{-1}, 77 K and 1 bar) reported for similar sized POCs. In this direct comparison, the increased CO_2- and H_2-philicity can only be explained by the beneficial effect of the introduction of fluorine atoms.

FC1 was further investigated in regards to its host-guest complex-forming abilities. Although the complexes that could be observed in the gas phase proved to be only supramolecular adducts, the fact that they survived the ionization process is indicative of their stability.

In an attempt to explore the solution phase properties of sparingly soluble **FC1**, the cage was reduced to the amine cage **RFC1**. Unfortunately, **RFC1** showed no signs of complex formation with aromatic compounds in neither solution phase nor the gas phase. Both the imine and the amine cages remain the subjects of further gas sorption and complex formation investigations.

Ultimately, the discovery of **FC1** and its investigation represent an important milestone in the field of fluorinated porous materials, as this is the first example in which the beneficial properties of fluorine substitution could be observed in cage-based materials.

3.4. Hybrid POC alloys

3.4.1. Introduction

During the investigation of small **Tri^{2}Di^3** cages, the use of the *para*-substituted fluorinated aldehyde resulted in the formation of **Tri^{4}Di^6** cages when the amines **Et-Amine** or **Me-Amine** were used, respectively.[1] As these cages should be large enough to feature a cavity in which gases or guests could be hosted, they represent an interesting subject of synthetic investigation. Furthermore, the incorporation of six fluorinated building blocks allows for the exploration of a stepwise substitution of these fluorinated ditopic aldehydes for their non-fluorinated isostructural analogues, to minutely examine the influence of fluorine substitution on the cage's properties.

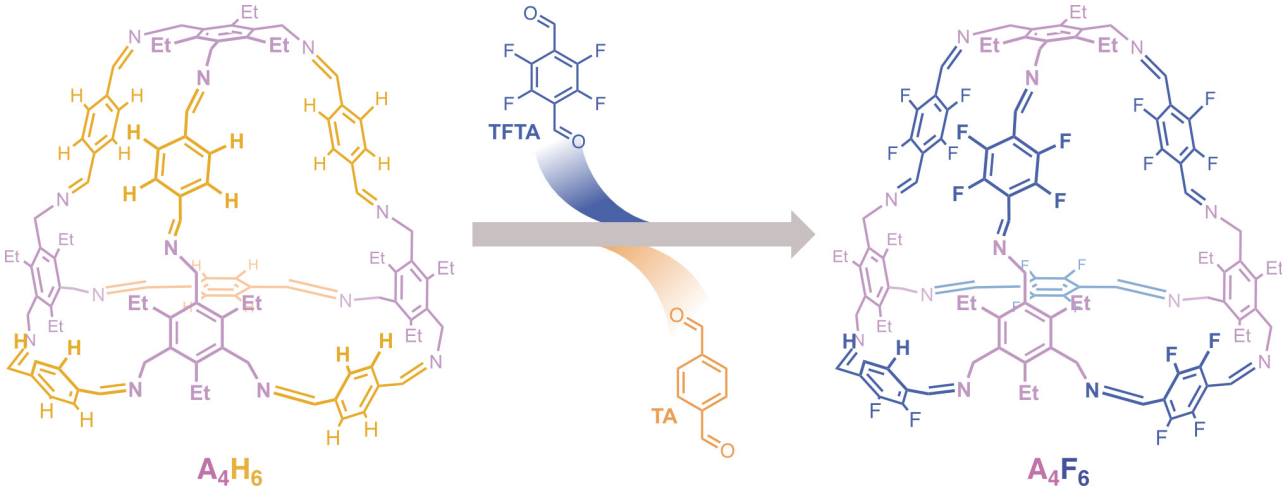

Figure 42: Stepwise substitution of the aldehyde building blocks in **A_4H_6** leads ultimately to the fluorinated cage **A_4F_6**, featuring six fluorinated aldehydes.

Choosing the **Tri^{4}Di^6** geometry, observed during the formation of **FPOC4**, as the subject of this study, it should be investigated how the stepwise substitution of terephthalaldehyde (**TA**), starting from cage **A_4H_6**, against tetrafluoroterephthalaldehyde (**TFTA**), leading to the fully fluorinated cage **A_4F_6**, influenced the cage's formation, crystallinity, thermal stability, and gas uptake (Figure 42). For the generated cage compounds, the systematic nomenclature **$A_4H_xF_{(6-x)}$** in which **A** relates to

[1]Large parts of this chapter were previously published: T. Kunde‡, T. Pausch‡ and B. M. Schmidt, Chem. Eur. J., 2021, 27, 8457–8460; ‡ – both authors contributed equally to this work. Several conclusions in this section were drawn from the master thesis: *Synthesis and Investigation of fluorinated/non-fluorinated porous hybrid materials* by Tobias Pausch.

the number of **Et-Amine** building blocks incorporated, **H** is used as an abbreviation for the count of **TA** molecules, and **F** is used for the count of **TFTA** molecules that are present inside the imine cage, shall be used. From the **Tri^{4}Di^6** topology, the sum of **TFTA** and **TA** molecules must always be equal to six. The large difference in the quadrupole moment and overall electron density between the two aldehydes should have a pronounced effect on the properties of the resulting material.

3.4.2. Synthesis

The library of imine cages that incorporate fluorinated as well as non-fluorinated building blocks, which will be called "hybrid" POCs, can be accessed in different ways. Hybrid cages can either be targeted directly, using **TA** and **TFTA** in the reaction with **Et-Amine,** or alternatively, **A_4H_6** or **A_4F_6** can be synthesized first and then be reacted with the corresponding aldehydes that are currently not incorporated. The former approach offers the precise targeting of every hybrid cage directly from the starting materials, whereas in the latter, the cages need to proceed through several other hybrid cage structures before being able to react to the targeted compound. When combining the building blocks in solution, the dynamic imine library that is created has the potential to reach different states of lower energy, whereas the substitution of a preformed cage introduces an energetic bias by starting from an already low-energy structure. To ensure an unbiased formation study of the hybrid organic cages, the building blocks were stoichiometrically reacted in solution with a specific cage composition as the targeted structure (Figure 43). Considering the regioisomeric structures of **$A_4H_2F_4$**, **$A_4H_3F_3$** and **$A_4H_4F_2$**, the formation of ten **Tri^{4}Di^6** cages is possible from the reaction of **Et-Amine** with 0–6 equivalents of **TA** and/or **TFTA**.

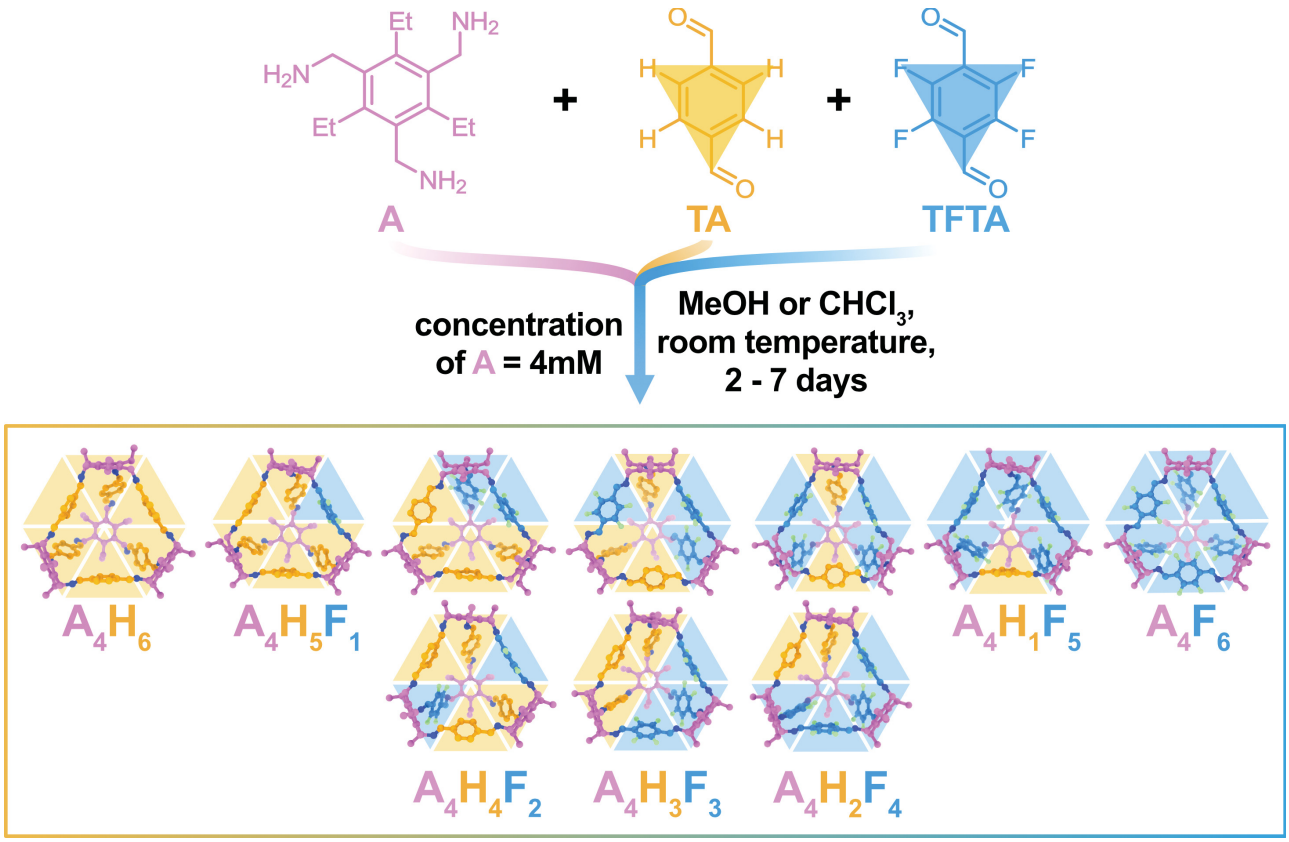

Figure 43: Synthetic scheme of the reaction of amine **A** with **TA** and fluorinated **TFTA**, in different feed ratios, targeting the hybrid cages $\mathbf{A_4H_XF_{(6-X)}}$; the hexagons indicate the corresponding compositions of the hybrid cages throughout the manuscript. This graphic was reproduced from ref. [83] with permission.

Using a slight excess, five equivalents of **Et-Amine** were reacted with various ratios of **TA** and **TFTA** in either methanol or $CHCl_3$ at an amine concentration of 4 mmol L^{-1}. After a period of two days, a colorless precipitate could be isolated by filtration directly from the reaction mixture when using methanol. When $CHCl_3$ is used, the cage along with short-chain oligomers remains dissolved. Analysis by ^1H NMR, ^{19}F NMR and DOSY experiments of the redissolved precipitates surprisingly revealed the formation of multiple cage species, that are observed as broad signals. From the DOSY spectrum the presence of multiple species that share roughly the same diffusion coefficient of D = 4.5 x 10^{-10} m^2 s^{-1} can be deduced. As the corresponding solvodynamic radius is with 9.0 Å similar to previously reported $\mathbf{Tri^4Di^6}$ cages, these results hint at the formation of more cages than just the targeted composition.[84] This hypothesis is confirmed when redissolved samples of the precipitate obtained from the reactions that target the individual hybrid POCs $\mathbf{A_4H_XF_{(6-X)}}$ are analyzed by MALDI MS.

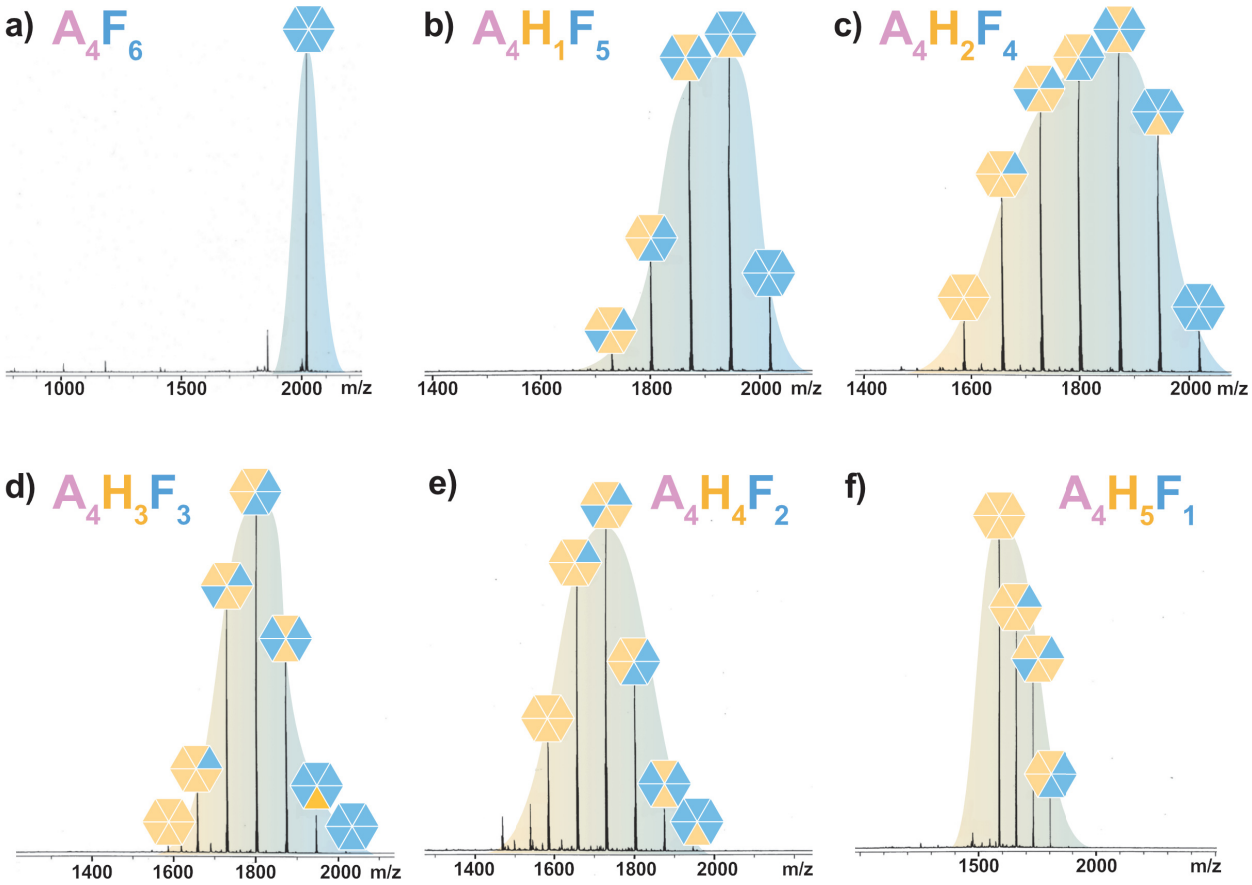

Figure 44: MALDI-MS spectra of pure cage compound a) $\mathbf{A_4F_6}$ and the isolated cage mixtures b) $\mathbf{A_4H_1F_5}$, c) $\mathbf{A_4H_2F_4}$, d) $\mathbf{A_4H_3F_3}$, e) $\mathbf{A_4H_4F_2}$, f) $\mathbf{A_4H_5F_1}$ obtained using different feed ratios of **TA** and **TFTA** with 5 equivalents of amine **A**, inlays each indicate the targeted composition. The compounds were isolated directly from the reaction mixture by either filtration or evaporation of the solvent at ambient temperatures. This graphic was reproduced from ref. [83] with permission.

A narrow gaussian-like distribution of the MS signals around the targeted composition of hybrid cages can be observed (Figure 44). From the MALDI MS spectra, the successful formation of all targeted hybrid cages, the fully fluorinated and the hydrogenated POC, could be confirmed.

The statistical outcome of the reaction is a clear sign that all cages are very similar in their total energy under the given conditions. The investigation, of all ten imine cages presented herein, by DFT calculations (conducted by Dr. Bernd M. Schmidt) revealed that the substitution of one **TA** building block for a **TFTA** building block increased the total energy of the cage compound by roughly 2.8 kcal mol^{-1}. The very low energetic difference between these cage compounds could explain why the reaction outcome follows a gaussian-like distribution. There is no clear energetic bias and also, there could be other effects that are not considered during the gas phase calculations that could reduce these minute energetic differences even further. Since the cages are precipitating from solution, the system could be out of its thermodynamic equilibrium. The observed hybrid cages that are deferring from the targeted composition could be a result of a

kinetic trap, which results in the precipitation of the cage. This causes the equilibrium in solution to be shifted, producing the observed gaussian-like distribution in the MALDI MS spectra.

Because **TFTA** bears highly electron-withdrawing substituents, the difference in reactivity compared to **TA** was investigated. In cases where the cage compound cleanly precipitates from a reaction solution, the completion of the reaction is visible to the naked eye and can also serve as an indicator for the reactivity of the used building blocks. To judge the completion of the reaction from the start of precipitation, the complete solubility of oligomeric intermediates must be ensured. In recent sections about fluorinated imine cages, chloroform was able to dissolve not only most of the cage compounds, but also no sign of precipitating oligomeric species was observed. Hence, methanol was used to study the reactivities of **TFTA** and **TA** with the naked eye, $\mathbf{A_4H_6}$ and the $\mathbf{A_4H_5F_1}$ mixture started to precipitate after 24 hours, whereas all cage alloys that incorporated more than one **TFTA** molecule into the targeted structure precipitated after less than 1 hour. This already hints at a faster reaction and therefore higher reactivity of the fluorine-containing building blocks.

To further strengthen the foundation of these initial results, the formation of $\mathbf{A_4H_3F_3}$ from the building blocks was investigated with ^{1}H NMR analysis (Figure 45).

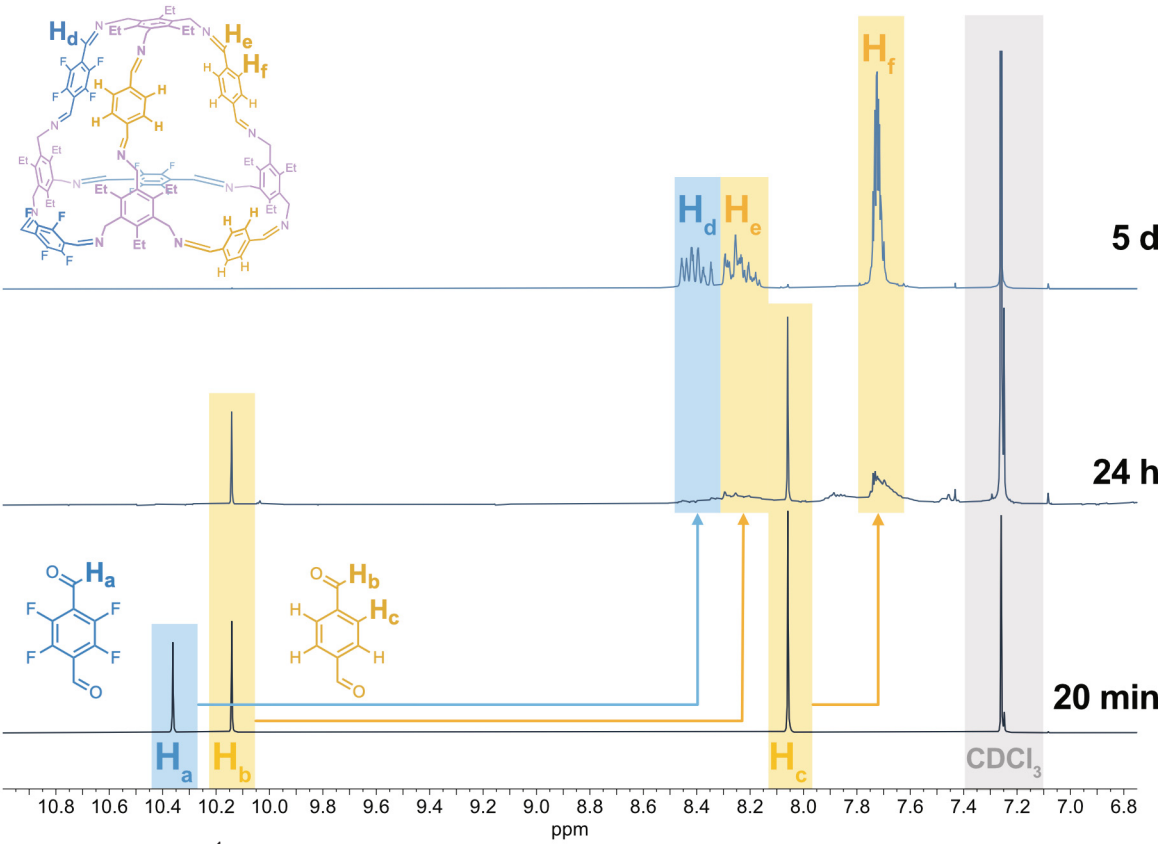

Figure 45: Stacked ^{1}H NMR spectra of the reaction mixture targeting the cage $\mathbf{A_4H_3F_3}$ after 20 minutes (bottom) and 24 hours (middle) and reference spectrum of the reaction mixture after 5 days in methanol (top). Blue lines indicate an assignment to the fluorinated building block, yellow lines where used to show the contributing non-fluorinated building blocks. This graphic was reproduced from ref. [83] with permission.

Initially, two signals corresponding to the chemically different deshielded formyl protons can be observed with their signals at ~10 ppm. After a few hours, the formation of precipitate could be observed along with the complete consumption of **TFTA** after 24 hours. The low intensity of new signals corresponding to imine formation, can be explained by the flexibility of the generated oligomeric and cage species. Additionally, precipitating oligomeric species that contain high amounts of fluorinated building blocks and act as reservoirs without being removed from the dynamic system completely, do not add to the signals intensity. Redissolved, low mass species can then react with the remaining, less reactive **TA** molecules to form a distribution of hybrid cage compounds around the targeted $\mathbf{A_4H_3F_3}$ cage accompanied by low mass oligomers, after 5 days.

The faster reaction of the fluorinated building blocks compared to **TA** can be attributed to their higher reactivity. Surprisingly, all $\mathbf{Tri^4Di^6}$ cages are very close in their total energy, which leads to the formation of a distribution of cage compounds around the targeted hybrid cage composition. These findings provide a valuable insight into the cage formation dynamics of fluorinated building blocks and are an important addition to the recent investigations of hydrogenated and deuterated $\mathbf{Tri^2Di^3}$ imine cage compounds.[64]

3.4.3. Solid state properties

Thermal stability

With increasing fluorine content in the series of hybrid cage alloys, the onset decomposition temperature of the material is increasing accordingly (Figure 46).

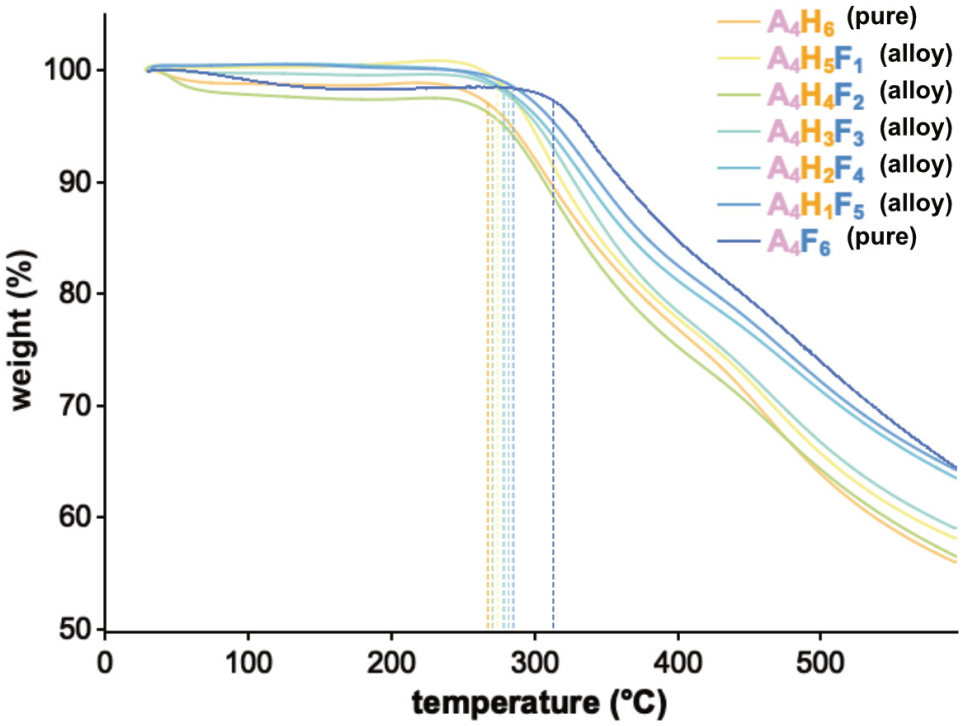

Figure 46: Thermogravimetric analyses of all hybrid cage alloys and the pure cage compounds; the dotted lines indicate the onset temperature of decomposition. This graphic was reproduced from ref. [83] with permission.

The decomposition temperature rises by about 5 °C with each subsequent substitution of a **TA** for a **TFTA** molecule, from 266 °C for $\mathbf{A_4H_6}$ to 313 °C for $\mathbf{A_4F_6}$. This result is in good agreement with the known effect of fluorine introduction on the thermal stability of porous framework materials.

Crystallinity

Single crystals of all alloys and $\mathbf{A_4F_6}$, except for $\mathbf{A_4H_6}$ and $\mathbf{A_4H_5F_1}$ could be grown by slow evaporation of a chloroform solution containing the redissolved precipitate of the targeted composition. The single-crystals of the hybrid cage compounds did *not* consist of only one cage structure, but featured the same gaussian-like distribution throughout the crystal lattice that could be observed in the as-synthesized samples. The macromolecular shape of the crystals is rhombohedral, and the cage alloys exhibit the highly symmetric rhombohedral space group *R-3*, with two *para*-substituted building blocks and one whole and a third molecule of **Et-Amine** in the asymmetric unit (Figure 47). The **TFTA** and **TA** motifs can be exchanged freely in the crystal lattice at the available two crystallographically independent positions and can also be moved by the representative symmetry operations. The average fluorine content was estimated from the diffraction data and is in excellent agreement with the data derived from MALDI MS signals in the spectra of the crystalline materials (see Section 5.5).

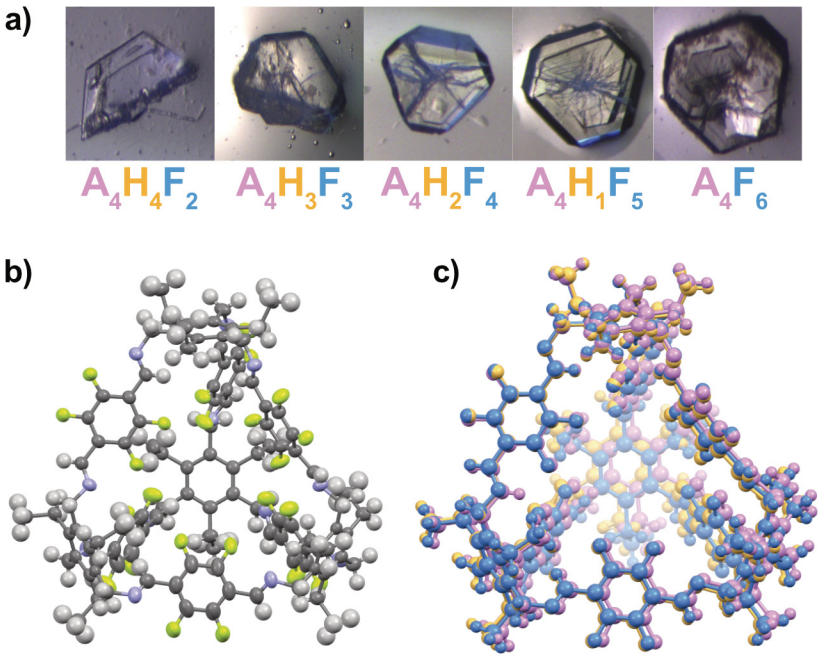

Figure 47: a) microscopic photographs taken of single-crystals before XRD measurements; b) Structure of $\mathbf{A_4H_2F_4}$ obtained from SXRD data; the structure was measured at 100 K and solved in the rhombohedral *R-3* with R_{Int} = 0.1182, R_1 = 0.0931 and wR_2 = 0.3157, the fluorine content is estimated to be 48 percent for both crystallographically unequal fluorobenzenes within the structure (the variance is the highest for $\mathbf{A_4H_2F_4}$ because of a low resolution and framework disorder, see the appendix); solvents are omitted for clarity (crystal structures were obtained and refined by Dr. Bernd M. Schmidt); c) overlay of the crystal structures for $\mathbf{A_4F_6}$ (blue), $\mathbf{A_4H_1F_5}$ (pink) and $\mathbf{A_4H_2F_4}$ (orange). This graphic was reproduced from ref. [83] with permission.

An overlay of the crystal structures for $\mathbf{A_4F_6}$, $\mathbf{A_4H_1F_5}$, and $\mathbf{A_4H_2F_4}$ shows very minute deviations from the tetrahedral geometry throughout the difference in fluorine substitution. As only the structures that contained the least number of fluorinated building blocks did *not* crystallize, two things can be deduced from this:

a) the introduction of fluorinated compounds into the crystal structure increases the crystallinity of the material while simultaneously leaving the cages' individual structures almost completely unaltered
b) the unprecedented interchangeability of the complete cage molecule combined with the interchangeability of individual building block motifs in the crystal lattice shows that fluorine and hydrogen are, albeit their very different electronic nature and their macroscopic influence on the material, very similar in their steric bulk.

Porosity

When the hybrid alloy crystals are investigated in their packing, the window-to-window packing motif between two adjacent cages can be observed. Two cages form an elliptical pore that is 18 Å in length. These “cage pairs” are connected by π–π stacking at a distance of 3.5 Å. The stacking of the **Et-Amine** motifs is hampered by the bulky ethyl substituents, leading to a larger distance of 4.5 Å between the amines of neighboring cages. Ultimately, the pores formed by the cage pairs remain isolated, creating a 0D pore inside the crystal lattice and essentially rendering the material non-porous. Extrinsic pores that are occupied with solvent molecules are too small in diameter to form a network in which guests or gas molecules could be incorporated.

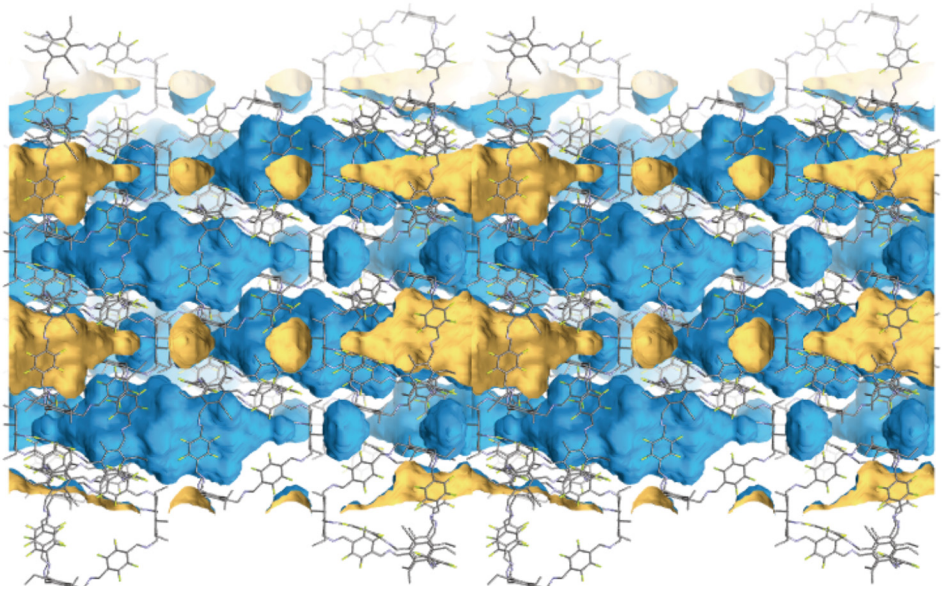

Figure 48: Solvent accessible surface area without solvents for a molecular probe with 1.2 Å radius (outer surface area = blue, inner surface = orange) within the crystal lattice of $\mathbf{A_4H_1F_5}$ (crystal structure was obtained and refined by Dr. Bernd M. Schmidt). This graphic was reproduced from ref. [83] with permission.

Therefore, it is of no surprise that after the thermal treatment of crystalline cage samples at 80 °C at 10^{-3} mbar for 16 hours, no porosity was observed during gas sorption measurements.

3.4.4. Summary

In this section, the influence of fluorine substitution on the synthesis, thermal stability, crystallinity, and porosity of imine cages was investigated. As a result, the formation of ten different $\mathbf{Tri^4Di^6}$ imine cages could be reported, of which nine are at least partially fluorinated. Using five equivalents of **Et-Amine** and varying equivalents of **TA** and **TFTA**, seven different cage compositions were targeted. By close examination of the rate of product formation, it could be proven that fluorinated aldehydes exhibit a higher reactivity in the cage formation reaction compared to

isostructural non-fluorinated building blocks. This is further supported by the faster formation of products and by the results of kinetic competition NMR experiments.

DFT calculations revealed that the resulting hybrid cage structures are all very close to each other in their total energies. This could be an explanation for the observed statistical distribution of cage compounds around a target composition instead of the clean formation of a single product.

Again, the beneficial effect of fluorine substitution on thermal stabilities could be observed as the subsequent introduction of more fluorinated building blocks led to an increase in the onset decomposition temperature from 266 °C to 313 °C.

Single crystals were obtained from all hybrid cage mixtures except for $\mathbf{A_4H_6}$ and $\mathbf{A_4H_5F_1}$. The crystal lattices did not consist of a single hybrid cage molecule but rather exhibited a gaussian-like distribution of hybrid cage molecules around the targeted structure, similar to the amorphous samples. The generation of crystalline hybrid cage alloys is proof of the beneficial influence of fluorinated building blocks on the material's crystallinity and culminates in the generation of a decernary crystal in which 10 different molecules (when isomeric structures are counted) co-exist in one singular crystal lattice.

Although two adjacent hybrid imine cages are packed in a window-to-window motif, the resulting 18 Å long cavity remains isolated due to unfavorable crystal packing and forms a zero-dimensional pore.

Nevertheless, the discovery of the hybrid cage alloys is unprecedented in the field of supramolecular chemistry and is also the first decernary co-crystal. Together with the proven beneficial influence on cage formation rate, thermal stability, and crystallinity, this study of fluorine substitution in organic imine cages marks another milestone for fluorinated POCs.

3.5. Large fluorinated cages

3.5.1. Introduction

The cages that were discussed in the previous sections, all but one, suffered from a cavity that was too small to accommodate either guests or gas molecules in the solid state. The best approach to generating larger cage compounds would be to increase the size of the cavity by either changing the topology or using building blocks in which the distance between the functional groups is increased compared to previously used building blocks.

Two structural motifs that would be very likely to ensure a cage with permanent porosity or enable the encapsulation of a variety of organic guests are shown in Figure 49.

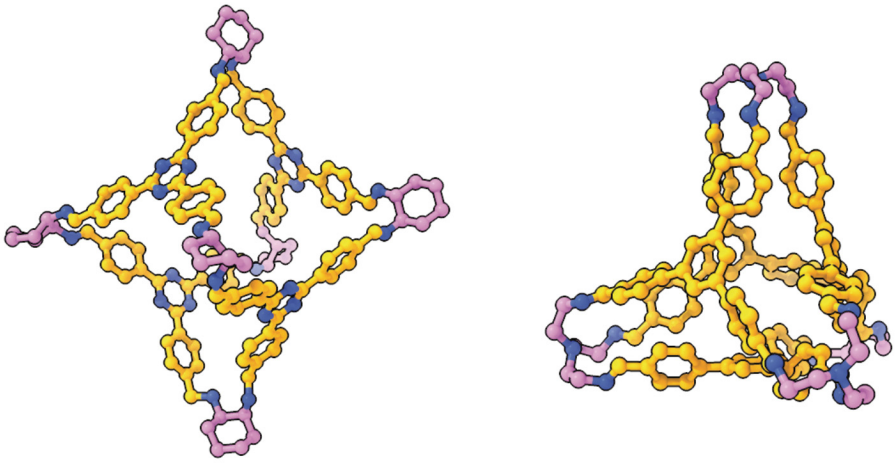

Wang *et al.* **Sessler *et al.***

Figure 49: Porous shape-persistent **Tri^{4}Di^6** cage investigated by Wang *et al.* (left) and **Tri^{4}Tri^4** imine cage that is able to encapsulate white phosphorous and was reported by Sessler *et al.* (right).[27,85]

In 2015, the Wang group reported the targeted synthesis of a large triazine-incorporating **Tri^{4}Di^6** cage. Using the geometry of Cooper's **CC3** cage and of Fujita's **M_6L_4** octahedron as inspiration, they designed and synthesized the cage from the reaction of four equivalents of 1,3,5-tris(4-formylphenyl)-2,4,6-triazine and six equivalents of (*R,R*)-**DACH**. The cage proved to be shape-persistent and featured a large apparent surface area of SA_{BET} = 1181 m^2 g^{-1}. It also exhibited a considerably high CO_2 uptake, which was attributed to the triazine core.[27,86]

Sessler *et al*. used four equivalents of TREN and four equivalents of 1,3,5-tris(4-formylphenyl)benzene to synthesize the **Tri^{4}Tri^4** cage that did not exhibit shape-persistency or porosity but was able to act as a host for the white phosphorous modification, P_4, by opening its windows. Interestingly, they reported that either fluorine substituents at the formyl-containing benzene rings or a triazine core, which causes the aldehyde to become planar, hampered the formation of the cage, resulting in the formation of an oligomeric mixture. These findings were attributed to C–H···π interactions between neighboring benzene rings at the TREN motifs, which are critical for successful cage formation and can only be formed when the aldehydes have at least a slight dihedral angle between the core and the phenyl substituents. No C–H···π interactions could be formed in the fluorine-containing aldehyde, and the C–F···π interactions appeared to be repulsive. The planar triazine aldehyde could also not form these stabilizing interactions as the geometrical shape of the molecule prohibited it.

The **Tri^{4}Di^6** and the **Tri^{4}Tri^4** motif presented here provide an excellent opportunity to study the formation and host behavior of large fluorinated imine cages in solution on the one hand and the synthesis and properties of larger fluorinated porous cages in the solid state on the other hand. The results of the investigations into the synthesis, solid-state and solution phase properties are discussed in this chapter.

3.5.2. Synthesis of the building blocks

Synthesis of the building blocks

One of the main features in both cage motifs presented is the use of a tritopic large aldehyde. If this motif could be reproduced using fluorinated aldehydes, this would open up a wide range of opportunities for cage molecules but also for framework materials and porous organic polymers alike.

A large tritopic fluorinated aldehyde that has previously been synthesized is 1,3,5-tris(4-formyltetrafluorophenyl)-benzene (**31**).[88] Aldehyde **31** has in the past been used for the synthesis of porous organic polymers and two-dimensional covalent organic frameworks. The linker either increased the uptake of CO_2[87a] or the crystallinity of the resulting material,[87b] making it an interesting candidate for the synthesis of fluorinated porous organic cages.

Aldehyde **31** could be synthesized in a four-step synthesis from 1,2,4,5-tetrafluorobenzene on a multi-gram scale (Scheme 29).

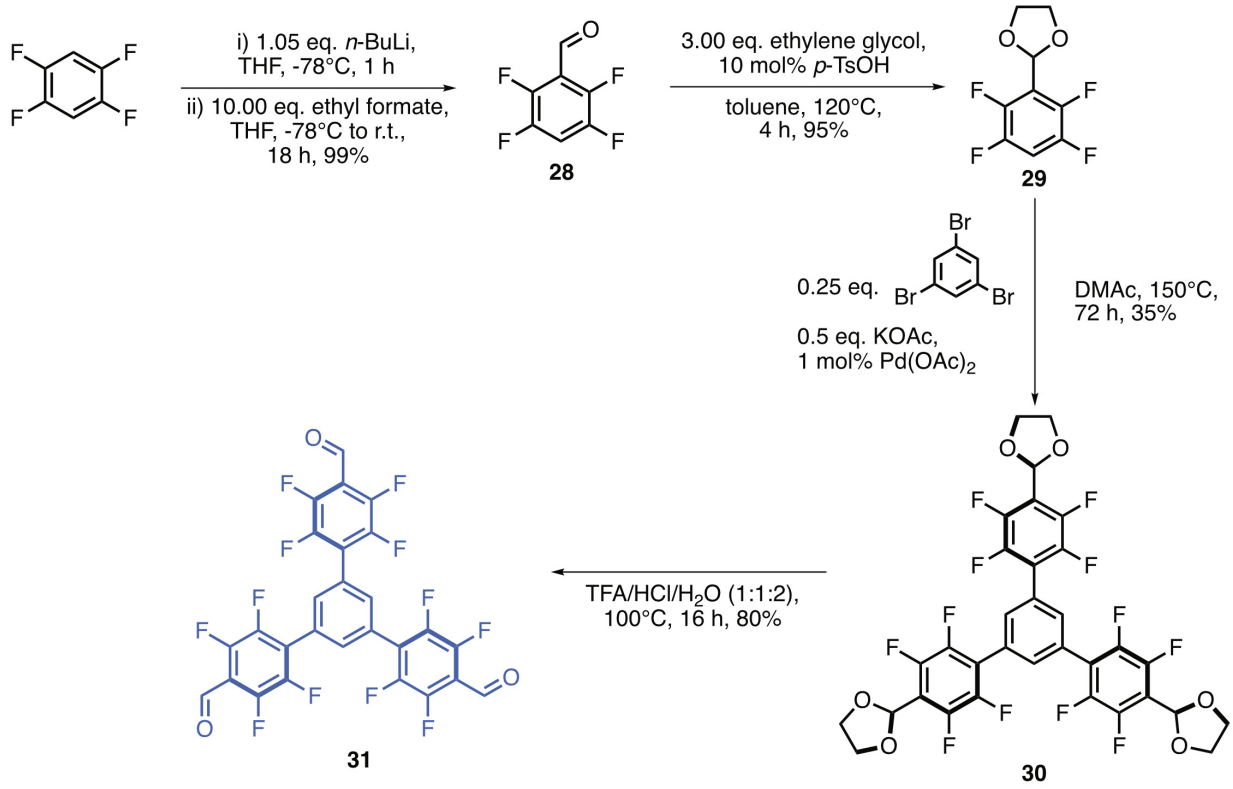

Scheme 29: Synthesis of the large tritopic fluorinated aldehyde **31** starting from tetrafluorobenzene.

In a first, high-yielding step, 1,2,4,5-tetrafluorobenzene is mono-lithiated and then reacted with ethyl formate to generate the formylated compound **28**. The protection of the aldehyde with ethylene glycol results in the almost quantitative formation of the acetal **29**. The trifold arene-coupling at the 1,3,5-tribromobenzene is realized in a 35% yield using an excess of acetal **29** in a C–H activation reaction. The resulting triacetal **30** can then be deprotected under harsh acidic conditions in very good yields, resulting in the formation of the tritopic aldehyde **31**. In this fluorinated aldehyde, the fluorine substituents are facing sterical repulsion between adjacent aromatic rings, resulting in a dihedral angle between the benzene core and the fluorinated rings. As this angle could become an obstacle during the synthesis of the targeted **Tri^{4}Di^6** cage, in which (*R,R*)-**DACH** is employed, another large tritopic aldehyde was designed.

The large fluorinated aldehyde **34** contains a triazine core instead of a benzene motif, which ensures the complete planarity of the aldehyde due to the absence of hydrogen atoms at the core. This aldehyde is isostructural to the triazine compound used during the synthesis of the large **Tri^{4}Di^6** cage designed by Wang *et al*. and is therefore even more promising to yield the targeted cage topology.

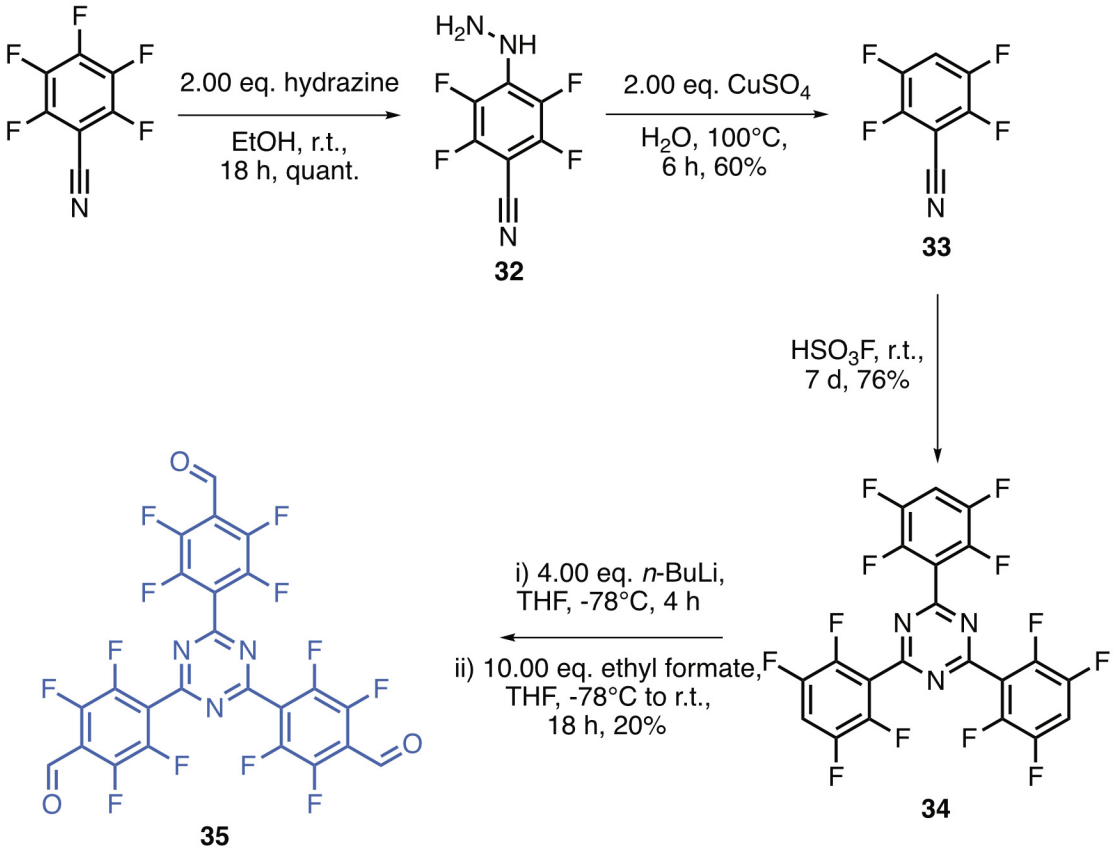

Scheme 30: Four step synthesis of the triazine aldehyde **35** starting from pentafluorobenzaldehyde.

Although the tetrafluorinated benzonitrile **33** is commercially available, its high price tag and long delivery times demand a fast and efficient route from cheaper starting materials (Scheme 30). When pentafluorobenzonitrile is reacted with hydrazine, the hydrazino group-containing compound **32** is obtained quantitatively. This compound could then be reacted using a copper-mediated cleavage reaction to yield benzonitrile **33**. Trimerization of **33** to the corresponding triazine compound **34** proceeds with good yields when performed in fluorosulfonic acid for 7 days. In the last step, the *para*-hydrogenated triazine compound was reacted with four equivalents of *n*-BuLi to yield a trifold lithiated compound after four hours. After the reaction with ethyl formate, a mixture of one-, di-, and triformylated compounds was obtained, which could then be separated by column chromatography to yield trialdehyde **35** in a 20% yield.

This highly fluorinated triazine aldehyde contains very electron-deficient aromatic rings that could possibly be utilized in framework and porous polymer syntheses alike. Although the last step of the synthesis is low-yielding, the cheap starting materials allow for the synthesis of multiple grams of the shelf-stable compound.

To further expand the diversity of large fluorinated tritopic aldehydes, a third molecule was synthesized. The aldehydes **31** and **35** both are considerably flat, extended aromatic panels that

feature a rather unpolar aromatic core. To generate an exception from that rule, the polar aldehyde **37** was designed (Scheme 31).

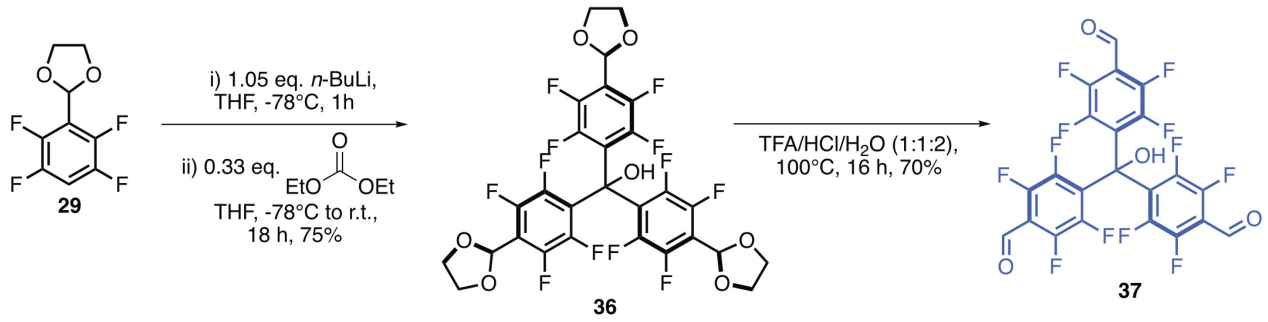

Scheme 31: Three step synthesis, starting from the acetal **29**, to yield the hydroxy-containing large fluorinated aldehyde **37**.

Utilizing the acetal **29** that was synthesized during the creation of the benzene core-containing aldehyde **31**, it was first lithiated with *n*-butyllithium and then reacted with diethyl carbonate to yield the triacetal **36**. This was then deprotected using the same conditions as for the deprotection of **30**, to yield the tritopic fluorinated aldehyde **37** with an overall good yield. The aldehyde **37** features a bonding angle of ~107° between the C–OH and each of the C–C_{ArF} bonds. The close proximity of the benzene rings causes a severe rotation of the aromatic rings to evade a steric clash of substituents. The central hydroxy group should exhibit considerably high acidity due to three very electron-withdrawing substituents at the adjacent carbon atom.

With three structurally similar but chemically different large fluorinated tritopic aldehydes, **31**, **35**, and **37**, in hand, a series of cage topologies were targeted and investigated.

3.5.3. TREN-based cages

Synthesis of the cage compounds

Starting with TREN as the amine building block, all three aldehydes were reacted in a 1/1.2 aldehyde to amine ratio to generate shape-flexible **Tri^{4}Tri^4** imine cages. When the aldehyde **31** is used, an isostructural compound of the non-fluorinated cage developed by Sessler *et al.* would be generated (**FPOC10**). If the triazine aldehyde **35** is reacted with TREN, the resulting cage **FPOC11** would contain very rigid planar aromatic panels that possibly feature a large binding site for electron-rich guests. Using the bent hydroxy containing aldehyde **37**, the resulting cage **FPOC12** would deviate from the truncated tetrahedral geometry that would largely be maintained by the

other derivatives, this could result in larger cage windows that are even more flexible as no aromatic core is featured in the panels (Figure 50).

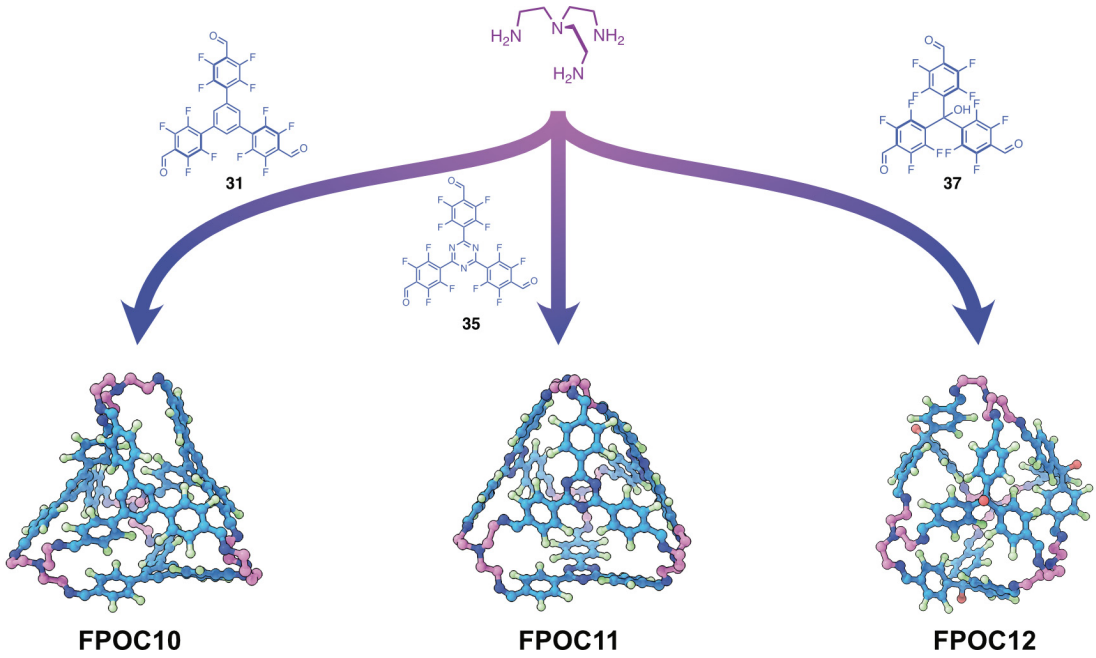

Figure 50: Reaction of TREN with different aldehydes leads to cages that are similar in their size and could be used to accomodate various guests in solution. Depicted structures were calculated using a universal force field (UFF-8) approach.

Different solvents and reaction conditions were screened for the synthesis of **FPOC10**. The most optimal conditions were the reaction of 4 equivalents of **31** with 4.8 equivalents of TREN in chloroform for 3 days. MALDI MS confirmed the clean formation of **FPOC10** as no oligomeric species could be observed ([**FPOC10**+H]$^+$ calculated: 2793.543 m/z, found: 2793.547 m/z). By adding *n*-hexane to the chloroform solution and evaporating the chloroform at room temperature under reduced pressure, the cage compound could be isolated in 60% yield as a yellow solid (Figure 51).

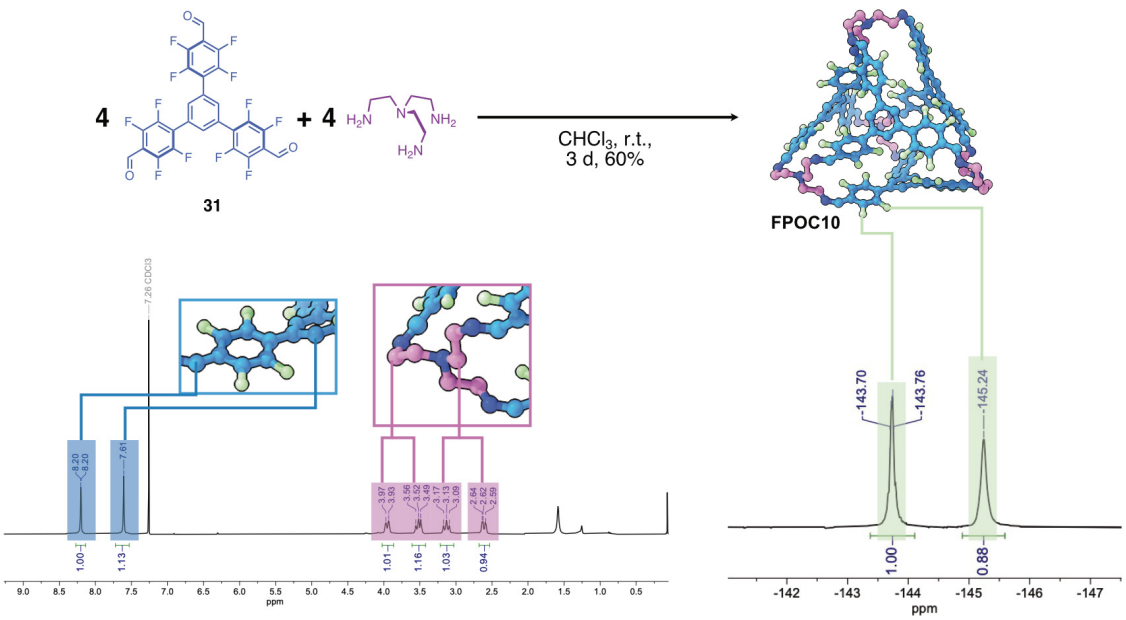

Figure 51: Synthetic scheme of the formation of **FPOC10** from the building blocks (top), ^{1}H NMR (bottom left) and ^{19}F NMR of a redissolved sample of the precipitate directly isolated from the reaction mixture by addition of *n*-hexane.

Only the two expected singlet signals can be observed in the ^{19}F NMR of the redissolved precipitate. In the ^{1}H NMR spectrum, the signals that correspond to the imine proton (8.20 ppm) and to the benzene core (7.61 ppm) can be observed. For the TREN motif, only two chemically distinct species are present, and therefore two doublet signals with an integral of 24 are expected in the NMR spectrum. The appearance of four multiplets each with an integral of 12 can be explained by the chirality that is exhibited by **FPOC10**. Sessler *et al.* reported in their study that because of the C–H···π interactions that stabilize the cage, aromatic panels can be incorporated with all outer aromatic rings rotated clockwise or counter-clockwise against the benzene core. This leads to a helical chirality that is exhibited by the cage. As four sets of signals are observed, this hints at the racemic formation of both the *P*- and *M*-isomer of the cage. The cage's successful formation, despite the absence of stabilizing C–H···π interactions, can be explained by the stabilizing C–F···π_F interactions that exist between neighboring fluorinated aromatic rings at the TREN motifs. Despite the fact that fluorinated aromatic rings have a completely different electronic distribution than non-fluorinated isostructural compounds, the presence of only fluorine substituents converts the observed hindrance of fluorine substitution into a favorable and attractive C–F···π_F interaction. In this regard, the introduction of fluorine atoms cannot be seen as generally unfavorable, but it has to be examined whether *enough* fluorine atoms were introduced to generate binding motifs that are structurally similar to hydrogenated motifs but completely inverted in their electronic nature.

From DOSY measurements, a diffusion coefficient of D = 8.14 x 10^{-10} m^2 s^{-1} was derived. That was calculated to correlate to a hydrodynamic radius of 4.6 Å. This value is considerably small for a **Tri^{4}Tri^4** cage of this size, but may be a result of the fast shape fluctuation that is introduced by the TREN motif.

Since the cavity of **FPOC10** should be large enough to accommodate guests, the encapsulation of isoflurane into the cavity was investigated. Isoflurane is a fluorinated, highly volatile hydrocarbon ether that was once used as an anesthetic but is also known to cause climate change. Therefore, its encapsulation and storage would be of great environmental interest. Different amounts of isoflurane (1, 5, 10, and 20 eq.) were introduced into chloroform solutions of the soluble **FPOC10**. In no scenario could signals that correlate to trapped isoflurane be observed in the ^{1}H NMR or ^{19}F NMR spectra. This either marks isoflurane as an unsuitable guest for the cage compound or is just indicative of chloroform's being an unsuitable solvent for guest encapsulation.

As **FPOC10** incorporates four TREN motifs, it was investigated whether the cage could host metals that could later be used in catalytic applications or act as additional binding sites for guests. When **FPOC10** is reacted with four equivalents of a copper(I) complex in solution, the yellow solution slowly turns red. Surprisingly, no decomposition of the imine cage was observed. Through slow evaporation of the solution, a single crystal suitable for SC–XRD could be grown (Figure 52).

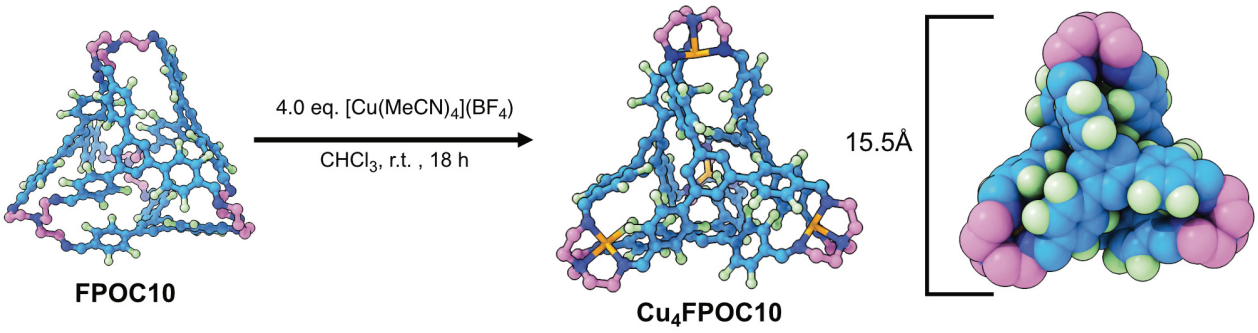

Figure 52: Synthetic scheme to generate the Cu(I)-coordinated cage **Cu$_4$FPOC10** (left), crystal structure with solvent molecules, hydrogen atoms and counter ions omitted for clarity (centre) and space filling model of the crystal structure (right).

In the crystal structure of **Cu$_4$FPOC10**, the encapsulation of four Cu(I) atoms is confirmed along with the hypothesized rotation of the fluorine rings all in a counter-clockwise direction. The overall height of the complex is with 15.5 Å in the range of the previously observed non-metal incorporating TREN-based **Tri^{4}Tri^4** cages. Cu···Cu distances are with 12.0 Å slightly longer than in the previously observed Cu-encapsulation **Tri^{2}Di^3** cage. The space-filling model visualizes that the encapsulation of Cu(I) ions closes the intrinsic pore in the solid state by reducing the distances

between adjacent aromatic panels. This could be a feature for incorporating guests into the empty cage **FPOC10** and then trapping them inside the cavity by the introduction of Cu(I) ions. Furthermore the Cu_4–tetrahedron that is formed inside the cage and is framed by very electron-deficient fluorinated walls, could allow for the rapid encapsulation of electron-rich aromatic guests. The high copper ion density inside this complex could also exhibit an extraordinarily high catalytic activity in copper-mediated reactions as four binding sites are in close proximity of one another. **FPOC10** and its Cu-complex (**Cu_4FPOC10**) remain the subjects for further studies on the host abilities of large fluorinated imine cages in solution.

FPOC10 and **Cu_4FPOC10** were investigated regarding their gas sorption properties, but were found to be non-porous after thorough activation at 80 °C for 18 hours at 10^{-3} mbar.

When the triazine aldehyde **35** is reacted in various solvents with 1.2 equivalents of TREN, only minute amounts of the targeted cage **FPOC11** can be observed in the MALDI MS spectra. Isolation, analogous to that of **FPOC10**, by precipitation results in only very low yields of a yellowish solid. If redissolved, this solid proved to be a mixture of various imine structures in which no clear indices of the cage compound were found in the NMR spectra.

Interestingly, when the aldehyde **37** is used, no signs of an imine cage can be found in either the MS nor the NMR spectra. These findings are thought to be the result of the previously mentioned critical C–H···π or C–F···π_F interactions, which appear to be required to form this cage geometry. In the planar aldehyde **35,** no rotation of the fluorinated rings is possible. As a result, no interactions between the neighboring rings in possible intermediates can be formed, so that no stabilization is gained. Aldehyde **37** exhibits a very different geometry from the other two fluorinated tritopic aldehydes and appears to be a “mismatch” in this delicate ‘puzzle’ of building block geometries, which prohibits the formation of **FPOC12**.

3.5.4. 1,3,5-Tris(aminomethyl)-based cages

After the discovery of **FC1** and its outstanding gas sorption properties, the synthesis of larger **Tri^4Tri^4** imine cages using even more extensively fluorinated building blocks was envisioned. By using the fluorinated aldehydes **31**, **35**, and **37** in conjunction with **Et-Amine,** the overall geometry of **FC1** should be maintained while simultaneously opening up the cage windows to increase the accessibility of the inner cavity.

Reacting four equivalents of **Et-Amine** with four equivalents of aldehyde **31** would lead to **FPOC13,** which features the slightly rotated fluorinated rings of the aromatic panels. This could either lead to a slightly smaller cavity when the fluorine atoms are pointing inwards, or simultaneously, this would enlarge the cage’s windows for improved guest uptake. It remains to be seen if

the inward rotation causes a sterical repulsion that could eventually even prevent the formation of **FPOC13** (Figure 53).

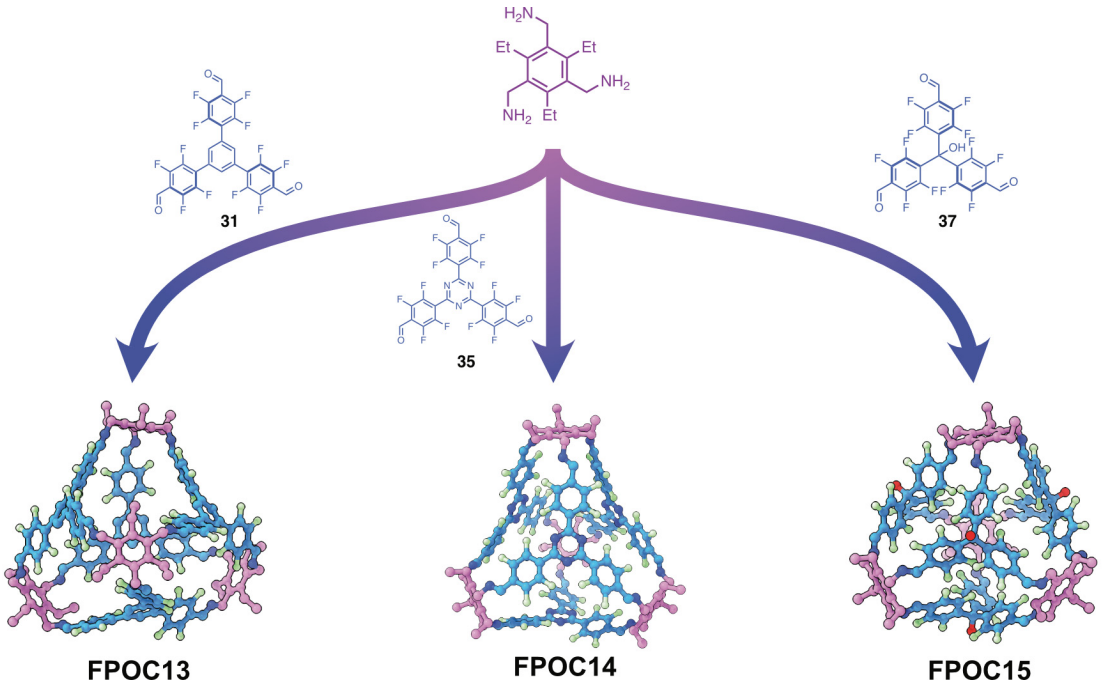

Figure 53: The reaction of **Et-Amine** with different tritopic aldehydes would lead to the formation of three **Tri^{4}Tri^4** cages that are all similar in size but each exhibit unique features that could influence the formation, gas uptake and guest encapsulation properties. The depicted structures are based on calculations using a universal force field approach.

If the triazine aldehyde **35** is used, the truncated tetrahedron introduced by **FC1** (section 3.3) is principally extended, creating **FPOC14**. This cage features very electron-deficient, large aromatic panels that are almost completely planar and could be very potent binding sites for electron-rich aromatic guests.

Using the polar, hydroxy group-incorporating aldehyde **37,** the expected geometry is a slightly distorted version of the truncated tetrahedral shape. The slight bend that is encoded in the aldehyde could increase the size of the cavity, making it slightly more spherical. Since the inward rotation of the fluorinated aldehydes is expected to be the largest of all three aldehydes, this cage (**FPOC15**) would offer an intriguing mixture of a comparatively polar external surface and a highly fluorinated, very hydrophobic inner surface.

The FPOC13 cage

In 52% yield, **FPOC13** could be synthesized from the reaction of 4 equivalents of aldehyde **31** with 4.8 equivalents of **Et-Amine** in a mixture of 1,4-dioxane and methanol. Interestingly, pure solvents either failed to yield the cage product, or a pure methanol precipitate formed after a few hours that

contained only oligomeric structures. In the dioxane/methanol mixture, a precipitate is formed that can be filtered off from the remaining mixture. When both the remainder of the solution and redissolved samples of the precipitate were investigated by MALDI MS analysis, only in the precipitate, signals that could be assigned to the clean formation of **FPOC13**, were found ([**FPOC13**+H]$^+$ calculated: 3205.813 m/z, found: 3205.803 m/z).
The cage proved to be very sparingly soluble in common organic solvents (Figure 54).

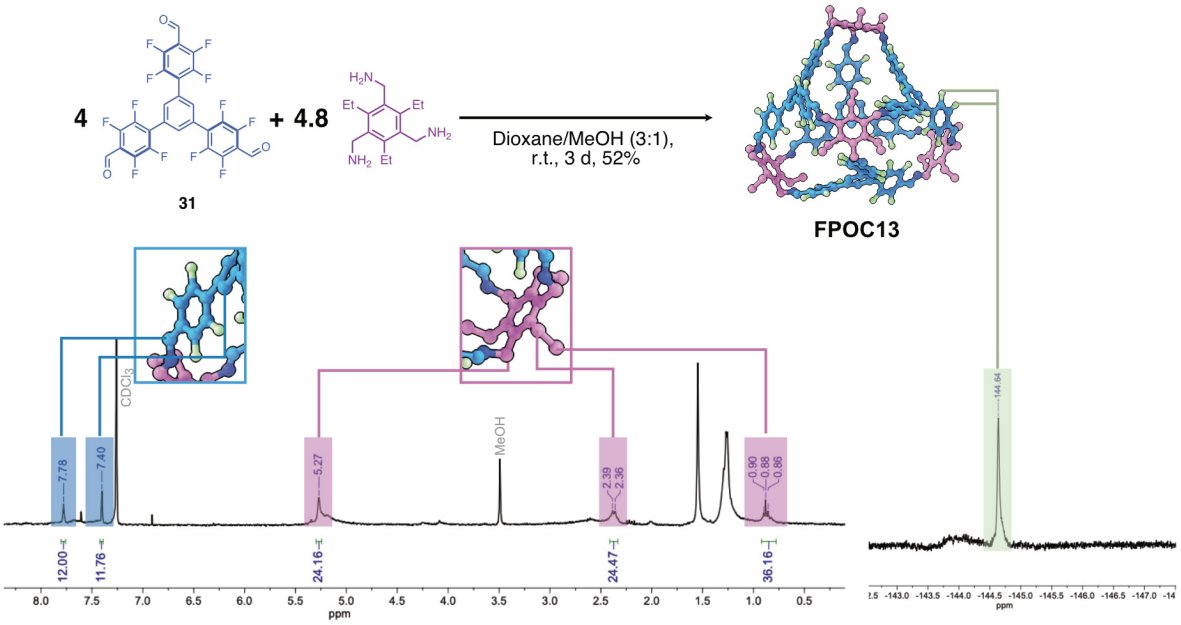

Figure 54: Synthetic scheme of the formation of **FPOC13** (top) and ^{1}H NMR spectrum (bottom left) and ^{19}F NMR spectrum (bottom right) of the sparingly soluble solid, obtained directly from the reaction mixture.

Signals at 7.76 ppm and 7.43 ppm in the ^{1}H NMR spectrum could be assigned to the imine proton and the benzene core in the fluorinated building block. Three signals could also be attributed to the **Et-Amine** motif (5.37, 2.38, and 0.88 ppm). Surprisingly, only one signal is observed in the ^{19}F NMR. Because no other species were detected in the ^{1}H NMR and MALDI MS spectra, and the aldehyde **31** is stable to decomposition under a wide range of conditions, this can only be explained by a shift of the outer fluorine signals, which overlapped with those corresponding to the inner fluorine atoms.

By layering the starting materials dissolved in a chloroform/methanol (1:1) mixture without stirring, large crystals suitable for SC–XRD could be grown. The crystals were heavily solvated, which necessitated the need for them to be measured at DESY's synchrotron diffraction beam line P11 at PETRA III by the team of Prof. Dr. C. Lehman (Max-Planck-Institut for Kohlenforschung, Mühlheim an der Ruhr). Even using synchrotron radiation, a sufficient enough dataset could not be obtained.

In Figure 55, a picture of the large tetrahedral crystals along with the powder X-ray diffraction (PXRD) pattern is shown. The sharp reflexes indicate a high degree of crystallinity throughout the whole sample.

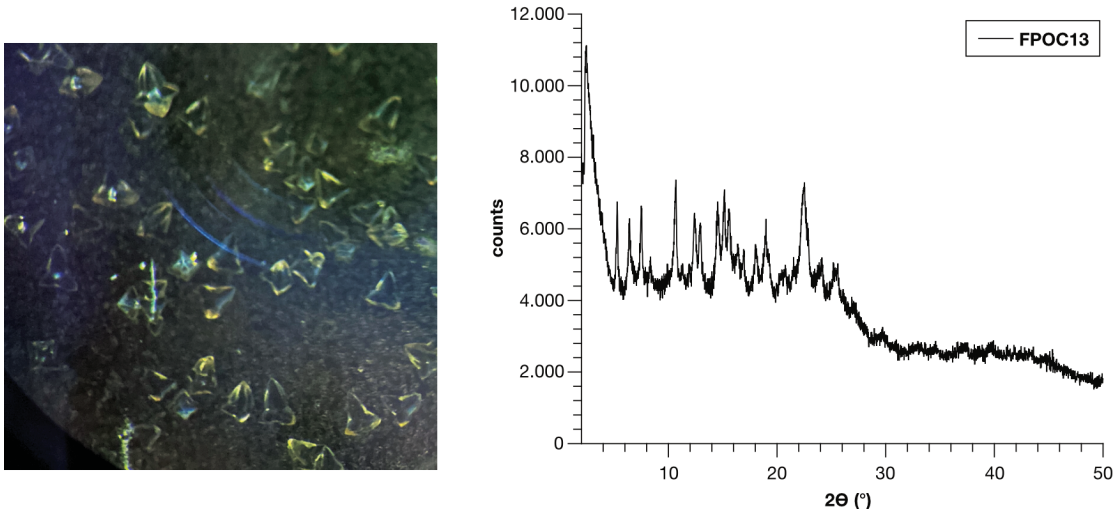

Figure 55: Microscopic image of the yellow tetrahedral crystals obtained directly from the layered reaction mixture (left) and PXRD pattern of the crystals (right).

FPOC13 continues the trend of thermally stable fluorinated imine compounds, as it exhibits a high onset decomposition temperature of 326.3 °C. With a thermally stable crystalline material in hand, the gas sorption properties of the FPOC-containing material were investigated.

The crystalline material featured a surface area of SA_{BET} = 510.6 m^2 g^{-1}. This surface area is comparable to the surface area exhibited by **FC1** (536 m^2 g^{-1}). As **FPOC13** features a cavity that is roughly 1.5 times the size of **FC1,** the surface was considered to be higher. Without a crystal structure, only hypotheses can be drawn as to what the reason behind this lower than expected surface area could be. An observation that has been made in the past for fluorinated organic framework materials is that the introduction of highly fluorinated building blocks reduces the surface area while keeping the gas uptake roughly constant. The larger fluorine substituents formally reduce the space that can be taken up by gas molecules inside the cavity, but the binding event is much stronger, resulting in no change in gas uptake.
Regardless of the surface area, **FPOC13** is able to incorporate up to 11.8 mmol g^{-1} of N_2 into its pores (Figure 56).

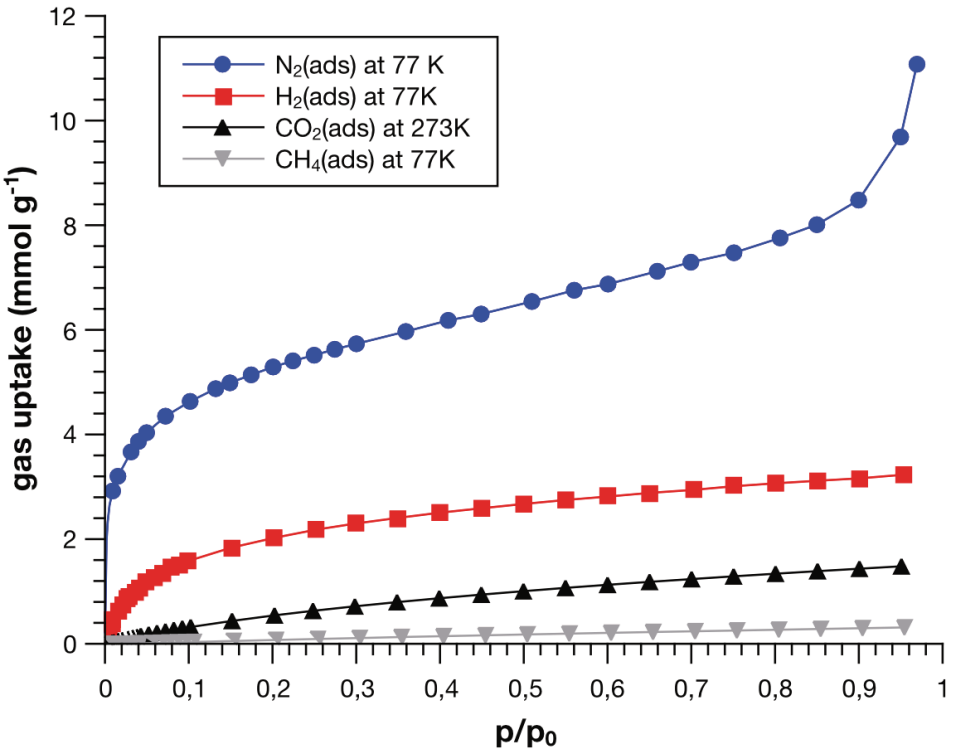

Figure 56: Adsorption isotherms for N_2 (blue), H_2 (red), CO_2 (black) and CH_4 (grey) of a crystalline, activated sample of **FPOC13**.

That is ~ 1.5 times the amount that could be incorporated into **FC1**, agreeing with the cavity size increase. Surprisingly, the porous material was only able to take up 3.2 mmol g^{-1} of H_2 (*vs.* 7.5 mmol g^{-1}, **FC1**) and 1.2 mmol g^{-1} of carbon CO_2 (*vs.* 4.2 mmol g^{-1}, **FC1**), which is a large decrease from the sorption properties exhibited by **FC1**. Furthermore, only minute amounts of the very bulky gas, CH_4, were adsorbed into the material's pores (0.9 mmol g^{-1}). Whether the decreased uptake was caused by an unfavorable crystal packing in which the window-to-window packing is inefficient or the cage's windows are blocked by the ethyl substituents is unknown until the crystal structure is determined. A sample that was not activated at 80 °C for 18 hours showed a remarkably lower surface area of <100 m^2 g^{-1}, hinting at the strong binding of residual solvent inside the cage's pores. Possibly, either a harsher activation protocol must be developed to fully desolvate the porous material and utilize the full potential of the material, or another polymporph of the crystal must be obtained that ensures more favorable packing.

Among similarly sized porous imine cages, **FPOC13** still exhibits good gas sorption properties and even excels in its N_2 uptake capabilities.[9]

FPOC13 marks the largest porous **Tri^4Tri^4** imine cage and the most extensively fluorinated POC reported to date.

Other Tri^4Tri^4 imine cages

When the triazine aldehyde **35** was reacted with 4.8 equivalents of **Et-Amine** in a methanol/

chloroform mixture, the formation of **FPOC14** could be confirmed by MALDI MS experiments ([**FPOC14**+H]$^+$ calculated: 3217.756 m/z found: 3217.786 m/z) along with oligomeric side products. By adding *n*-hexane to the reaction mixture and evaporating the chloroform under reduced pressure, precipitation of a bright yellow solid could be induced. The solid proved to be even less soluble in organic solvents than **FPOC13**. By redissolving a sample of the precipitate in $CDCl_3$, it could be confirmed that **FPOC14** formed in 35% yield (Figure 57).

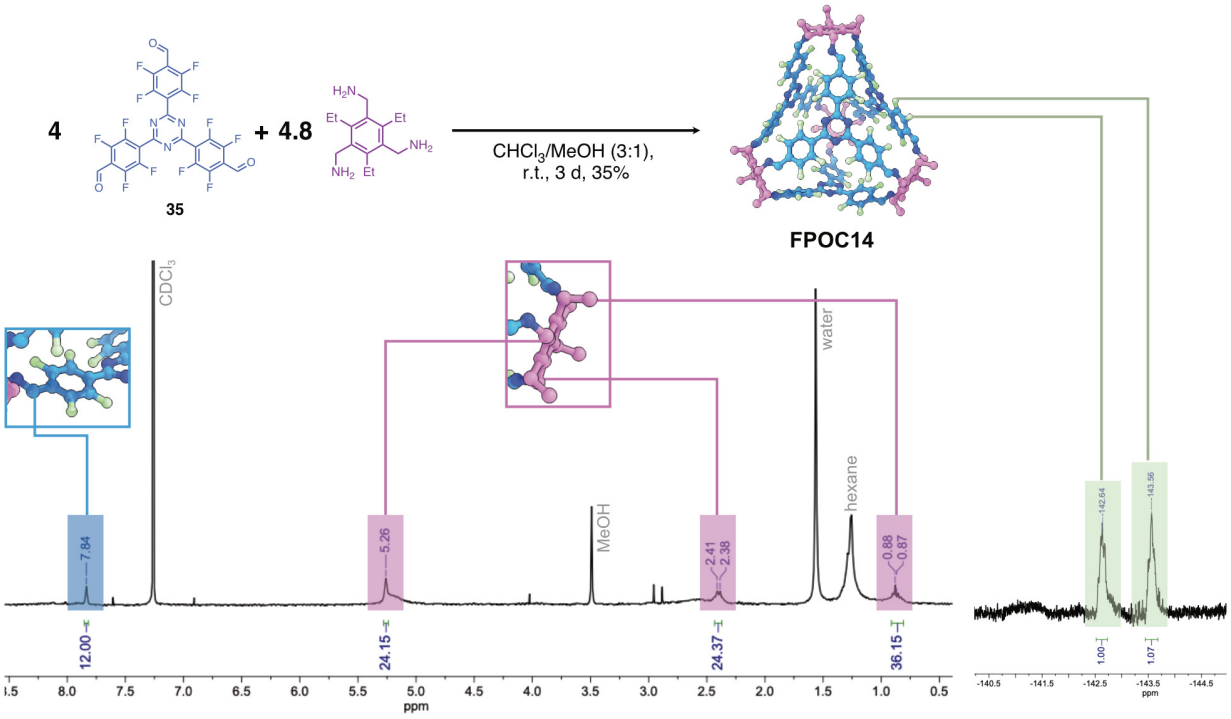

Figure 57: Synthetic scheme of the formation of **FPOC14** from **Et-Amine** and aldehyde **35** in 35% yield (top). The ^{1}H NMR spectrum (bottom left) and the ^{19}F NMR spectrum (bottom right) of the sparingly soluble precipitate indicate the successful formation of **FPOC14**.

A large remainder of the precipitated solid could not be dissolved in any organic solvent. All attempts to crystallize **FPOC14** by either layering the products or recrystallizing it from the obtained precipitate from optimal synthetic conditions, only resulted in the formation of oligomeric species. Since the formation of oligomeric species was observed in the MALDI MS spectrum of both the reaction mixture as well as the precipitate, the macroscopic properties of **FPOC14** were not further investigated, as the amount of oligomers in the samples remains unknown. Clearly, either the isolation of clean **FPOC14** by either crystallization or optimized precipitation must be investigated to make this cage compound accessible for further studies.

Combining four equivalents of aldehyde **37** and 4.8 equivalents of **Et-Amine** in chloroform/ methanol (1:1) leads to the precipitation of a colorless solid that prove to be the least soluble in the series of **Tri^{4}Tri^4** imine cages investigated. Only in the MALDI MS spectrum signals that could be assigned to the formation of **FPOC15** were observed ([**FPOC15**+H]$^+$ calculated: 3021.730 m/z

found: 3021.649 m/z). Signals, that can be assigned to lower mass oligomeric species are also observed in the MALDI MS spectrum (Figure 58).

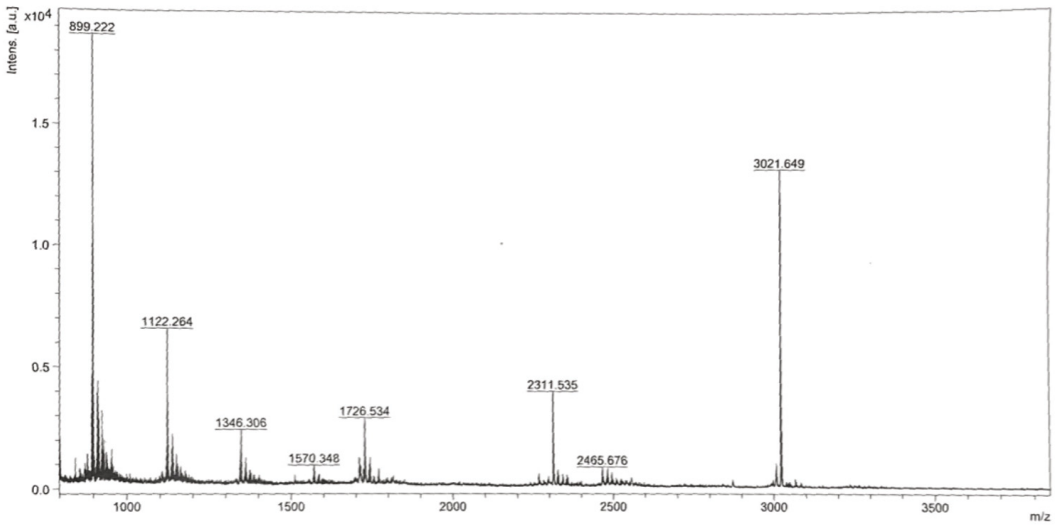

Figure 58: MALDI MS spectrum of an aliquot from the reaction mixture of the synthesis of **FPOC15.**

The solid proved to be not soluble enough for the recording of NMR spectra, rendering further structural investigation impossible. **FPOC15** was not further investigated in terms of its thermal stability and gas sorption properties because the amount of oligomeric structures could not be determined and the isolation of the clean cage compound was not possible.
More elaborate research on the formation and isolation of **FPOC15** is needed to render this cage compound suitable for the creation of a porous material.

3.5.5. DACH-based cages

The last cage topology that is going to be investigated in this work is the **Tri^{4}Di^6** cage that resembles an octahedron. In these cage compounds, the fluorinated tritopic aldehydes occupy half of the faces of a regular octahedron, with the ditopic amines acting as the corners of the polyhedron. This geometry has been exploited multiple times by metal-organic cages and organic cages alike and was proven to be a versatile and stable platform for the generation of porous materials. [8,26,27]

The reaction of four equivalents of aldehyde **31** with six equivalents of (*R,R*)-**DACH** would lead to the formation of **FPOC16** (Figure 59). In this cage, the occupied faces of the octahedron are not completely planar but could experience a strong inward rotation of the fluorinated aromatic rings, as the close proximity of opposing aromatic panels at the amines could lead to a steric repulsion.

Whether this "clash of substituents" would prevent the cage's formation or lead to opened windows is an interesting investigation subject.

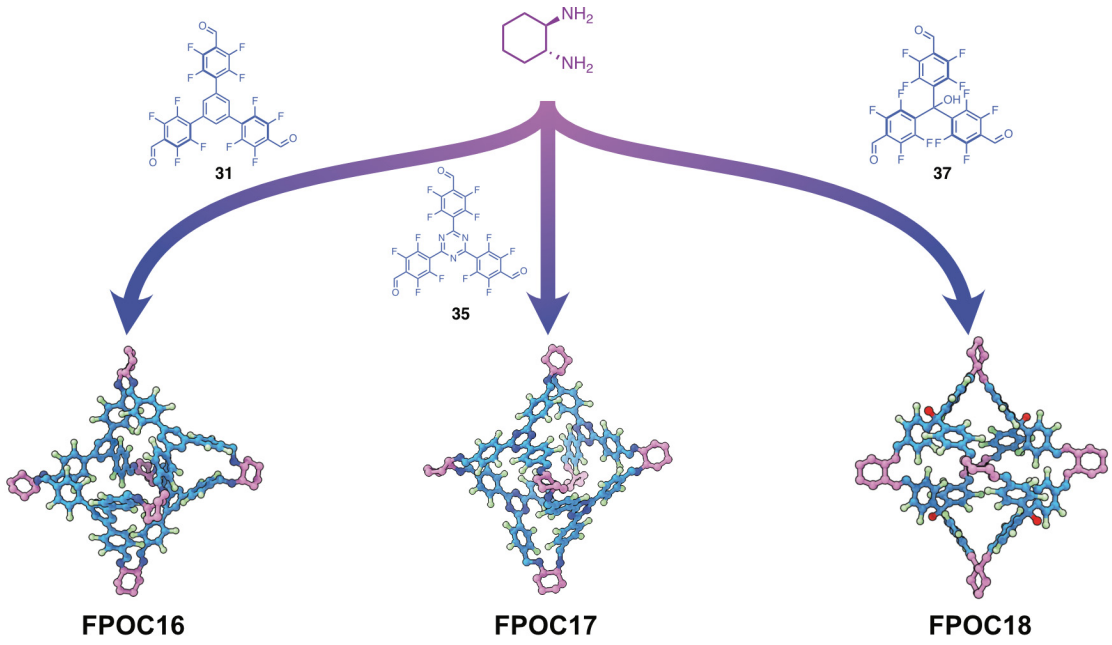

Figure 59: Reactions of (*R,R*)-**DACH** with different fluorinated tritopic aldehydes results in the formation of various **Tri^{4}Di^6** cages that all should exhibit a similar octahedral geometry. The depicted structures were calculated using an universal force field approach (UFF-8). The hydrogen atoms in all structures were omitted for clarity.

The use of the triazine aldehyde **35** would result in the formation of the isostructural highly fluorinated analogue (**FPOC17**) to the cage reported by Wang *et al.* In this structure, the aromatic panels should be completely planar, providing an interesting binding site for gases to interact with. Using the polar aldehyde **37** would result in the formation of **FPOC18**. From the UFF calculations, this cage provides the most inward rotation of the fluorinated aromatic rings, which is encoded inside the aldehyde **37**. But nevertheless, the cage would exhibit a very strict adaptation of the octahedral geometry observed in other **Tri^{4}Di^6** cages.

FPOC16

When four equivalents of the trialdehyde **31** are reacted with six equivalents of (*R,R*)-**DACH** for three days in chloroform, the formation of **FPOC16** can be confirmed by the presence of signals that could be assigned to the singly charged molecular ion, along with the formation of oligomeric products ([**FPOC16**+H]$^+$ calculated: 2893.625 m/z, found: 2893.660 m/z). The addition of *n*-hexane, accompanied by the evaporation of chloroform under reduced pressure at room tempera-

ture, again led to the formation of a bright yellow solid. This could be identified by NMR analysis to be **Tri^{4}Di^6** cage **FPOC16** (Figure 60).

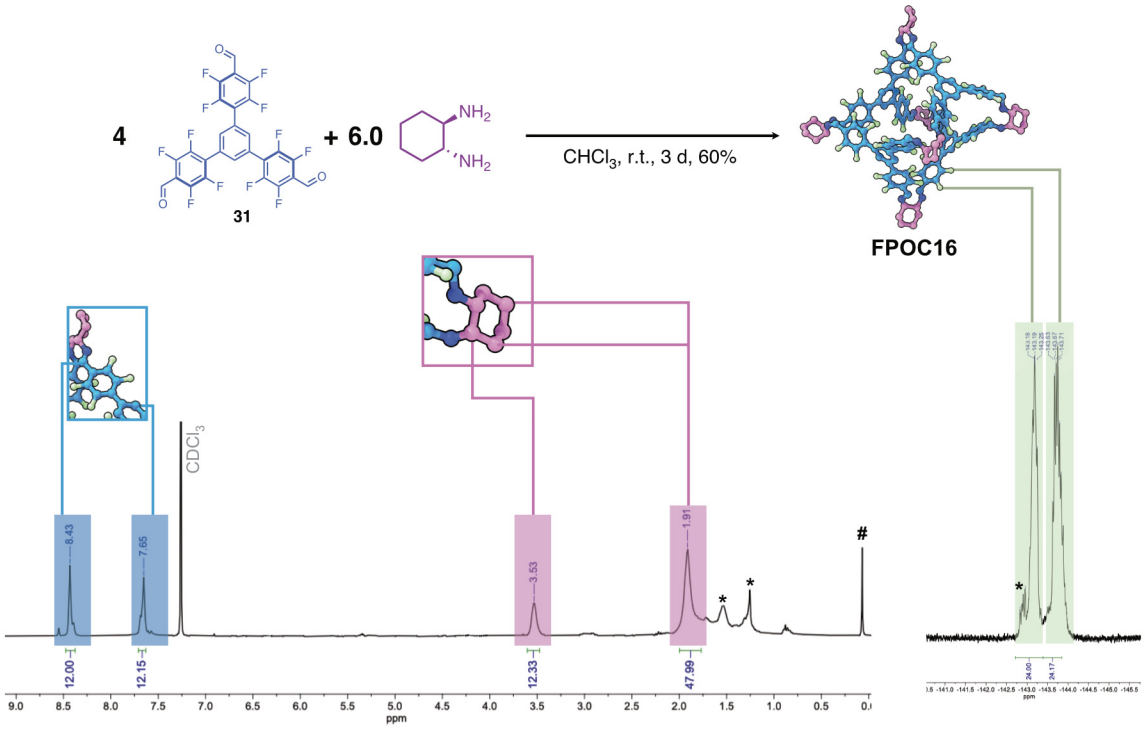

Figure 60: Synthetic scheme of the formation of **FPOC16** from the precursors in 60% yield (top). ^{1}H NMR (bottom left) and ^{19}F NMR spectrum (bottom right) of the redissolved precipitate indicating the formation of a cage compound. * – oligomers from precipitation; # – H grease

In the ^{19}F NMR spectrum, two multiplets of roughly the same intensity can be observed. These can be assigned to the inner and outer fluorine atoms in the aromatic rings. From the UFF-calculated structure, it is apparent that these rings experience different degrees of rotation, which would reduce the overall symmetry of the cage, leading to the observance of multiple signals. The ^{1}H NMR spectrum features the expected imine and phenylene core signals for the fluorinated aromatic motif (8.43 ppm and 7.65 ppm) and a sharp singlet for the C–H group that is adjacent to the amino group (3.53 ppm). A broad singlet is observed at 1.91 ppm, which is a result of the overlappingsignals for CH_2 groups of the cyclohexane ring in the **DACH** motif. **FPOC16** is very well soluble in chlorinated solvents and was therefore subjected to DOSY NMR analysis. Surprisingly, signals corresponding to the formation of *two* species could be observed (Figure 61). The smaller species exhibit a diffusion coefficient of D = 3.08 x 10^{-10} m^2 s^{-1} which translates to a solvodynamic radius of 11.9 Å. This value is in good accordance with values reported for other **Tri^{4}Di^6** cages of the same size.[26] The larger species exhibit a diffusion coefficient of D = 2.65 x 10^{-10} m^2 s^{-1}, which corresponds to a solvodynamic radius of 14.6 Å. Although DOSY NMR analysis cannot be

considered a very accurate method as many values are just approximated, this difference in solvodynamic radii is too pronounced to be a measuring error.

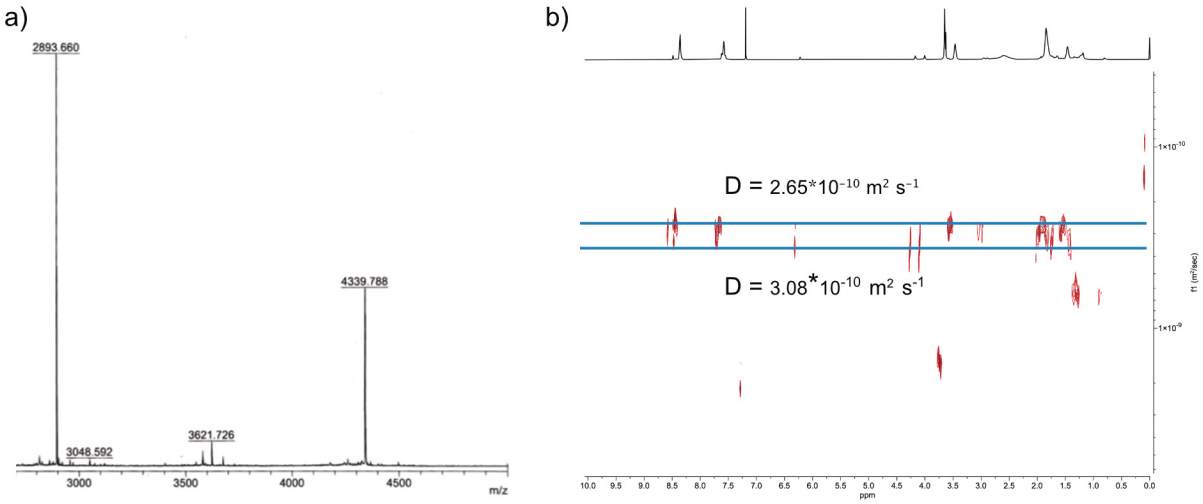

Figure 61: a) MALDI MS spectrum of the redissolved precipitate of the reaction for **FPOC16**; b) DOSY spectrum indicating the formation of two macromolecular species.

The analysis of the redissolved solid by MALDI MS analysis reveals the presence of a higher mass ion signal that can be attributed to the formation of a **Tri^{6}Di^9** cage ([**Tri^{6}Di^9**+H]$^+$ calculated: 4339.940 m/z, found: 4339.788 m/z). Jelfs *et al*. predicted the formation of a **Tri^{6}Di^9** cage, but at the time of writing, only one example is known to exist that features a templating effect of palladium to achieve this geometry.[18,30] The larger version of **FPOC16** would be the first organic imine cage to feature such a rare geometry (Figure 62).

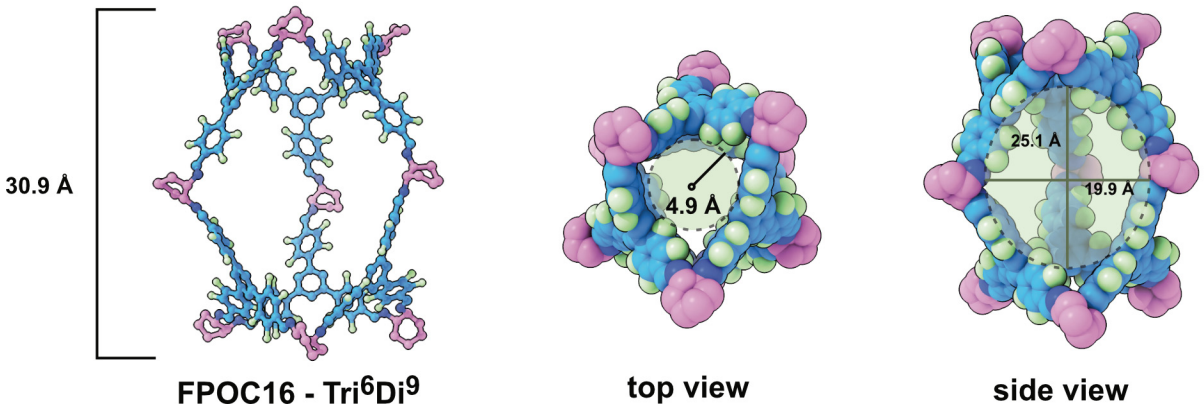

Figure 62: Calculated structure of a **Tri^{6}Di^9** cage from the reaction of aldehyde **31** with (*R,R*)-DACH using an universal force field (UFF) approach (left). The space-filling model is shown from the top (middle) and from a side angle (right).

There is no regular polyhedron that resembles the geometry of a **Tri^{6}Di^9** cage. The structural features can rather be described as similar to a "barrel", with two smaller windows at the top and bottom, at which three amine motifs can be located on each side. These two subunits of three aldehydes and three amines on each side are interconnected with three **DACH** motifs in the middle, creating the "barrel-shape". The calculated structure features a height of 30.9 Å and two types of windows. The smaller, almost circular window exhibits a radius of 4.9 Å, whereas the large elliptical window has a height of 25.1 Å and a width of 19.9 Å. This cage geometry should feature a very large cavity that would be interesting to investigate for the storage of gases, as it contains very large windows at the equatorial sites.

A possible cause for the formation of such an unusual topology could lie in the connection of two aromatic panels at the **DACH** motif. As previously mentioned, the large inward rotation of the fluorinated aromatic rings could result in a sterical clash at the corners of an octahedral geometry. In the calculated **Tri^{6}Di^9** structure, the average binding angle at the **DACH** motif is increased, resulting in less sterical strain between adjacent fluorinated aromatic rings.

Attempts to separate these two compounds based on their different in size using a GPC have so far not proven to be fruitful, as the solubility in THF is considerably lower and, due to the reversible imine bonds, the distribution between **Tri^{4}Di^6** and **Tri^{6}Di^9** cages seems to be concentration-dependent (GPC seperation experiments were conducted by Laura zur Horst in the group of Prof. Dr. S. Höger at Universität Bonn). At low concentrations, the system was observed to shift its equilibrium towards the formation of more **Tri^{4}Di^6** cages, sacrificing the larger cage in the process.

By conducting the reaction at lower concentrations, the **Tri^{4}Di^6** cage **FPOC16** could be synthesized individually. Higher concentrations unfortunately did not lead to the exclusive formation of the **Tri^{6}Di^9** cage, but rather of oligomeric species. A separation of the mixture by crystallization only yielded polymeric foils or sparingly soluble precipitates. Future efforts will be focused on finding methods to synthesize the larger cage exclusively or to isolate it after the synthesis.

The isolated **Tri^{4}Di^6** cage **FPOC16** was further investigated for its thermal stability, crystallinity, and gas sorption properties. The cage features an early onset decomposition temperature of 310.1 °C. Although this is slightly lower than the **Tri^{4}Di^6** cage by Wang *et al*. exhibits the stability of **FPOC16,** rendering it viable for use as a material under elevated temperatures.

Since the material proved to be thermally stable, the precipitated solid was washed with *n*-hexane and the solvent was exchanged to diethyl ether and then activated at 120 °C at 10^{-3} mbar for 18 hours. Gas sorption measurements prove the **FPOC16**-derived material to indeed exhibit porosity.

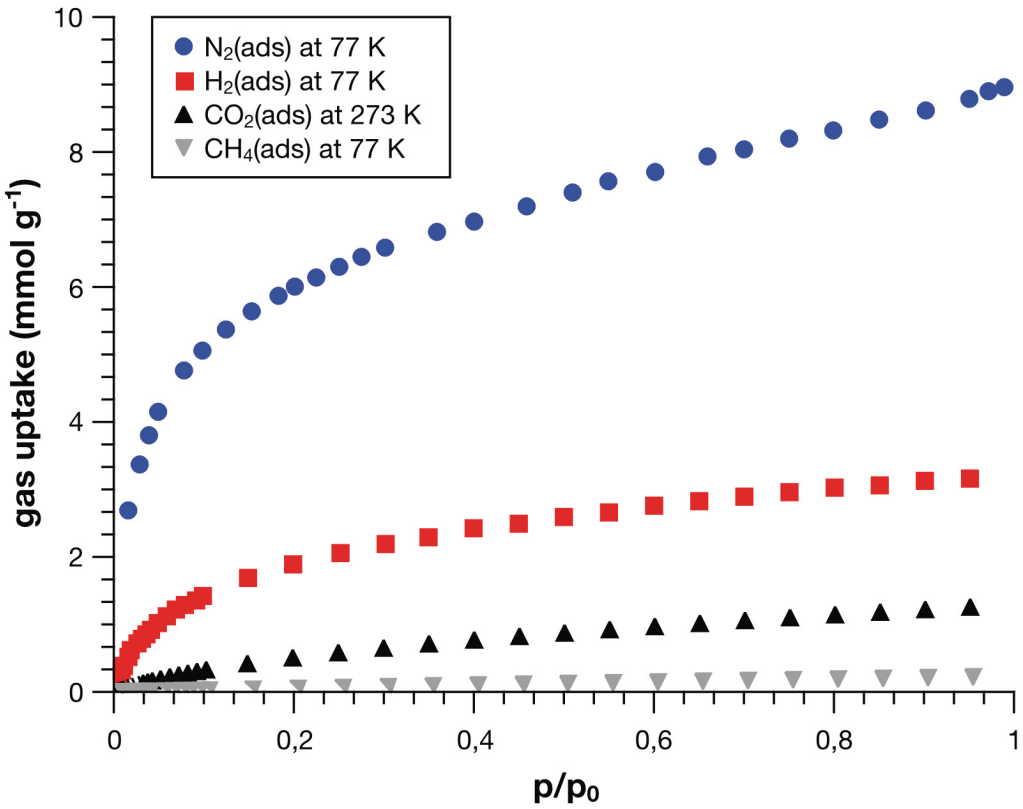

Figure 63: Stacked isotherms of N_2 (blue), H_2 (red), CO_2 (black) and CH_4 (grey) uptake of **FPOC16** after activation.

The semi-crystalline material (see Section 5.6) exhibits an apparent surface area of SA_{BET} = 521.5 $m^2\ g^{-1}$. This is less than half of the similar-sized crystalline cage reported by Wang. An explanation of this can either be given by the fluorine atoms, which take up more space compared to hydrogen atoms, thereby reducing the available space, or to an unfavorable packing in the semicrystalline material. As there is possibly no extended pore network present inside the semicrystalline material, the overall porosity remains low. This is also reflected in the exhibited gas uptake. **FPOC16** can adsorb up to 8.97 mmol g^{-1} of N_2 at 77 K, 3.18 mmol g^{-1} of H_2 at 77 K, 1.26 mmol g^{-1} of CO_2 at 273 K and 0.22 mmol g^{-1} of CH_4 at 77 K. Interestingly, although the surface area of **FPOC16** is profoundly less than what the cage of Wang *et al*. exhibited and the uptake of N_2, CO_2, and CH_4 is roughly half or less compared to Wang's uptake, the amount of H_2 that is adsorbed is very similar to that reported by Wang *et al*. (3.18 mmol g^{-1} **FPOC16** *vs*. 3.57 mmol g^{-1} Wang *et al*.).[27]
Considering that these values are observed in a semicrystalline material, it would be intriguing to obtain a crystalline material in which the highly ordered structure would possibly feature a pore network and its impact on the gas sorption properties. The presented results are encouraging in the investigation of larger fluorinated POCs and their properties, as they suggest that the beneficial influence of fluorine substitution on the material's properties that was previously observed in medium- and smaller-sized POCs will be maintained.

FPOC17

If four equivalents of the fluorinated triazine aldehyde **35** are combined with six equivalents of (*R,R*)-**DACH**, a **Tri^{4}Di^6** cage that is isostructural to the imine cage reported by Wang *et al*. is created. Similar to **FPOC16,** the reaction yielded optimal results when conducted at room temperature in chloroform for three days (Figure 64).

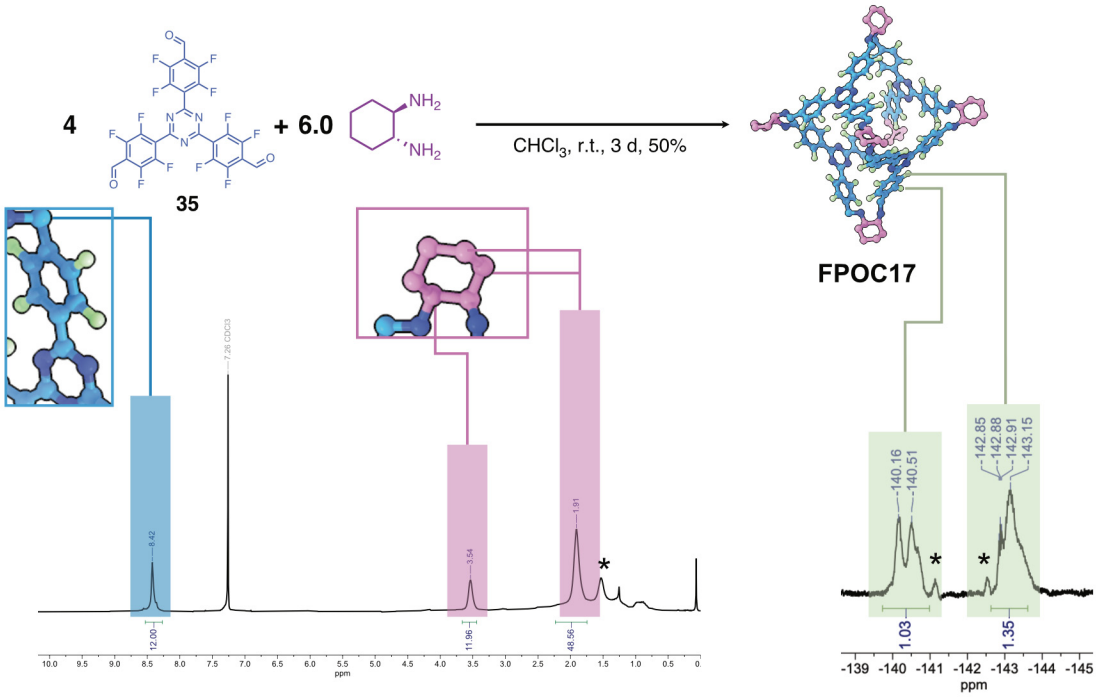

Figure 64: Synthetic scheme for the synthesis of **FPOC17** in chloroform from the precursors (top), ^{1}H NMR spectrum (left) and ^{19}F NMR spectrum (right) of the redissolved precipitate in $CDCl_3$ at room temperature. The depicted structure was calculated using a universal force-field (UFF) approach. * – oligomers precipitated together with product

The cage could be isolated as a bright yellow solid with a 50% yield by adding *n*-hexane to the chloroform solution and evaporating the chloroform at room temperature under reduced pressure, which induced precipitation. Although the presence of the **Tri^{4}Di^6** cage ([**FPOC17**+H]$^+$ calculated: 2905.568 m/z, found: 2905.510 m/z) along with a signal that could either correspond to a **Tri^{6}Di^9** cage or a catenane of the **Tri^{4}Di^6** and a **Tri^{2}Di^3** cage was observed in the MALDI MS spectrum ([**Tri^{6}Di^9**+H]$^+$ calculated: 4357.855 m/z, found: 4357.580 m/z), only one species was observed in the DOSY experiment (Figure 65).

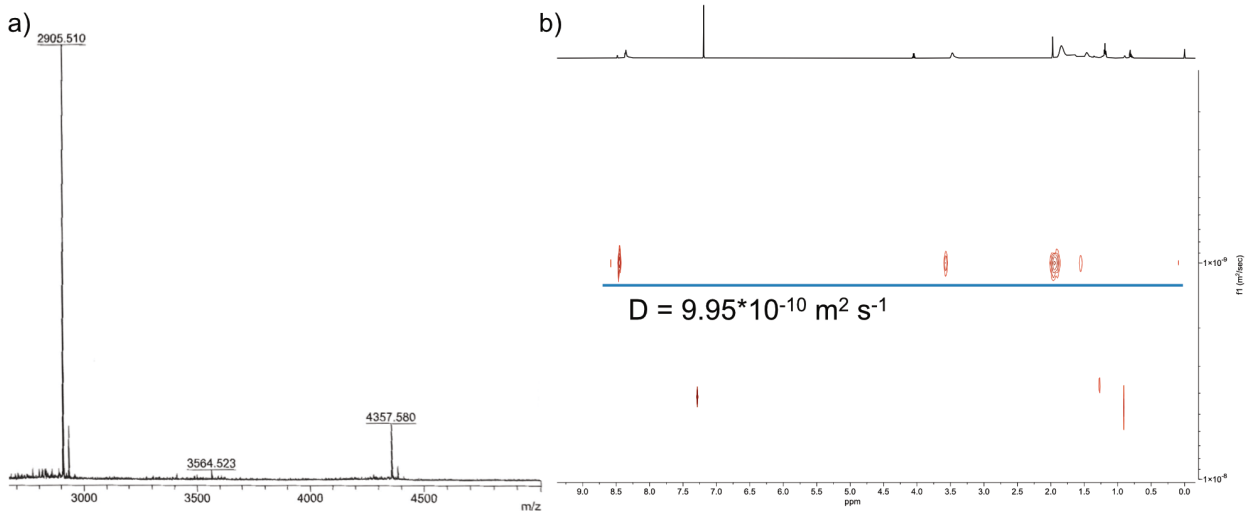

Figure 65: a) MALDI MS spectrum; b) DOSY NMR spectrum (right) of the precipitate dissolved in $CDCl_3$.

The observed diffusion coefficient corresponds to a solvodynamic radius of 3.9 Å, which is much lower than expected for the **Tri^{4}Di^6** geometry that is targeted. An explanation could be given by an erroneous experiment, as the diffusion coefficient of $CDCl_3$ is also much lower than expected, or by a severe contraction of the cage in solution, which is rather unlikely as the similar **DACH**-based imine cages have always exhibited a high degree of shape-persistency.

All attempts to either recrystallize the obtained solid or to directly synthesize a crystalline material by layering the starting materials resulted only in the formation of an oligomer-rich off-white precipitate. Therefore, the obtained precipitate was used to investigate the solid-state properties of **FPOC17**.

The material features an onset decomposition temperature of 258.0 °C, which is much lower than the structurally related cage **FPOC16** exhibited. Triazine-based compounds have in the past been attributed with outstanding thermal stability, which makes these findings even more unexpected. Possible explanations could be the evolution of HF during the decomposition process which then increases the rate of decomposition. This observation marks the first deviation from the trend in which FPOCs usually exhibit improved thermal stability. Nevertheless, **FPOC17** proved to be stable enough to be investigated with regard to the material's gas sorption abilities.

The obtained precipitate was washed with *n*-hexane and the pores were soaked with a more volatile compound by exchanging the solvent to diethyl ether. Investigation of the sample by PXRD analysis revealed that the material was mostly amorphous but possessed crystalline subdomains, making it an interesting candidate for further crystallization studies. After the activation at 80 °C and 10^{-3} mbar for 18 hours, the material was investigated by gas sorption measurements.

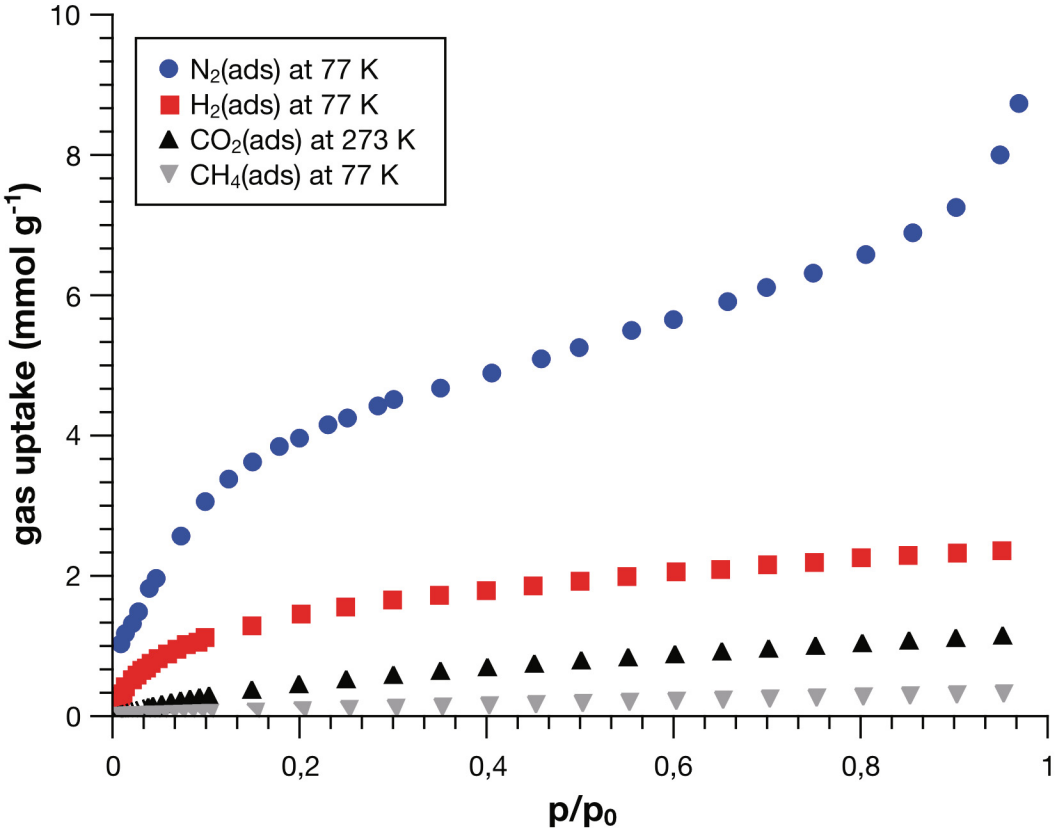

Figure 66: Stacked isotherms of N_2 (blue), H_2 (red), CO_2 (black) and CH_4 (grey) uptake of the semicrystalline **FPOC17**-based material.

FPOC17 features an apparent surface area of SA_{BET} = 395.2 m^2 g^{-1}, which is again considerably lower than the isostructural non-fluorinated **Tri^{4}Di^6** cage. The porous material is able to adsorb 8.73 mmol g^{-1} of N_2 at 77 K, 2.36 mmol g^{-1} of H_2 at 77 K, 1.15 mmol g^{-1} of CO_2 at 273 K, and 0.32 mmol g^{-1} of CH_4 at 77 K (Figure 66). Surprisingly, this material features an even lower gas uptake and surface area than **FPOC16,** although the aromatic fluorinated panels feature complete planarity and should hence allow for a larger cavity and surface area. The most probable explanation is the lack of crystallinity that is exhibited by the analyzed sample. Since the influence of the crystallinity on the porosity of the material is profound, **FPOC17** remains the target for further crystallization studies to generate a porous, crystalline material. Since these initial results for **FPOC16** and **FPOC17** are based on semicrystalline or amorphous materials, it is difficult to determine, if the introduction of fluorine into porous organic cage structures leads to an increase in gas uptake. However, these findings show that even semicrystalline or amorphous fluorinated POC-based materials exhibit porosity, which is possibly only enhanced when the material can be recrystallized.

FPOC18

The aldehyde **37** features a geometry that has so far not been explored in the field of porous organic cages. Compared to the planar benzene-based aldehyde **31** and triazine-based aldehyde

35, the tertiary alcohol motif in the center of aldehyde **37** introduces a tetrahedral angle between the three fluorinated benzene rings. This results in a reduced distance between the rings, which leads to severe sterical repulsion that is resolved by the rotation of the aromatic planes away from each other. This results in all formyl groups needing to have favorable angles between each other to create a highly symmetric imine cage.

When four equivalents of **37** are combined with six equivalents of (*R,R*)-**DACH** in chloroform, the reaction mixture turns yellow after one day but does not exhibit any cloudiness or precipitate formation. The investigation of the reaction mixture reveals the clear formation of the **Tri^{4}Di^6** cage **FPOC18** ([**FPOC18**+H]$^+$ calculated: 2709.542 m/z, found: 2905.490 m/z). The isolation of the cage proved to be difficult, as its solubility in *n*-hexane is considerably high. By evaporating the chloroform mixture to a minimum and adding cold *n*-hexane (-10°C), precipitation of an off-white solid could be induced. The redissolved solid is confirmed to be **FPOC18** by NMR analysis (Figure 67).

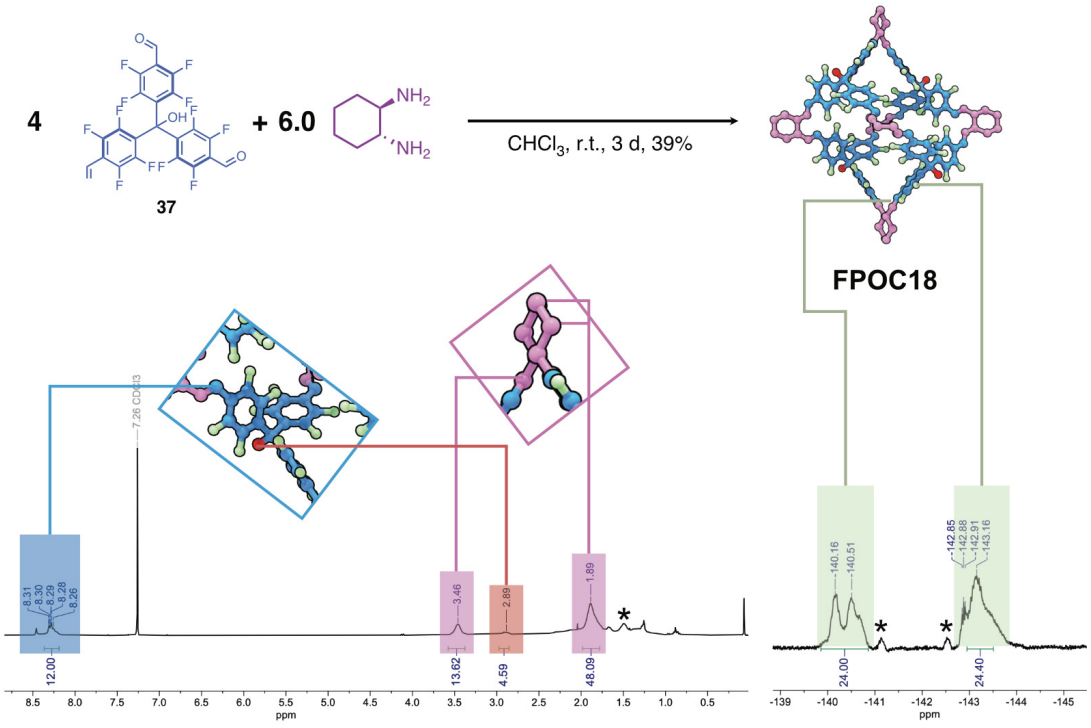

Figure 67: Synthetic scheme for the formation of **FPOC18** from the precursors in chloroform (top), ^{1}H NMR spectrum (left) and ^{19}F NMR spectrum (right) of the redissolved precipitate isolated directly from the reaction mixture. The depicted structure was calculated using a universal force field (UFF) approach. * – oligomeric structures

In the ^{1}H NMR and ^{19}F NMR, multiple signals around the expected shifts for the imine-corresponding signal (8.30 ppm, ^{1}H) and the fluorine-corresponding signals (-141.4 and 142.1 ppm, ^{19}F) can be observed. A possible explanation for these signals could be the formation of helical isomers.

Due to the pronounced sterical hindrance between the fluorinated aromatic rings, the aldehyde **37** could exhibit helical isomerism in the cage molecule. This would lead to the generation of *P*- and *M*-isomer-containing structures. If the geometry of **FPOC18** is flexible enough to incorporate both isomers into a single structure, this would explain the multitude of signals. The signals corresponding to the cyclohexane motif at 1.89 ppm and 3.49 ppm remain largely unaffected by this asymmetrical influence.

When the recrystallization of **FPOC18** from the precipitated sample was investigated, the formation of very thin needles could be observed when a mixture of acetonitrile and $CHCl_3$ (1:9) was slowly evaporated (Figure 68, left).

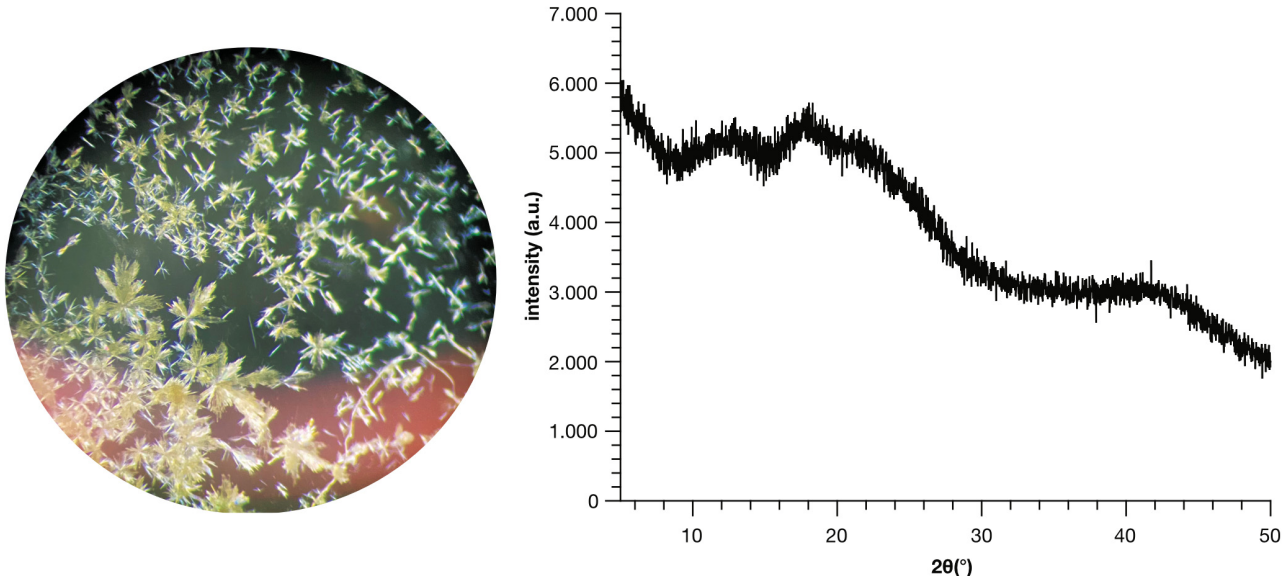

Figure 68: Microscopic image of crystals obtained from the slow evaporation of a acetonitrile/chloroform (1:9) mixture (left), PXRD pattern of the as-synthesized precipitate obtained by filtering off the precipitate from the reaction mixture (right).

The crystals proved to be too small and possibly systematically twinned to be investigated with SC-XRD. When trying to harvest the crystals for analysis with PXRD, they were found to be very fragile and quickly decomposed. Due to the low yield during crystallization, no suitable PXRD pattern could be recorded. Suitable crystallization methods need to be further investigated to obtain a porous crystalline material that can then be fully investigated regarding its material properties. For the investigation of solid-state properties, the amorphous sample of **FPOC18** obtained from precipitating the cage by the addition of cold *n*-hexane was analyzed (Figure 68, right).

The thermogravimetric analysis of the amorphous sample revealed a very low onset decomposition temperature of 139.8 °C. This is in good accordance with the fragility of the obtained crystals.

Although the material did not exhibit high thermal stability, **FPOC18** was investigated regarding its gas sorption properties. The amorphous sample was subjected to gas sorption measurements after activation for 18 hours at 60 °C and 10^{-3} mbar. The **FPOC18**-based material features a very low apparent surface area of SA_{BET} = 50.5 m^2 g^{-1}, which hints at a loss of porosity during the isolation or activation of the sample. This argument is further strengthened by the inherent low thermal stability of the cage compound. Ultimately, this very likely renders **FPOC18** an unsuitable compound for the generation of a porous material, which is dependent on the generation of a crystalline material that could exhibit much altered macroscopic properties. Nevertheless, **FPOC18** features remarkable solubility in a wide array of organic solvents, making it an interesting candidate structure for future investigation of its solution-phase properties.

3.5.6. Summary

In this section, three highly fluorinated tritopic aldehydes, of which **35** and **37** have not previously been synthesized, were investigated for their potential formation of large, fluorinated POCs. When combined with three structurally very different amines, the generation of nine new cage compounds was possible. Seven of these could be synthesized successfully and were investigated with regard to their solid-state properties.

The large **Tri^4Tri^4** cage **FPOC13** could be obtained as a highly crystalline material that exhibited excellent thermal stability up to 326.3 °C and proved to be shape-persistent. Although the apparent surface area of SA_{BET} = 510.55 m^2 g^{-1} is comparable to that of **FC1**, the cage was able to adsorb 1.5 times the amount of N_2 (11.8 mmol g^{-1} *vs.* 7.9 mmol g^{-1}, **FC1**). This is indicative of an improved gas uptake that could be facilitated by the presence of more fluorine atoms inside the cavity. When the crystal structure becomes available, future investigations could be directed towards an increase in porosity due to different activation or crystallization conditions.

The large **Tri^4Di^6** cages **FPOC16** and **FPOC17** also exhibited porosity, albeit they could only be obtained as amorphous materials. Future efforts need to focus on the generation of crystalline materials that would be able to incorporate an extended pore network, leading to enhanced gas uptake abilities. The successful synthesis, isolation, and shape-persistency of these cages is the validation for fluorinated building blocks to be an important consideration in the investigation of new cage compounds.

Surprisingly, during the formation of **FPOC16,** the formation of an unprecedented geometry could be observed. A **Tri^6Di^9** cage could be identified in the DOSY NMR spectrum as well as in the MALDI MS spectrum. At the time of writing, this unusual geometry could only be facilitated with a templating effect in a metal-organic cage by Nitschke *et al*.[18] The formation of this geometry, can

presumably be attributed to the strong attractive interactions between C–F bonds and the highly fluorinated aromatic rings. Isolation of this unprecedented geometry could open up new possibilities for targeting cage structures that have so far been inaccessible under the use of non-fluorinated building blocks.

The synthesis of a large TREN-based **Tri^{4}Tri^4** cage, **FPOC10**, supports this claim, as the synthesis of this highly flexible cage motif necessitates the presence of strong interactions between neighboring aromatic panels. This property was thought to be unique to the formation of C–H···π interactions, but it was demonstrated in this study that the use of electronically inverse, highly fluorinated compounds can replicate these interactions in the form of C–F···π_F interactions. **FPOC10** is very soluble in a wide range of solvents and can form a Cu(I) complex by binding four copper(I) ions in a tetrahedral geometry inside its cavity (**Cu$_4$FPOC10**). This complex provides an interesting candidate for catalytic and guest-binding applications, as this combination of highly fluorinated aromatic walls with metal binding sites is unprecedented so far.

Ultimately, the variety of uses of fluorinated building blocks for the synthesis of different supramolecular materials has been demonstrated in terms of stability, crystallinity, porosity, and guest-binding. The transfer of knowledge that has been gathered on the properties of the fluorine substitution effects to another supramolecular material shall be investigated in the last section of this work.

3.6. Fluorinated trianglimines

3.6.1. Introduction

In the field of supramolecular chemistry, the dynamic imine bond formation has mostly been used to either generate large framework structures, porous polymers or organic cage compounds[1]. A feature that all these compound classes share is their inherent multidimensionality. Porous polymers and POCs always exhibit a three-dimensional pore since the incorporated linkers need to exhibit this three-dimensional connectivity to generate the porous network inside the material. Only in COFs have two-dimensional structures been reported that form porous networks by stacking their 2D layers above one another, creating porosity in the third dimension. Analogous to how POCs represent the isolated three-dimensional pores similar to those of 3D-COFs and MOFs, macrocycles represent the isolated two-dimensional pore similar to 2D-COFs. These isolated "rings" possess a hole, which is the definition of a two-dimensional pore, that can be connected with another hole of an adjacent macrocycle to ultimately form a three-dimensional channel. The difference between macrocycles and 2D-COFs lies in their connectivity. Whereas in 2D-COFs infinitely stretching layers are stacked, in macrocycles each molecule remains individually accessible for either post-synthetic modification, dissolving, or reorganization.

The most prominent class of macrocycles featuring a reversible imine bond, is the class of trianglimines. They are formed from the reaction of three ditopic aldehydes with three ditopic amines. Most often the aldehydes are *meta*- or *para*-substituted arenes and the amines are cycloalkane-*trans*-1,2-diamines (e.g. (*R,R*)-**DACH**, Scheme 32).

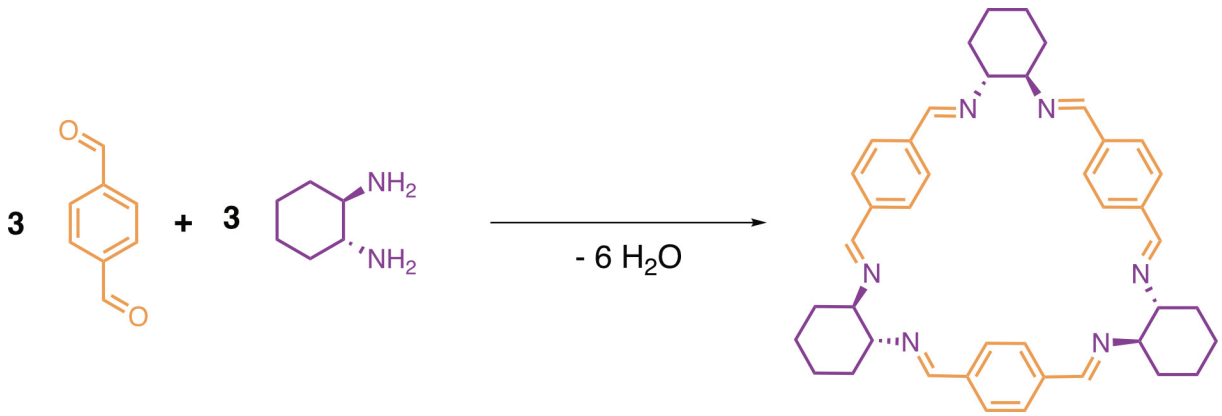

Scheme 32: Synthetic scheme of the sixfold condensation between three aldehydes and three amines to form the triangular shaped macrocycle, trianglimine.

[1] Large parts of this chapter have previously been published: T. Kunde‡, T. Pausch‡, G. J. Reiss and B. M. Schmidt, *Synlett*, 2022, **33**, 161–165; ‡ – both authors contributed equally to this work

The first examples of this compound class were highlighted in the early 2000s by the group of Gawronski, who investigated the exact example in Scheme 32, amongst others.[89] In these early works, the formation of an inclusive complex, where multiple rings were stacked and formed a tubular channel around the solvents, was reported, but no particular effort was undertaken to create a porous material from that observation.[89a] The group of Kuhnert did a tremendous amount of work on this compound class, enabling the precise controllability of ring and hole size by using substituted aldehydes, that had varying distances between their formyl groups.[90] Similar to POCs, trianglimines can be reduced, using almost identical conditions, to the trianglamines that feature six *amine bonds* instead of *imine bonds*, which in turn can also be "tied" to improve the shape-persistency of the compounds.[89a,91]

In recent years, the slumbering potential for the formation of supramolecular porous frameworks has been uncovered. The group of Janiak demonstrated that the porosity of the stacked macrocycles is not only influenced by the interactions between neighboring molecules but can actually be overridden by the introduction of elongated molecules that fit nicely into the macrocycle's pores. By using long-chain alcohols, they were able to thread the trianglimines like beads onto the alcohol. When they evaporated the alcohol under reduced pressure, the tubular channel-like structure remained intact, with the resulting material exhibiting porosity.[92]

The group of Khashab demonstrated the tremendous separation capabilities of this compound class. By precisely engineering the ring and hole sizes of their trianglimines, they reported the separation of various compound mixtures, most prominently the separation of ethylbenzene from styrene (Figure 69).[93]

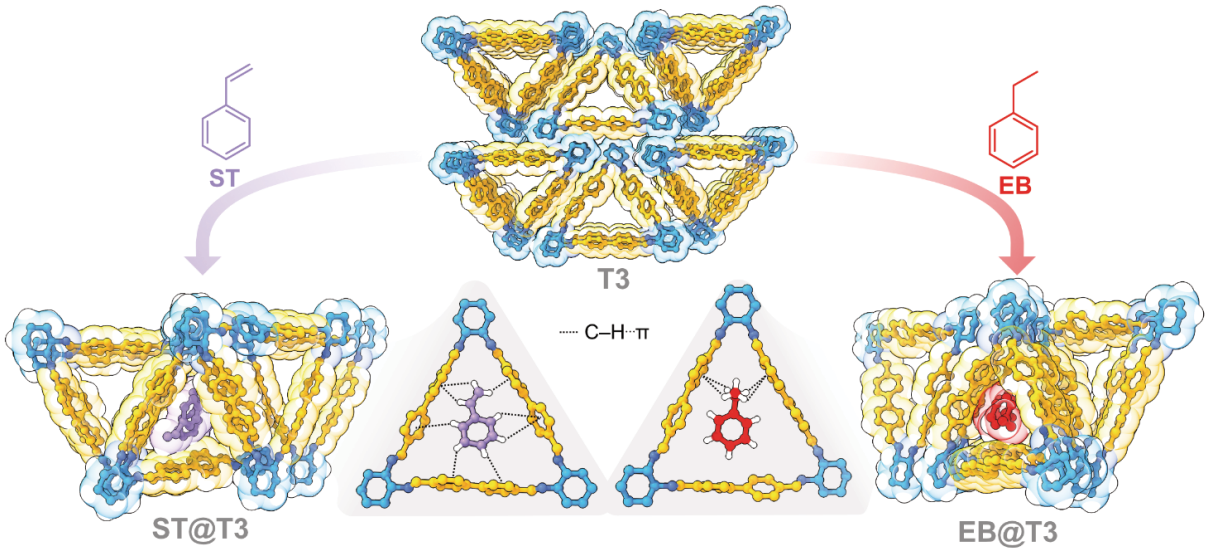

Figure 69: Crystalline macrocycle stacks of the trianglimine stack (T3) readily adsorbed ethylbenzene (EB) and styrene (ST) individually in the intrinsic pore, facilitated by C–H···π interactions between the methyl groups of the guests. This graphic was reproduced with permission from ref. [9].

The same group was also able to generate an ultra thin membrane that incorporated different trianglimines to achieve the mentioned effect of a cut-out board, where only specific solvents can permeate through the membrane, that are selected by their shape.[94]
Cooper *et al*. showed that, in addition to their separation abilities, the chirality of the amines used, influences the supramolecular frameworks (SOFs) created by these trianglimines.[95] When only one enantiomer of the *iso*-aldehyde containing trianglimine is crystallized, the resulting material is nonporous due to unfavorable crystal packing. This could be overcome by heterochiral packing, resulting in an apparent surface area of SA_{BET} = 355 m^2 g^{-1}. The groups of Cooper and Khashab could further demonstrate that the desolvated structures of the trianglimines and trianglamines were suitable to separate gas mixtures by either shape selection or sorption phenomena similar to columns used in gas chromatography.[93d,95]

In summary, trianglimines provide an interesting field of supramolecular materials, due to their ease of preparation, variety of regulation possibilities, and analyzability compared to covalent framework materials. Up until now, the influence of fluorine substitution on this emerging material class has not been investigated. With knowledge about the synthesis of highly fluorinated imine cages in hand, the synthesis and characterization of the first extensively fluorinated trianglimine were investigated.

3.6.2. Synthesis

Since fluorine atoms exhibit a higher sterical demand compared to hydrogen atoms, their introduction into porous structures can lead to a decrease in porosity. In the case of the small **Tri^2Di^3** cages presented in this work, this led to the complete closure of the cage pores. To prevent this from occurring during the synthesis of trianglimines, the fluorinated biphenyl aldehyde **23** was chosen for the generation of a fluorinated macrocycle. From the works of Kuhnert *et al*., it can be deduced that biphenyl-incorporating trianglimines feature a hole size height of approximately 13.5 Å, which is roughly 3 Å larger than for the monophenyl derivative.[89c] This could make a big difference when the fluorine atoms are considered to point into the hole.
A colorless solid precipitated directly from the reaction mixture after reacting three equivalents of **23** with three equivalents of (*R,R*)-**DACH** in acetonitrile at room temperature for 18 hours. The precipitate could easily be dissolved in chloroform and the formation of the highly fluorinated trianglimine **RRF24** was confirmed by MALDI MS and NMR analysis ([**RRF24**+H]$^+$ calculated: 1279.269 m/z, found: 1279.269 m/z).

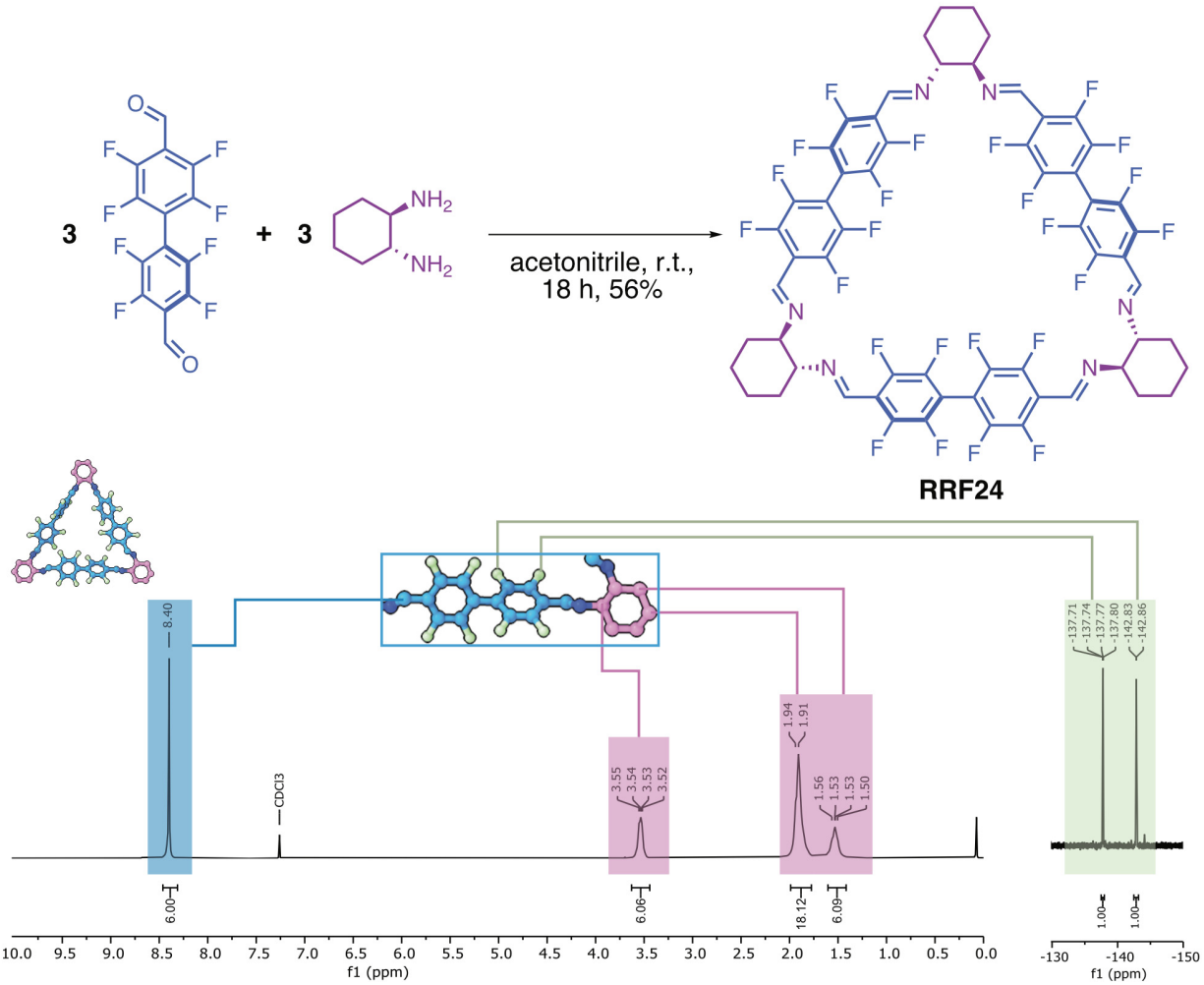

Figure 70: Synthetic scheme of the reaction to form **RRF24** from the precursors in acetonitrile (top), ^{1}H NMR spectrum (bottom left) and ^{19}F NMR spectrum (bottom right).

In Figure 70 the clean formation of the trianglimine is reflected in the clean and sharp NMR signals in the ^{1}H and ^{19}F NMR spectra. The presence of an oligomeric structure would broaden the signals, which is not observed.

In $CDCl_3$, DOSY NMR analysis determined a diffusion coefficient of D = 4.4 x 10-10 m^2 s^{-1}, corresponding to a solvodynamic radius of 9.3 Å. Subtracting the diameter of the cyclohexane motifs, this value is in good agreement with the hole size that was reported by Kuhnert *et al.*[89c]

3.6.3. Solid-state properties

By slow evaporation of a chloroform/acetonitrile (9:1) mixture, crystals suitable for SC–XRD could be obtained.

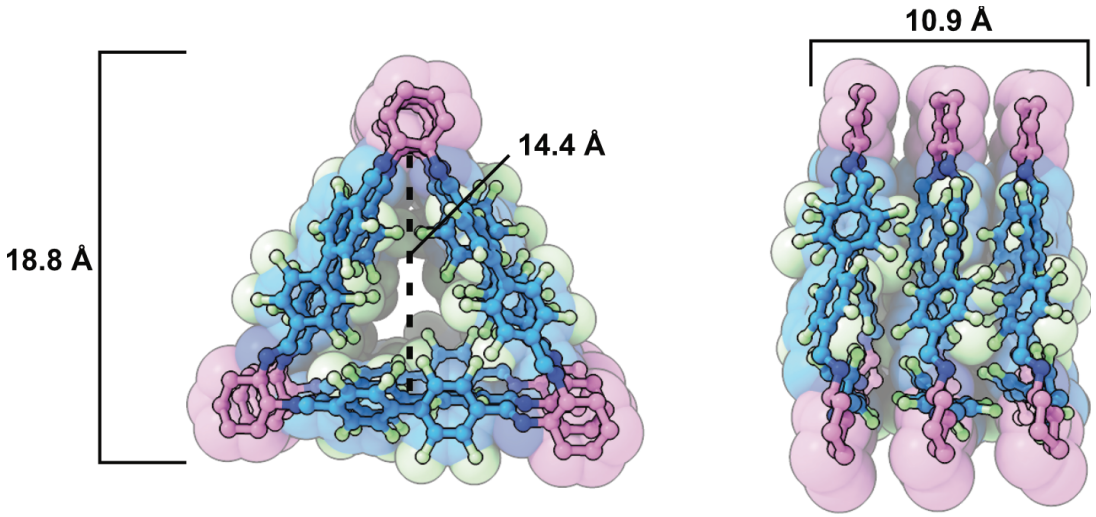

Figure 71: Crystal structure of **RRF24** obtained from acetonitrile, solvent molecules and hydrogen atoms were omitted for clarity. The frontal view (left) shows the formation of tubular channels throughout the crystal. A side view of the asymmetric unit (right) reveals the presence of three macrocycles in a tightly packed stack. Space-filling models are shown with reduced opacity (crystal structures were obtained and refined by Dr. Bernd M. Schmidt).

RRF24 crystallizes in the monoclinic space group $P2_1$ and features a trio of crystallographically independent macrocycles and three acetonitrile molecules in the asymmetric unit (Figure 71). As a consequence, each circular void is different, leading to three different orientations of the acetonitrile molecules inside of the voids. Crystallographically, this stack exhibits pseudo geometry, as one trianglimine is rotated 120° in one direction and then moved to the next point in the stack, resulting in a full rotation of the triangular shaped macrocycle after three repetition units. This is a result of the twisted conformation of the octafluorobiphenyl units, which are possibly trying to maximize the C–F$\cdots\pi_F$ interactions between neighboring trianglimines. The resulting one-dimensional strands are slightly offset by about 2.6 Å. The tubular pores formed inside of the linear stacks can be approximated as helical tubular channels that are occupied with acetonitrile molecules.

The long, needle-shaped crystals were isolated from the mother liquor, washed with fresh acetonitrile, and the solvent was exchanged to *n*-pentane. The pentane was then evaporated at ambient pressure and temperature for 24 hours, followed by an activation at 80 °C and 10^{-3} mbar for 16 hours, before the sample was being subjected to gas sorption measurements.

The material proved to be porous, as it exhibited an apparent surface area of SA_{BET} = 88 m^2 g^{-1}. Only N_2 was investigated as a sorption gas, and **RRF24** was able to adsorb 1.25 mmol g^{-1} of N_2.

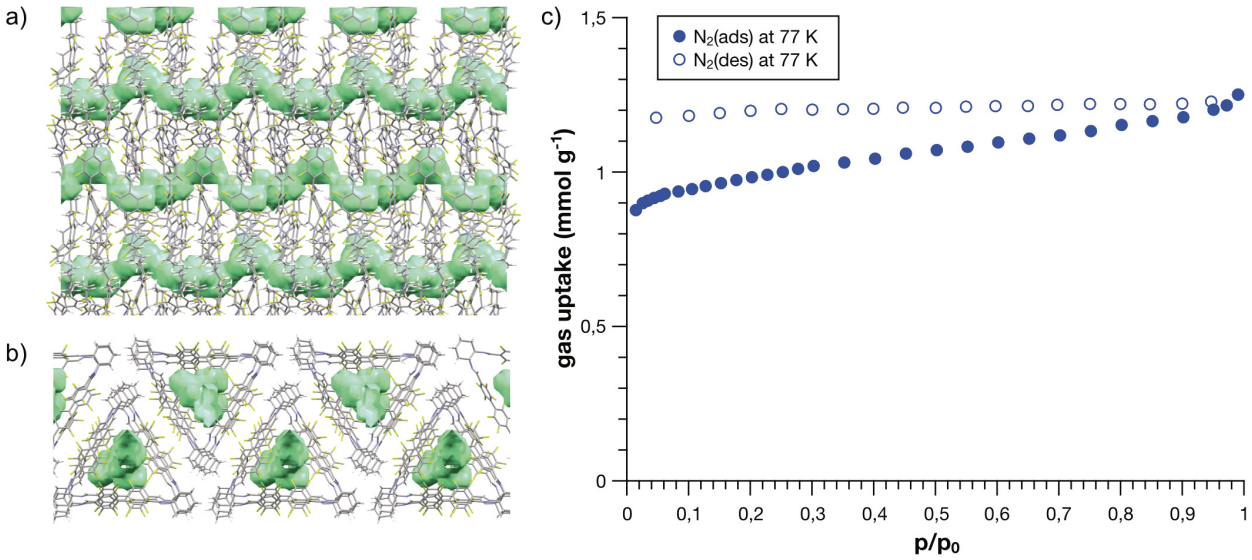

Figure 72: a) Crystal packing of **RRF24** shown along the crystallographic *b* axis; b) Crystal packing of **RRF24** shown along the crystallographic *a* axis (bottom). The tubular pores were visualized by manually deleting the incorporated solvent molecules and using a probe radius of 1.2 Å to visualize the accessible void space; c) The adsorption (blue, filled) and desorption (blue, outlined) isotherms of **RRF24** measured for N_2 at 77 K (right).

This value is somewhat lower than that of a structurally related supramolecular organic framework (**T-SOF-1**) in which terephthalaldehyde and **DACH** were reacted to form a trianglimine, which was then reduced to the trianglamine.[92d] This is possibly a result of the larger fluorine atoms pointing into the voids, which cannot be prevented, as the octafluorobiphenyl motif is encoded with a conformational twist. It has to be noted, though, that the porosity in **T-SOF-1** was a feature of the amine structures that were stabilized by chlorine interactions and resulted in the formation of a large extrinsic pore in between the macrocycle stacks. When the isostructural non-fluorinated biphenyl trianglimine was used for the comparison, this material did not even exhibit porosity in its imine form.[92a]

Therefore, **RRF24** marks another example in which the introduction of fluorine resulted in the formation of a highly crystalline supramolecular framework that exhibited porosity in its imine form. More precisely, in this case, the material exhibited helical and tubular channels that could be accessed with gases.

To investigate whether the influence of the fluorine atoms in the biphenyl motif on adjacent macrocycles that led to the formation of a helix in **RRF24** could be transferred to the non-fluorinated trianglimine, the formation of a cocrystal between **RRF24** and its non-fluorinated analogue (**RRH24**) was attempted. **RRH24** was prepared according to the literature procedure, and an equimolar amount of **RRF24** was dissolved in the same chloroform/acetonitrile mixture.[89c] Since C-F$\cdots\pi_F$ and C–H$\cdots\pi$ interactions should be the most favorable, due to their electronic nature, the formation of a supramolecular ABAB co-polymer was anticipated. The formation of crystals that

were suitable for SC–XRD could be observed.

Surprisingly, from the crystal structure, no formation of a supramolecular co-polymer could be observed, but rather the formation of a hybrid trianglimine, in which one biphenyl motif was substituted for an octafluorobiphenyl moiety (Figure 73).

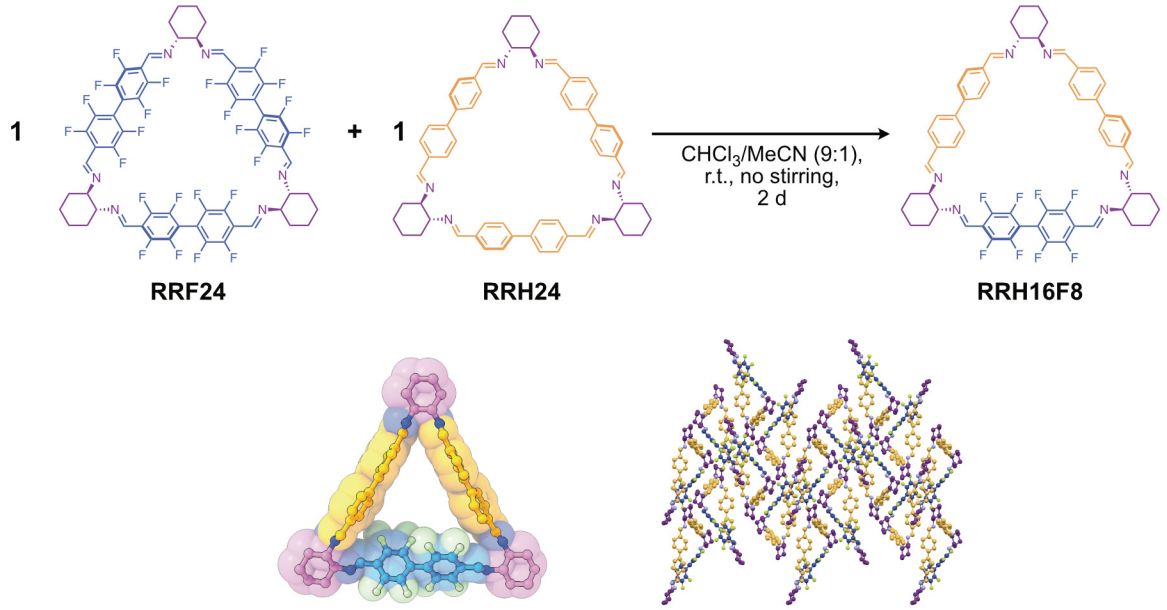

Figure 73: Mixing of equimolar amounts of **RRF24** and **RRH24** results in the formation of the mixed trianglimine **RRH16F8** (top). The crystal structure reveals a larger circular void in the center of the macrocycle (bottom left), but the crystal packing is unfavorable for porosity of the material. Solvent molecules and hydrogen atoms were omitted for clarity.

The mixed trianglimine **RRH16F8** crystallizes in the tetragonal space group $P4_32_12$. The hydrogenated biphenyl motifs are planar, and the aromatic planes of both biphenyl motifs are oriented perpendicular to the plane of the trianglimine, forming a large opening in the center of this macrocycle. Unfortunately, the overall crystal packing does not result in the formation of tubular stacks but rather in vertex-to-window crystallization. The highly crystalline material does not exhibit porosity. Still, these results provide an interesting starting point for the synthesis of partially fluorinated trianglimines, as the use of a suitable crystallization solvent could lead to the formation of stacks. The tubular pores would then be large enough to substantially adsorb gases, while simultaneously featuring an electron-deficient side to which electron-rich guests could be bound.

3.6.4. Summary

In this section, the successful synthesis of a highly fluorinated trianglimine, **RRF24**, was described. The macrocycle could be obtained as a crystalline material in which the individual molecules form a one-dimensional, tightly packed stack. Adjacent macrocycles of this stack are rotated 120° counter-clockwise in the trianglimine plane, resulting in three subunits being a full rotation. This is accompanied by the formation of a helical chirality that is induced by the twisted conformations of the octafluorobiphenyl motifs. By maximizing the C-F$\cdots\pi_F$ interactions between neighboring aromatic rings, a severe helical twist is induced, transferring the chirality between the molecules.

In the generated material, this results in the formation of helical channels which are occupied by the crystallization solvent. Careful activation of the material made it possible to generate a porous material that exhibited moderate uptake of nitrogen. The presence of fluorine atoms played a vital role in the stability of the tightly packed, shape-persistent stacks that do not require reduction to amine bonds to remain intact. The inherent helical chirality of the channels will be the subject of future studies as it could be used to achieve chiral seperation of molecules, further expanding the nano filtration capabilities of trianglimine-based materials.

When a co-crystal consisting of alternating fluorinated and non-fluorinated trianglimines was targeted, due to the dynamic nature of the imine bond, a hybrid trianglimine compound was formed. The crystal structure revealed that this compound exhibited a large circular void while simultaneously featuring one highly fluorinated side of the triangle, at which the binding or adsorption of electron-rich guests seemed possible. The generation of a highly ordered crystal structure is needed in the investigation of this material for gas sorption applications.

Ultimately, the first highly fluorinated trianglimine was investigated and proved once more that the introduction of fluorine into existing supramolecular motifs is often accompanied by positive influences on the material’s properties.

4. Conclusion

In this work, the influence of fluorine substitution on the solid-state and solution phase properties of fluorinated cage compounds was investigated.
Prior to the studies presented herein, only two examples of fluorinated imine cages were reported. Over the course of this study, 15 novel highly fluorinated organic cages, plus 8 partially fluorinated organic imine cages and one fluorinated macrocycle, could be synthesized, isolated, and investigated in regards to their material properties.

The investigation of the trigonal prismatic **Tri^{2}Di^3** cages (**FPOC1-3**) offered insights into the formation of imine cages using highly fluorinated building blocks. These results could be utilized to synthesize thermally stable imine cages that could be reduced to the corresponding amine cages, which exhibit fluorescence upon contact with anions. This was used to detect various anions with the naked eye. Similar indicator-like properties were exhibited by larger **Tri^{2}Di^3** imine cages (**FPOC7-8**), which featured a highly acidic methylene bridge in their fluorinated building blocks.

The targeted synthesis of a **Tri^{4}Di^6** cage using octafluorobiphenyl-containing aldehyde (**23**) resulted in the formation of a dense **Tri^{2}Di^3** cage (**FPOC9**) instead. A possible explanation for the formation of this sterically crowded cage molecule was found in the formation of multiple attractive C–F$\cdots\pi_F$ interactions.

When the fluorinated **Tri^{4}Tri^4** cage **FC1** was synthesized, it was proven that not only the thermal stability of the cage compound is increased upon the introduction of fluorinated building blocks into the structure, but furthermore, the gas sorption properties are enhanced as well. **FC1** exhibits one of the highest CO_2- and H_2-philicity observed in similarly sized imine cages (CO_2: 4.2 mmol g^{-1} at 273 K and 1 bar, H_2: 7.5 mmol g^{-1} at 77 K and 1 bar) and could potentially be used in hydrogen-storing applications. A crystalline material can be generated in high yields directly from the reaction of the starting materials, which is facilitated by the presence of the fluorine substituents in the amine building block.

In a study of the subsequential substitution of hydrogen-containing aldehydes for highly fluorinated aldehydes inside a **Tri^{4}Di^6** cage, the influence on the material's properties was investigated. Not only could the thermal stability of the material be increased as a function of degree of fluorination, but, the material's crystallinity followed the same trend. Crystalline samples of the hybrid cage-containing alloy, in which different imine cages co-exist in the same crystal lattice, could be prepared. This culminated in the preparation of a rare decernary co-crystal in which not only the

positions of the different hybrid cage molecules but also the positions of the hydrogen-containing aldehydes and fluorinated aldehydes are interchangeable.

A trianglimine-based supramolecular organic framework could be obtained from the transfer of knowledge about fluorinated imine cages to the field of macrocycles. Incorporating three highly fluorinated aldehydes into trianglimine **RRF24** led to the formation of a highly crystalline material. This was analyzed to be the result of a one-dimensional stacking of macrocycles to form a tubular channel. Due to C–F$\cdots\pi_F$ interactions between adjacent macrocycles, chirality is transferred between them, resulting in the introduction of a helical twist along the channel axis. This trianglimine-based material exhibited porosity towards N_2 (SA_{BET} = 88 m^2 g^{-1}; uptake: 1.25 mmol g^{-1}) after successful activation, which is indicative of the outstanding stability of the supramolecular stacks.

By targeting larger fluorinated imine cages, the effect of fluorine substitution could be investigated more thoroughly. The formation of a **Tri^{4}Tri^4** cage (**FPOC10**), that employs a flexible TREN-motif was enabled by stabilizing C–F$\cdots\pi_F$ interactions. These findings mark a profound addition to the intermolecular interactions that are considered important for the formation of hollow cage structures.
When the formation of a highly crystalline material based on **FC1** was taken as a blueprint for the synthesis of **Tri^{4}Tri^4** cages, that incorporate larger fluorinated aldehydes, another highly crystalline sample based on **FPOC13** could be obtained. The material featured a similar surface area (SA_{BET} = 510.6 m^2 g^{-1}) and an increased uptake of N_2 (11.8 mmol g^{-1}). Although the CO_2 and H_2 uptake is lower than for **FC1**, these results are the foundation for further research on the crystallinity and porosity of **FPOC13**.

Lastly, the synthesis of highly fluorinated octahedral cages, a motif that could previously often be attributed with high porosity and stability, was investigated. During the synthesis of the **Tri^{4}Di^6** cage **FPOC16**, based on (*R,R*)-**DACH** and phenylene-based aldehyde **31**, the formation of a **Tri^{6}Di^9** cage could be observed in the MALDI and the DOSY NMR spectra. This cage topology has remained elusive to supramolecular chemists to this date. Further optimization in synthetic conditions and purification procedures are required to isolate this compound and fully characterize the material.
Additionally, two porous materials based on **Tri^{4}Di^6** cages were obtained that exhibited moderate porosity (**FPOC16**: SA_{BET} = 521.5 m^2 g^{-1}; **FPOC17**: SA_{BET} = 395.2 m^2 g^{-1}) and uptake of N_2 (**FPOC16**: 8.97 mmol g^{-1}; **FPOC17**: 8.73 mmol g^{-1}). Since the thermal stability was lower than for **FC1**, further optimization of the material properties is needed.

The increase in thermal stability, crystallinity, and gas uptake that depends on the introduction of fluorinated building blocks into the cage molecules has been observed in numerous cases throughout this work. This undoubtedly proves the importance that fluorinated imine cages have

for the field of supramolecular organic chemistry. The successful transfer of these beneficial attributes to supramolecular organic frameworks has not only introduced fluorinated building blocks into another field of supramolecular chemistry but has also cemented the importance of intermolecular C–F···π_F interactions for the formation of stable materials and molecules.

5. Experimental Details

5.1. Methods

Solvents and commercial starting materials were purchased from Sigma Aldrich, TCI, Fisher Scientific, J&K scientific and abcr GmbH and used as received. Dry solvents were obtained from an MBraun solvent purification system. Reactions were monitored by thin layer chromatography (TLC) carried out on silica gel plates (ALUGRAM® Xtra SIL G/UV254, Macherey Nagel) using UV light for detection. Column chromatography was carried out with silica gel (Silica 60 M, 0.04-0.063 mm, Macherey Nagel) using eluents as specified. Flash column chromatography was carried out on a Biotage® Selekt system using the SNAP Sphär60 columns.

NMR measurements

NMR spectra were recorded on a Bruker Avance III 300 and a Bruker Avance III 600 spectrometer at 25 °C using residual protonated solvent signals as internal standards for ^{1}H and $^{13}C\{^{1}H\}$ spectra (^{1}H: $\delta(CDCl_3)$ = 7.26 ppm; $^{13}C\{^{1}H\}$: $\delta(CDCl_3)$ = 77.16 ppm). Splitting patterns are abbreviated as follows: singlet (s), doublet (d), triplet (t), quartet (q), quintet (p), heptet (hept), multiplet (m), and broad (br).

DOSY experiments

DOSY NMR experiments were recorded at 298 K and calibrated using known self-diffusion values for the solvents used (D_{solv}).[96] The hydrodynamic radii were estimated using the unmodified Stokes-Einstein- equation. This equation was solved for r_S using values for η from the literature.[97]

$$D = \frac{k_B T}{6\pi\eta r_H}$$

D is the measured diffusion coefficient ($m^2\ s^{-1}$)

k_B is the Boltzmann constant ($1.3806485 * 10^{-23}\ m^2\ kg\ s^{-2}\ K^{-1}$) T is the temperature (K)

r_H is the hydrodynamic radius of the analyte (m)

η is the viscosity of the solvent at temperature T ($kg\ m^{-1}\ s^{-1}$)

IR

Infrared spectra were recorded using a Shimadzu IR Affinity-1 with AT-IR sampling technique.

Mass spectrometry (MALDI)

Matrix-assisted Laser Desorption/Ionization mass spectrometry was performed on a MALDI-TOF/TOF UltrafleXtreme (Bruker Daltonics, Billerica, Massachusetts) using dithranol as matrix.

BET measurements

The BET surfaces of porous samples were determined *via* BET-isothermal analysis on a QUANTACHROME Nova 4200e S/N (Quantachrome Instruments, Florida, USA). Sample preparations are indicated at the corresponding graphs.

TGA

Thermogravimetric analysis was carried out under argon using a PerkinElmer Thermogravimetric Analyzer Pyris 1 or a Netzsch TG 209 F3 Tarsus in a temperature range from 30 °C to 800 °C at a step rate of 10 °C/min and holding a constant temperature at 800 °C for 5 minutes. All samples were analyzed twice to minimize possible errors.

PXRD

Powder X-ray diffraction data were collected on a Panalytical X'pert pro multi-purpose diffractometer (MPD) in reflection Bragg-Brentano geometry operating with a Cu anode at 40 kV 40 mA. Samples were mounted as loose powder between two 40 µm thin PTFE foils. PXRD patterns were collected in 100 2 minute scans with a step size of 0.00657 degrees 2 theta and scan time of 115 s/step over 10 – 50 deg 2 theta on a sample stage rotating at 2s/rotation. The incident X-ray beam was conditioned with 0.04 rad Soller slits, automatic divergence slit 1/8 deg, mask (15 mm) and anti-scatter slit of 1/4 deg. The diffracted beam passed through an automatic antiscatter slit (5 mm), 0.04 rad Soller slits and Ni filter before processing by the PIXcel detector operating in scanning mode.

SC–XRD

Single-crystals were mounted using a microfabricated polymer film crystal-mounting tool (dual-thickness MicroMount, MiTeGen) or a cactus needle, using low viscosity oil (perfluoropolyalkylether; viscosity 1800 cSt, ABCR). A Bruker D8 Venture single-crystal X-ray diffractometer with area detector, a Rigaku XtaLAB Synergy diffractometer or a Rigaku Oxford Diffraction Gemini ultra single-crystal X-ray diffractometer using Mo-*K*α (λ = 0.71073 Å) radiation or Cu-K α(λ = 1.54178 Å) were used for data collection at the temperature stated for each compound. Multiscan absorption corrections implemented in SADABS[101] were applied to the data. The structures were solved by intrinsic phasing (SHELXT-2013)[102] and refined by full-matrix least-

squares methods on F^2 (SHELXL-2014)[103] The hydrogen atoms were placed at calculated positions and refined by using a riding model. All SC-XRD measurements and refinements were carried out by Dr. B. M. Schmidt, except the measurement for the mixed macrocycle, which was measured by Dr. B. M. Schmidt and solved together with Dr. Guido Reiß.

5.2. Experimental Details for Section 3.1

Parts of this section were reproduced with permission from refs. [79, 83].

Synthesis of 1,3,5-triethylbenzene (8)

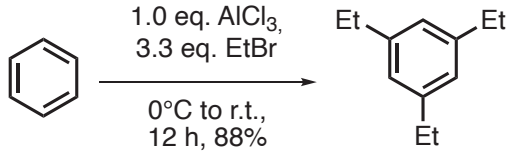

8

Aluminum chloride (8.80 g, 66.00 mmol, 1.10 eq.) was placed in a two-necked round bottom flask equipped with a septum and reflux condenser. At 0 °C bromoethane was added (10.00 mL, 134.00 mmol, 2.20 eq.). Benzene (5.30 mL, 60.00 mmol, 1.00 eq.) was added slowly followed by the remaining bromoethane (5.20 mL, 70.00 mmol, 1.20 eq.). The reaction was allowed to warm to room temperature while stirring for 12 hours. The mixture was poured on ice and the resolving solution was extracted with diethyl ether (3 x 150 mL). The combined organic phases were washed with 50 mL water, 50 mL aqueous 1 N NaOH and 50 mL water. The solution was dried over $MgSO_4$ and the solvent was removed under reduced pressure yielding 8.59 g (88 %) of 1,3,5-triethylbenzene as a colorless oil.

^{1}H NMR (300 MHz, $CDCl_3$): δ 6.87 (s, 3H, **H_{Ar}**), 2.62 (q, J = 7.6 Hz, 6H, C**H_2**), 1.24 (t, J = 7.6 Hz, 9H, C**H_3**).

All further spectral data was in accordance with the literature.[66]

Synthesis of 1,3,5-tris(bromomethyl)-2,4,6-triethyl benzene (9)

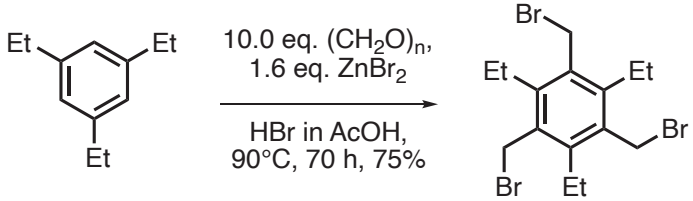

8 **9**

To a suspension of 1,3,5-triethylbenzene (10.00 mL, 53.00 mmol, 1.00 eq.) and paraformaldehyde (16.00 g, 530.00 mmol, 10.00 eq.) in hydrobromic acid (100 mL, 33 % in acetic acid), zinc bromide (19.79 g, 88.00 mmol, 1.60 eq.) was added in small portions. The mixture was stirred at 90 °C for 70 hours. The mixture was cooled to room temperature and 100 mL of water were added. The precipitate was filtered off and washed with water. The brown solid was solved in DCM and washed with saturated $NaHCO_3$ solution and 1 N NaOH solution. The solvent was removed under reduced pressure to give 17.53 g (75 %) of 1,3,5-tris(bromomethyl)-2,4,6-triethylbenzene as a beige solid.

^{1}H NMR (300 MHz, $CDCl_3$): δ 4.58 (s, 6H, C**H_2**-Br), 2.94 (q, J = 7.6 Hz, 6H, C**H_2**-CH_3), 1.34 (t, J = 7.6 Hz, 9H, C**H_3**).

All further spectral data was in accordance with the literature.[66]

Synthesis of 1,3,5-tris(azidomethyl)-2,4,6-triethyl benzene (10)

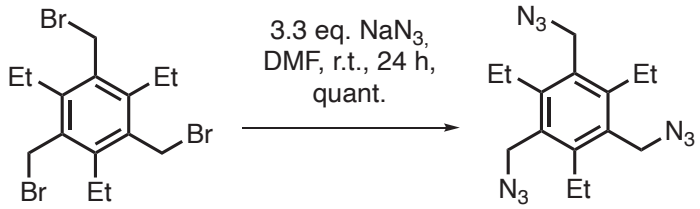

9 **10**

1,3,5-Tris(bromomethyl)-2,4,6-triethylbenzene (14.33 g, 32.50 mmol, 1.00 eq.) was dissolved in 300 mL DMF. Sodium azide (6.97 g, 107.00 mmol, 3.30 eq.) was slowly added and the mixture was stirred at room temperature for 24 hours. The mixture was diluted with 200 mL brine and stirred for an additional hour. It was extracted with DCM (5 x 100 mL) and the combined organic phases were washed with brine (5 x 50 mL). The solvent was removed under reduced pressure and the remaining DMF was evaporated yielding 10.59 g (100%.) 1,3,5-tris(azidomethyl)-2,4,6-triethylbenzene as a brown solid.

^{1}H NMR (300 MHz, $CDCl_3$): δ 4.49 (s, 6H, C**H_2**-N_3), 2.85 (q, J = 7.6 Hz, 6H, C**H_2**-CH_3), 1.24 (t, J = 7.6 Hz, 9H, C**H_3**).

All further spectral data was in accordance with the literature.[66]

Synthesis of 1,3,5-tris(aminomethyl)-2,4,6-triethylbenzene (Et-Amine)

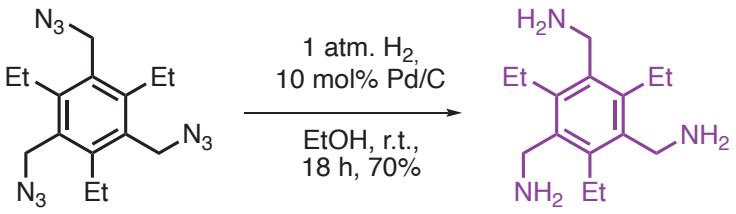

10 **Et-Amine**

Palladium on charcoal (430.00 mg, 0.60 mmol, 20 mol%) was added to a solution of 1,3,5-tris(azidomethyl)-2,4,6-triethylbenzene (10.59 g, 32.30 mmol, 1.00 eq.) in 200 mL ethanol and the mixture was stirred under a hydrogen atmosphere for 72 hours. The catalyst was filtered of and the solvent was removed under reduced pressure. The obtained red solid was purified by dissolving it in DCM and precipitation in cyclohexane to give 5.38 g (67 %) 1,3,5-tris(aminomethyl)-2,4,6-triethylbenzene as a colorless solid.

^{1}H NMR (300 MHz, $CDCl_3$): δ 3.87 (s, 6H, C**H$_2$**-NH_2), 2.81 (q, J = 7.5 Hz, 6H, C**H$_2$**-CH_3), 1.23 (t, J = 7.5 Hz, 9H, C**H$_3$**).

All further spectral data was in accordance with the literature.[66]

Synthesis of 1,3,5-tris(bromomethyl)-2,4,6-trimethylbenzene (11)

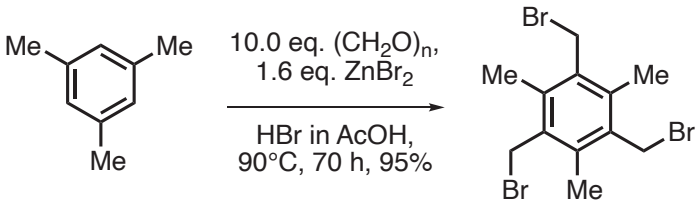

11

Mesitylene (13.97 g, 100.00 mmol, 1.00 eq.) and paraformaldehyde (10.77 g, 330.00 mmol, 3.30 eq.) were dissolved in hydrobromic acid (40 mL, 33 % in acetic acid). The mixture was stirred at 90 °C for 70 hours. The mixture was cooled to room temperature and 100 mL of water were added. The precipitate was filtered off and washed with water. The brown solid was solved in DCM and washed with saturated $NaHCO_3$ solution and 1 N NaOH solution. The solvent was removed under reduced pressure to give 31.30 g (95 %) of 1,3,5-tris(bromomethyl)-2,4,6-trimethylbenzene as a beige solid.

^{1}H NMR (300 MHz, $CDCl_3$) δ 4.58 (s, 6H, C**H$_2$**-Br), 2.46 (s, 9H, C**H$_3$**).

All further spectral data was in accordance with the literature.[28]

Synthesis of 1,3,5-tris(azidomethyl)-2,4,6-trimethyl benzene (12)

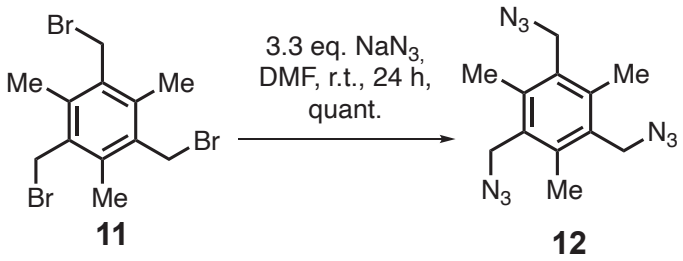

11 **12**

To a solution of 1,3,5-tris(bromomethyl)-2,4,6-trimethylbenzene (9.98 g, 25.00 mmol, 1.00 eq.) in dry DMF (25 mL) was added NaN_3 (5.36 g, 82.50 mmol, 3.30 eq.) at 0 °C in portions over a period of 20 min. The reaction mixture was stirred at room temperature for 24 h. It was then quenched with water (5 mL), and the solution was extracted with EtOAc (3 x 20 mL). The combined organic layers were repeatedly washed with water (5 x 5 mL) and brine, dried with Na_2SO_4, and concentrated to afford 1,3,5-tris(azidomethyl)-2,4,6-trimethyl benzene (7.13 g, 100 % yield) as a colorless solid.

^{1}H NMR (300 MHz, $CDCl_3$) δ 4.50 (s, 6H, C**H$_2$**-N_3), 2.46 (s, 9H, C**H$_3$**)

All further spectral data was in accordance with the literature.[28]

Synthesis of 1,3,5-tris(aminomethyl)-2,4,6-trimethylbenzene (Me-Amine)

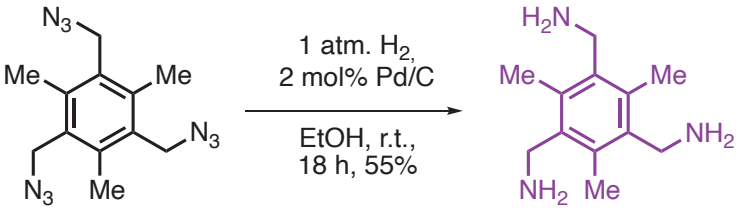

12 **Me-Amine**

Palladium on charcoal (532.00 mg, 0.50 mmol, 20 mol%) was added to a solution of 1,3,5-tris(azidomethyl)-2,4,6-triethylbenzene (7.13 g, 25.00 mmol, 1.00 eq.) in 200 mL ethanol and the mixture was stirred under a hydrogen atmosphere for 72 hours. The catalyst was filtered of and the solvent was removed under reduced pressure. The obtained red solid was purified by dissolving it in DCM and precipitation in cyclohexane to give 2.85 g (55 %) 1,3,5-tris(aminomethyl)-2,4,6-trimethylbenzene as a colorless solid.

^{1}H NMR (300 MHz, $CDCl_3$) δ 3.91 (s, 6H, C**H$_2$**-NH_2), 2.44 (s, 9H, C**H$_3$**), 1.21 (bs, 6H, N**H$_2$**).

All further spectral data was in accordance with the literature.[28]

Synthesis of 1,3,5-tris(chloromethyl)-2,4,6-trifluorobenzene (13)

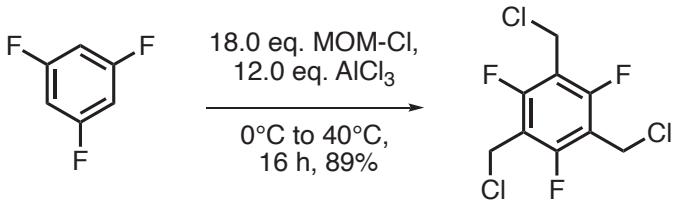

13

A two-neck round bottomed flask was charged with 1,3,5-trifluorbenzene (2.10 mL, 20.00 mmol 1.00 eq.) and freshly distilled chloromethyl methyl ether (27.30 mL, 360.00 mmol, 18.00 eq.) was added. The solution was degassed *via* nitrogen bubbling and $AlCl_3$ (32.0 g, 240 mmol, 12 eq.) was added in 8 portions under a continuous nitrogen stream over 30 min. at 0 °C. After complete addition, the resulting orange mixture was stirred at 0 °C for 60 min and was then heated to 40 °C for 16 h. After that time the reaction mixture was poured on ice and stirred for two hours. The mixture was filtrated and the precipitate was purified by recrystallization from benzene/DCM (9:1) yielding 4.96 g (89 %) 1,3,5-tris(chloromethyl)-2,4,6-trifluorobenzene as yellow crystals.

^{1}H NMR (300 MHz, $CDCl_3$) δ 4.64 (s, 6H, C**H_2**-Cl); **^{19}F NMR** (282 MHz, $CDCl_3$): δ -114.57 (s, **F_{Ar}**); **^{13}C{^{1}H} NMR** (75 MHz, $CDCl_3$) δ = 159.51 (dt, J = 257.6, 10.4 Hz, **C**-F), 111.27 (dd, J = 24.4, 19.8 Hz, **C**-CH_2), 32.03 ppm (s); IR: = 3041.7, 2991.6, 2789.1, 1722.4, 1660.7, 1622.1, 1469.8, 1438.9, 1365.6, 1267.2, 1257.6, 1190.1, 1097.5, 995.3, 974.4, 937.4, 787.0, 760.0, 734.9, 713.7, 694.4, 667.4, 638.4, 615.3 cm^{-1}; **CI-MS**: $[M\text{-}Cl+H]^+$ calc.: 241 m/z; found: 241 m/z

Synthesis of 1,3,5-tris(azidomethyl)-2,4,6-trifluorobenzene (14)

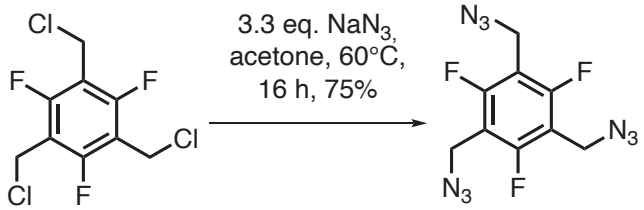

13 **14**

1,3,5-Tris(chloromethyl)-2,4,6-trifluorobenzene (3.00 g, 10.81 mmol, 1.00 eq.) and sodium azide (2.32 g, 35.68 mmol, 3.30 eq.) were dissolved in 35 mL acetone. The mixture was stirred at 60 °C for 16 hours. After cooling to room temperature, the solution was diluted with diethyl ether and washed with water. The combined organic phases were dried over sodium sulfate. The solvent was removed under reduced pressure. 2.43 g (75 %) 1,3,5-tris(azidomethyl)-2,4,6-trifluorobenzene were obtained as a light-yellow oil.

^{1}H NMR (300 MHz, $CDCl_3$) δ 4.45 (s, 6H, C**H_2**-N_3); **^{19}F NMR** (282 MHz, $CDCl_3$): δ -114.52 (s, **F_{Ar}**); **^{13}C{^{1}H} NMR** (75 MHz, $CDCl_3$) δ = 160.04 (dt, J = 254.2, 10.9 Hz), 108.91 (dd, J = 25.6, 20.8 Hz), 42.05 – 41.61 ppm (m); IR: = 2467.0, 2420.7, 2090.8, 1722.4, 1626.0, 1467.8, 1450.5, 1342.5, 1251.8, 1219.0, 1097.5, 1008.8, 881.5, 858.3, 779.2, 752.2, 715. 6, 640.4, 625.0, 603.7 cm^{-1}; due to the very labile nature of the triazide, high-resolution MS data could not be obtained, ionization

by different techniques led to unspecific fragments; **CI-MS**: $[M-N_3+H]^+$ calc.: 255 m/z; found: 255 m/z

Synthesis of 1,3,5-tris(aminomethyl)-2,4,6-trifluorobenzene (F-Amine)

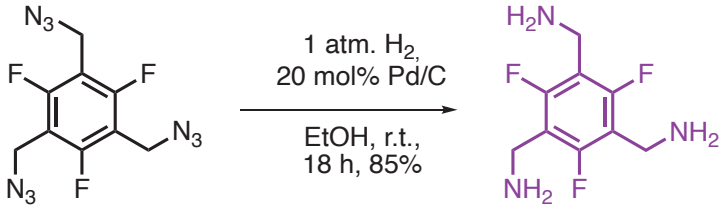

14 **F-Amine**

In a 250 mL Schlenk flask, 1,3,5-tris(azidomethyl)-2,4,6-trifluorobenzene (4) (2.40 g, 8.00 mmol, 1.00 eq.) was dissolved in 100 mL absolute ethanol. To this solution, palladium on carbon (300.00 mg, 20 mol%) was added. The atmosphere inside the flask was exchanged with H_2 gas twice before it was stirred for four hours under 1 bar of hydrogen gas. The resulting suspension was filtered through two filter papers and the solvent was evaporated under reduced pressure to give 1,3,5-tris(aminomethyl)-2,4,6-trifluorobenzene (**2**) as an off-white hygroscopic solid (1.50 g, 85%). **^{1}H NMR** (300 MHz, $CDCl_3$) δ 3.89 (s, 6H, C**H_2**), 1.45 ppm (broad s, 6H, N**H_2**); **^{19}F NMR** (282 MHz, $CDCl_3$) δ -123.61 ppm (s, 3F, **F_{Ar}**); **^{13}C{^{1}H} NMR** (75 MHz, $CDCl_3$) δ = 158.4 (dt, J = 246.1, 12.1 Hz, **C**-F), 115.6 - 115.0 (m, **C**-CH_2), 34.3 ppm (s, **C**H_2); IR: = 3361.3, 3289.4, 2951.5, 2885.0, 2667.1, 1621.8, 1457.0, 1383.7, 1312.3, 1170.6, 1089.6, 913.1, 821.5, 744.4, 622.9, 607.5, 537.1, 520.7 cm^{-1}; **ESI-HRMS**: calc. $[C_9H_{12}F_3N_3 + H]^+$ = 220.1056 m/z, found: 220.1059 m/z

Synthesis of 1,3-diformyl-2,4,5,6-tetrafluorobenzene (15)

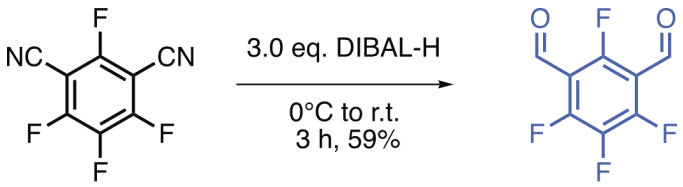

15

A 100 mL Schlenk flask was charged with 2,4,5,6-tetrafluoroisophthalonitrile (1.00 g, 5.00 mmol, 1.00 eq.) and 40 mL of dry toluene. The solution was purged with nitrogen and the DIBAL-H solution (1.0 M in hexanes, 15.00 mL, 3.00 eq.) was added dropwise at 0 °C. The reaction was allowed to reach room temperature while stirring for three hours. The solution was cooled to 0 °C, before ethyl acetate (1 mL) and 2 N HCl (20 mL) were added slowly. The phases were separated and the aqueous layer was extracted with CH_2Cl_2 (2 x 30 mL). The solvent was removed under reduced pressure. The crude product was solved in toluene and filtered over a silica plug to give 0.67 g (59 %) of 2,4,5,6-tetrafluoroisophthalaldehyde as pale-yellow crystals.

^{1}H-NMR (300 MHz, $CDCl_3$) δ 10.29 (s, 6H, C**H**O); **^{19}F-NMR** (282 MHz, $CDCl_3$) δ -124.85 (dt, J = 13.3, 3.6 Hz, 1F, **F_{ortho}**), -125.35 (dd, J = 20.7, 3.3 Hz, 2F, **F_{para}**), -160.72 (td, J = 20.7, 13.4 Hz, 1F, **F_{meta}**).

All further spectral data was in accordance with the literature.[36]

Synthesis of FPOC1

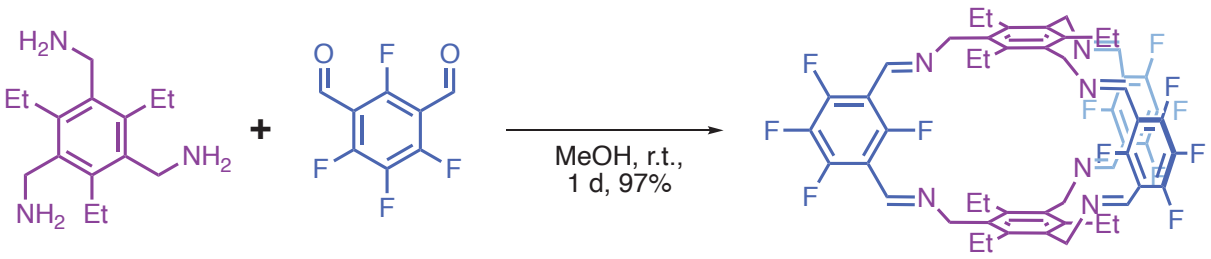

FPOC1

To a solution of **15** (124.00 mg, 6.00 mmol, 1.20 eq.) in 50 mL of methanol inside a 250 mL round-bottomed flask, a solution of **Et-Amine** (125.00 mg, 5.00 mmol, 1.00 eq.) in 50 mL of methanol was added dropwise over the course of 1 hour. After successful addition, the resulting mixture was stirred at room temperature for 24 hours. The resulting precipitate was filtered off and was carefully washed with cold methanol (3 x 25 mL) to yield **FPOC1** as a yellow solid (242.00 mg, 97%).

^{1}H NMR (300 MHz, $CDCl_3$) δ 7.86 (s, 6H, C**H**O), 5.19 (d, J = 2.4 Hz, 12H, C**H_2**-N), 2.27 (q, J = 7.4 Hz, 12H, C**H_2**-CH_3), 1.21 (t, J = 7.4 Hz, 18H, C**H_3**); **^{19}F NMR** (282 MHz, $CDCl_3$) δ -129.25 (d, J = 20.3 Hz, 6F, **F_{para}**), -130.14 (d, J = 5.5 Hz, 3F, **F_{ortho}**), -162.94 (t, J = 19.9 Hz, 3F, **F_{meta}**); **^{13}C{^{1}H} NMR** (75 MHz, $CDCl_3$) δ 148.2 (s, **C**HN), 144.9 (s, **C_q**-CH_2-N), 130.6 (s, **C_q**-Et), 56.1 (s, CH_2-N), 23.9 (s, CH_2-CH_3), 16.1 (s, CH_3).

FT-IR (ATR): $\tilde{\nu}$(cm^{-1}) = 2966.52, 2927.94, 2897.08, 2873.94, 2850.79, 1633.71, 1614.42, 1531.48,1479.40, 1454.33, 1417.68, 1381.03, 1323.17, 1280.73, 1192.01, 1151.50, 1026.13, 966.34, 794.67.

Signals corresponding to the carbons of the fluorinated aromatics could not be identified due to a low signal to noise ratio and strong coupling.

MALDI-MS: [**FPOC1**+H]$^{+}$ calculated: 1009.382 m/z, found: 1009.363 m/z.

Synthesis of FPOC2

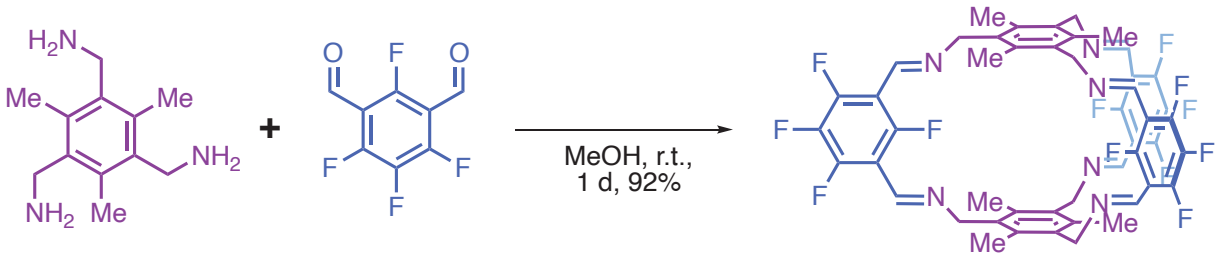

FPOC2

To a solution of **15** (124.00 mg, 6.00 mmol, 1.20 eq.) in 50 mL of methanol inside a 250 mL round-bottomed flask, a solution of **Me-Amine** (104.00 mg, 5.00 mmol, 1.00 eq.) in 50 mL of methanol was added dropwise over the course of 1 hour. After successful addition the resulting mixture was stirred at room temperature for 24 hours. The resulting precipitate was filtered off the remaining solution and was carefully washed with cold methanol (3 x 25 mL) to yield **FPOC2** as a yellow solid (212.50 mg, 92%).

^{1}H NMR (300 MHz, $CDCl_3$) δ 7.88 (s, 6H, C**H**O), 5.14 (d, J = 2.4 Hz, 12H, C**H$_2$**-N), 2.08 (s, 18H, C**H$_3$**); **^{19}F NMR** (282 MHz, $CDCl_3$) δ -129.07 (d, J = 20.1 Hz, 6F, **F$_{para}$**), -130.17 (d, J = 4.7 Hz, 3F, **F$_{ortho}$**), -162.94 (t, J = 19.6 Hz, 3F, **F$_{meta}$**); **^{13}C{^{1}H} NMR** (75 MHz, $CDCl_3$) δ 148.1 (s, **C**HN), 138.4 (s, **C$_q$**-CH_2-N), 131.3 (s, **C$_q$**-Et), 57.6 (s, **C**H_2-N), 16.1 (s, **C**H_3).

FT-IR (ATR): $\tilde{\nu}$(cm^{-1}) = 1627.92, 1517.98, 1477.47, 1458.18, 1411.89, 1382.96, 1327.03, 1284.59, 1246.02, 1190.08, 1149.571101.35, 1024.2, 989.48, 950.91, 744.52, 732.95, 704.02, 665.44,.

Signals corresponding to the carbons of the fluorinated aromatics could not be identified due to an unfavorable signal to noise ratio.

MALDI-MS: [**FPOC2**+H]$^+$ calculated: 925.288 m/z, found: 925.301 m/z.

Synthesis of FPOC3

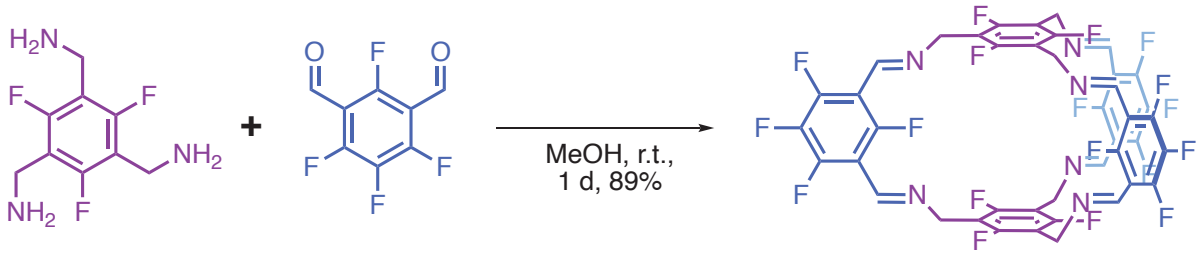

FPOC3

To a solution of **15** (124.00 mg, 6.00 mmol, 1.20 eq.) in 50 mL of methanol inside a 250 mL round-bottomed flask, a solution of **Me-Amine** (110.00 mg, 5.00 mmol, 1.00 eq.) in 50 mL of methanol was added dropwise over the course of 1 hour. After successful addition the resulting mixture was stirred at room temperature for 24 hours. The resulting precipitate was filtered off the remaining solution and was carefully washed with cold methanol (3 x 25 mL) to yield **FPOC3** as a yellow solid (211.80 mg, 89%).

^{1}H NMR (300 MHz, $CDCl_3$) δ 7.88 (s, 6H, C**H**N), 5.14 (d, J = 2.4 Hz, 12H, C**H$_2$**-N), 2.08 (s, 18H, **CH$_3$**); **^{19}F NMR** (282 MHz, $CDCl_3$) δ -115.87 (s, 6H, **F$_{Amine}$**), -124.83 (dt, J = 13.3, 3.6 Hz, 3F, **F$_{ortho}$**), -125.32 (dd, J = 20.9, 3.6 Hz, 6F, **F$_{para}$**), -160.69 (td, J = 20.7, 13.3 Hz, 3F, **F$_{meta}$**). Due to the low solubility of the compound, no ^{13}C spectrum could be obtained.

FT-IR (ATR): $\tilde{\nu}$(cm^{-1}) = 1624,06, 1544.98, 1533.41, 1477.47, 1458.18, 1413.82, 1388.75, 1340.53, 1327.03, 1284.59, 1192.01, 1147.65, 1101.35, 1049.28, 999.13, 921.97, 833.25, 767.67, 744.52, 715.59, 696.30, 669.30, 632.65.

MALDI-MS: [**FPOC3**+H]$^+$ calculated: 949.137 m/z, found: 949.125 m/z.

General procedure for the reduction of imine cages to amine cages (RFPOC1-3)

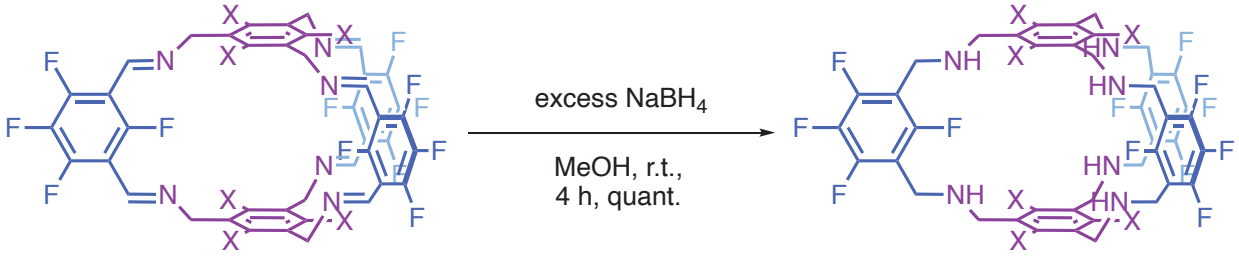

FPOC1, X = Et
FPOC2, X = Me
FPOC3, X = F

RFPOC1, X = Et
RFPOC2, X = Me
RFPOC3, X = F

To a suspension of the corresponding cage in methanol, sodium borohydride (20.0 eq.) was added in portions. The reaction temperature was maintained below 40°C. During the addition of sodium borohydride, the suspension started to clear. After stirring the mixture for 4 hours at room temperature, the solvent was evaporated completely under reduced pressure and the remaining solvent was dispersed in chloroform. The resulting suspension was stirred for 2 hours at room temperature and was then filtered. The solvent of the filtrate was evaporated under reduced pressure to yield the amine cages as colorless solids in quantitative yields.

FPOC1 to **RFPOC1**: 202.00 mg (0.20 mmol) of **FPOC1** yielded 204.0 mg (0.20 mmol, 100%) of **RFPOC1**.

^{1}H NMR (300 MHz, $CDCl_3$) δ 3.82 (s, 12H, ArF-C**H$_2$**-N), 3.78 (s, 12H, ArH-C**H$_2$**-N), 2.74 (q, J = 7.4 Hz, 12H, C**H$_2$**-CH_3), 1.21 (t, J = 7.4 Hz, 18H, C**H$_3$**); **^{19}F NMR** (282 MHz, $CDCl_3$) δ -125.88 (d, J = 11.2 Hz, 3F, **F$_{ortho}$**)), -139.85 (d, J = 22.1 Hz, 6F, **F$_{para}$**), -164.90 (td, J = 22.0, 11.1 Hz, 3F, **F$_{meta}$**); **^{13}C{^{1}H} NMR** (75 MHz, $CDCl_3$) δ 155.37 (d, J = 240.5 Hz, **C**F), 147.79 (d, J = 252.5 Hz, **C**F), 142.70, 139.06 – 134.98 (m, **C**F), 129.17 (s, **C$_q$**-CH_2-N), 128.36 (s, **C$_q$**-Et), 125.44 (s, **C$_{ArF}$**), 48.21 (s, Ar_F-**C**H_2-N), 41.25 (s, Ar_H-**C**H_2-N), 22.62 (s, **C**H_2(Et)), 16.95 (s, **C**H_3(Et)). Signals corresponding to the carbons of the fluorinated aromatics could not be identified due to an unfavorable signal to noise ratio.

FT-IR (ATR): $\tilde{\nu}$(cm^{-1}) = 2966.52, 2929.87, 2900.94, 2873.94, 1965.46, 1691.57, 1639.49, 1568.13, 1489.05, 1452.40, 1375.25, 1319.31, 1280.73, 1236.37, 1192.01, 1155.36, 1109.07, 1078.21, 1045.42, 1028.06, 995.27, 966.34, 871.82, 810.10, 769.60, 738.74, 729.09, 711.73, 603.72.
MALDI-MS: [**RFPOC1**+H]$^+$ calculated: 1021.476 m/z, found: 1021.462 m/z.

FPOC2 to **RFPOC2**: 210.0 mg (22.40 mmol) of **FPOC2** to 212.4 mg (22.40 mmol, 100%) of **RFPOC2**.
^{1}H NMR (300 MHz, $CDCl_3$) δ 3.84 (s, 12H, Ar_F-C**H$_2$**-N), 3.80 (s, 12H, Ar_H-C**H$_2$**-N), 2.35 (s, 18H, CH_3); **^{19}F NMR** (282 MHz, $CDCl_3$) δ -125.46 (d, J = 11.1 Hz, 3F, **F$_{ortho}$**), -139.82 (d, J = 21.9 Hz, 6F, **F$_{para}$**), -164.90 (dd, J = 22.0, 11.2 Hz, 3F, **F$_{meta}$**).
MALDI-MS: [**RFPOC2**+H]$^+$ calculated: 937.382 m/z, found: 937.375 m/z
FT-IR (ATR): $\tilde{\nu}$(cm^{-1}) = 2912.51, 2900.94, 2856.58, 1643.35, 1489.05, 1454.33, 1417.68, 1377.17, 1361.74, 1323.17, 1278.81, 1257.59, 1242.16, 1219.01, 1197.79, 1107.14, 1078.21, 1064.71, 1018.41, 995.27, 966.34, 933.55, 883.40, 750.31, 721.38, 713.66, 663.51, 628.79.
Due to the low solubility in common NMR solvents, no ^{13}C NMR spectrum could be obtained.

FPOC3 to **RFPOC3**: 206.1 mg (21.45 mmol) of **FPOC3** to 208.5 mg (21.45 mmol, 100%) of **RFPOC3**.
^{1}H NMR (300 MHz, $CDCl_3$) δ 3.79 (s, 12H, Ar_F-C**H$_2$**-N), 3.76 (s, 12H, Ar_H-C**H$_2$**-N); **^{19}F NMR** (282 MHz, $CDCl_3$) δ -120.15 (s, 6F, **F$_{Amine}$**), -126.64 (d, J = 11.0 Hz, 3F, **F$_{ortho}$**), -138.40 (d, J = 21.7 Hz, 6F, **F$_{para}$**), -164.35 (dd, J = 21.8, 11.2 Hz, 3F, **F$_{meta}$**).
FT-IR (ATR): $\tilde{\nu}$(cm^{-1}) = 2916.37, 2848.86, 1643.35, 1606.70, 1489.05, 1454.33, 1377.17, 1336.67, 1278.81, 1261.45, 1217.08, 1195.87, 1161.15, 1111.00, 1080.14, 1001.06, 945.12, 877.61, 821.68, 775.38, 756.10, 711.73, 665.44, 605.65.
MALDI-MS: [**RFPOC3**+H]$^+$ calculated: 961.231 m/z, found: 961.224 m/z
Due to the low solubility in common NMR solvents, no ^{13}C NMR spectrum could be obtained.

Synthesis of 2,4,6-trifluorobenzaldehyde (16)

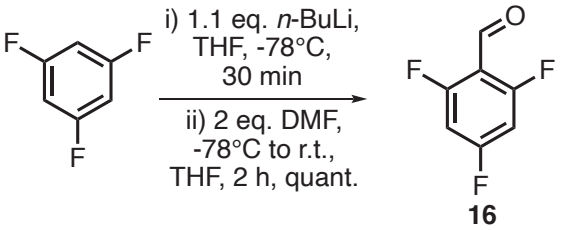

16

In a 50 mL flask THF was cooled down to -78 °C (aceton/dry ice) under nitrogen. 1,3,5-Trifluorbenzene (0.31 mL, 3.00 mmol, 1.00 eq.) was added. *n*-BuLi (1.6M in hexane, 2.10 mL, 3.30 mmol, 1.10 eq.) was added dropwise and the solution was stirred at -78 °C for 30 min. DMF (0.26 mL, 3.30 mmol, 1.10 eq.) was added dropwise and the solution was warmed up to room temperature.

NH_4Cl was added and the mixture was extracted with ethyl acetate. The combined organic layers were washed with brine and dried over $MgSO_4$. The solvent was evaporated to give the final product as colorless solid (480.30 mg, 100% yield).

^{1}H NMR (300 MHz, $CDCl_3$): δ = 10.25 (s, 1H, C**H**O), 6.81 – 6.70 (m, 2H, $\mathbf{H_{meta}}$); **^{19}F NMR** (282 MHz, $CDCl_3$): δ = -95.45 (t, J = 11.5 Hz, 1F, $\mathbf{F_{para}}$), -110.71 (d, J = 11.6 Hz, 2F, $\mathbf{F_{ortho}}$).

All further spectral data was in accordance with the literature.[74]

Synthesis of (E)-N-benzyl-1-(2,4,6-trifluorophenyl)methanimine (17)

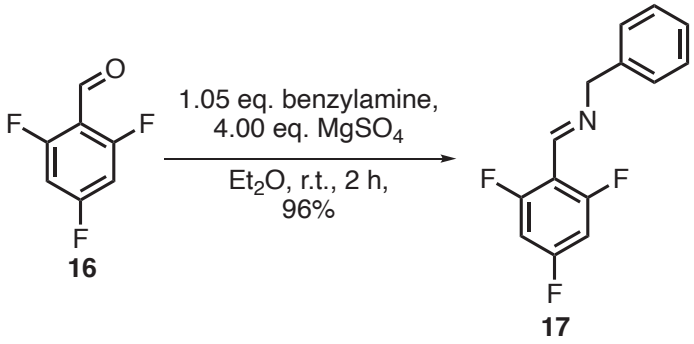

In a round-bottom flask, $MgSO_4$ (1.71 g, 14.24 mmol, 4.00 eq.) was stirred in diethyl ether (4 mL/mmol) for 15 min. Then 2,4,6-trifluorobenzaldehyde (570.00 mg, 3.56 mmol, 1.00 eq.) was added. While stirring, the benzylamine (0.39 mL, 3.63 mmol, 1.02 eq.) was added. The reaction solution was allowed to stir at rt for 4 h. The solution was filtered and the solvent was evaporated, under reduced pressure to yield the imine (**17**) as yellow solid (851.80 mg, 96%).

Imine **17** was directly used in the next step, as further purification led to a decomposition of the compound.

Synthesis of N-benzyl-1-(2,4,6-trifluorophenyl)methanamine (18)

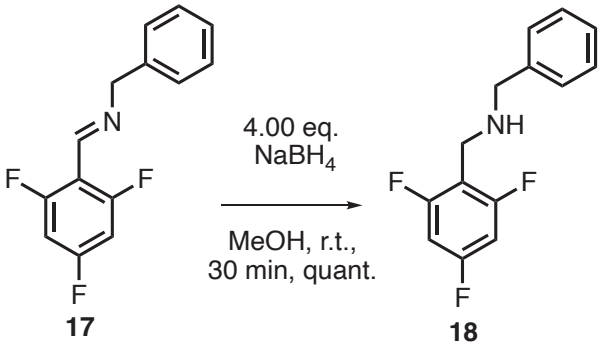

In a round-bottom flask imine **17** (698.00 mg, 2.80 mmol, 1.00 eq) was stirred in methanol (5 mL/mmol). $NaBH_4$ (424.00 mg, 11.20 mmol, 4.00 eq) is added and the reaction was stirred for 30 min at rt until no more gas development was seen. The solvent was evaporated and the crude product

was dissolved in 2M HCl and was then made basic with 4M KOH. The aqueous phase was extracted with dichloromethane (3 x 20 mL). The organic phase was dried over $MgSO_4$ and the solvent was evaporated under reduced pressure to yield the amine as a colorless solid (703.50 mg, 100%)

^{1}H NMR (300 MHz, $CDCl_3$): δ = 7.33 (d, J = 4.3 Hz, 4H, **H_{Ph}**), 7.30 – 7.21 (m, 1H, **H_{Ph}**), 6.72 – 6.60 (m, 2H, **H_{meta}**), 3.87 (s, 2H, Ar_F-C**H_2**-N), 3.78 (s, 2H, Ar_H-C**H_2**-N), 1.77 (s, 1H, NH); **^{19}F NMR** (282 MHz, $CDCl_3$): δ = -109.33 (t, J = 6.0 Hz, 1F, **F_{para}**), -112.93 (d, J = 6.0 Hz, **F_{ortho}**).

All further spectral data was in accordance with the literature.[74]

Synthesis of 3-benzyl-5,7-difluoro-1-phenyl-3,4-dihydroquinazoline-2(1H)-thione (19)

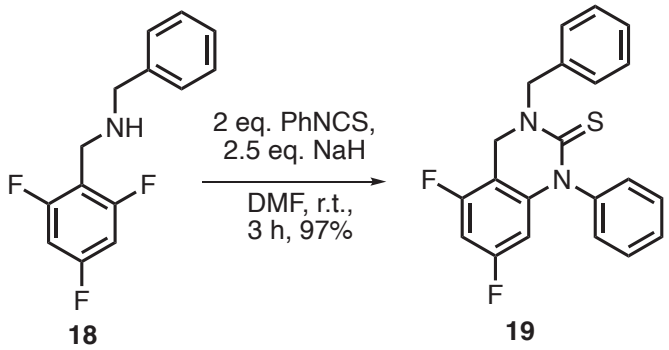

18 **19**

In a 10 mL test tube, the amine (57.00 mg, 0.20 mmol, 1.00 eq.) was stirred in DMF (5 mL/mmol). NaH (60 wt% in parrafin, 20.00 mg, 0.50 mmol, 2.50 eq) was added slowly. Then phenylisothiocyanate (48.00 µL, 0.40 mmol, 2.00 eq) was added and the reaction was allowed to stir at rt for 16 h. The reaction solution was extracted with dichloromethane (3 x 30 mL), washed with brine and dried over $MgSO_4$. Solvents were evaporated in vacuum. The final product could be isolated after column chromatography (cyclohexane:ethyl acetate 10:1) as a bright yellow solid (71.40 mg, 97%).

^{1}H NMR (300 MHz, $CDCl_3$): δ = 7.61 – 7.44 (m, 5H, CH_2-**H_{Ph}**), 7.40 – 7.28 (m, 2H, SCN-**H_{Ph}**), 6.47 (td, J = 8.9, 2.3 Hz, 1H, **H_{meta}**), 5.71 (d, J = 10.6 Hz, 1H, **H_{ortho}** to ring closure), 5.41 (s, 2H, Ar_F-C**H_2**-N), 4.53 (s, 2H, Ar_H-**CH_2**-N); **^{19}F NMR** (282 MHz, $CDCl_3$): δ = -108.81 (d, J = 7.6 Hz, 1F, **F_{para}**), -116.20 (d, J = 7.2 Hz, 1F, **F_{meta}**); **^{13}C{^{1}H} NMR** (151 MHz, $CDCl_3$): δ = 163.3 (s, **C_{ArF}-F**), 161.8 (s, **C_{ArF}-F**), 158.9 (s, **C_{ArF}-F**), 157.3 (s, **C_{ArF}**), 154.58 (s, **C_{ArF}**), 142.7 (s, *tert*-**C_{ArF}**), 136.8 (s, **C_{Ar}**), 128.7 (s, **C_{Ar}**), 128.0 (s, **C_{Ar}**), 127.6 (s, *tert*-**C_{Ar}**), 105.5 (s, **C_{Ar}**), 105.3 (s, **C_{Ar}**), 97.9 (s, **C_{Ar}**), 97.8 (s, **C_{Ar}**), 96.6 (s, *tert*-**C_{Ar}**), 58.9 (s, **C**H_2-N), 40.9 (s, **C**H_2-N).

FT-IR (ATR): $\tilde{\nu}$(cm^{-1}) = 3097.68, 3080.32, 3051.39, 3032.10, 2918.30, 1631.78, 1616.35, 1593.20, 1519.91, 1485.19, 1440.83, 1431.18, 1411.89, 1373.32, 1359.82, 1317.38, 1296.16, 1263.37, 1244.09, 1205.51, 1178.51, 1157.29, 1138.00, 1114.86, 1083.99, 1022.27, 993.34, 972.12, 950.91,

920.05, 896.90, 875.68, 835.18, 817.82, 808.17, 796.60, 777.31, 734.88, 717.52, 694.37, 659.66, 636.51.

ESI-HRMS (m/z): [**19**+H]$^+$ calculated: 367.1075 m/z, found: 367.1071 m/z.

Synthesis of the mono- (20) and difunctionalized (21) RFPOC1

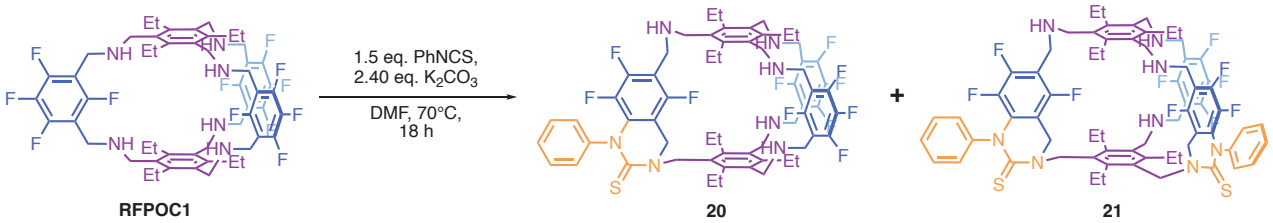

RFPOC1 (51.00 mg, 0.05 mmol, 1.00 eq.) was dissolved in DMF and K_2CO_3 (16.60 mg, 0.12 mmol, 2.40 eq.) were added under intense stirring. After the addition of phenylisothiocyanate (10.5 µL, 0.08 mmol, 1.50 eq.) the reaction mixture was heated to 70°C for 18 hours. The solvent was evaporated under reduced pressure and the residue was dissolved in 50 mL of dichloromethane and washed with saturated $NaHCO_3$ solution (3 x 50 mL). The organic phase was separated and dried over anhydrous $MgSO_4$. Ultimately, the solvent of the filtrate was evaporated under reduced pressure to yield the crude mixture as a brown solid.

^{1}H NMR (300 MHz, $CDCl_3$) δ 7.48 – 7.30 (m, 5H, **H_{Ph}**), 3.83 (s, 9H, Ar_F-C**H_2**-N), 3.78 (s, 9H, Ar_H-C**H_2**-N), 2.73 (t, J = 7.4 Hz, 9H, C**H_2**-C**H_3**), 1.34 – 1.21 (m, 27H, C**H_3**).

^{19}F NMR (282 MHz, $CDCl_3$) δ -125.52 (d, J = 11.4 Hz), -125.90 (dd, J = 19.0, 11.0 Hz), -130.69, -138.62 (d, J = 22.3 Hz), -139.83 (d, J = 22.0 Hz), -141.27 – -141.88 (m), -148.48 – -149.02 (m), -164.17 – -165.04 (m).

Due to the complexity of the ^{19}F NMR spectrum no assignment of the signals could be made. The low solubility of the product mixture prevented the recording of ^{13}C NMR spectra.

ESI (HR)MS: [**20**+H]$^+$ calculated: 1136.4828 m/z, found: 1136.4838 m/z; [**21**+2H]$^{2+}$ calculated: 626.2497 m/z, found: 626.2490 m/z.

Anion sensing experiments

20 mg of **RFPOC1** or **RFPOC2** were dissolved in 1 mL of 10 wt% acetic acid. To this solution, NBu_4Cl (1 or 10 eq.) were added. The resulting mixture was then sonicated at room temperature for 20 minutes and afterwards subjected to NMR analysis.

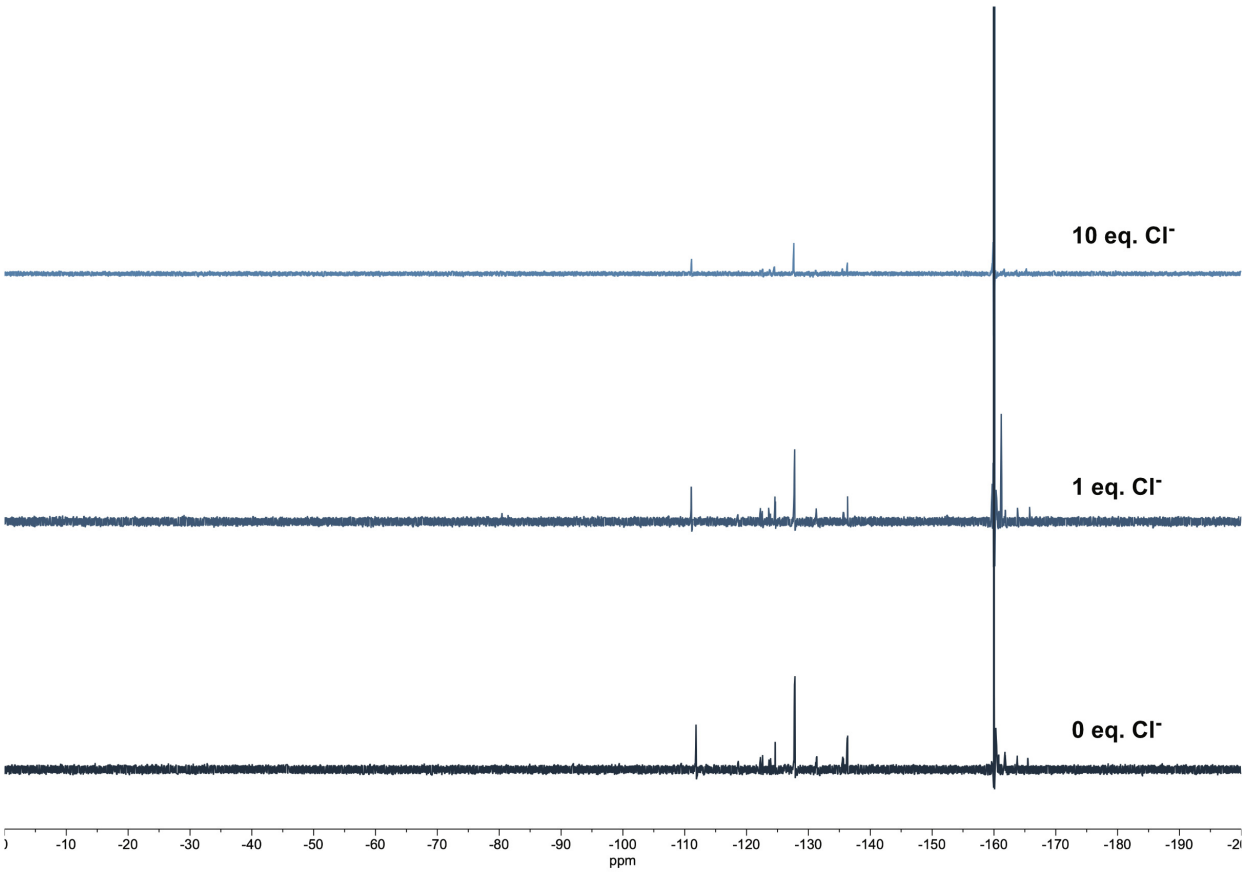

Figure S1: Stacked 19F NMR spectra of a solution of RFPOC1 in 10 wt% acetic acid with Hexafluorobenzene as an internal standard (at -180.0 ppm).

Thermogravimetrical analysis

Table S1: Overview about onset decomposition temperatures of the small fluorinated **Tri^{2}Di^3** cages.

Sample name	Onset decomposition temperature (°C)
FPOC1	322.2
FPOC2	347.5
FPOC3	336.5

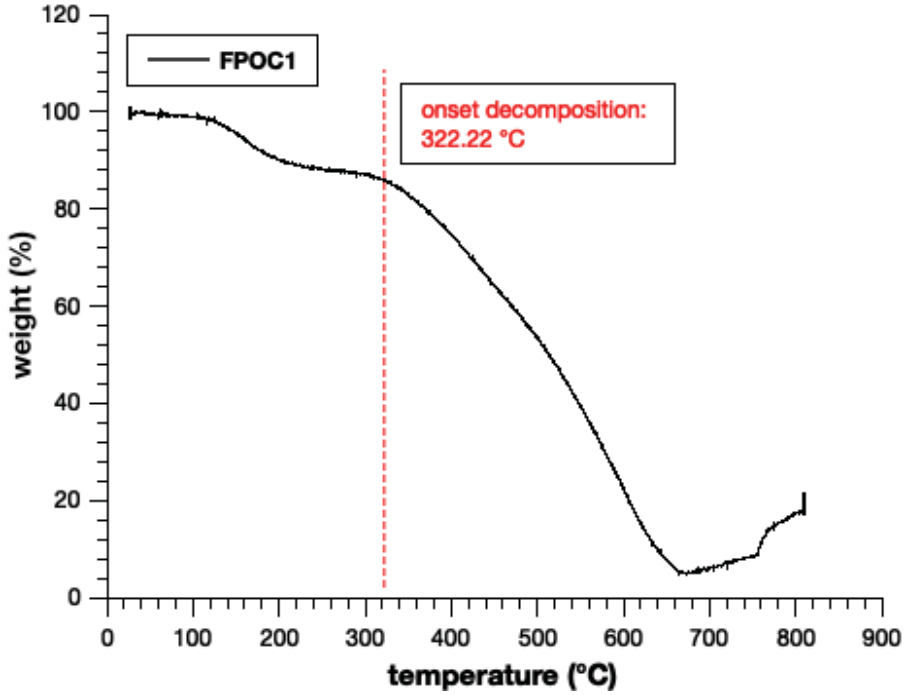

Figure S2: TGA graph of **FPOC1**, which was precipitated, washed with methanol and then dried at 40 °C for 24 hours prior to measurement.

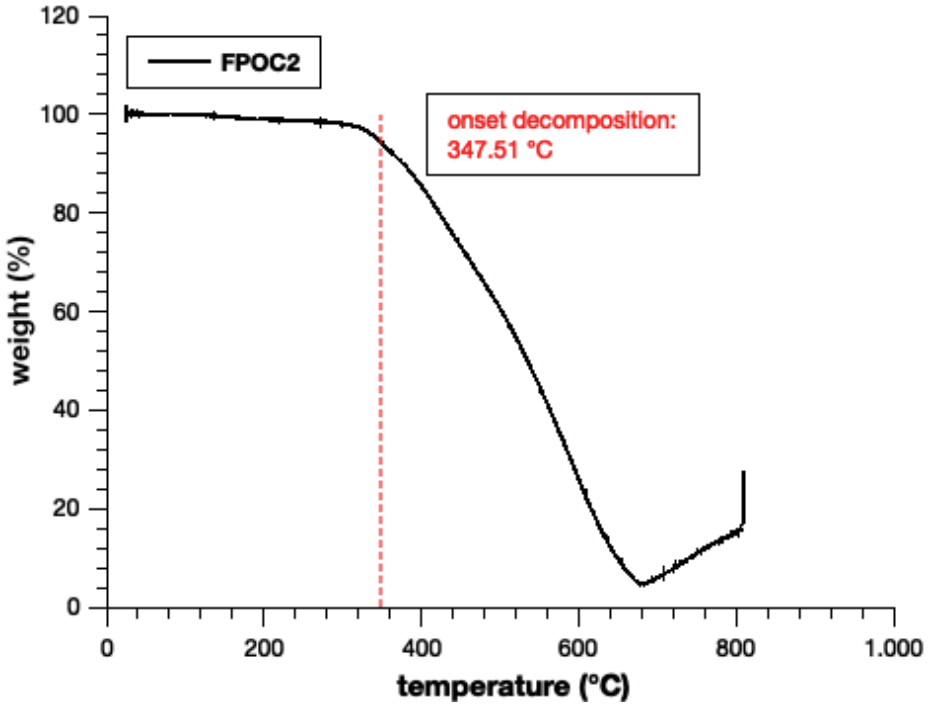

Figure S3: TGA graph of **FPOC2**, which was precipitated, washed with methanol and then dried at 40 °C for 24 hours prior to measurement.

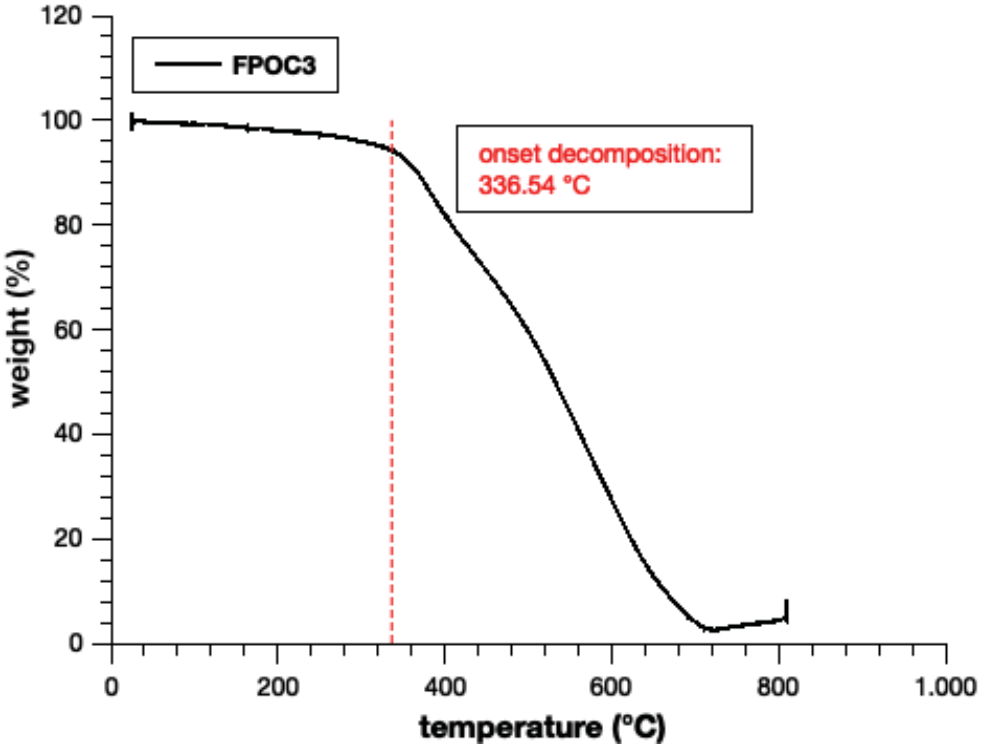

Figure S4: TGA graph of **FPOC3**, which was precipitated, washed with methanol and then dried at 40 °C for 24 hours prior to measurement.

Gas sorption studies

The apparent surface area was determined in a single point measurement experiment, as the area was too low for the recording of an isothermal curve for all three FPOCs.

Table 2: Apparent surface areas determined by a single point measurement method according to the BET-model measured using nitrogen as sorption gas.

Sample name	SA_{BET} ($m^2\,g^{-1}$)
FPOC1	4
FPOC2	11
FPOC3	3

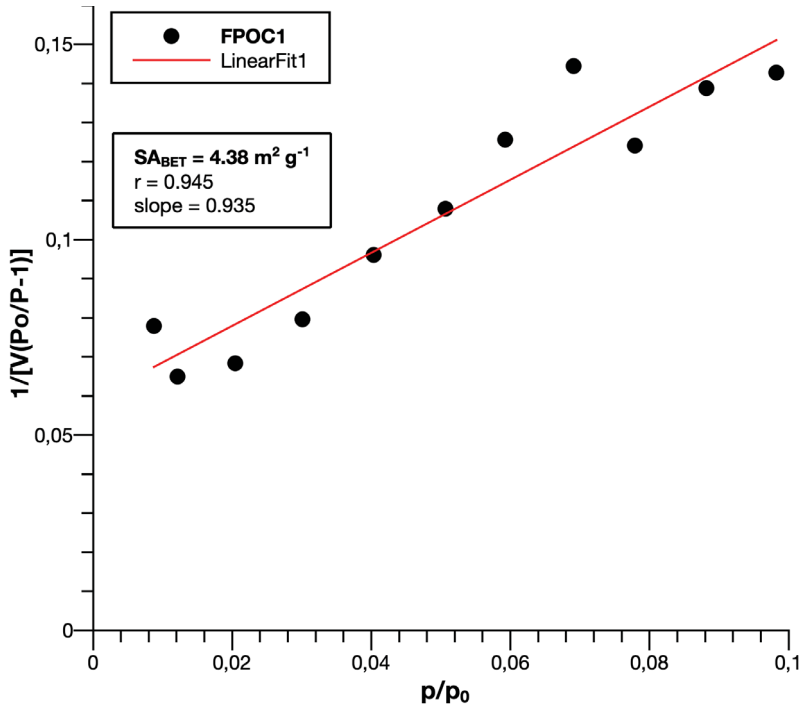

Figure S5: BET plot of an amorphous sample of **FPOC1**.

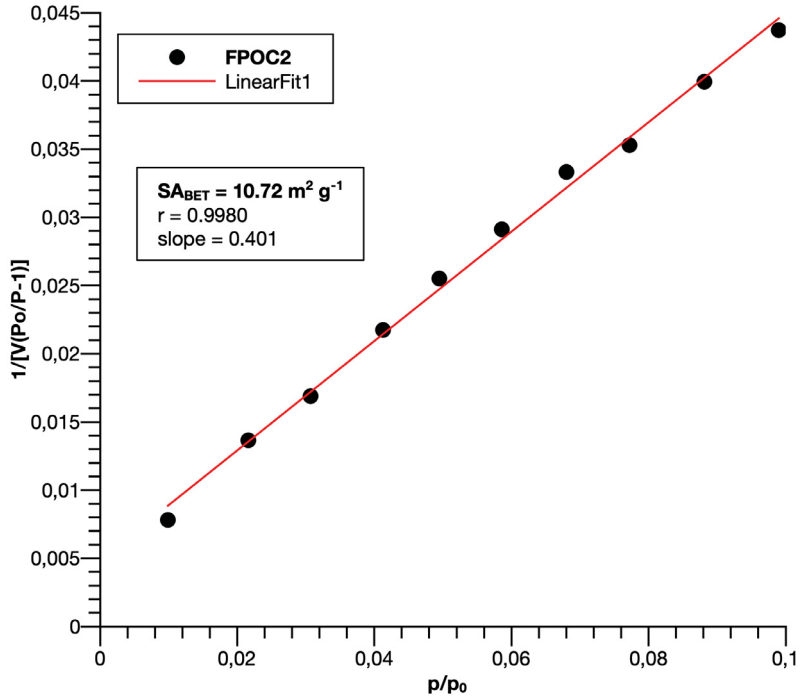

Figure S6: BET plot of an amorphous sample of **FPOC2**.

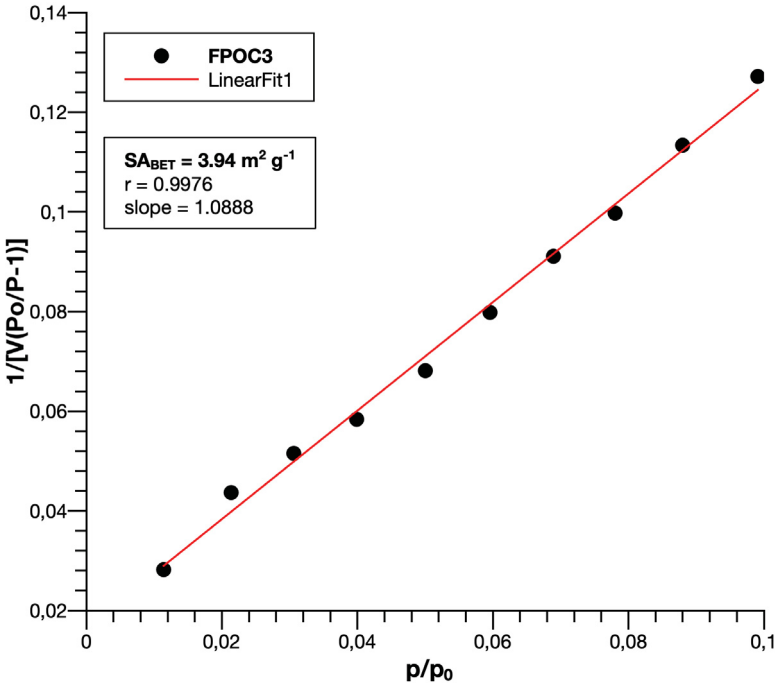

Figure S7: BET plot of an amorphous sample of **FPOC3**.

Crystal structures

Crystallographic data for **FPOC1**

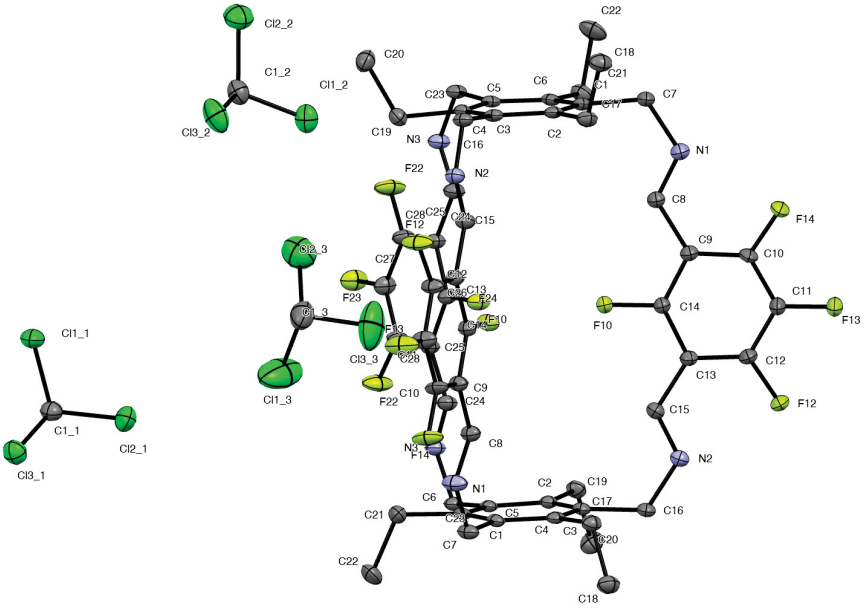

Figure S8: ORTEP-drawing (50% probability thermal ellipsoids) of the molecular structure of **FPOC1** in the single-crystal as determined by X-ray diffraction. Hydrogens are omitted for clarity.

Crystal data	
Chemical formula	$C_{54}H_{48}F_{12}N_6 \cdot 6(CHCl_3)$
M_r	1725.19
Crystal system, space group	Monoclinic, P2/n
Temperature (K)	118
a, b, c (Å)	15.439 (3), 10.696 (2), 23.775 (5)
b (°)	98.32 (3)
V (Å^3)	3884.9 (14)
Z	2
D_x (Mg m^{-3})	1.475
Radiation type	Cu Ka
m (mm^{-1})	6.42
Crystal shape	Prism
Colour	Colorless
Crystal size (mm)	0.86 × 0.44 × 0.24
Data collection	
Diffractometer	Bruker D8 VENTURE
Radiation source	Incoatec Microfocus Source
Scan method	f and w scans
Absorption correction	Multi-scan SADABS (Bruker-AXS)
T_{min}, T_{max}	0.311, 0.754
No. of measured, independent and observed [I > 2s(I)] reflections	69127, 8320, 7811
R_{int}	0.054
q values (°)	q_{max} = 79.9, q_{min} = 3.2
$(\sin q/l)_{max}$ (Å^{-1})	0.639
Range of h, k, l	h = -19→18, k = -13→12, l = -30→29
Refinement	
Refinement on	F^2
R[F^2 > 2s(F^2)], wR(F^2), S	0.058, 0.168, 1.05
No. of reflections	8320
No. of parameters	439

H-atom treatment	H-atom parameters constrained
$D\rho_{max}$, $D\rho_{min}$ (e Å^{-3})	0.97, -0.87

Computer programs: Bruker APEX2, Bruker SAINT, SHELXL2018/3 (Sheldrick, 2018).

Crystallographic data for model compound **19**

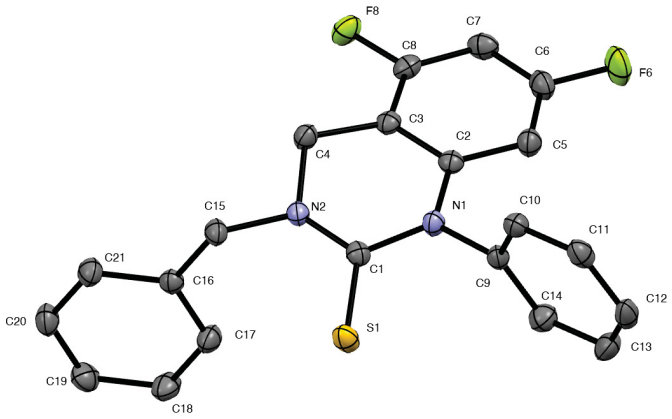

Figure S9 ORTEP-drawing (50% probability thermal ellipsoids) of the molecular structure of the ring- closed **19** in the single-crystal as determined by X-ray diffraction. Hydrogens are omitted for clarity.

Crystal data	
Chemical formula	$C_{21}H_{16}F_2N_2S$
M_r	366.42
Crystal system, space group	Orthorhombic, Pbca
Temperature (K)	140
a, b, c (Å)	7.1002 (3), 21.0704 (9), 23.2216 (10)
V (Å^3)	3474.0 (3)
Z	8
D_x (Mg m^{-3})	1.401
Radiation type	Cu Ka
m (mm^{-1})	1.89
Crystal shape	Rod
Colour	Colorless
Crystal size (mm)	0.30 × 0.14 × 0.11
Data collection	
Diffractometer	Bruker D8 VENTURE

Radiation source	Incoatec Microfocus Source
Scan method	f and w scans
Absorption correction	Multi-scan SADABS (Bruker-AXS)
No. of measured, independent and observed [I > 2s(I)] reflections	47547, 3296, 3166
R_{int}	0.044
q values (°)	q_{max} = 70.4, q_{min} = 4.2
$(\sin q/l)_{max}$ (Å^{-1})	0.611
Range of h, k, l	h = -8→8, k = -20→25, l = -28→28
Refinement	
Refinement on	F^2
R[F^2 > 2s(F^2)], wR(F^2), S	0.028, 0.076, 1.04
No. of reflections	3296
No. of parameters	235
No. of restraints	1
H-atom treatment	H-atom parameters constrained
$D\rho_{max}$, $D\rho_{min}$ (e Å^{-3})	0.26, -0.25

Computer programs: Bruker APEX3, Bruker SAINT, SHELXT 2014/5 (Sheldrick, 2014), SHELXL2018/3 (Sheldrick, 2018).

5.3. Experimental Details for Section 3.2

Parts of this section were reproduced with permission from ref. [88].

Synthesis of 4,4'-methylenebis(2,3,5,6-tetrafluorobenzonitrile) (24)

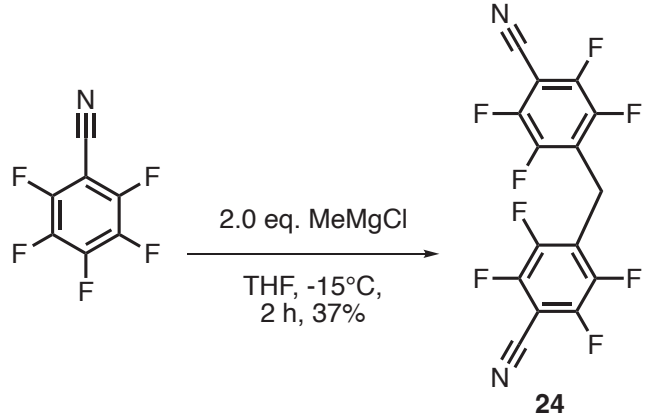

24

Pentafluorobenzonitrile (3.78 mL, 30.00 mmol, 1.00 eq.) was dissolved in 75 mL of dry THF. To this solution methyl magnesium chloride (3.0 M in THF, 20 mL, 60 mmol, 2.0 eq.) were added dropwise

at -15°C. During the addition, the temperature was maintained below -10°C. After stirring for two hours at -15°C, the reaction was quenched by the addition of 100 mL of 2 M hydrochloric acid solution and was allowed to reach room temperature. The organic layer was separated and was evaporated under reduced pressure. The remaining slurry was dissolved in 100 mL of dichloromethane and was washed with saturated $NaHCO_3$ solution (3 x 25 mL) and brine (3 x 25 mL). The organic phase was dried over $MgSO_4$ and was evaporated under reduced pressure. The dinitrile **24** could be isolated after column chromatography (cyclohexane/ethyl acetate 9:1) as a yellow solid (1.95 g, 5.30 mmol, 37%).

^{1}H NMR (300 MHz, $CDCl_3$) δ 4.29 (t, J = 1.4 Hz, 2H, C**H_2**); **^{19}F NMR** (282 MHz, $CDCl_3$) δ -131.15 – -131.55 (m, 4F, **F_{inner}**), -138.18 – -138.63 (m, 4F, **F_{outer}**).

All further spectral data were in accordance with the literature.[76]

Synthesis of 4,4'-methylenebis(2,3,5,6-tetrafluorobenzaldehyde) (22)

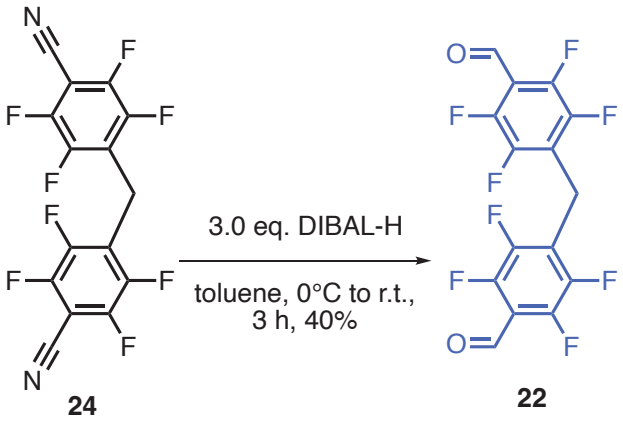

24 **22**

To a stirred solution of **24** (1.56 g, 4.30 mmol, 1.00 eq.) in dry toluene 50 mL, DIBAL-H in toluene (1.00 M, 12.90 mL, 12.90 mmol, 3.00 eq.) was added dropwise at 0 °C under argon. After complete addition, the reaction was allowed to reach room temperature and was stirred for 3 hours. Then, the reaction was quenched by the addition of 20 mL of 2 M hydrochloric acid solution and was stirred for 10 minutes. The organic layer was separated and the aqueous layer was washed with ethyl acetate (3 x 25 mL). The combined organic layers were dried over $MgSO_4$ and were evaporated under reduced pressure. The crude product was subjected to column chromatography (toluene) to yield **22** (0.63 g, 1.70 mmol, 40%) as an off-white crystalline solid.

^{1}H NMR (300 MHz, $CDCl_3$) δ 10.39 – 10.21 (m, 2H, C**H**O), 4.28 (t, J = 1.4 Hz, 2H, C**H_2**); **^{19}F NMR** (282 MHz, $CDCl_3$) δ -140.92 (d, J = 6.6 Hz, 4F, **F_{inner}**), -144.77 (d, J = 6.5 Hz, 4F, **F_{outer}**); **^{13}C{^{1}H} NMR** (151 MHz, $CDCl_3$) δ 182.27 (s, **C**HO), 146.69 (dd, J = 222.7, 13.9 Hz, **C**F_{outer}), 145.03 (dd, J = 222.7, 13.9 Hz, **C**F_{inner}), 121.38 (d, J = 17.3 Hz, **C**-CHO), 114.84 (t, J = 9.6 Hz, **C**-CH_2), 27.03 (s, **C**H_2).

FT-IR (ATR): $\tilde{\nu}$(cm^{-1}) = 1492.90, 1479.40, 1330.88, 1309.67, 1292.31, 1278.81, 1029.99, 931.62, 900.76, 630.72, 613.36.

CI-MS: calculated: [**22**+H]$^+$ 368.0 m/z, found: 368.0 m/z.

Synthesis of 2,2',3,3',5,5',6,6'-octafluoro-[1,1'-biphenyl]-4,4'-dicarbonitrile (25)

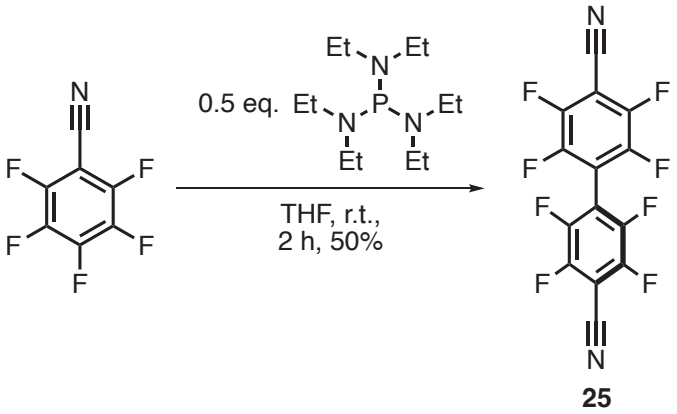

25

Pentafluorobenzonitrile (8.10 mL, 12.30 g, 64.00 mmol, 1.00 eq.) was dissolved in 200 mL of dry THF and Tris(diethylamino)phosphine (8.16 g, 33.28 mmol, 0.52 eq.) were added dropwise under nitrogen and stirring. The mixture was allowed to stir for 2 hours at room temperature. After the TLC indicated the complete consumption of the starting material, the reaction was quenched via the addition of 40mL 2N hydrochloric acid. The mixture was extracted with diethyl ether (3 x 50 mL) and was dried over anhydrous magnesium sulphate. After evaporation of the solvent the oily residue was left to crystallize to yield 25 (5,68 g, 16 mmol, 50 % yield) as faint yellow crystalline blocks.

^{19}F NMR (282 MHz, $CDCl_3$): δ -129.65 (d, Ar-**F_{inner}**), -133.47 (d, Ar-**F_{outer}**).

Synthesis of 2,2',3,3',5,5',6,6'-octafluoro-[1,1'-biphenyl]-4,4'-dialdehyde (23)

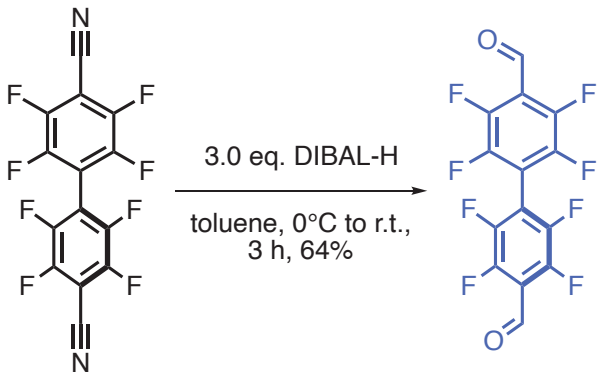

25 **23**

Biphenyl **25** (2.00 g, 5.74 mmol, 1.00 eq.) was dissolved in toluene (50 mL) and the resulting solution was thoroughly degassed *via* purging with argon for 15 minutes. A solution of DIBAL-H in toluene (1.50 M, 11.50 mL, 17.22 mmol, 3.00 eq.) was added dropwise over a period of 30 minutes at 0 °C. After complete addition, the resulting mixture was allowed to reach room temperature and was stirred for additional 4 hours. The reaction was then cooled again to 0 °C and was quenched by addition of 10 mL of ethyl acetate and 30 mL of 2 N hydrochloric acid. The organic phase was separated and the aqueous phase was extracted with dichloromethane (2 x 100 mL). The

combined organic phases were dried over $MgSO_4$ and the solvent was evaporated under reduced pressure to yield **23** (1.60 g, 4.51 mmol, 79 % yield) as a colorless powder.

^{1}H NMR (300 MHz, $CDCl_3$): δ 10.39 (s, -C**H**O); **^{19}F NMR** (282 MHz, $CDCl_3$): δ -136.15 (m, Ar-**F_{inner}**), -143.70 (m, Ar-**F_{outer}**); **^{13}C{^{1}H} NMR** (75 MHz, $CDCl_3$) δ 181.90 (s, Ar-**C**HO), 147.24 (d, J = 210.5 Hz, **C_{Ar}**-F_{outer}), 143.76 (d, J = 207.0 Hz, **C_{Ar}**-F_{inner}), 117.05 (t, J = 9.8 Hz, **C_{Ar}**-CHO), 111.89 (m, **C_q/$C_{q'}$**); FT-IR (ATR): $\tilde{\nu}$(cm^{-1}) = 2910.6 (w), 2358.9 (w), 2339.7 (w), 1712.8 (s), 1651.1 (m), 1575.8 (w), 1473.6 (s), 1408.0 (m), 1381.0 (m), 1357.9 (w), 1317.4 (w), 1298.1 (m), 1276.9 (s), 1114.9 (w), 1018.4 (s), 1003.0 (s), 989.5 (s), 956.7 (s), 914.3 (m), 800.5 (m), 721.4 (s); **EI-MS** (80 °C): calc. for $[C_{14}H_2F_8O_2–H]^+$ = 352.9843 m/z; found: 353.0 m/z (100%, $[M-H]^+$), 324.9 (27 %, $[M-CHO]^+$), 297.0 m/z (26 %, $[M-2(CHO)+H]^+$), 278.0 m/z (48 %, $[M(297\ m/z)-F]^+$); M_p: 144.8-145.1 °C.

Synthesis of FPOC9 (Tri^{2}Di^3)

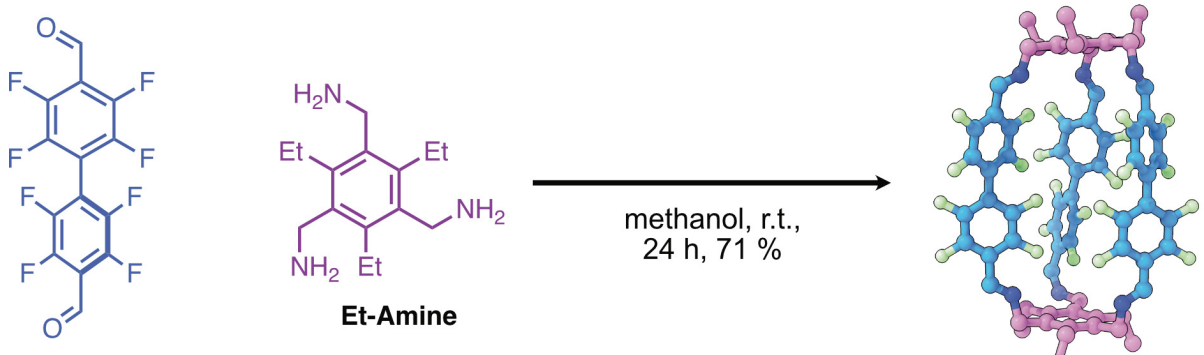

23 **Et-Amine** **FPOC9**

To a stirred solution of aldehyde **23** (210.00 mg, 0.60 mmol, 1.20 eq.) in 50 mL of methanol, **Et-Amine** (120.00 mg, 0.50 mmol, 1.00 eq.) in 50 mL of methanol was added dropwise over the course of 90 minutes. After complete addition the reaction was stirred for 24 hours, during which time a yellow precipitate formed. The precipitate was filtered off the solution, washed with methanol and was dried at 40°C under reduced pressure for 18 hours to yield **FPOC9** (254.30 mg, 71 %) as a bright yellow solid.

^{1}H NMR (300 MHz, $CDCl_3$) δ 7.87 (s, 6H, C**H**N), 5.15 (s, 12H, C**H_2**-N), 2.64 (d, J = 7.6 Hz, 12H, C**H_2**-CH_3), 0.85 (t, J = 7.9 Hz, 18H, C**H_3**); **^{19}F NMR** (282 MHz, $CDCl_3$) δ -138.87 (s, 12F, **F_{outer}**), -144.26 (s, 12F, **F_{inner}**).

Due to the low solubility of the cage in common NMR solvents, no ^{13}C NMR spectrum could be obtained.

FT-IR (ATR): $\tilde{\nu}$(cm^{-1}) = 2983.88, 2966.52, 2900.94, 2872.01, 2856.58, 1645.28, 1469.76, 1454.33, 1435.04, 1377.17, 1346.31, 1319.31, 1265.30, 1018.41, 981.77, 723.31.

ESI-HRMS: [**FPOC9**+H]$^+$ calculated: 1453.3630 m/z, found: 1453.3622 m/z

Synthesis of FPOC7

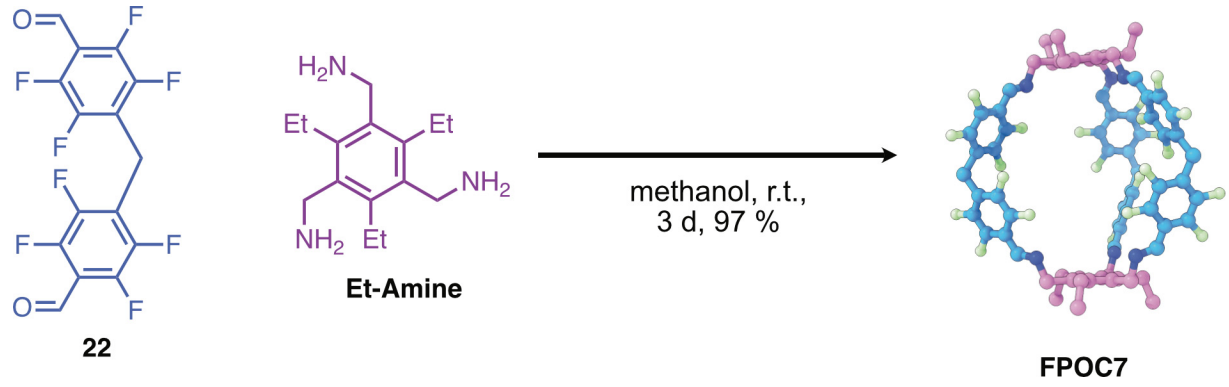

To a stirred solution of aldehyde **22** (101.60 mg, 0.28 mmol, 1.20 eq.) in 25 mL of methanol, **Et-Amine** (57.40 mg, 0.23 mmol, 1.00 eq.) in 25 mL of methanol was added dropwise over the course of 90 minutes. After complete addition the reaction was stirred for 3 days, during which time a yellow precipitate formed. The precipitate was filtered off the solution, washed with methanol and was dried at 40 °C under reduced pressure for 18 hours to yield **FPOC9** (166.80 mg, 97 %) as a bright yellow solid.

^{1}H NMR (300 MHz, $CDCl_3$) δ 8.13 (s, 6 H, C**H**N), 5.04 (d, J = 1.9 Hz, 12 H, C**H$_2$**-N), 4.11 (s, 12 H, Ar_F-C**H$_2$**-Ar_F), 2.67 (d, J = 7.6 Hz, 12 H, C**H$_2$**-CH_3), 1.26 (s, 18 H, C**H$_3$**); **^{19}F NMR** (282 MHz, $CDCl_3$) δ -143.27 – -143.47 (m, 12 F, **F$_{inner}$**), -144.25 (dd, J = 20.7, 12.5 Hz, 12 F, **F$_{outer}$**).

Due to the low solubility of the cage in common NMR solvents, no ^{13}C NMR spectrum could be obtained.

FT-IR (ATR): $\tilde{\nu}$(cm^{-1}) = 2970.38, 2929.87, 2900.94, 2879.72, 2358.94, 1639.49, 1485.19, 1473.62, 1379.10, 1294.24, 1282.66, 1028.06, 995.27, 977.91, 873.75.

MALDI-MS: [**FPOC9**+H]$^+$ calculated: 1495.510 m/z, found: 1495.512 m/z.

Synthesis of FPOC8

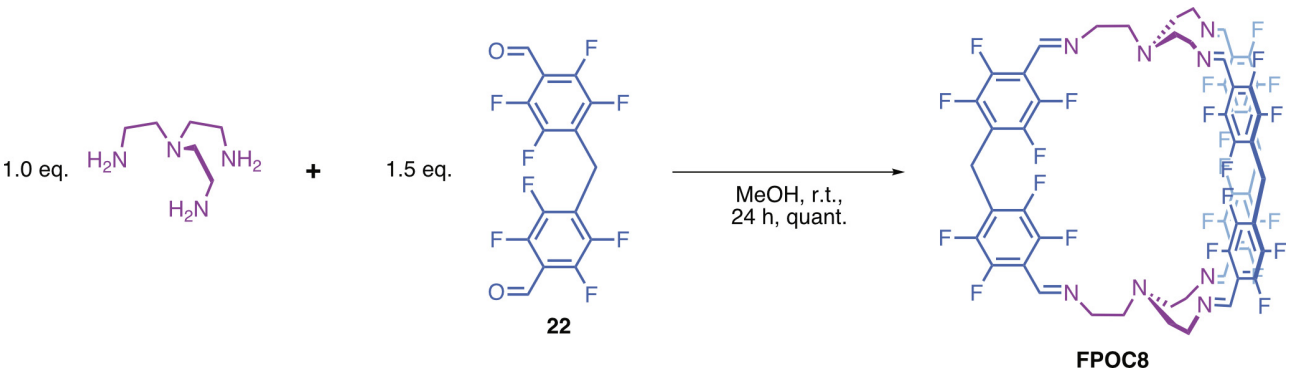

To a stirred solution of aldehyde **22** (276.10 mg, 0.75 mmol, 1.50 eq.) in 75 mL of methanol, TREN (73.50 mg, 0.50 mmol, 1.00 eq.) in 75 mL of methanol was added dropwise over the course of 90 minutes. After complete addition the reaction was stirred for 24 hours, during which time the

solution turned yellow. The solvent was evaporated at room temperature under reduced pressure, to yield **FPOC8** as a yellow solid (322.10 mg, 100 %).

^{1}H NMR (300 MHz, $CDCl_3$) δ 8.21 (s, 6 H, C**H**N), 4.14 (s, 12H, Ar_F-C**H_2**-Ar_F), 3.68 (s, 12H, CHN-C**H_2**), 2.91 (s, 12H, C**H_2**-N); **^{19}F NMR** (282 MHz, $CDCl_3$) δ -143.50 (s, 12 F, **F_{inner}**), -145.02 (s, 12 F, **F_{outer}**).

Due to a too low signal-to-noise ratio and strong coupling, no ^{13}C NMR spectrum could be obtained.

FT-IR (ATR): $\tilde{\nu}$(cm^{-1}) = 2943.37, 2887.44, 2829.57, 2818.00, 2362.80, 1643.35, 1471.69, 1384.89, 1367.53, 1340.53, 1288.45, 1064.71, 1014.56, 997.20, 968.27, 906.54, 889.18, 750.31, 688.59, 669.30, 623.01.

MALDI-MS: [**FPOC8**+H]$^+$ calculated: 1289.275 m/z, found: 1289.346 m/z.

Synthesis of RFPOC8

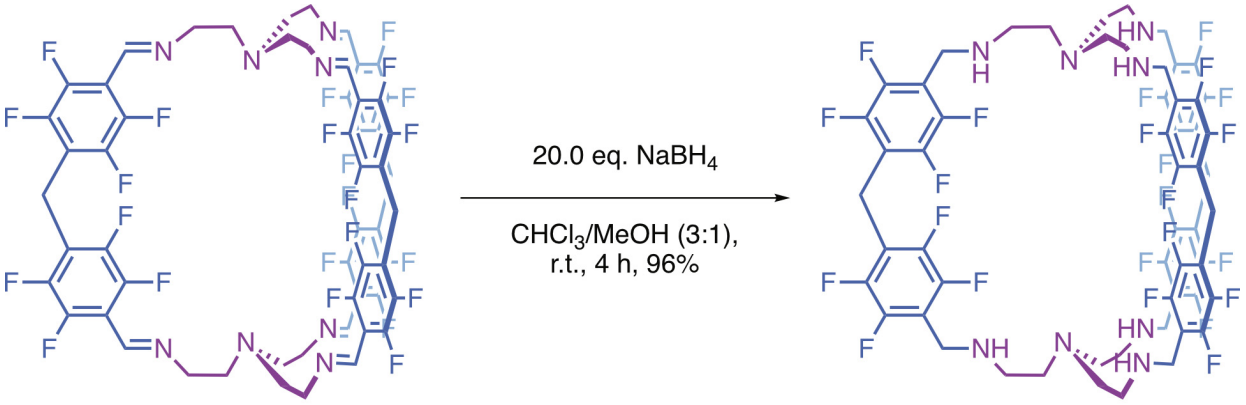

FPOC8 **RFPOC8**

FPOC8 (322.00 mg, 0.25 mmol, 1.00 eq.) were dissolved in a chloroform/methanol (3:1) mixture and $NaBH_4$ (189.20 mg, 5.00 mmol, 20.00 eq.) was added in portions at room temperature. The reaction turned colorless and was stirred for 4 more hours. Then, the solvent was evaporated under reduced pressure and the residue was suspended in chloroform (100 mL) and was filtered. The filtrate was washed with saturated $NaHCO_3$ solution (3 x 25 mL) and brine (3 x 25 mL) and was dried over $MgSO_4$. The solvent was evaporated under reduced pressure to yield **RFPOC8** as an off-white solid (318.00 mg, 0.24 mmol, 96%).

^{1}H NMR (300 MHz, $CDCl_3$) δ 4.07 (s, 12 H, Ar_F-C**H_2**-N), 3.68 (s, 12 H, Ar_F-C**H_2**-Ar_F), 2.58 – 2.56 (m, 12 H, N-C**H_2**-CH_2), 2.51 – 2.48 (m, 12 H, N-CH_2-C**H_2**); **^{19}F NMR** (282 MHz, $CDCl_3$) δ -143.67 (t, J = 16.1 Hz, 12 F, **F_{inner}**), -145.70 (dd, J = 22.5, 11.4 Hz, 12 F, **F_{outer}**).

Due to a too low signal-to-noise ratio and strong coupling, no ^{13}C NMR spectrum could be obtained.

FT-IR (ATR): $\tilde{\nu}$(cm^{-1}) = 2945.30, 2918.30, 2887.44, 2825.72, 1645.28, 1633.71, 1481.33, 1396.46, 1381.03, 1338.60, 1269.16, 1211.30, 1161.15, 1111.00, 1099.43, 1060.85, 1022.27, 933.55, 916.19, 844.82, 773.46, 736.81, 713.66, 686.66, 617.22.

ESI-MS: [**RFPOC8**+H]$^+$ calculated: 1315.5 m/z, found: 1315.4 m/z.

Deprotonation experiments

20.0 mg of either **FPOC7**, **FPOC8** or **RFPOC8** were dissolved in dry dichloromethane and either 10 µL of DBU or 10 mg of sodium hydride (60 wt% in paraffin) were added to the solution. The resulting mixture was sonicated for 5 minutes which lead to the rapid formation of a colored solution (**FPOC7** + **FPOC8** = purple, **RFPOC8** = orange).

Synthesis of Cu_2RFPOC8

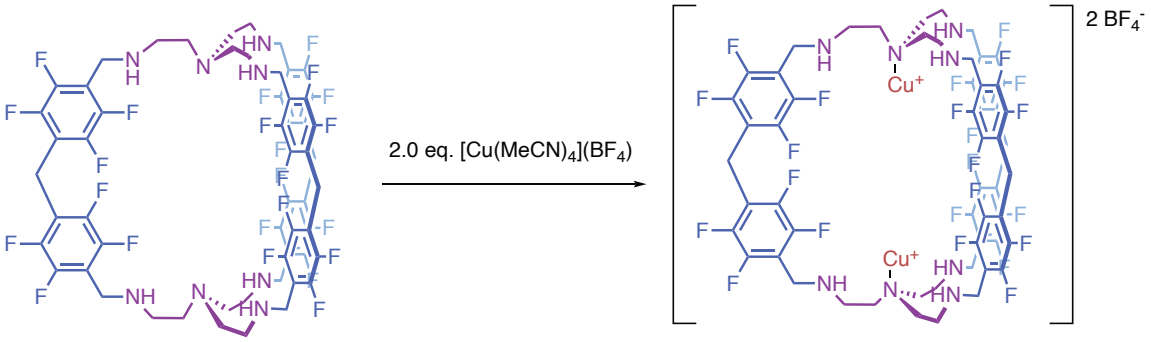

RFPOC8 **Cu_2RFPOC8**

RFPOC8 (20.0 mg, 15.4 µmol, 1.0 eq.) were dissolved in 2 mL of dry chloroform and $[Cu(MeCN)_4]BF_4$ (9.6 mg, 30.8 µmol, 2.0 eq.) was added. The solution was sonicated for 10 minutes, during which the color changed from yellow to red. By slow evaporation of the solvent over 7 days **Cu_2RFPOC8** was obtained as a deep red crystalline solid (20.1 mg, 82%).

Encapsulation studies of PFOA with Cu_2RFPOC8

10.0 mg of **Cu-RFPOC8** were dissolved in $CDCl_3$ and 1.0 equivalents (1.4 µL) of PFOA were added, along with hexafluorobenzene as internal standard.

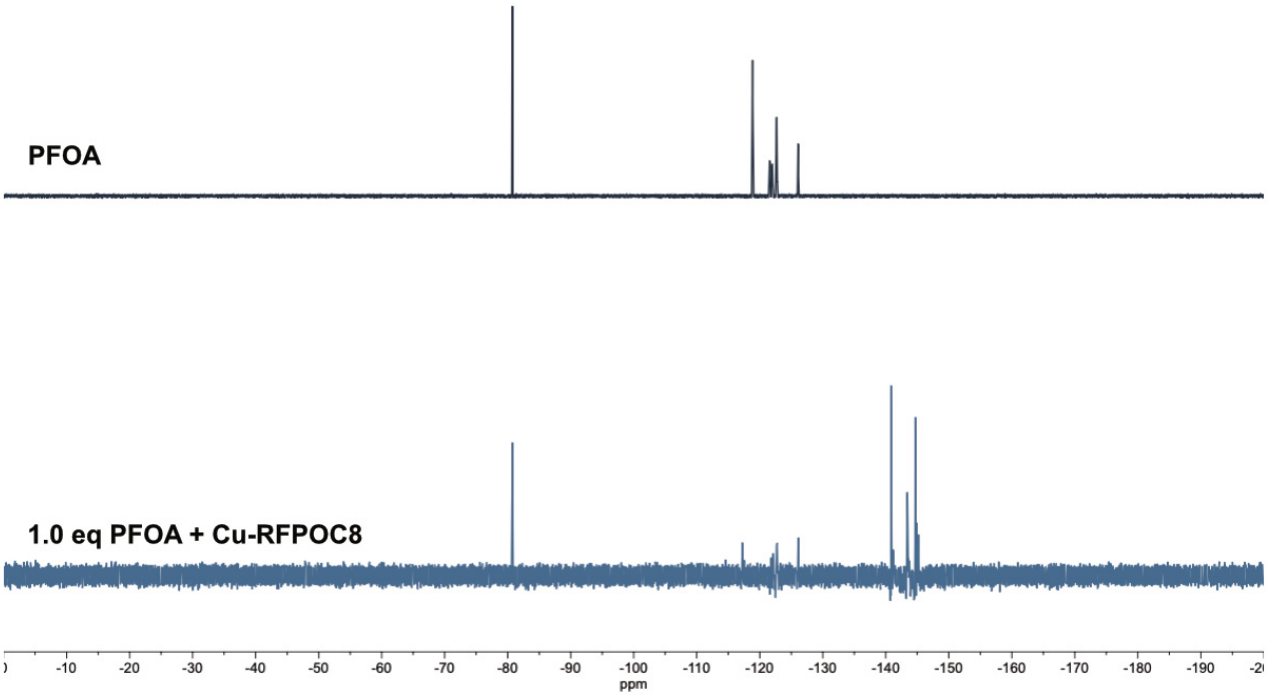

Figure S10: ^{19}F NMR (282 MHz) spectrum of pure PFOA (top) and 1.0 eq. of PFOA with **Cu_2RFPOC8** in $CDCl_3$.

Crystallographic Details

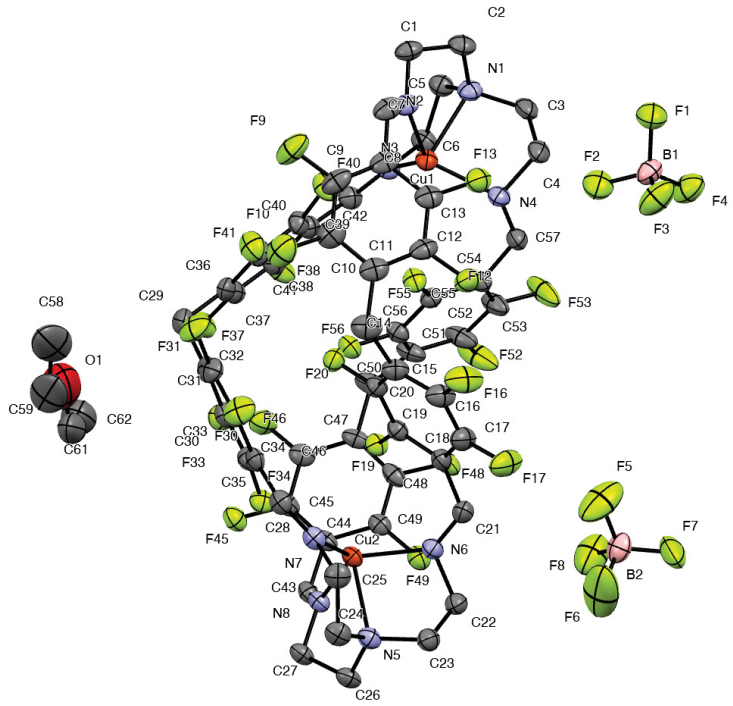

Figure S9: ORTEP-drawing (50% probability thermal ellipsoids) of the molecular structure of the complex **Cu_2RFPOC8** in the single-crystal as determined by X-ray diffraction. Hydrogens are omitted for clarity.

Crystal data	
Chemical formula	$C_{30.25}H_{22.38}BCuF_{16}N_4O_{0.44}$
M_r	827.30
Crystal system, space group	Triclinic, P–1
Temperature (K)	100
a, b, c (Å)	12.4981 (6), 12.6498 (6), 23.2502 (12)
a, b, g (°)	75.650 (2), 79.451 (2), 67.610 (1)
V (Å^3)	3276.5 (3)
Z	4
D_x (Mg m^{-3})	1.677
Radiation type	Cu Ka
m (mm^{-1})	2.08
Crystal size (mm)	0.38 × 0.18 × 0.16
Data collection	
Diffractometer	Bruker D8 VENTURE
Absorption correction	–

No. of measured, independent and observed [I > 2s(I)] reflections	87753, 12667, 11596
R_{int}	0.056
q values (°)	q_{max} = 74.8, q_{min} = 3.9
$(\sin q/l)_{max}$ (Å^{-1})	0.626
Range of h, k, l	h = -15→15, k = -15→15, l = -29→29
Refinement	
R[F^2 > 2s(F^2)], wR(F^2), S	0.075, 0.189, 1.12
No. of reflections	12667
No. of parameters	958
No. of restraints	61
H-atom treatment	H-atom parameters constrained
	w = 1/[$s^2(F_o^2)$ + (0.0531P)^2 + 16.5619P] where P = (F_o^2 + 2F_c^2)/3
$D\rho_{max}$, $D\rho_{min}$ (e Å^{-3})	1.46, -0.76

Computer programs: SHELXT 2014/5 (Sheldrick, 2014), SHELXL2018/3 (Sheldrick, 2018).

5.4. Experimental Details for Section 3.3

This section was largely reproduced and adapted from ref. [79] with permission by the authors.
For the synthesis of **F-Amine**, please see Section 3.1.

Synthesis of trimethylbenzene-1,3,5-tricarboxylate (26)

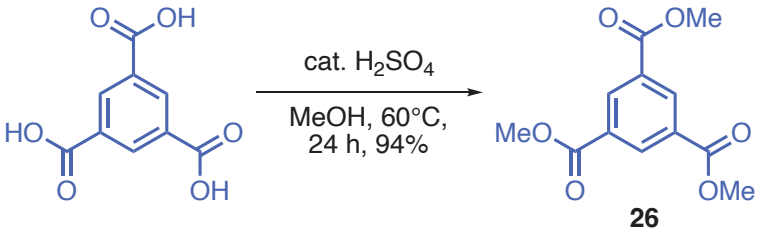

26

Benzene-1,3,5-tricarboxylic acid (10.00 g, 47.59 mmol, 1.00 eq.) was suspended in a mixture of 150 mL methanol and concentrated sulfuric acid (3.10 mL, 58.16 mmol, 1.20 eq.) and heated to 60 °C for 21 hours. The suspension was allowed to cool to room temperature and saturated $NaHCO_3$ solution was added slowly. The mixture was filtered and the residue was washed with 150 mL water while the filtrate was extracted with diethyl ether (2 x 100 mL). The combined organic phases were dried over Na_2SO_4. The precipitate and the organic phase were combined and the solvent

was removed under reduced pressure to give trimethyl-1,3,5-benzenetricarboxylate (**26**) as a colourless solid (11.26 g, 44.74 mmol, 94 %).

^{1}H NMR (300 MHz, $CDCl_3$): δ = 8.86 (s, 3 H, Ar-**H**), 3.98 ppm (s, 9 H, C**H$_3$**-O).

All further spectral data were in accordance with the literature.[29]

Synthesis of 1,3,5-tris(hydroxymethyl)benzene (27)

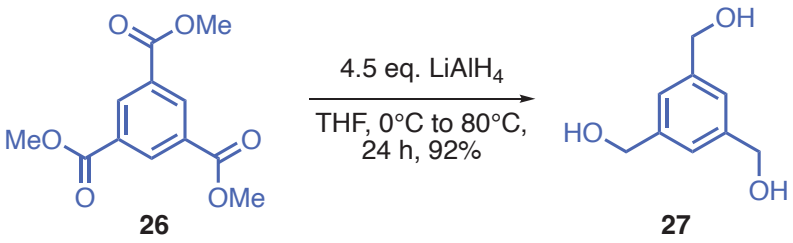

26 **27**

Trimethyl-1,3,5-benzenetricarboxylate (**26**) (10.57 g, 41.90 mmol, 1.00 eq.) in 170 mL dry THF was added dropwise to a suspension of $LiAlH_4$ (7.10 g, 187.10 mmol, 4.50 eq.) in 80 mL dry THF at 0 °C. After addition, the mixture was allowed to warm to room temperature while stirring for 14 hours under a nitrogen atmosphere. 100 g of a 1:1 mixture of Celite and $NaHSO_4$ were added in small portions. At 0 °C, 7 mL water and 7 mL 15 % NaOH solution were added dropwise. The mixture was diluted with THF and filtered and the residue was washed with diethyl ether. The solvent was removed under reduced pressure yielding 1,3,5-tris(hydroxymethyl)benzene (**27**) as a pale-yellow solid (6.49 g, 38.60 mmol, 92 %).

^{1}H NMR (300 MHz, D_2O): δ = 7.32 (s, 3H, Ar-**H**), 4.65 ppm (s, 6H, C**H$_2$**).

All further spectral data were in accordance with the literature.[29]

Synthesis of 1,3,5-triformylbenzene (TFB)

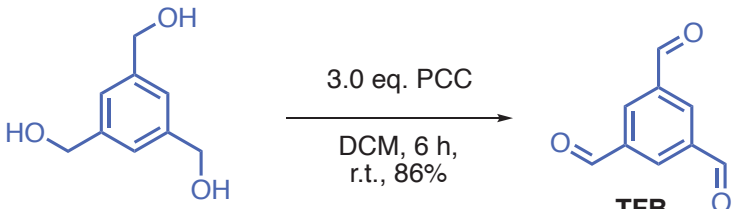

27 **TFB**

1,3,5-Tris(hydroxymethyl)benzene (**27**) (4.082 g, 24.27 mmol) was suspended in 240 mL CH_2Cl_2. 7.5 g Celite were added and the suspension was stirred for 15 minutes. PCC (15.70 g, 72.81 mmol, 3.0 eq.) was added and the mixture was stirred overnight. The reaction mixture was diluted with diethyl ether (80 mL) and stirred for another 30 minutes. The precipitate was filtered off. The residue was extracted with CH_2Cl_2. The solvent was removed under reduced pressure. The crude product was dissolved in CH_2Cl_2 and filtered over silica gel to give 1,3,5-triformylbenzene (**TFB**) as

a colorless solid (3.402 g, 20.87 mmol, (86 %).

^{1}H NMR (300 MHz, $CDCl_3$): δ = 10.21 (s, 3H, C**H**O), 8.64 ppm (s, 3H, Ar-**H**).

All further spectral data were in accordance with the literature.[29]

Synthesis of FC1

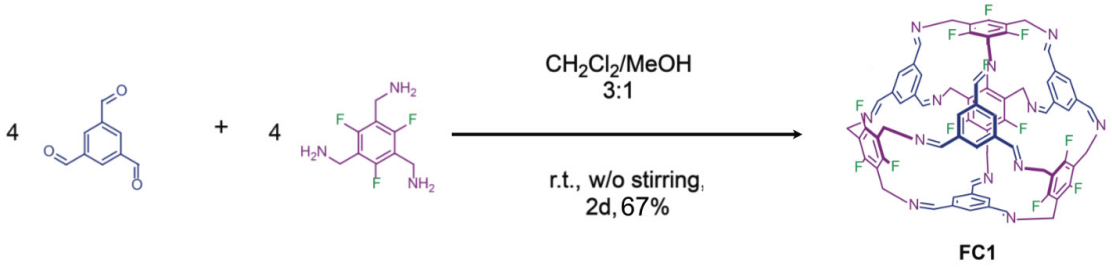

Method A:

1,3,5-Triformylbenzene (**TFB**) (104.00 mg, 6.40 mmol, 0.80 eq.) was dissolved in 100 mL of dry methanol inside a 250 mL round bottomed flask. A solution of 1,3,5-tris(aminomethyl)-2,4,6-trifluorobenzene (**F-Amine**) (175.00 mg, 8.00 mmol, 1.00 eq.) in 100 mL dry methanol was added dropwise over the period of one hour. The resulting solution was stirred for two days at room temperature. The resulting precipitate was filtered off and washed with 50 mL of cold methanol to give the imine cage **FC1** as a white solid (200.00 mg, 1.50 mmol, 95%).

Method B:

1,3,5-Triformylbenzene (**TFB**) (104.00 mg, 6.40 mmol, 0.80 eq.) was dissolved in 100 mL of DCM/methanol 3:1 inside a 250 mL Erlenmeyer flask. A solution of 1,3,5-tris(aminomethyl)-2,4,6-trifluorobenzene (**F-Amine**) (175.00 mg, 8.00 mmol, 1.00 eq.) in 100 mL DCM/methanol 3:1 was carefully layered on top of the **TFB** solution. The resulting bi-layered solution was left standing without stirring for three days. The resulting precipitate was filtered off and washed with cold methanol (50 mL) to yield the imine cage **FC1** as transparent thin needles (140.00 mg, 1.10 mmol, 67%).

^{1}H NMR (300 MHz, $CDCl_3$): δ = 8.37 (s, 12H, Ar-**H**), 7.97 (s, 12H, C**H**N), 4.76 ppm (s, 24H, C**H_2**-N); ^{19}F NMR (282 MHz, $CDCl_3$): δ = -119.17 ppm (s, 12F, **F_{amine}**); due to the poor solubility of **FC1** no $^{13}C\{^1H\}$ spectrum could be obtained, we provided an elemental analysis additionally; **IR**: ṽ = 2987.7, 2968.5, 2868.2, 1672.3, 1643.4, 1624.1, 1464.0, 1452.0, 1388.8, 1365.6 1330.9, 1253.7, 1224.8, 1149.6, 1041.6, 1018.4, 993.3, 970.2, 891.1, 866.0, 702.1, 684.7, 655.8, 611.4 cm^{-1}; **ESI-HRMS**: calc. $[C_{72}H_{48}F_{12}N_{12}+H]^+$ = 1309.4006 m/z, found: 1309.3985 m/z;

Elemental Analysis: calculated. for $C_{72}H_{48}F_{12}N_{12}$ x 4.5 H_2O: C: 62.20, H: 4.13, N: 12.09; found: C: 62.36, H: 4.30, N: 12.41.

Synthesis of RFC1

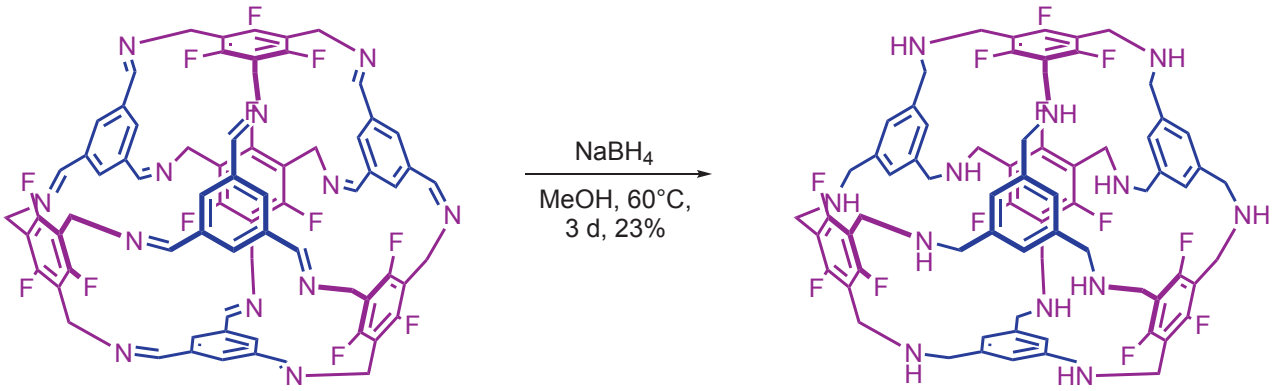

FC1 (100 mg, 0.80 mmol, 1.00 eq.) was suspended in 200 mL of methanol and $NaBH_4$ (500 mg, excess) was added in portions at room temperature. After one hour, the reaction mixture was heated to reflux and more $NaBH_4$ (300 mg) was added. The resulting mixture was refluxed for two days. After allowing the mixture to cool to room temperature, the solvent was evaporated and the residue was taken up with 100 mL of 2 M HCl and made basic with 4M KOH again. The aqueous phase was extracted with dichloromethane (3 x 100mL) and the combined organic phases were dried over $MgSO_4$. The solvent was evaporated under reduced pressure to yield the locked cage **RFC1** as a white solid (24.00 mg, 0.18 mmol, 23% yield).

^{1}H NMR (300 MHz, $CDCl_3$): δ = 6.98 (s, 12H, Ar-**H**), 3.82 - 3.64 (m, 48H, C**H$_2$**-NH$_2$-C**H$_2$**), 1.58 ppm (br s, 24H, NH_2); **^{19}F NMR** (282 MHz, $CDCl_3$): δ = -120.65 ppm (s, 12F, Ar-**F)**; Due to the low solubility of the compound sufficient ^{13}C NMR data could not be obtained. **FT-IR (ATR)**: $\tilde{\nu}(cm^{-1})$ = 2989.7, 2968.5, 2953.02, 2900.9, 2881.7, 2866.2, 2850.8, 2833.4, 1726.3, 1668.43, 1622.1, 1600.9, 1504.5, 1452.4, 1444.7, 1363.7, 1325.1, 1317.4, 1236.4, 1220.94, 1192.01, 1157.29, 1097.5, 1089.8, 1057.0, 995.3, 925.8, 854.5, 841.0, 748.4, 731.0, 719.5, 663.5, 619.2, 607.6; **ESI-HRMS**: calc. $[C_{72}H_{48}F_{12}N_{12}+3H]^{3+}$ = 445.2010 m/z, found: 445.2007 m/z; calc. $[C_{72}H_{48}F_{12}N_{12}+2H]^{2+}$ = 667.2978 m/z, found: 667.2968 m/z.

DOSY experiments

The hydrodynamic radii were estimated to be r_S = 0.71 nm for **FC1** and r_S = 0.76 nm for **RFC1** respectively.

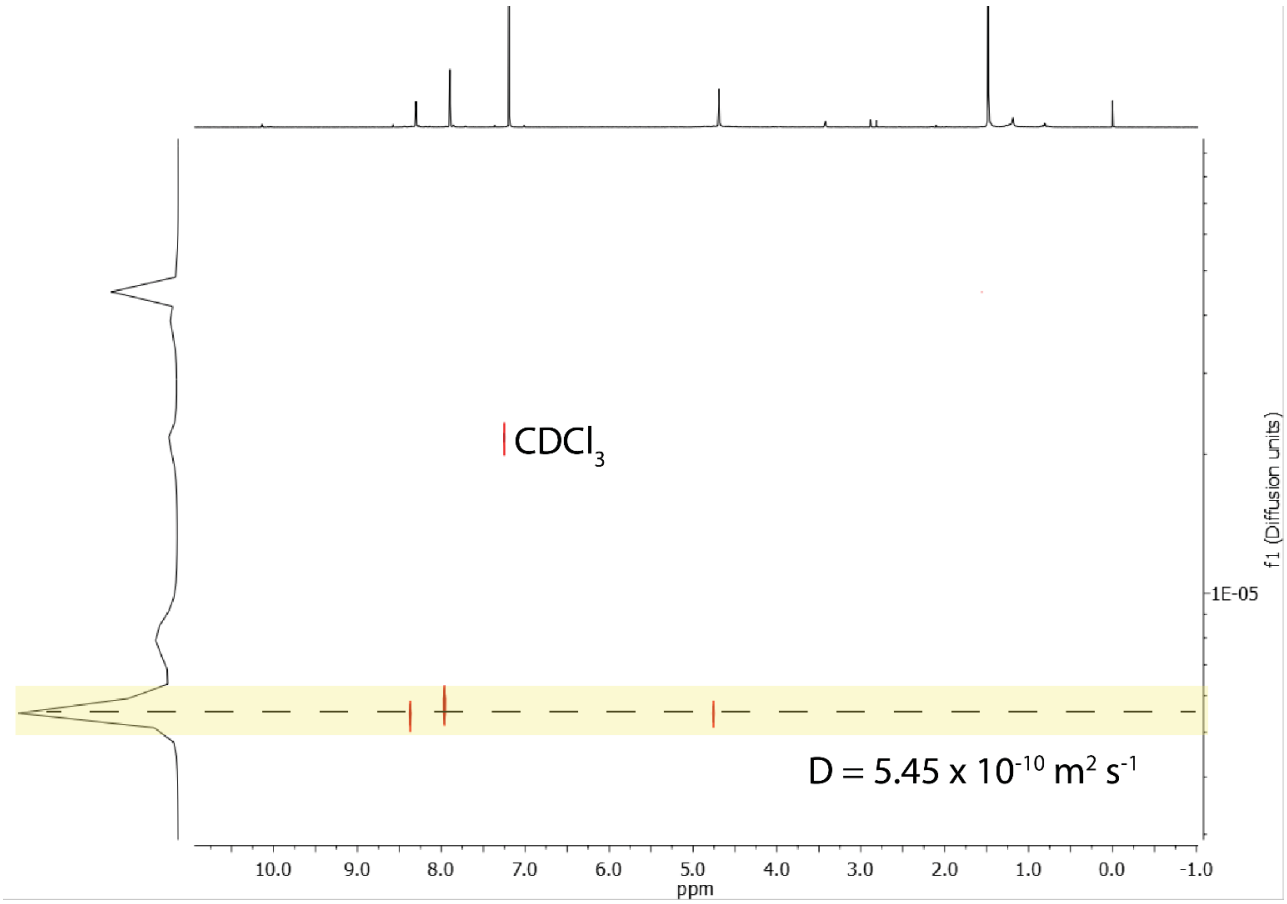

Figure S11: DOSY NMR spectrum (600 MHz, $CDCl_3$, 298 K) of **FC1**.

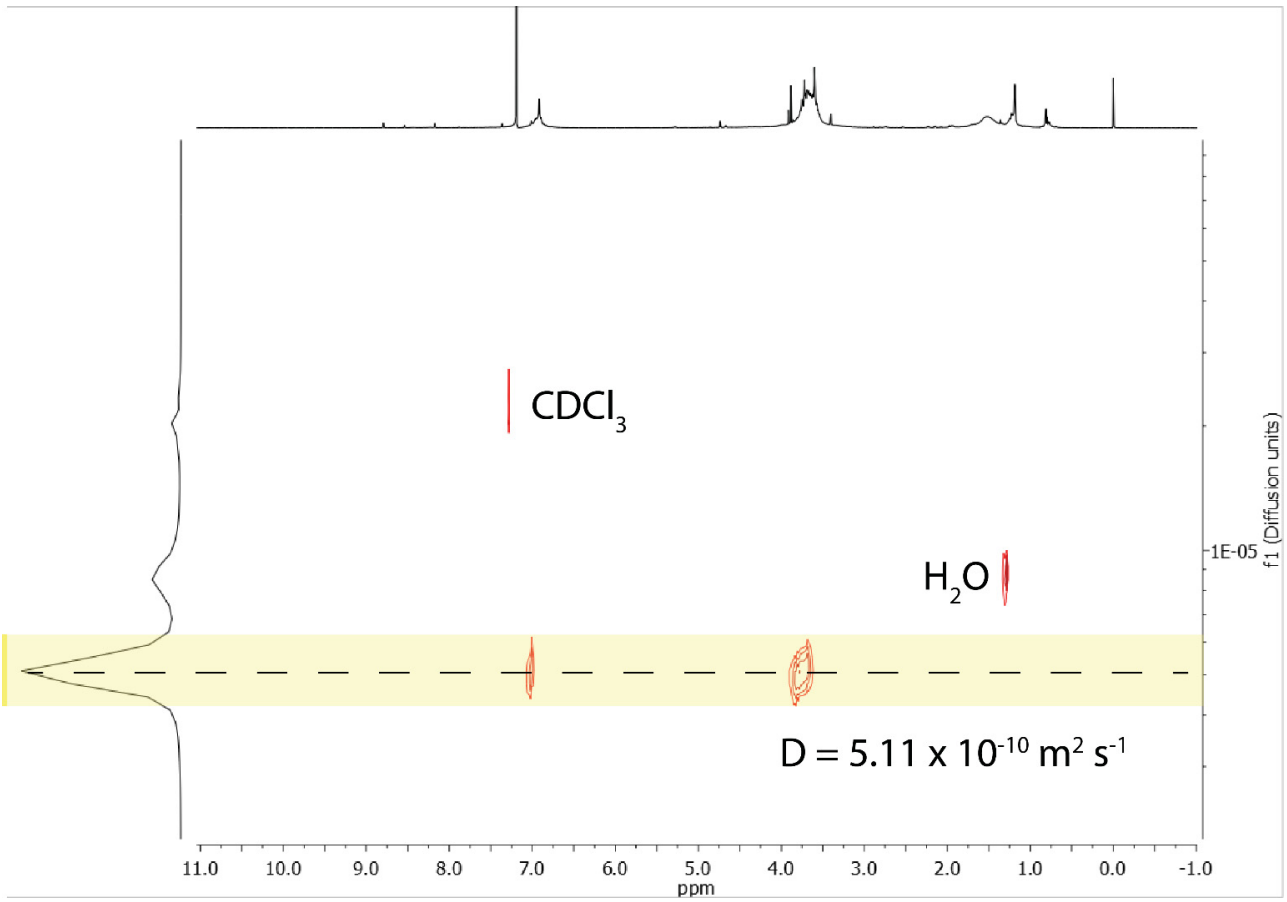

Figure S12: DOSY NMR spectrum (600 MHz, $CDCl_3$, 298 K) of **RFC1**.

Computational Details

Quantum mechanical calculations were performed by applying density functional theory All geometry optimizations were performed with the Gaussian16 program.[98] Geometries were optimized using first B3LYP, followed by M062X functionals and the def2-TZVP basis set for H, C, N and F atoms. Stationary points were characterized by vibrational analyses. Figure S13 gives an overview of all optimized structures. The geometries are nearly equivalent for B3LYP and M062X, therefore only M062X-optimized ones are shown. These calculations were performed and evaluated by Dr. Bernd M. Schmidt.

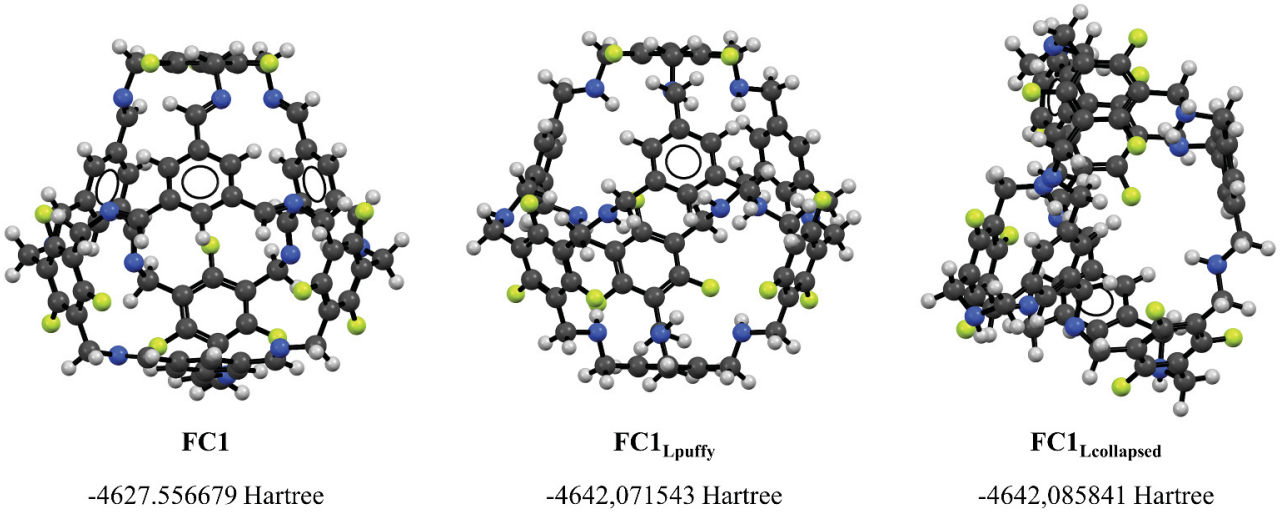

Figure S13: DFT-optimized geometries of **FC1**, **RFC1$_{puffy}$** and **FC1L$_{collapsed}$** (from left to right) using M062X/ def2- TZVP level of theory. The collapsed geometry of **RFC1** is more stable than the puffy geometry of **RFC1** by 9.6 kcal mol^{-1}.

MM2 calculations

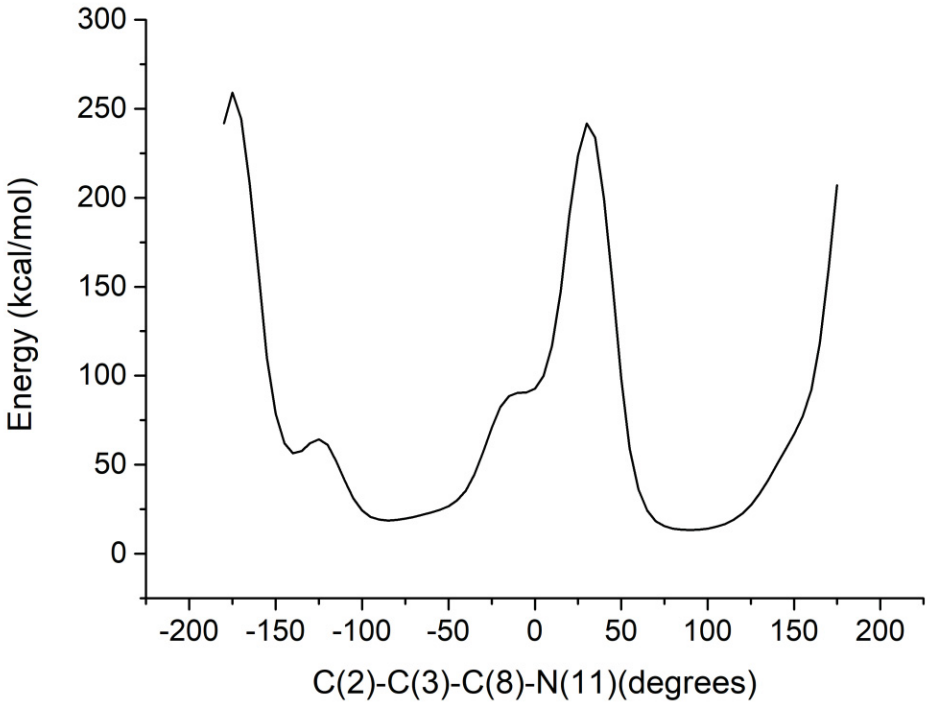

Figure S14: Energy plot of the rotation around the C_{sp^2}–C_{sp^3} bond of an aminomethyl substituent of **Et-Amine** (MM2 calculation).

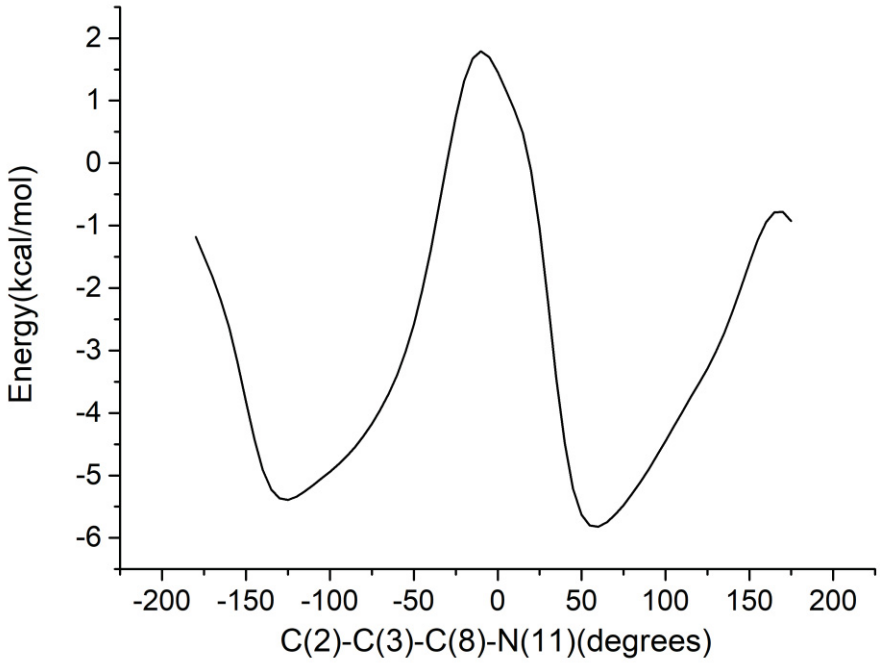

Figure S15: Rotational energy around the C_{sp^2}–C_{sp^3} bond of an aminomethyl substituent of 1,3,5-tris(aminomethyl)-2,4,6-trifluorobenzene (**F-Amine**) (MM2 calculations).

Thermogravimetrical Analysis

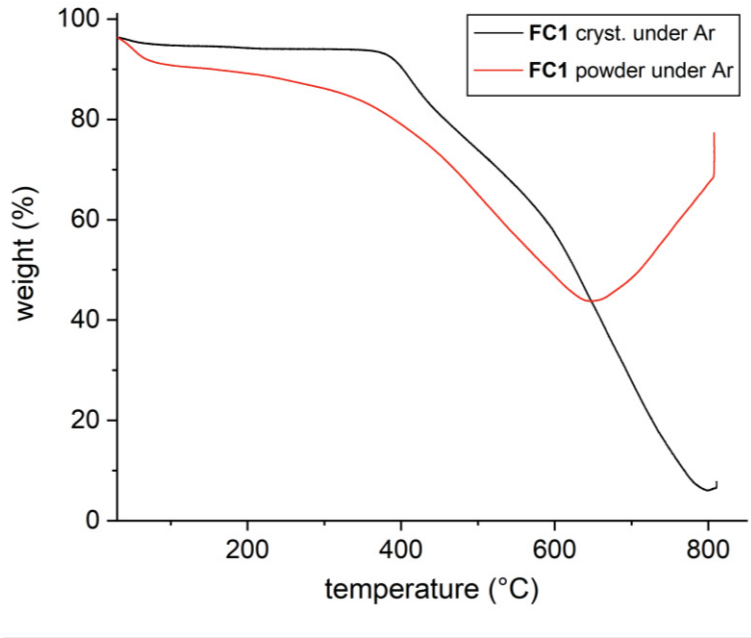

Figure S16: Thermogravimetric curves of a crystalline sample of **FC1** (black line) and of a powdered sample of **FC1** (red line). The initial dip in the red curve stems from remaining moisture, even though the sample

was previously evacuated at 40 °C and 10^{-2} mbar for 24 hours. The increase in weight starting at about 680 °C is caused by a corrosion of the instruments by release of HF due to the moisture in the gas flow. Onset decomposing temperatures are 361.5 °C (powdered **FC1**) and 373.1 °C (crystalline **FC1**).

Gas sorption analysis

Table S3: Gas uptake of differently processed samples of **FC1**.

Gas	**FC1** (cryst.)		**FC1** (powder)	
	uptake (mmol/g)	in weight %	uptake (mmol/g)	in weight %
N_2	7.6	22.14	6.8	19.10
H_2	7.5	1.51	5.4	11.42
CO_2	4.2	18.98	2.6	1.06

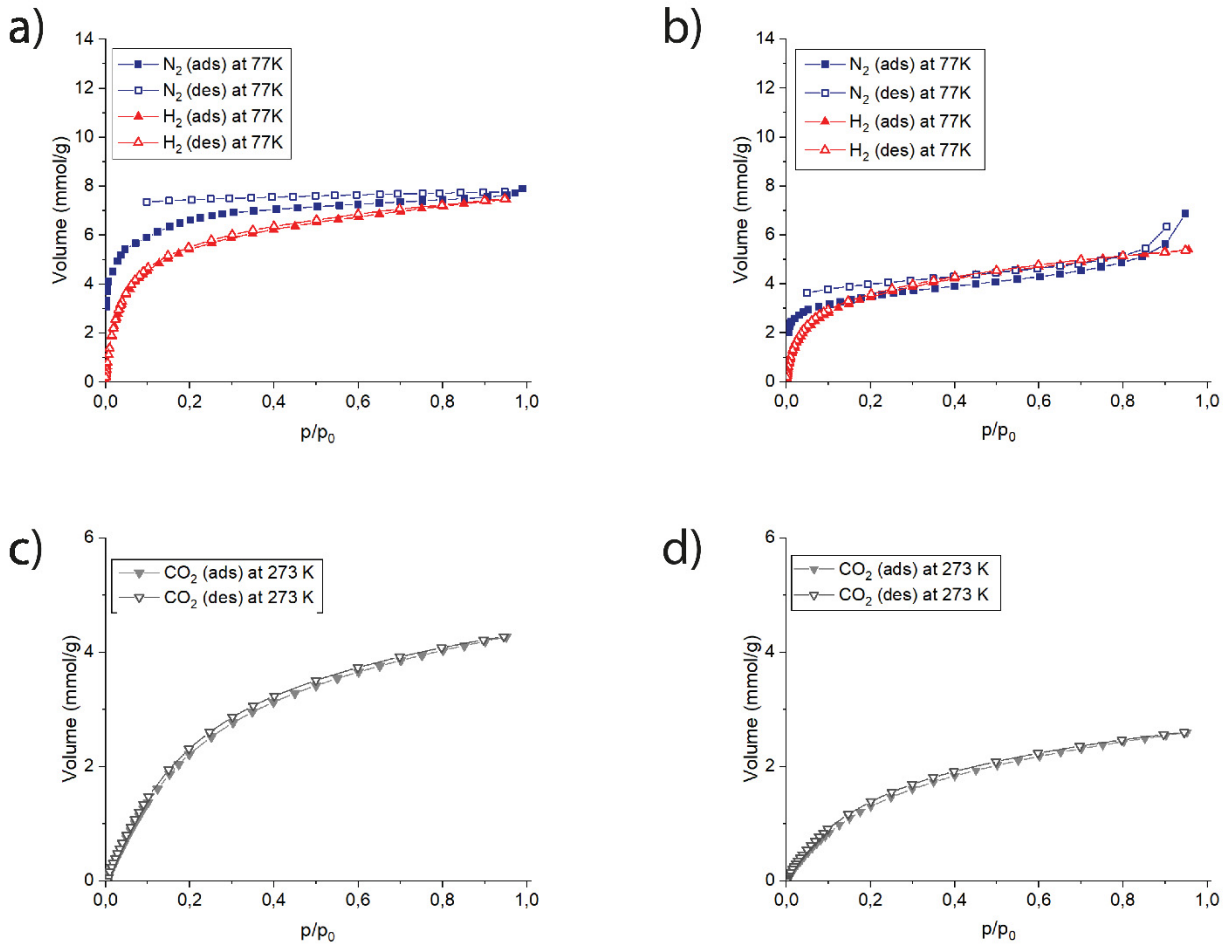

Figure S17: a) adsorption (solid symbol) and desorption (hollow symbol) of N_2 (blue) and H_2 (red) for a crystalline **FC1** sample; b) adsorption (solid symbol) and desorption (hollow symbol) of N_2 (blue) and H_2 (red) for a powdered **FC1** sample; c) adsorption (solid symbol) and desorption (hollow symbol) for CO_2 of a

crystalline **FC1** sample; d) adsorption (solid symbol) and desorption (hollow symbol) for CO_2 of a powdered **FC1** sample.

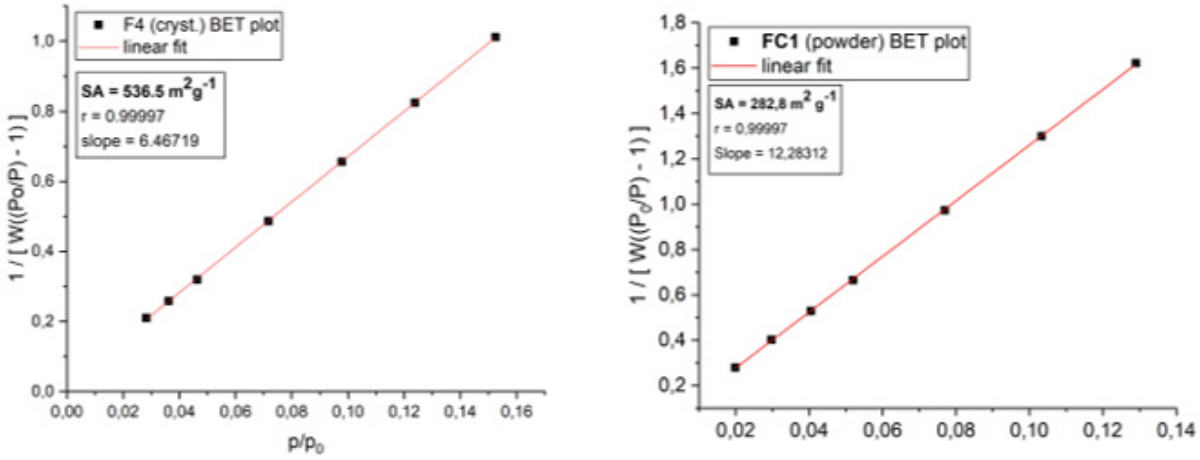

Figure S18: BET plots of a crystalline (left) and a powdered (right) **FC1** sample

Crystallographic details

Single crystals used directly as obtained from the synthetic mixture were mounted using a microfabricated polymer film crystal-mounting tool (dual-thickness MicroMount, MiTeGen) using low viscosity oil perfluoropolyether PFO-XR75 to reduce the X-ray absorption and scattering. A data set of a colourless needle with dimensions of 157.0 x 34.0 x 33.4 µm of **FC1** was collected at the P11 beamline at PETRA III, DESY[99,100] in August 2019 with a wavelength of 0.619900 Å and a PILATUS detector, using P11 Crystallography Control GUI at 200(2) K. Initial data reduction was carried out using XDS (V. 1 Nov 2016). The structure was then refined by full-matrix least-squares methods on F2 (SHELXL-2014).[101-103] The hydrogen atoms were placed at calculated positions and refined by using a riding model.

The crystal structures were measured by the team of Prof. Dr. C. Lehmann (Max-Planck-Institut for Kohlenforschung, Mülheim an der Ruhr) and refined by Dr. Bernd M. Schmidt.

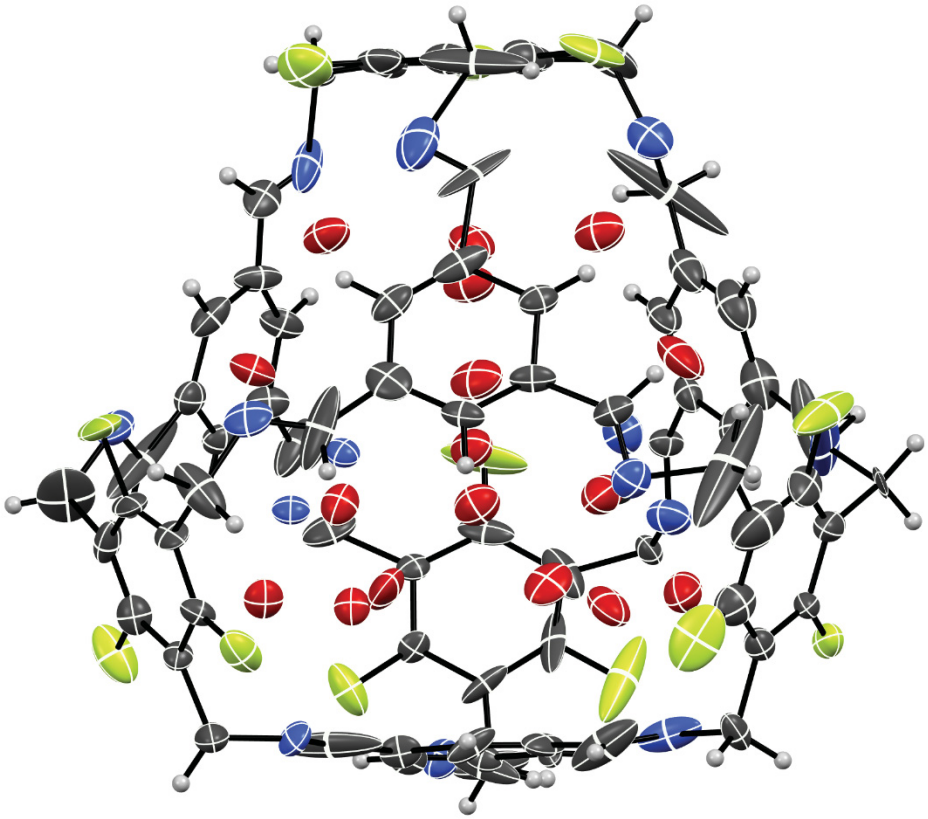

Figure S19: Synchrotron data set of **FC1** showing the asymmetric unit with thermal ellipsoids set at 50% probability. The structure was measured at 200 K and solved in the monoclinic space group $P2_1$ with R_{Int} = 0.0693, R_1 = 0.2287 and wR_2 = 0.5134. The structure shows various C-H···F contacts between alternating hydrogenated and fluorinated ports of the windows.

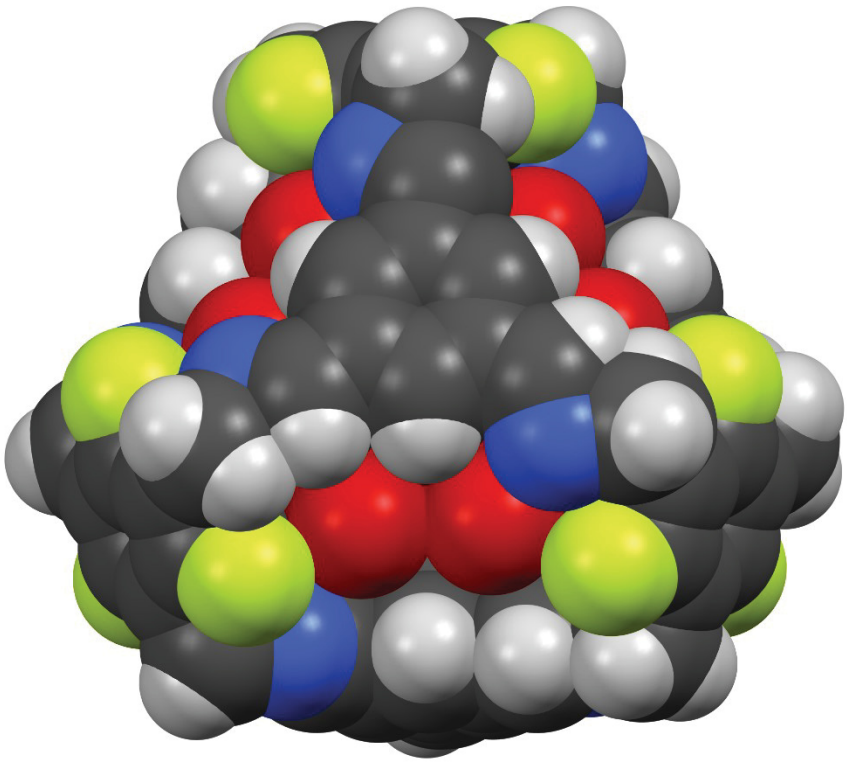

Figure S20: Asymmetric unit of **FC1** showing the asymmetric unit with a space-filling representation.

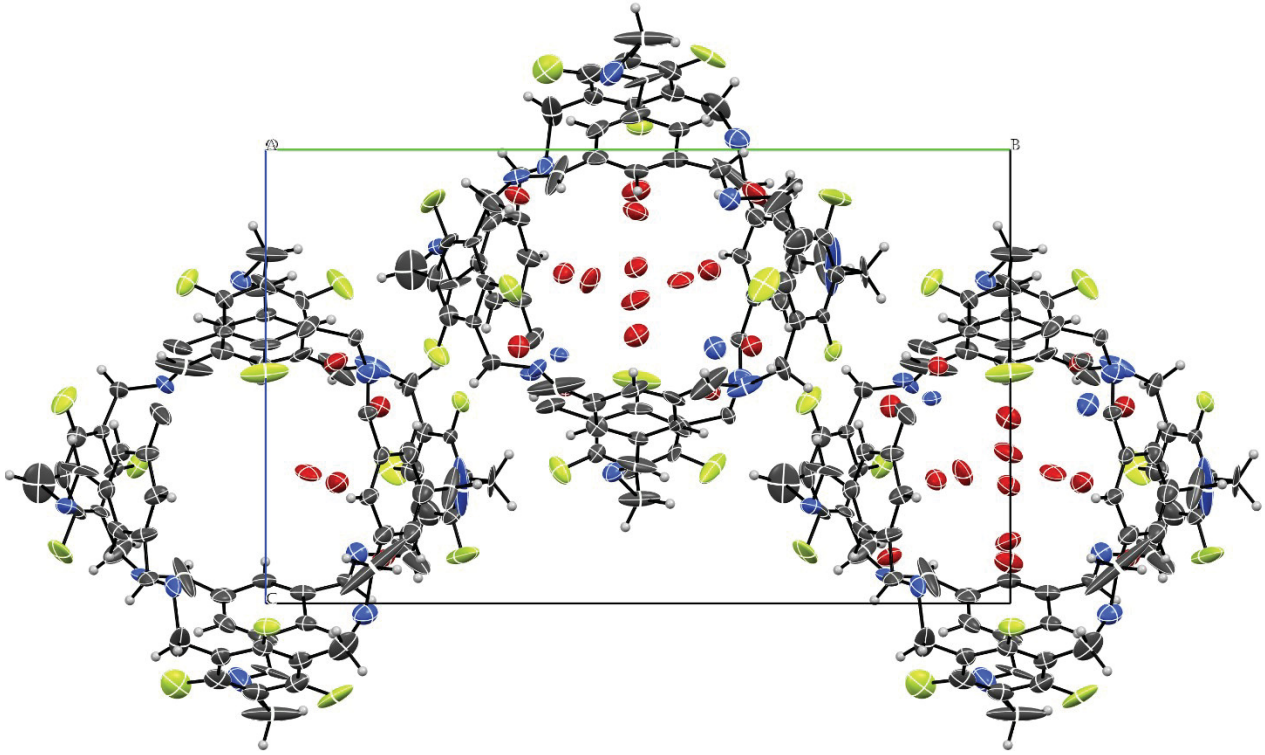

Figure S21: View of the unit cell of **FC1** along the crystallographic *a* axis. The infinite pores along the cages can be clearly seen.

PXRD

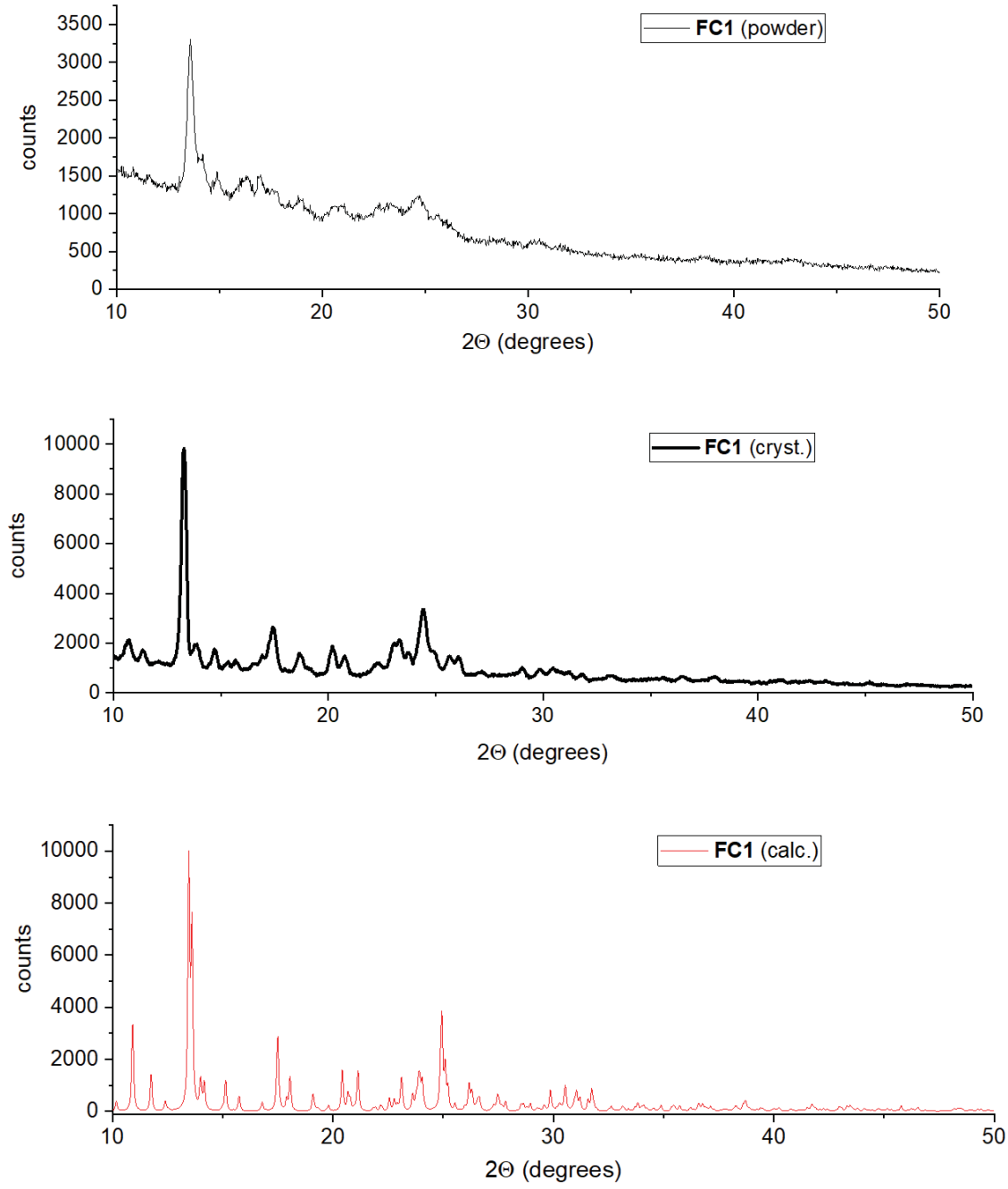

Figure S22: PXRD spectra of a powder (top) and crystalline (middle) **FC1** sample. The spectra at the bottom was calculated from the SC-XRD data and is in good agreement with the crystalline sample. As can be seen by the broader signals and the noise in the spectrum in the top the crystallinity of the powdered sample is the lowest.

MS and CID experiments

All MS/MS and CID experiments were performed by Hendrik V. Schröder in the group of Prof. Dr. C. A. Schalley (FU Berlin). MS measurements and collision-induced dissociation (CID) tandem MS

experiments were conducted on a Synapt G2-S HDMS (Waters Co., Milford, MA, USA) with a flow rate of 10 µL/min, a spray voltage of 2.63 kV, source temperature of 80 °C, sample cone voltage of 121 V and source offset of 64 V, respectively. For CID, a nitrogen-containing trap cell was used with collision voltages between 0 and 60 V. All ions were generated by electrospray ionization (ESI) in the positive mode. Samples were sprayed from CH_2Cl_2/CH_3CN (9:1) solutions at concentration of ~10 µM. Host- guest complexes were generated by addition of 20 µL of the corresponding aromatic guest to 1 mL of the 10 µM host solution and subsequent vortexing.

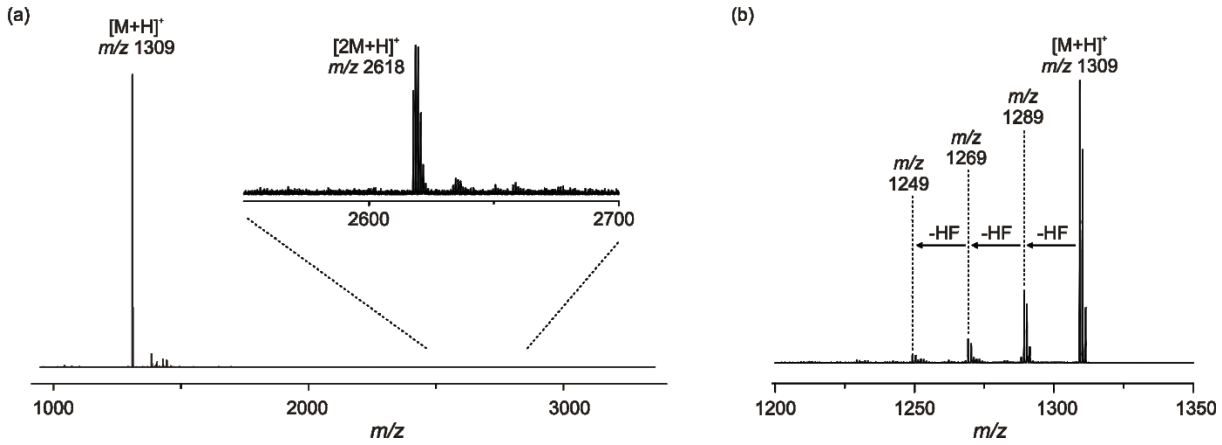

Figure S23: (a) ESI-MS spectrum (CH_2Cl_2/CH_3CN = 9:1) of the protonated imine cage [**FC1**+H]$^+$, inlet showing the weak dimer signal at m/z 2618. (b) CID Experiment (collision voltage: 60 V) of the mass-selected signal m/z 1309.

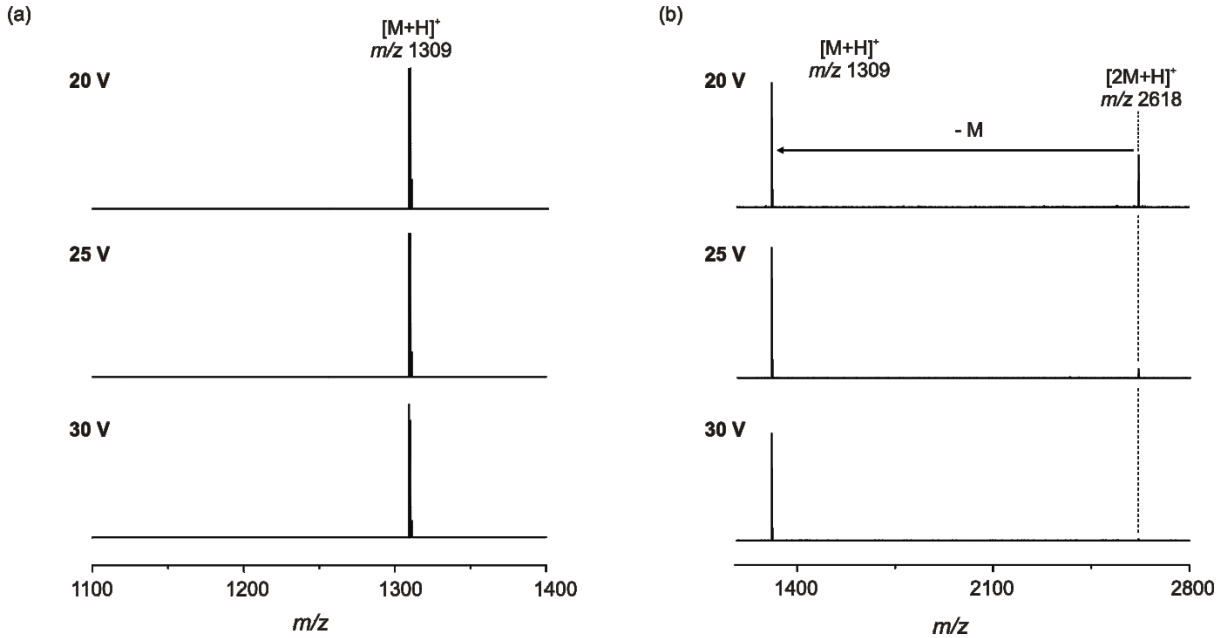

Figure S24: CID experiments of the imine cage **FC1** with mass selected signals (a) m/z 1309 and (b) m/z 2618 at different collision voltages.

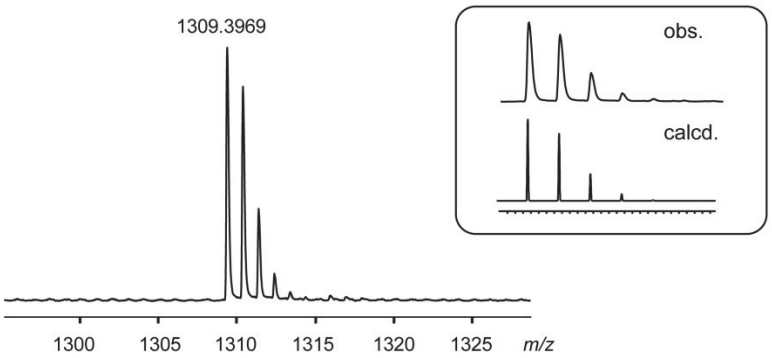

Figure S25: High resolution mass spectrum of the protonated imine cage [**FC1**+H]$^+$ m/z calcd. for $C_{72}H_{48}N_{12}F_{12}$: 1309.4006 [**FC1**+H]$^+$, found: 1309.3969 (Δ = 2.8 ppm).

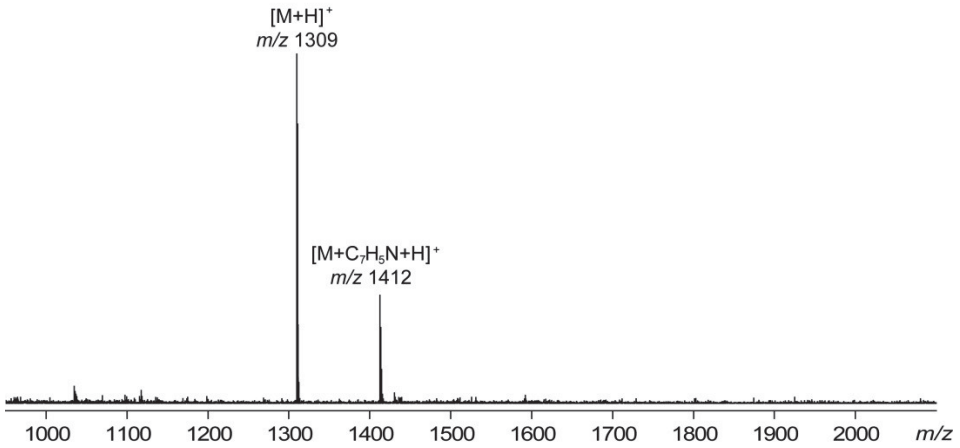

Figure S26: ESI-MS spectrum (CH_2Cl_2/CH_3CN = 9:1) of the protonated imine cage [**FC1**+H]$^+$ and its benzonitrile complex.

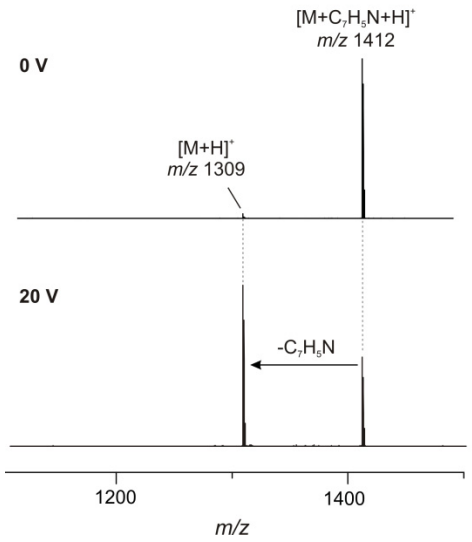

Figure S27: CID experiments with imine cage **FC1** and its benzonitrile complex: mass-selected signal for the protonated host-guest complex at m/z 1412 before (top) and after increase of collision voltage to 20 V (bottom).

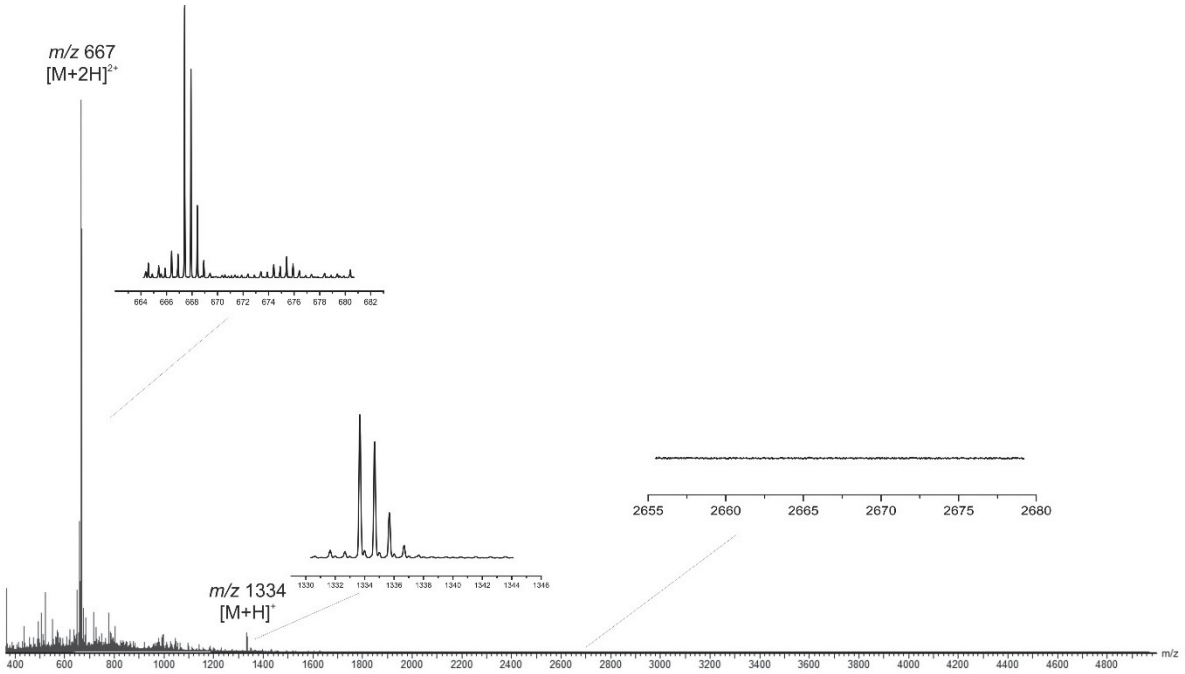

Figure S28: ESI-MS spectrum H_2O/iPrOH/HCOOH (50:50:1) of the protonated amine cage [**RFC1**+2H]$^{2+}$ m/z at 667, inlet showing the weak single charged ion [**RFC1**+H]$^{+}$ signal at m/z 1334.

Table S4: Qualitative screening of guests for the imine cage **FC1** and amine cage **RFC1**.

	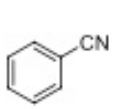	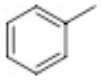	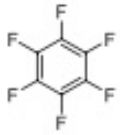	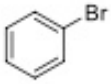	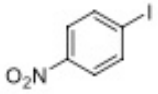
FC1 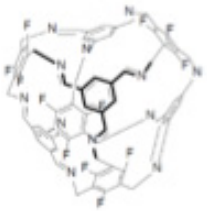	✓ *m/z* 1412	✗	✓ *m/z* 1495	✗	✓ *m/z* 1558 (weak)
FC1$_L$ 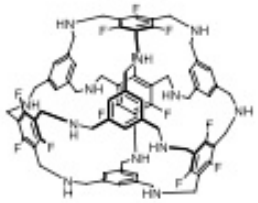	✗	✗	✗	✗	✗

For NMR titration experiments, the same substrates as listed above were used. A stock solution of **FC1** in $CDCl_3$ (c = 0.16 mM) was mixed with a stock solution of the substrates (1 and 10 eq.) in $CDCl_3$. The mixture was sonicated at room temperature for 30 min and the corresponding solutions were then subjected to NMR analysis. In neither case, a shift in neither ^1H nor ^{19}F NMR could be observed for the substrates.

5.5. Experimental Details for Section 3.4

Large Parts of this section were reproduced with permission from ref. [83].

For the synthesis of **Et-Amine** please see Section 5.2. Tetrafluoroterephthalaldehyde and terephthalaldehyde were obtained from commercial sources and were used without further purification.

Synthesis of A_4H_6

Cage compound $\mathbf{A_4H_6}$ was obtained following literature known procedures. All obtained analytical data were in accordance with literature.[84]

Synthesis of A_4F_6

To a solution of 2,3,5,6-tetrafluoroterephthalaldehyde **TFTA** (124.00 mg, 600.00 µmol, 1.20 eq.) in methanol (75 mL) a solution of **Et-Amine** (125.00 mg, 500.00 µmol, 1.00 eq in methanol (75 mL) was added dropwise over 4 h. After stirring the reaction mixture for 3 d at room temperature the precipitate was collected by filtration and washed with methanol (3 x 50 ml). Extraction of the solid

with dichloromethane (3 x 20 mL) and removal of the solvent in vacuo (30 °C) gave cage **A_4F_6** (54.00 mg, 27.00 µmol, 27%) pale-yellow solid.

^{1}H NMR (600 MHz, $CDCl_3$): δ 8.34 (s, 12H, Ar_F-C**H**=N), 5.02 (s, 24H, N-C**H_2**-Ar), 2.72 (q, J = 7.5 Hz, 24H, Ar-C**H_2**-CH_3), 1.26 (t, J = 7.5 Hz, 36H, Ar-CH_2-C**H_3**); **^{19}F NMR** (565 MHz, $CDCl_3$): δ -143.70 (s, 24F, **F_{Ar}**); **^{13}C{^{1}H} NMR** (151 MHz, $CDCl_3$): δ 150.24 (s, Ar_F-**C**H=N), 146.06 (s, Ar_F**C**-1/4), 144.40 (s, Ar**C**-1/3/5), 131.88 (s, Ar**C**-2/4/6), 117.15 (s, Ar_F**C**-2/3/5/6), 59.27 (s, N-**C**H_2-Ar), 23.16(s, Ar-**C**H_2-CH_3), 15.76 (s, Ar-CH_2-**C**H_3).

FT-IR (ATR): ṽ(cm^{-1}) = 2966.5, 2931.8, 2875.9, 1641.4, 1477.5, 1460.1, 1379.1, 1296.2, 1273.0, 1234.4, 1074.4, 1045.4, 1035.7, 1016.49, 991.4, 977.9, 956.7, 923.9, 898.8, 781.2, 758.0, 742.6, 667.4, 619.2.

MALDI-MS: calc. $[C_{108}H_{96}F_{24}N_{12}+H]^+$ = 2017.758 m/z, found: 2017.716 m/z

Mp.: 318 °C

Synthesis of scrambled cages

General procedure: To a solution of terephthalaldehyde (**TA**) and tetrafluoroterephthaldehyde (**TFTA**) in methanol (50 mL) a solution of **Et-Amine** (125.00 mg, 500.00 µmol, 1.00 eq) in methanol (75 mL) was added dropwise over 1 h. After stirring the reaction mixture for 3 days at room temperature the precipitate was collected by filtration and washed with methanol (3 x 50 mL). Extraction of the solid with dichloromethane (3 x 20 mL) and removal of the solvent under reduced pressure (30 °C) gave the scrambled cages as pale-yellow solids.

Synthesis of $A_4H_5F_1$

$A_4H_5F_1$ was synthesized according to the general procedure using **TFTA** (20.60 mg, 100.00 µmol, 0.20 eq.) and **TA** (67.10 mg, 500.00 µmol, 1.00 eq.).

Yield: 52.10 mg (24%)

^{1}H NMR (600 MHz, $CDCl_3$): δ 8.45 – 8.39 (m, 2H, Ar_F-C**H**=N), 8.30 – 8.21 (m, 10H, Ar_HC**H**=N), 7.77 – 7.69 (m, 20H, Ar_H-**H**), 5.01 (s, 4H, Ar_F-CH=N-C**H_2**), 4.94 (s, 20H, Ar_H-CH=N-C**H_2**), 2.79 – 2.68 (m, 24H, Ar-C**H_2**-CH_3), 1.29 – 1.24 (m, 36H, Ar-CH_2-C**H_3**); **^{19}F NMR** (565 MHz, $CDCl_3$): δ -143.56 – -143.67 (m). δ -143.60 (s, A_4H_5**F_1**), -143.64 (s, A_4H_4**F_2**).

Due to the low solubility in common NMR solvents, no ^{13}C NMR spectrum could be obtained.

FT-IR (ATR): ṽ(cm^{-1}) = 2962.7, 2927.9, 2893.2, 2870.1, 2362.8, 1635.6, 1566.2, 1477.5, 1452.4, 1375.3, 1313.5, 1298.1, 1261.5, 1234.4, 1215.2, 1166.9, 1087.9, 1074.4, 1043.5, 1016.5, 974.1, 923.9, 910.4 823.6, 756.1, 733.0, 694.4, 677.0, 650.0.

MALDI-MS: calc. $[C_{108}H_{120}N_{12}+H]^+$ = 1585.984 m/z, found: 1586.015 m/z (**A_4H_6**); calc. $[C_{108}H_{116}F_4N_{12}+H]^+$ = 1657.946 m/z, found: 1657.956 m/z (**$A_4H_5F_1$**); calc. $[C_{108}H_{112}F_8N_{12}+H]^+$ =

1729.908 m/z, found: 1729.940 m/z (**$A_4H_4F_2$**); calc. $[C_{108}H_{108}F_{12}N_{12}+H]^+$ = 1801.871 m/z, found: 1801.901 m/z (**$A_4H_3F_3$**).

Mp.: 269 °C

Synthesis of $A_4H_4F_2$

$A_4H_4F_2$ was synthesized according to the general procedure using **TFTA** (41.20 mg, 200.00 µmol, 0.40 eq.) and **TA** (53.70 mg, 400.00 µmol, 0.80 eq.).

Yield: 48.70 mg (20%)

^{1}H NMR (600 MHz, $CDCl_3$): δ 8.46 – 8.34 (m, 1H, Ar_F-C**H**=N), 8.30 – 8.18 (m, 3H, Ar_HC**H**=N), 7.82 – 7.64 (m, 7H, Ar_H-**H**), 5.01 (s, 2H, Ar_F-CH=N-C**H_2**), 4.94 (s, 6H, Ar_H-CH=N-C**H_2**), 2.82 – 2.64 (m, 9H, Ar-C**H_2**-CH_3), 1.33 – 1.18 (m, 15H, Ar-CH_2-C**H_3**); **^{19}F NMR** (565 MHz, $CDCl_3$): δ -139.37 – -147.45 (m). Or -143.60 (s, **$A_4H_5F_1$**), -143.64 (s, **$A_4H_4F_2$**).

Due to the low solubility in common NMR solvents, no ^{13}C NMR spectrum could be obtained.

FT-IR (ATR): $\tilde{\nu}$(cm^{-1}) = 2962.7, 2929.9, 2872.0, 2839.2, 1699.3, 1637.6, 1566.2, 1477.5, 1452.4, 1379.1, 1313.5, 1296.2, 1213.2, 1043.5, 976.0, 908.5, 850.6, 825.5, 775.4, 731.0.

MALDI-MS: calc. $[C_{108}H_{120}N_{12}+H]^+$ = 1585.984 m/z, found: 1586.072 m/z (**A_4H_6**); calc. $[C_{108}H_{116}F_4N_{12}$ + H$]^+$ = 1657.946 m/z, found: 1658.036 m/z (**$A_4H_5F_1$**); calc. $[C_{108}H_{112}F_8N_{12}+H]^+$ = 1729.908 m/z, found: 1730.001 m/z (**$A_4H_4F_2$**); calc. $[C_{108}H_{108}F_{12}N_{12}+H]^+$ = 1801.871 m/z, found: 1801.965 m/z (**$A_4H_3F_3$**); calc. $[C_{108}H_{104}F_{16}N_{12}+H]^+$ = 1873.833 m/z, found: 1873.926 m/z (**$A_4H_1F_5$**); calc. $[C_{108}H_{100}F_{20}N_{12}+H]^+$ = 1945.795 m/z, found: 1945.886 m/z (**$A_4H_1F_5$**).

Mp.: 277 °C

Synthesis of $A_4H_3F_3$

$A_4H_3F_3$ was synthesized according to the general procedure using **TFTA** (61.80 mg, 300.00 µmol, 0.60 eq.) and **TA** (40.20 mg, 300.00 µmol, 0.60 eq.).

Yield: 62.76 mg (25%)

^{1}H NMR (600 MHz, $CDCl_3$): δ 8.48 – 8.32 (m, 1H, Ar_F-C**H**=N), 8.30 – 8.16 (m, 1H, Ar_HC**H**=N), 7.77 – 7.68 (m, 2H, Ar_H-**H**), 5.01 (s, 2H, Ar_F-CH=N-C**H_2**), 4.95 (s, 3H, Ar_H-CH=N-C**H_2**), 2.91 – 2.58 (m, 5H, Ar-C**H_2**-CH_3), 1.33 – 1.20 (m, 8H, Ar-CH_2-C**H_3**); **^{19}F NMR**(565 MHz, $CDCl_3$): δ -143.55 – -143.71 (m). Or -143.60 (s, **$A_4H_5F_1$**).

Due to the low solubility in common NMR solvents, no ^{13}C NMR spectrum could be obtained.

FT-IR (ATR): $\tilde{\nu}$(cm^{-1}) = 2968.5, 2929.9, 2872.0, 2358.9, 2337.7, 1639.5, 1477.5, 1460.1, 1408.0, 1373.3, 1298.1, 1261.5, 1232.5, 1074.4, 1043.5, 1016.5, 976.0, 908.5, 821.7, 767.7, 729.1.

MALDI-MS: calc. $[C_{108}H_{120}N_{12}+H]^+$ = 1585.984 m/z, found: 1586.037 m/z (**A_4H_6**); calc. $[C_{108}H_{116}F_4N_{12}+H]^+$ = 1657.946 m/z, found: 1658.005 m/z (**$A_4H_5F_1$**; calc. $[C_{108}H_{112}F_8N_{12}+H]^+$ = 1729.908 m/z, found: 1729.973 m/z (**$A_4H_4F_2$**); calc. $[C_{108}H_{108}F_{12}N_{12}+H]^+$ = 1801.871 m/z, found:

1801.941 m/z (**$A_4H_3F_3$**); calc. $[C_{108}H_{104}F_{16}N_{12}+H]^+$ = 1873.833 m/z, found: 1873.908 m/z (**$A_4H_2F_4$**); calc. $[C_{108}H_{100}F_{20}N_{12}+H]^+$ = 1945.795 m/z, found: 1945.872 m/z (**$A_4H_1F_5$**).
Mp.: 284 °C

Synthesis of $A_4H_2F_4$

$A_4H_2F_4$ was synthesized according to the general procedure using **TFTA** (82.40 mg, 400.00 µmol, 0.80 eq.) and **TA** (26.80 mg, 200.00 µmol, 0.40 eq.).
Yield: 49.79 mg (19%)
^{1}H NMR (600 MHz, $CDCl_3$): δ 8.53 – 8.32 (m, 1H, Ar_F-C**H**=N), 8.29 – 8.14 (m, 1H, Ar_HC**H**=N), 7.79 – 7.66 (m, 1H, Ar_H-**H**), 5.13 – 4.98 (m, 2H, Ar_F-CH=N-C**H_2**), 4.98 – 4.90 (m, 2H, Ar_H-CH=N-C**H_2**), 2.87 – 2.61 (m, 2H, Ar-C**H_2**-CH_3), 1.32 – 1.19 (m, 5H, Ar-CH_2-C**H_3**); **^{19}F NMR** (565 MHz, $CDCl_3$): δ -143.50 – -143.78 (m). Observed -143.70 (s, **A_4F_6**).
Due to the low solubility in common NMR solvents, no ^{13}C NMR spectrum could be obtained.
FT-IR (ATR): $\tilde{\nu}$(cm^{-1}) = 2987.7, 2966.5, 2929.9, 2900.9, 2873.9, 1639.5, 1477.5, 1460.1, 1379.1, 1298.1, 1232.5, 1101.4, 1045.4, 1016.5, 991.4, 976.0, 954.8, 906.5, 823.6, 765.7, 731.0.
MALDI-MS: calc. $[C_{108}H_{112}F_8N_{12}+H]^+$ = 1729.908 m/z, found: 1729.942 m/z (**$A_4H_4F_2$**); calc. $[C_{108}H_{108}F_{12}N_{12}+H]^+$ = 1801.871 m/z, found: 1801.908 m/z (**$A_4H_3F_3$**); calc. $[C_{108}H_{104}F_{16}N_{12}+H]^+$ = 1873.833 m/z, found: 1873.874 m/z (**$A_4H_2F_4$**); calc. $[C_{108}H_{100}F_{20}N_{12}+H]^+$ = 1945.795 m/z, found: 1945.840 m/z (**$A_4H_1F_5$**); calc. $[C_{108}H_{96}F_{24}N_{12}+H]^+$ = 2017.758 m/z, found: 2017.804 m/z (**A_4F_6**).
Mp.: 289 °C

Synthesis of $A_4H_1F_5$

$A_4H_1F_5$ was synthesized according to the general procedure using **TFTA** (103.00 mg, 500.00 µmol, 1.00 eq.) and **TA** (13.38 mg, 100.00 µmol, 0.20 eq.).
Yield: 60.34 mg (22%)
^{1}H NMR (600 MHz, $CDCl_3$): δ 8.53 – 8.32 (m, 10H, Ar_F-C**H**=N), 8.29 – 8.14 (m, 2H, Ar_HC**H**=N), 7.78 – 7.66 (m, 4H, Ar_H-**H**), 5.05 – 4.98 (m, 20H, Ar_F-CH=N-C**H_2**), 4.98 – 4.90 (m, 4H, Ar_H-CH=N-C**H_2**), 2.87 – 2.61 (m, 24H, Ar-C**H_2**-CH_3), 1.32 – 1.19 (m, 36H, Ar-CH_2-C**H_3**); **^{19}F NMR** (565 MHz, $CDCl_3$): δ -143.55 – -143.80 (m). Or δ -143.70(s, **A_4F_6**).
Due to the low solubility in common NMR solvents, no ^{13}C NMR spectrum could be obtained.
FT-IR (ATR): $\tilde{\nu}$(cm^{-1}) = 2987.7, 2970.4, 2885.5, 2358.9, 2339.7, 1701.2, 1639.5, 1477.5, 1458.2, 1406.1, 1379.1, 1296.2, 1228.7, 1045.4, 1014.6, 950.9, 906.5, 864.1, 829.4, 814.0, 777.3, 727.2.
MALDI-MS: calc. $[C_{108}H_{112}F_8N_{12}+H]^+$ = 1729.908 m/z, found: 1729.948 m/z (**$A_4H_3F_3$**); calc. $[C_{108}H_{108}F_{12}N_{12}+H]^+$ = 1801.871 m/z, found: 1801.912 m/z (**$A_4H_2F_4$**); calc. $[C_{108}H_{104}F_{16}N_{12}+H]^+$ = 1873.833 m/z, found: 1873.878 m/z (**$A_4H_1F_5$**); calc. $[C_{108}H_{100}F_{20}N_{12}+H]^+$ = 1945.795 m/z, found: 1945.846 m/z; calc. $[C_{108}H_{96}F_{24}N_{12}+H]^+$ = 2017.758 m/z, found: 2017.813 m/z (**A_4F_6**).
Mp.: 295 °C

Kinetic NMR experiments

The kinetic experiments were recorded in $CDCl_3$ (Sigma-Aldrich, ≥ 99.8%), because the solubilities of intermediate oligomeric species and the final cage species were too low in MeOH-d^4 to be monitored. During the experiments some precipitation still occurred therefore we added an external standard of 1,3,5-trifluorobenzene in $CDCl_3$ at 80 µM concentration to follow the concentration of oligomer and starting materials present in the reaction solution.

Experimental procedure I

Stock solution A: **Et-Amine** (5.0 mg, 20 µmol) was dissolved in 2.5 mL $CDCl_3$.

Stock solution B: **TFTA** (2.5 mg, 12 µmol) and **TA** (1.6 mg, 12µmol) were dissolved in 2.5 mL $CDCl_3$.

In an NMR tube 0.5 ml of stock solution A (4 µmol of **Et-Amine**) were added to 0.5 mL of stock solution B (2.4 µmol per aldehyde) and mixed by shaking the resulting solution for 5 min.

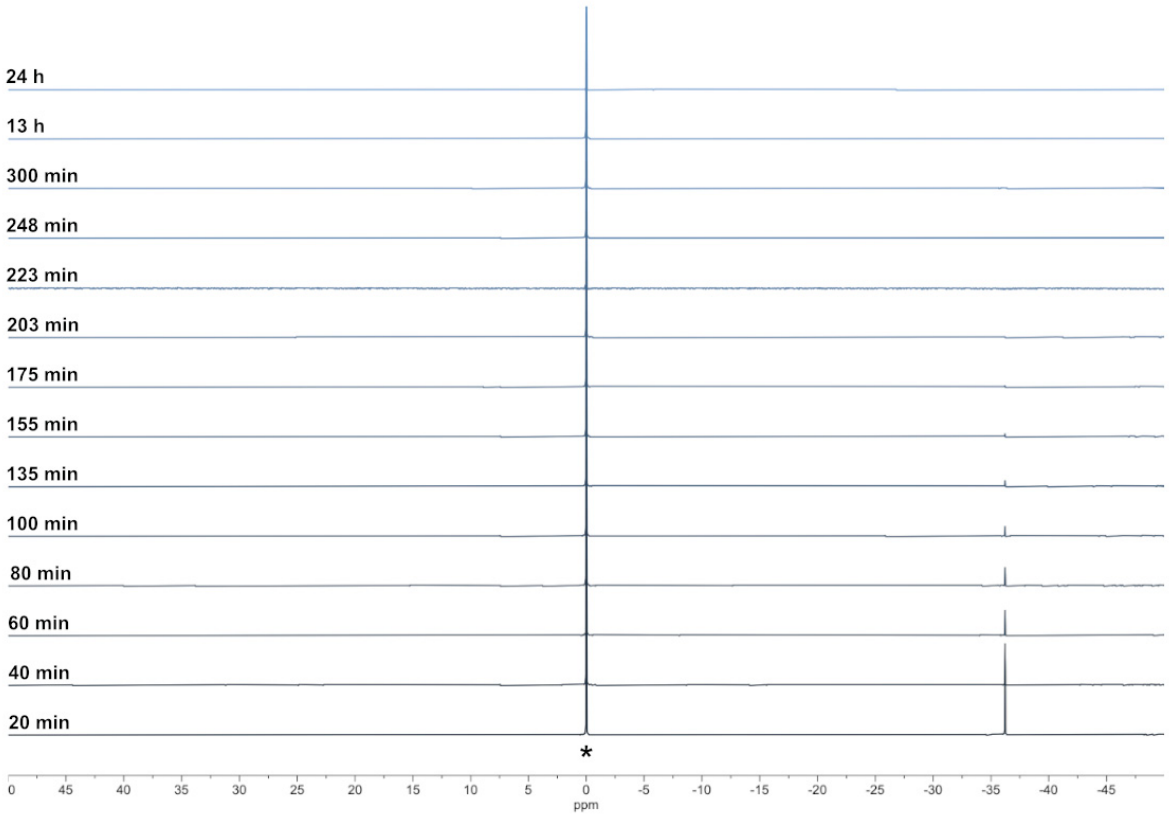

Figure S29: Overlay of ^{19}F NMR spectra recorded for the formation of $\mathbf{A_4H_3F_3}$ in specified time intervals (see inlay). The signal at -36.23 ppm corresponds to the fluorine atoms of **TFTA**. 1,3,5-Trifluorobenzene (*) was used as a reference (0 ppm) and as an external standard for monitoring the concentration of **TFTA** during the experiments.

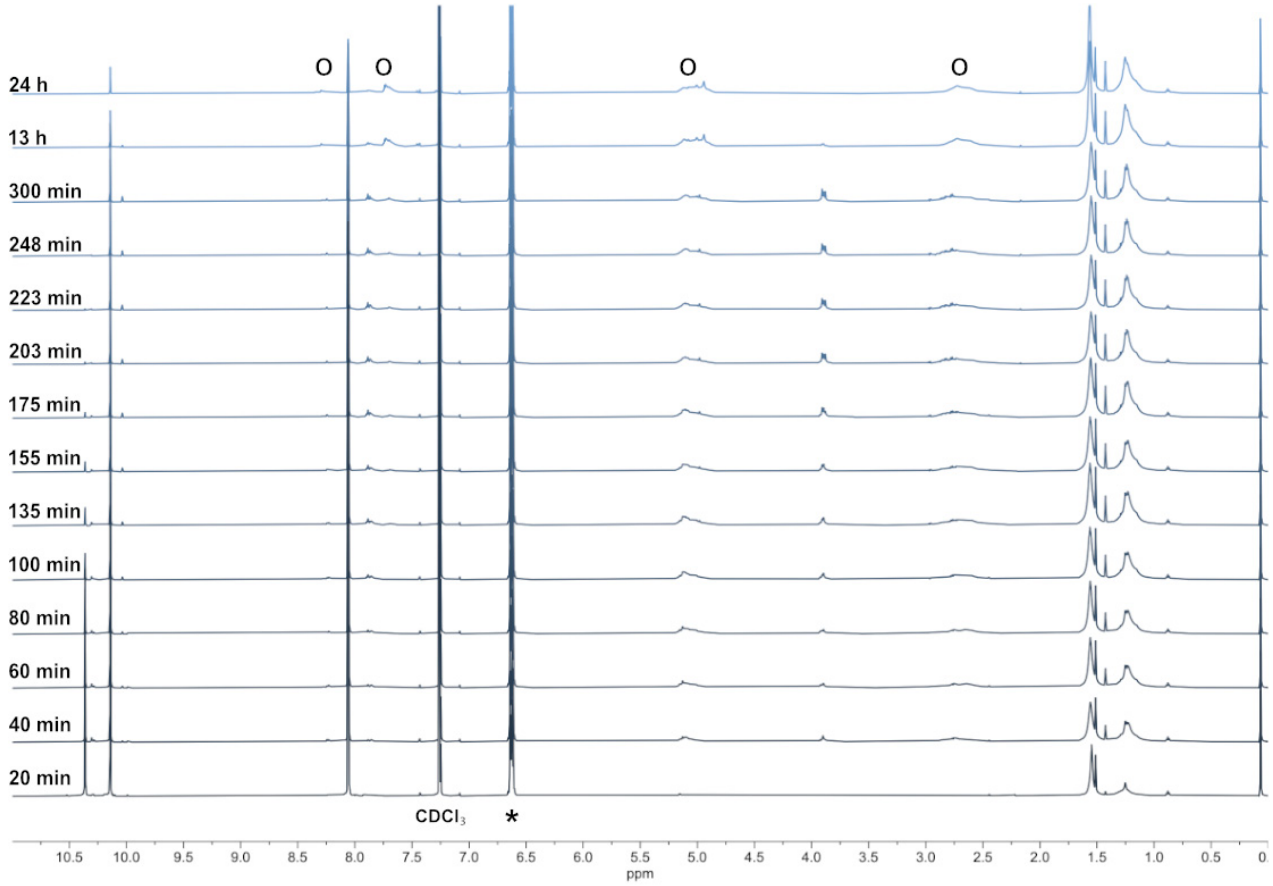

Figure S30: Overlay of ^{1}H NMR spectra of the formation of $\mathbf{A_4H_3F_3}$ recorded in specified time intervals (see inlay) in $CDCl_3$. 1,3,5-Trifluorobenzene (*) was used as an external standard to monitor the concentration of the compounds. The decrease of the **TFTA** signal at 10.36 ppm is caused by the precipitation of oligomeric products due to the fast reaction with **Et-Amine**. This explains the absence of all amine signals after just 20 minutes. These **TFTA**-containing oligomers function as reservoirs for the formation of pre-ordered hybrid oligomeric structures (O-symbol). These are solubilized nicely in $CDCl_3$, eventually resulting in the formation of $\mathbf{A_4H_3F_3}$ after 5 days.

Experimental procedure II

The kinetic experiments on the formation of $\mathbf{A_4H_3F_3}$ were repeated under competitive conditions. The concentration of both aldehydes was chosen so that both cage species $\mathbf{A_4H_6}$ and $\mathbf{A_4F_6}$ were possible to form without formation of hybrid species.

Stock solution A: **Et-Amine** (5.0 mg, 20 µmol) was dissolved in 2.5 ml $CDCl_3$.

Stock solution B: **TFTA** (5.0 mg, 24 µmol) and **TA** (3.2 mg, 24 µmol) were dissolved in 2.5 mL $CDCl_3$.

In an NMR tube 0.5 mL of stock solution A (4 µmol of **Et-Amine**) were added to 0.5 mL of stock solution B (4.8 µmol per aldehyde) and mixed by shaking the resulting solution for 5 min. The

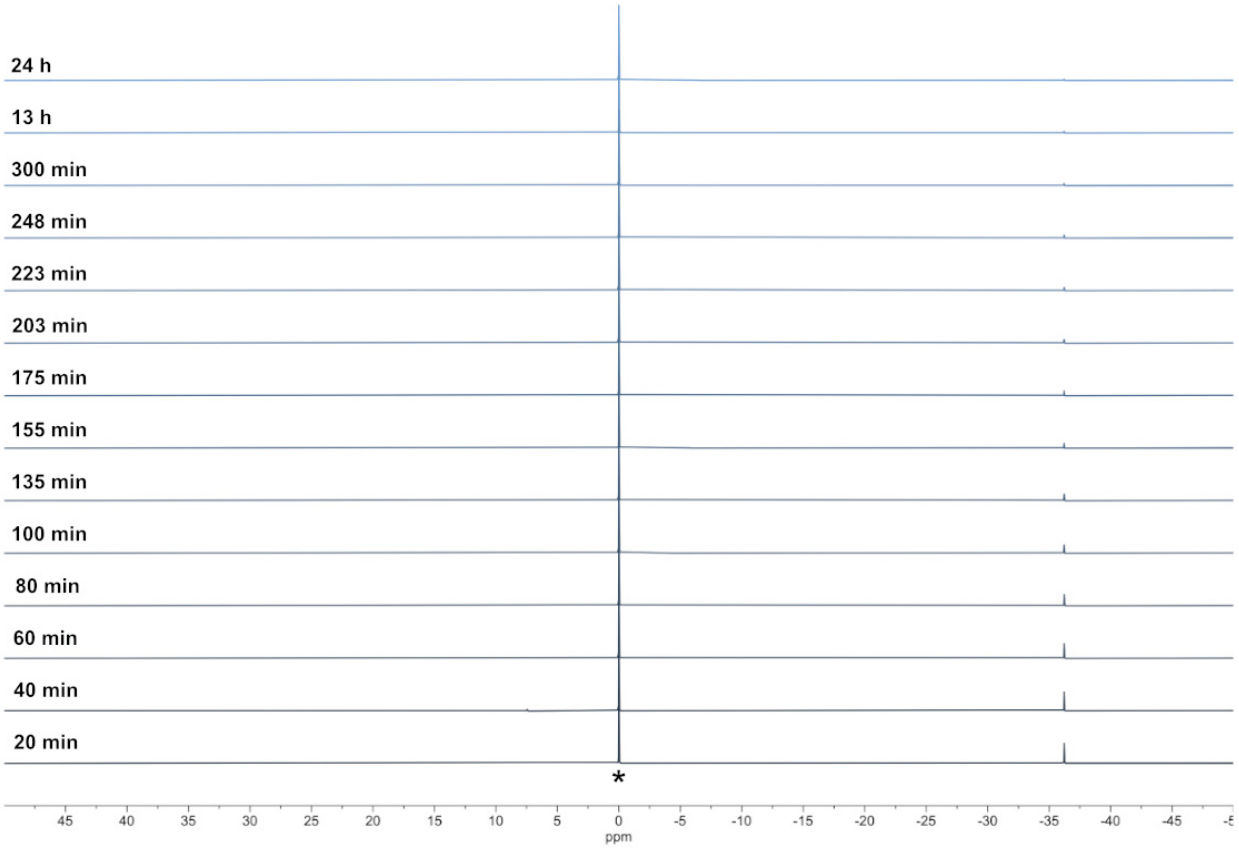

Figure S31: Overlay of ^{19}F NMR spectra recorded for the formation of $\mathbf{A_4H_3F_3}$ under competitive conditions in specified time intervals (see inlay). The signal at -36.23 ppm corresponds to the fluorine atoms of **TFTA**. 1,3,5-Trifluorobenzene (*) was used as a reference (0 ppm) for monitoring the concentration of **TFTA** during the experiments.

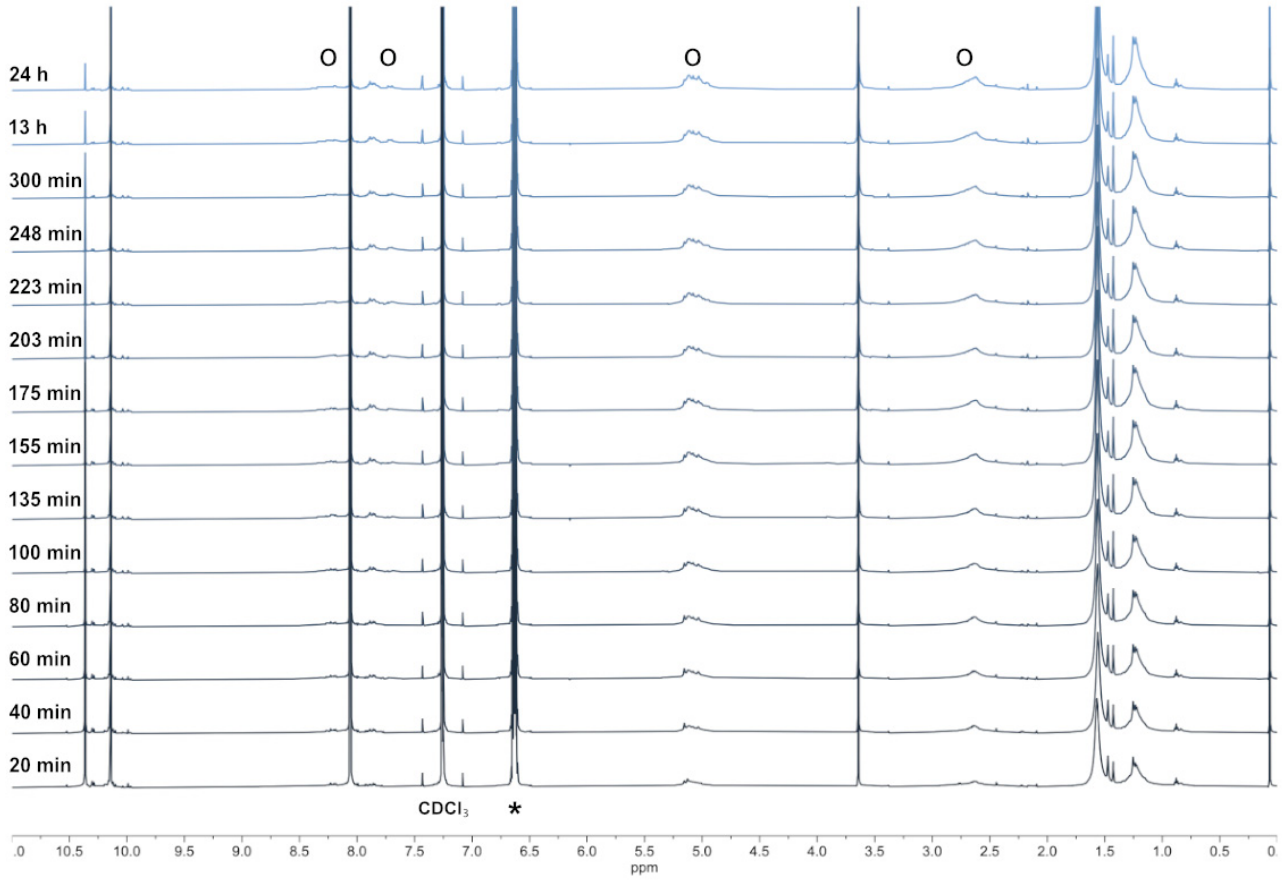

Figure S32: Overlay of ^{1}H NMR spectra of the formation of $\mathbf{A_4H_3F_3}$ recorded in specified time intervals (see inlay) in $CDCl_3$. 1,3,5-Trifluorobenzene (*) was used as an external standard to monitor the concentration of the compounds. The decrease of the **TFTA** signal at 10.36 ppm is caused by formation of oligomeric products due to the fast reaction with **Et-Amine**. Due to the lower availability of amine A under competitive conditions, the **TA** molecules are incorporated into the hybrid oligomeric species faster than under standard conditions. This results in the fast formation of solubilized oligomeric species (O-symbols) and a faster decrease of the **TA** signal than under standard conditions. The **TFTA** molecules remain partially unreacted and are liberated from the oligomers as the system starts equilibrating towards the formation of $\mathbf{A_4H_6}$ and $\mathbf{A_4H_5F_1}$ eventually.

Thermodynamic experiments

Invesigating the amine stoichiometry

Et-Amine (24.92 mg, 100.00 µmol, 1.00 eq.), **TFTA** (24.71 mg, 120.00 µmmol, 1.20 eq.) and **TA** (16.08 mg, 120.00 µmol, 1.20 eq.) were suspended in methanol (25 mL) and stirred for 3 d at room temperature. The formed precipitate was washed with methanol (3 x 15 mL) and analyzed by NMR and MALDI-MS.

For comparison **Et-Amine** (24.9 mg, 100 µmol, 1.00 eq.), **TFTA** (12.4 mg, 60.0 µmmol, 0.60 eq.) and **TA** (8.1 mg, 60 µmol, 0.60 eq.) were suspended in methanol (25 mL) and stirred for 3 d at room temperature. The formed precipitate was washed with methanol (3 x 15 mL) and analyzed by NMR and MALDI-MS.

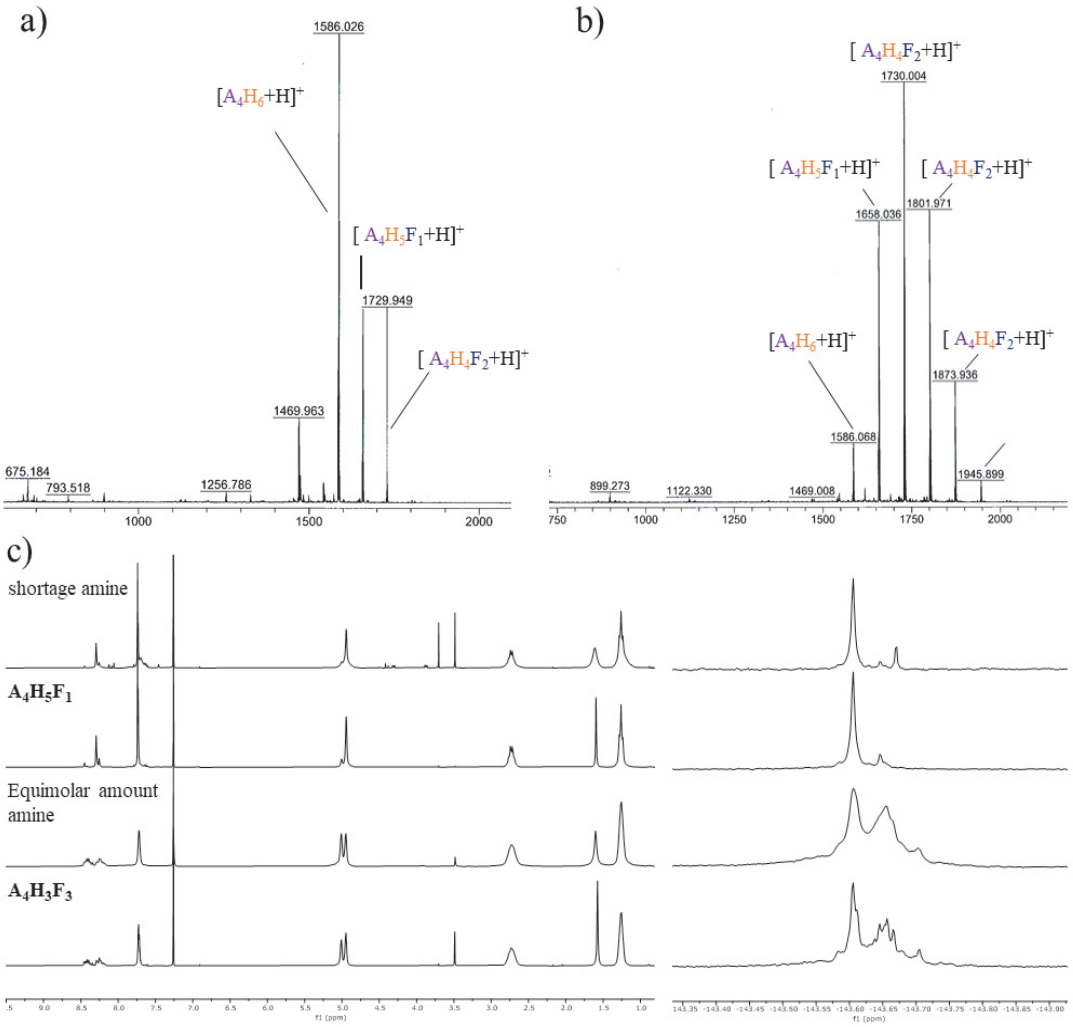

Figure S33: a) MALDI-MS spectrum of the obtained solid using an amine: aldehyde ratio of 2.5:6 instead of 5:6, b) MALDI-MS spectrum of the obtained reference solid using an amine: aldehyde ratio of 5:6 and c) stacked ^{1}H NMR (left) and ^{19}F NMR (right) spectra of the obtained solids and previously synthesised hybrid materials $\mathbf{A_4H_5F_1}$ and $\mathbf{A_4H_3F_3}$ for comparison.

Exchange experiments

Mixing the cages $\mathbf{A_4H_6}$ and $\mathbf{A_4F_6}$

Procedure: Cages $\mathbf{A_4H_6}$ (3.22 mg 2.00 µmol) and $\mathbf{A_4F_6}$ (4.03 mg 2.00 µmol) were stirred in 2 mL of the respective solvent (methanol or $CDCl_3$) at either room temperature or 60 °C for 10 d. In the case of solvent systems containing methanol the solvent was removed in vacuo at room temperature and the solid was analysed by NMR as well as MALDI-MS while in $CDCl_3$ a sample for NMR and MALDI-MS was taken of the solution after 3 d and 10 d.

After 3 d in $CDCl_3$ at 60 °C an exchange between the cages could be observed, which increased over the next 7 d. No exchange was observed in methanol nor $CDCl_3$ at room temperature even after stirring for 10 d.

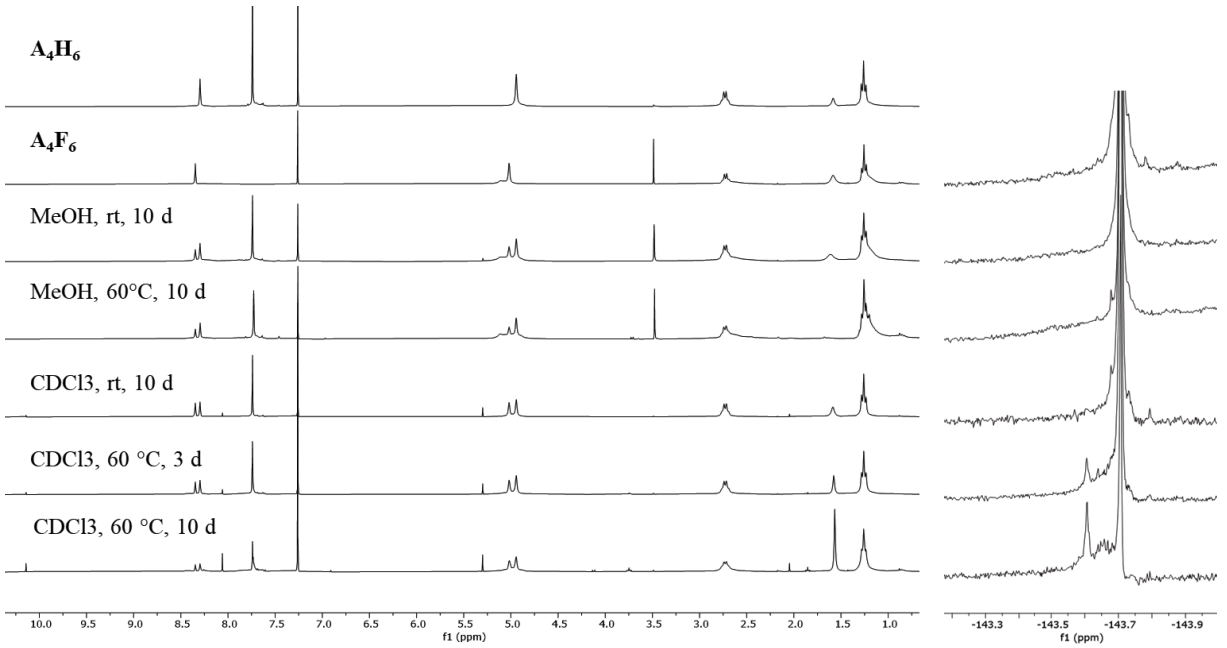

Figure S34: ^{1}H-NMR spectra (left) and ^{19}F-NMR spectra (right) of exchange experiments between cages $\mathbf{A_4H_6}$ and $\mathbf{A_4F_6}$.

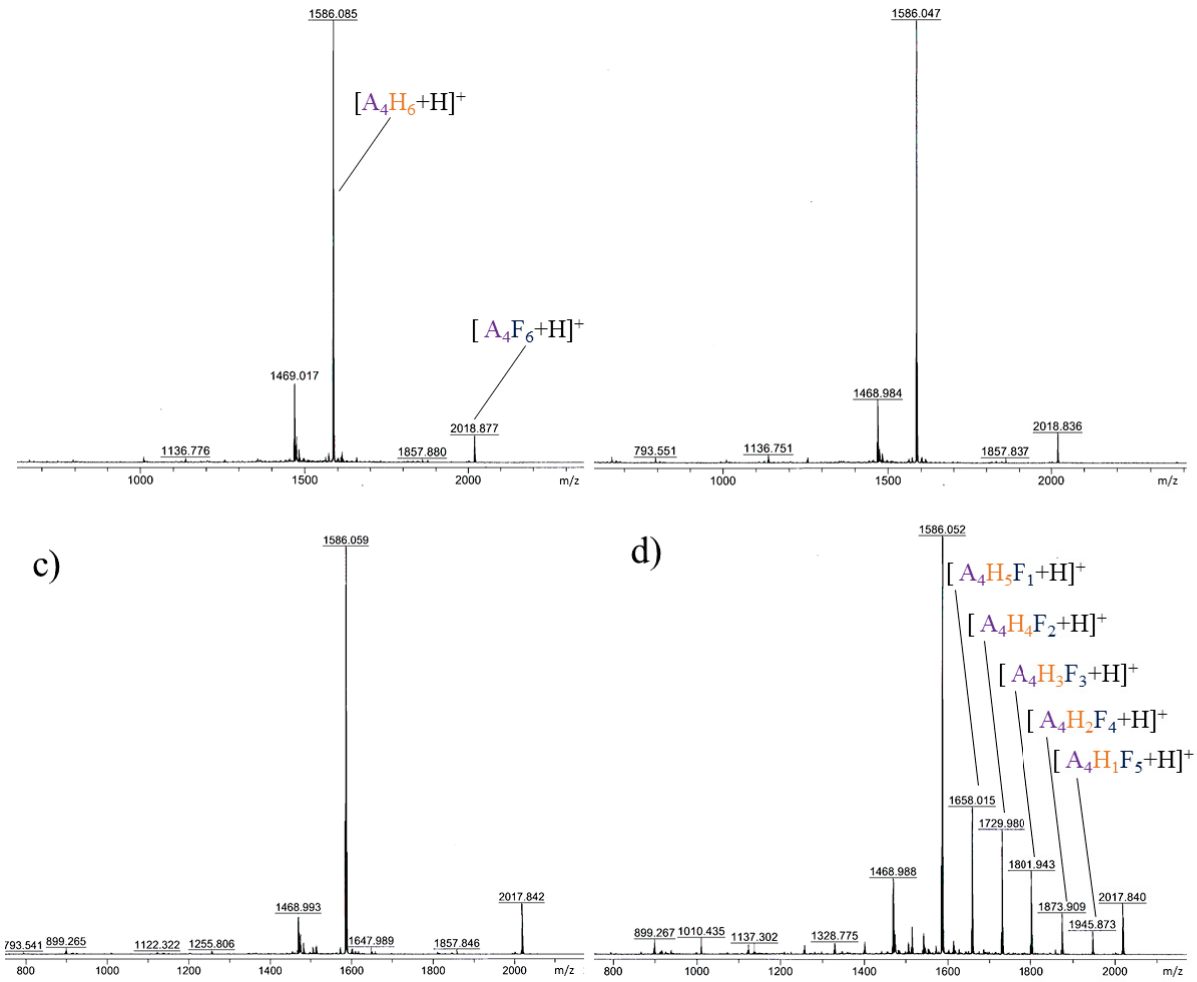

Figure S35: MALDI-MS spectra of exchange experiments between $\mathbf{A_4H_6}$ and $\mathbf{A_4F_6}$, in a) methanol at r.t. for 10 d, b) methanol at 60 °C for 10 d, c) $CDCl_3$ at r.t. for 10 d or d) $CDCl_3$ at 60°C for 10 d.

Mixing cages $\mathbf{A_4H_6}$ and $\mathbf{A_4F_6}$ with TFTA or TA

Mixing ***A_4H_6*** *with* ***TFTA***

Procedure: Cage $\mathbf{A_4H_6}$ (16.02 mg, 10.00 µmol) was solved/suspended in 5.0 mL solvent (methanol or $CHCl_3$). To 1 mL of this stock solution 1 mL either 2 mM (1.00 eq.), 10 mM (5.00 eq.) or 40 mM (20.00 eq.) **TFTA**-solution (same solvent) was added. The resulting mixture was stirred for 3 d at room temperature. The solvent was removed in vacuo and the obtained solids were analysed by MALDI-MS.

Using only 1 eq. of **TFTA** in either methanol or $CHCl_3$ led to an exchange between the aldehydes and the formation of the scrambled cages $\mathbf{A_4H_5F_1}$ and $\mathbf{A_4H_4F_2}$. Using 5 eq. **TFTA** or more led to a complete decomposition of the cage and primarily oligomeric products were formed.

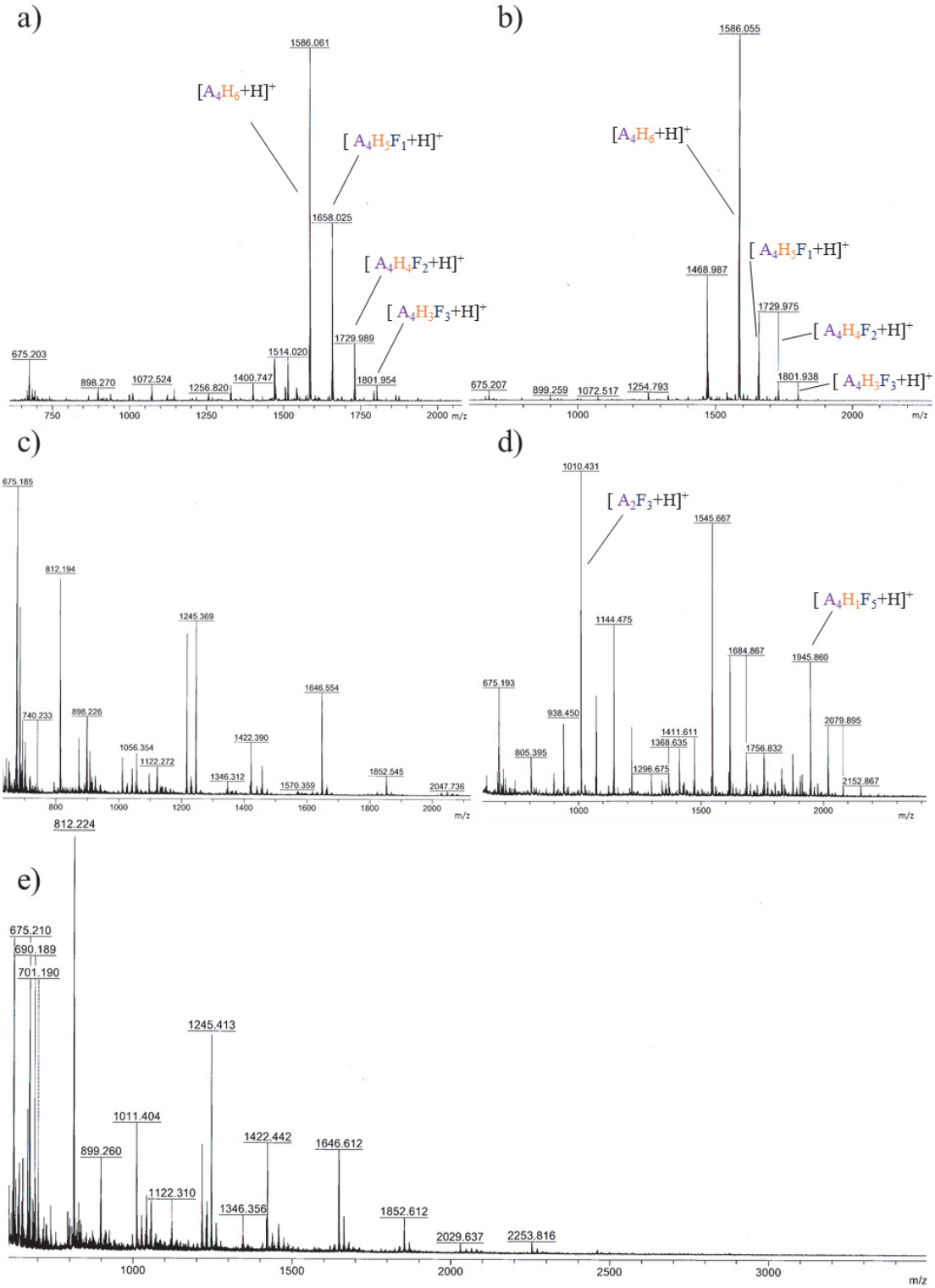

Figure S36: MALDI-MS spectra of exchange experiments between $\mathbf{A_4H_6}$ and **TFTA** after 3 d at room temperature with a) 1.00 eq. **TFTA** in methanol, b) 1.00 eq. **TFTA** in $CHCl_3$, b) 5.00 eq. **TFTA** in methanol, d) 5.00 eq. **TFTA** in $CHCl_3$ or e) 20.00 eq. **TFTA** in $CHCl_3$ showing the complete decomposition of the cage.

*Mixing **A_4F_6** with **TA***

Procedure: Cage **A_4F_6** (20.00 mg, 10.00 µmol) was solved/suspended in 5.0 mL solvent (MeOH or $CHCl_3$). To 1 mL of this stock solution 1 mL either 2 mM (1.00 eq.) or 10 mM (5.00 eq.) **TA**-solution (same solvent) was added. The resulting mixture was stirred for 3 d at room temperature. The solvent was removed in vacuo and the obtained solids were analysed by MALDI-MS.

As in the previous experiment using only 1 eq. of **TA** in $CHCl_3$ led to an exchange between the aldehydes and the formation of the scrambled cage **$A_4H_1F_5$** as well as a the **Tri^2Di^3** imine cage **A_2F_3**. Using 5 eq. **TA** or more in $CHCl_3$ led to a complete decomposition of the cage and primarily oligomeric products were formed and the formation of the **Tri^2Di^3** cage was increased. In methanol, no exchange could be observed supposedly due to the low solubility of **A_4F_6**.

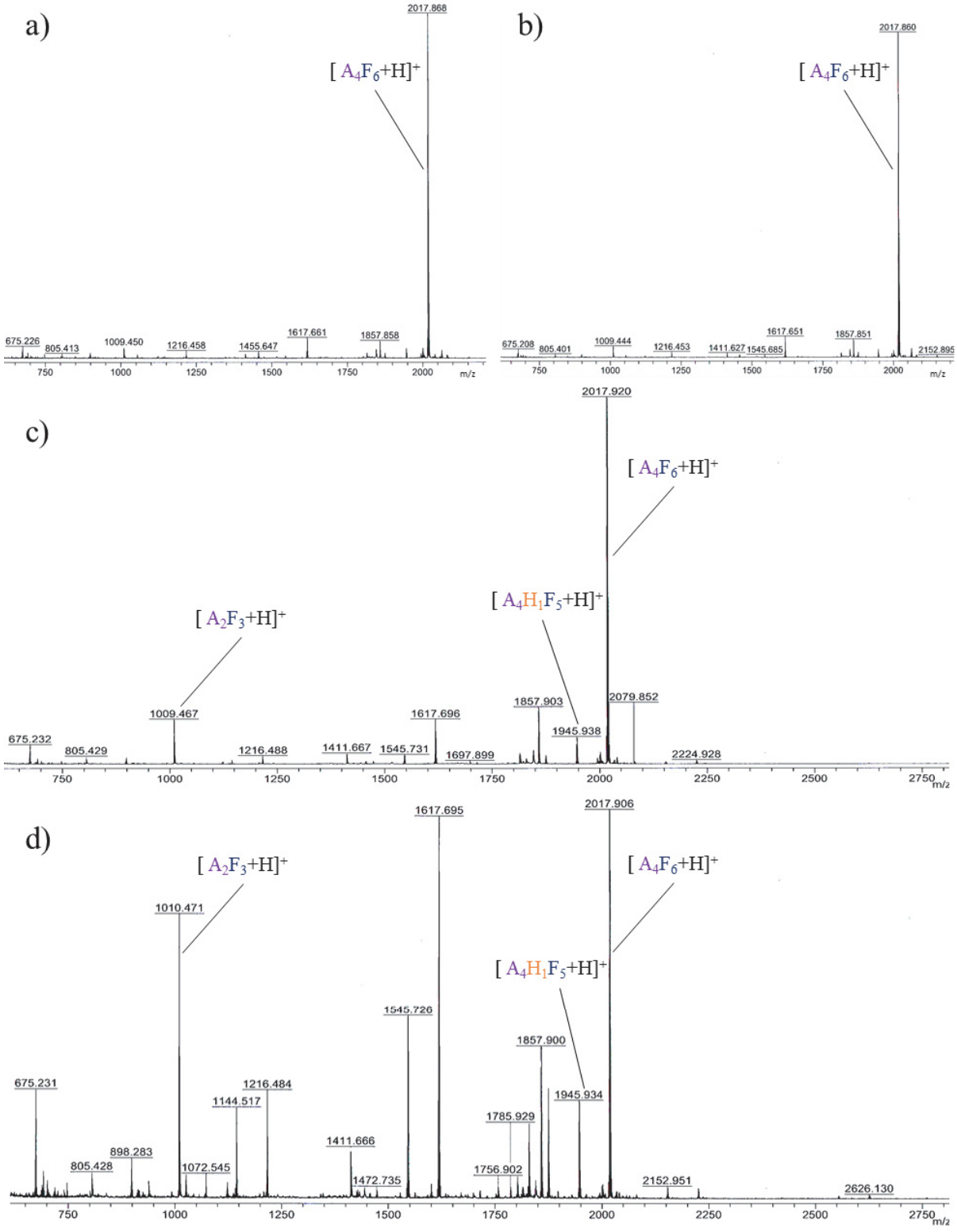

Figure S37: MALDI-MS spectra of exchange experiments between $\mathbf{A_4F_6}$ and **TA** after 3 d at room temperature with a) 1.00 eq. **TFTA** in methanol, b) 5.00 eq. **TA** in methanol, b) 1.00 eq. **TA** in $CHCl_3$ or d) 5.00 eq. **TA** in $CHCl_3$.

DOSY experiments

Table S5: Estimated hydrodynamic radii (r_S) using parameters from literature and diffusion coefficients (D) measured by DOSY NMR.

Compound/Mixture	log(D) [log(m^2s^{-1})]	D x 10^{-10} [m^2 s^{-1}]	r_S (Å)
$\mathbf{A_4H_5F_1}$	-9.34	4.57	8.85
$\mathbf{A_4H_4F_2}$	-9.27	5.37	7.53
$\mathbf{A_4H_3F_3}$	-9.37	4.27	9.48
$\mathbf{A_4H_2F_4}$	-9.35	4.47	9.05
$\mathbf{A_4H_1F_5}$	-9.33	4.68	8.65
$\mathbf{A_4F_6}$	-9.31	4.90	8.26

All cages show similar diffusion coefficients which are comparable to previous reported diffusion coefficients of cage compound $\mathbf{A_4H_6}$ (D_{Lit}= 4.69 x 10^{-9} m^2 s^{-1}). Hence even the highly complex cage mixtures show only a single set of signals.

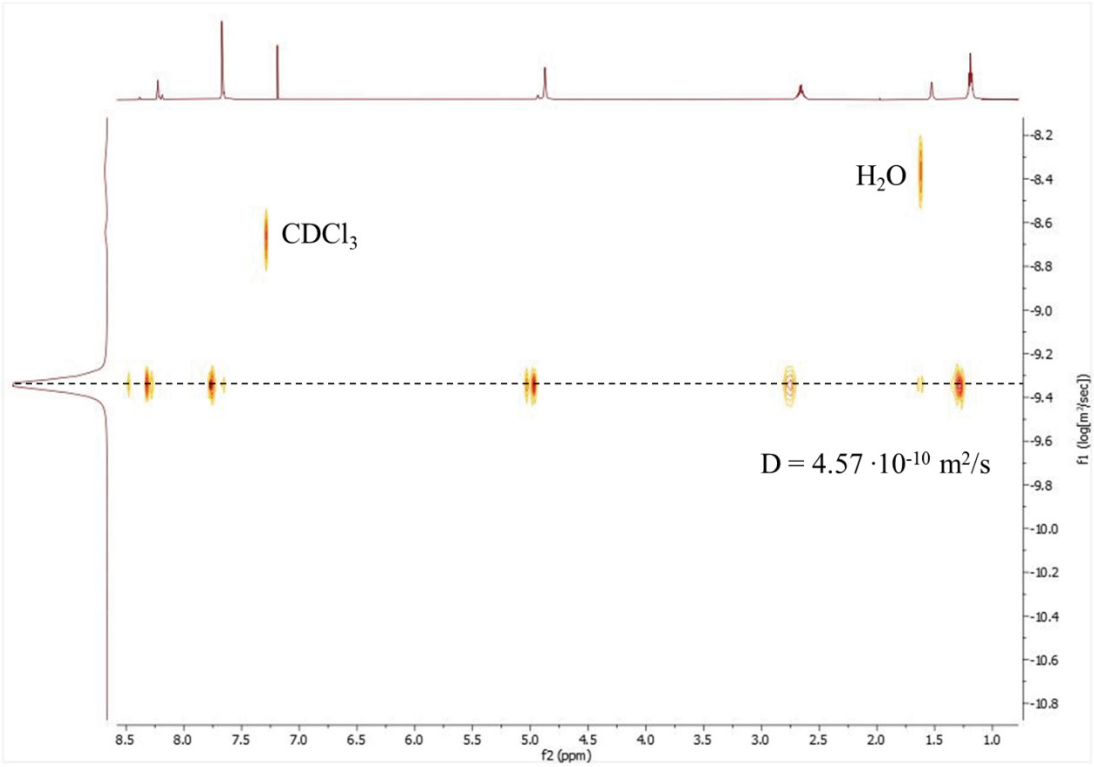

Figure S38: DOSY NMR spectrum (600 MHz, $CDCl_3$, 298 K) of hybrid cage mixture $\mathbf{A_4H_5F_1}$.

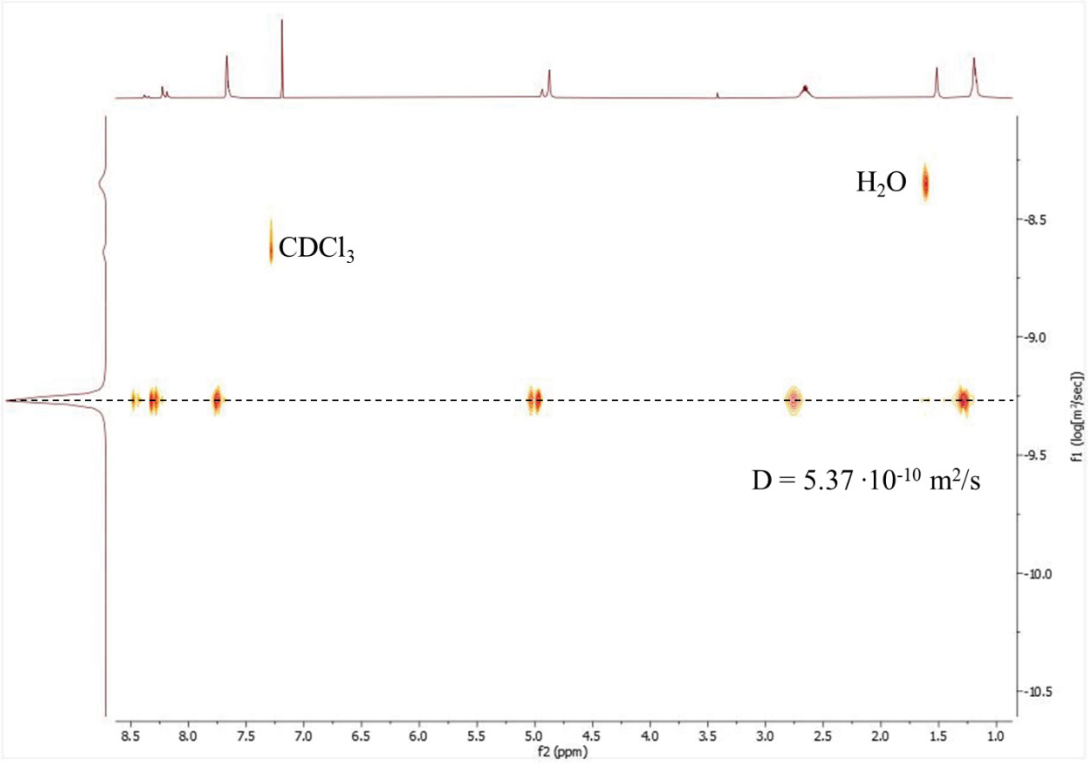

Figure S39: DOSY NMR spectrum (600 MHz, $CDCl_3$, 298 K) of hybrid cage mixture **$A_4H_4F_2$**.

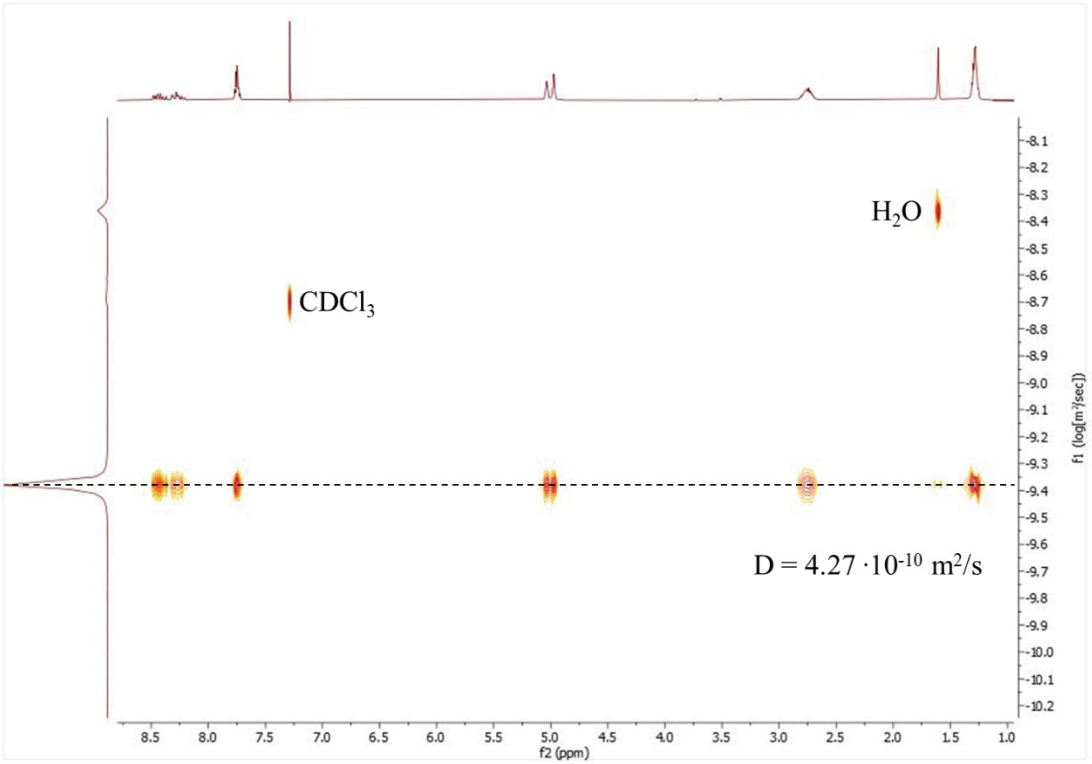

Figure S40: DOSY NMR spectrum (600 MHz, $CDCl_3$, 298 K) of hybrid cage mixture **$A_4H_3F_3$**.

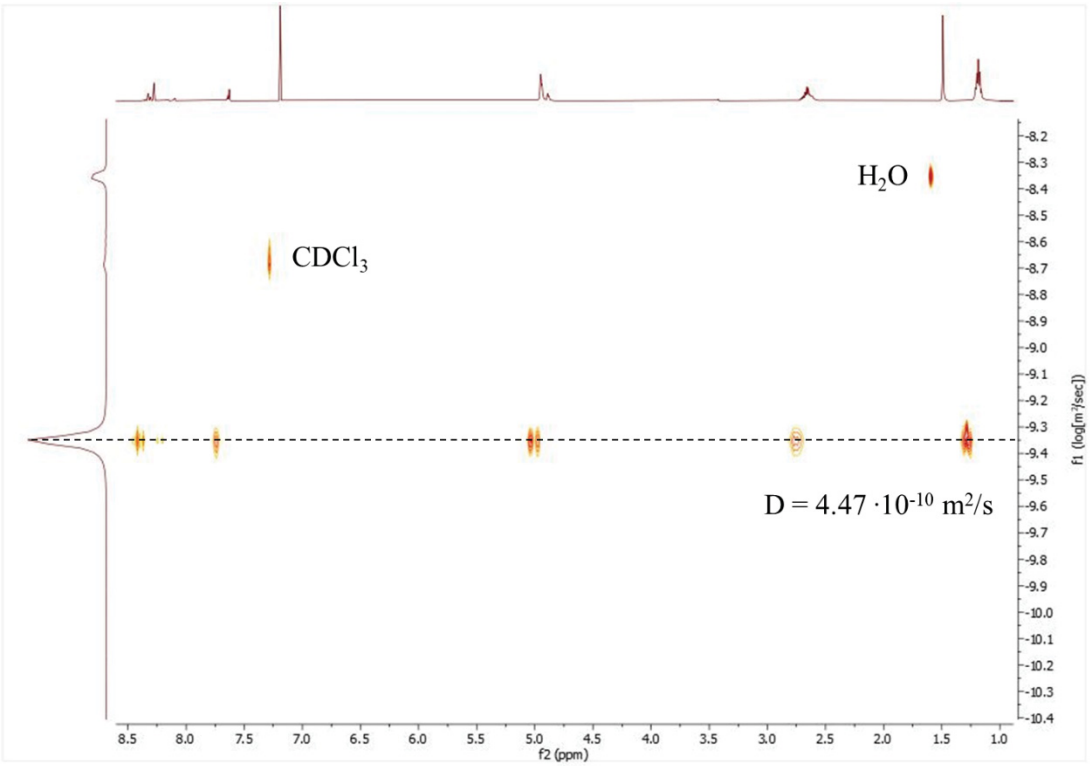

Figure S41: DOSY NMR spectrum (600 MHz, $CDCl_3$, 298 K) of hybrid cage mixture $\mathbf{A_4H_2F_4}$.

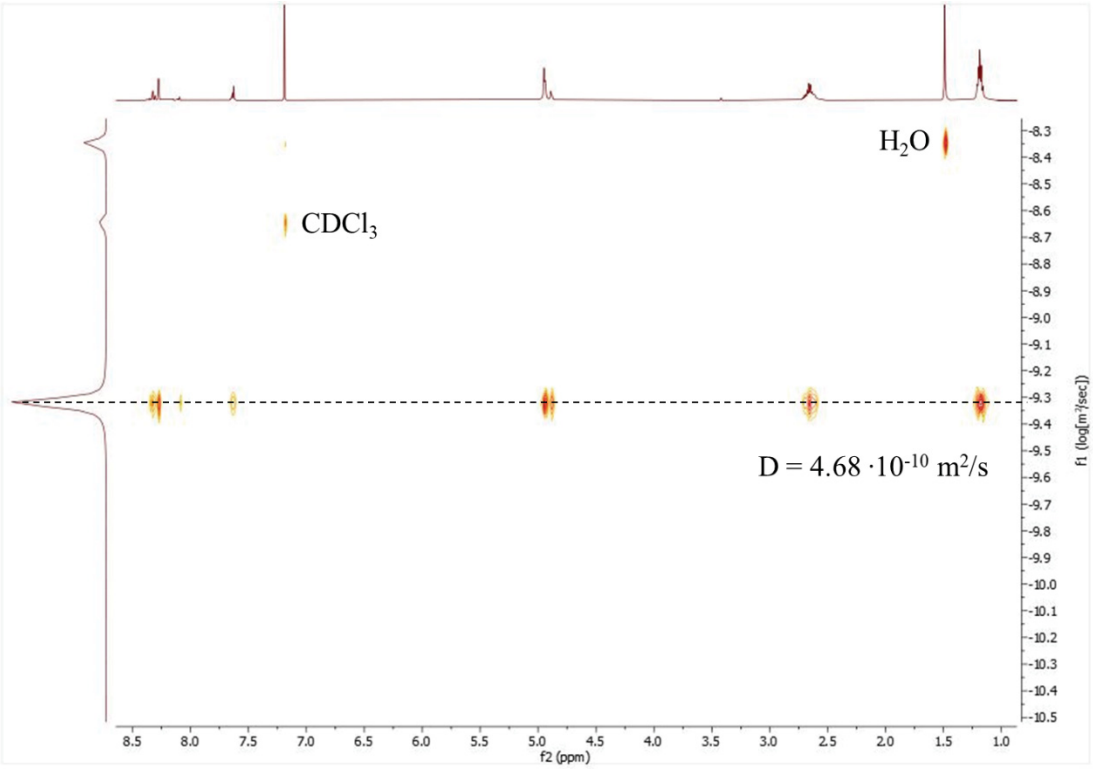

Figure S42: DOSY NMR spectrum (600 MHz, $CDCl_3$, 298 K) of hybrid cage mixture $\mathbf{A_4H_1F_5}$.

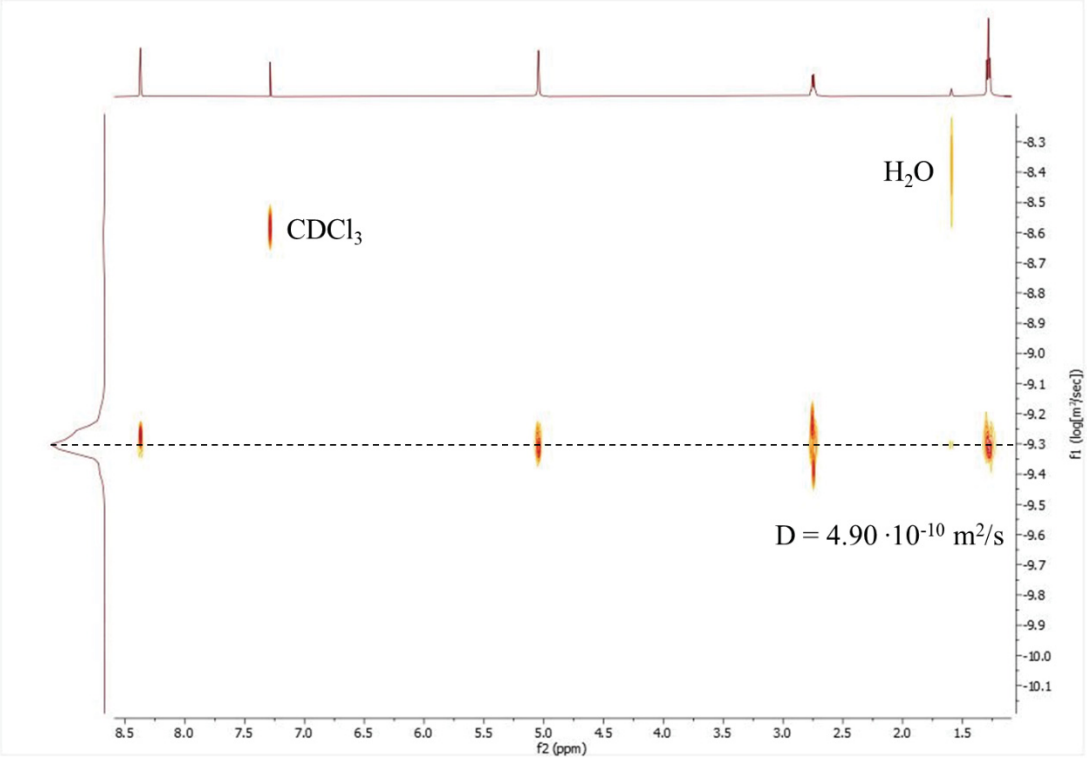

Figure S43: DOSY NMR spectrum (600 MHz, $CDCl_3$, 298 K) of cage compound **A_4F_6**.

Computational Details

Quantum mechanical calculations were performed by applying density functional theory. Single-point energies of all studied hybrid cages were calculated using Gaussian16 program.[98] Stationary points were characterized by vibrational analyses. Figure S44 gives an overview of all structures used to determine the differences in energy. For the calculation of the differences in total energy, additionally water (-76,415215 Hartree), **TFTA** (-855,76929 Hartree), **TA** (-458,835478 Hartree) and **Et-Amine** (-752,028315 Hartree) were employed, following the approach of Jelfs and co-workers.[28a]

All calculations were performed and evaluated by Dr. Bernd M. Schmidt.

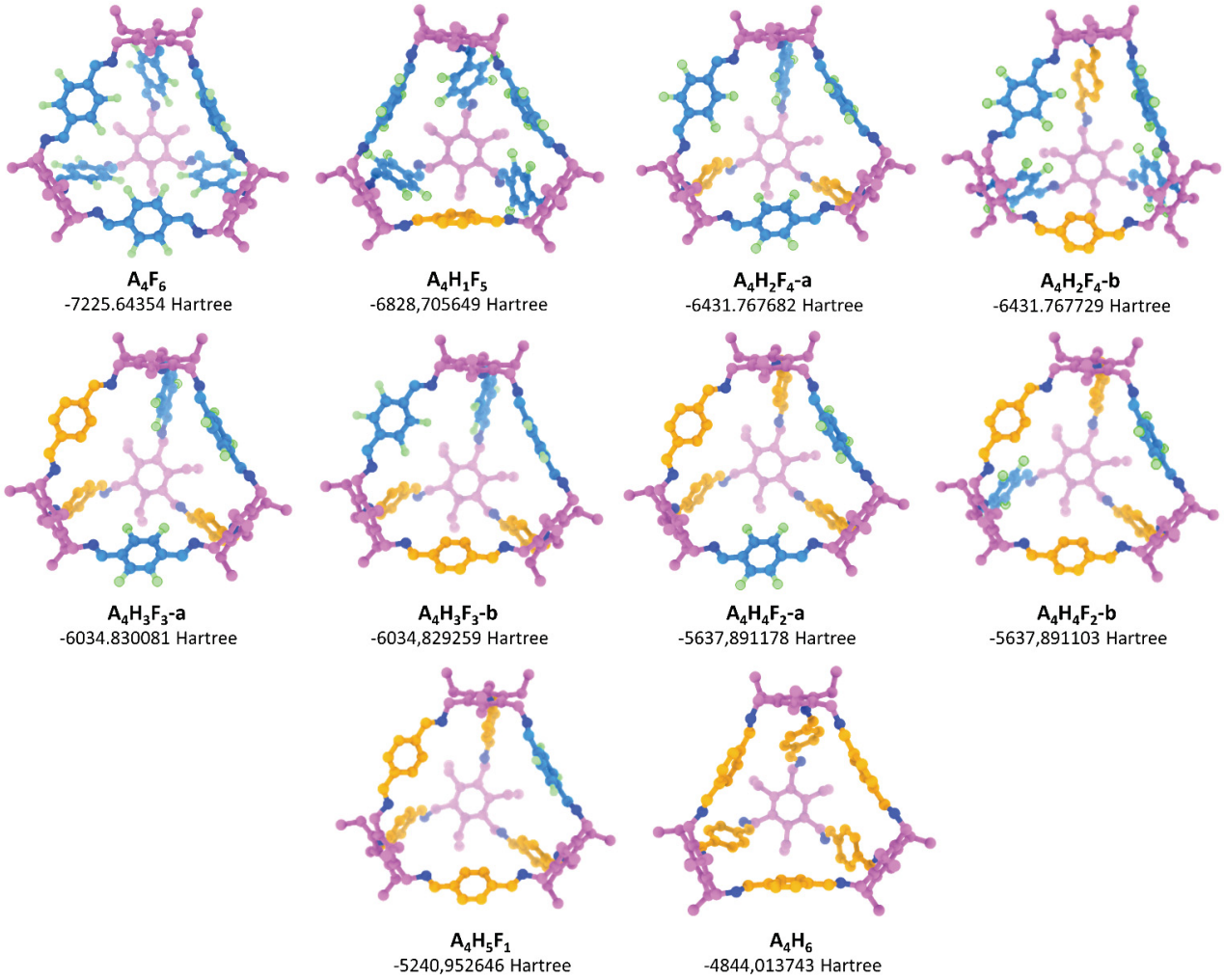

Figure S44: DFT single-point energies obtained by using B3LYP/6-311G level of theory.

Thermogravimetrical analysis

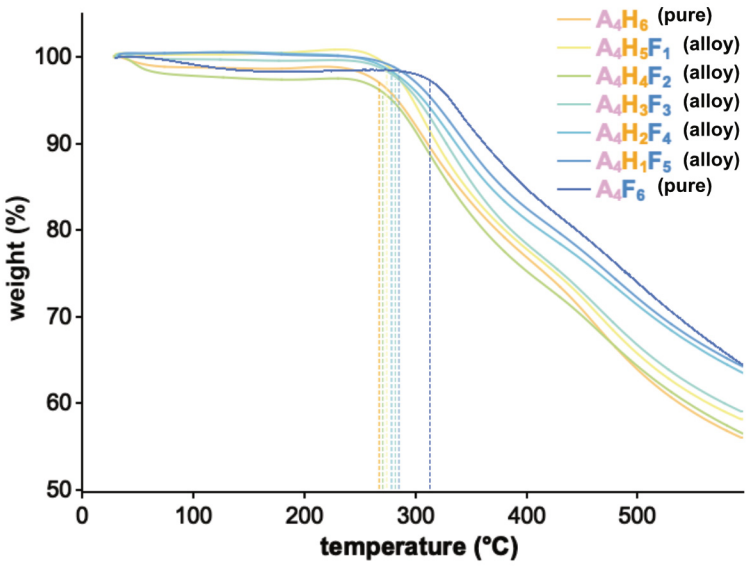

Figure S45: Thermogravimetric analysis curves of amorphous samples of the hybrid and symmetric cages. The initial dip is due to evaporation of residual water even though all samples were evacuated at 40 °C and 10^{-2} mbar for 24 hours prior to the measurement.

Table S6: Onset decomposition temperatures derived from thermogravimetric analysis curves through tangent evaluation.

	A_4H_6	$A_4H_5F_1$ alloy	$A_4H_4F_2$ alloy	$A_4H_3F_3$ alloy	$A_4H_2F_4$ alloy	$A_4H_1F_5$ alloy	A_4F_6
T_{onset} (°C)	266.1	273.5	271.2	281.8	278.8	285.0	313.3

Gas sorption analysis

Table S7: Gas uptake of the two symmetric cages A_4H_6 and A_4F_6.

	uptake (mmol g^{-1})	
Gas	A_4H_6	A_4F_6
N_2	2.8	1.9

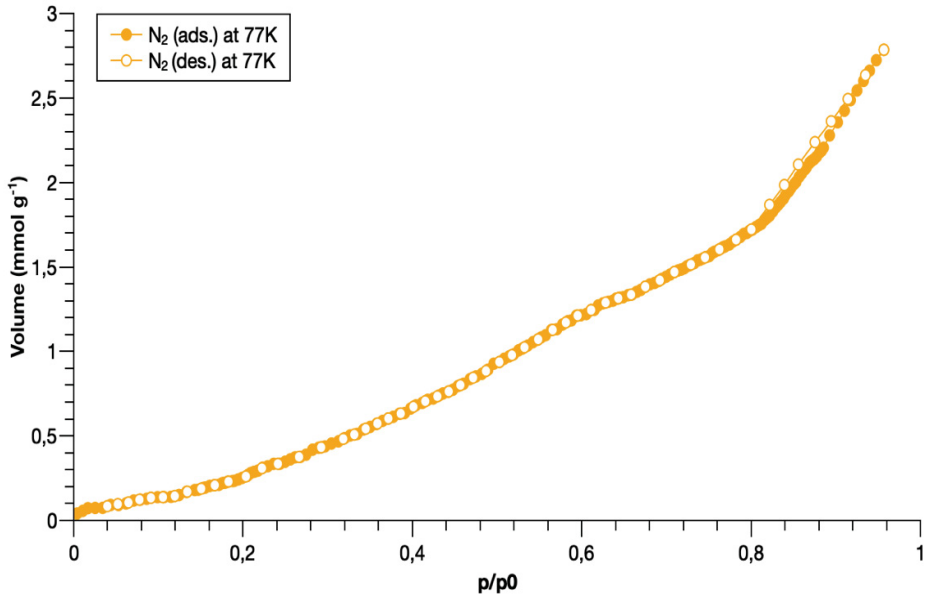

Figure S46: Adsorption (solid symbol) and desorption (hollow symbol) of nitrogen at 77 K of the symmetric A_4H_6 cage compound as isolated from the reaction mixture. The sample was evacuated at 40 °C and 10^{-2} mbar for 24 hours prior to the measurement.

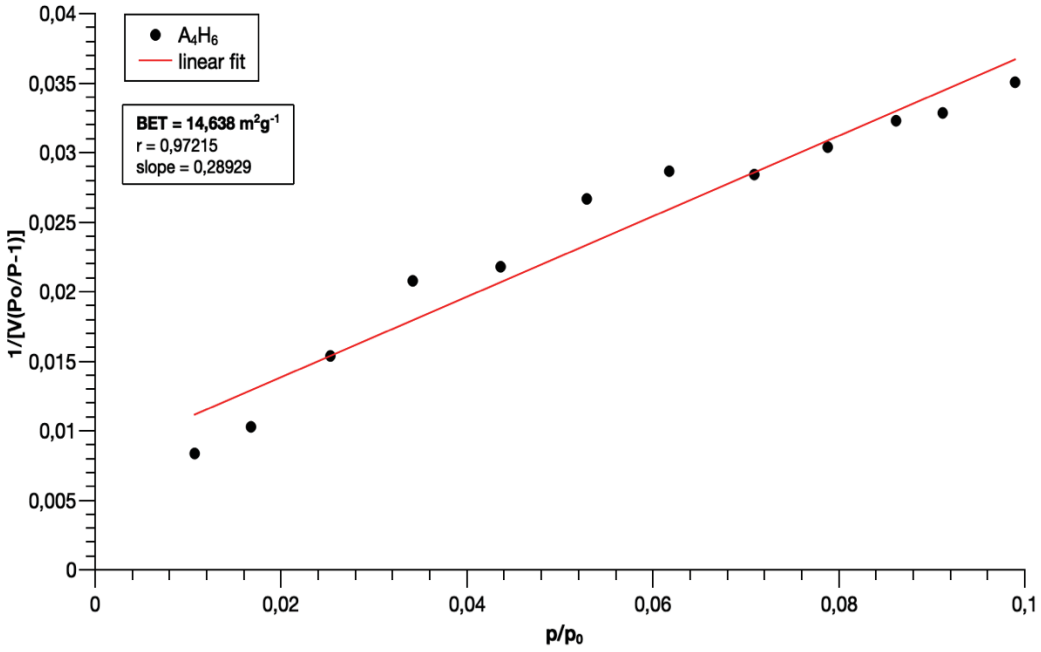

Figure S47: BET plot of a crystalline $\mathbf{A_4H_6}$ sample. The BET surface area was calculated using a microporous assumption.

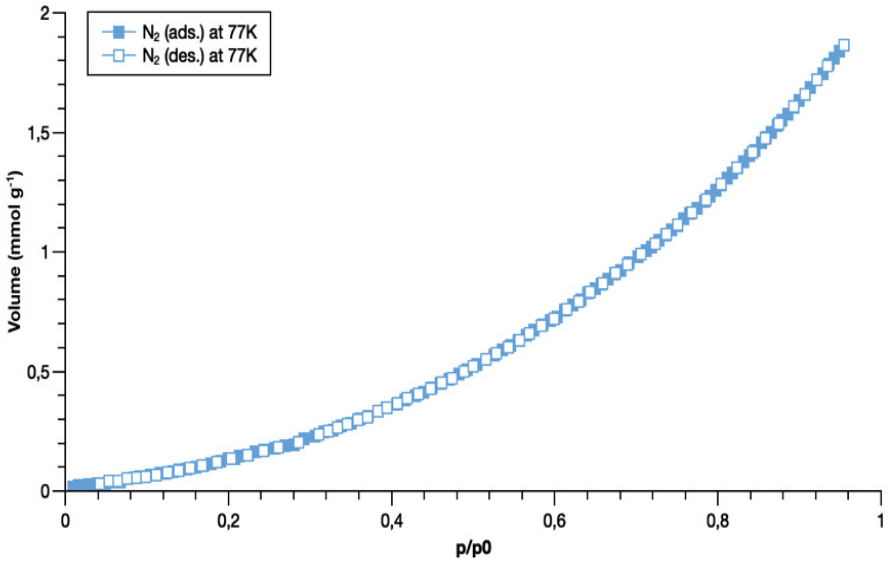

Figure S48: Adsorption (solid symbol) and desorption (hollow symbol) of nitrogen at 77 K of the symmetric $\mathbf{A_4F_6}$ cage compound as isolated from the reaction mixture. The sample was evacuated at 40 °C and 10^{-2} mbar for 24 hours prior to the measurement.

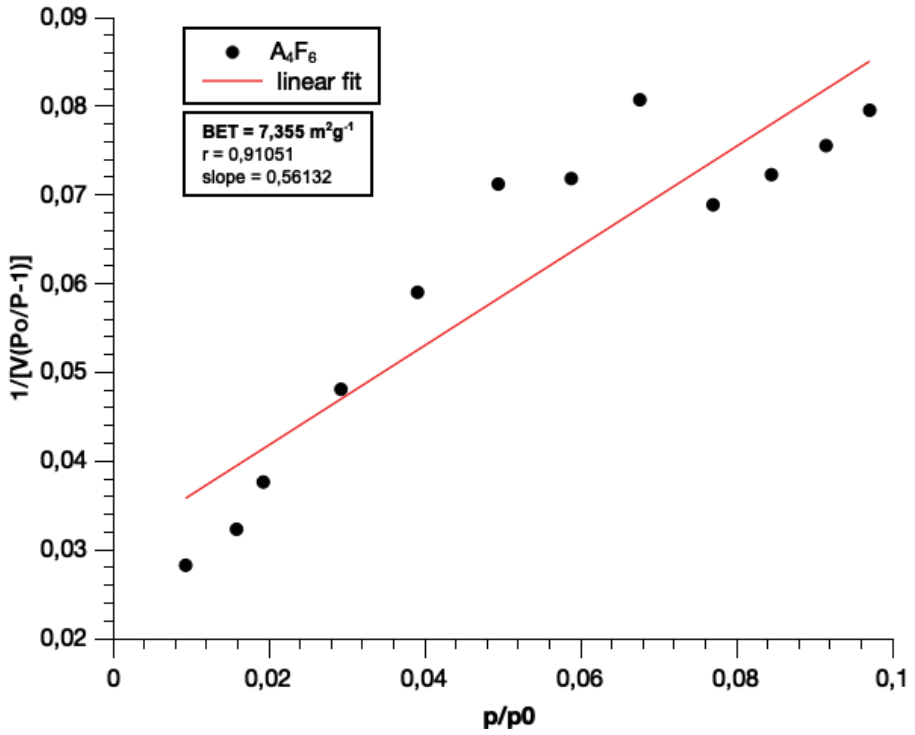

Figure S49: BET plot of a crystalline A_4F_6 sample. The BET surface area was calculated using a microporous assumption.

Crystallographic details

CCDC 2047255 (**A_4F_6**), 2047256 (**$A_4H_1F_5$**) and 2047257 (**$A_4H_2F_4$**) contain the supplementary crystallographic data for the cage compound and the corresponding alloys. These data can be obtained free of charge from The Cambridge Crystallographic Data Centre.

A_4F_6

Crystals of **A_4F_6** were grown by slow evaporation of a chloroform acetonitrile solution. A colourless, hexagonal prism was mounted and the structure was obtained at 140 K using Cu-K αradiation.

$A_4H_1F_5$

Crystals of **$A_4H_1F_5$** were grown by slow evaporation of a chloroform acetonitrile solution. Fluorine atoms were treated with fvar refinement, and the fluorine content is estimated to be 80 percent for both crystallographically unequal fluorobenzenes within the structure.

$A_4H_2F_4$

Crystals of **$A_4H_2F_4$** were grown by slow evaporation of chloroform and acetonitrile solution. Fluorine atoms were treated with fvar refinement, and the fluorine content is estimated to be 69-73 % percent for both crystallographically unequal fluorobenzenes within the structure.

$A_4H_4F_2$

Crystals of **$A_4H_4F_2$** were grown by slow evaporation of a chloroform and n-pentane solution. Fluorine atoms were treated with fvar refinement, and the fluorine content is estimated to be 48 percent for both crystallographically unequal fluorobenzenes within the structure.

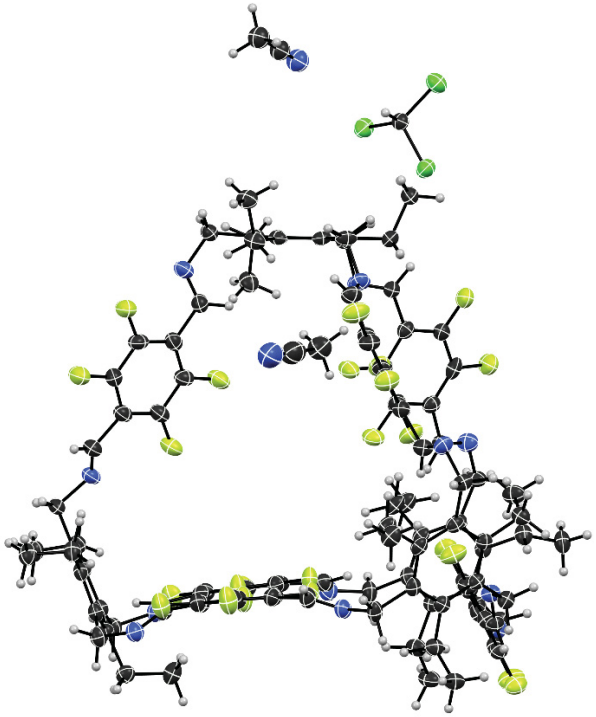

Figure S50: Data set of **A_4F_6** showing the cage and one chloroform molecule with thermal ellipsoids set at 50% probability. The structure was measured at 140 K and solved in the rhombohedral space group R-3 with R_{Int} = 0.1053, R_1 = 0.0961 and wR_2 = 0.3148.

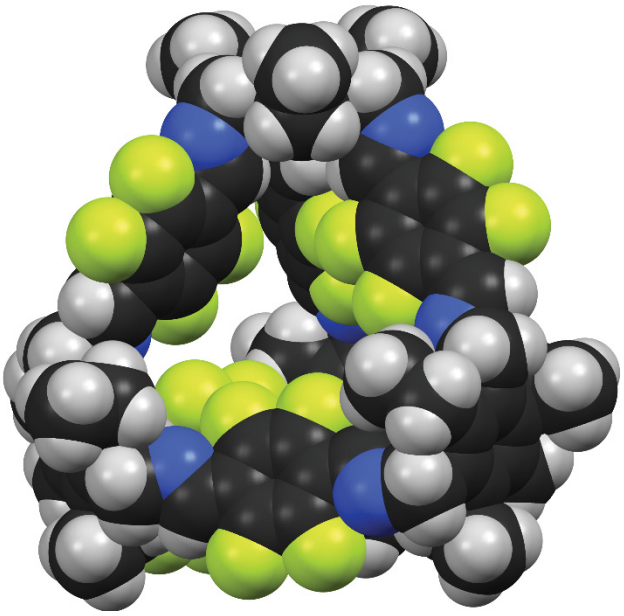

Figure S51: Cage unit of **A_4F_6** in a space-filling representation with all solvents omitted.

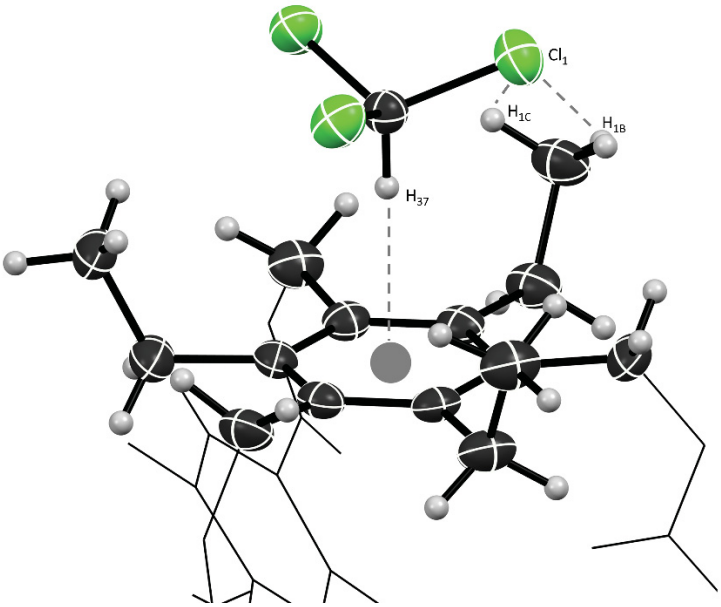

Figure S52: Excerpt showing the well-ordered chloroform molecule sitting above the substituted benzene of **A_4F_6**. Selected bond lengths [Å]: H_{37}–centroid 2.331, Cl_1–H_{1B} 3.020, Cl_1–H_{1C} 3.470. Due to the symmetry of the space group, all other contacts are identical.

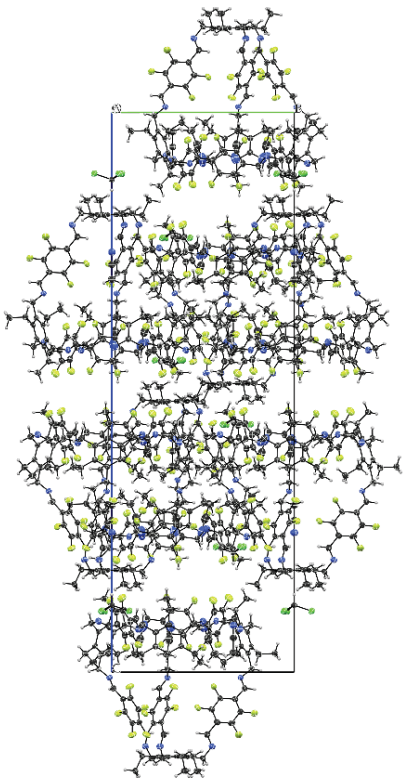

Figure S53: View of the unit cell of $\mathbf{A_4F_6}$ along the crystallographic a axis.

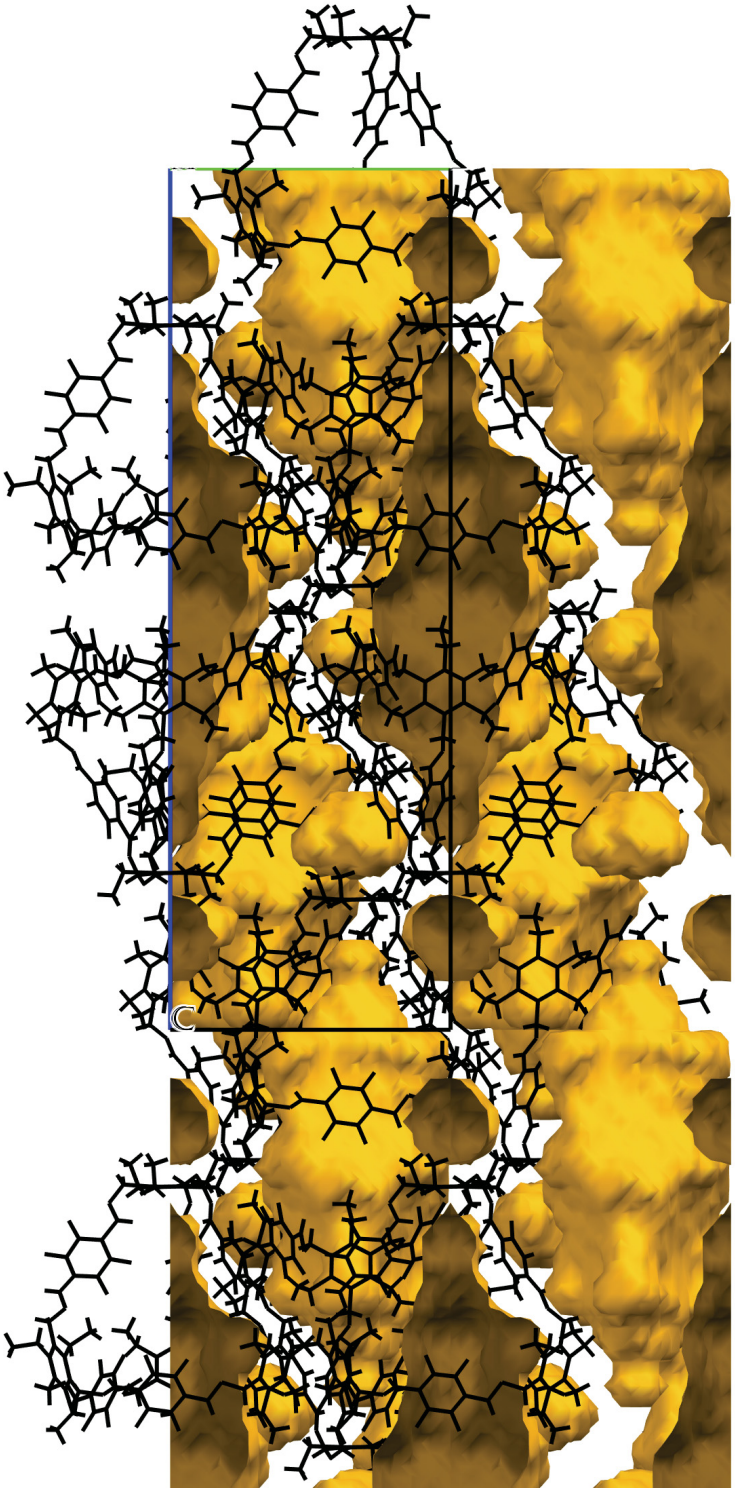

Figure S54: View of the extended unit cell of $\mathbf{A_4F_6}$ along the crystallographic a axis, voids calculated using a probe of 1.2 Å and shown in orange.

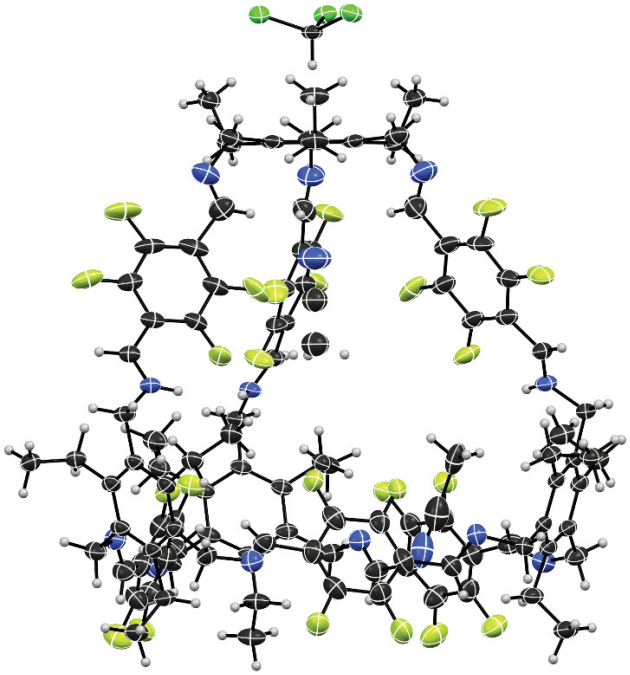

Figure S55: Data set of $\mathbf{A_4H_1F_5}$ showing the cage and one chloroform molecule with thermal ellipsoids set at 50% probability. The structure was measured at 100 K and solved in the rhombohedral space group R-3 with R_{Int} = 0.0826, R_1 = 0.1248 and wR_2 = 0.4358.

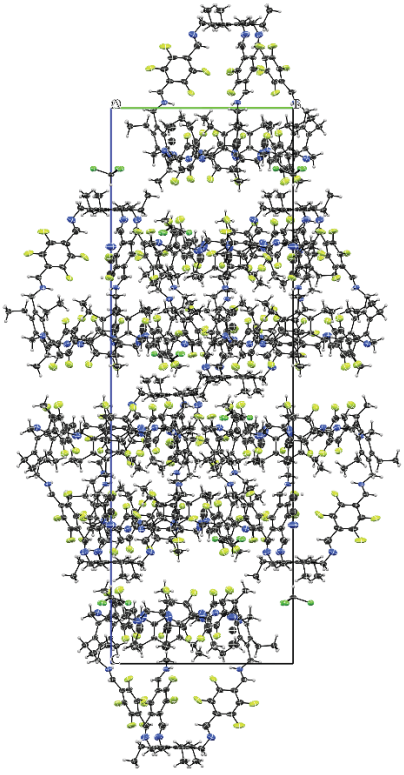

Figure S56: View of the unit cell of $\mathbf{A_4H_1F_5}$ along the crystallographic a axis.

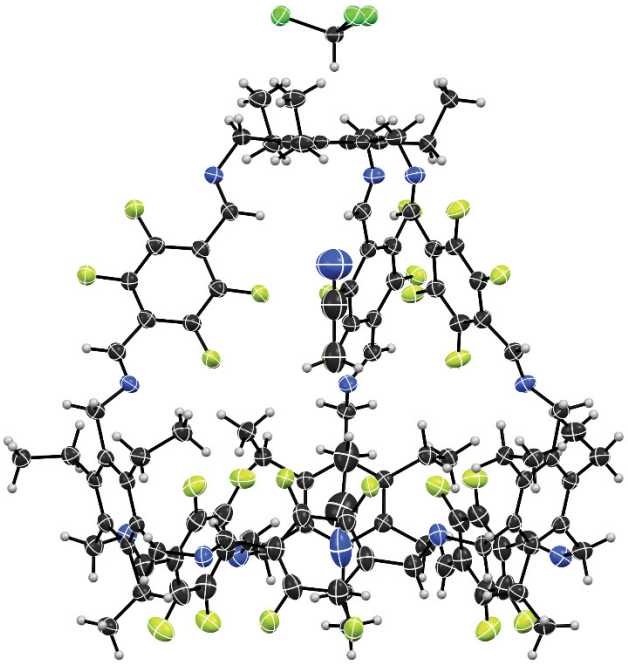

Figure S57: Data set of $\mathbf{A_4H_2F_4}$ showing the cage and one chloroform molecule with thermal ellipsoids set at 50% probability. The structure was measured at 100 K and solved in the rhombohedral space group R-3 with R_{Int} = 0.1182, R_1 = 0.0931 and wR_2 = 0.3157.

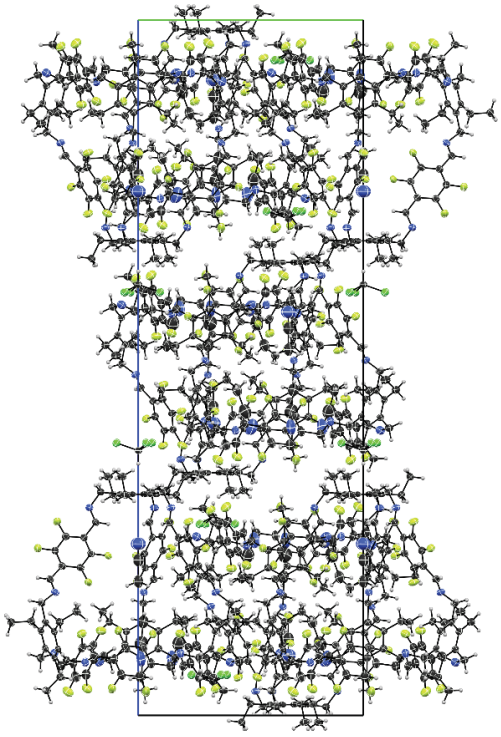

Figure S58: View of the unit cell of $\mathbf{A_4H_2F_4}$ along the crystallographic a axis.

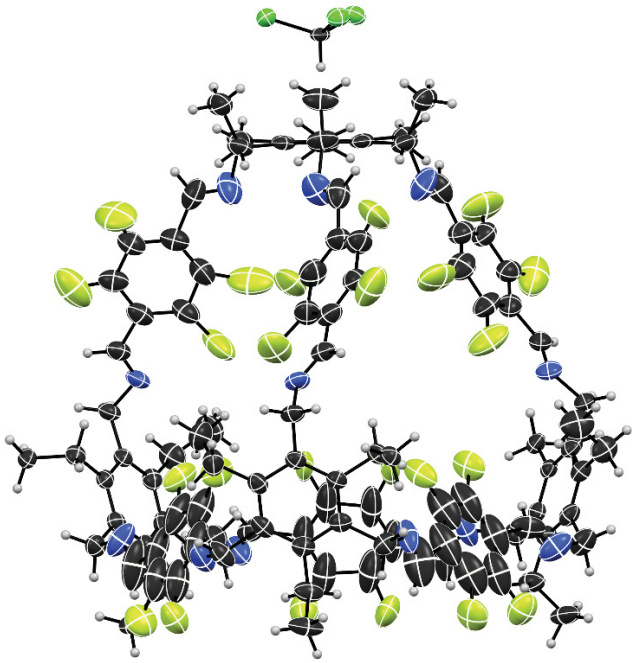

Figure S59: Data set of $\mathbf{A_4H_2F_4}$ showing the cage and one chloroform molecule with thermal ellipsoids set at 50% probability. The structure was measured at 100 K and solved in the rhombohedral space group R-3 with R_{Int} = 0.0714, R_1 = 0.1863 and wR_2 = 0.5439.

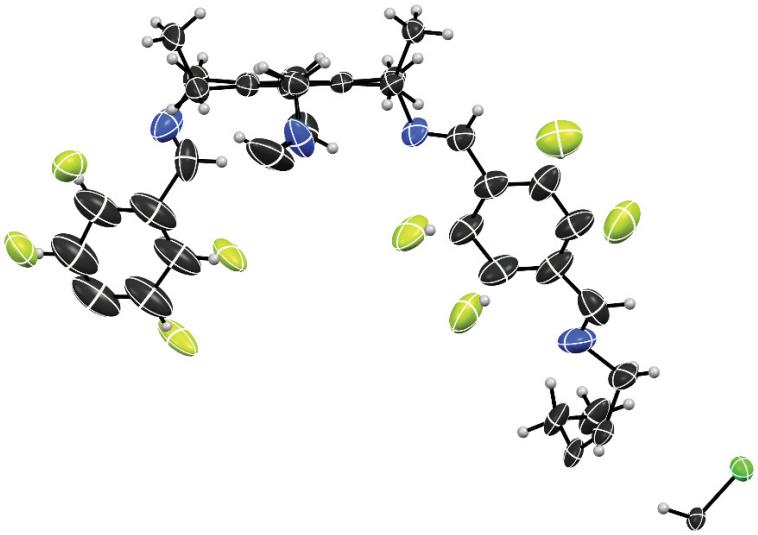

Figure S60: Asymmetric unit of $\mathbf{A_4H_2F_4}$ showing the disordered fluorinated phenyl and fluorophenyl units in the crystal, thermal ellipsoids set at 50% probability.

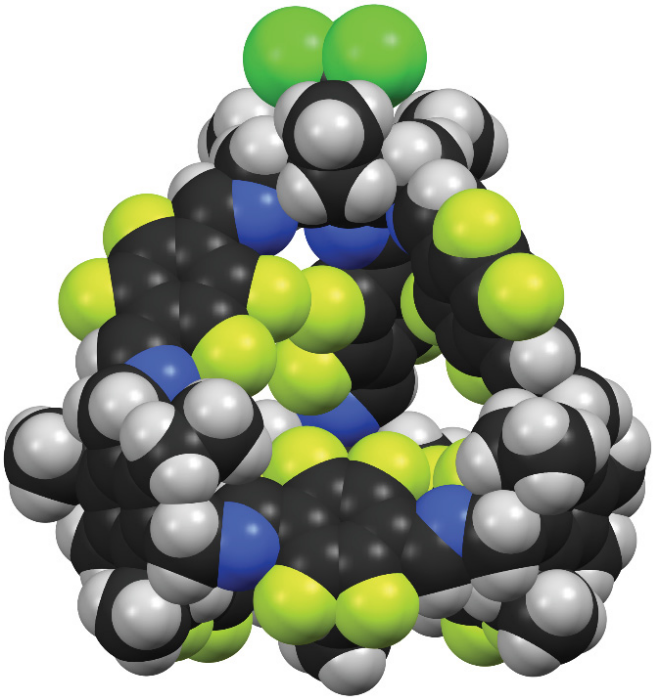

Figure S61: Cage unit $\mathbf{A_4H_2F_4}$ and one chloroform molecule in a space-filling representation.

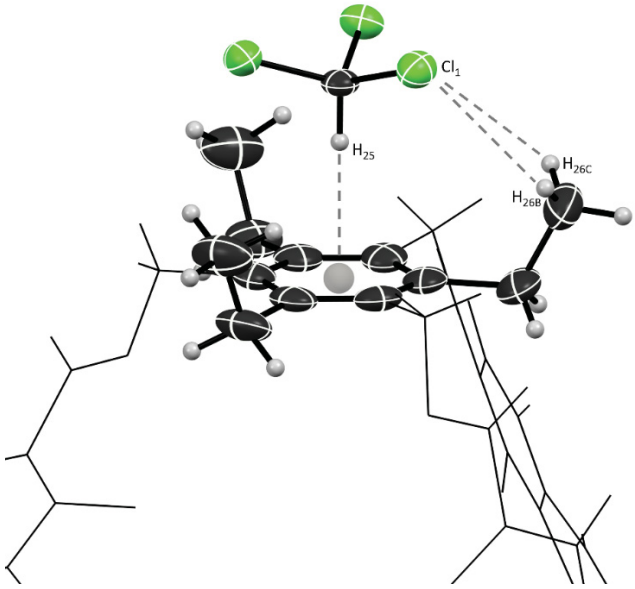

Figure S62: Excerpt showing the well-ordered chloroform molecule sitting above the substituted benzene. Selected bond lengths [Å]: H_{25}–centroid 2.310, Cl_1–H_{26B} 2.962, Cl_1–H_{26C} 3.568. Due to the symmetry of the space group, all other contacts are identical.

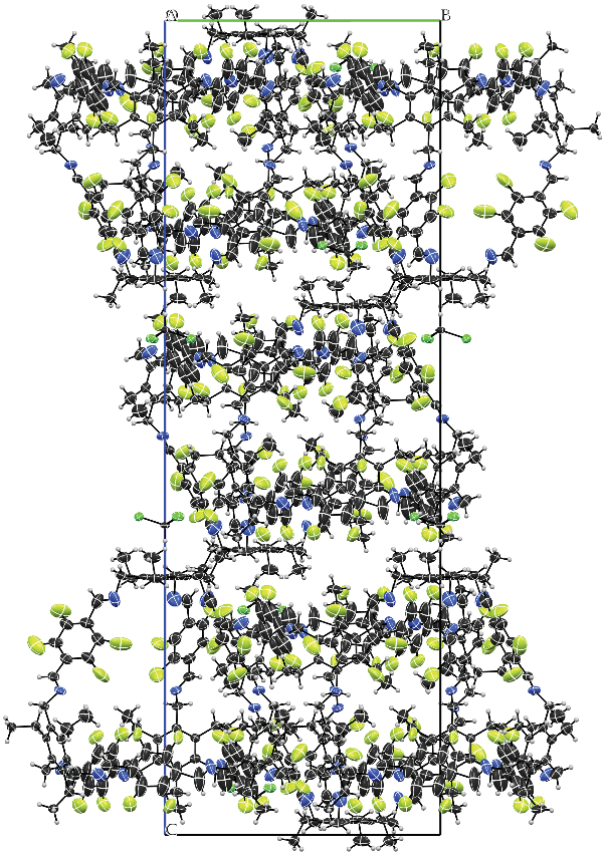

Figure S63: View of the unit cell of $\mathbf{A_4H_4F_2}$ along the crystallographic *a* axis.

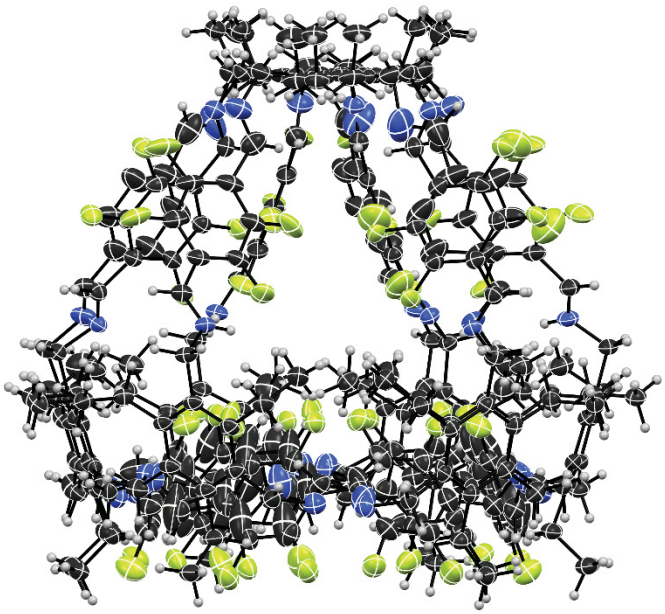

Figure S64: Overlap of the cages $\mathbf{A_4F_6}$, $\mathbf{A_4H_2F_4}$ and $\mathbf{A_4H_4F_2}$, solvents omitted for clarity.

Photographs of single crystals

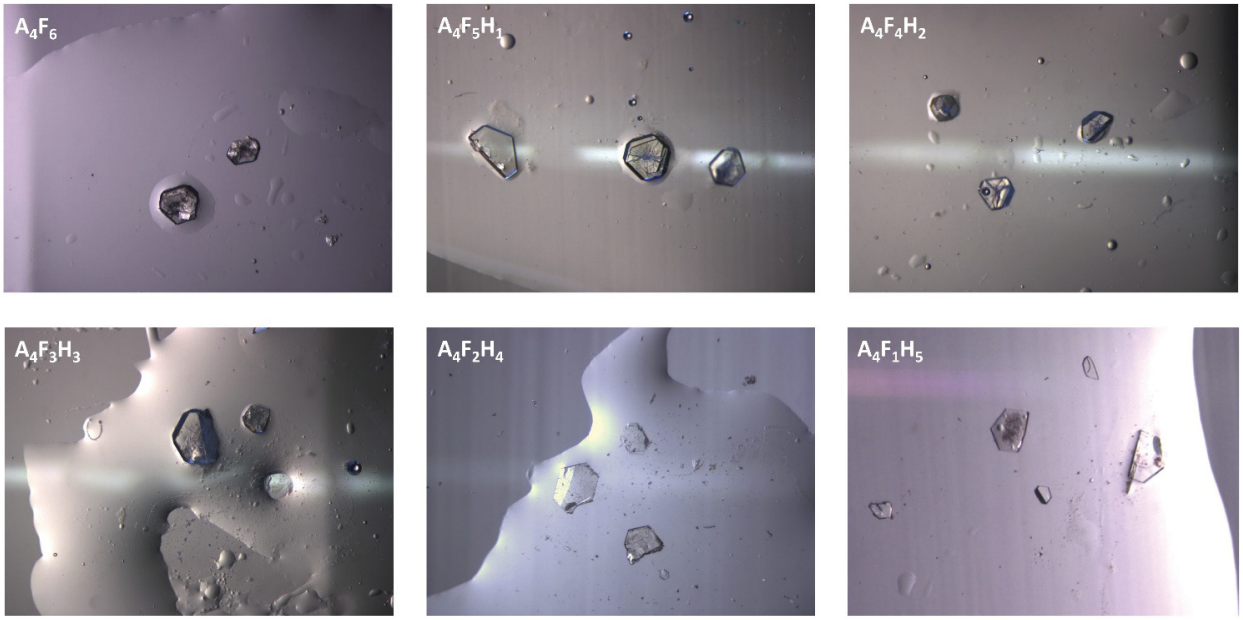

Figure S65: Microscope photographs of single-crystals obtained from slow evaporation of a chloroform/ acetonitrile solution of the corresponding cage compounds $\mathbf{A_4F_6}$, $\mathbf{A_4F_5H_1}$ alloy, $\mathbf{A_4F_4H_2}$ alloy, $\mathbf{A_4F_3H_3}$ alloy, $\mathbf{A_4F_2H_4}$ alloy and $\mathbf{A_4F_1H_5}$ alloy.

PXRD

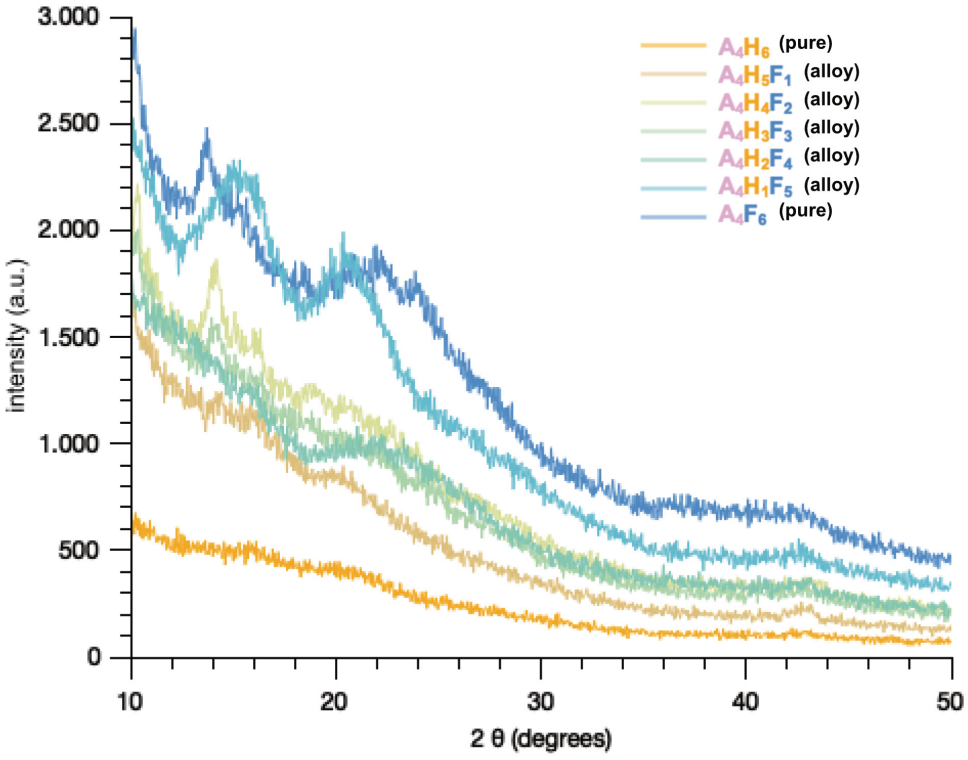

Figure S66: Overlay of PXRD spectra of the different hybrid cage alloys and cage compounds as isolated directly from the reaction mixture. All compounds exhibit either amorphous or only semi-crystalline behaviour.

5.6. Experimental Details for Section 3.5

Synthesis of 2,3,5,6-Tetrafluorobenzaldehyde (28)

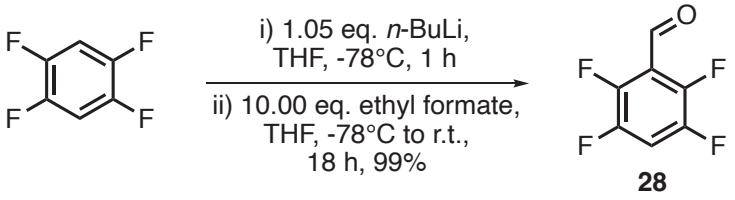

Tetrafluorobenzene (5.58 mL, 50.00 mmol, 1.00 eq.) was dissolved in dry THF (100 mL) and was cooled to -78 °C under nitrogen. *n*-Butyl lithium (2.50 M in hexane, 21.00 mL, 52.50 mmol, 1.05 eq.) was added dropwise to the reaction mixture over the course of 30 minutes. The resulting reaction mixture was then stirred for one additional hour at -78 °C before ethyl formate (8.08 mL, 100.00 mmol, 2.00 eq.) was added. The reaction was stirred for 20 minutes at -78 °C and was then allowed to reach room temperature during 18 hours. The reaction was ended by the addition of 2 M HCl solution (20 mL) and the phases were separated. The organic phase was washed with saturated $NaHCO_3$ solution (3 x 25 mL) and brine (3 x 25 mL) and was dried over anhydrous $MgSO_4$. After evaporation of the solvent under reduced pressure, the aldehyde (**28**) could be obtained as a colorless oil (8.81 g, 99%).

^{1}H NMR (300 MHz, $CDCl_3$) δ 10.33 (t, J = 1.1 Hz, 1H, C**H**O), 7.34 (tt, J = 9.3, 7.3 Hz, 1H, *p*-**H**); **^{19}F NMR** (282 MHz, $CDCl_3$) δ -137.23 (d, J = 6.2 Hz, 2F, *meta*-**F**), -143.76 – -145.18 (m, 2F, *ortho*-**F**).

All further spectral data was in accordance with the literature.[88]

Synthesis of 2-(2,3,5,6-tetrafluorophenyl)-1,3-dioxolane (29)

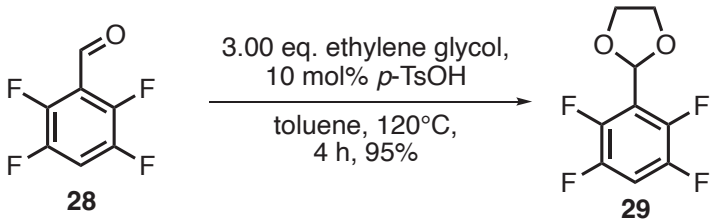

Aldehyde **28** (7.84 g, 44.00 mmol, 1.00 eq.) was dissolved in toluene (100 mL) and para-toluene sulfonic acid (0.76 g, 4.40 mmol, 0.10 eq.) together with ethylene glycol (8.19 g, 132.00 mmol, 3.00 eq.) were added. The reaction mixture was heated to 120 °C in a Dean-Stark apparatus for 4 hours. The mixture was then washed with saturated $NaHCO_3$ solution (3 x 25 mL) and brine (3 x

25 mL) and the organic phase was dried over anhydrous $MgSO_4$. Evaporation of the solvent under reduced pressure yielded the acetal **29** as a bright yellow oil (9.29 g, 95%).

^{1}H NMR (300 MHz, $CDCl_3$) δ 7.08 (tt, J = 9.6, 7.4 Hz, 1H, *para*-**H**), 6.25 (d, J = 0.6 Hz, 1H, O-C**H**-O), 4.30 – 4.13 (m, 2H, C**H$_2$**), 4.13 – 3.98 (m, 2H, C**H$_2$**); **^{19}F NMR** (282 MHz, $CDCl_3$) δ -138.38 – -139.84 (m, 2F, *meta*-**F**), -143.89 – -146.05 (m, 2F, *ortho*-**F**).

All further spectral data was in accordance with the literature.[88]

Synthesis of 2,2'-(5'-(4-(1,3-dioxolan-2-yl)-2,3,5,6-tetrafluorophenyl)-2,2'',3,3'',5,5'',6,6''-octafluoro-[1,1':3',1''-terphenyl]-4,4''-diyl)bis(1,3-dioxolane) (30)

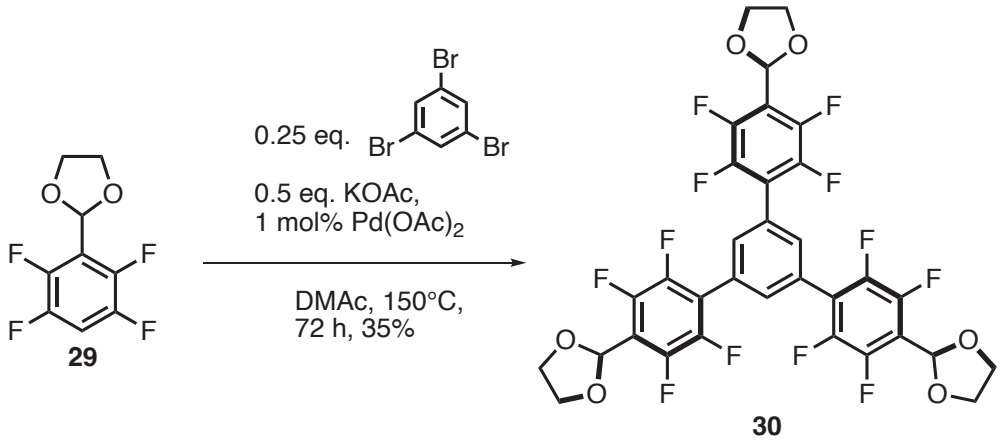

1,3,5-Tribromobenzene (2.52 g, 8.00 mmol, 1.00 eq.), potassium acetate (1.57 g, 16.00 mmol, 2.00 eq.) and acetal **29** (7.11 g, 32.00 mmol, 4.00 eq.) were added to a Schlenk flask and dimethyl acetamide (20 mL) was added. The resulting mixture was purged with argon three times and palladium acetate (35.90 mg, 0.08 mmol, 1 mol%) was added. The mixture was heated to 150 °C under argon and the flask was sealed. The reaction was stirred at this temperature for 72 hours. After filtration of the solids, the filtrate was evaporated under reduced pressure (70 °C bath temperature, 1 x 10^{-2} mbar). The crude oil was purified by column chromatography (cyclohexane/ ethyl acetate 3:1) to yield the triacetal **30** as an off-white, fluffy solid (2.35 g, 35%).

^{1}H NMR (600 MHz, $CDCl_3$) δ 7.67 (s, 3H, Ar-**H**), 6.30 (s, 3H, O-C**H**-O), 4.36 – 4.15 (m, 6H, C**H$_2$**), 4.15 – 3.99 (m, 6H, C**H$_2$**); **^{19}F NMR** (565 MHz, $CDCl_3$) δ -143.70 – -143.80 (m, 6F, **F$_{inner}$**), -143.93 (dd, J = 22.2, 13.2 Hz, 6F, **F$_{outer}$**).

All further spectral data was in accordance with the literature.[88]

Synthesis of 2,2'',3,3'',5,5'',6,6''-octafluoro-5'-(2,3,5,6-tetrafluoro-4-formylphenyl)-[1,1':3',1''-terphenyl]-4,4''-dicarbaldehyde (31)

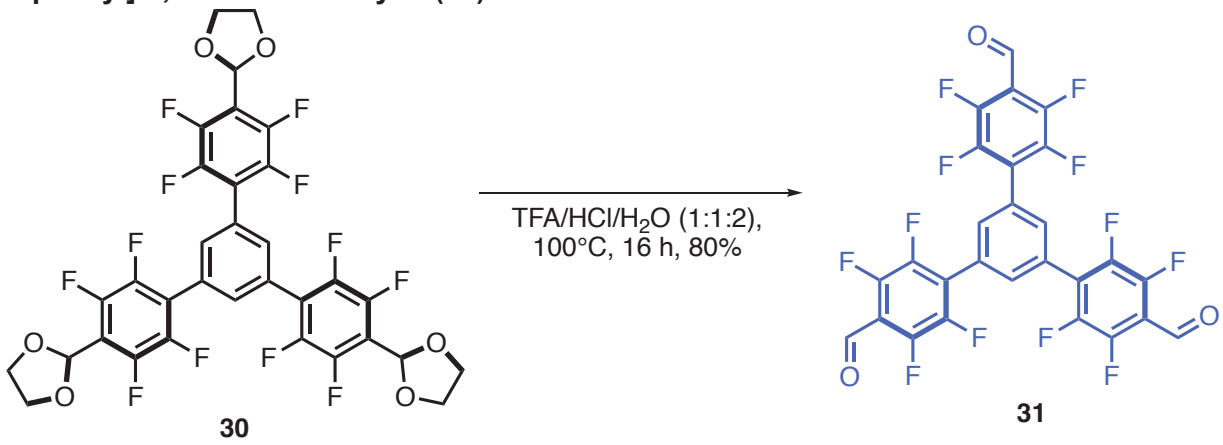

30 **31**

The acetal **30** (1.10 g, 1.50 mmol, 1.00 eq.) was dissolved in trifluoroacetic acid (5 mL) and water (20 mL) and concentrated HCl (5 mL) were added. The resulting suspension was heated to 100 °C for 16 hours under intense stirring. The solvent was evaporated under reduced pressure and the residue was taken up in methanol (50 mL) and filtered. The precipitate was washed with diethyl ether to yield the aldehyde **31** as an off-white solid (0.89 g, 80%).

^{1}H NMR (300 MHz, DMSO-d^{6}) δ 10.26 (t, J = 1.1 Hz, 3H, C**H**O), 8.10 (s, 3H, Ar-**H**); **^{19}F NMR** (282 MHz, DMSO-d^{6}) δ -143.14 – -143.47 (m, 6F, $\mathbf{F_{inner}}$), -145.80 – -146.08 (m, $\mathbf{F_{outer}}$).

All further spectral data was in accordance with the literature.[88]

Synthesis of 4-hydrazino-2,3,5,6-tetrafluorobenzonitrile (32)

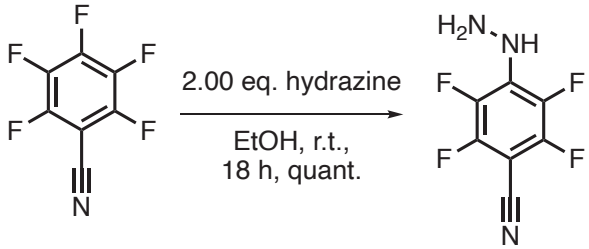

32

Pentafluorobenzonitrile (12.16 mL, 100.0 mmol, 1.0 eq.) was dissolved in ethanol. An aqueous hydrazine solution (66 wt%, 9.71 g, 200.0 mmol, 2.0 eq.) was added dropwise over the course of 2 hours. During the addition the temperature was monitored to stay below 25 °C. The resulting mixture was stirred for 18 hours at room temperature. Ice water (500 mL) was added to induce precipitation. After stirring for additional 20 minutes, the precipitate was isolated by filtration and washed with 50 mL of cold diethyl ether (-20 °C) to yield the hydrazine compound **32** as a colorless solid (20.15 g, 100%).

^{1}H NMR (300 MHz, $CDCl_3$) δ 5.78 (s, 1H, N**H**-NH_2), 4.12 (s, 2H, N$\mathbf{H_2}$); **^{19}F NMR** (282 MHz, $CDCl_3$) δ -134.42 (d, J = 12.8 Hz, 2F, $\mathbf{F_{ortho}}$), -159.16 (d, J = 12.8 Hz, 2F, $\mathbf{F_{meta}}$).

All further spectral data was in accordance with spectra from commercial sources.

Synthesis of 2,3,5,6-Tetrafluorobenzonitrile (33)

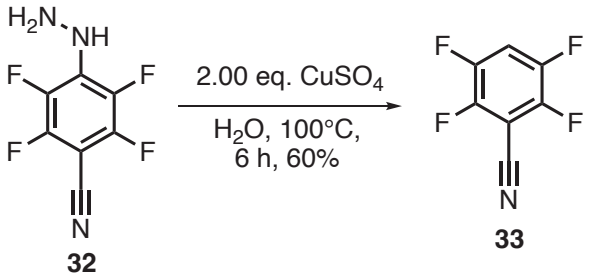

32 **33**

Hydrazine compound **32** (20.51 g, 100.00 mmol, 1.00 eq.) was dispersed in 100 mL of water and the suspension was heated to 90 °C. To this mixture an aqueous $CuSO_4$ (49.93 g, 200.00 mmol, 2.00 eq.) solution was added over the course of two hours. The reaction mixture was heated to 105 °C in a Dean-Stark-apparatus for four additional hours. During this time two phases were forming in the cooling trap. After 4 hours the organic phase was diluted with diethyl ether (100 mL), washed with brine (3 x 25 mL) and was dried over anhydrous $MgSO_4$. The evaporation of the solvent under reduced pressure yielded the tetrafluoro compound **33** as colorless crystals (10.50 g, 60%).

^{1}H NMR (300 MHz, $CDCl_3$) δ 7.40 (tt, J = 9.4, 7.3 Hz, 1H, Ar-**H**); **^{19}F NMR** (282 MHz, $CDCl_3$) δ -131.60 – -132.03 (m, 2F, **F**(2,6)), -134.67 – -135.10 (m, 2F, **F**(3,5)).

All further spectral data was in accordance with spectra from commercial sources.

Synthesis of 2,4,6-tris(2,3,5,6-tetrafluorophenyl)-1,3,5-triazine (34)

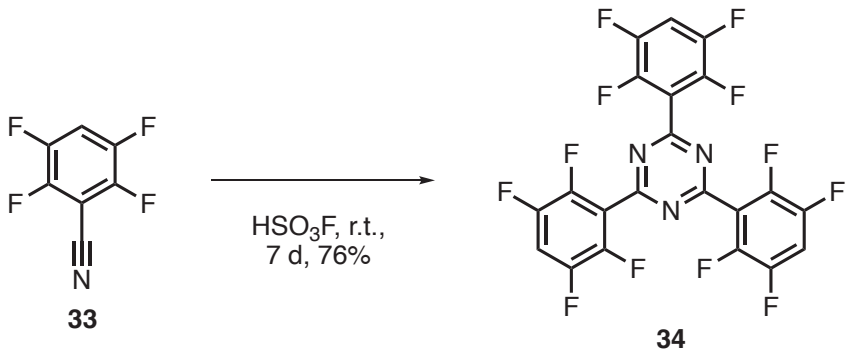

33 **34**

Tetrafluorobenzonitrile **33** (0.53 g, 3.00 mmol, 1.00 eq.) was dissolved in fluorosulfonic acid (4 mL) and the resulting mixture was stirred for 7 days at room temperature. The mixture was added dropwise into ice water, while keeping the temperature below 10 °C. The precipitate was filtered off and washed with diethyl ether to yield the triazine **34** as a colorless solid (0.40 g, 76%).

^{1}H NMR (300 MHz, $CDCl_3$) δ 7.32 (ddd, J = 9.5, 7.2, 2.3 Hz, 3H, Ar-**H**); **^{19}F NMR** (282 MHz, $CDCl_3$) δ -136.82 – -137.28 (m, 6F, $\mathbf{F_{outer}}$), -141.04 – -141.37 (m, 6F, $\mathbf{F_{inner}}$). Due to the very low solubility in common NMR solvents, no ^{13}C NMR spectrum could be obtained.

FT-IR (ATR): $\tilde{\nu}$(cm^{-1}) = 1732.08, 1647.21, 1525.69, 1502.55, 1487.12, 1463.97, 1436.97, 1392.61, 1348.24, 1323.17, 1280.73, 1240.23, 1190.08, 1174.65, 1130.29, 1064.71, 1002.98, 970.19, 935.48, 881.47, 867.97, 858.32, 840.96, 779.24, 769.60, 729.09, 700.16, 680.87, 630.72, 611.43.

CI-MS: calculated: [**34**+H]$^+$ 526.0 m/z, found: 526.0 m/z.

Synthesis of 4,4',4''-(1,3,5-triazine-2,4,6-triyl)tris(2,3,5,6-tetrafluorobenzaldehyde) (35)

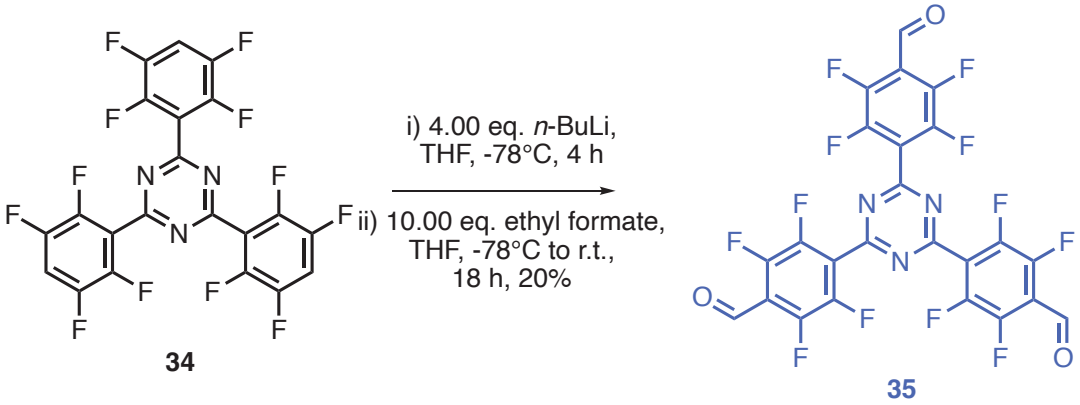

34 **35**

Compound **34** (1.05 g, 2.00 mmol, 1.00 eq.) was dissolved in dry THF (100 mL) and was cooled to -78 °C. To this chilled mixture *n*-butyl lithium (2.50 M in hexanes, 3.20 mL, 8.00 mmoL, 4.00 eq.) was added dropwise to keep the reaction temperature below -70 °C. After complete addition the mixture was stirred for additional 4 hours. Ethyl formate (1.48 g, 20.00 mmol, 10.00 eq.) was added and the reaction was allowed to reach room temperature overnight (18 hours). The purple suspension was diluted with 2 M HCl solution and the organic phase was washed with brine and dried over anhydrous $MgSO_4$. After evaporation of the solvent under reduced pressure, the crude product was purified by column chromatography to yield **35** as a colorless wax-like solid (0.23 g, 20%).

^{1}H NMR (300 MHz, $CDCl_3$) δ 10.50 – 10.34 (m, 3H, C**H**O); **^{19}F NMR** (282 MHz, $CDCl_3$) δ -139.28 – -139.61 (m, 6F, $\mathbf{F_{inner}}$), -143.22 – -143.55 (m, 6F, $\mathbf{F_{outer}}$); **^{13}C NMR** (75 MHz, CDCl3) δ 182.13 (**C**HO), 167.30 (s, 1C, $\mathbf{C_q}$-CHO), 147.80 (d, J = 124.3 Hz, 1C, **C**F_{outer}), 144.32 (d, J = 121.6 Hz, 1C, **C**F_{inner}), 120.44 (s, 1C, $\mathbf{C_q}$-Trz), 117.31 (s, 1C, $\mathbf{C_{Trz}}$).

FT-IR (ATR): $\tilde{\nu}$(cm^{-1}) = 1708.93, 1521.84, 1479.40, 1471.69, 1408.04, 1354.03, 1309.67, 1278.81, 1265.30, 1180.44, 1078.21, 1035.77, 993.34, 947.05, 920.05, 709.80, 624.94.

CI-MS: calculated: [**35**-H]$^-$ 609.0 m/z, found: 608.9 m/z.

Synthesis of tris(4-(1,3-dioxolan-2-yl)-2,3,5,6-tetrafluorophenyl)methanol (36)

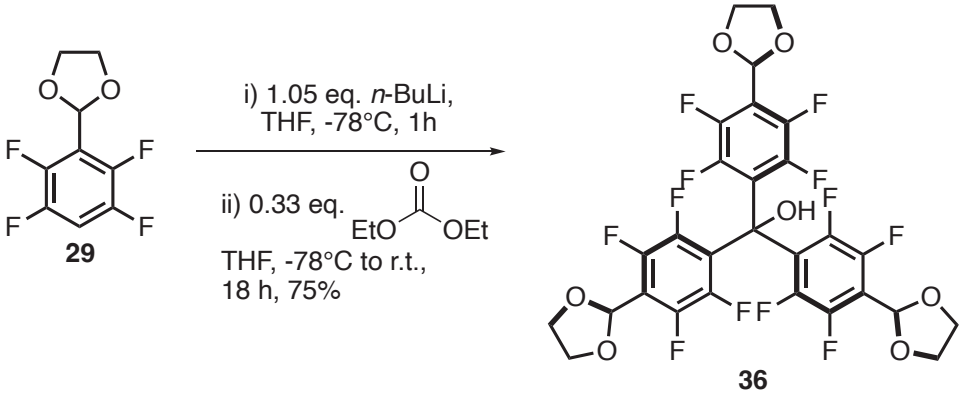

29 **36**

The acetal **29** (6.44 g, 29.00 mmol, 1.00 eq.) was dissolved in dry THF (80 mL) and cooled to -78 °C. To the reaction mixture *n*-butyl lithium (2.50 M in hexanes, 12.20 mL, 30.50 mmol, 1.05 eq.) was added dropwise. After the addition the reaction mixture was stirred for an additional hour, after which diethyl carbonate (1.16 g, 9.60 mmol, 0.33 eq.) was added. The reaction was allowed to reach room temperature overnight (18 hours) and 2M HCl solution (20 mL) was added. The mixture was washed with saturated $NaHCO_3$ (3 x 25 mL) solution and brine (3 x 25 mL) and the combined organic phases were dried over anhydrous $MgSO_4$. After evaporation of the solvent under reduced pressure the crude product was purified by column chromatography to yield the triacetal **36** as a bright yellow foam (1.30 g, 75%).

^{1}H NMR (300 MHz, $CDCl_3$) δ 6.25 (s, 3H, O-C**H**-O), 4.41 (s, 1H, O**H**), 4.27 – 4.17 (m, 6H, C$\mathbf{H_2}$), 4.10 – 3.97 (m, 6H, C$\mathbf{H_2}$); **^{19}F NMR** (282 MHz, $CDCl_3$) δ -140.17 – -140.52 (m, 6F, $\mathbf{F_{inner}}$), -143.47 – -143.77 (m, 6F, $\mathbf{F_{outer}}$).

Due to the low solubility in common NMR solvents, no ^{13}C NMR spectrum could be obtained.

FT-IR (ATR): $\tilde{\nu}$(cm^{-1}) = 3336.85, 2914.44, 1481.33, 1390.68, 1363.67, 1352.10, 1282.66, 1215.15, 1147.65, 1116.78, 1089.78, 1076.28, 995.27, 983.70, 948.98, 908.47, 889.18, 858.32, 800.46, 785.03, 761.88, 721.38, 705.95, 673.16, 661.58, 646.15, 624.94, 611.43.

Synthesis of 4,4',4''-(hydroxymethanetriyl)tris(2,3,5,6-tetrafluorobenzaldehyde) (37)

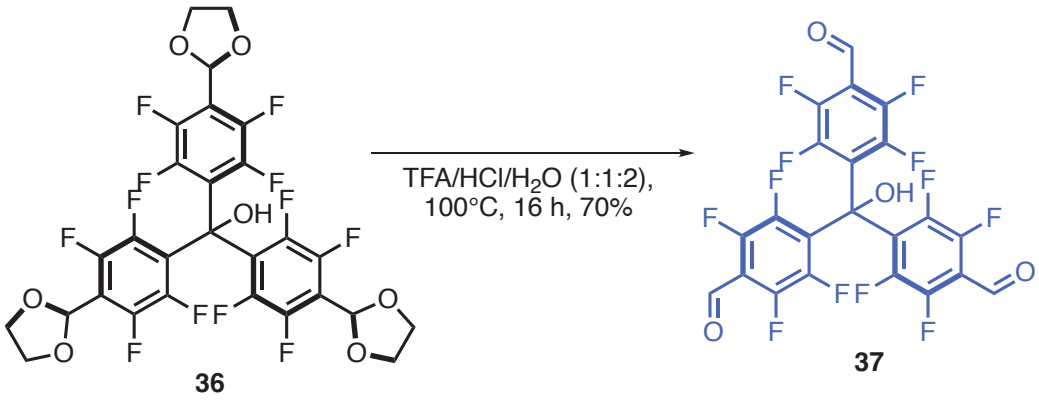

36 **37**

The triacetal **36** (3.53 g, 5.10 mmol, 1.00 eq.) was dissolved in trifluoroacetic acid (10 mL) and water (50 mL) was added, followed by concentrated aqueous HCl (10 mL). The resulting suspension was stirred intensively at 100 °C for 16 hours. The solvent was then evaporated under reduced pressure and the residue was taken up in chloroform (50 mL) and was washed with saturated $NaHCO_3$ (3 x 25 mL) and brine (3 x 25 mL). After drying over anhydrous $MgSO_4$ the solvent was evaporated under reduced pressure to yield aldehyde **37** as a colorless foam (2.50 g, 70%).

^{1}H NMR (300 MHz, $CDCl_3$) δ 10.42 – 10.23 (m, 3H, C**H**O), 4.55 (s, 1H, O**H**); **^{19}F NMR** (282 MHz, $CDCl_3$) δ -138.23 – -138.97 (m, 6F, $\mathbf{F_{inner}}$), -143.15 – -143.66 (m, 6F, $\mathbf{F_{outer}}$).

Due to the low solubility, no ^{13}C NMR spectrum could be obtained.

FT-IR (ATR): $\tilde{\nu}$(cm^{-1}) = 1788.01, 1708.93, 1651.07, 1473.62, 1408.04, 1388.75, 1290.38, 1263.37, 1215.15, 1168.86, 1149.57, 1112.93, 1089.78, 995.27, 975.98, 948.98, 856.39, 798.53, 769.60, 759.95, 700.16, 624.94.

Synthesis of FPOC10

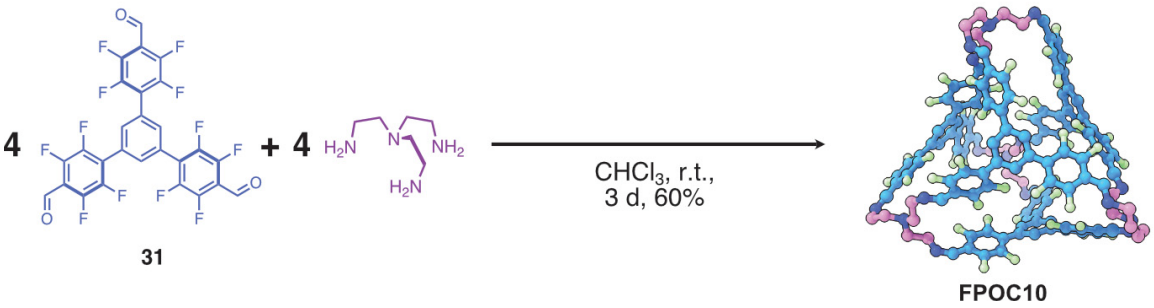

31 **FPOC10**

Aldehyde **31** (212.20 mg, 0.35 mmol, 1.00 eq.) was dissolved in dry chloroform (40 mL) and TREN (56.50 mg, 0.35 mmol, 1.00 eq.) dissolved in 40 mL chloroform was added dropwise to the reaction mixture. The resulting solution was stirred at room temperature for 3 days, during which a bright yellow color developed. Half of the solvent was evaporated under reduced pressure at room temperature and *n*-hexane was added to the solution, resulting in the precipitation of a bright yellow solid. The solid was isolated by filtration and washed with *n*-hexane to yield **FPOC10** (146.6 mg, 60%) as a yellow solid.

^{1}H NMR (300 MHz, $CDCl_3$) δ 8.20 (d, J = 1.6 Hz, 12H, C**H**N), 7.61 (s, 12H, Ar-**H**), 3.95 (d, J = 11.9 Hz, 12H, C**H$_2$**-N=C), 3.61 – 3.46 (m, 12H, C**H$_2$**-N=C), 3.13 (t, J = 12.1 Hz, 12H, C**H$_2$**–CH_2), 2.78 – 2.47 (m, 12H, C**H$_2$**–CH_2); **^{19}F NMR** (282 MHz, $CDCl_3$) δ -143.74 (dq, J = 12.7, 6.6 Hz, 24F, **F$_{inner}$**), -145.24 (s, 24 F, **F$_{outer}$**). Due to the low solubility in chloroform, no ^{13}C NMR spectrum could be obtained.

FT-IR (ATR): $\tilde{\nu}$(cm^{-1}) = 2943.37, 2887.44, 2829.57, 2818.00, 2362.80, 1643.35, 1471.69, 1384.89, 1367.53, 1340.53, 1288.45, 1064.71, 1014.56, 997.20, 968.27, 906.54, 889.18, 750.31, 688.59, 669.30, 623.01

ESI-HRMS: [**FPOC10**+4H]$^{4+}$ calculated: 699.3920 m/z; found: 699.3934 m/z.

Synthesis of Cu_4FPOC10

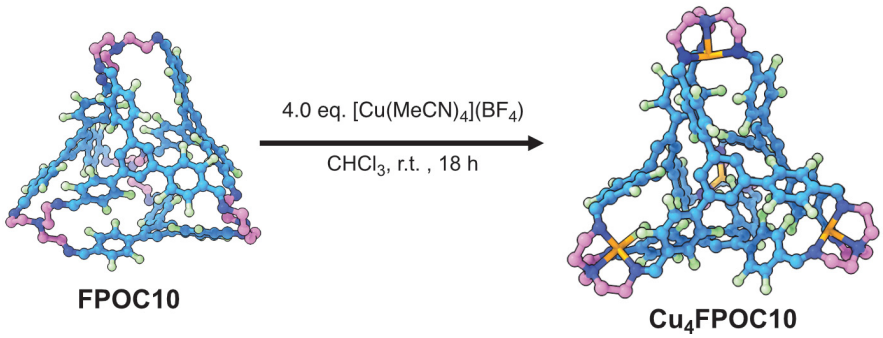

FPOC10 (20.00 mg, 7.20 µmol) was dissolved in chloroform (2.0 mL) and four equivalents of $[Cu(MeCN)_4]BF_4$ (10.70 mg, 28.80 µmol, 4.00 eq.) were added.

The reaction mixture was left standing at room temperature for 18 hours. The solvent was evporated at ambient pressure and temperature to yield **Cu_4FPOC10** as red crystals.

ESI-MS: [**Cu-FPOC10**+4H]$^{4+}$ calculated: 762.1 m/z; found: 762.1 m/z.

Due to the very low amount of product, no NMR and IR spectra could be obtained.

Synthesis of FPOC13

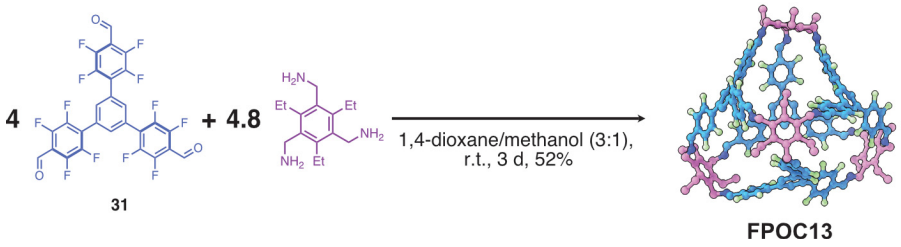

Procedure for semicrystalline material:

Aldehyde **31** (303.20 mg, 0.50 mmol, 1.00 eq.) was suspended in a 1,4-dioxane/methanol (3:1) mixture (50 mL) and **Et-Amine** (149.60 mg, 0.60 mmol, 1.20 eq.) dissolved in the same solvent mixture (50 mL) was added dropwise. During the addition, the reaction formed a clean solution which was then stirred for 3 days after complete addition. During the reaction time, an off-white precipitate formed that was isolated by filtration, washed with methanol and dried at 40 °C for 24 hours under reduced pressure. This yielded **FPOC13** (208.40 mg, 52%) as an off-white fluffy solid.

Procedure for crystalline material:

Solid aldehyde **31** (60.60 mg, 0.10 mmol, 1.00 eq.) was scattered on the bottom of a 25 mL glass vial. **Et-Amine** (25.00 mg, 0.12 mmol, 1.20 eq.) dissolved in a chloroform/methanol (1:1) mixture (20 mL) was carefully layered on top of the solid. Over the course of 2 days, large, yellow, tetrahedral crystals grew on the vial's bottom and walls. After careful decantation of the solvent, **FPOC13** could be isolated as a crystalline material (32.00 mg, 40%).

^{1}H NMR (300 MHz, $CDCl_3$) δ 7.78 (s, 12H, C**H**O), 7.40 (s, 12H, Ar-**H**), 5.27 (s, 24H, C**H_2**-N=C), 2.37 (d, J = 8.1 Hz, 24H, C**H_2**-CH_3), 1.27 (s, 36H, C**H_3**); **^{19}F NMR** (282 MHz, $CDCl_3$) δ -144.64 (s, 48F, **F_{inner}** and **F_{outer}**). Due to the very low solubility, no ^{13}C NMR spectra could be obtained.

FT-IR (ATR): ṽ(cm^{-1}) = 2933.73, 2860.43, 1645.28, 1471.69, 1384.89, 1342.46, 1290.38, 1091.71, 981.77, 966.34, 927.76, 781.17, 709.80, 678.94, 665.44.
ESI-HRMS: [**FPOC13**+2H]$^{2+}$ calculated: 1603.9116 m/z; found: 1603.9099 m/z.

Synthesis of FPOC14

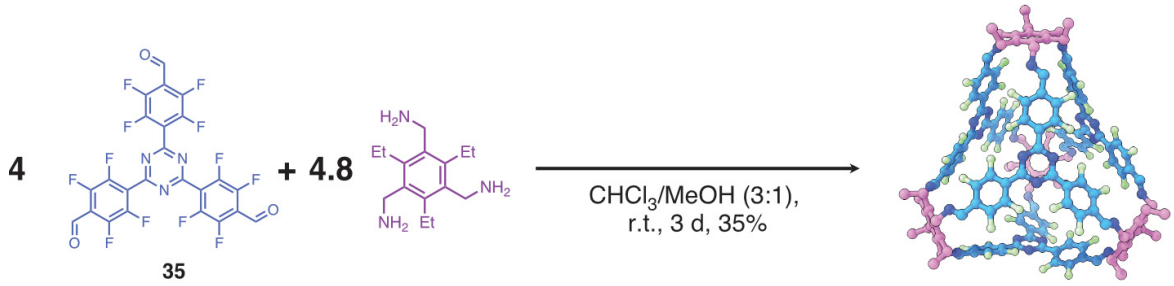

Aldehyde **35** (121.20 mg, 0.20 mmol, 1.00 eq.) was dissolved in a chloroform/methanol (3:1) mixture (25 mL) and a solution (25 mL) of **Et-Amine** (54.90 mg, 0.24 mmol, 1.20 eq.) in chloroform/methanol (3:1) was added dropwise. Half of the solvent was evaporated under reduced pressure at room temperature and n-hexane was added to the solution, resulting in the precipitation of a bright yellow solid. The solid was isolated by filtration and washed with *n*-hexane to yield **FPOC14** (56.30 mg, 35%) as a yellow solid.
^{1}H NMR (300 MHz, $CDCl_3$) δ 7.84 (s, 12H, C**H**O), 5.26 (s, 24H, C**H$_2$**-N=C), 2.40 (d, J = 7.9 Hz, 24H, C**H$_2$**-CH_3), 0.87 (d, J = 7.5 Hz, 36H, C**H$_3$**); **^{19}F NMR** (282 MHz, $CDCl_3$) δ -142.65 (s, 24F, **F$_{inner}$**), -143.57 (s, 24F, **F$_{outer}$**). Due to the very low solubility, no ^{13}C NMR spectrum could be obtained.
FT-IR (ATR): ṽ(cm^{-1}) = 2960.73, 2931.80, 2872.01, 1743.65, 1697.36, 1693.50, 1639.49, 1581.63, 1521.84, 1475.54, 1402.25, 1354.03, 1317.38, 1269.16, 1232.51, 1172.72, 1136.07, 1085.92, 1074.35, 1043.49, 985.62, 920.05, 850.61, 756.10, 709.80, 665.44.
MALDI MS: [**FPOC14**+H]$^{+}$ calculated: 3217.756; found: 3217.786 m/z.

Synthesis of FPOC15

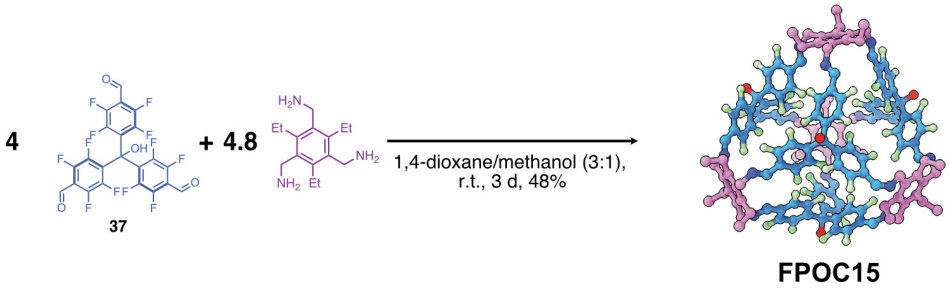

Aldehyde **37** (67.20 mg, 0.12 mmol, 1.00 eq.) was dissolved in a 1,4-dioxane/methanol (3:1) mixture (15 mL) and **Et-Amine** (35.90 mg, 0.14 mmol, 1.20 eq.) dissolved in the same solvent mixture (15 mL) was added dropwise. During the addition the reaction formed a clean solution which was then stirred for 3 days after complete addition. Over the course of the reaction, an off-white precipitate formed that was isolated by filtration, washed with methanol and dried at 40 °C for 24 hours under reduced pressure. This yielded **FPOC15** (40.20 mg, 48%) as an off-white fluffy solid.

MALDI MS: [**FPOC15**+H]$^+$ calculated: 3021.730 m/z; found: 3021.649 m/z).

Due to the insolubility of the cage in common NMR solvents, no NMR spectrum could be recorded.

Synthesis of FPOC16 + Tri^{6}Di^9

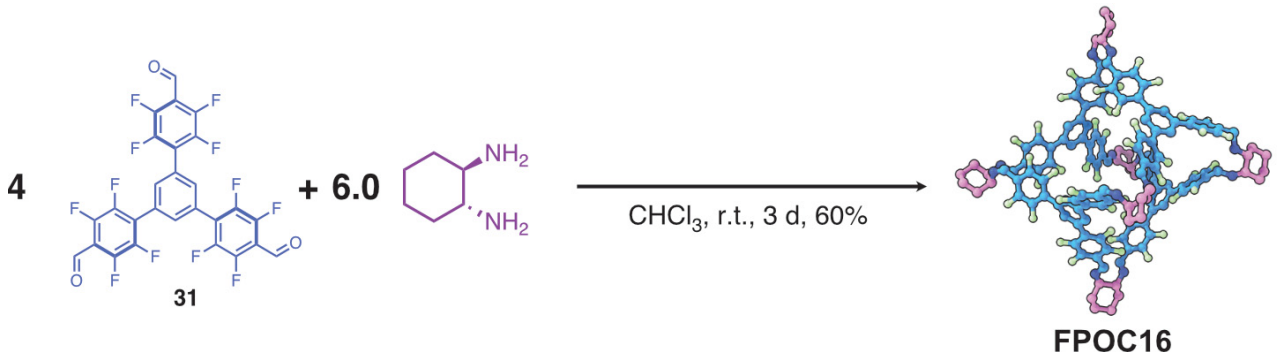

Aldehyde **31** (303.20 mg, 0.50 mmol, 1.00 eq.) was dissolved in dry chloroform (60 mL) and (*R,R*)-**DACH** (79.90 mg, 0.75 mmol, 1.50 eq.) dissolved in 60 mL chloroform was added dropwise to the reaction mixture. The resulting solution was stirred at room temperature for 3 days, during which a bright yellow color developed. Half of the solvent was evaporated under reduced pressure at room temperature and n-hexane was added to the solution, resulting in the precipitation of a bright yellow solid. The solid was isolated by filtration and washed with n-hexane to yield **FPOC16** as a mixture with the larger **Tri$_6$Di$_9$** cage (216.90 mg, 60%) as a yellow solid.

*Procedure for the isolation of **FPOC16** under high dilution*

Aldehyde **31** (156.70 mg, 0.25 mmol, 1.00 eq.) was dissolved in dry chloroform (60 mL) and (*R,R*)-**DACH** (39.90 mg, 0.38 mmol, 1.50 eq.) dissolved in 60 mL chloroform was added dropwise to the reaction mixture. The resulting solution was stirred at room temperature for 3 days, during which a bright yellow color developed. Half of the solvent was evaporated under reduced pressure at room temperature and n-hexane was added to the solution, resulting in the precipitation of a bright yellow solid. The solid was isolated by filtration and washed with n-hexane to yield **FPOC16** (144.60 mg, 40%) as a yellow solid.

^{1}H NMR (300 MHz, $CDCl_3$) δ 8.43 (s, 12H, C**H**N), 7.65 (s, 12H, Ar-**H**), 3.53 (s, 12H, C**H**-N), 1.91 (s, 48H, C$\mathbf{H_2}$-cyhex); **^{19}F NMR** (282 MHz, $CDCl_3$) δ -142.69 – -143.39 (m, 24F, $\mathbf{F_{inner}}$), -143.75 (tt, J = 25.4, 13.1 Hz, 24F, $\mathbf{F_{outer}}$). Due to the very low solubility, no ^{13}C NMR spectrum could be recorded.
FT-IR (ATR): ṽ(cm^{-1}) = 2933.73, 2860.43, 2358.94, 2158.35, 1643.35, 1602.85, 1494.83, 1471.69, 1423.47, 1388.75, 1346.31, 1301.95, 1199.72, 1176.58, 1091.71, 1033.85, 991.41, 968.27, 927.76, 891.11, 858.32, 800.46, 777.31, 721.38, 700.16, 677.01, 632.65, 609.51.
MALDI MS: [**FPOC16**+H]$^+$ calculated: 2893.625 m/z, found: 2893.660 m/z; [**Tri^{6}Di^9** + H]$^+$ calculated: 4339.940 m/z, found: 4339.788 m/z.

Synthesis of FPOC17

Aldehyde **35** (127.90 mg, 0.21 mmol, 1.00 eq.) was dissolved in dry chloroform (25 mL) and (*R,R*)-**DACH** (33.60 mg, 0.32 mmol, 1.50 eq.) dissolved in 25 mL chloroform was added dropwise to the reaction mixture. The resulting solution was stirred at room temperature for 3 days, during which a bright yellow color developed. Half of the solvent was evaporated under reduced pressure at room temperature and *n*-hexane was added to the solution, resulting in the precipitation of a bright yellow solid. The solid was isolated by filtration and washed with *n*-hexane to yield **FPOC17** (76.20 mg, 50%) as a yellow solid.
^{1}H NMR (300 MHz, $CDCl_3$) δ 8.43 (t, J = 2.8 Hz, 12H, C**H**O), 3.54 (s, 12H, C**H**-N), 2.04 – 1.76 (m, 48H, C$\mathbf{H_2}$-cyhex); **^{19}F NMR** (282 MHz, $CDCl_3$) δ -141.26 (dd, J = 21.6, 13.8 Hz, 24F, $\mathbf{F_{inner}}$), -142.08 (tt, J = 28.1, 11.6 Hz, 24F, $\mathbf{F_{outer}}$). Due to the low solubility, no ^{13}C NMR spectrum could be obtained.
FT-IR (ATR): ṽ(cm^{-1}) = 2933.73, 2864.29, 1643.35, 1589.34, 1521.84, 1475.54, 1452.40, 1396.46, 1355.96, 1313.52, 1267.23, 1242.16, 1178.51, 1147.65, 1132.21, 1089.78, 1035.77, 989.48, 943.19, 931.62, 848.68, 806.25, 748.38, 709.80, 665.44, 648.08.
MALDI MS: [**FPOC17**+H]$^+$ calculated: 2905.568 m/z, found: 2905.510 m/z.

Synthesis of FPOC18

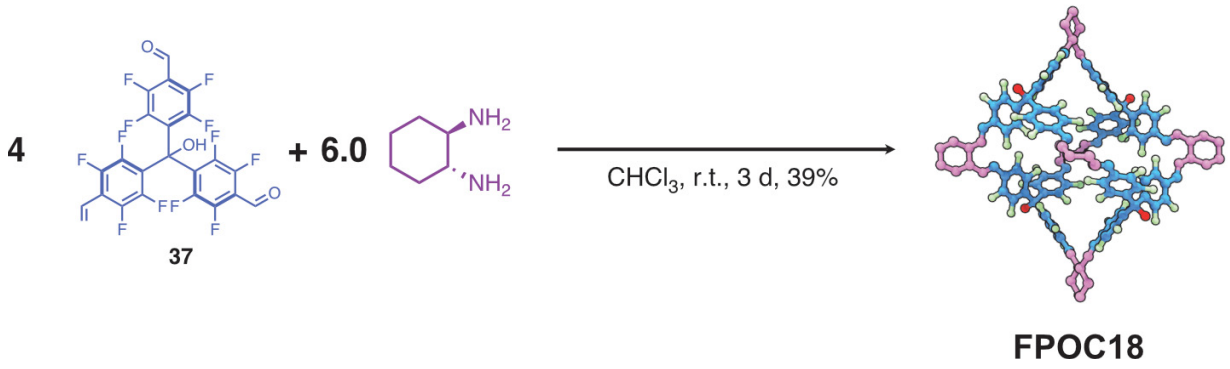

Aldehyde **37** (112.10 mg, 0.20 mmol, 1.00 eq.) was dissolved in dry chloroform (25 mL) and (*R,R*)-**DACH** (34.30 mg, 0.30 mmol, 1.50 eq.) dissolved in 25 mL chloroform was added dropwise to the reaction mixture. The resulting solution was stirred at room temperature for 3 days, during which a bright yellow color developed. The solvent volume was reduced to 5 mL by evaporation under reduced pressure at room temperature and *n*-hexane was added to the solution, resulting in the precipitation of a bright yellow solid. The solid was isolated by filtration and washed with *n*-hexane to yield **FPOC18** (52.80 mg, 39%) as a yellow solid.

^{1}H NMR (300 MHz, $CDCl_3$) δ 8.29 (d, J = 15.3 Hz, 12H, C**H**O), 4.45 (s, 4H, O**H**), 3.46 (s, 12H, C**H**-N), 1.87 (s, 48H, C$\mathbf{H_2}$-cyhex); **^{19}F NMR** (282 MHz, $CDCl_3$) δ -140.34 (d, J = 99.7 Hz, 24F, $\mathbf{F_{inner}}$), -143.02 (d, J = 80.2 Hz, 24F, $\mathbf{F_{outer}}$). Due to the low solubility, no ^{13}C NMR spectrum could be recorded.

FT-IR (ATR): $\tilde{\nu}$(cm^{-1}) = 1643.35, 1473.62, 1384.89, 1342.46, 1290.38, 1130.29, 1091.71, 1014.56, 981.77, 968.27, 927.76, 781.17, 767.67, 759.95, 707.88, 682.80, 665.44.

MALDI MS: [**FPOC18**+H]$^{+}$ calculated: 2709.542 m/z, found: 2709.490 m/z.

DOSY experiments

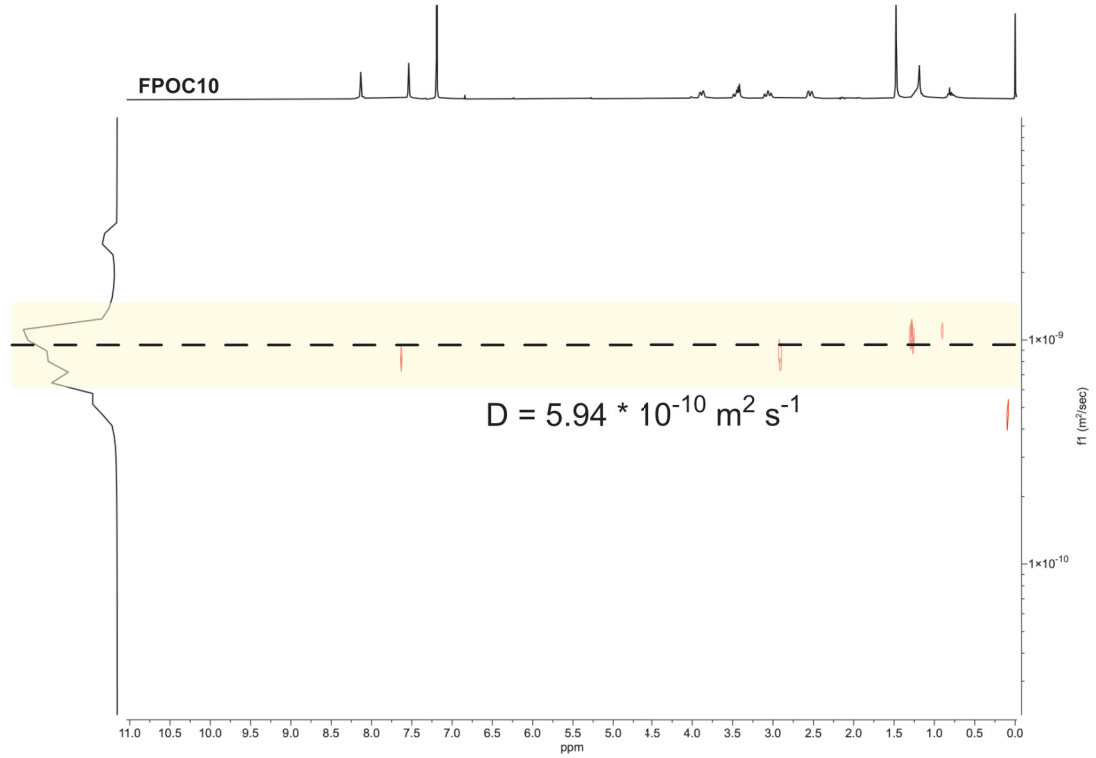

Figure S67: DOSY NMR spectrum (600 MHz, $CDCl_3$, 298 K) of **FPOC10**.

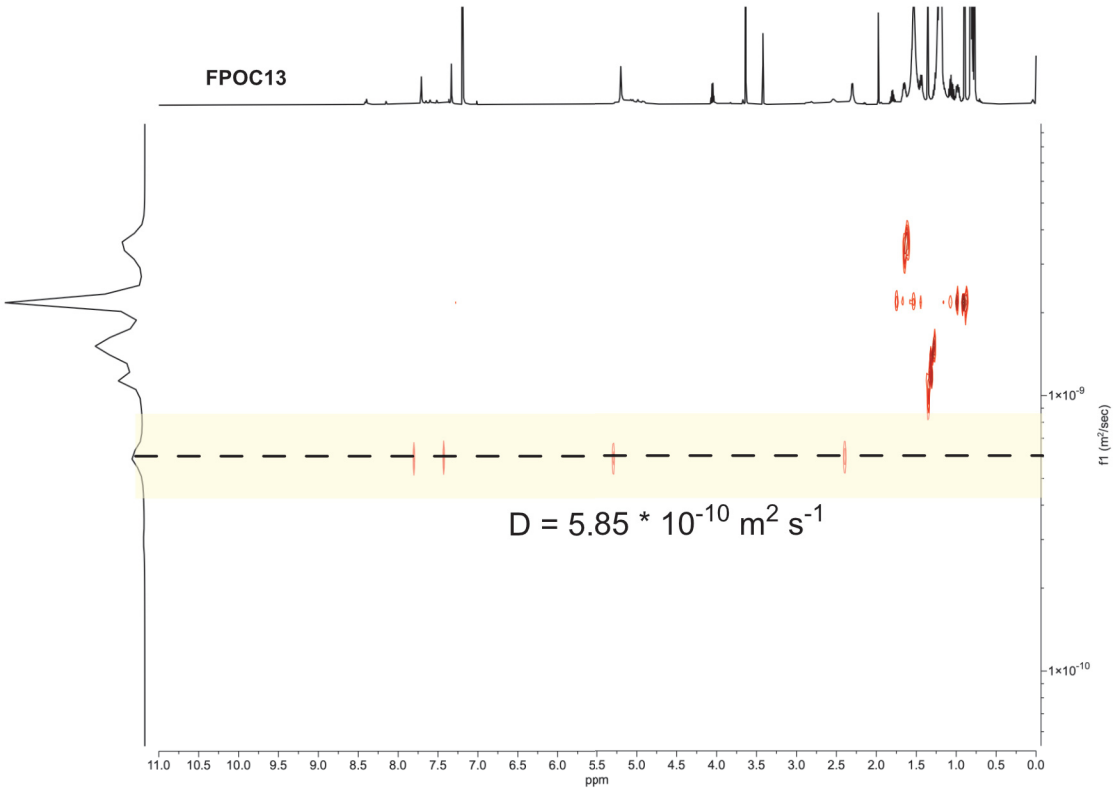

Figure S68: DOSY NMR spectrum (600 MHz, $CDCl_3$, 298 K) of **FPOC13**.

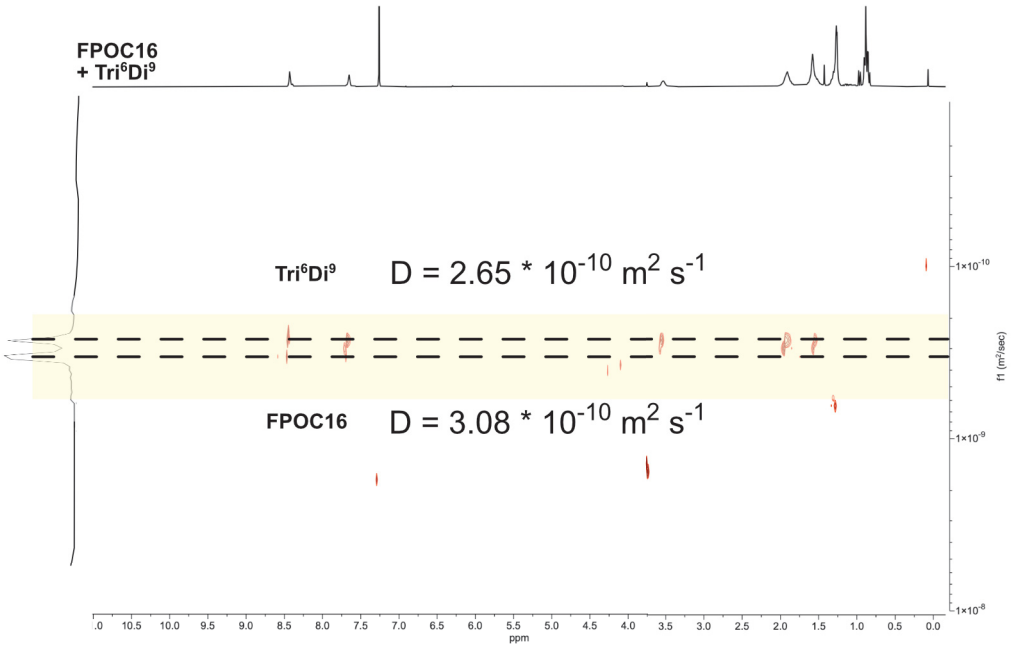

Figure S69: DOSY NMR spectrum (600 MHz, $CDCl_3$, 298 K) of **FPOC16** and the **Tri⁶Di⁹** cage.

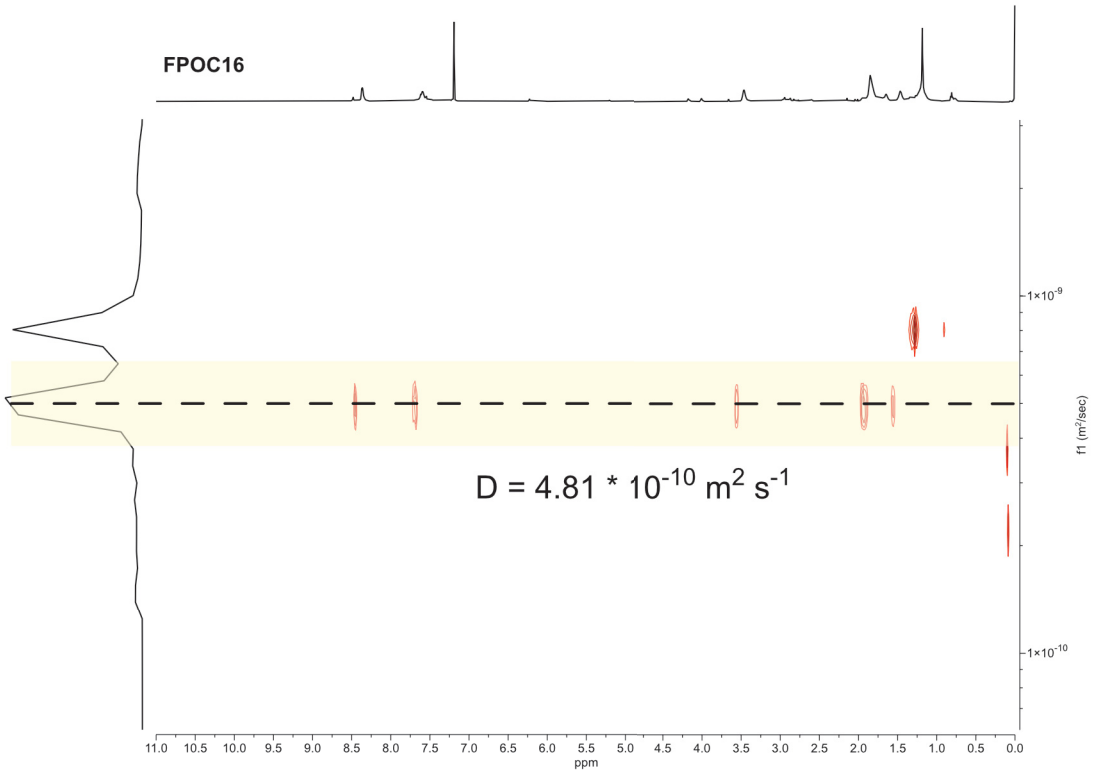

Figure S70: DOSY NMR spectrum (600 MHz, $CDCl_3$, 298 K) of **FPOC16**.

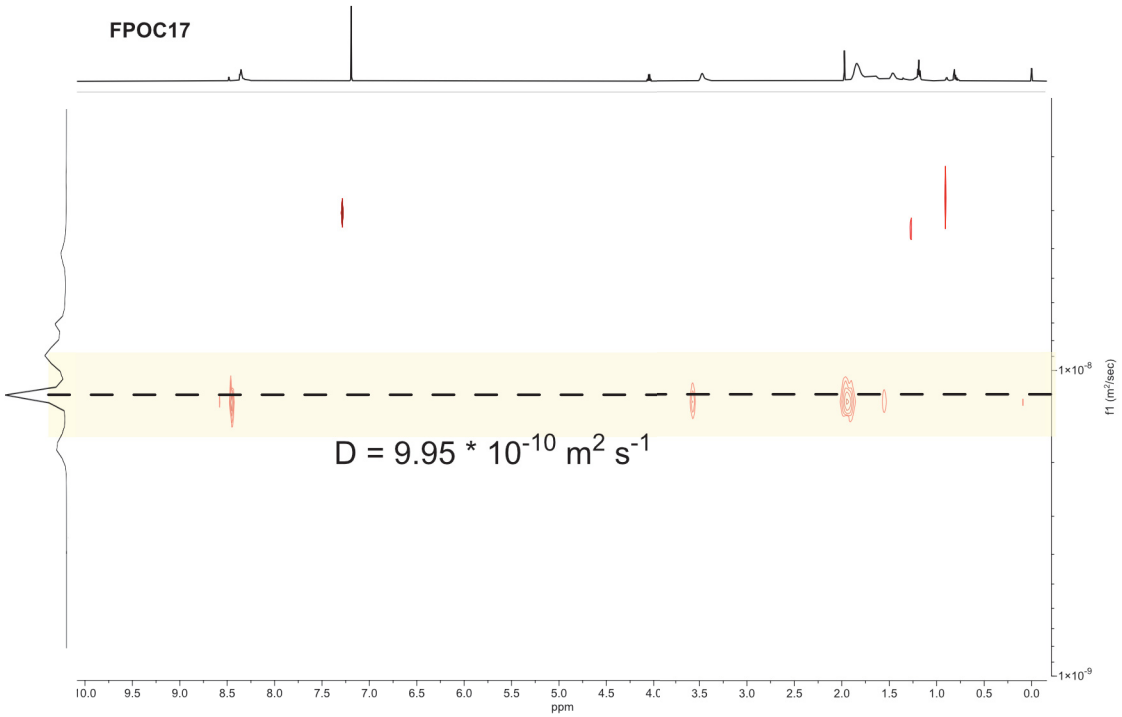

Figure S71: DOSY NMR spectrum (600 MHz, $CDCl_3$, 298 K) of **FPOC17**.

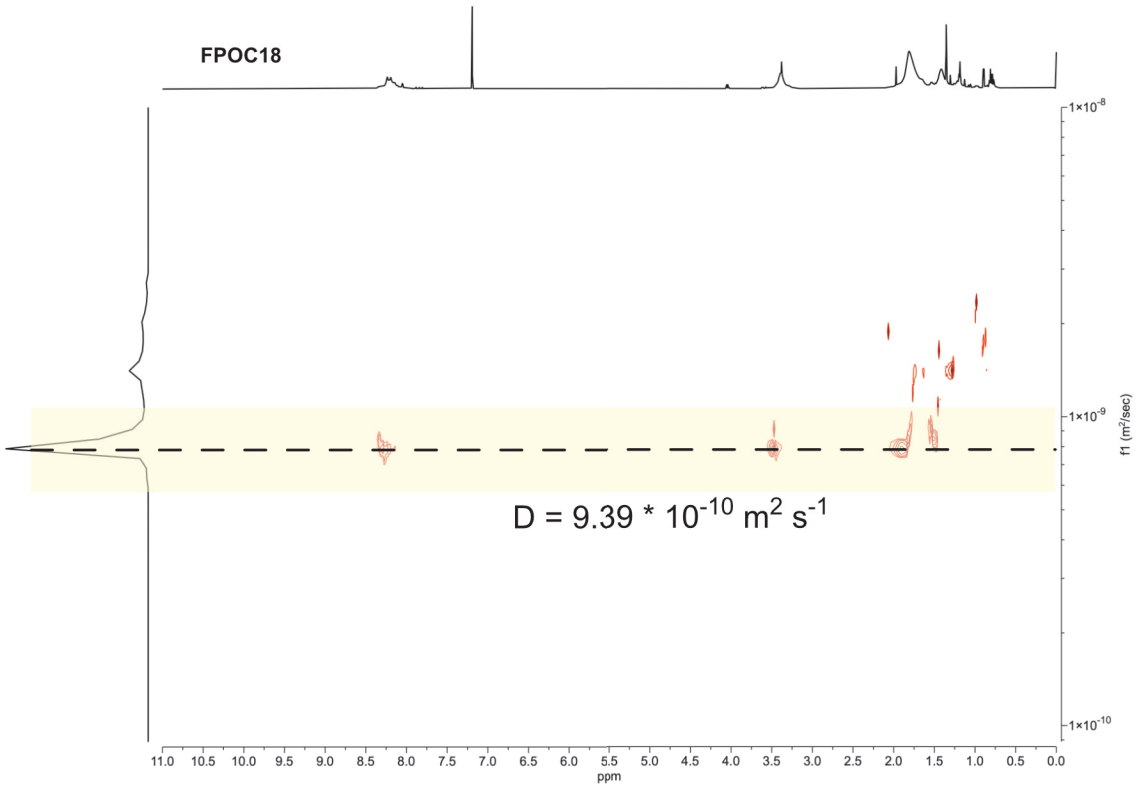

Figure S72: DOSY NMR spectrum (600 MHz, $CDCl_3$, 298 K) of **FPOC18**.

Thermogravimetrical analysis

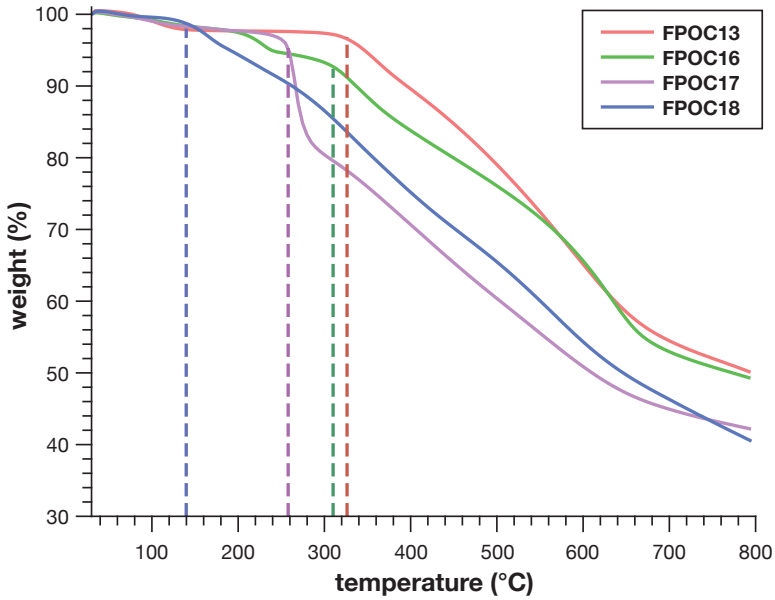

Figure S73: Thermogravimetric analysis curves of amorphous samples of the large cages. The initial dip is due to evaporation of residual water even though all samples were evacuated at 40 °C and 10^{-2} mbar for 24 hours prior to the measurement.

Table S8: Onset decomposition temperatures derived from thermogravimetric analysis curves through tangent evaluation.

	FPOC13	FPOC16	FPOC17	FPOC18
T_{onset} (°C)	326.3	310.1	258.0	139.8

Gas sorption analysis

Before the sorption analysis, all cage samples were washed with the precipitation/crystallization solvent and were soaked in diethyl ether for 24 hours before evaporation at ambient temperature and pressure for an additional 24 hours. Afterwards the samples were thermally activated for 18 hours at 80 °C.

Table S9: Apparent surface areas (BET model) derived from nitrogen isotherms of the respective materials.

	FPOC13	FPOC16	FPOC17	FPOC18
SA_{BET} ($m^2\ g^{-1}$)	510.6	521.5	395.2	50.5

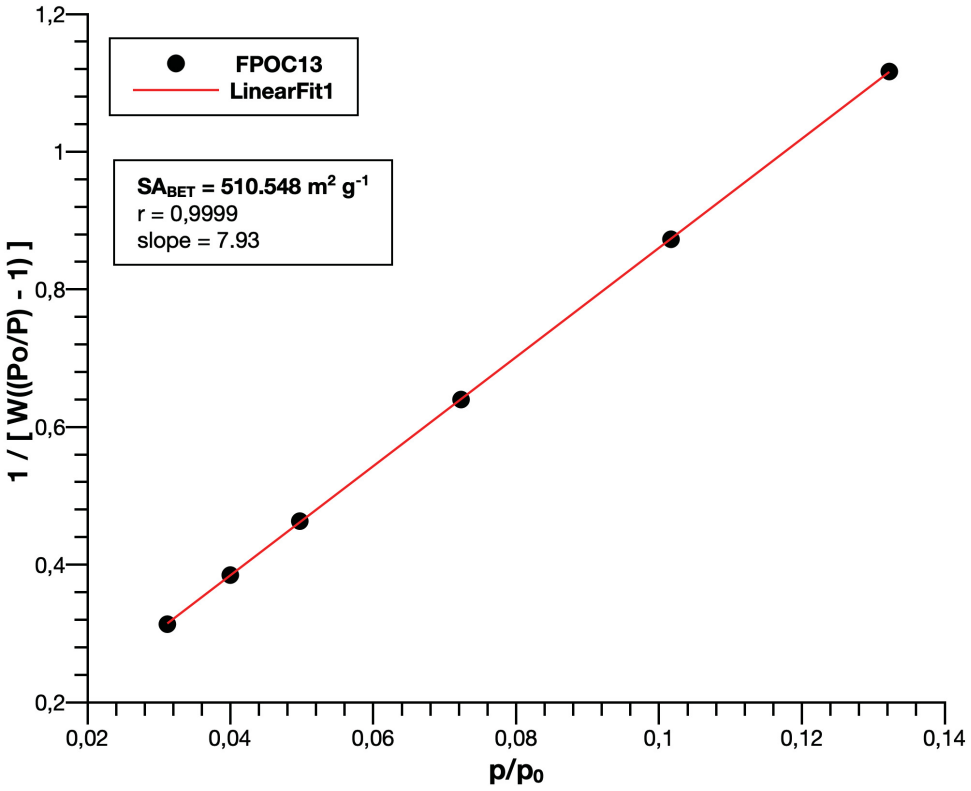

Figure S74: BET plot of a crystalline **FPOC13** sample.

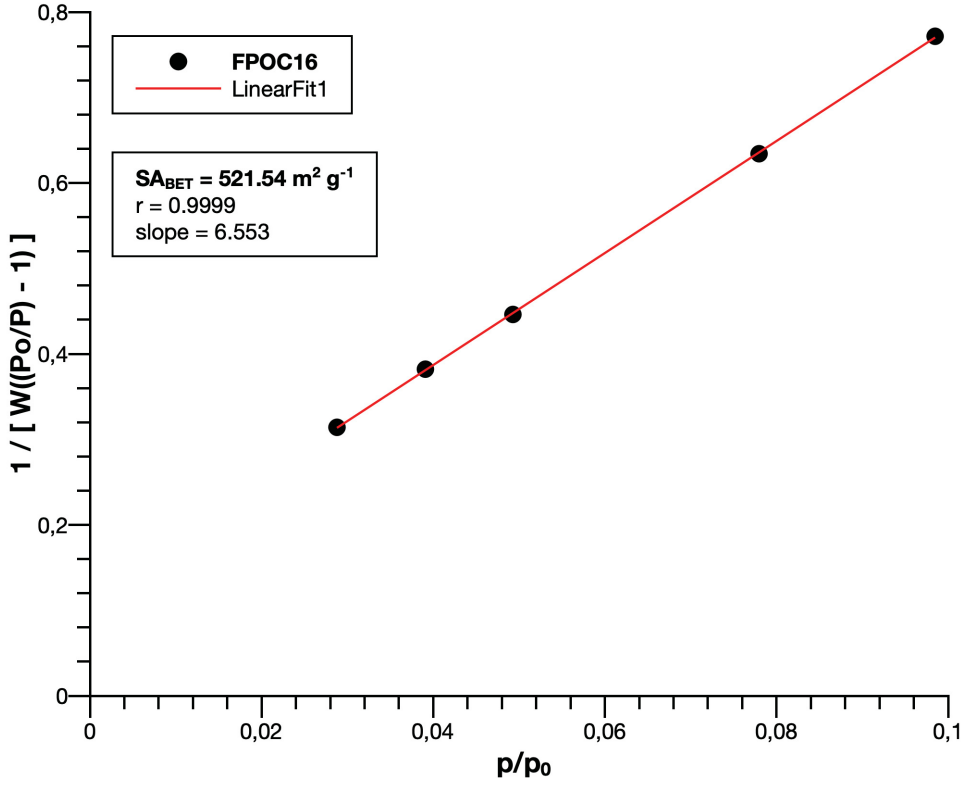

Figure S75: BET plot of an amorphous **FPOC16** sample.

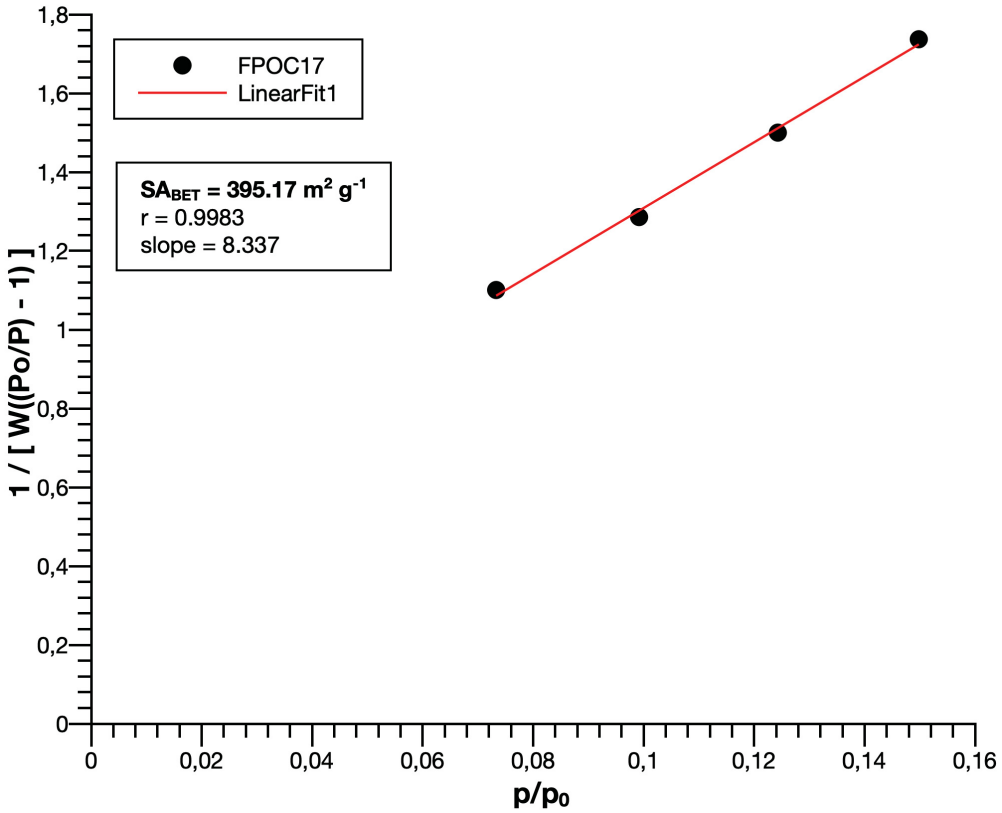

Figure S76: BET plot of an amorphous **FPOC17** sample.

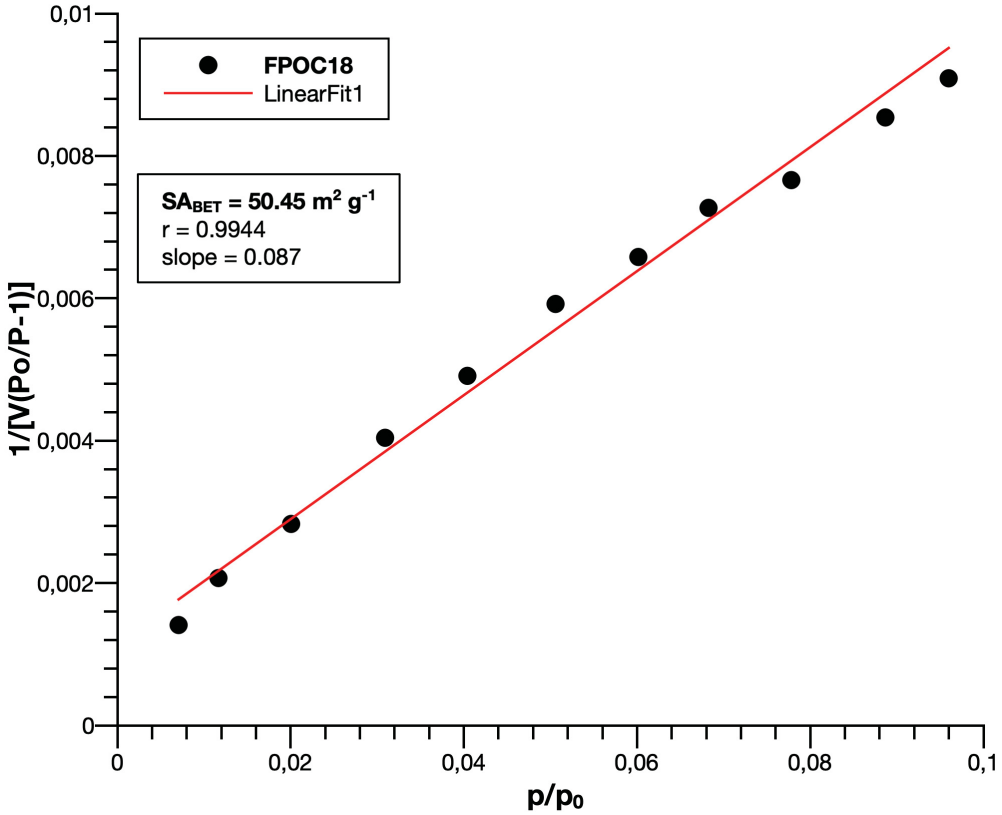

Figure S77: BET plot of an amorphous **FPOC18** sample.

Table S10: Uptake of various gases inside the pores of the different large FPOCs.

	Gas uptake (mmol g^{-1})			
	N_2	H_2	CO_2	CH_4
FPOC13	11.80	3.17	1.18	0.92
FPOC16	8.97	3.18	1.26	0.22
FPOC17	8.73	2.36	1.15	0.32

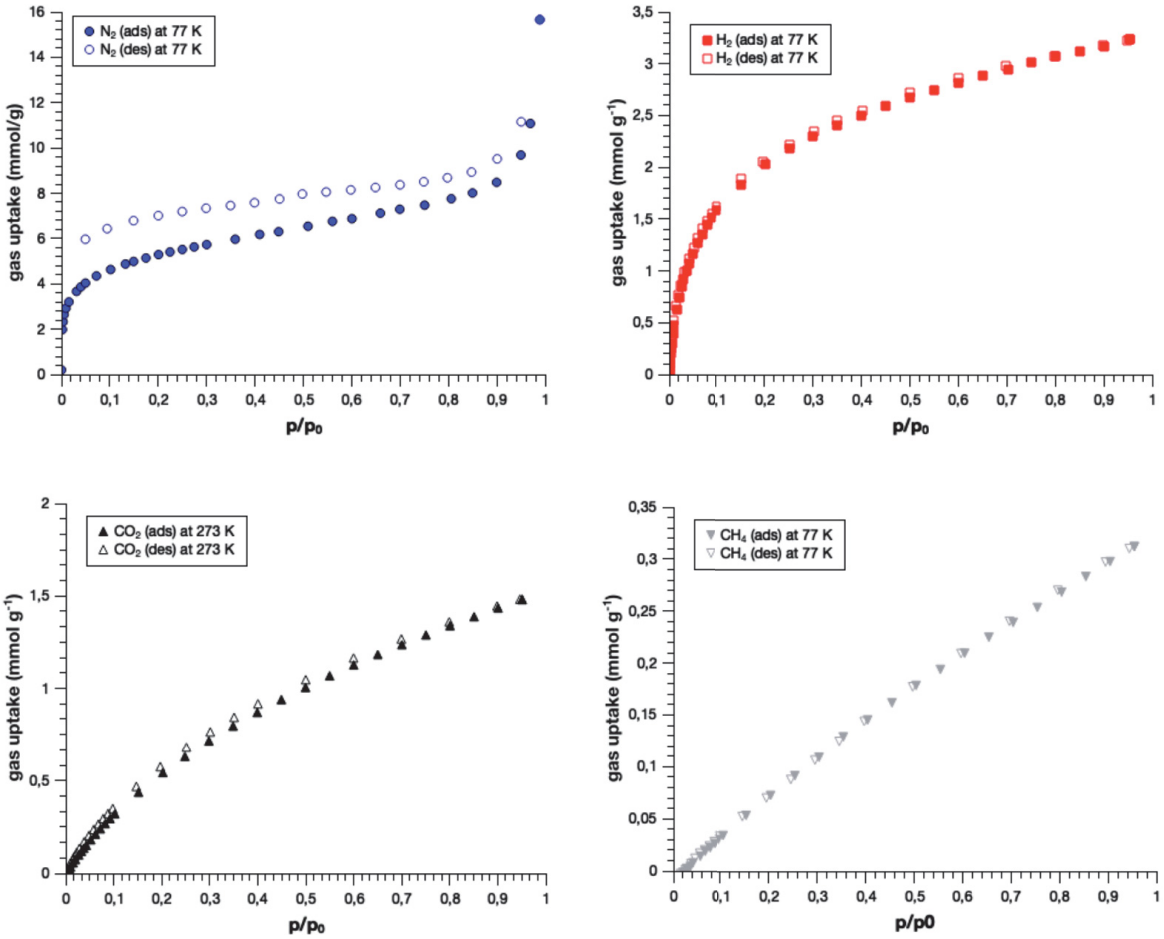

Figure S78: Adsorption (filled) and desorption (hollow) isotherms of N_2 (top left), H_2 (top right), CO_2 (bottom left) and CH_4 (bottom right) measured for **FPOC13**.

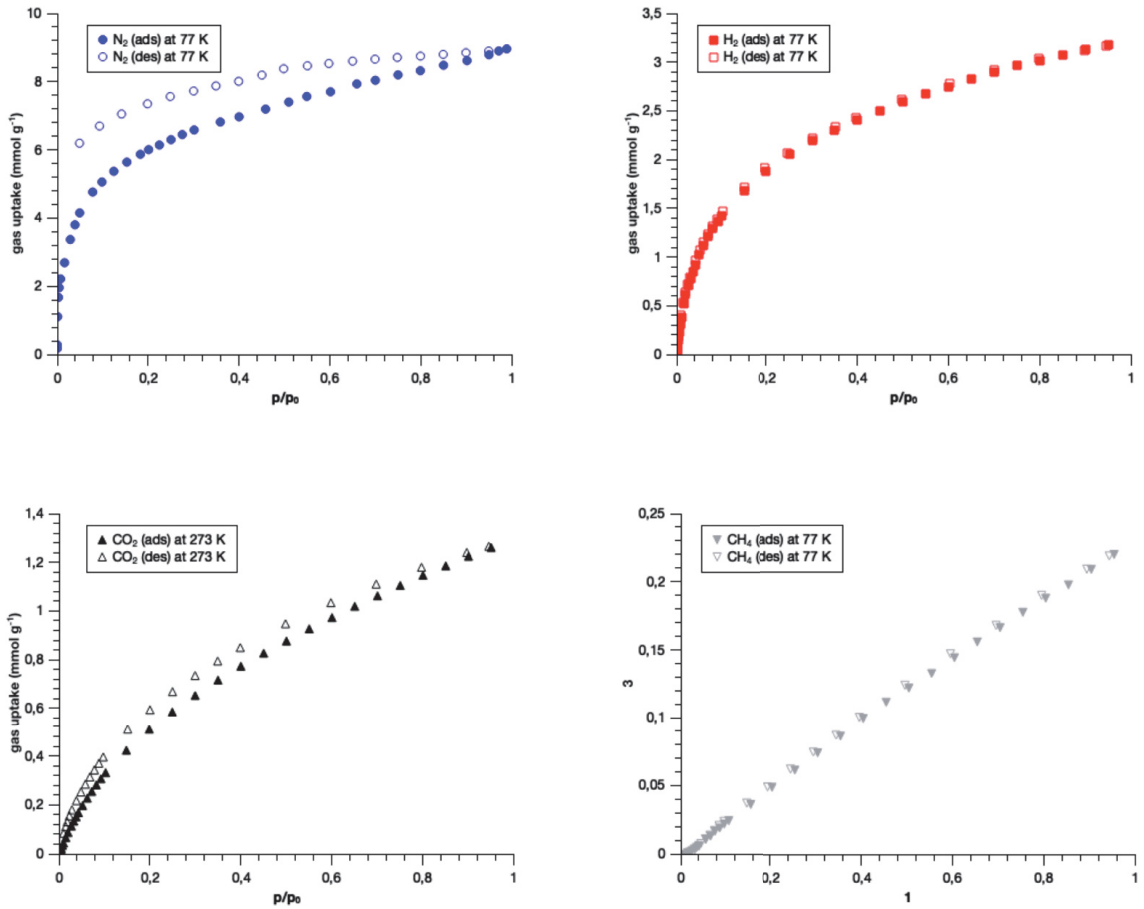

Figure S79: Adsorption (filled) and desorption (hollow) isotherms of N_2 (top left), H_2 (top right), CO_2 (bottom left) and CH_4 (bottom right) measured for **FPOC16**.

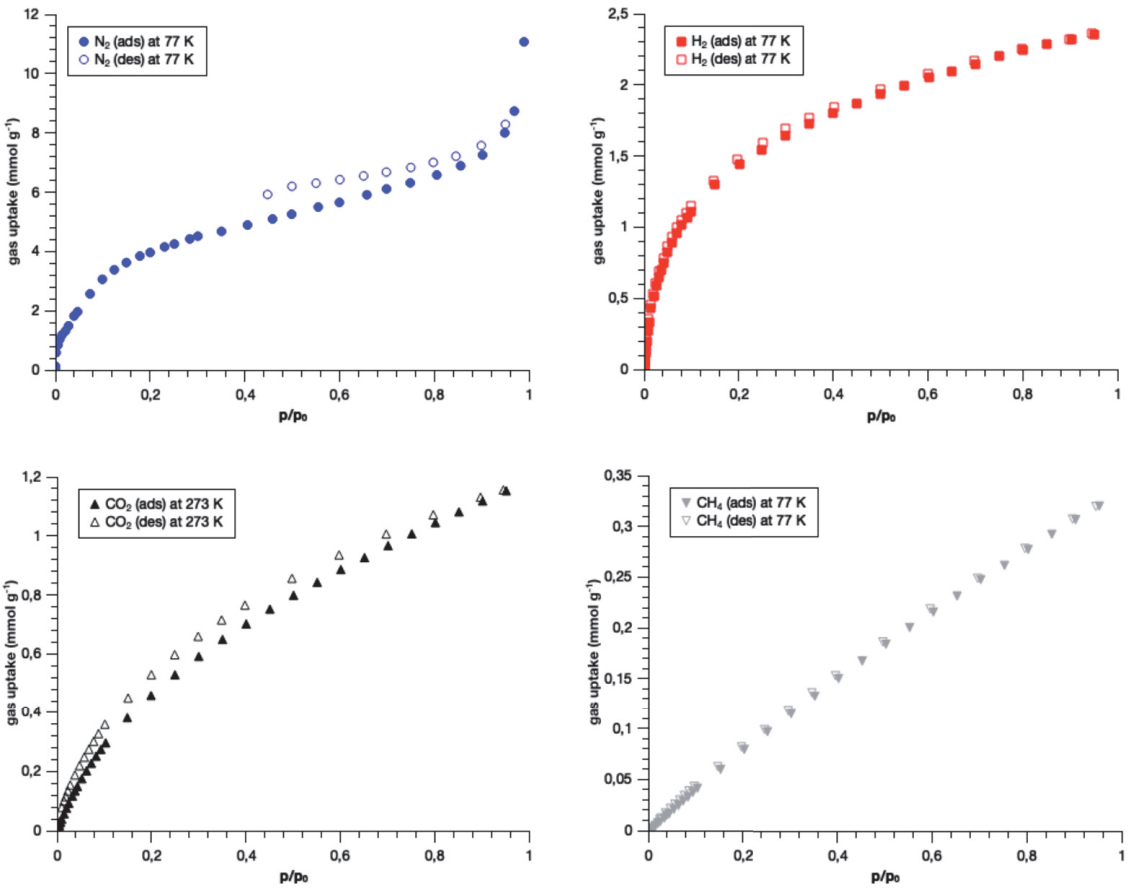

Figure S80: Adsorption (filled) and desorption (hollow) isotherms of N_2 (top left), H_2 (top right), CO_2 (bottom left) and CH_4 (bottom right) measured for **FPOC17**.

Crystallographic data

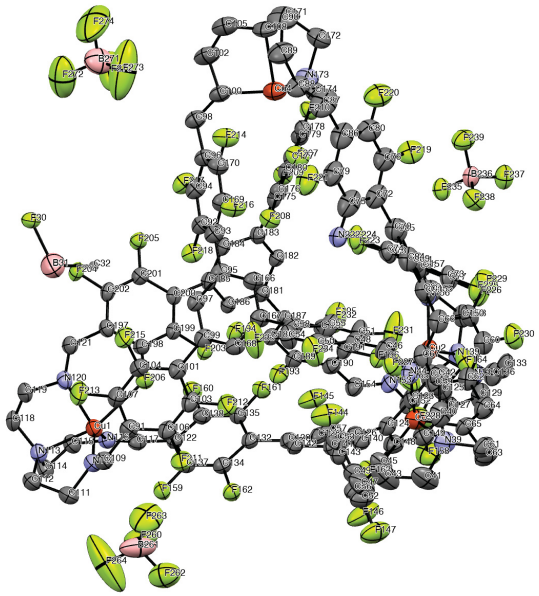

Figure S81: Crystal structure obtained from SC-XRD analysis of a red block-shaped crystal obtained after slow evaporation of a chloroform mixture containing **Cu_4FPOC10**.

The crystal structure of **Cu_4FPOC10** was obtained from a preliminary data set. Due to major errors during the refinement of the crystallographic data it was decided, that a second data set must be obtained by repeating the measurement to generate sufficient structural accuracy.

PXRD

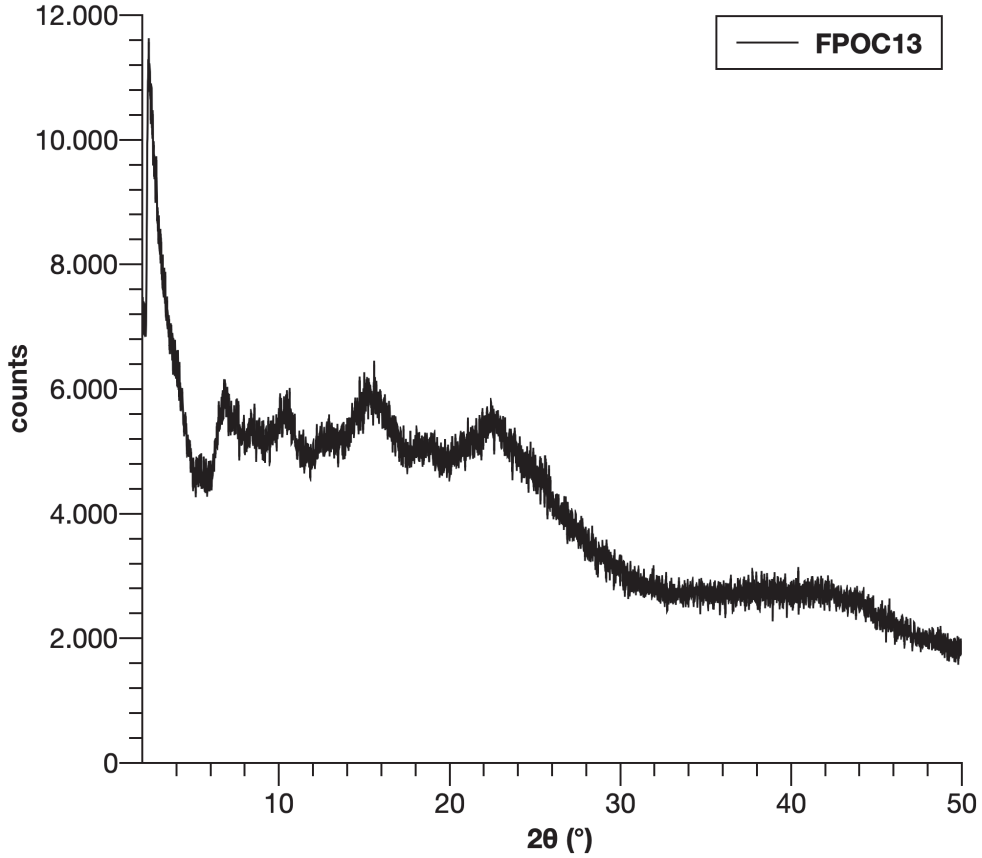

Figure S82: PXRD pattern of an amorphous **FPOC13** sample isolated from the reaction mixture by filtration.

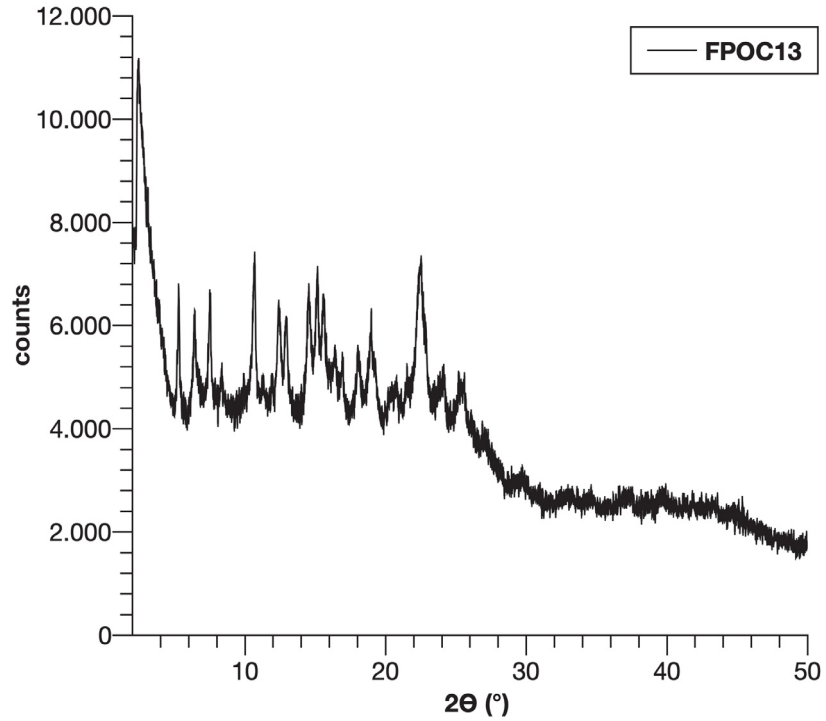

Figure S83: PXRD pattern of a crystalline **FPOC13** sample isolated from the reaction mixture using the layering approach.

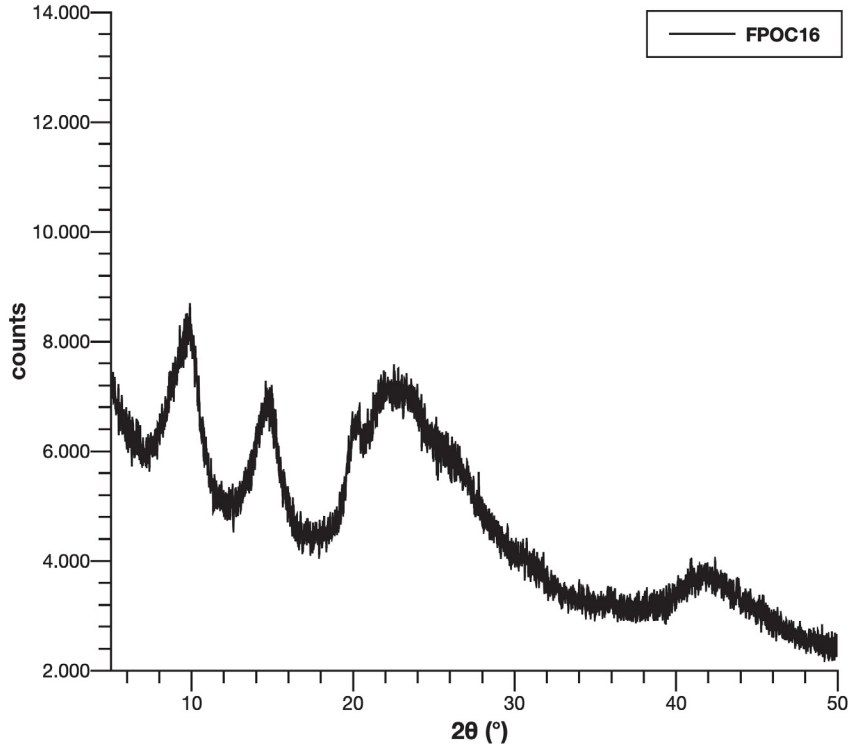

Figure S84: PXRD pattern of an amorphous **FPOC16** sample isolated from the reaction mixture by filtration.

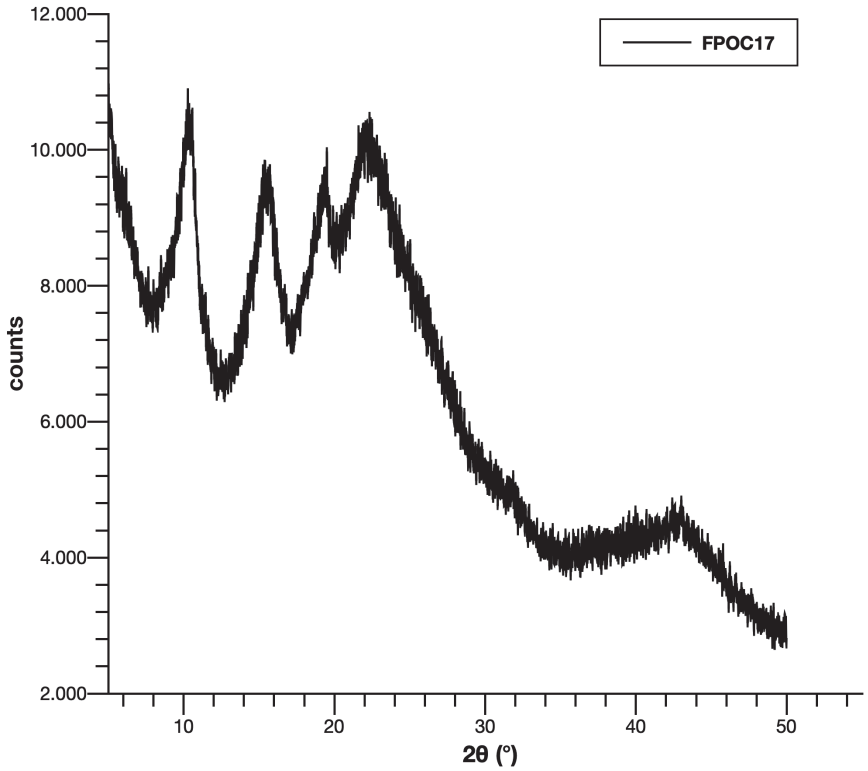

Figure S85: PXRD pattern of a semicrystalline **FPOC17** sample isolated from the reaction mixture by filtration.

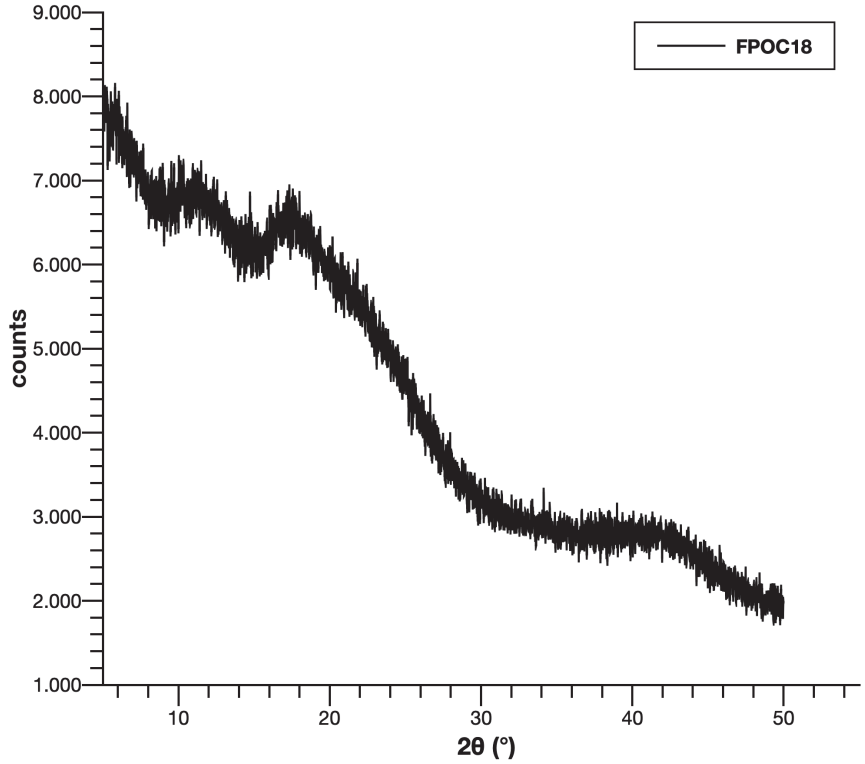

Figure S86: PXRD pattern of an amorphous **FPOC18** sample isolated from the reaction mixture by filtration.

5.7. Experimental Details for Section 3.6

For the synthesis of aldehyde **23** please look into the synthetic procedures for section 3.2. The synthesis of **RRH24** has been previously been reported.[89c] Large parts of these experimental procedures have already been published and were adapted with permission from the authors.[88]

Synthesis of fluorinated trianglimine macrocycle RRF24

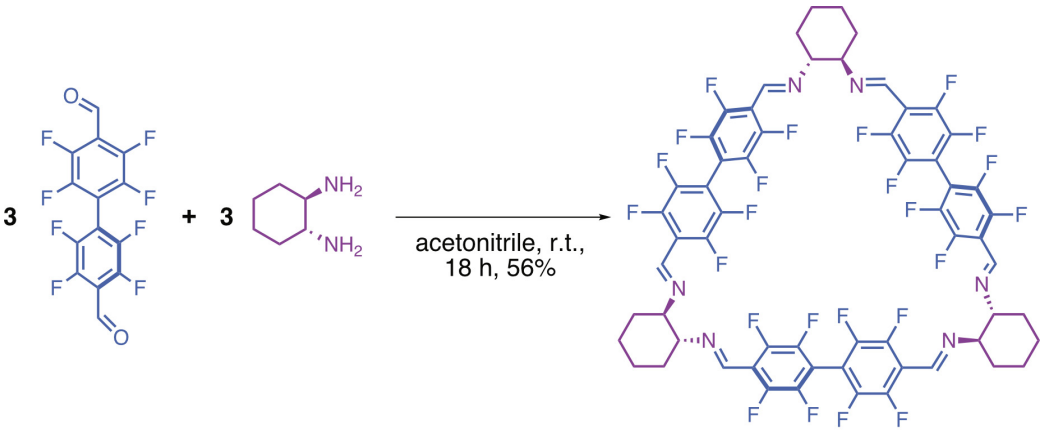

RRF$_{24}$

To a stirring solution of aldehyde **2** (283.00 mg, 800.00 µmol, 1.00 eq) in 10 mL MeCN a solution of (*R,R*)-**DACH** (91.40 mg, 800.00 µmol, 1.00 eq) in 15 mL MeCN was added dropwise over the course of 1 h. The resulting solution was stirred overnight at room temperature, the formed precipitate was isolated by filtration and washed with 2 x 5 mL MeCN yielding in 195.00 mg (150 µmol, 56 %) of macrocycle **RRF24** as colorless powder.

^{1}H NMR (300 MHz, $CDCl_3$): δ 8.40 (s, 2H, -C**H**N), 3.84 – 3.22 (m, 2H, C**H**-N=), 2.12 – 1.72 (m, 6H, -C**H$_2$**- (DACH), 1.75 – 1.34 (m, 2H, C**H$_2$** (DACH)); **^{19}F NMR** (282 MHz, $CDCl_3$): δ -137.77 (dd, J = 16.8, 9.6 Hz, 4F, Ar-**F$_{outer}$**), -142.38 – -143.31 (m, 4F, Ar-**F$_{inner}$**); **^{13}C{^{1}H} NMR** (126 MHz, $CDCl_3$): δ 149.68(Ar-**C**HN), 145.57 (dd, J = 257.3, 11.8 Hz, **C$_{Ar}$**-F$_{outer}$), 143.72 (dd, J = 254.5, 15.5 Hz, **C$_{Ar}$**-F$_{inner}$), 117.90 (t, J = 12.7 Hz, **C$_{Ar}$**-CHN), 108.05 (t, J = 16.2 Hz, Ar-**C$_{Ar}$**), 75.91(-**C**-N=), 32.35(-**C**-H), 24.27(-**C**-H);

FT-IR (ATR): $\tilde{\nu}$(cm^{-1}) = 2933.7 (w), 2862.4 (w), 1643.4 (w), 1469.8 (s), 1384.9 (w)1278.8 (m), 1263.4 (w), 1089.8 (w), 1033.9 (w), 987.6 (m), 927.8 (m), 862.2 (w), 723.3 (s);

HRMS (ESI): calc. for [**RRF24**+H]$^+$ = 1297.2691 m/z, found: 1297.2688 m/z;

Synthesis of the mixed macrocycle RRH16F8

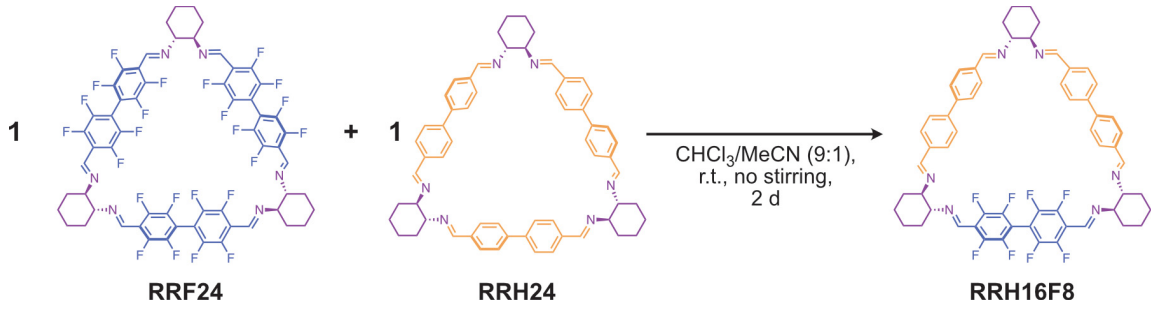

Inside of 25 mL vial **RRF24** (25.90 mg, 0.01 mmol, 1.00 eq.) was dissolved in 10 mL of a chloroform/acetonitrile (9:1) mixture and **RRH24** (17.30 mg, 0.01 mmol, 1.00 eq.) dissolved in 10 mL of the same solvent mixture was layered on top the solution. The resulting biphasic system was sealed and left standing for 2 days without stirring. During the reaction time, rhombohedral crystals formed on the bottom of the vial. After careful decantation of the solvent, crystalline **RRH16F8** could be obtained.

Due to the low amount of product, no NMR or IR spectra could be obtained.

DOSY experiments

Table S11: Estimated solvodynamic radii (r_S) using parameters from literature and diffusion coefficient (D) measured by DOSY NMR.

Compound/ Mixture	log(D) [log(m^2 s^{-1})]	D · 10^{-10} [m^2 s^{-1}]	r_S [nm]
RRF24	-9.36	4.37	0.926

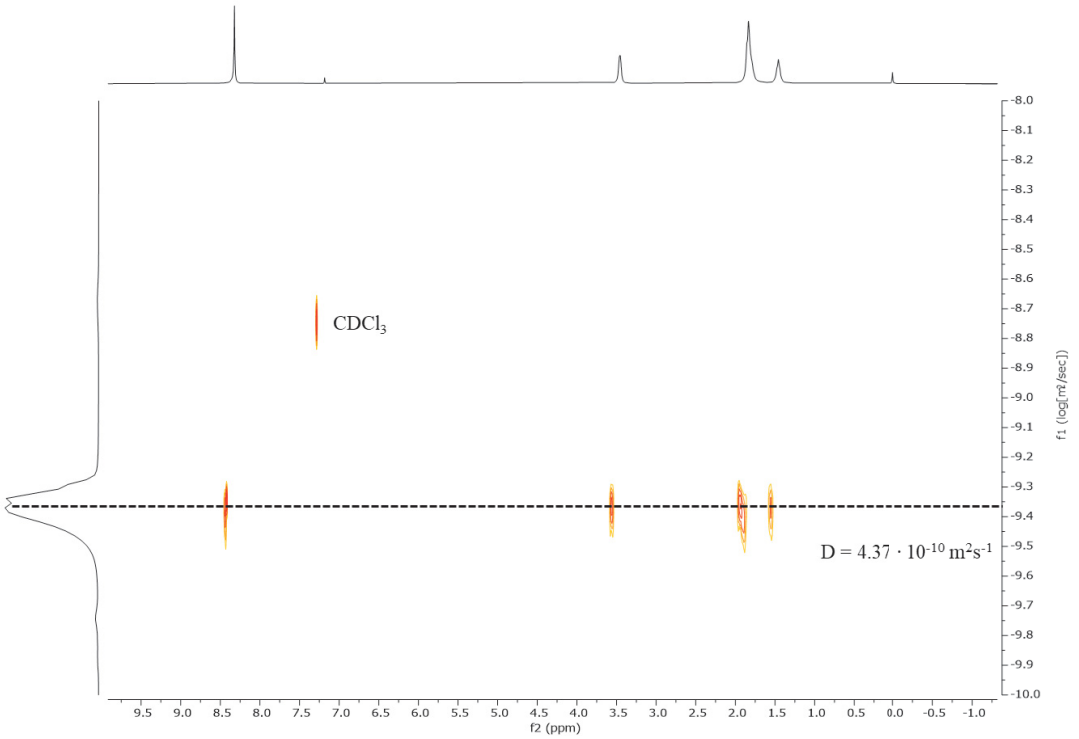

Figure S87: DOSY NMR spectrum (600 MHz, $CDCl_3$, 298 K) of macrocycle **RRF24**.

Gas adsorption analysis

Sample preparation:

Crystalline samples of macrocycle **RRF24** were obtained by slow evaporation from a DCM/MeCN (3/1) solution over the course of 3-5 days. The resulting 0.1 to even 1.0 cm long colorless needles were carefully washed by layering MeCN on top, which was again carefully decanted the next day, this procedure was repeated two times. To remove residue solvent from the channels, two methods were employed for activation.

Method A - **RRF24** (MeCN): The obtained needles were as obtained dried in a dynamic vacuum at 40 °C for 20 h prior degassing at the BET-Station.

Method B - **RRF24** (soaked with *n*-pentane): The obtained needles were carefully layered with n-pentane and were allowed to soak, after 10 h, 24 h and 34 h, the solvent was exchanged and after 48 h the solvent was decanted. The n-pentane soaked crystals were then allowed to stand in a fume hood for 1 day prior to degassing at the BET-Station.

Table S12: Gas uptake of the two crystalline **RRF24** samples.

	uptake ($cm^3\ g^{-1}$)	
gas	**RRF24** (MeCN)	**RRF24** (*n*-pentane soaked)
N_2	20.52	28.02

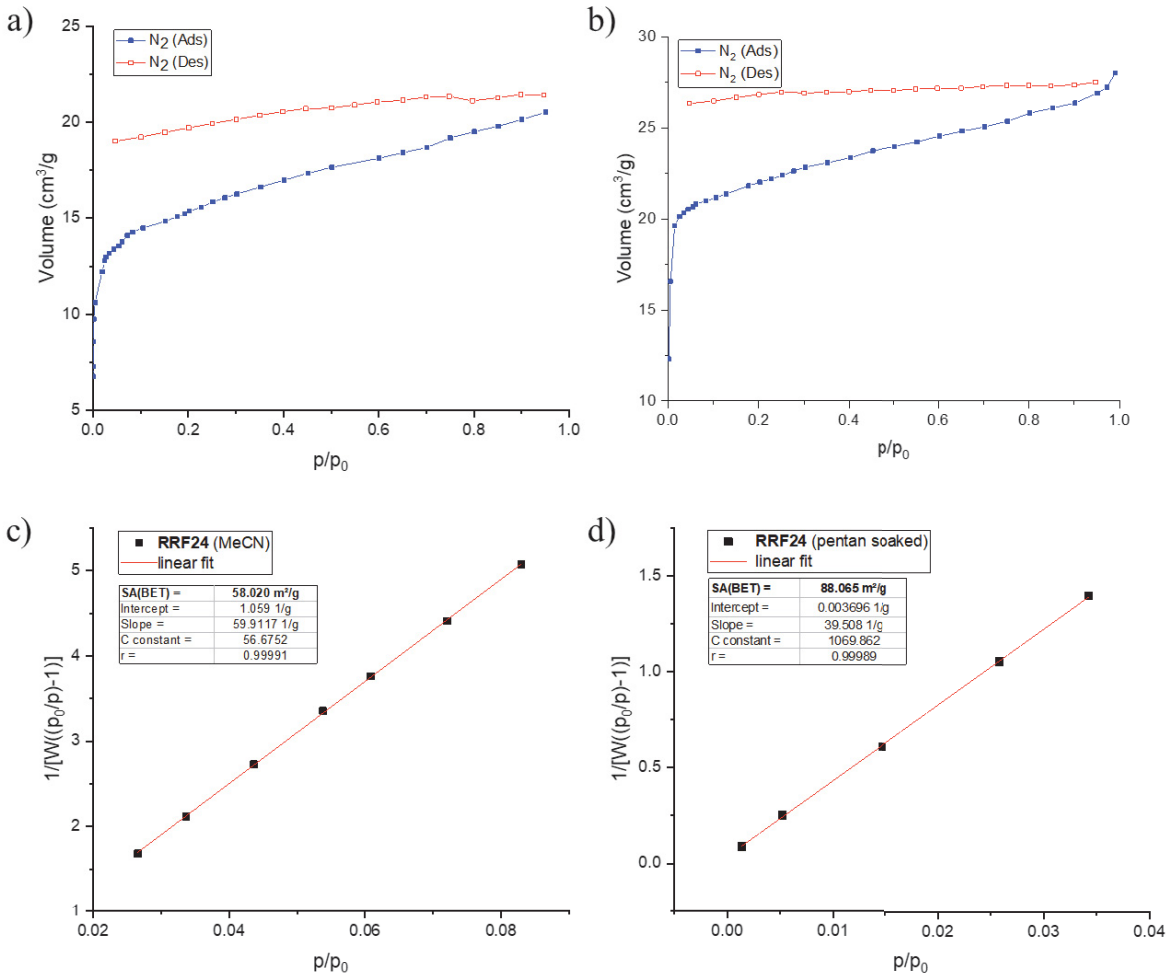

Figure S88: a) adsorption (blue, solid symbol) and desorption (red, hollow symbol) of N_2 for a crystalline **RRF24** sample activated according to method A (soaking with MeCN); b) adsorption (blue, solid symbol) and desorption (red, hollow symbol) of N_2 for a crystalline **RRF24** sample activated according to method B (soaking with n-pentane); c) BET plot of a crystalline **RRF24** sample activated according to method A; d) BET plot of a crystalline **RRF24** sample activated according to method B.

Crystallographic details

CCDC 2071124 (**RRF24**) contains the supplementary crystallographic data for this macrocycle. These data can be obtained free of charge from The Cambridge Crystallographic Data Centre.

RRF24

Crystals of **RRF24** were grown by slow evaporation of a chloroform acetonitrile solution.

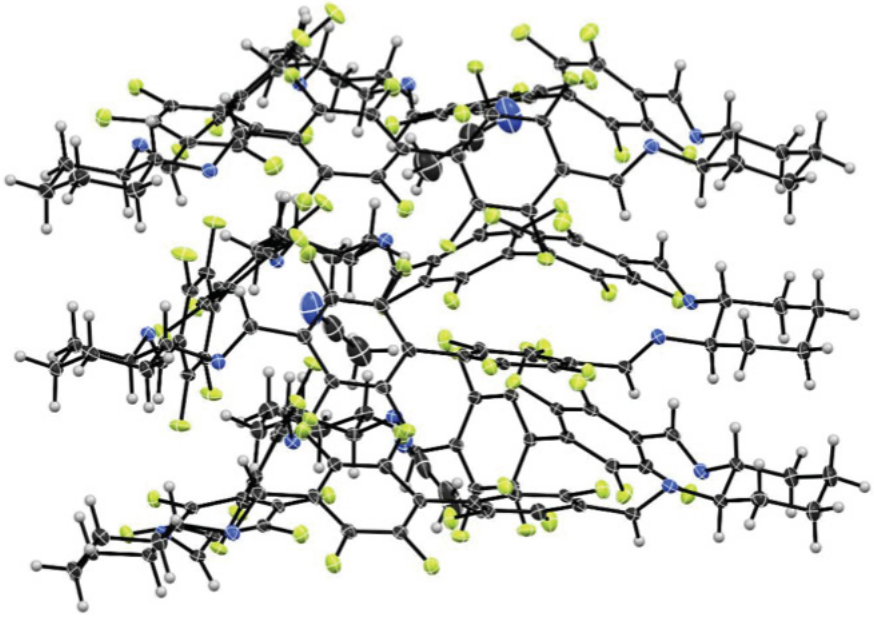

Figure S89: Data set of **RRF24** showing the asymmetric unit bearing three unique **RRF24** molecules including three unique acetonitrile molecules with thermal ellipsoids set at 50% probability. The structure was measured at 100 K and solved in the monoclinic space group $P2_1$ with R_{Int} = 0.0766, R_1 = 0.0363 and wR_2 = 0.0882. This graphic was reproduced from ref. [88] with permission from the authors.

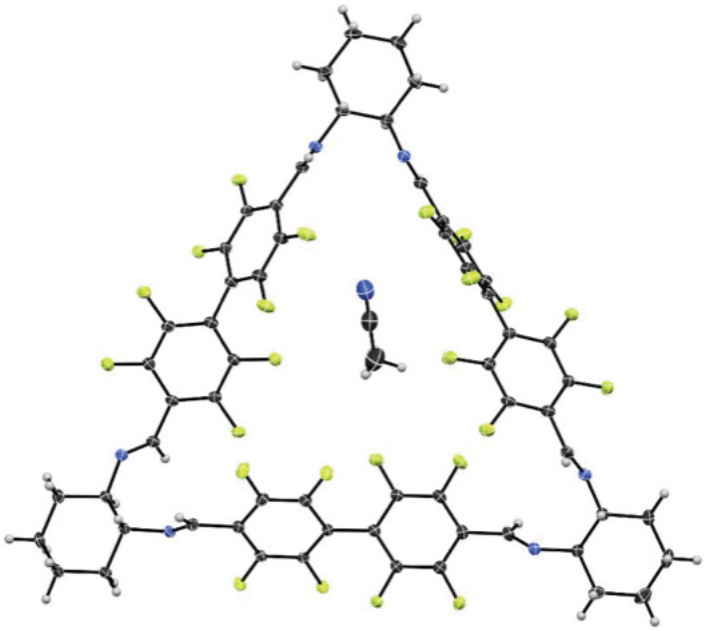

Figure S90: Data set of **RRF24** showing the molecular structure of one trianglimine within the asymmetric unit.

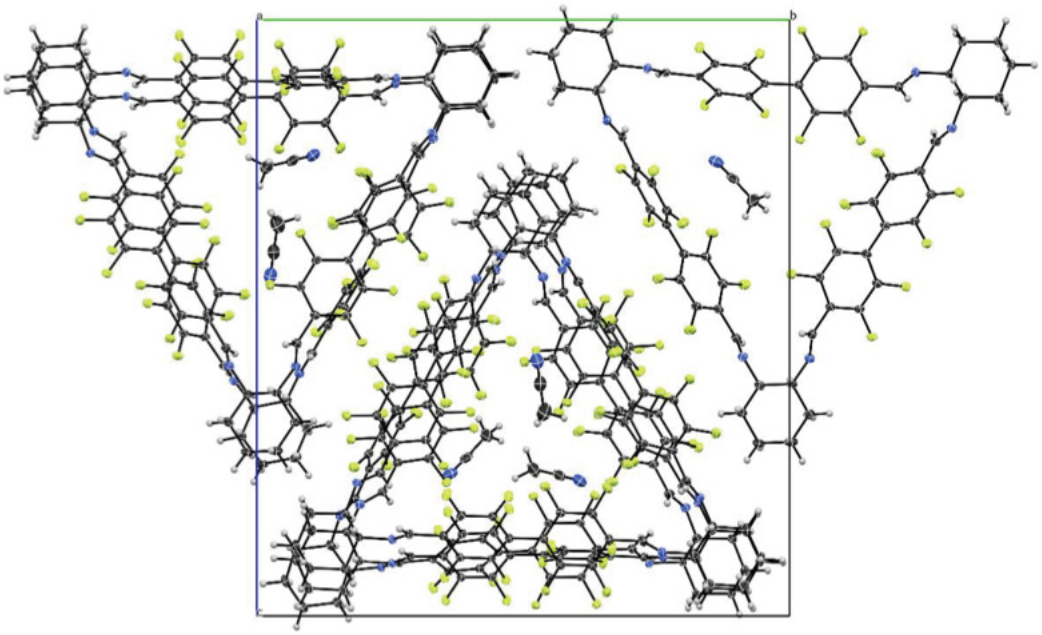

Figure S91: View of the unit cell of **RRF24** along the crystallographic *a* axis.

RRH16F8

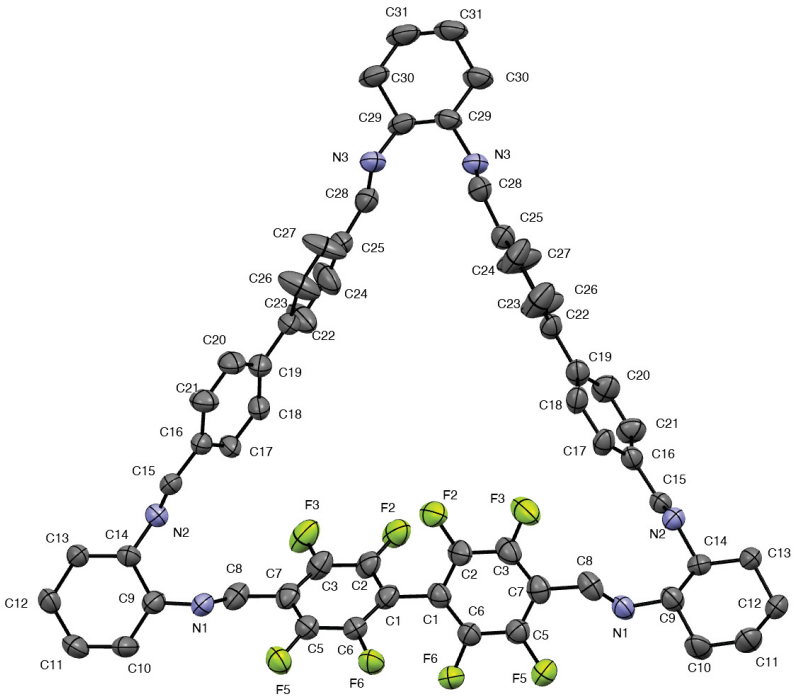

Figure S92: ORTEP-drawing (50% probability thermal ellipsoids) of the molecular structure of the mixed macrocycle **RRH16F8** in the single-crystal as determined by X-ray diffraction. Hydrogens and solvent molecules are omitted for clarity.

Crystal data

Chemical formula	$C_{20}H_{10}F_5N_5O_5$
M_r	495.33
Crystal system, space group	Tetragonal, $P4_32_12$
Temperature (K)	100
a, c (Å)	15.2467 (2), 23.7328 (3)
V (Å^3)	5516.97 (16)
Z	8
Radiation type	Cu Ka
No. of reflections for cell measurement	9675
q range (°) for cell measurement	3.5–63.0
m (mm^{-1})	0.97
Crystal shape	Fragment
Colour	Colourless
Crystal size (mm)	0.18 × 0.10 × 0.03
Data collection	
Diffractometer	Bruker D8 VENTURE
Radiation source	Incoatec Microfocus Source
Absorption correction	Multi-scan SADABS (Bruker-AXS)
No. of measured, independent and observed [I > 2s(I)] reflections	98051, 4833, 4236
R_{int}	0.074
q values (°)	q_{max} = 66.6, q_{min} = 11.1
$(\sin q/l)_{max}$ (Å^{-1})	0.595
Range of h, k, l	h = -18→18, k = -18→18, l = -28→28
Refinement	
Refinement on	F^2
R[F^2 > 2s(F^2)], wR(F^2), S	0.075, 0.231, 1.09
No. of reflections	4833
No. of parameters	334
No. of restraints	0
H-atom treatment	H-atom parameters constrained
$D\rho_{max}$, $D\rho_{min}$ (e Å^{-3})	0.53, -0.31

Absolute structure	Flack x determined using 1650 quotients [(I+)-(I-)]/[(I+)+(I-)] (Parsons, Flack and Wagner, Acta Cryst. B69 (2013) 249-259).
Absolute structure parameter	0.04 (5)

6. Spectra

6.1. Spectra for Section 3.1

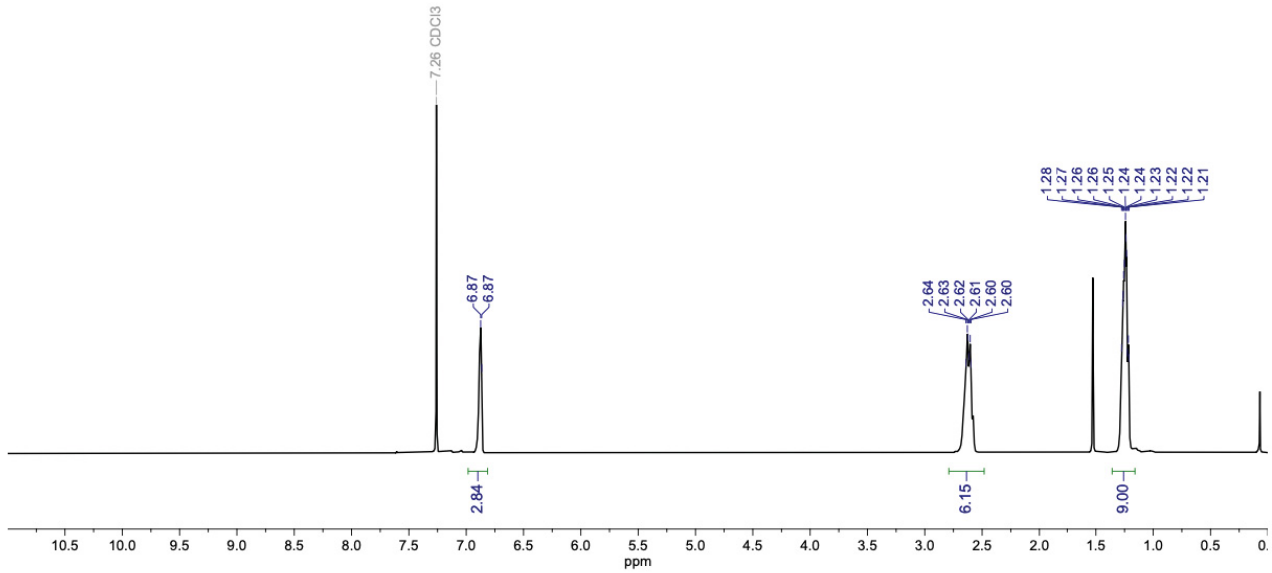

Figure S93: ^{1}H NMR spectrum (300 MHz, $CDCl_3$) of **8**.

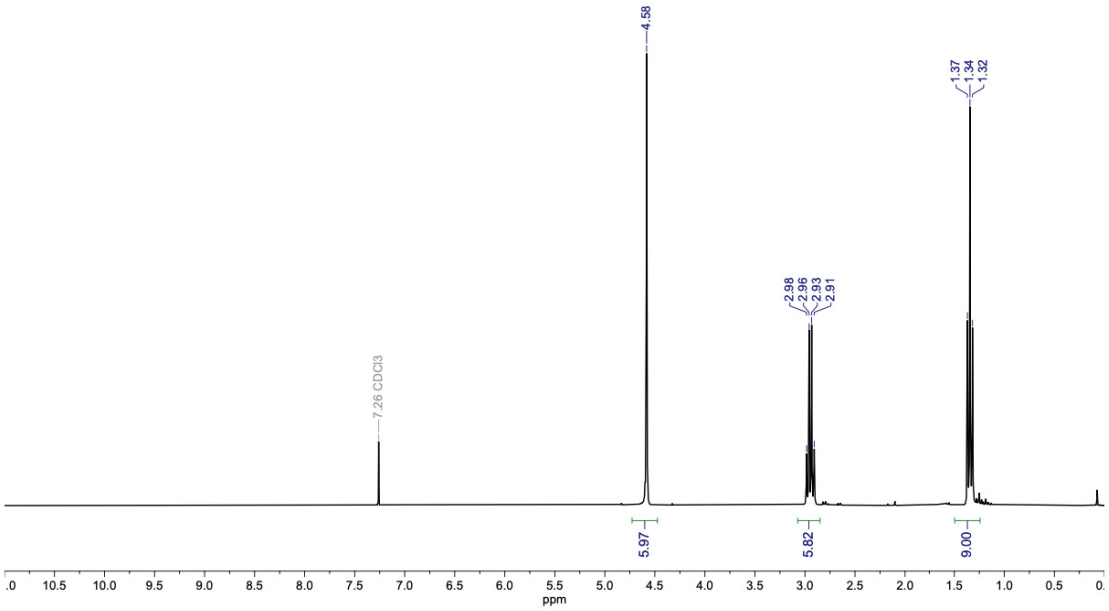

Figure S94: ^{1}H NMR spectrum (300 MHz, $CDCl_3$) of **9**.

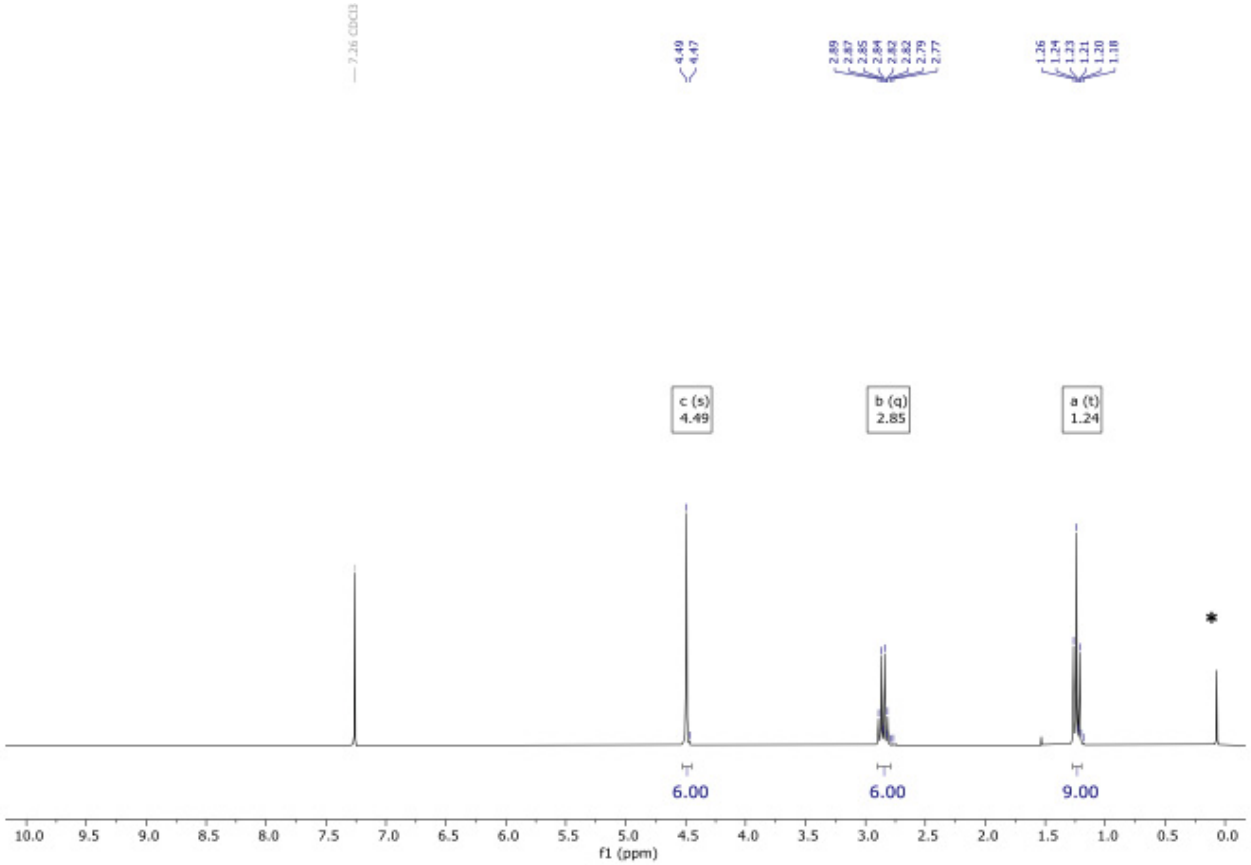

Figure S95: ^{1}H NMR spectrum (300 MHz, $CDCl_3$) of **10**, asterisk indicates the presence of H grease.

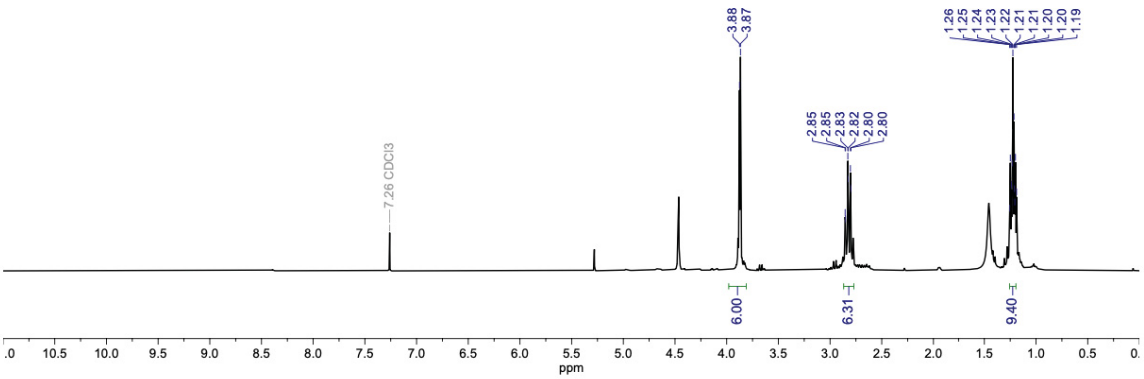

Figure S96: ^{1}H NMR spectrum (300 MHz, $CDCl_3$) of **Et-Amine**.

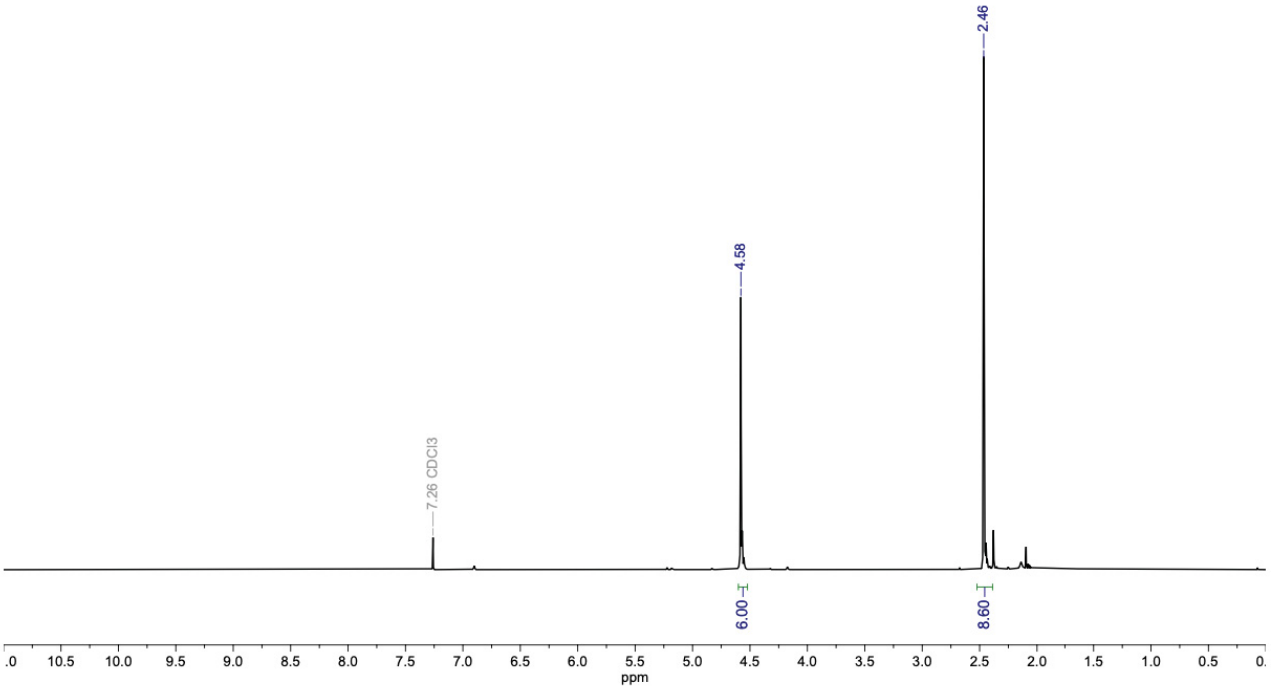

Figure S97: ^{1}H NMR spectrum (300 MHz, $CDCl_3$) of **11**.

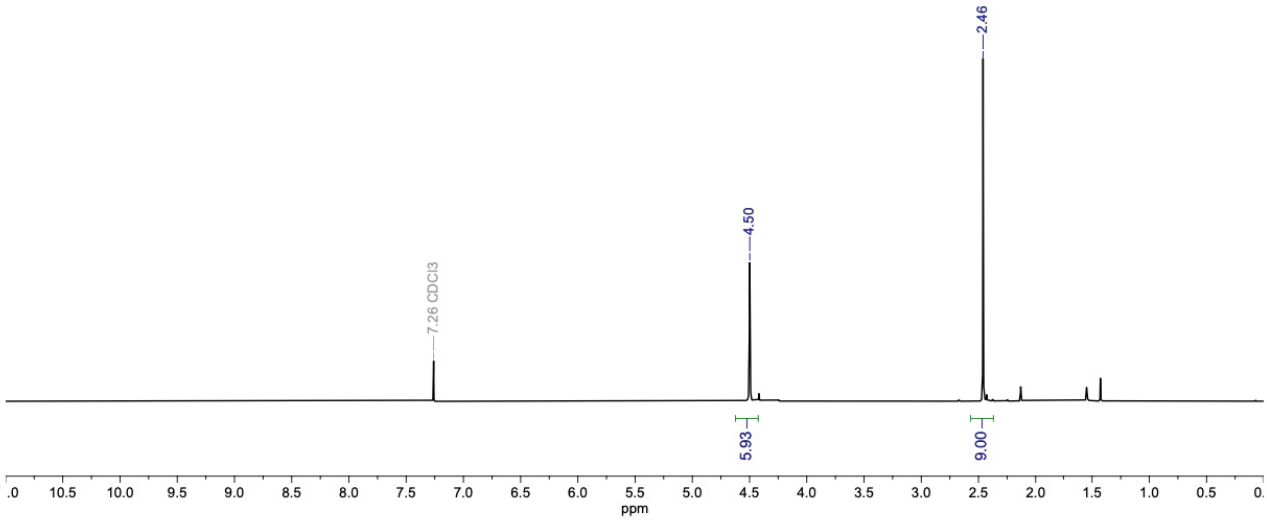

Figure S98: ^{1}H NMR spectrum (300 MHz, $CDCl_3$) of **12**.

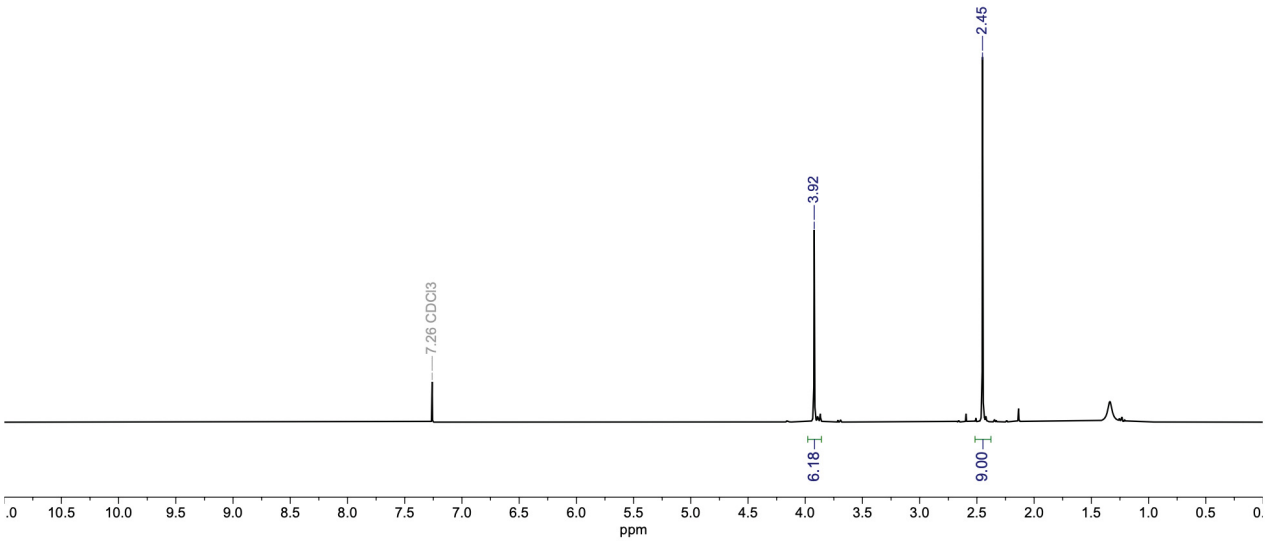

Figure S99: ^{1}H NMR spectrum (300 MHz, $CDCl_3$) of **Me-Amine**.

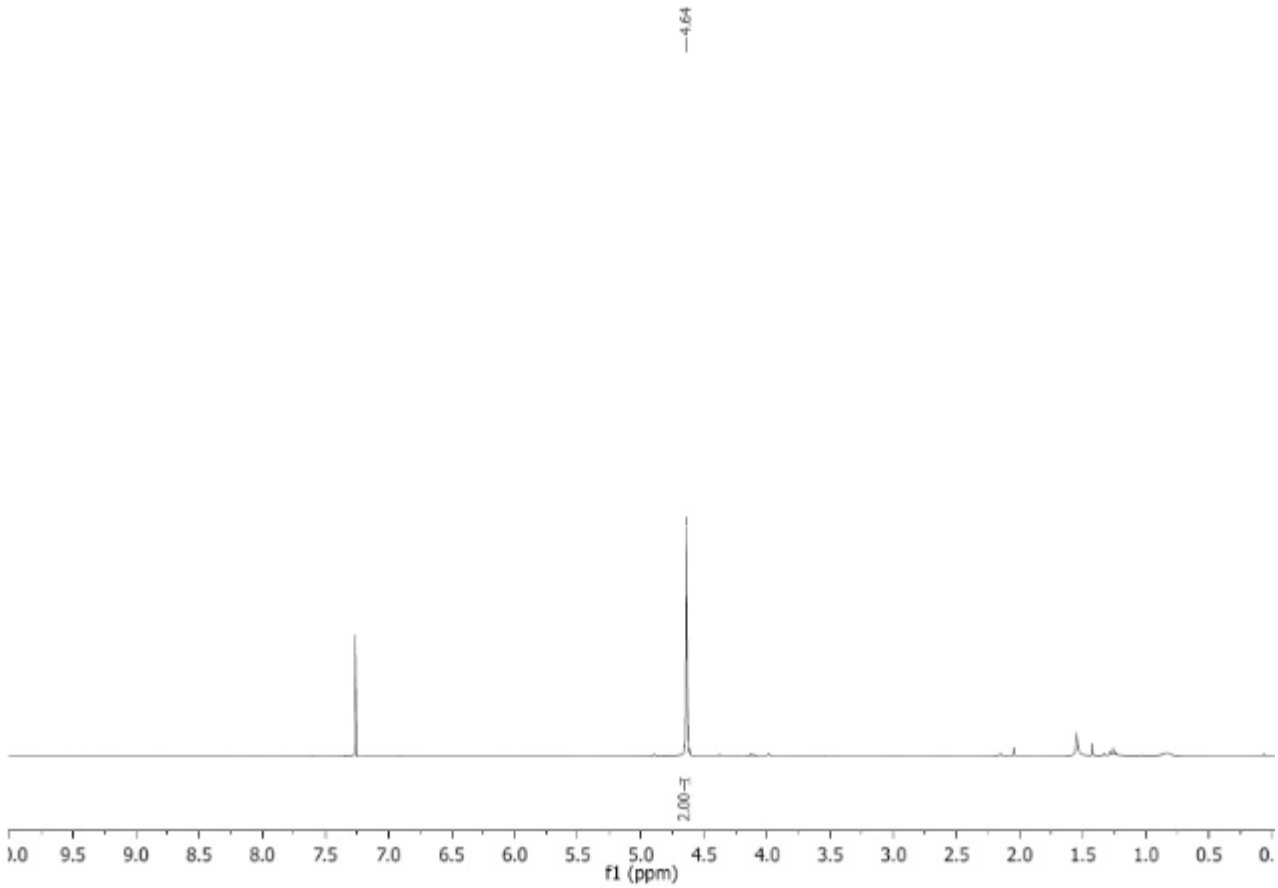

Figure S100: ^{1}H NMR spectrum (300 MHz, $CDCl_3$) of **13**.

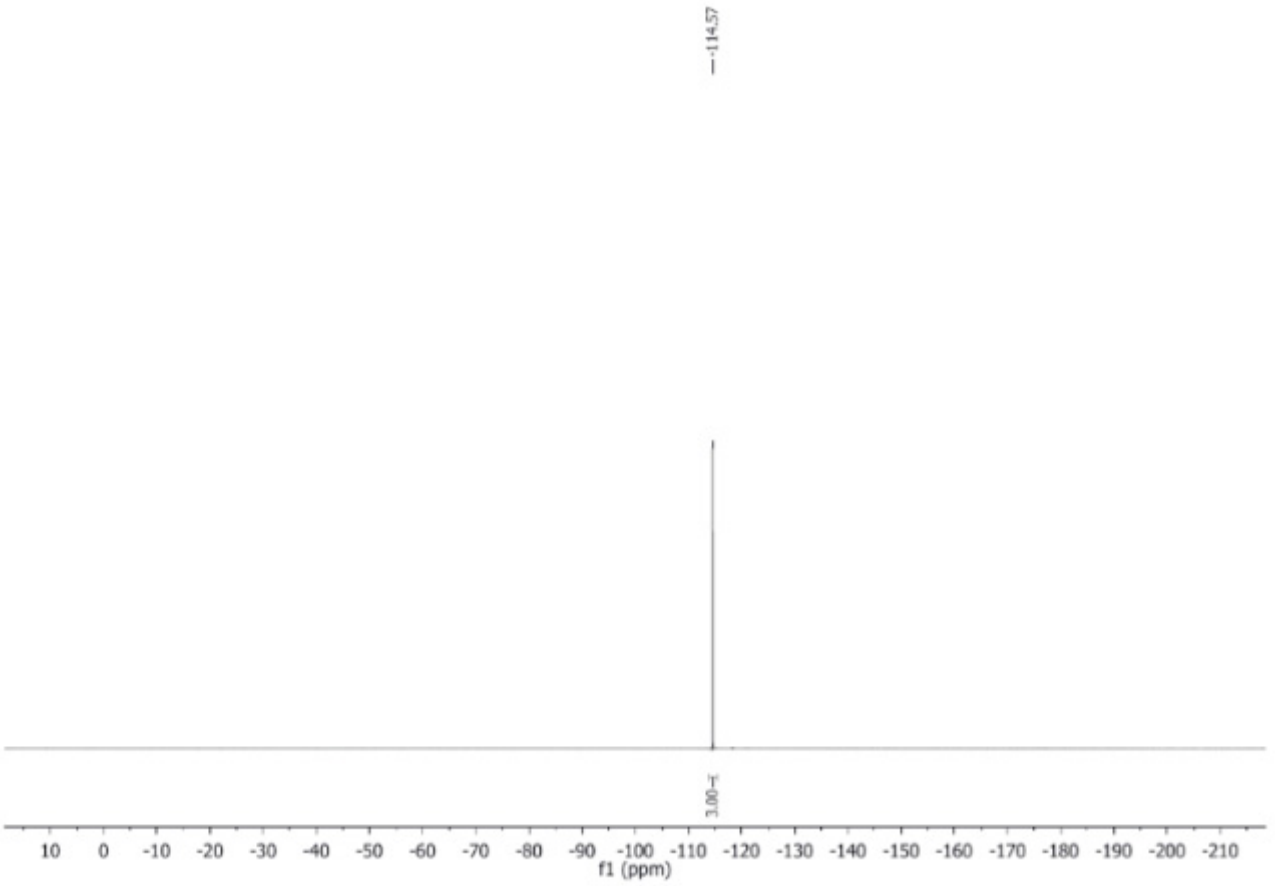

Figure S101: ^{19}F NMR spectrum (282 MHz, $CDCl_3$) of **13** .

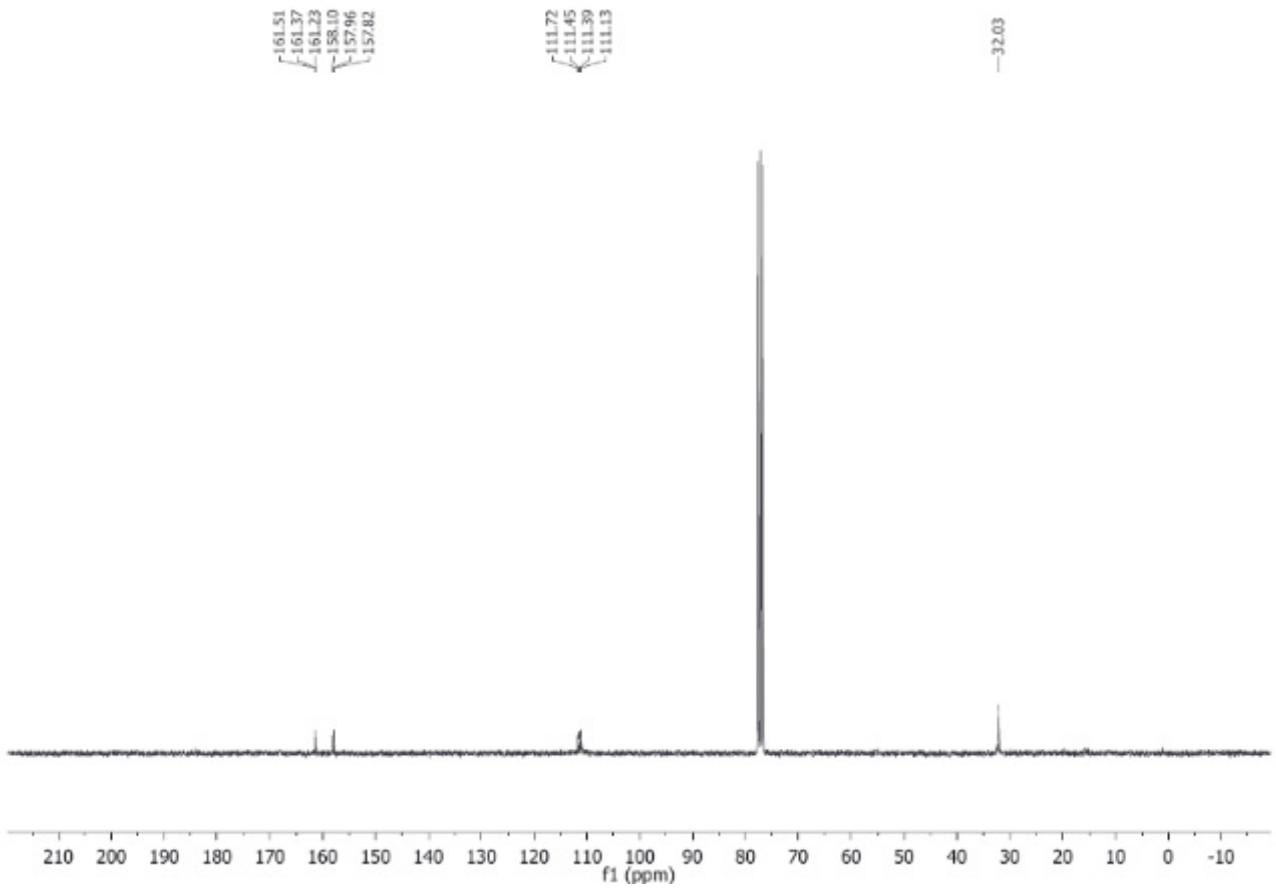

Figure S102: ^{13}C NMR spectrum (75 MHz, $CDCl_3$) of **13**.

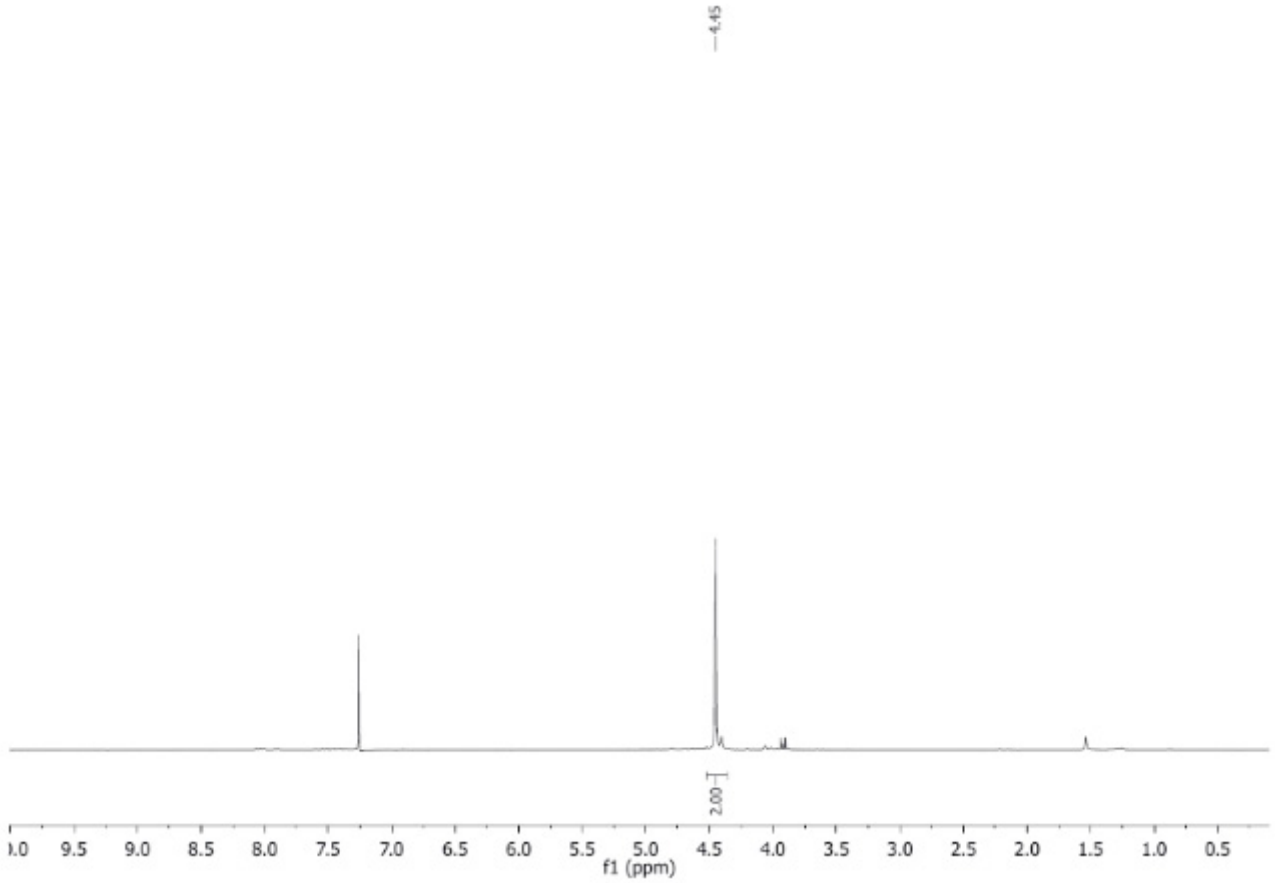

Figure S103: ^{1}H NMR spectrum (300 MHz, $CDCl_3$) of **14**.

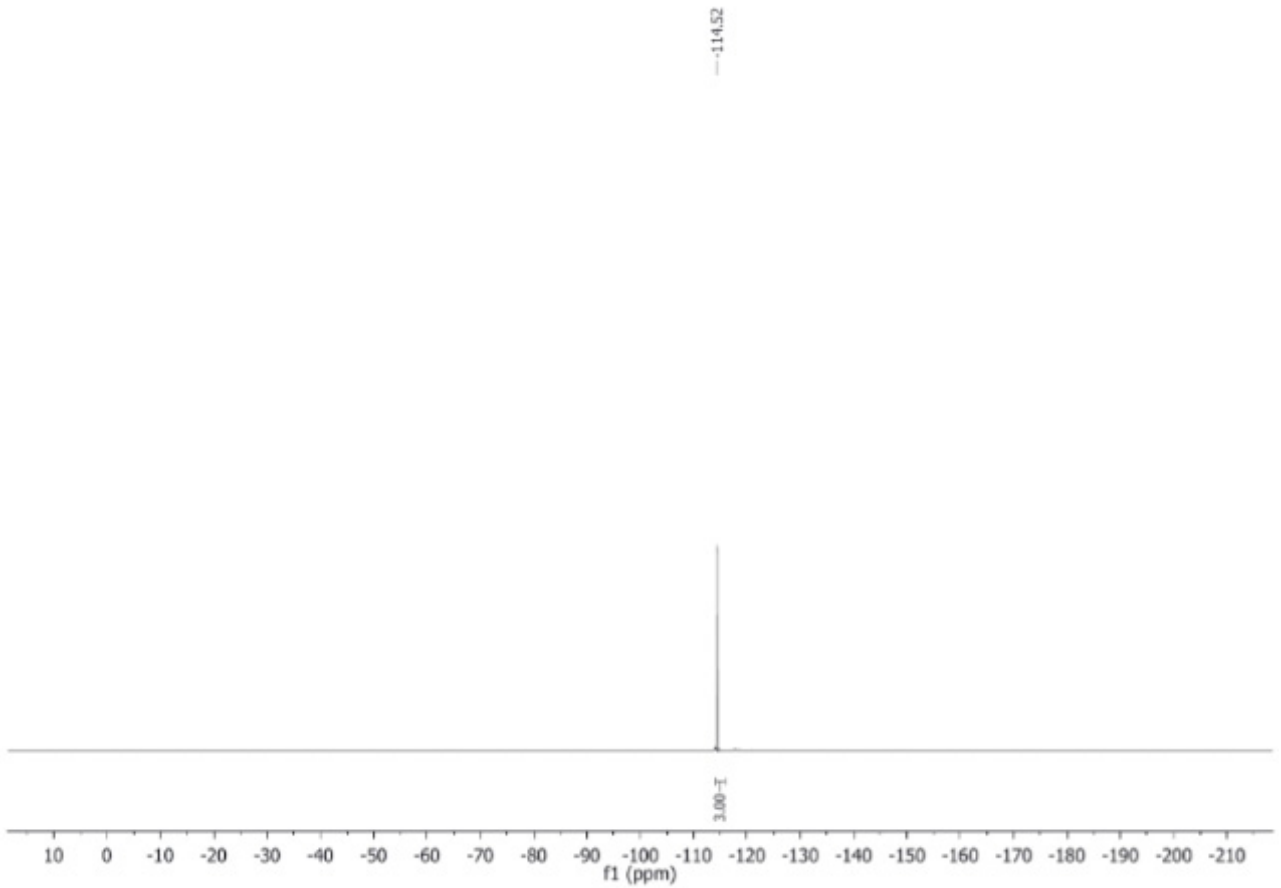

Figure S104: ^{19}F NMR spectrum (282 MHz, $CDCl_3$) of **14**.

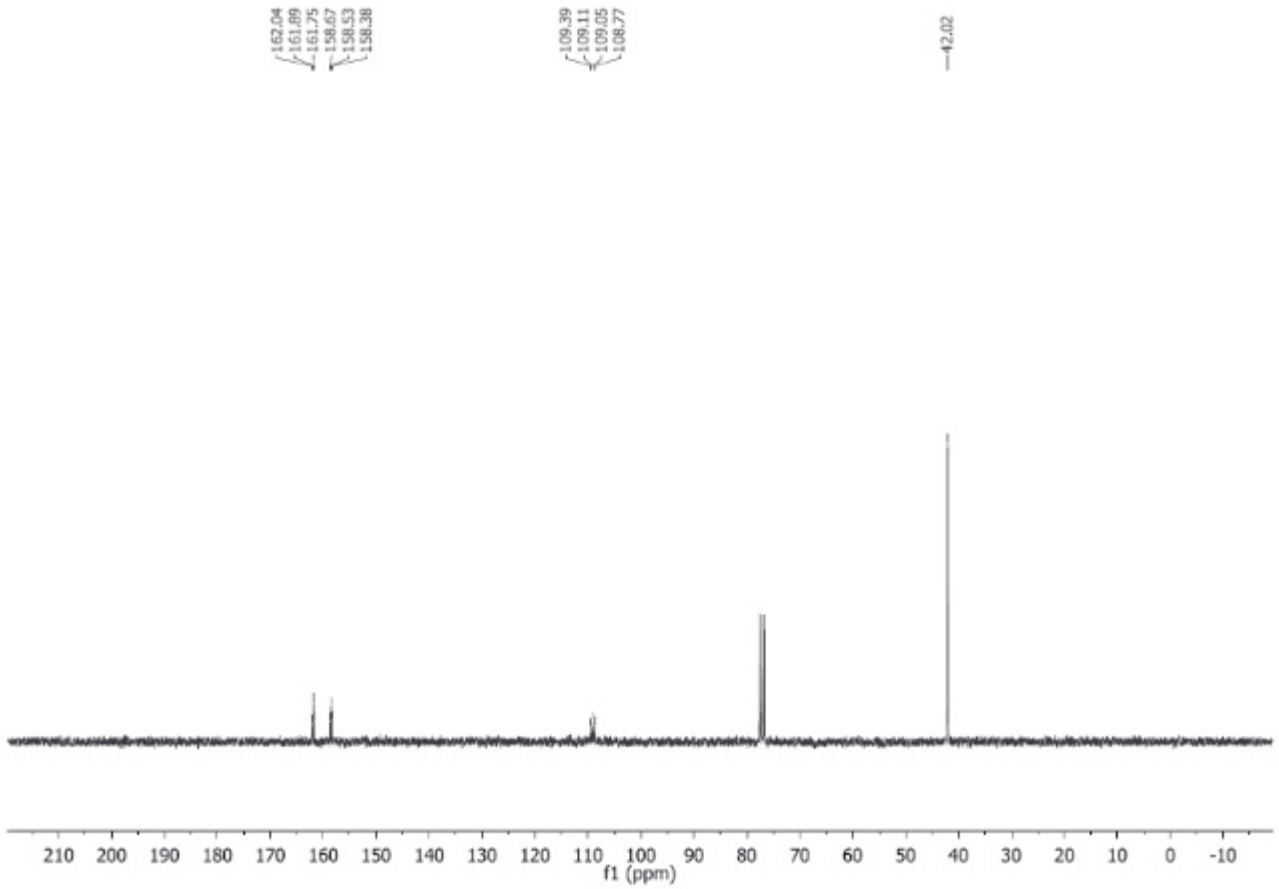

Figure S105: ^{13}C NMR spectrum (75 MHz, $CDCl_3$) of **14**.

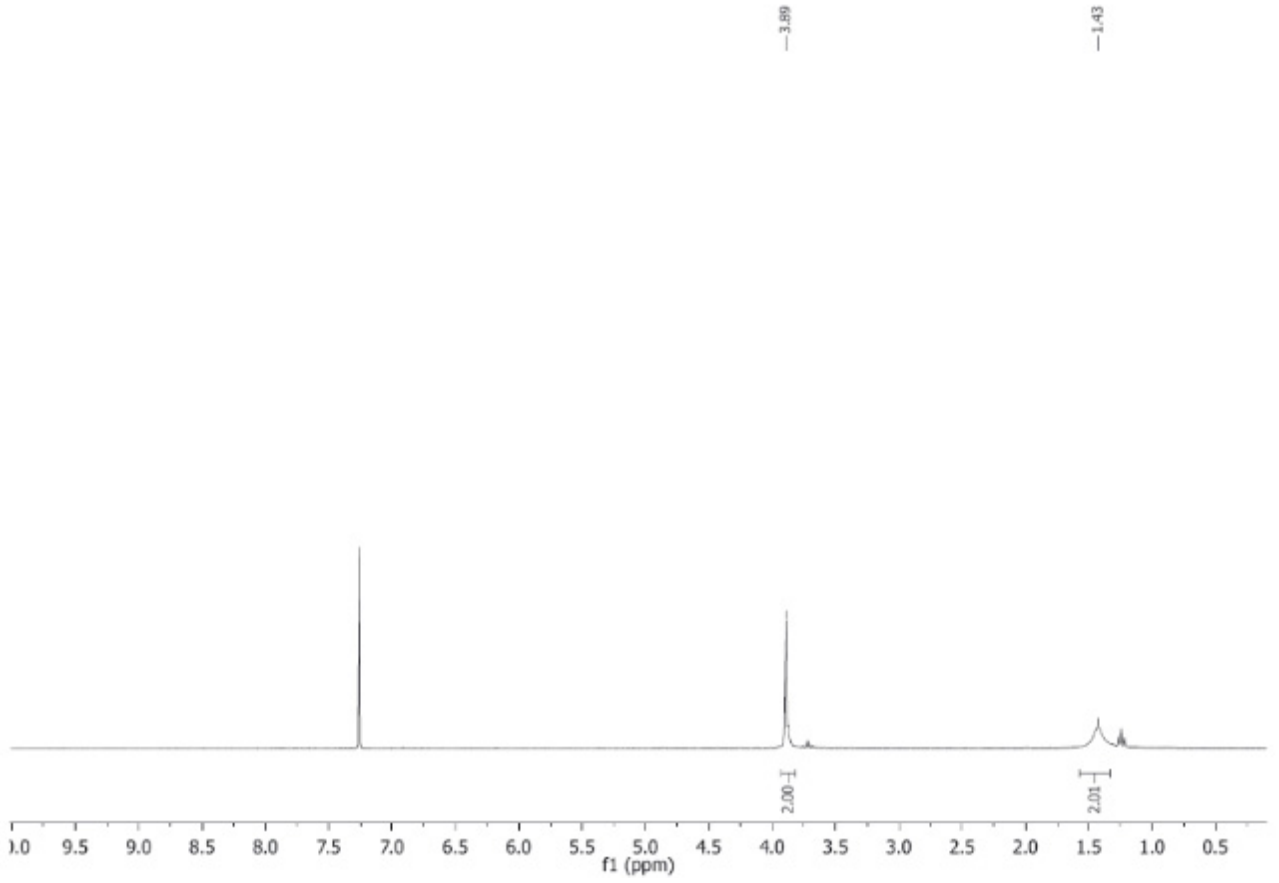

Figure S106: ^{1}H NMR spectrum (300 MHz, $CDCl_3$) of **F-Amine**.

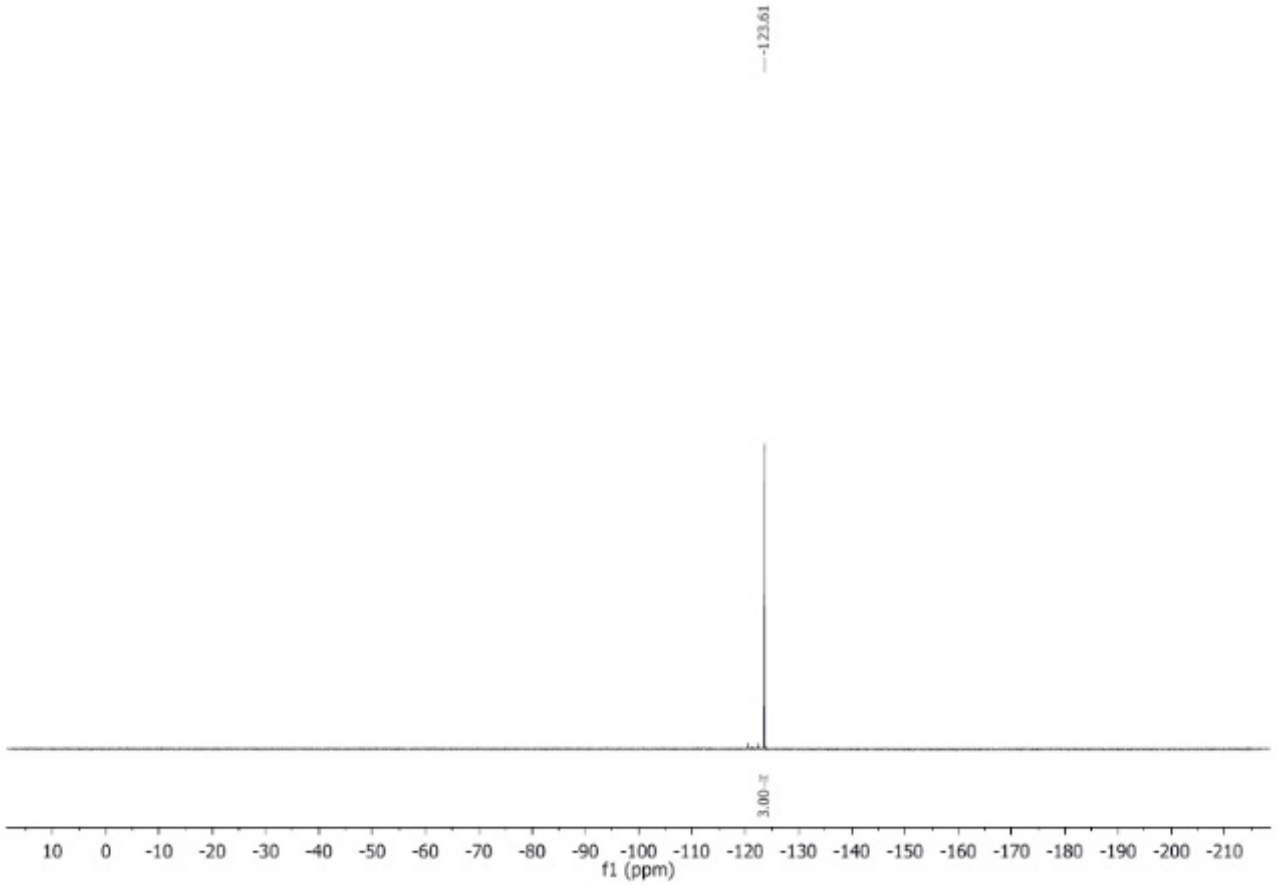

Figure S107: ^{19}F NMR spectrum (282 MHz, $CDCl_3$) of **F-Amine**.

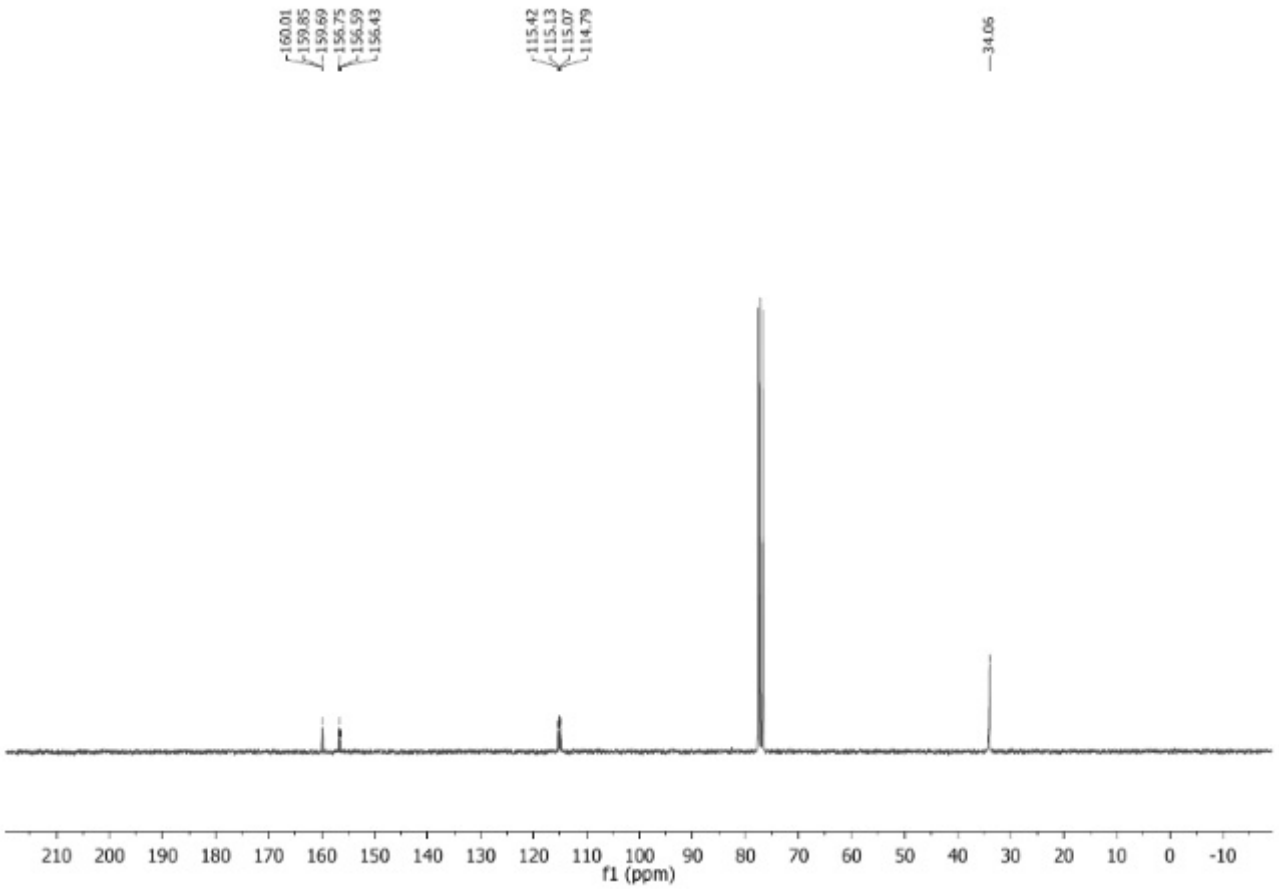

Figure S108: ^{13}C NMR spectrum (75 MHz, $CDCl_3$) of **F-Amine**.

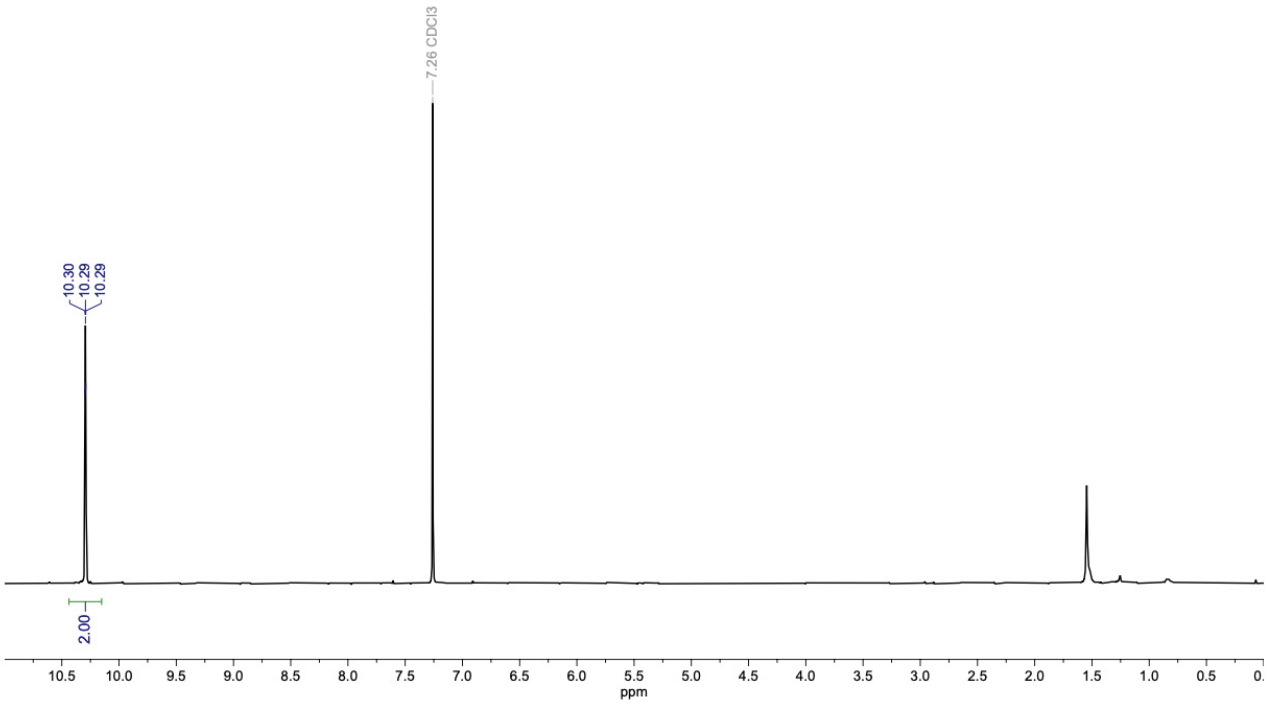

Figure S109: ^{1}H NMR spectrum (300 MHz, $CDCl_3$) of **15**.

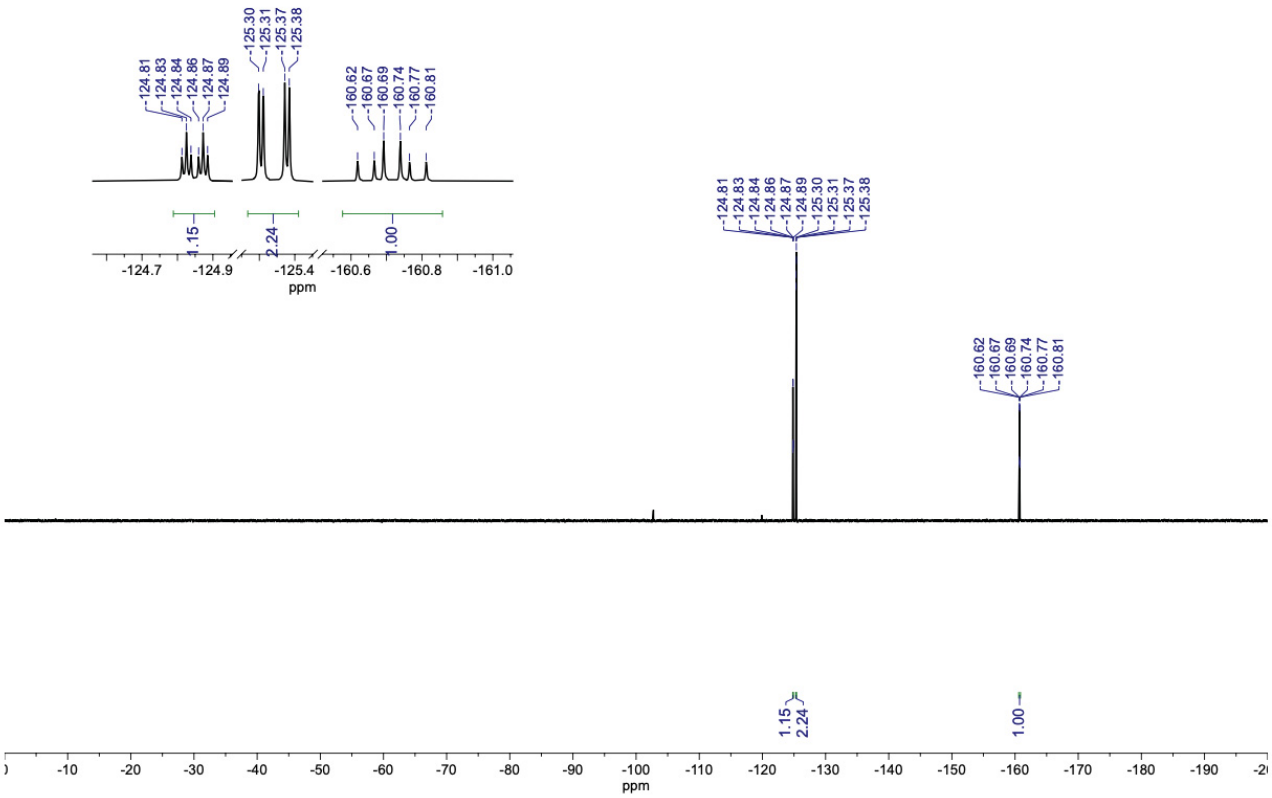

Figure S110: ^{19}F NMR spectrum (282 MHz, $CDCl_3$) of **15**.

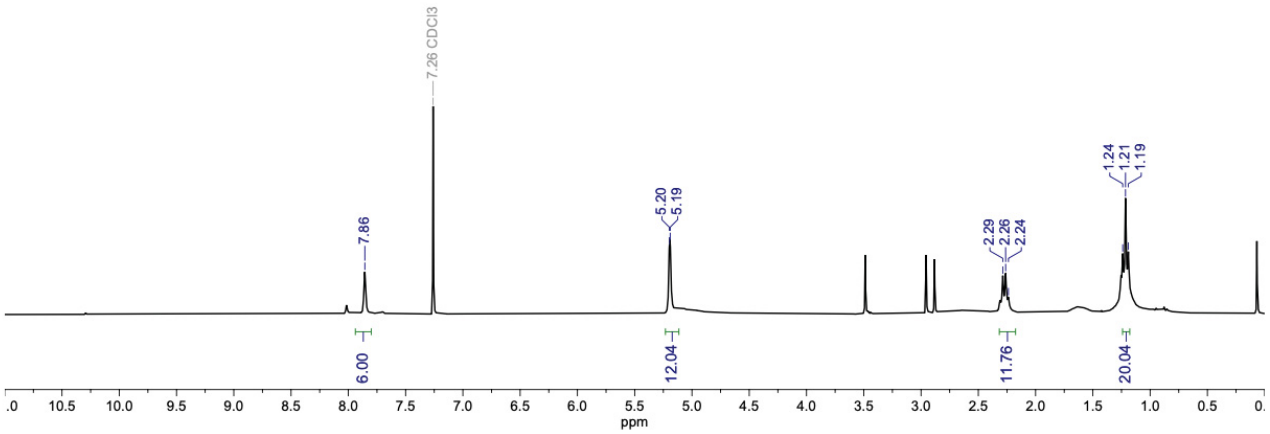

Figure S111: ^{1}H NMR spectrum (300 MHz, $CDCl_3$) of **FPOC1**.

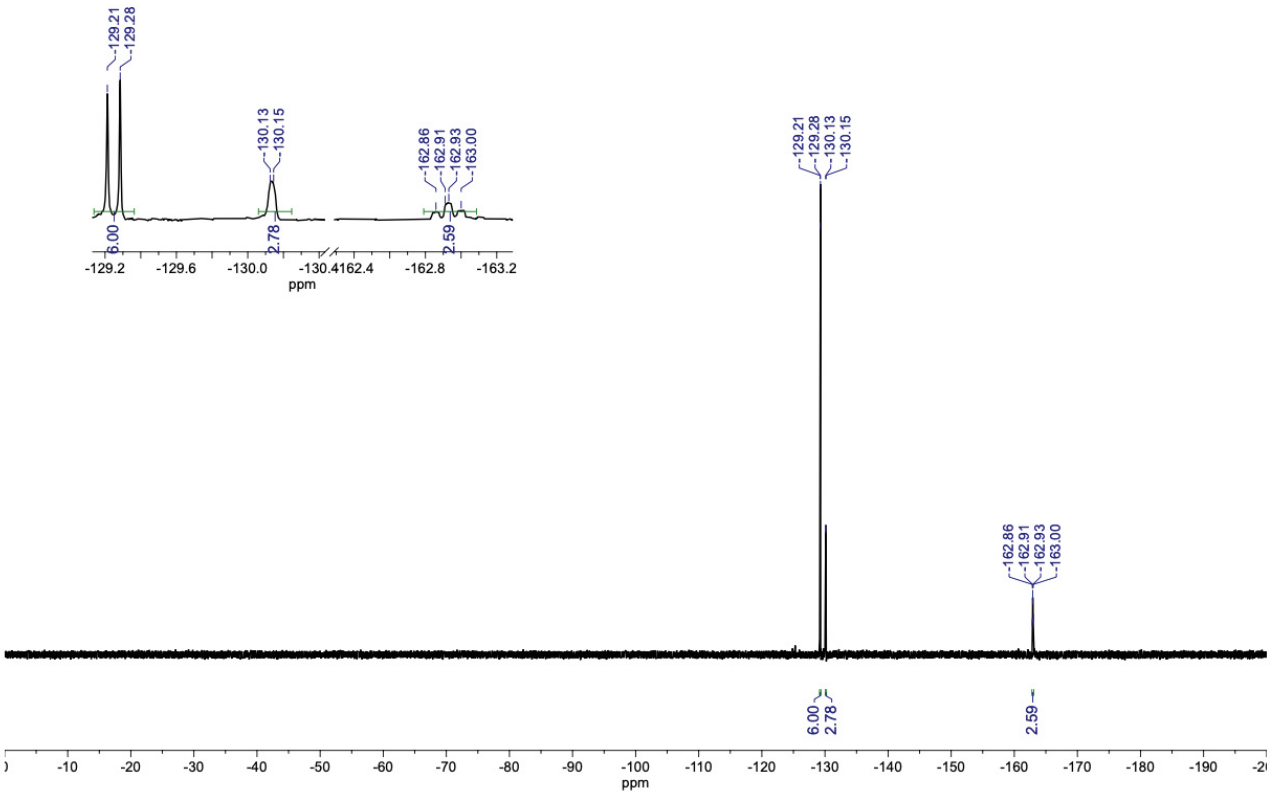

Figure S112: ^{19}F NMR spectrum (282 MHz, $CDCl_3$) of **FPOC1**.

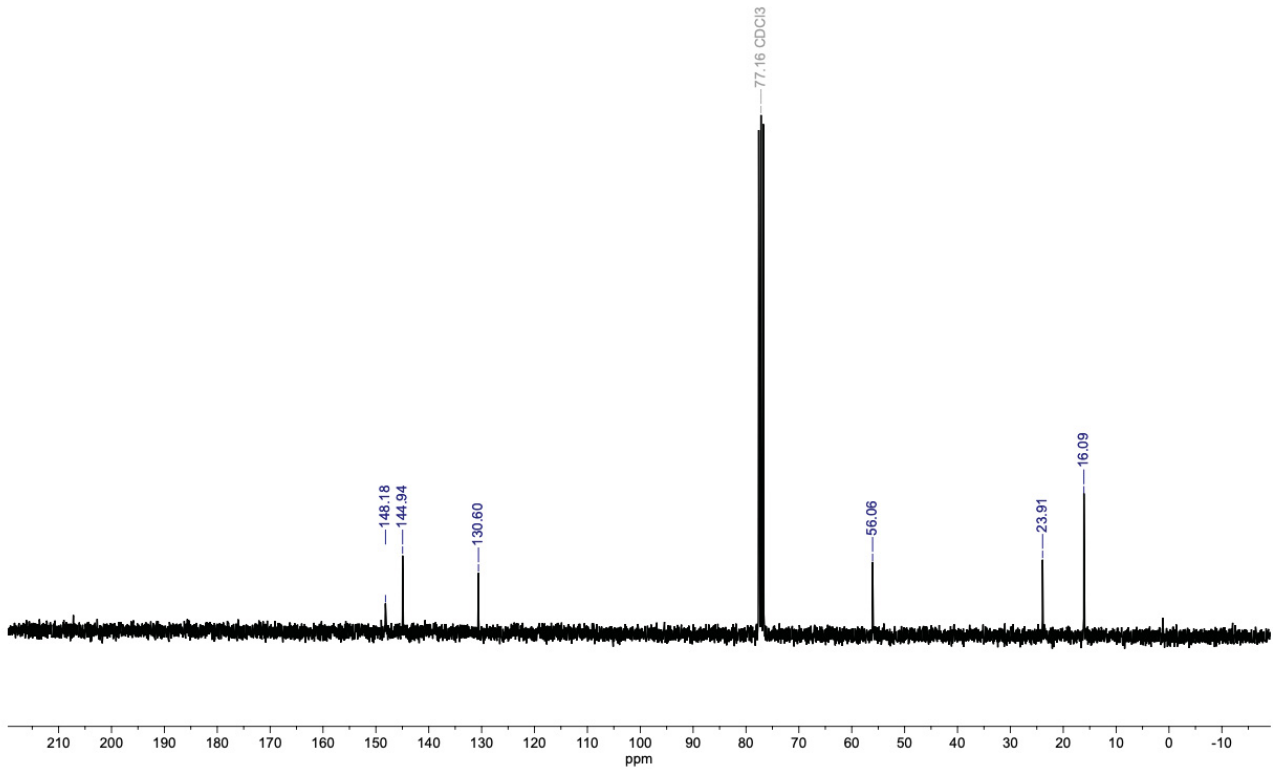

Figure S113: ^{13}C NMR spectrum (75 MHz, $CDCl_3$) of **FPOC1**.

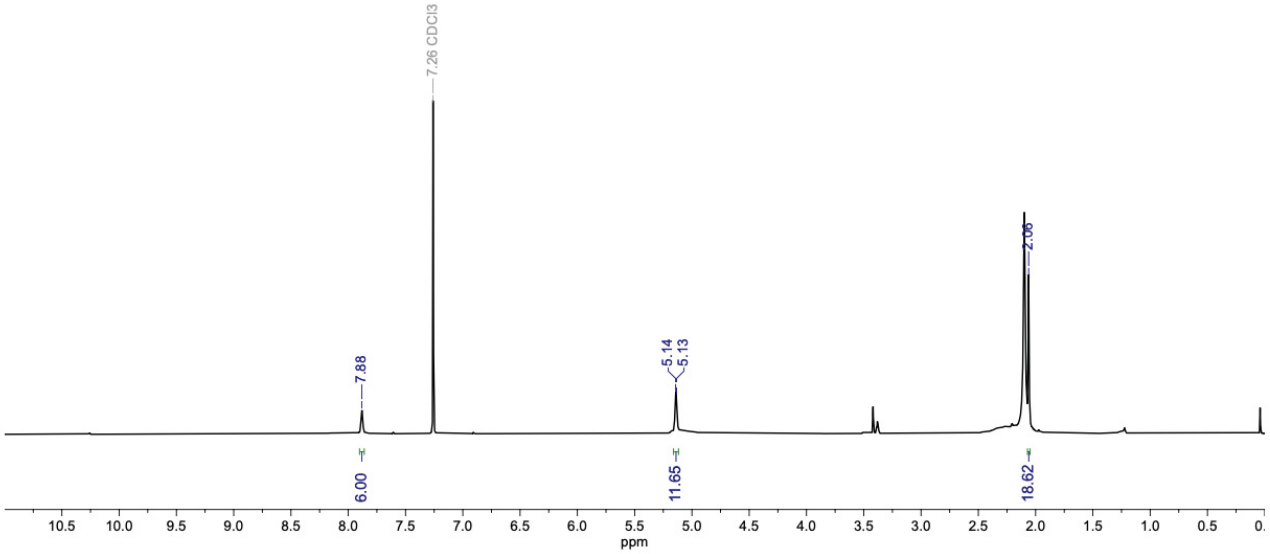

Figure S114: ^{1}H NMR of **FPOC2** (300 MHz, $CDCl_3$).

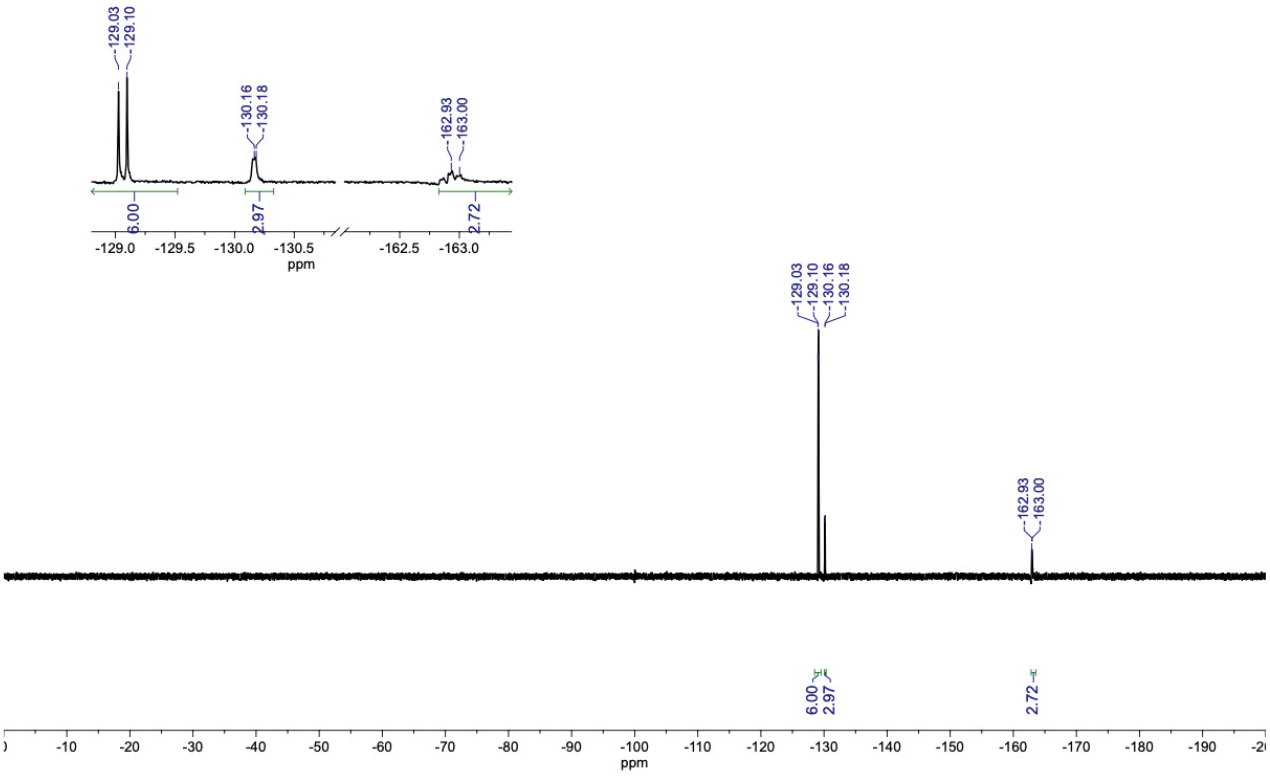

Figure S115: ^{19}F NMR spectrum (282 MHz, $CDCl_3$) of **FPOC2**.

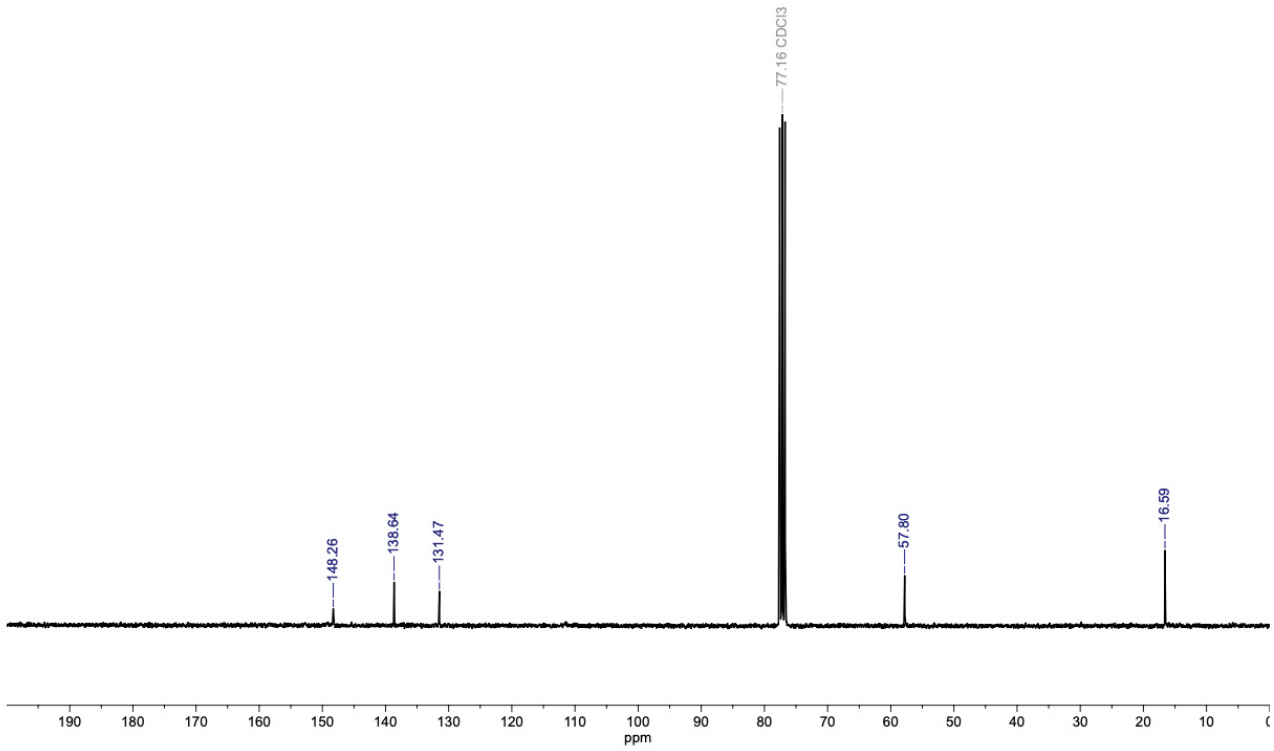

Figure S116: ^{13}C NMR spectrum (75 MHz, $CDCl_3$) of **FPOC2**.

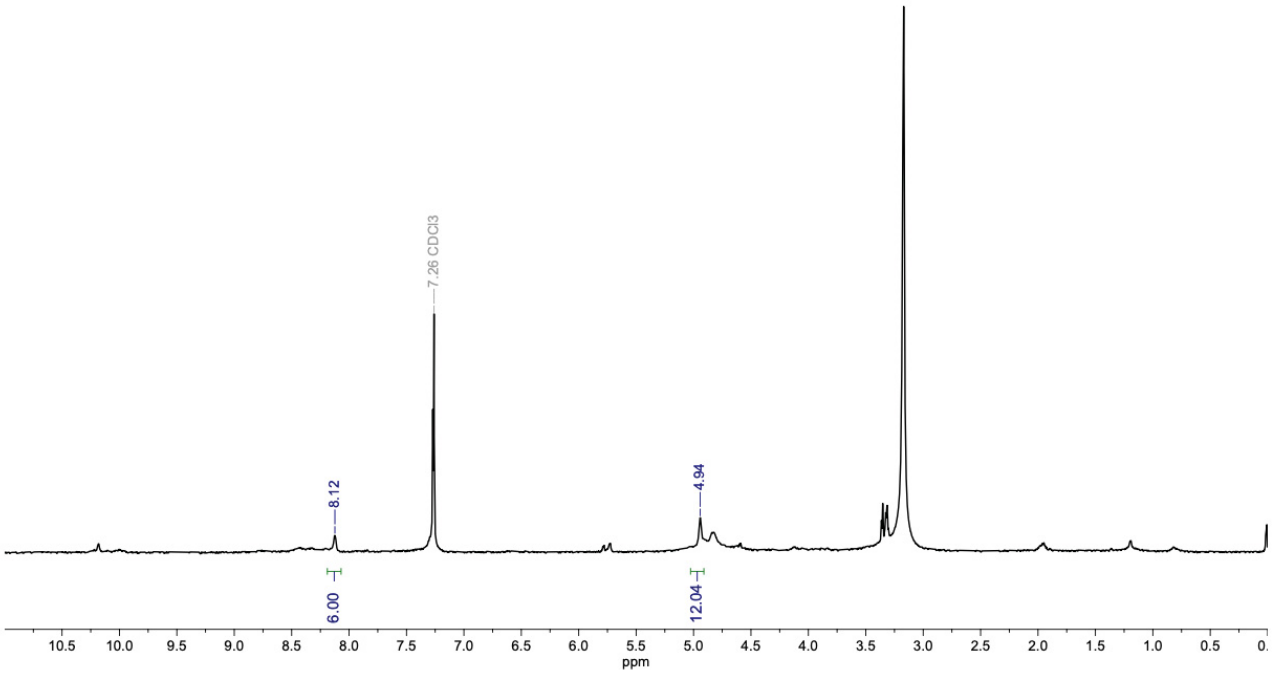

Figure S117: ^{1}H NMR of **FPOC3** (300 MHz, $CDCl_3$). Low intensity signals can be attributed to the formation of lower mass oligomers, that precipitate from the solution along with the cage compound.

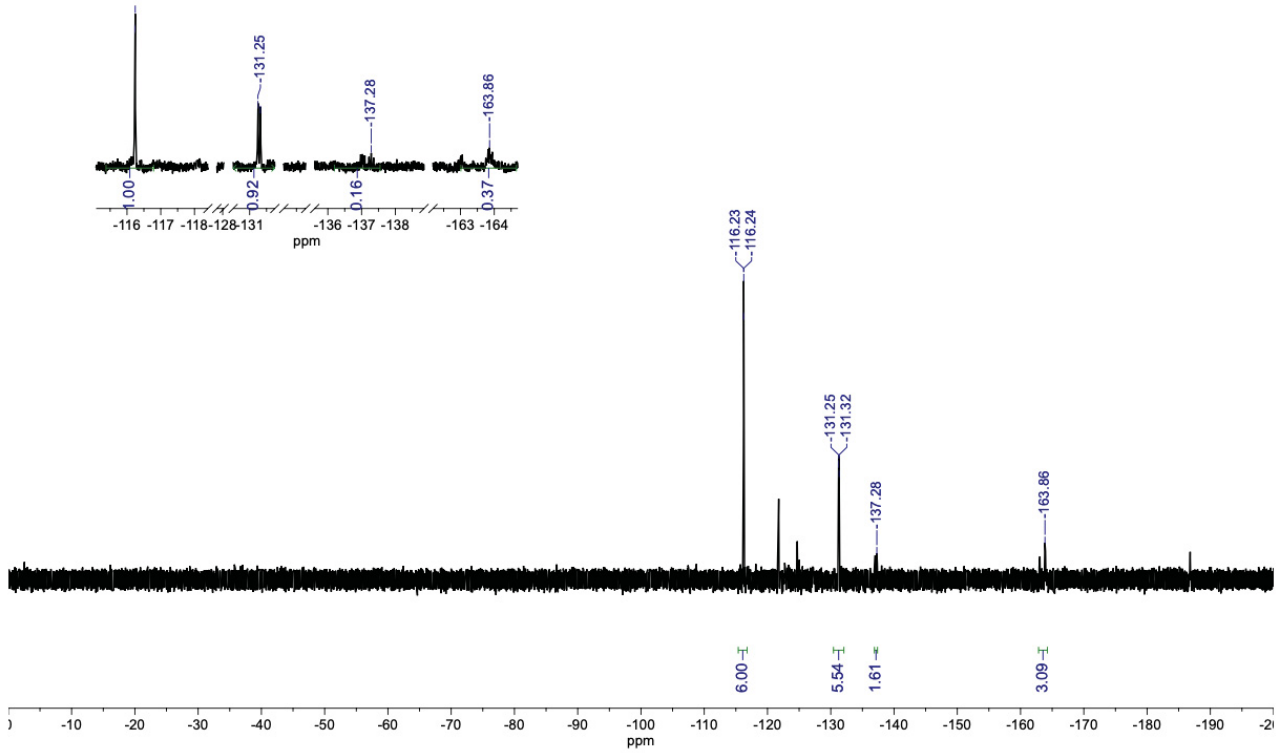

Figure S118: ^{19}F NMR spectrum (282 MHz, $CDCl_3$) of **FPOC3**. Low intensity signals can be attributed to the formation of lower mass oligomers, that precipitate from the solution along with the cage compound.

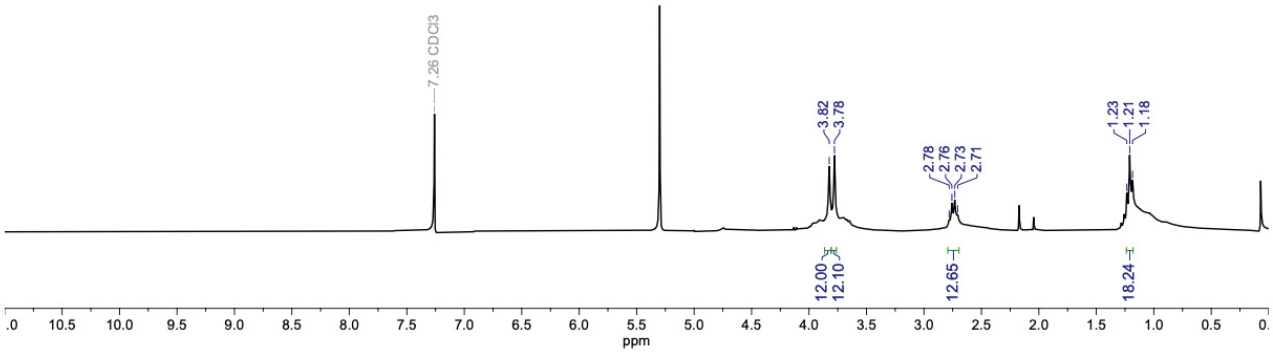

Figure S119: ^{1}H NMR spectrum (300 MHz, $CDCl_3$) of **RFPOC1**.

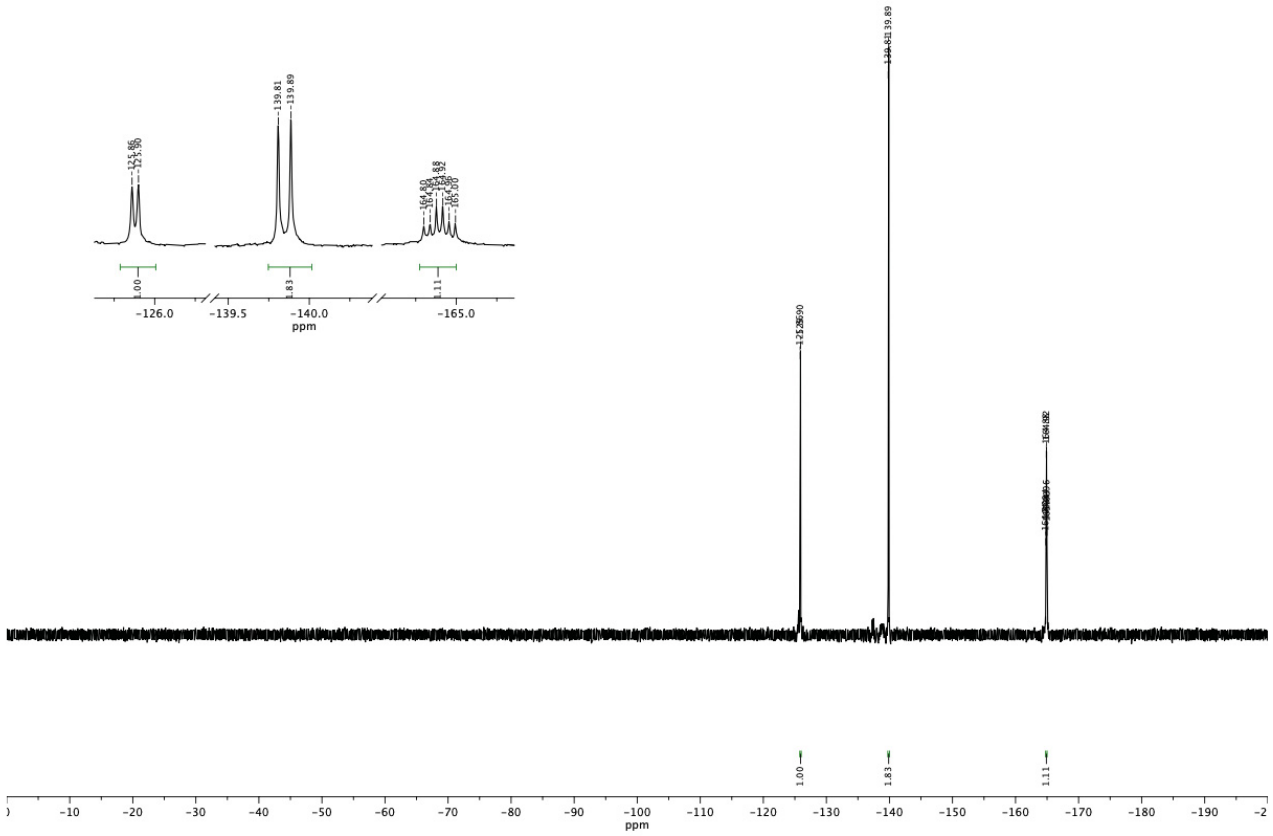

Figure S120: ^{19}F NMR spectrum (282 MHz, $CDCl_3$) of **RFPOC1**.

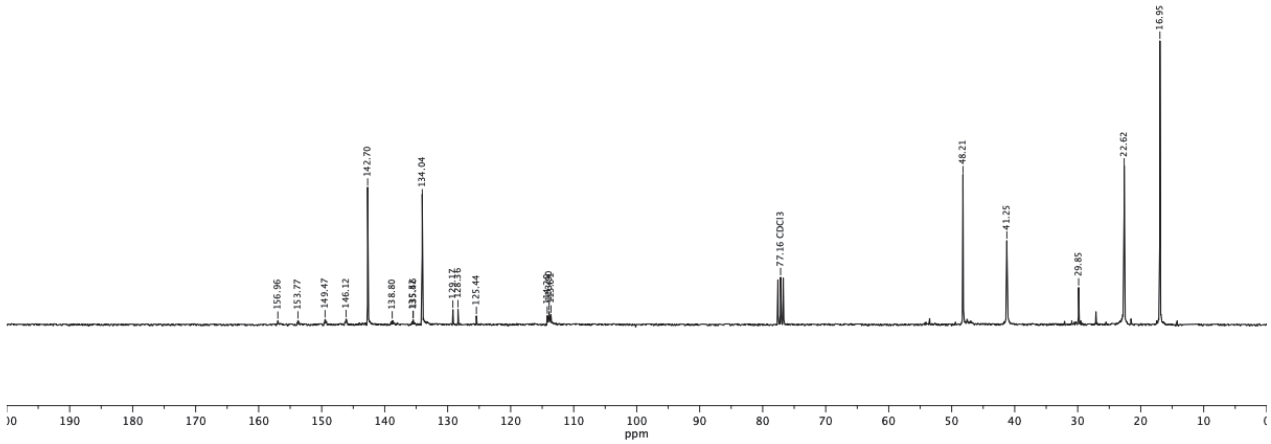

Figure S121: ^{13}C NMR spectrum (75 MHz, $CDCl_3$) of **RFPOC1**.

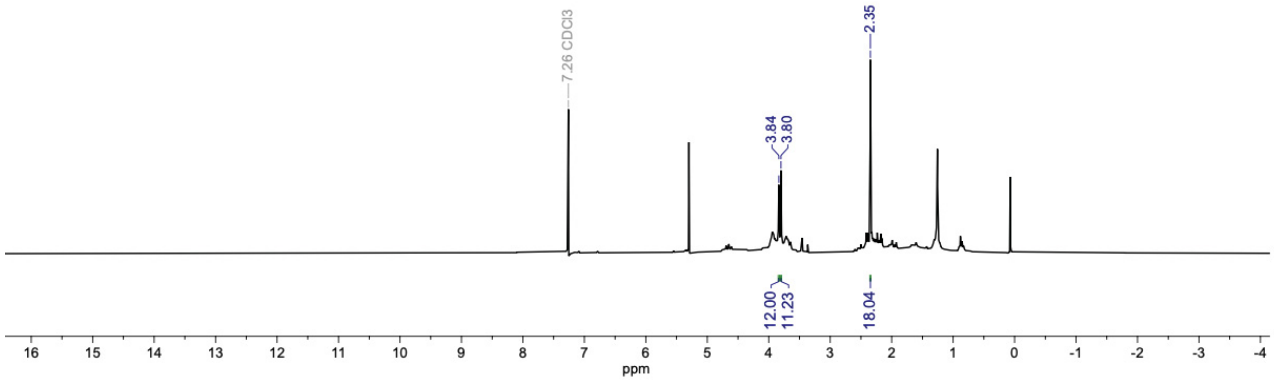

Figure S122: ^{1}H NMR spectrum (300 MHz, $CDCl_3$) of **RFPOC2**.

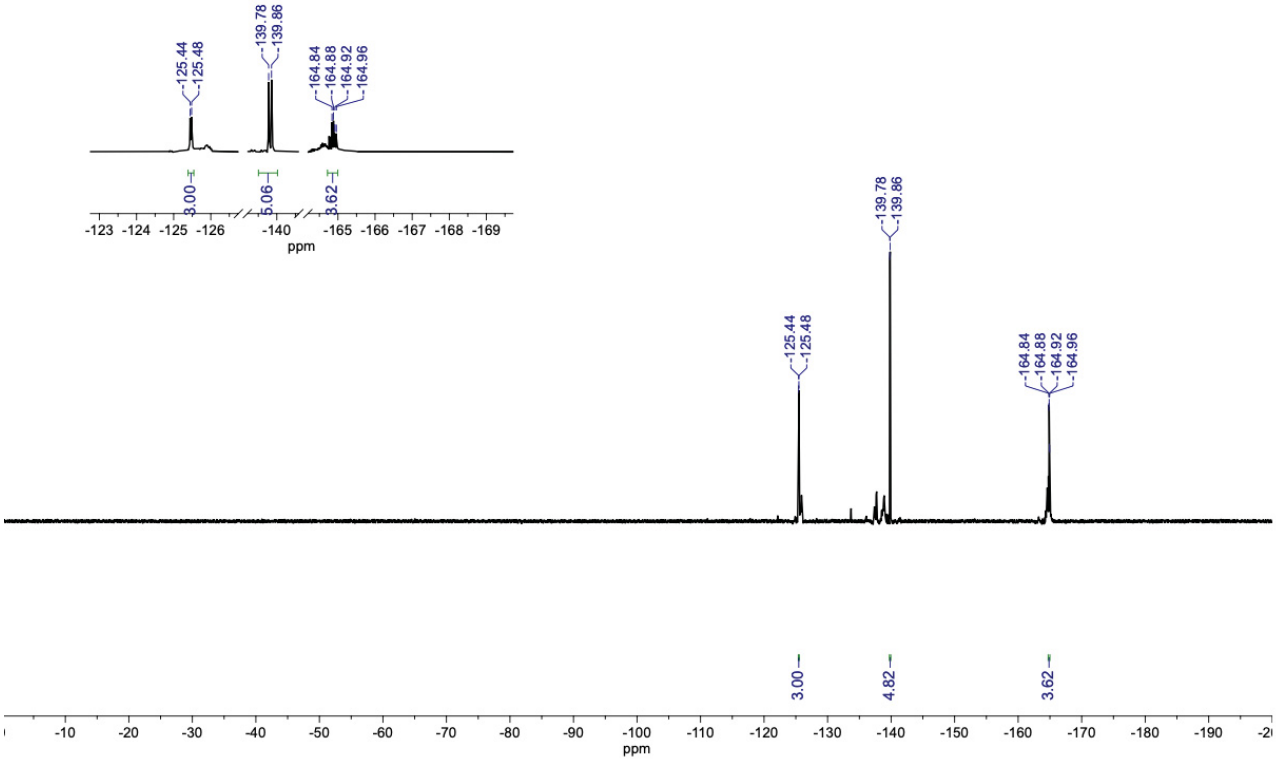

Figure S123: ^{19}F NMR spectrum (282 MHz, $CDCl_3$) of **RFPOC2**.

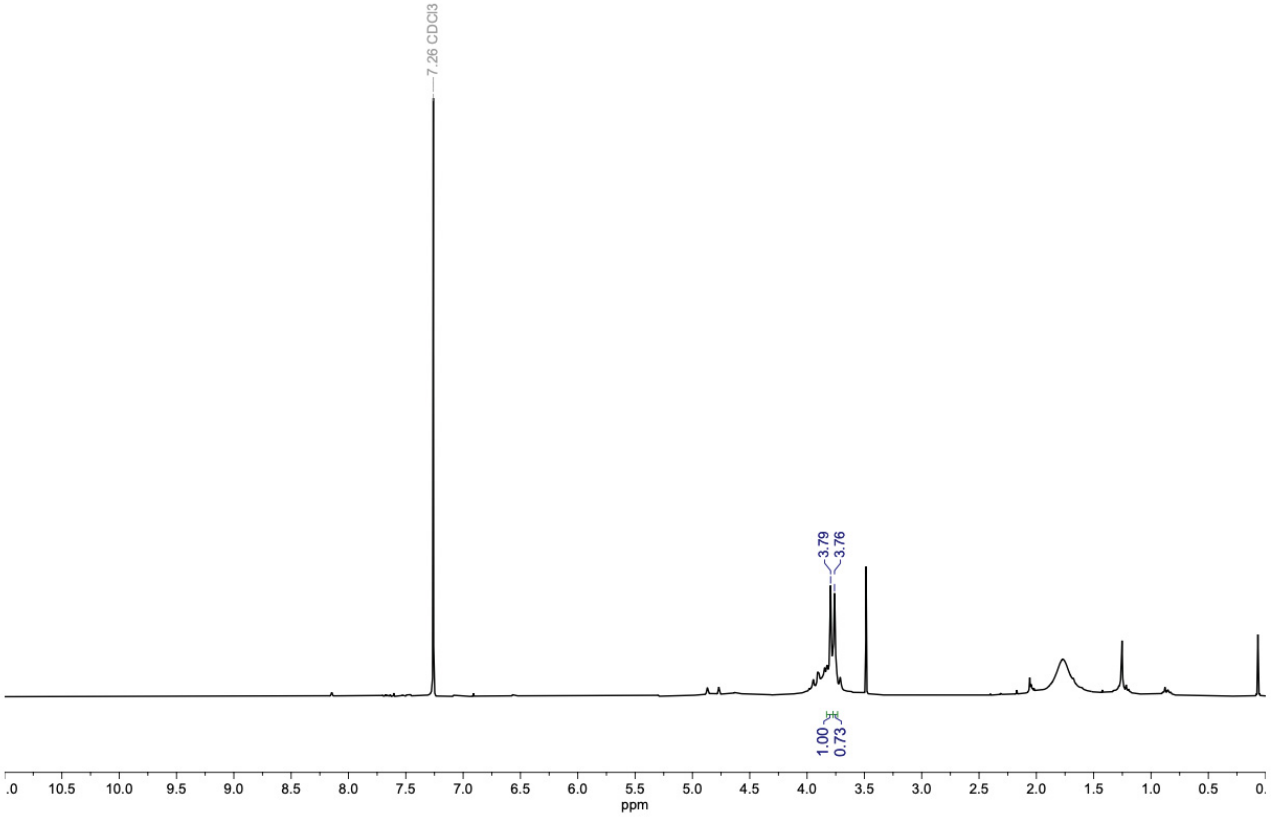

Figure S124: ^{1}H NMR spectrum (300 MHz, $CDCl_3$) of **RFPOC3**.

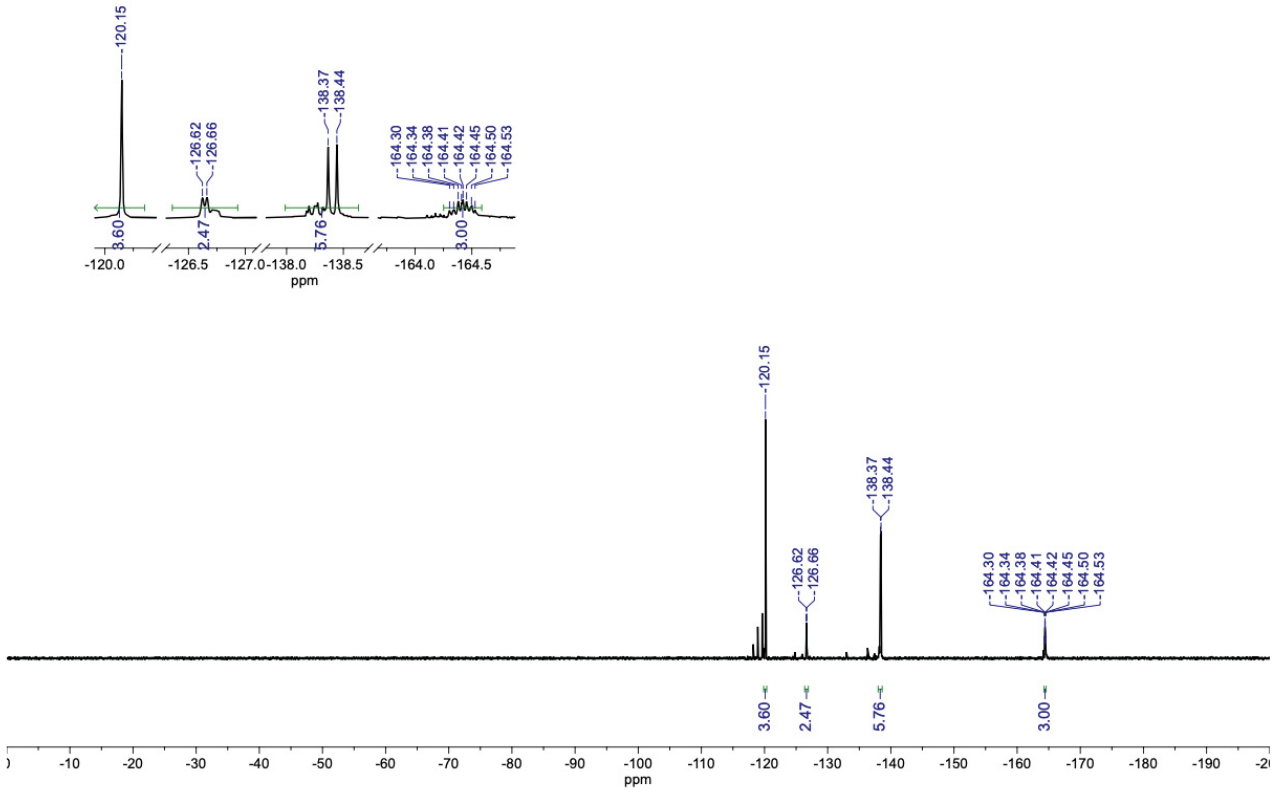

Figure S125: ^{19}F NMR spectrum (282 MHz, $CDCl_3$) of **RFPOC3**. Signals with lower intensity can be assigned to decomposed oligomeric structures of **FPOC3**.

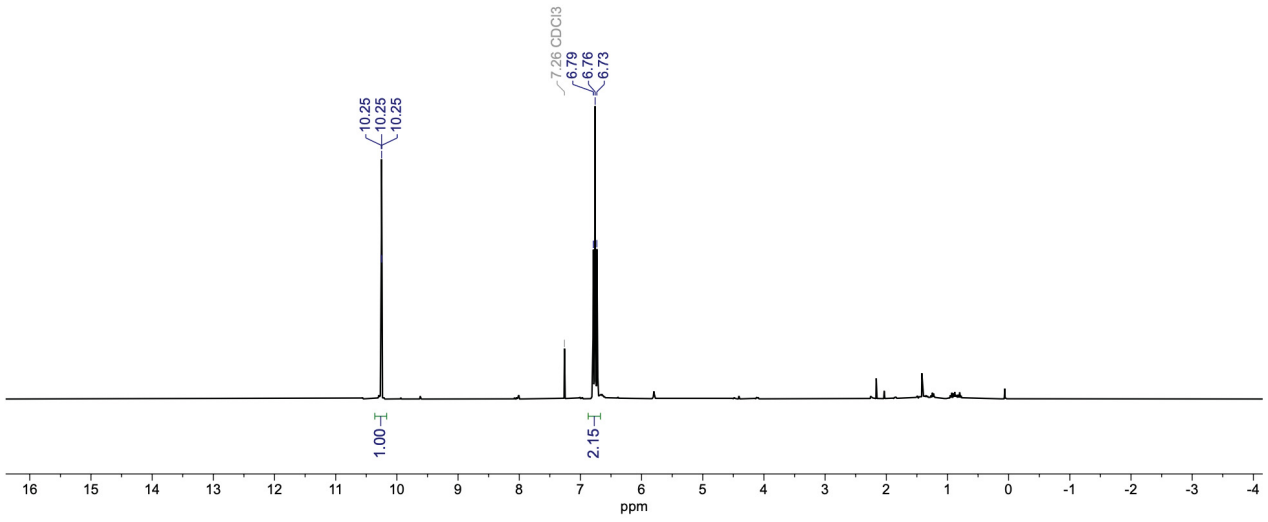

Figure S126: ^{1}H NMR of **16** (300 MHz, $CDCl_3$).

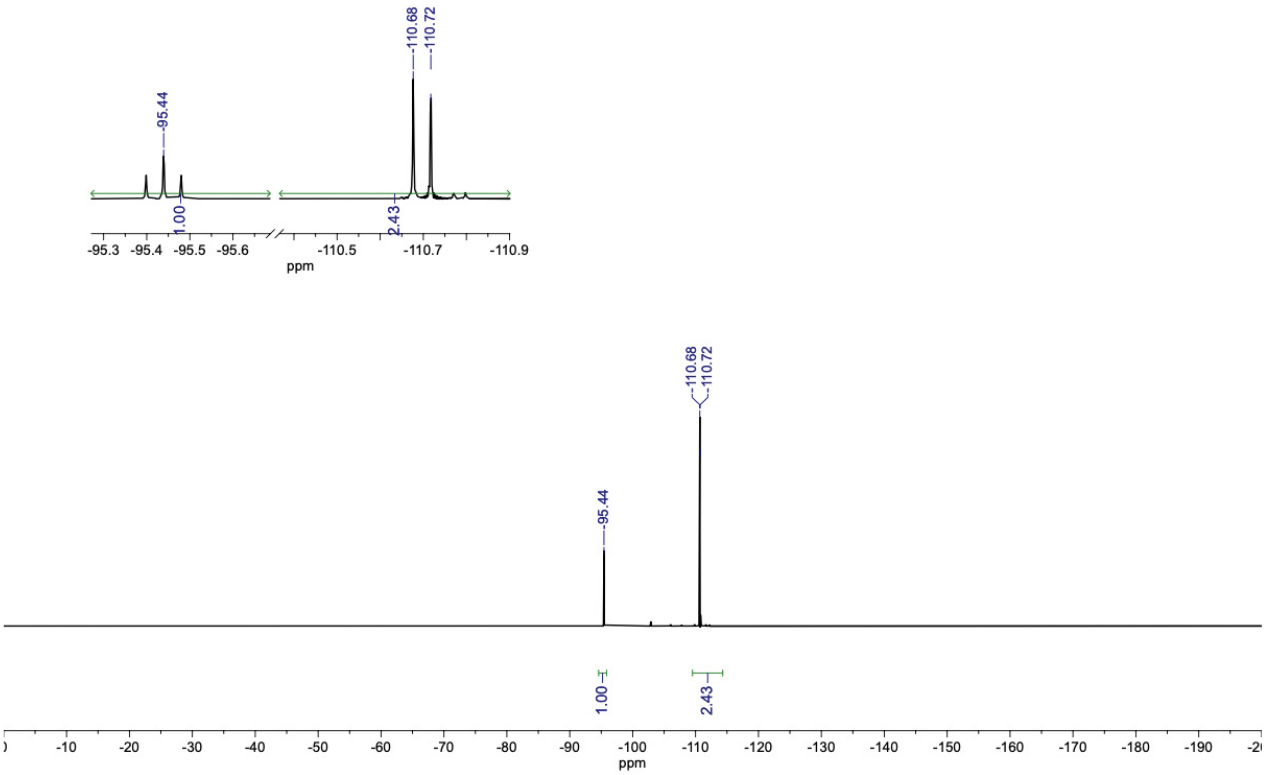

Figure S127: ^{19}F NMR spectrum (282 MHz, $CDCl_3$) of **16**.

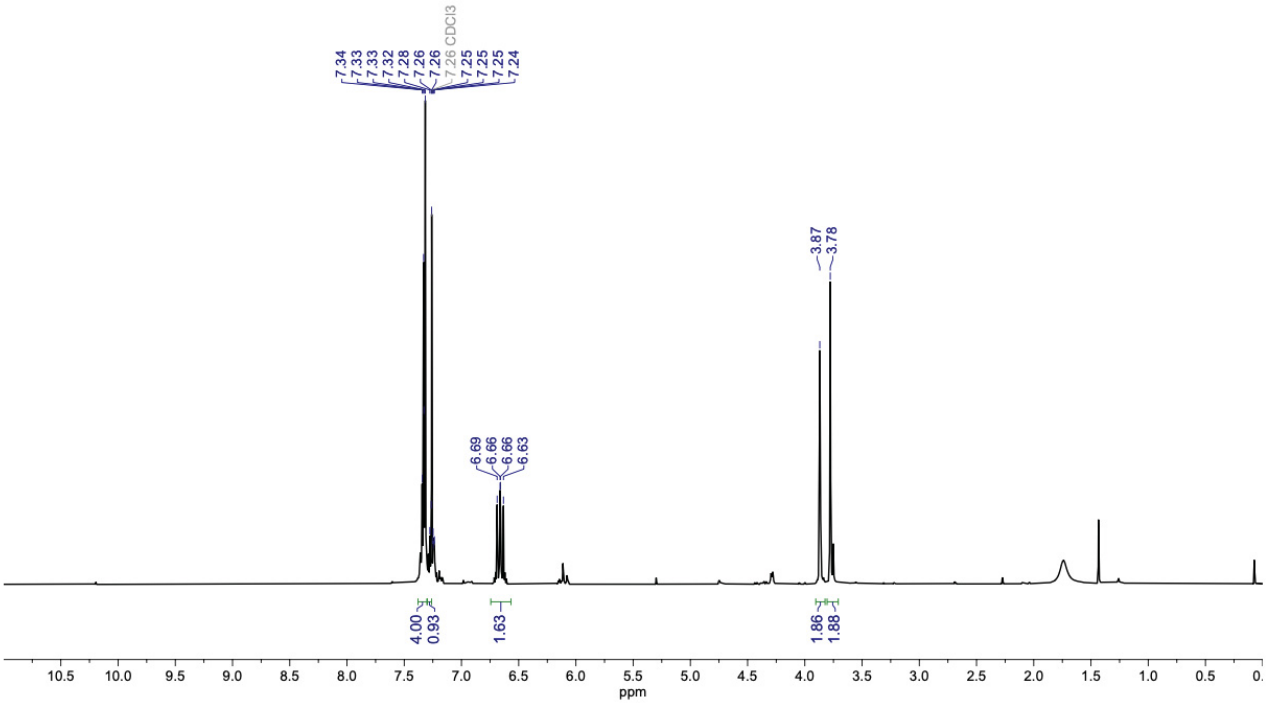

Figure S128: ^{1}H NMR spectrum (300 MHz, $CDCl_3$) of **18**.

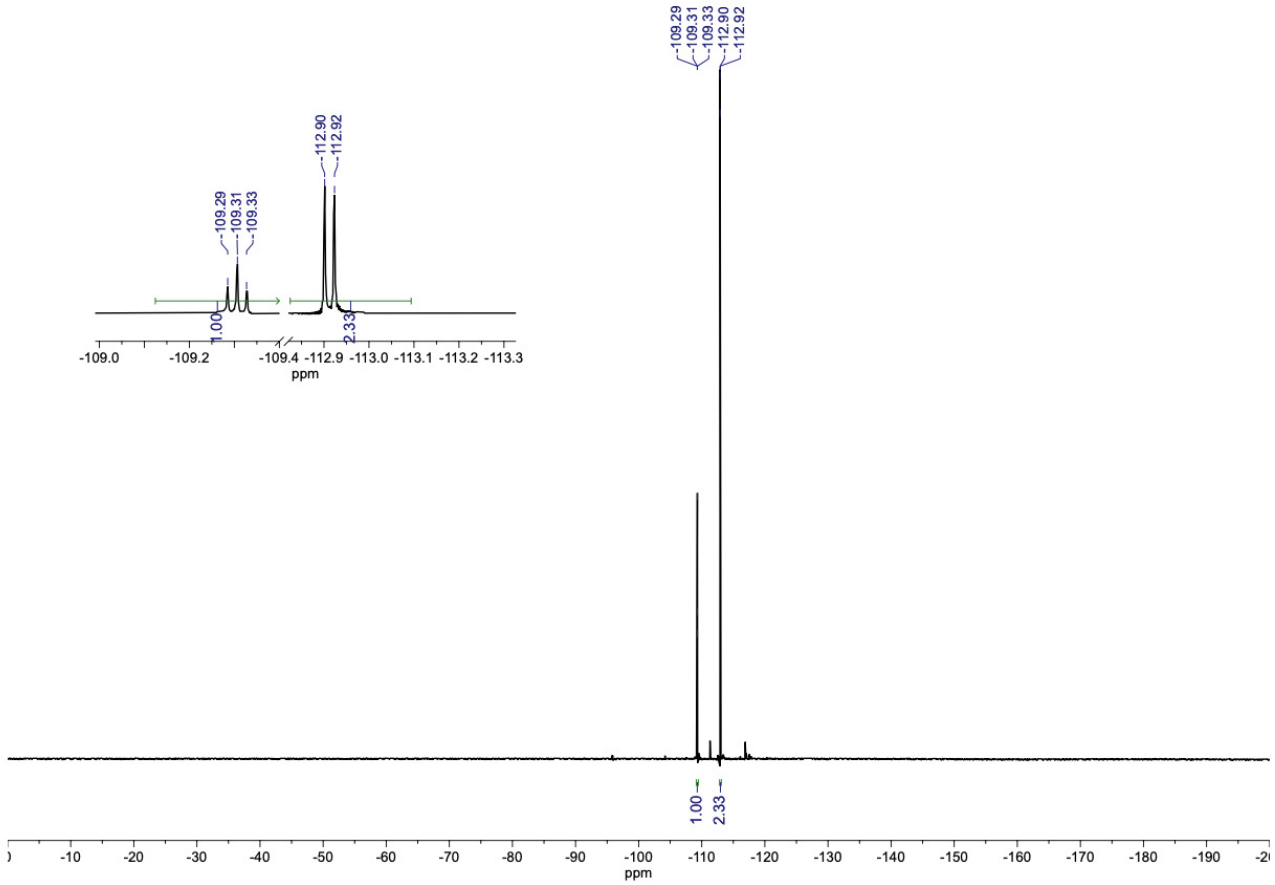

Figure S129: ^{19}F NMR spectrum (282 MHz, $CDCl_3$) of **18**.

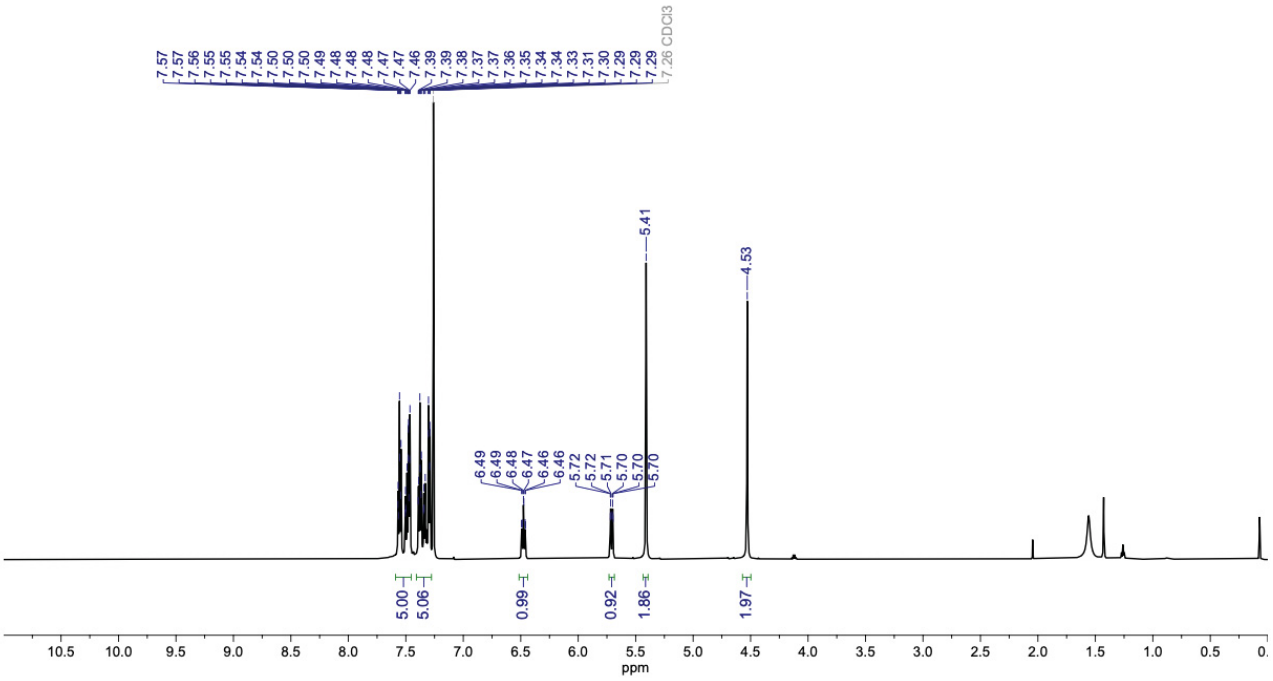

Figure S130: ^{1}H NMR spectrum (300 MHz, $CDCl_3$) of **19**.

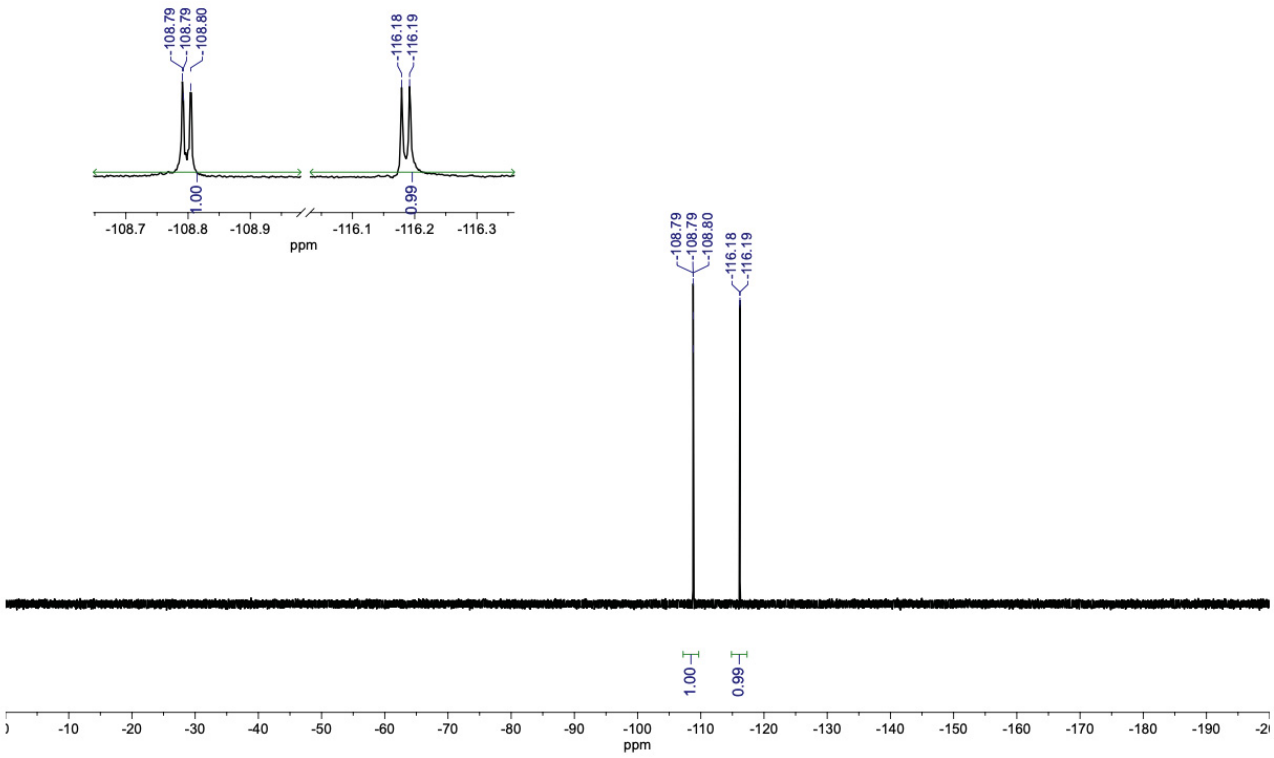

Figure S131: ^{19}F NMR spectrum (300 MHz, $CDCl_3$) of **19**.

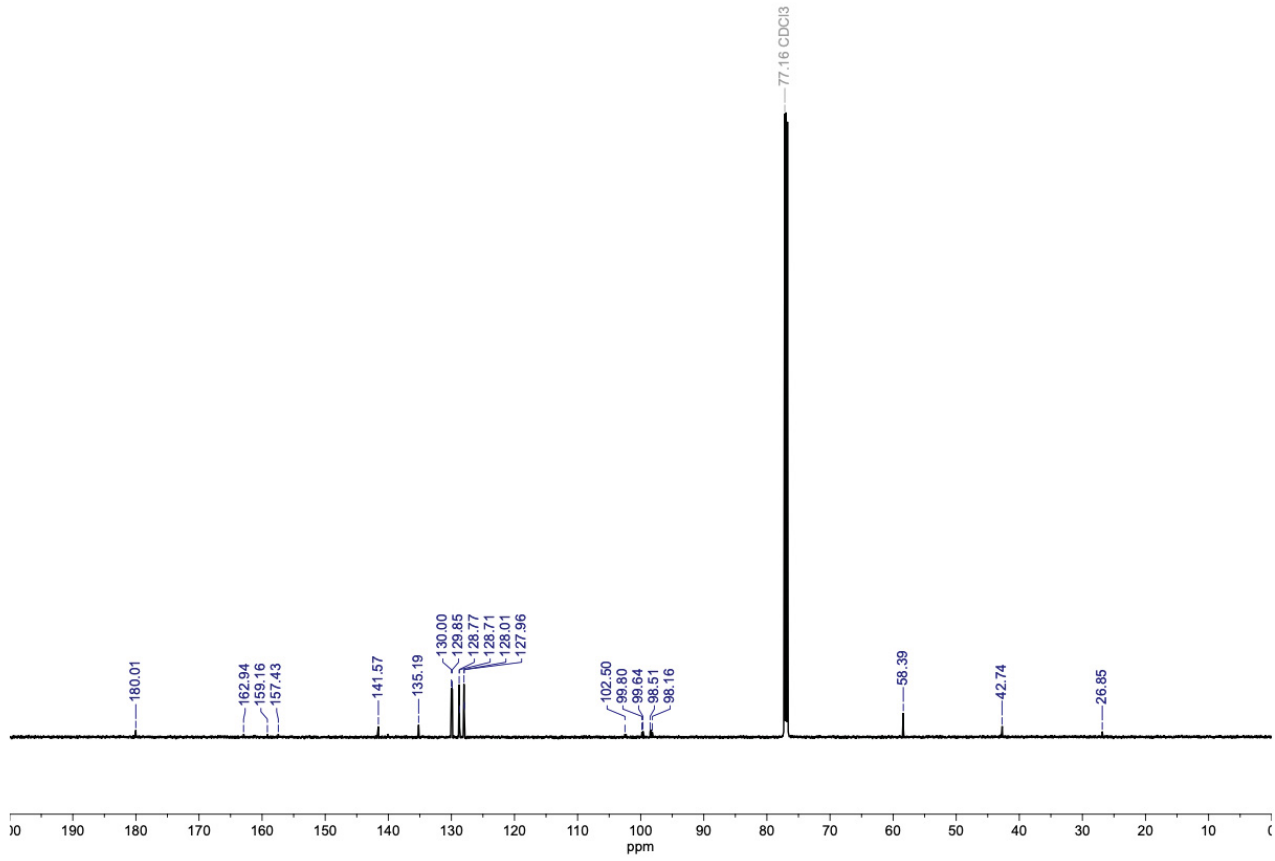

Figure S132:^{13}C NMR spectrum (300 MHz, $CDCl_3$) of **19**.

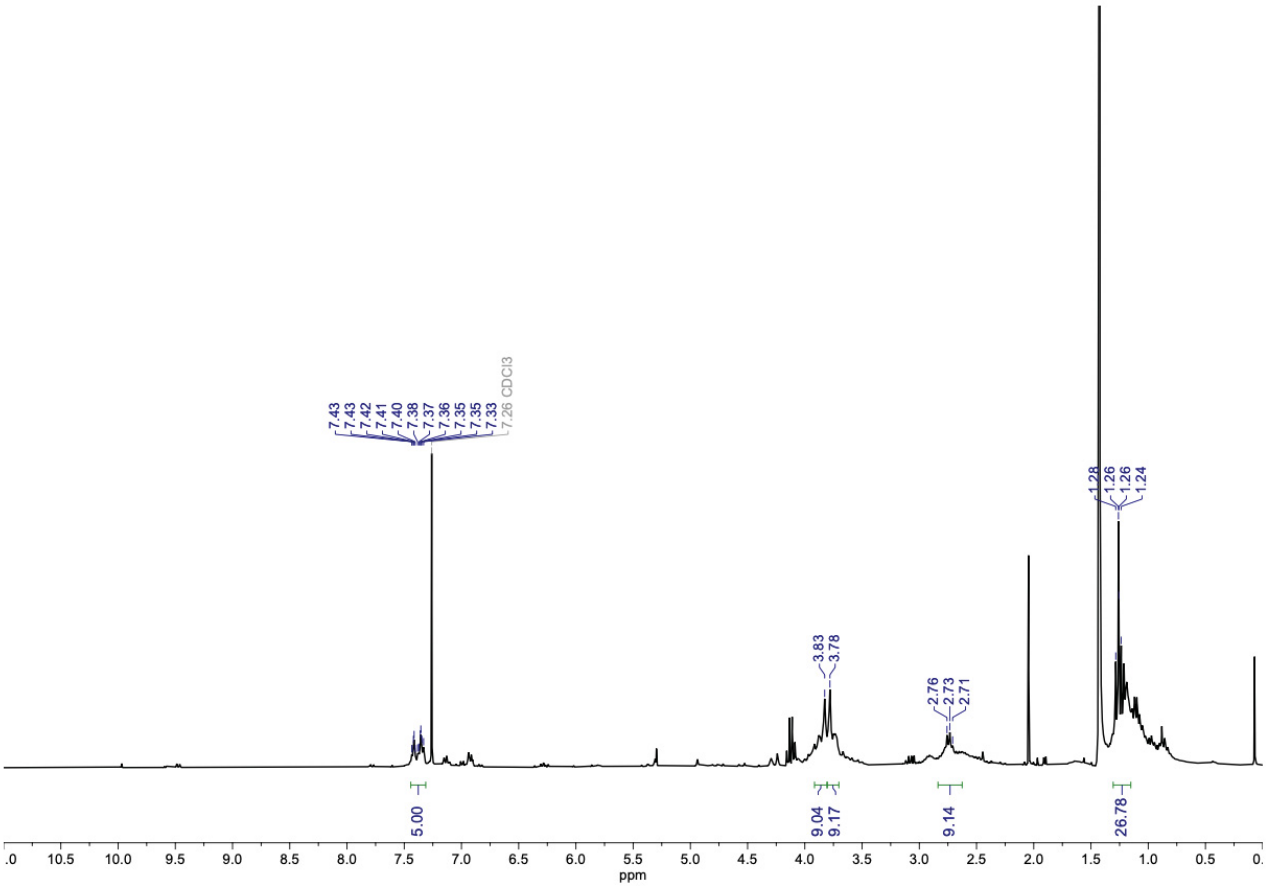

Figure S133: ^{1}H NMR spectrum (300 MHz, $CDCl_3$) of the product mixture **20** + **21**.

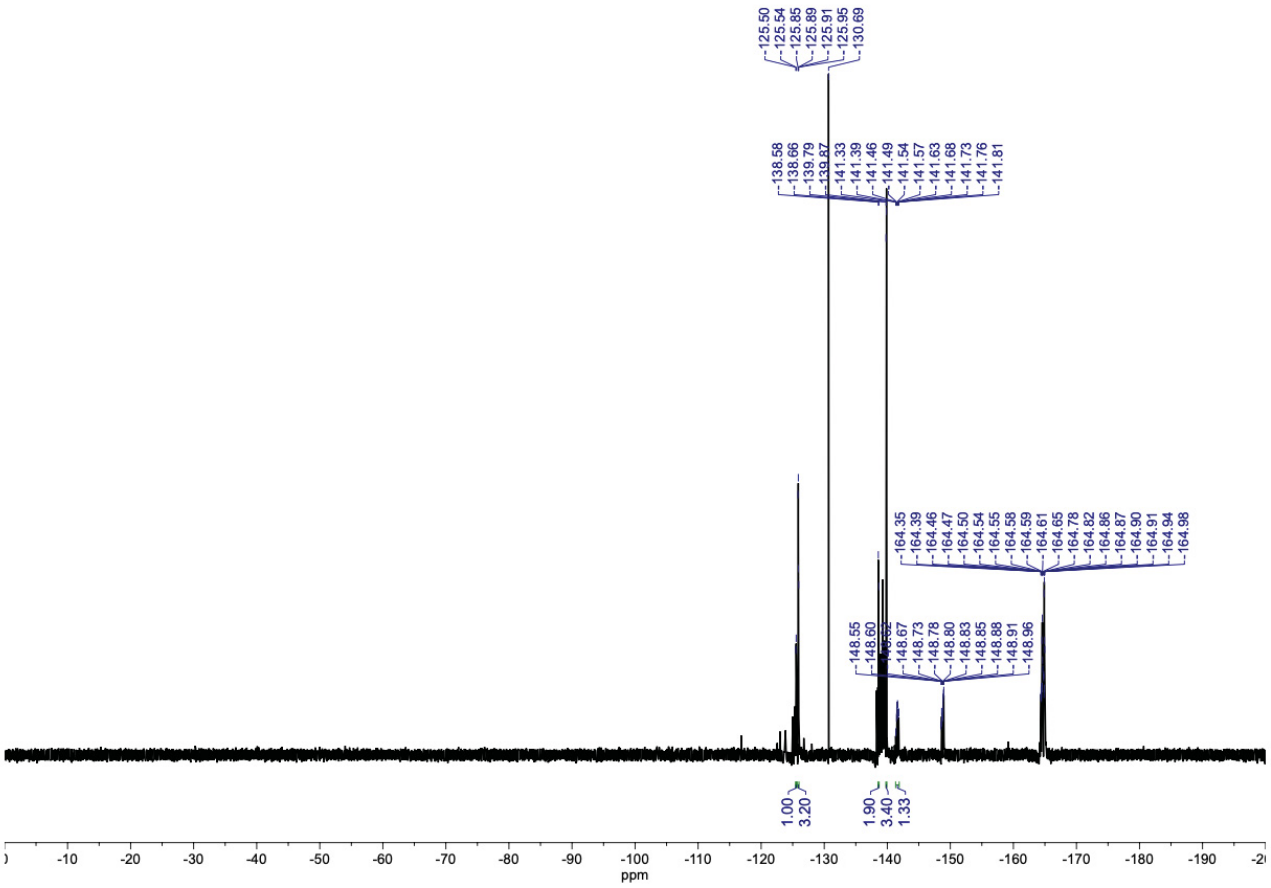

Figure S134: ^{19}F NMR spectrum (282 MHz, $CDCl_3$) of the product mixture **20** + **21**.

IR spectra

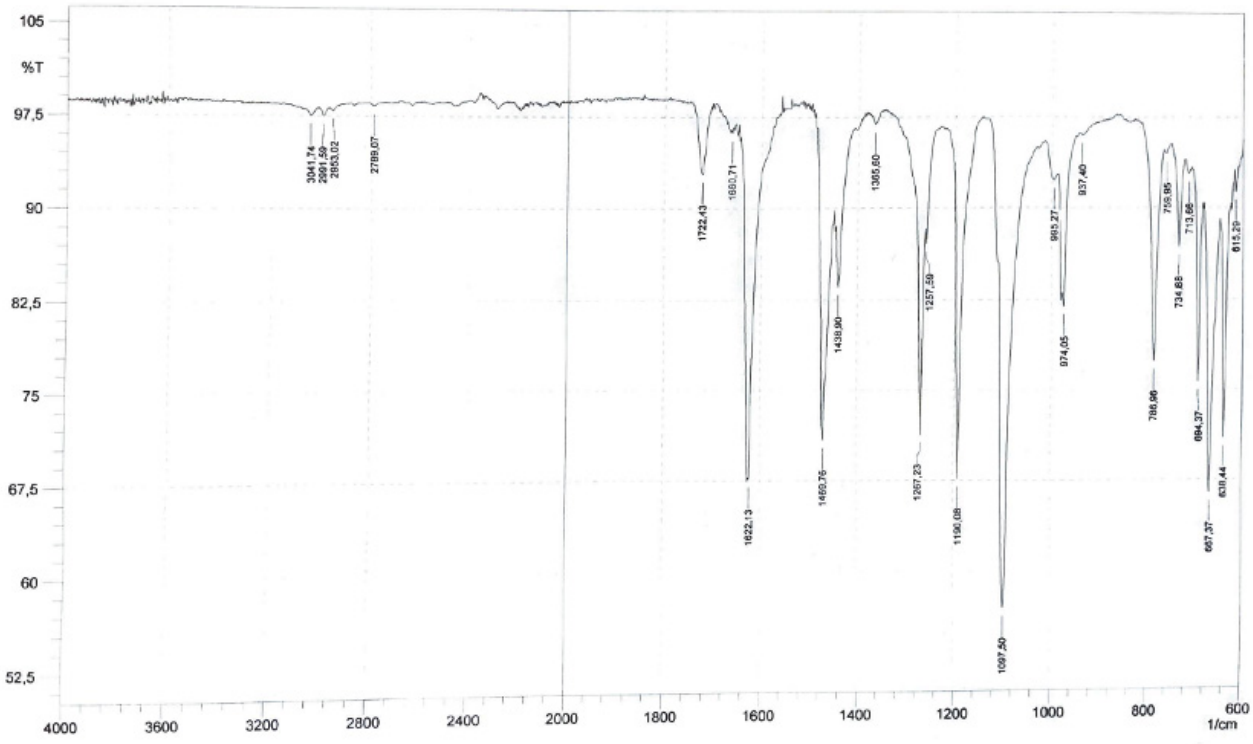

Figure S135: AT-IR spectrum of **13.**

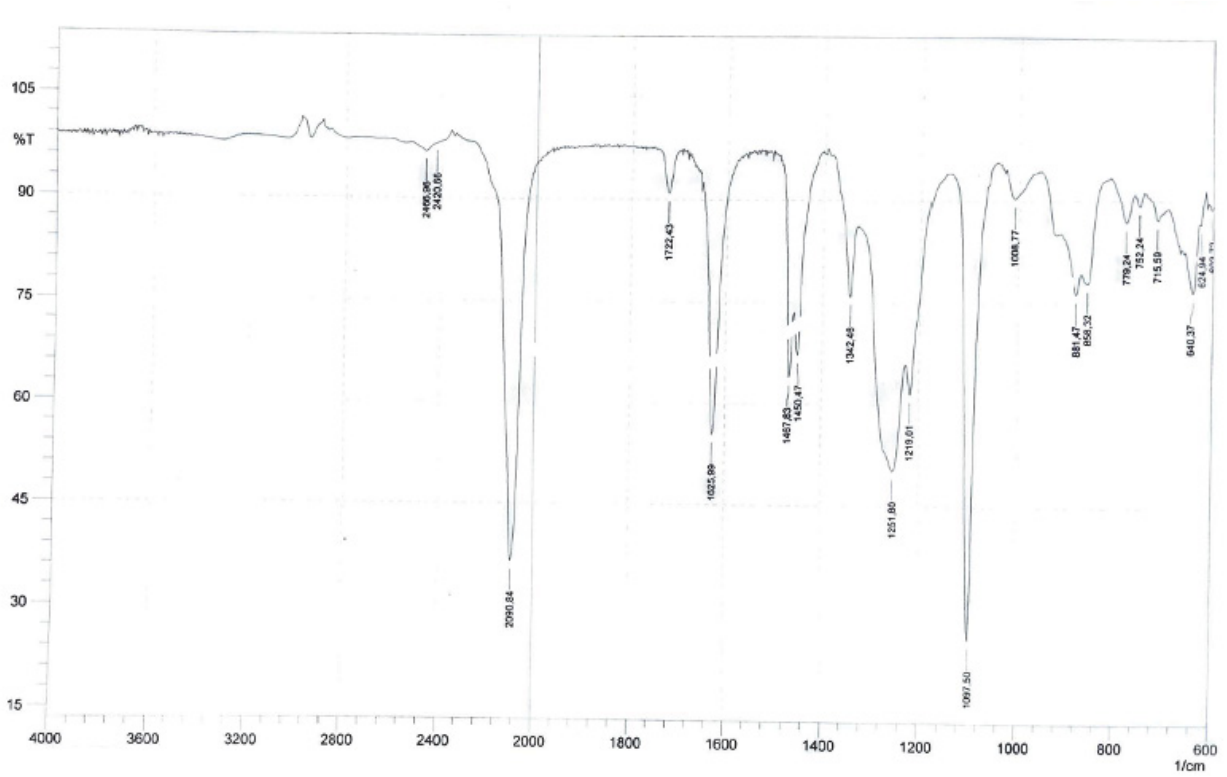

Figure S136: AT-IR spectrum of **14.**

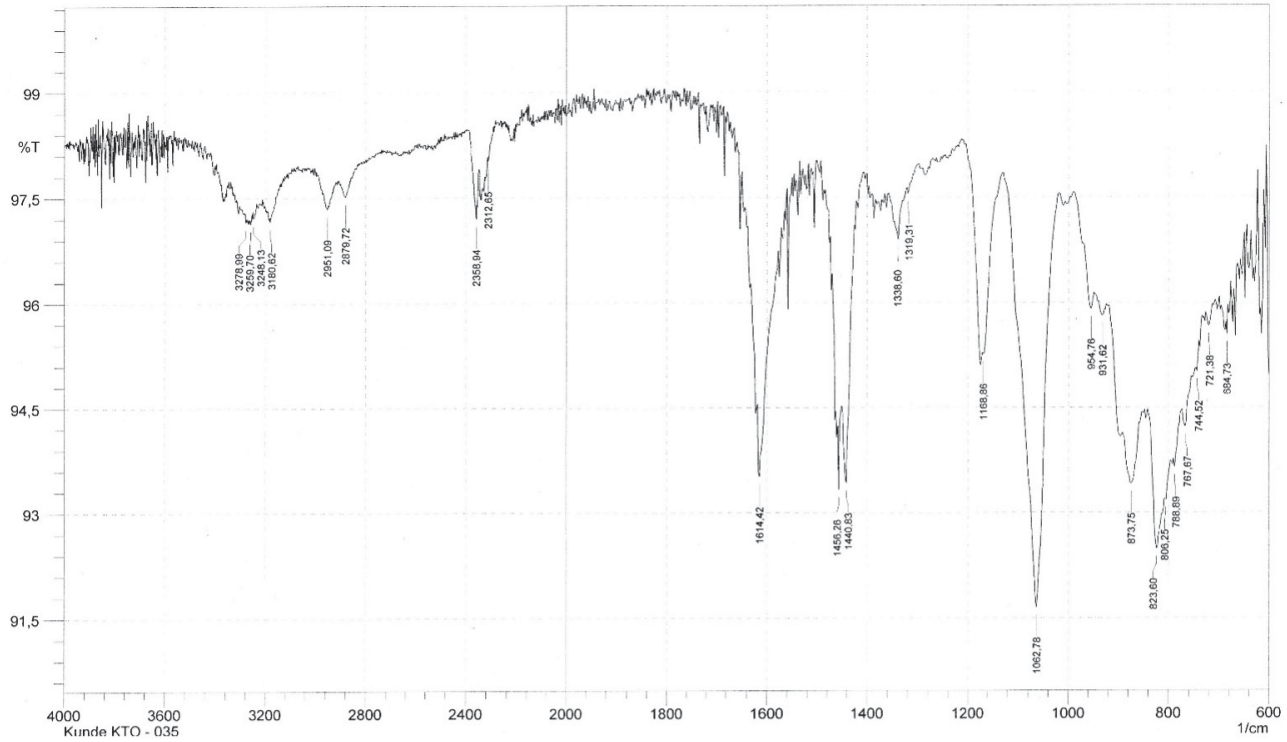

Figure S137: AT-IR spectrum of **15.**

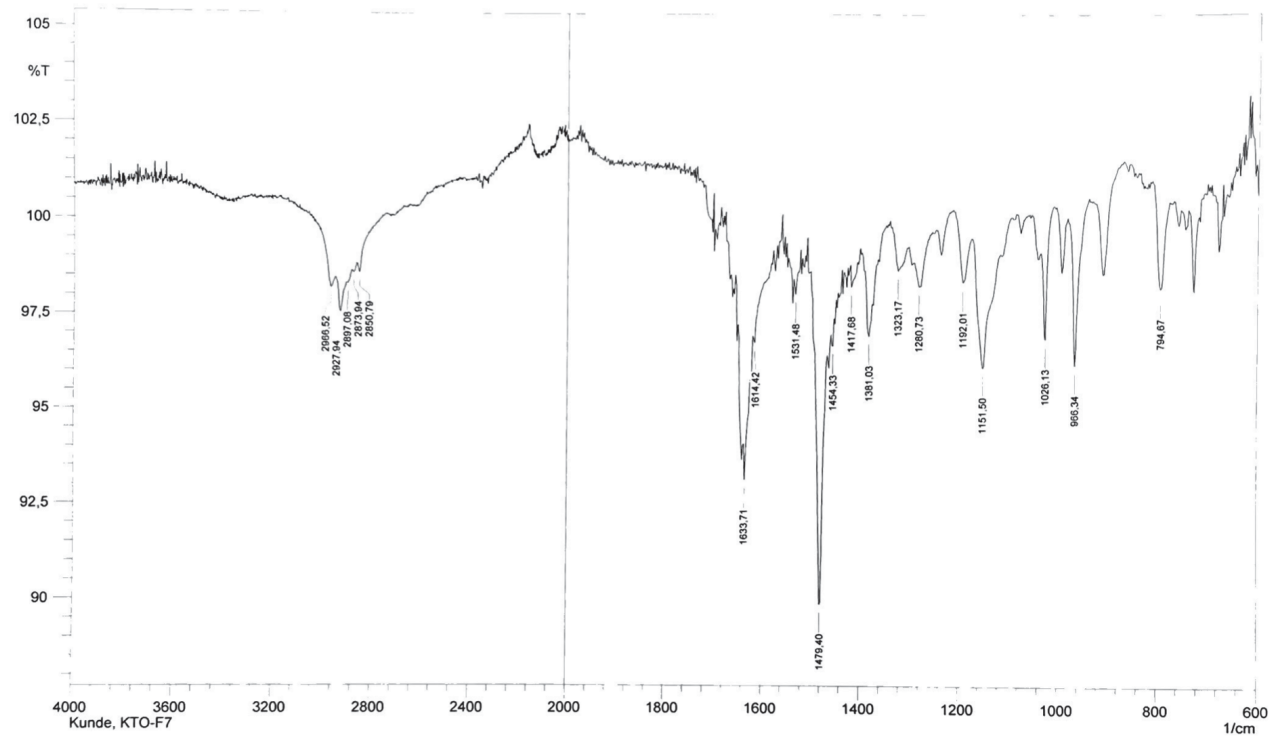

Figure S138: AT-IR spectrum of **FPOC1.**

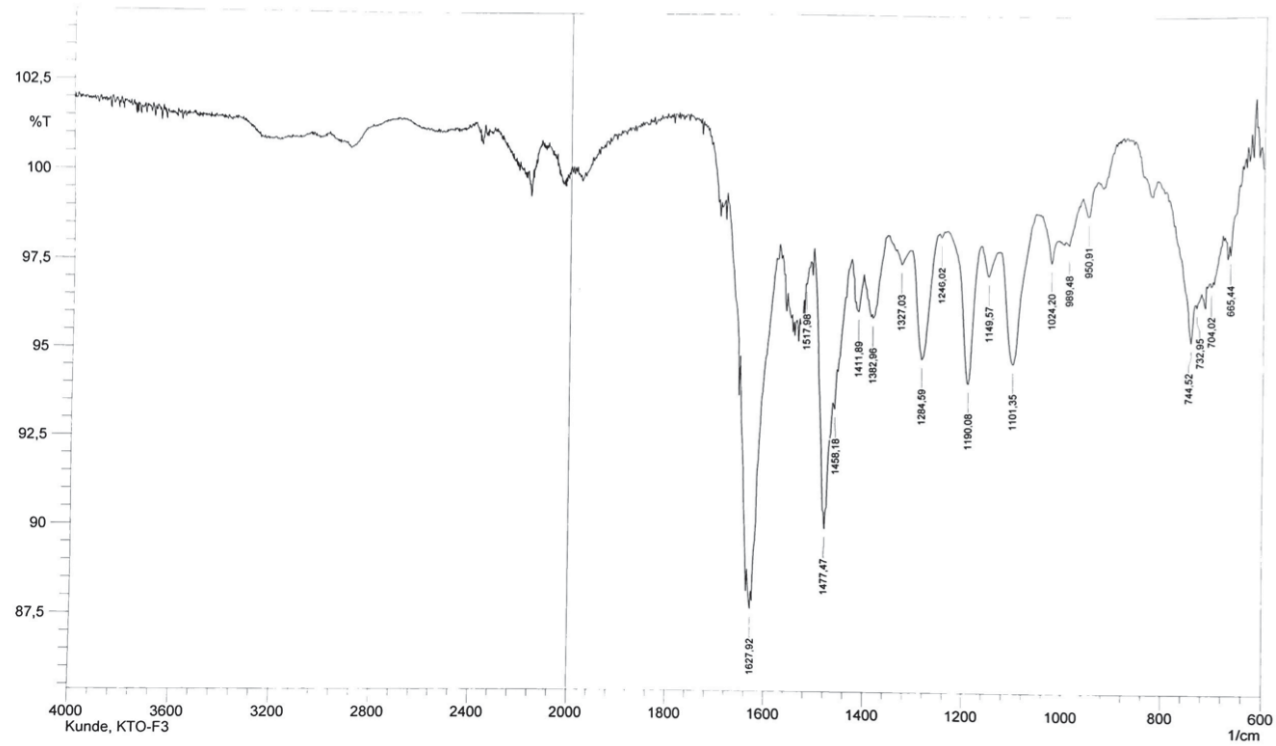

Figure S139: AT-IR spectrum of **FPOC2.**

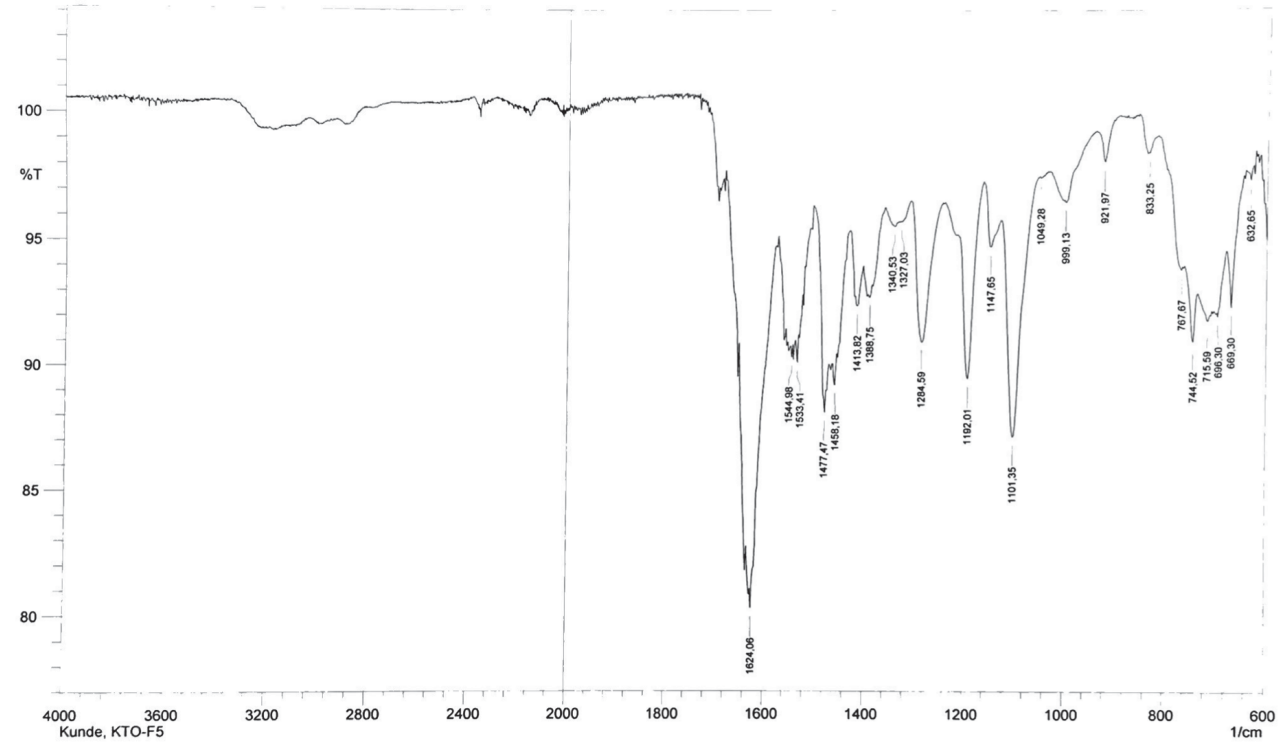

Figure S140: AT-IR spectrum of **FPOC3.**

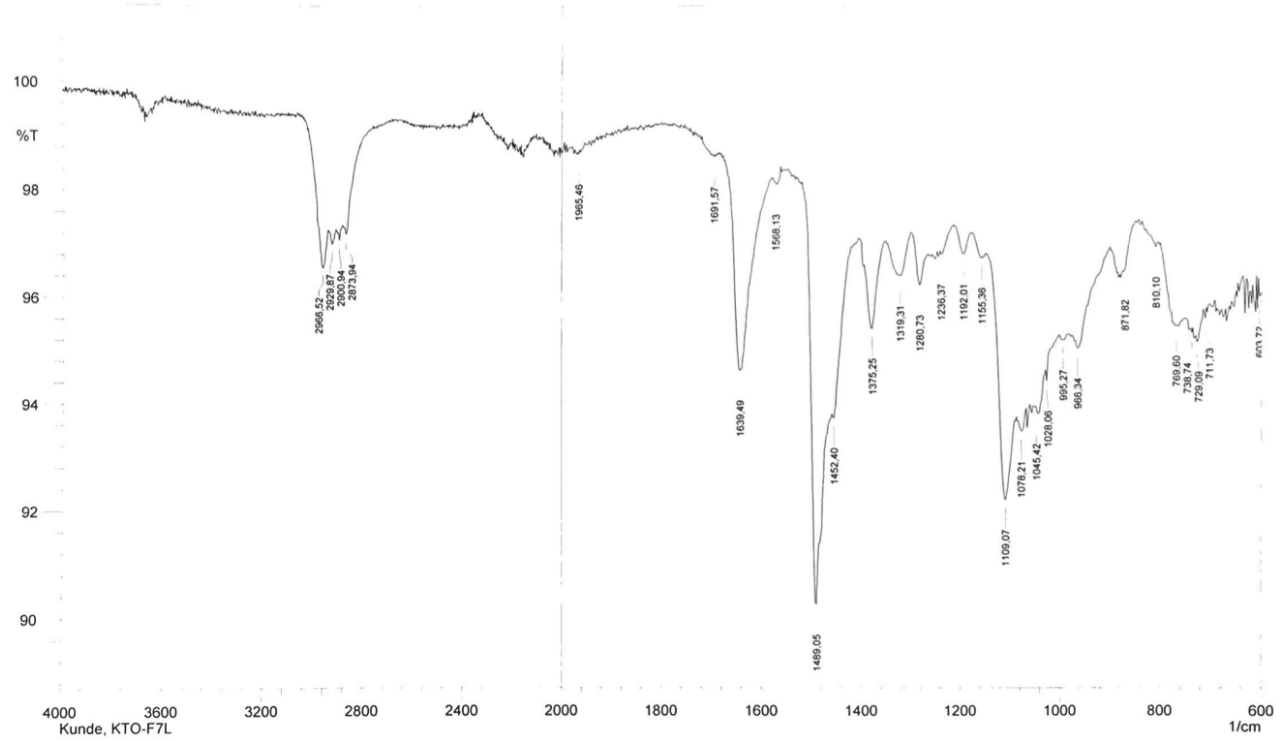

Figure S141: AT-IR spectrum of **RFPOC1.**

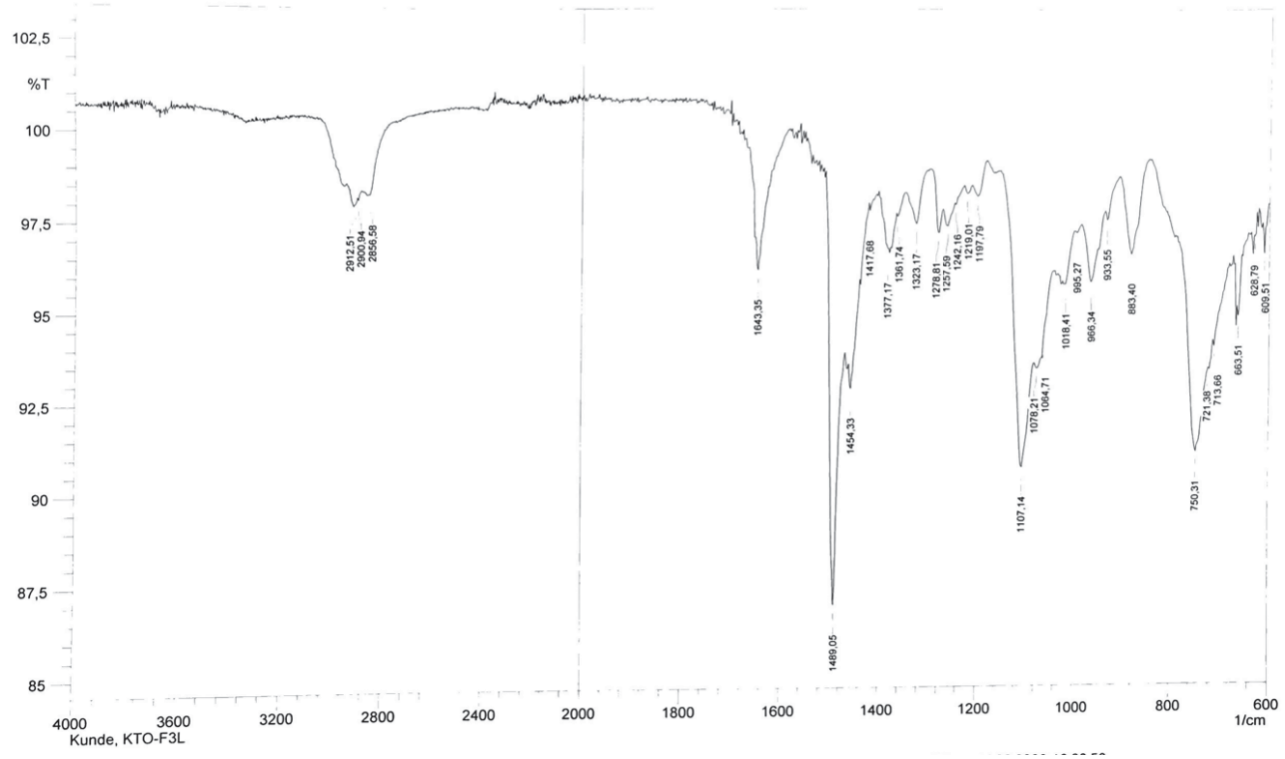

Figure S142: AT-IR spectrum of **RFPOC2.**

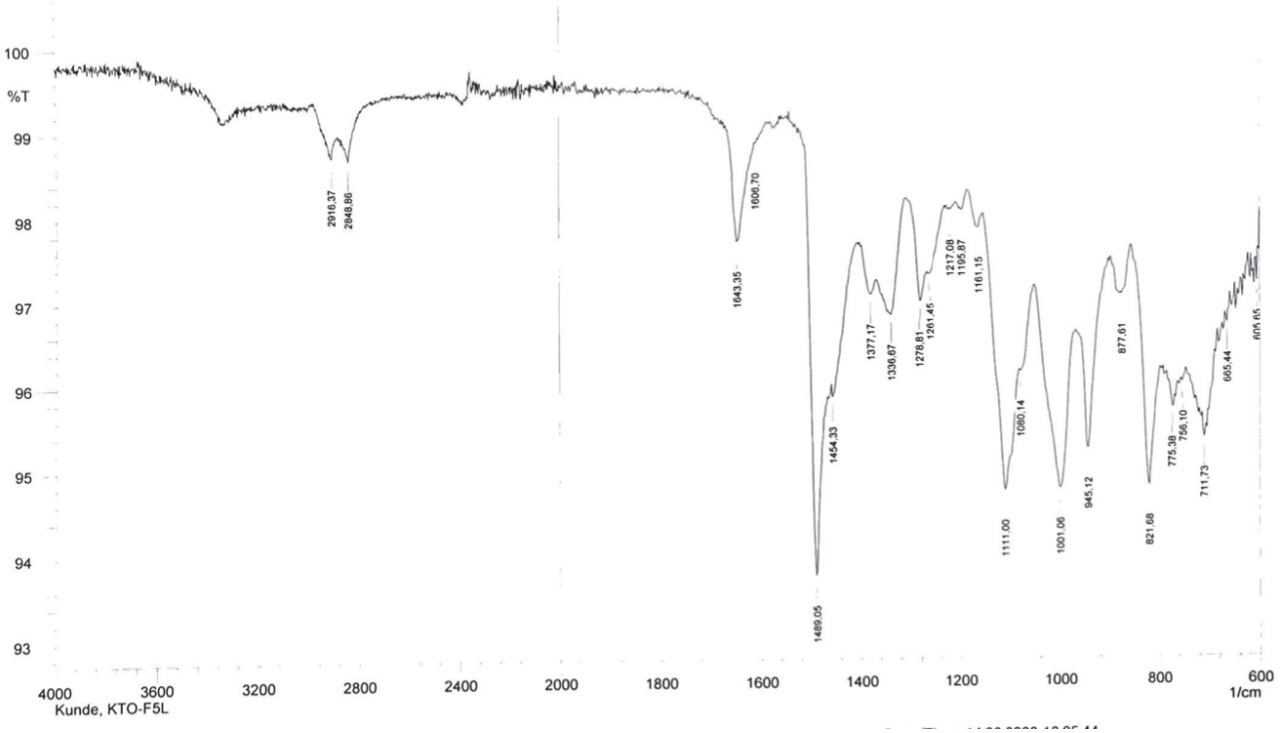

Figure S143: AT-IR spectrum of **RFPOC3.**

MS spectra

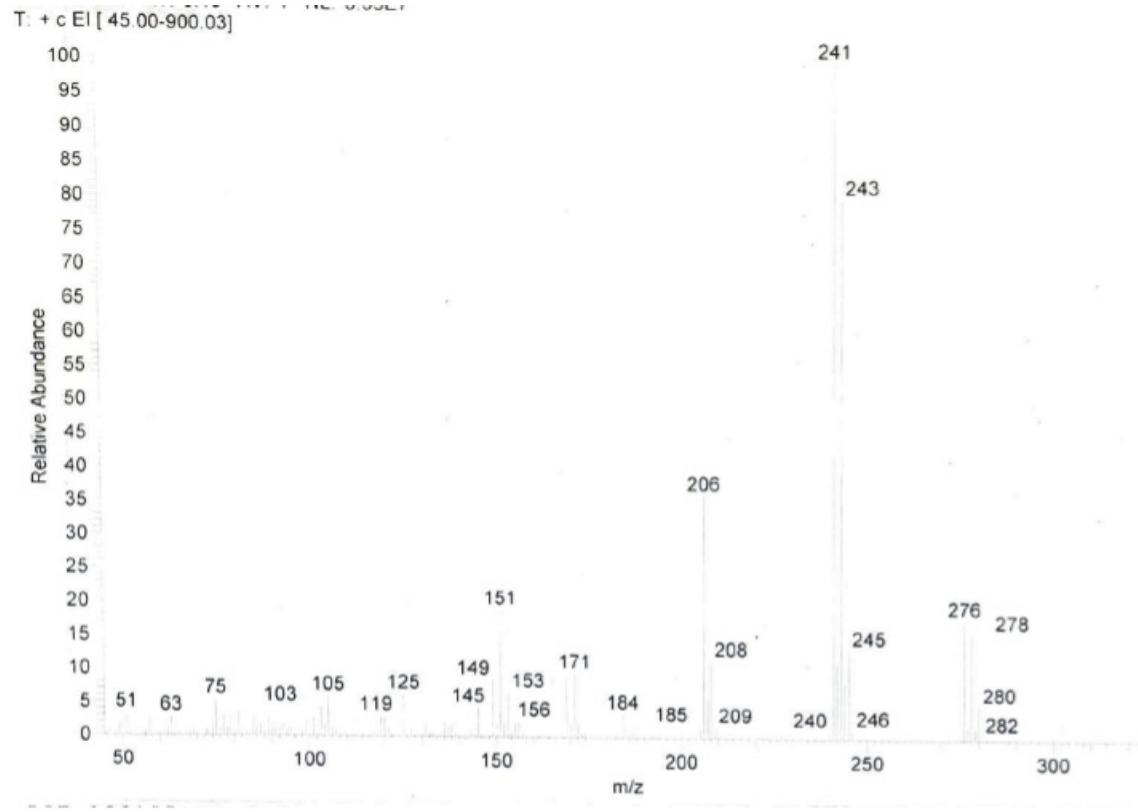

Figure S144: CI-MS spectrum of **13**, the found mass ion of 241 m/z corresponds very well to the calculated species $[M\text{-}Cl+H]^+$ calc.: 241 m/z.

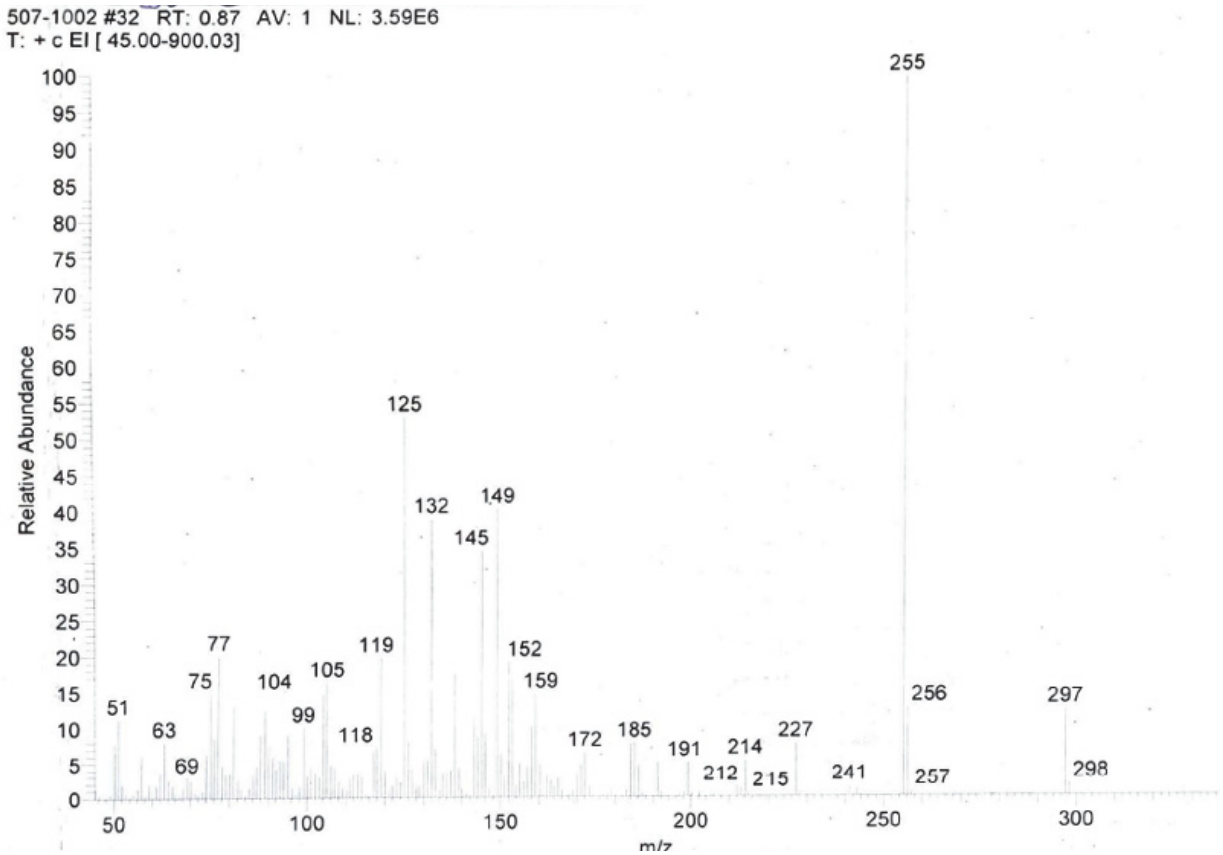

Figure S145: CI-MS spectrum of **14**, the found mass ion of 255 m/z corresponds very well to the calculated species $[M\text{-}N_3+H]^+$ calc.: 255 m/z.

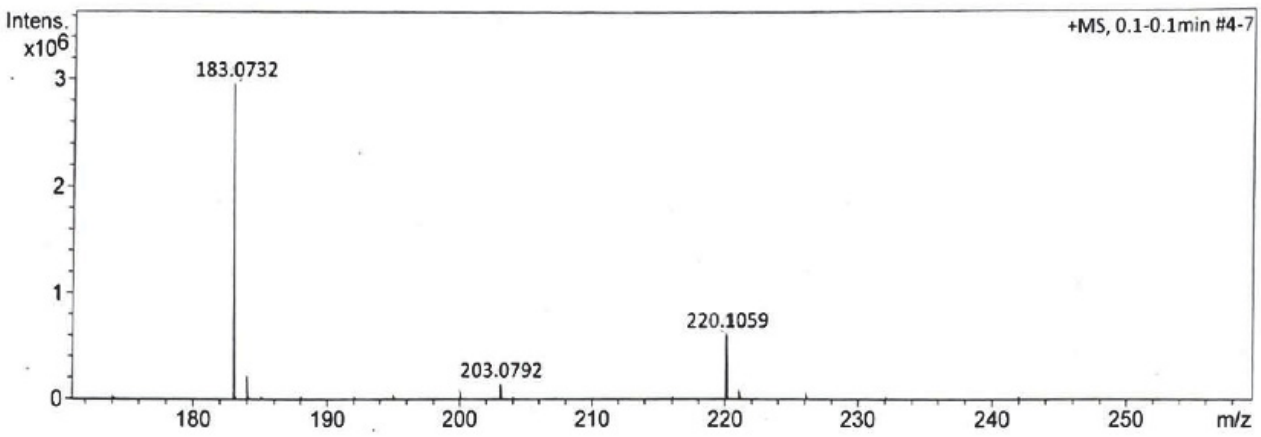

Figure S146: ESI-HRMS spectrum of **15**, the found mass ion of 220.1059 m/z corresponds very well to the calculated species [**15**+H]$^+$ calc.: 220.1056 m/z.

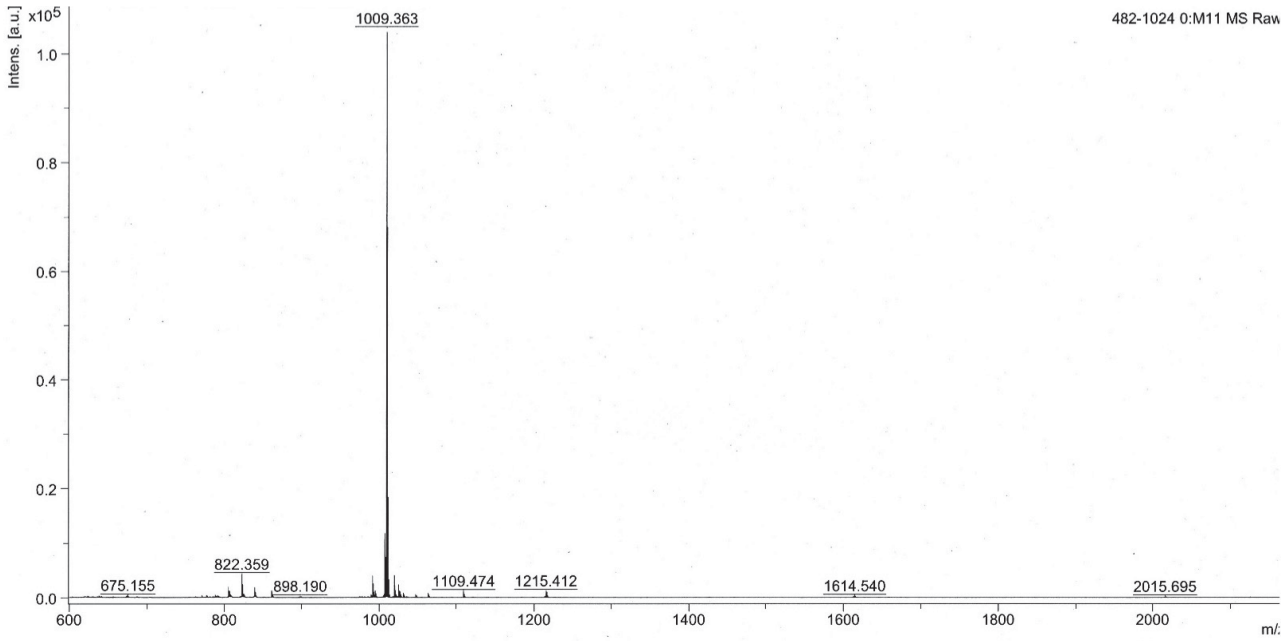

Figure S147: MALDI-MS spectrum of **FPOC1**, the found mass ion of 1009.363 m/z corresponds very well to the calculated species [**FPOC1**+H]$^+$ calc.: 1009.382 m/z.

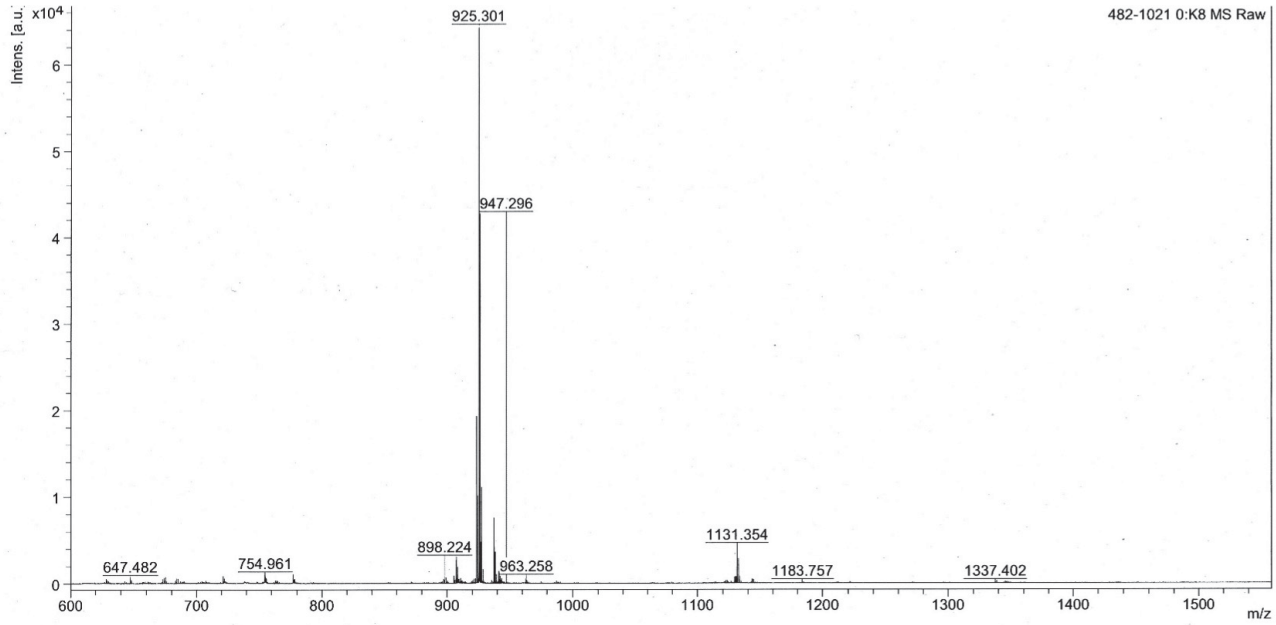

Figure S148: MALDI-MS spectrum of **FPOC2**, the found mass ion of 925.301 m/z corresponds very well to the calculated species [**FPOC2**+H]$^+$ calc.: 925.288 m/z.

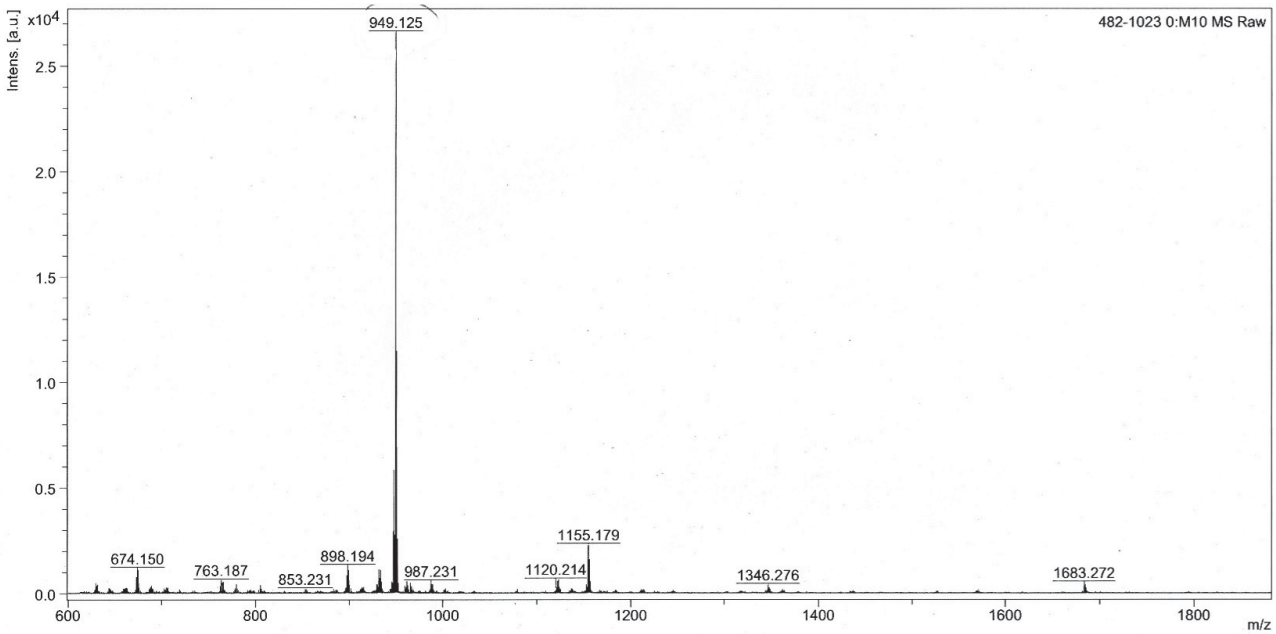

Figure S149: MALDI-MS spectrum of **FPOC3**, the observed mass ion of 949.125 m/z corresponds very well to the calculated species [**FPOC3**+H]$^+$ calc.: 949.137 m/z.

E

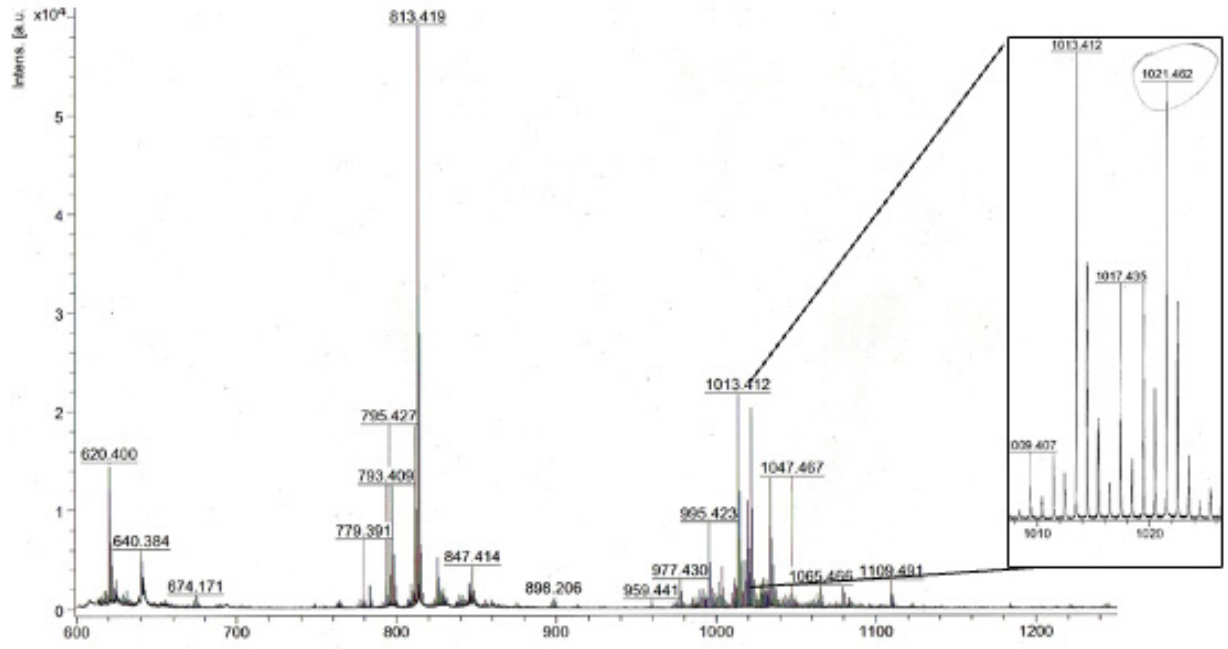

Figure S150: MALDI-MS spectrum of **RFPOC1**, the observed mass ion of 1021.462 m/z corresponds very well to the calculated species [**RFPOC1**+H]$^+$ calc.: 1021.476 m/z.

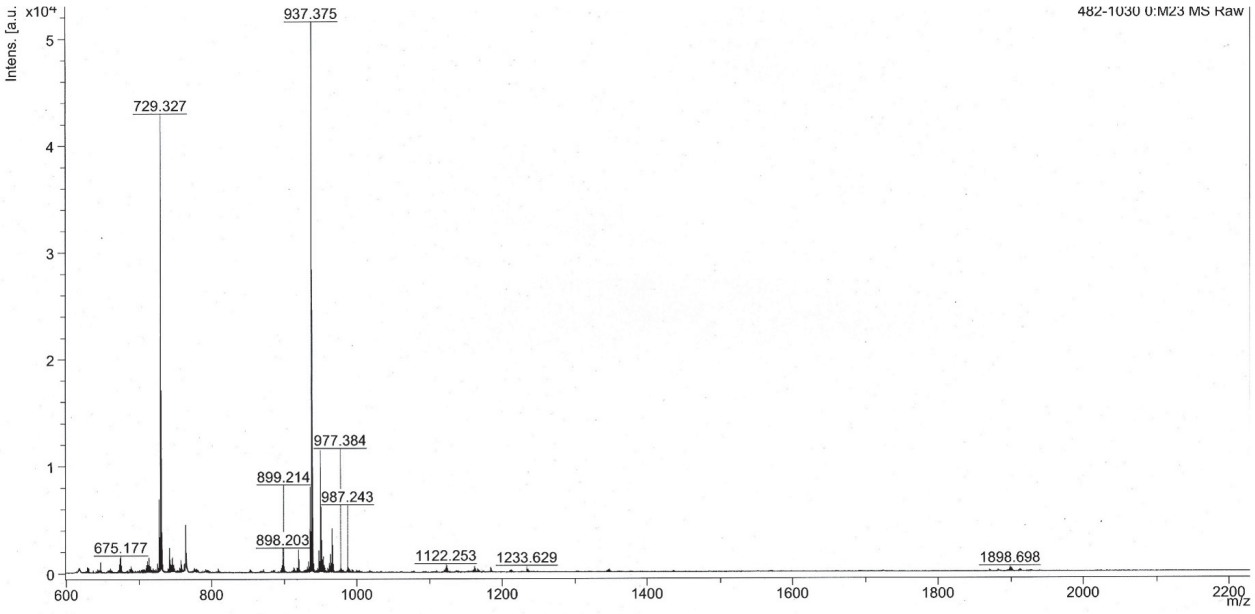

Figure S151: MALDI-MS spectrum of **RFPOC2**, the observed mass ion of 937.375 m/z corresponds very well to the calculated species [**RFPOC2**+H]$^+$ calc.: 937.382 m/z.

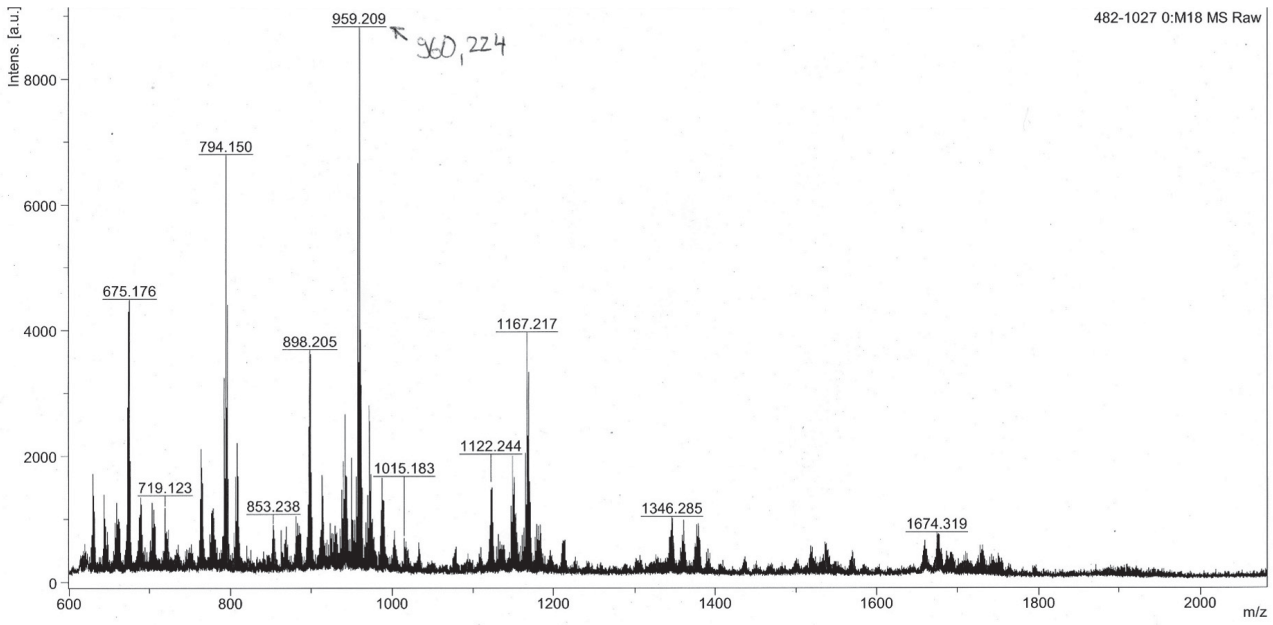

Figure S152: MALDI-MS spectrum of **RFPOC3**, the observed mass ion of 961.224 m/z corresponds very well to the calculated species [**RFPOC3**+H]$^+$ calc.: 961.231 m/z.

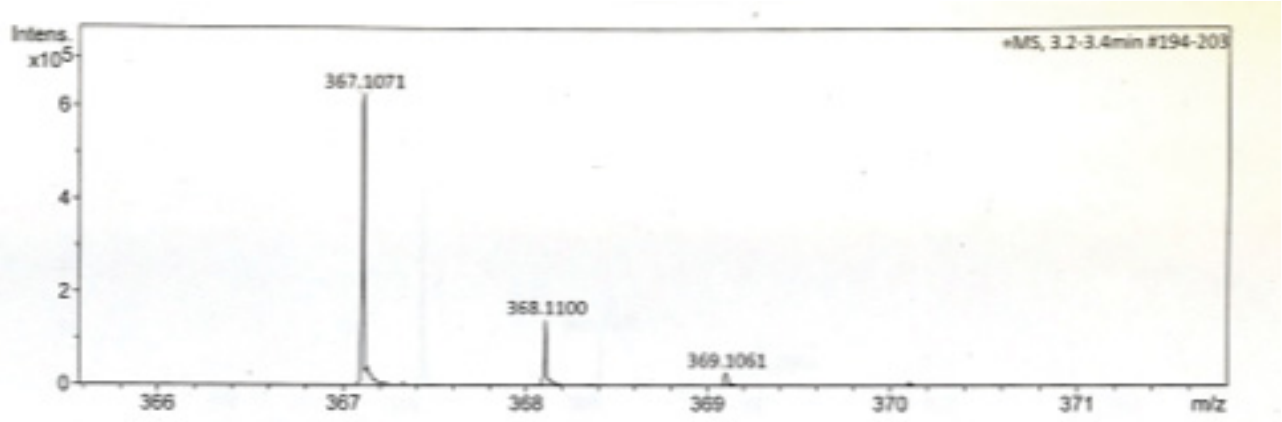

Figure S153: ESI-HRMS spectrum of **19**, the observed mass ion of 367.1071 m/z corresponds very well to the calculated species [**19**+H]$^+$ calc.: 367.1075 m/z.

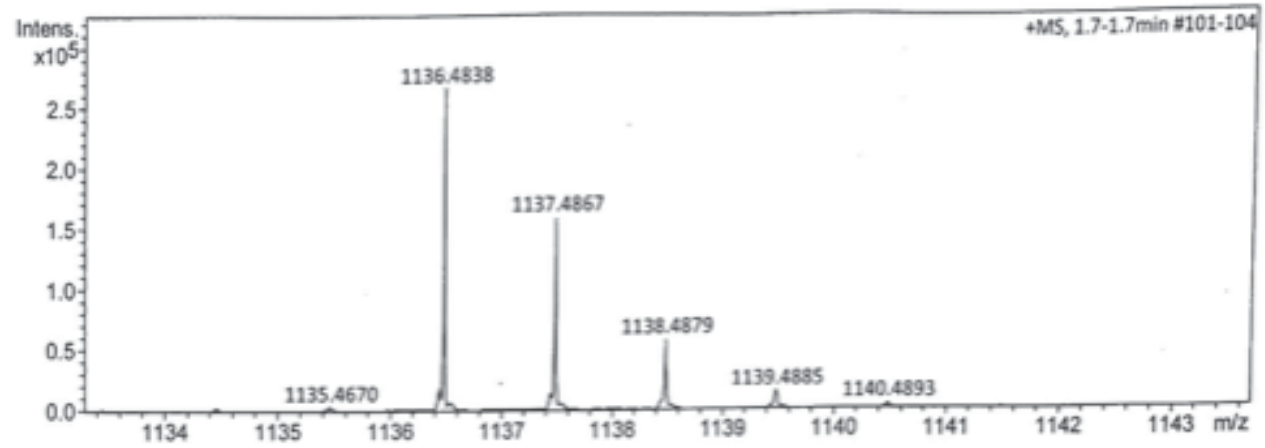

Figure S154: ESI-HRMS spectrum of **20**, the observed mass ion of 1136.4838 m/z corresponds very well to the calculated species [**20**+H]$^{+}$ calc.: 1136.4828 m/z.

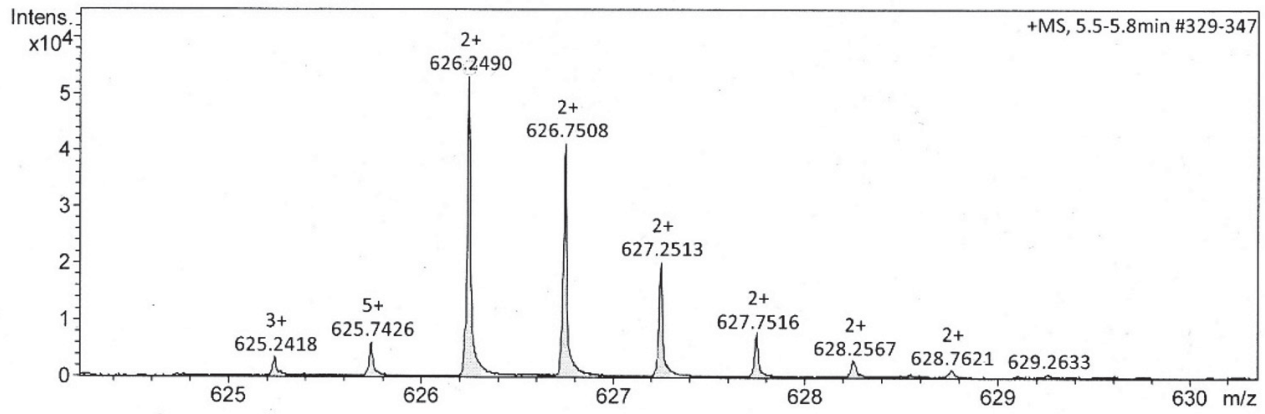

Figure S155: ESI-HRMS spectrum of **21**, the observed mass ion of 626.2490 m/z corresponds very well to the calculated species [**20**+2H]$^{2+}$ calc.: 626.2497 m/z.

6.2. Spectra for Section 3.2

NMR spectra

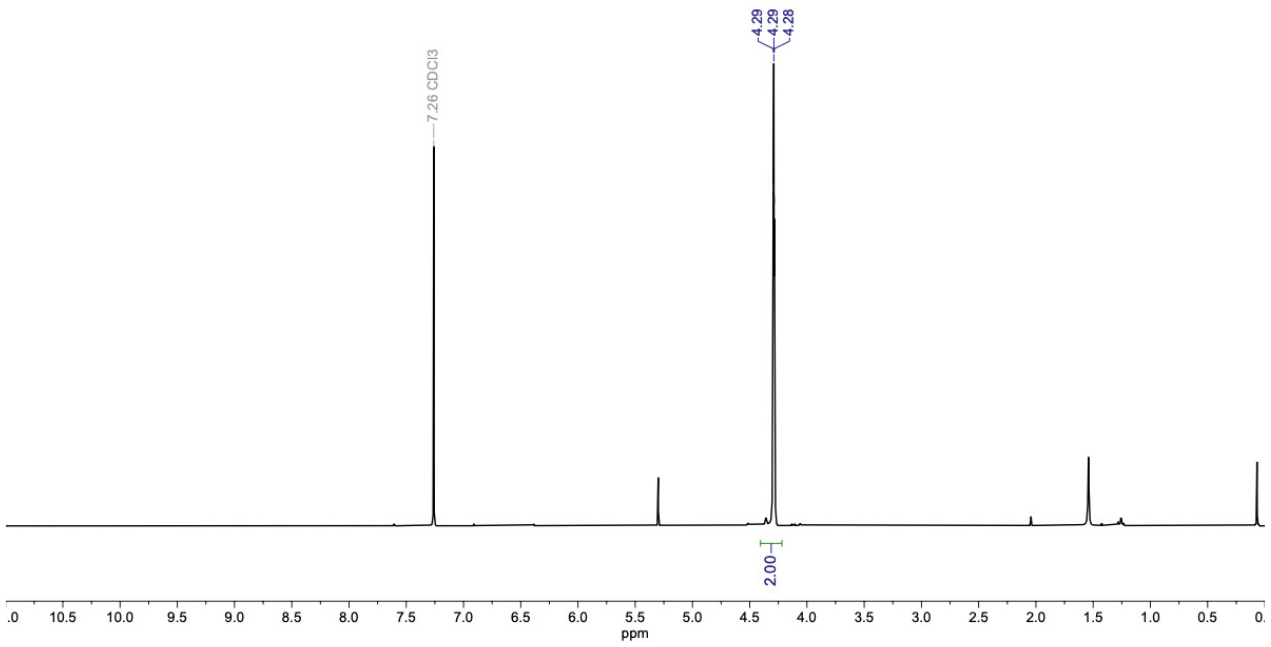

Figure S156: ^{1}H NMR spectrum (300 MHz, $CDCl_3$) of **24**.

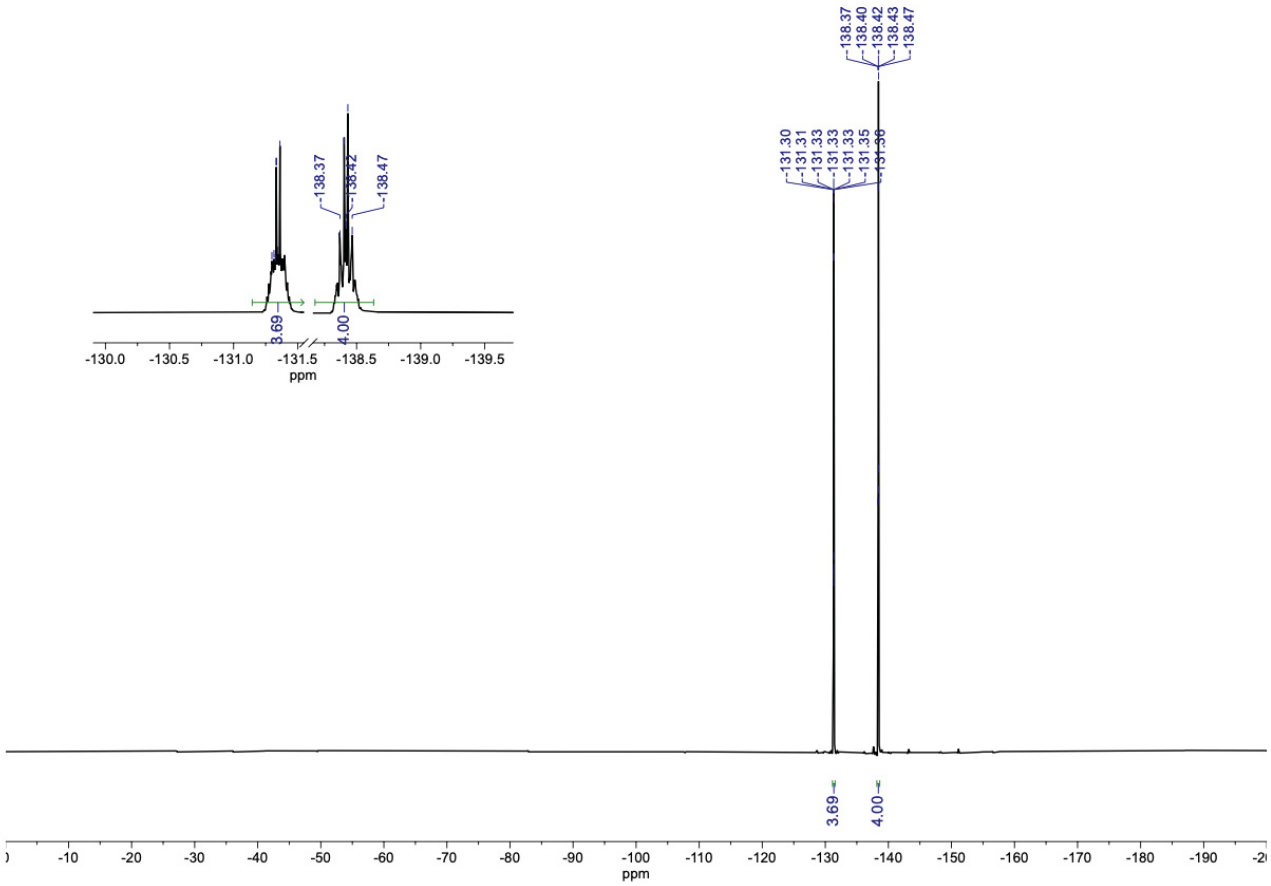

Figure S157: ^{19}F NMR spectrum (282 MHz, $CDCl_3$) of **24**.

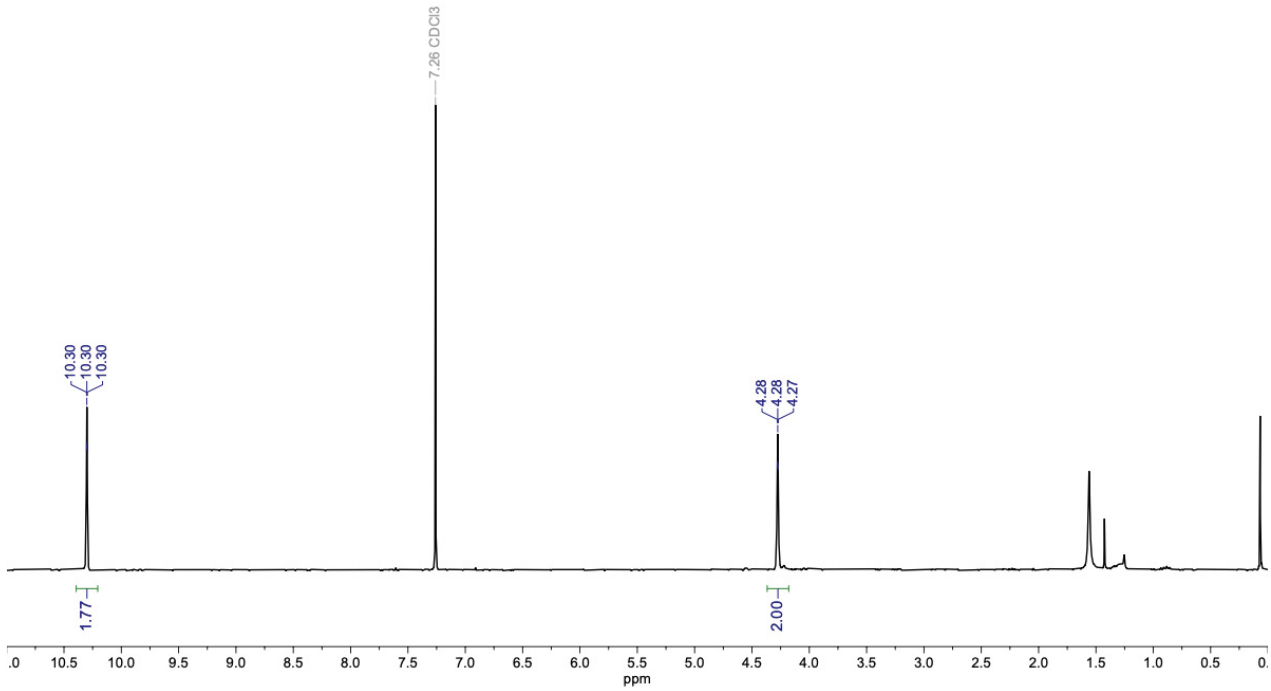

Figure S158: ^{1}H NMR spectrum (300 MHz, $CDCl_3$) of **22**.

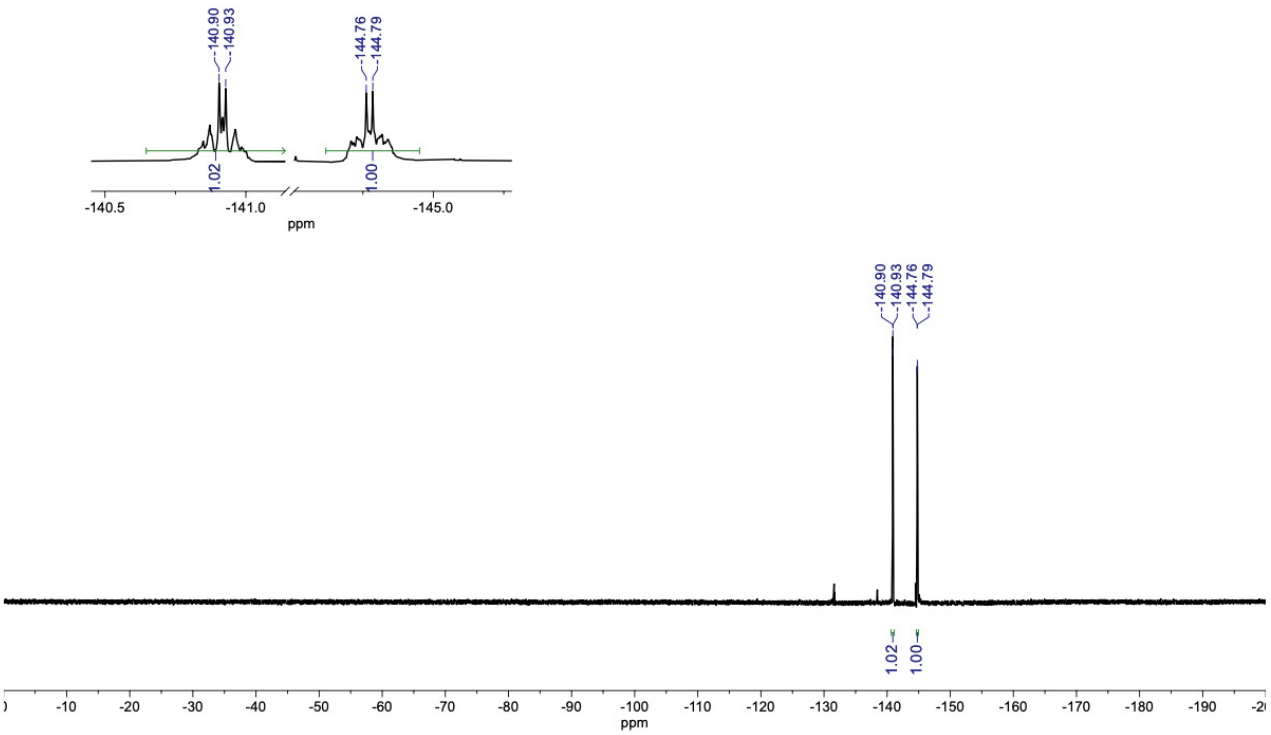

Figure S159: ^{19}F NMR spectrum (282 MHz, $CDCl_3$) of **22**.

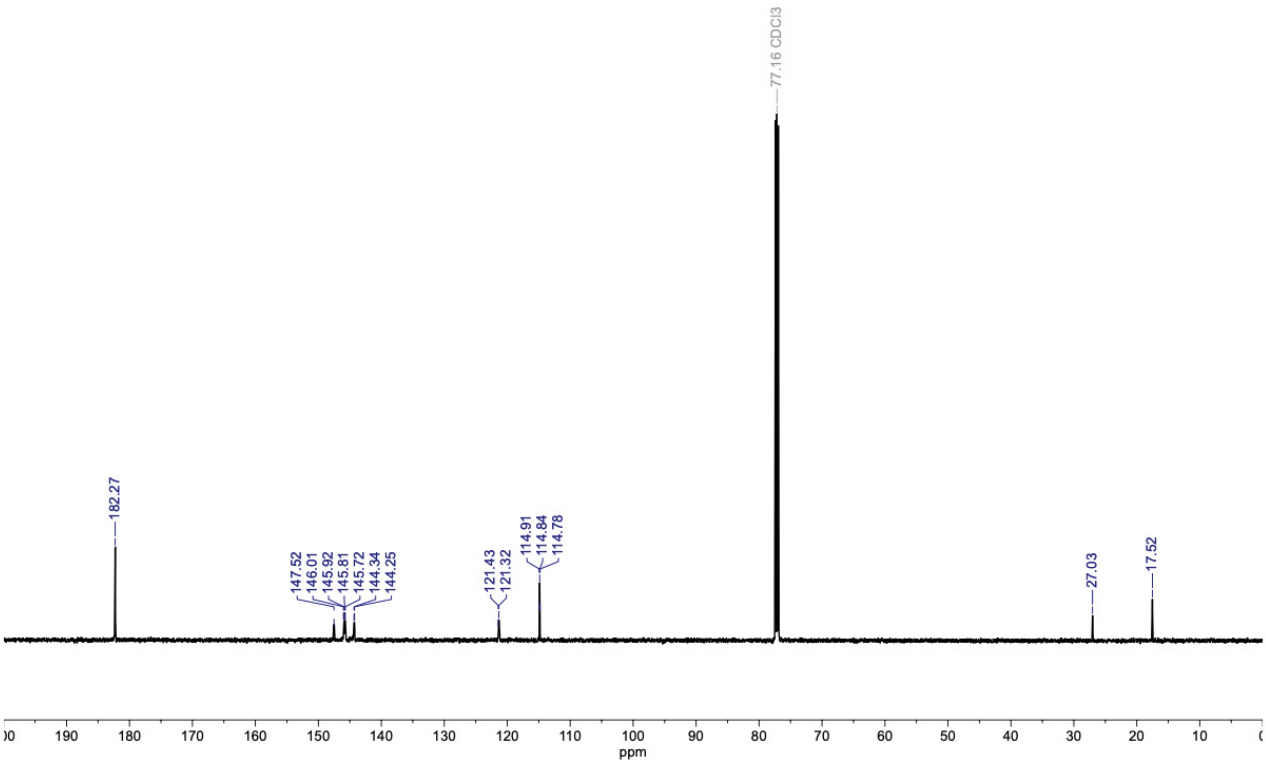

Figure S160: ^{13}C NMR spectrum (75 MHz, $CDCl_3$) of **22**.

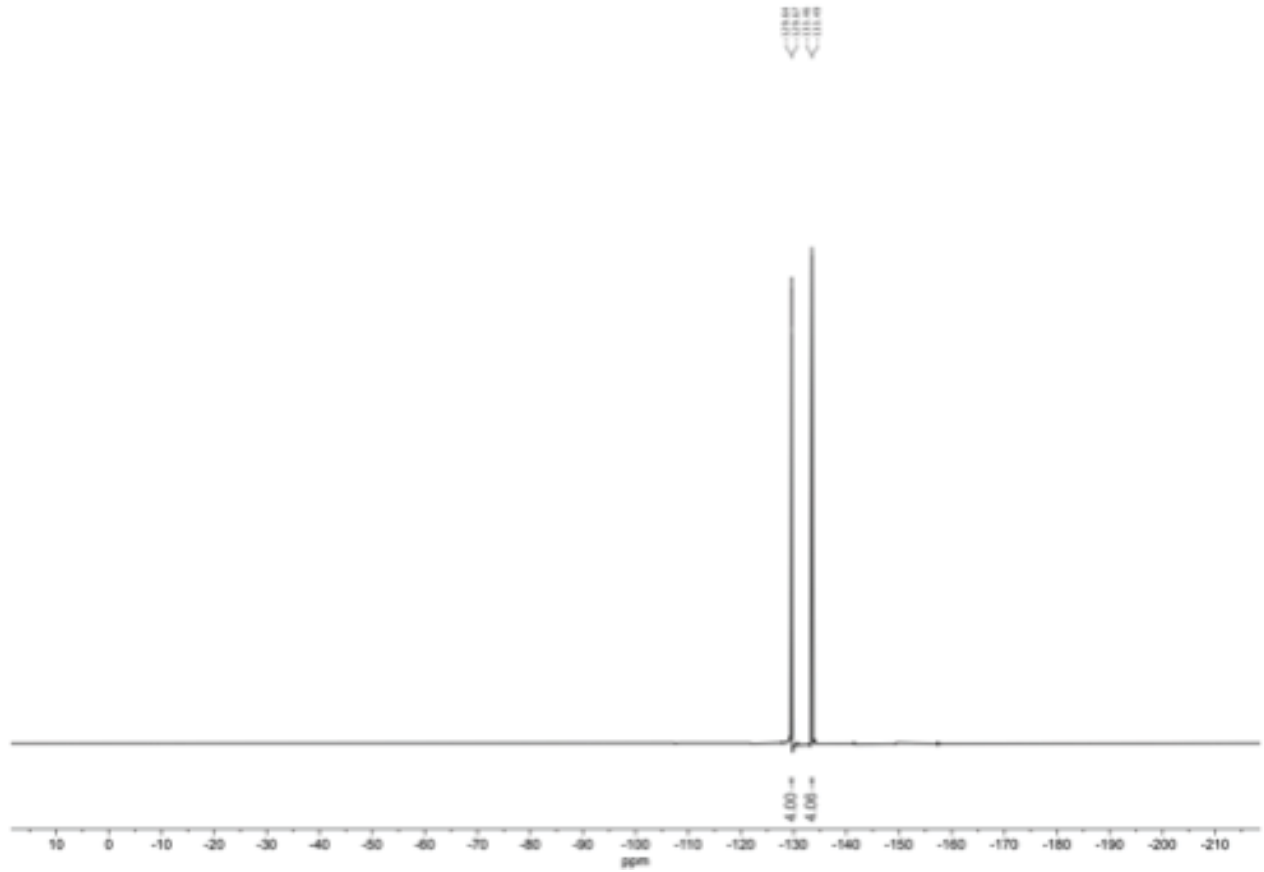

Figure S161: ^{19}F NMR spectrum (282 MHz, $CDCl_3$) of **25**.

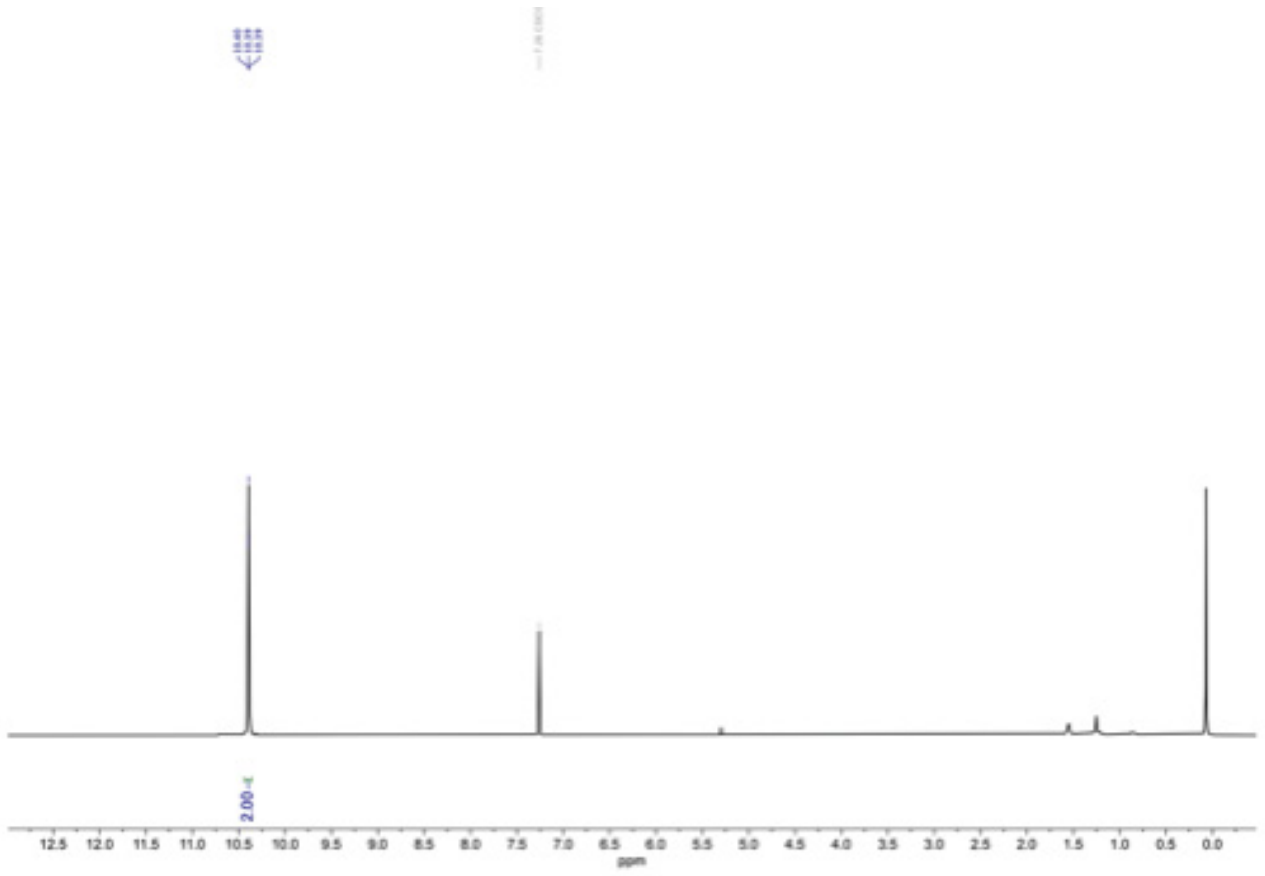

Figure S162: ^{1}H NMR spectrum (300 MHz, $CDCl_3$) of **23**.

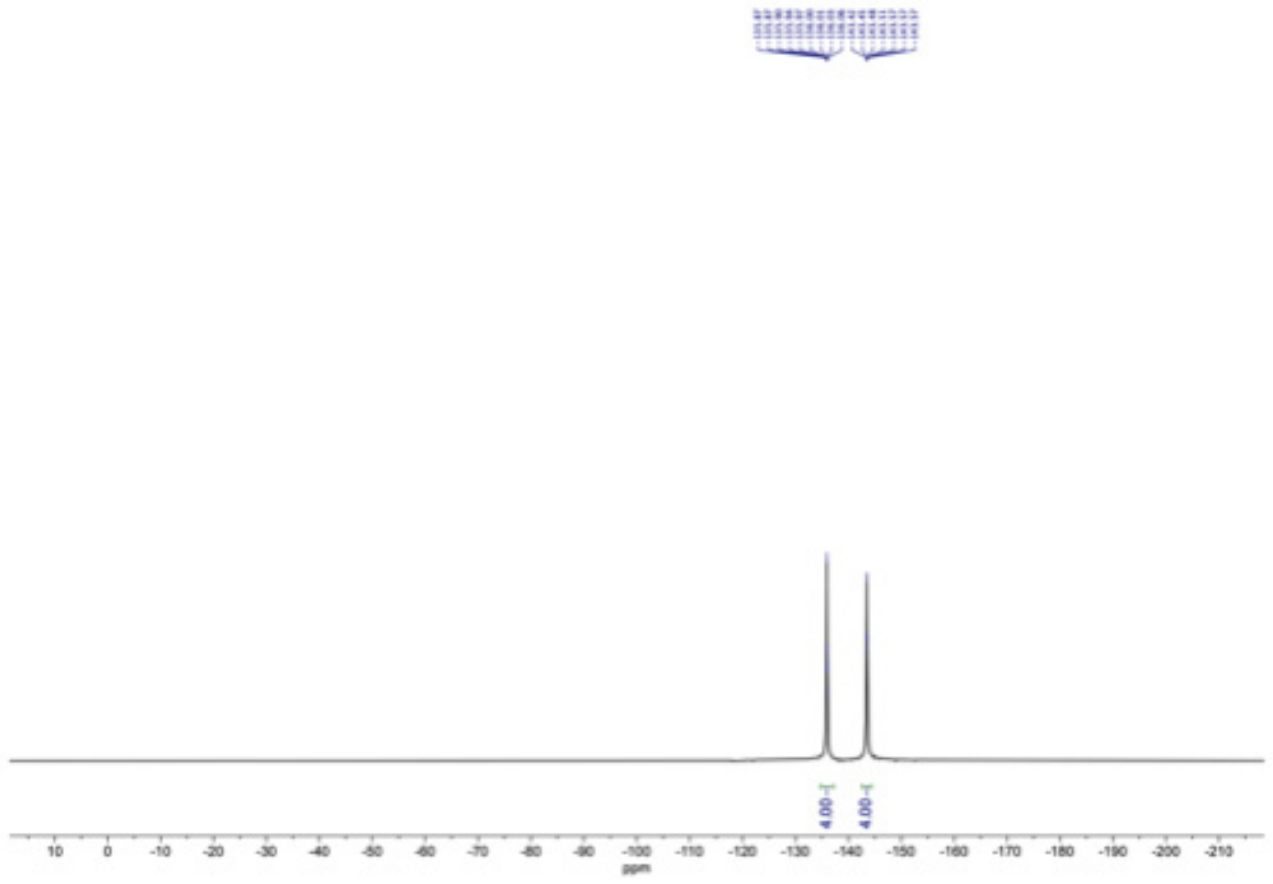

Figure S163: ^{19}F NMR spectrum (282 MHz, $CDCl_3$) of **23**.

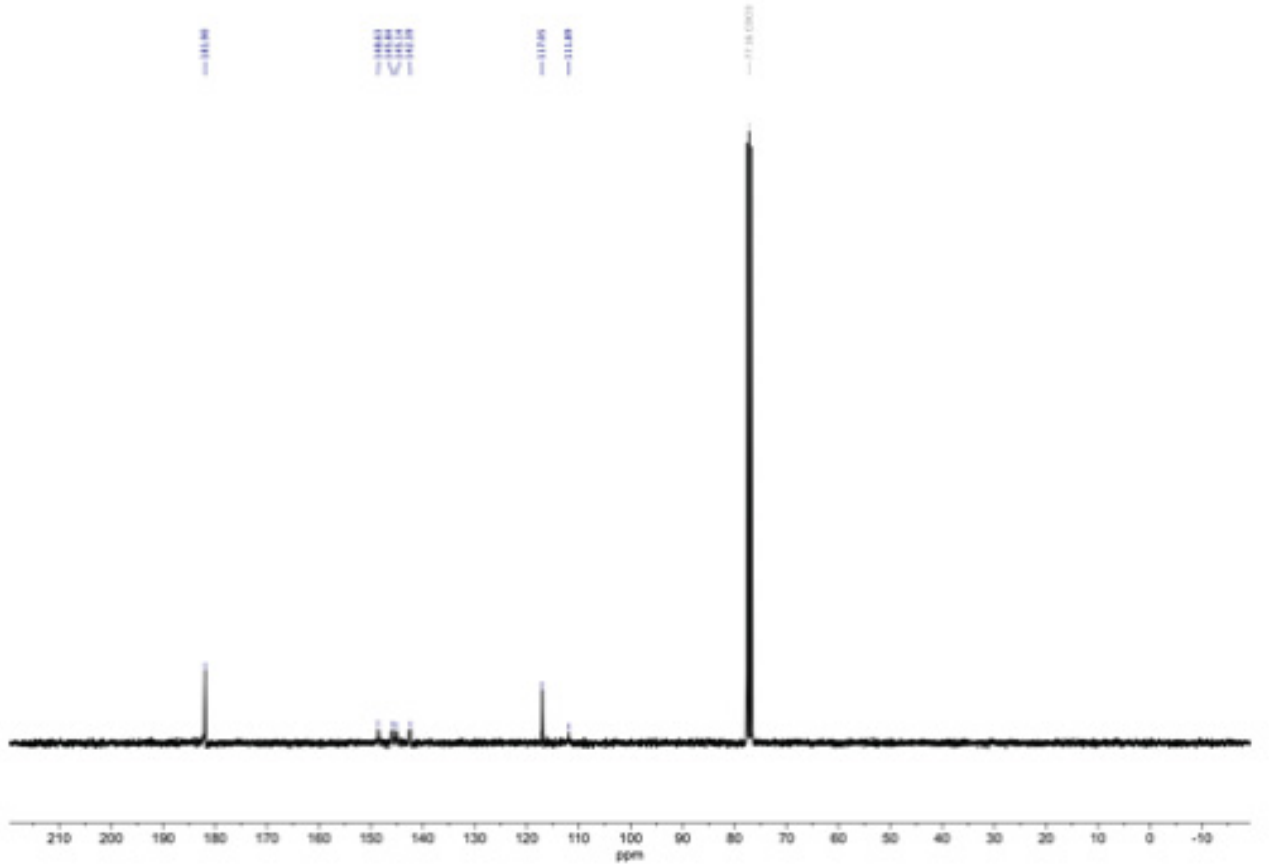

Figure S164: ^{13}C NMR spectrum (75 MHz, $CDCl_3$) of **23**.

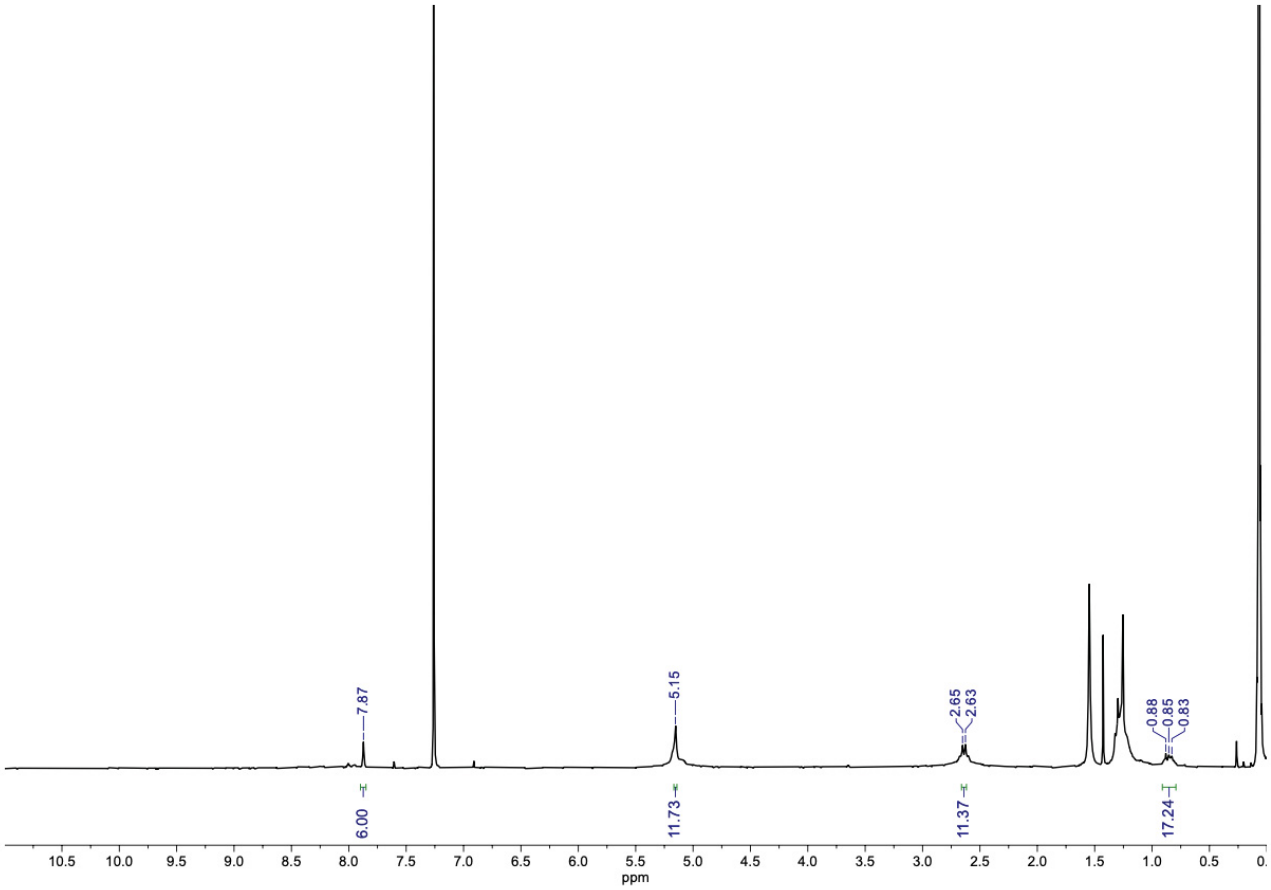

Figure S165: ^{1}H NMR spectrum (300 MHz, $CDCl_3$) of **FPOC9**.

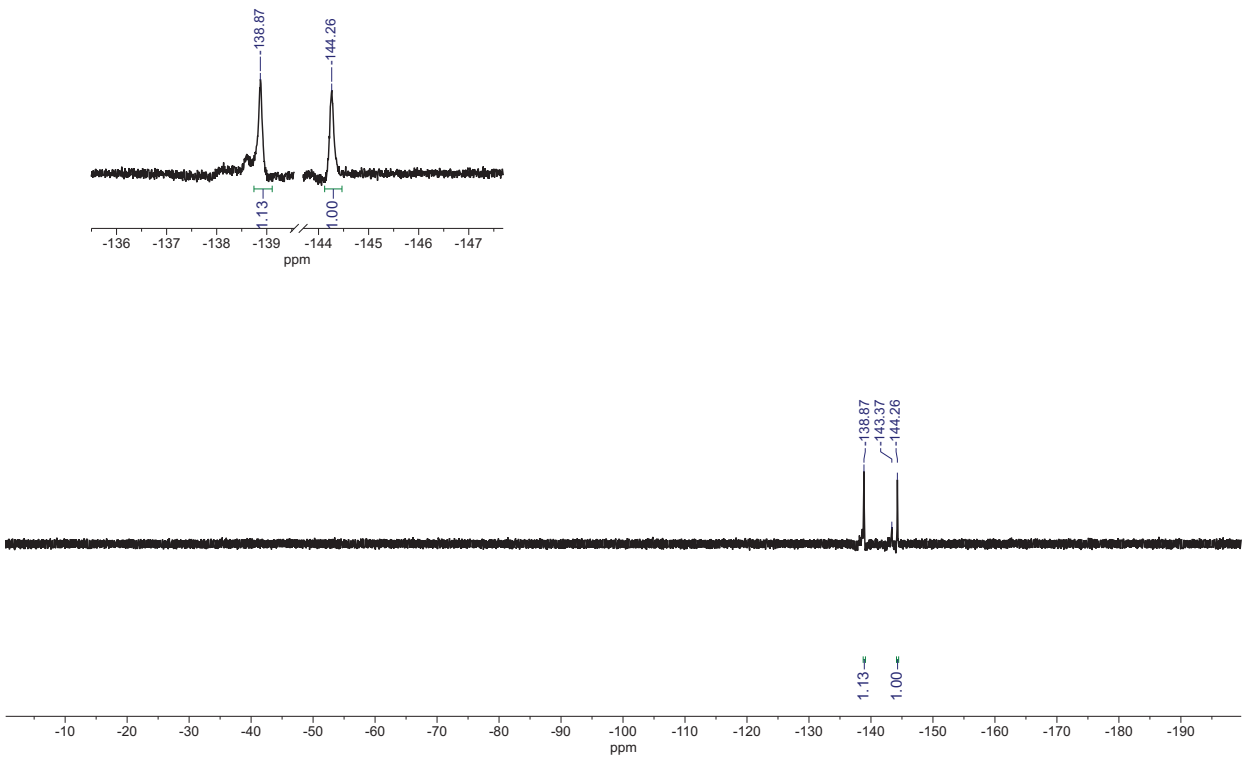

Figure S166: ^{19}F NMR spectrum (282 MHz, $CDCl_3$) of **FPOC9**.

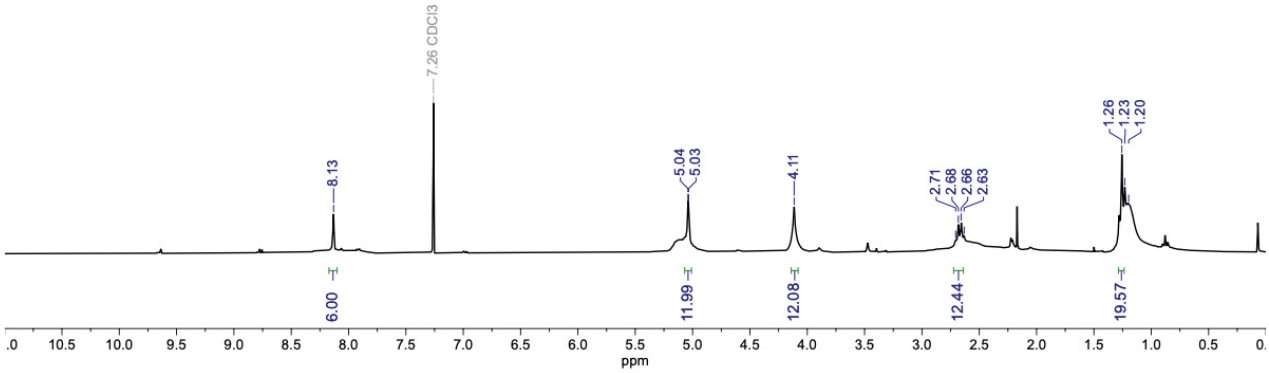

Figure S167: ^{1}H NMR spectrum (300 MHz, $CDCl_3$) of **FPOC7**.

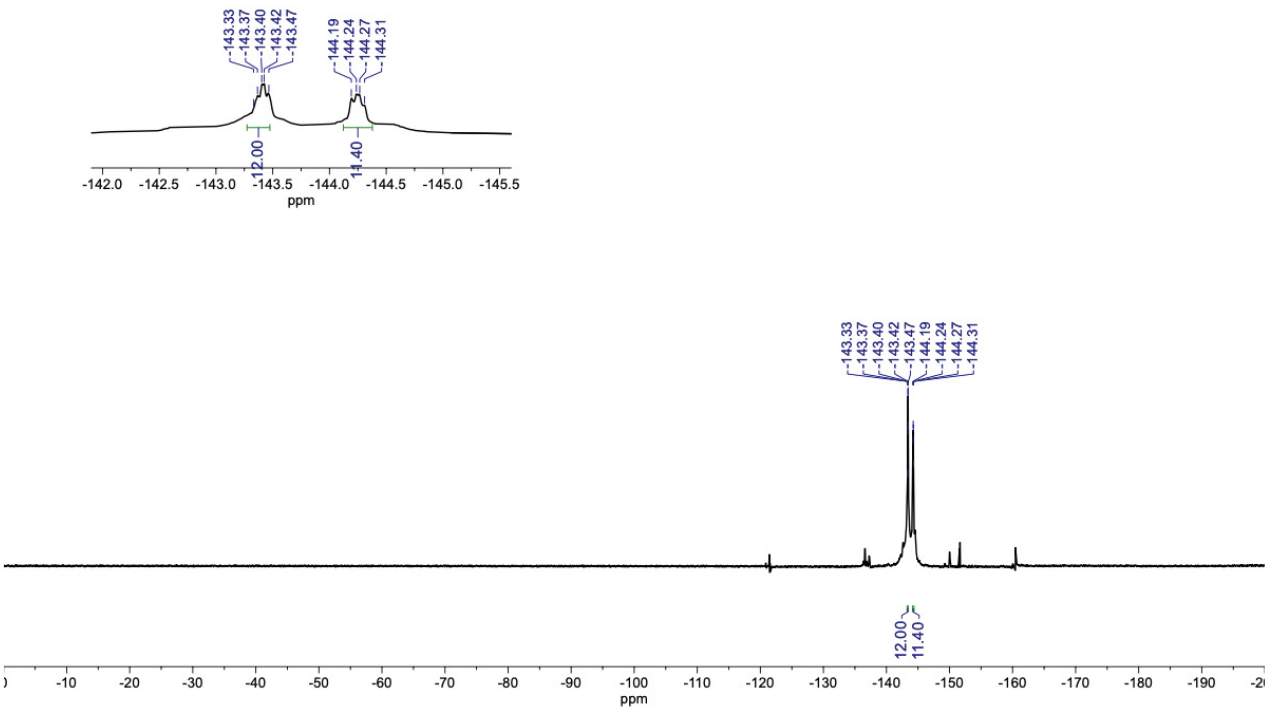

Figure S168: ^{19}F NMR spectrum (282 MHz, $CDCl_3$) of **FPOC7**. Lower intensity signals can be assigned to the formation of lower mass oligomeric side products, that could not be separated from the cage compound.

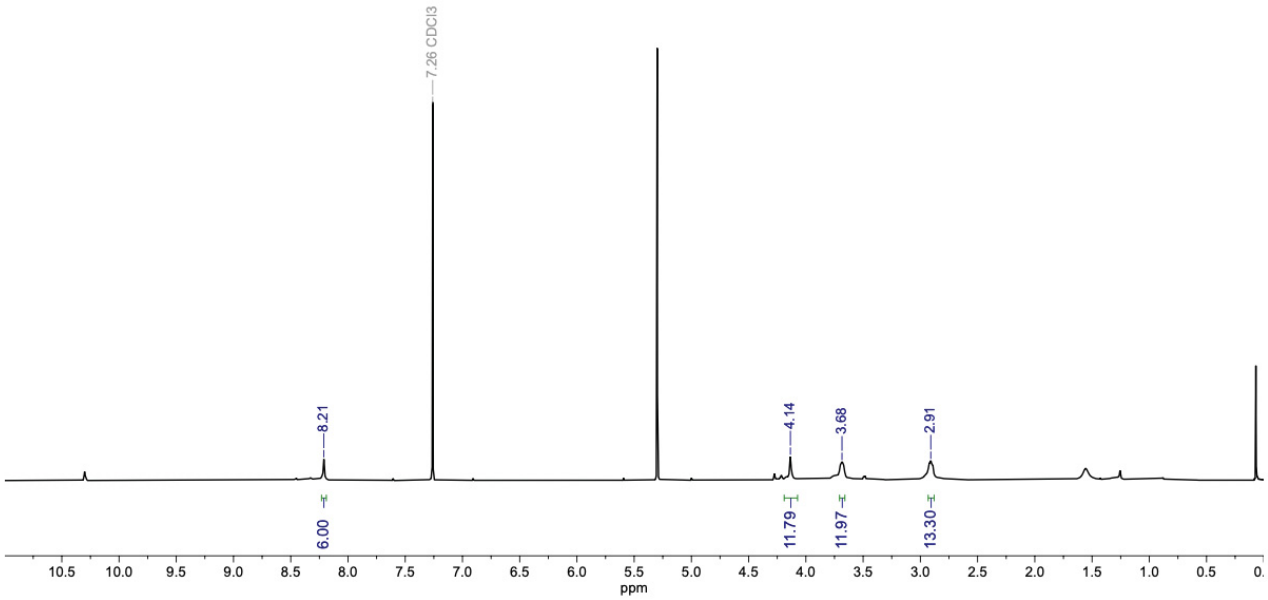

Figure S169: ^{1}H NMR spectrum (300 MHz, $CDCl_3$) of **FPOC8**.

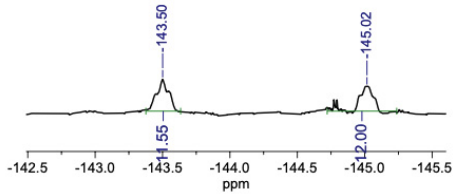

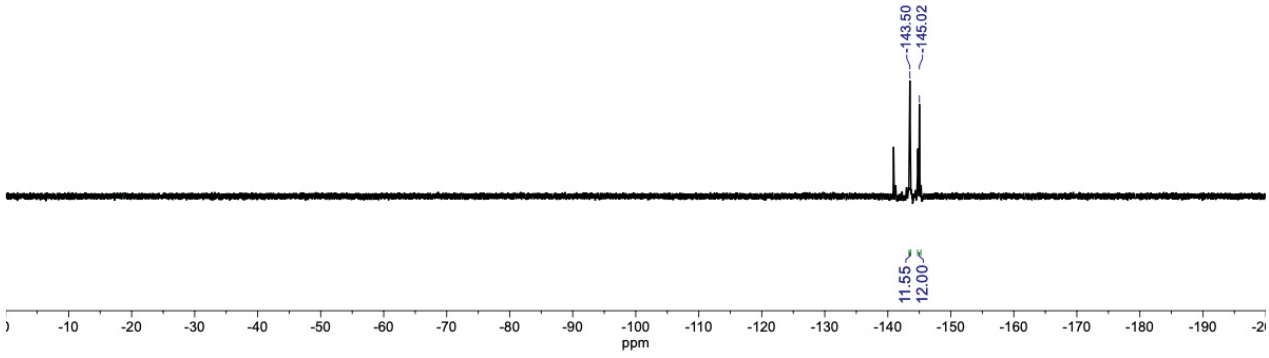

Figure S170: ^{19}F NMR spectrum (282 MHz, $CDCl_3$) of **FPOC8**.

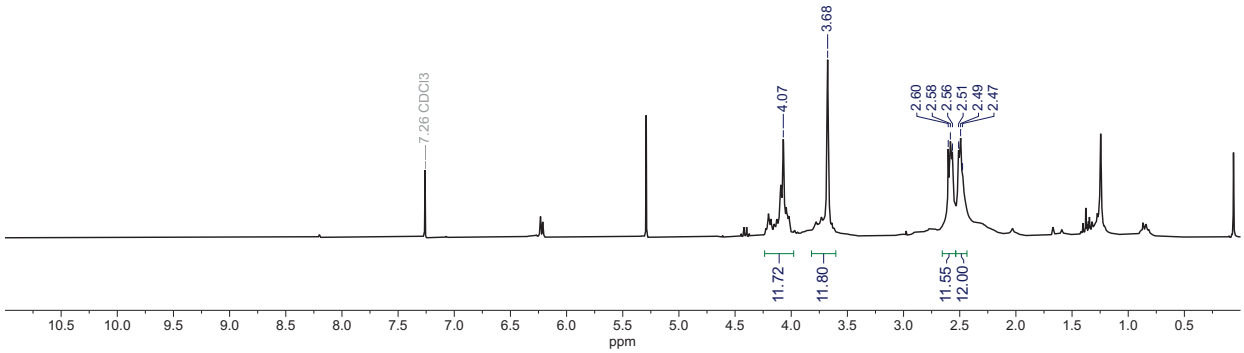

Figure S171: ^{1}H NMR spectrum (300 MHz, $CDCl_3$) of **RFPOC8**. 5.27 ppm - DCM, 1.28 - water.

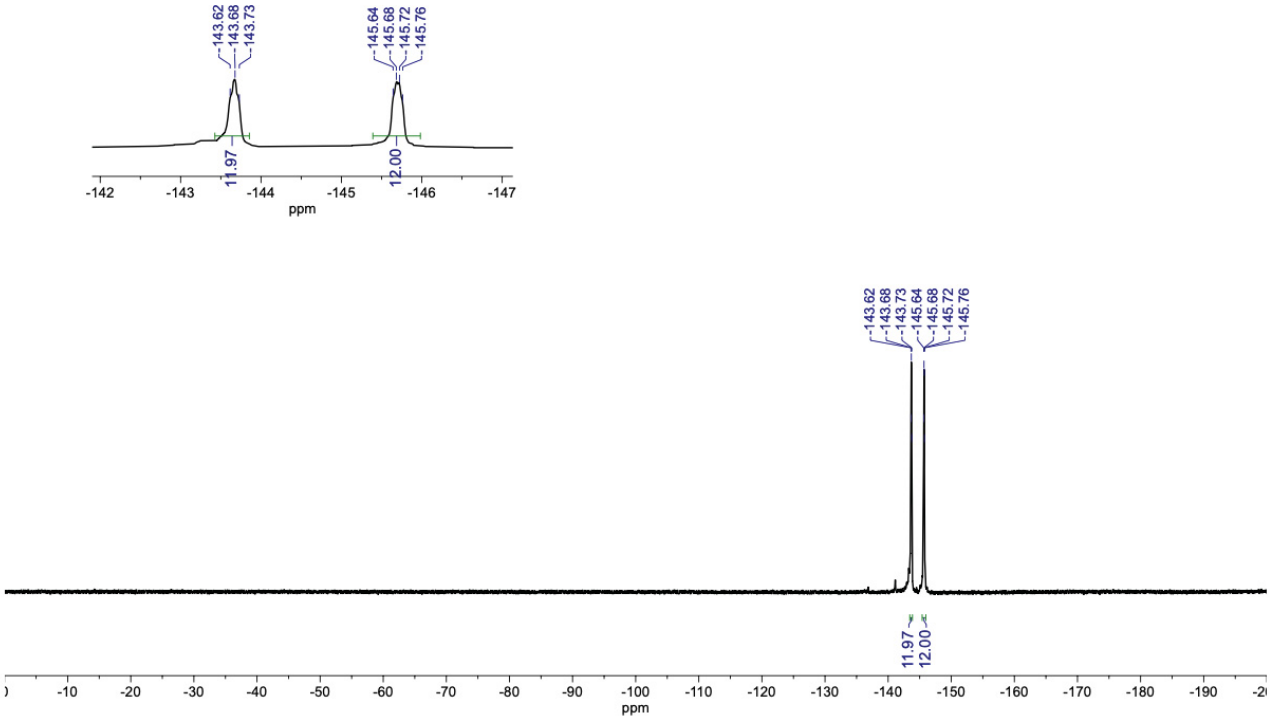

Figure S172: ^{19}F NMR spectrum (282 MHz, $CDCl_3$) of **RFPOC8**.

IR spectra

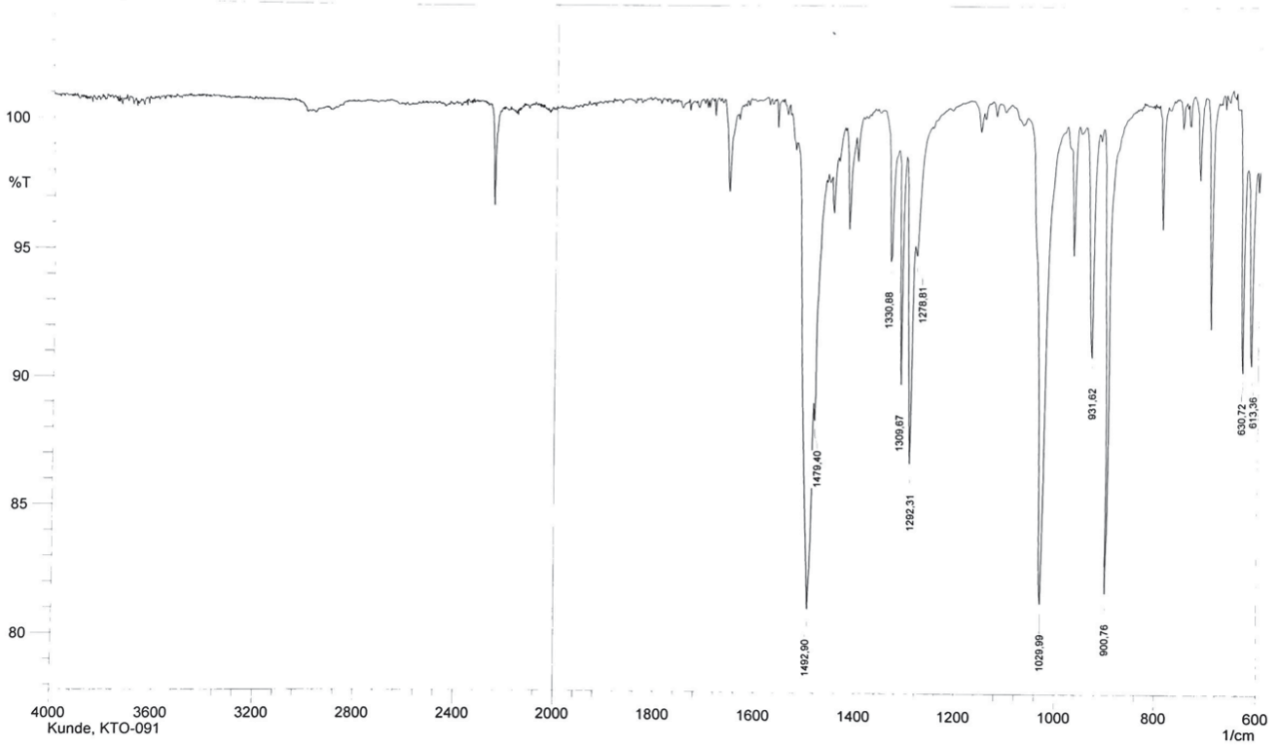

Figure S173: AT-IR spectrum of dinitrile **24**.

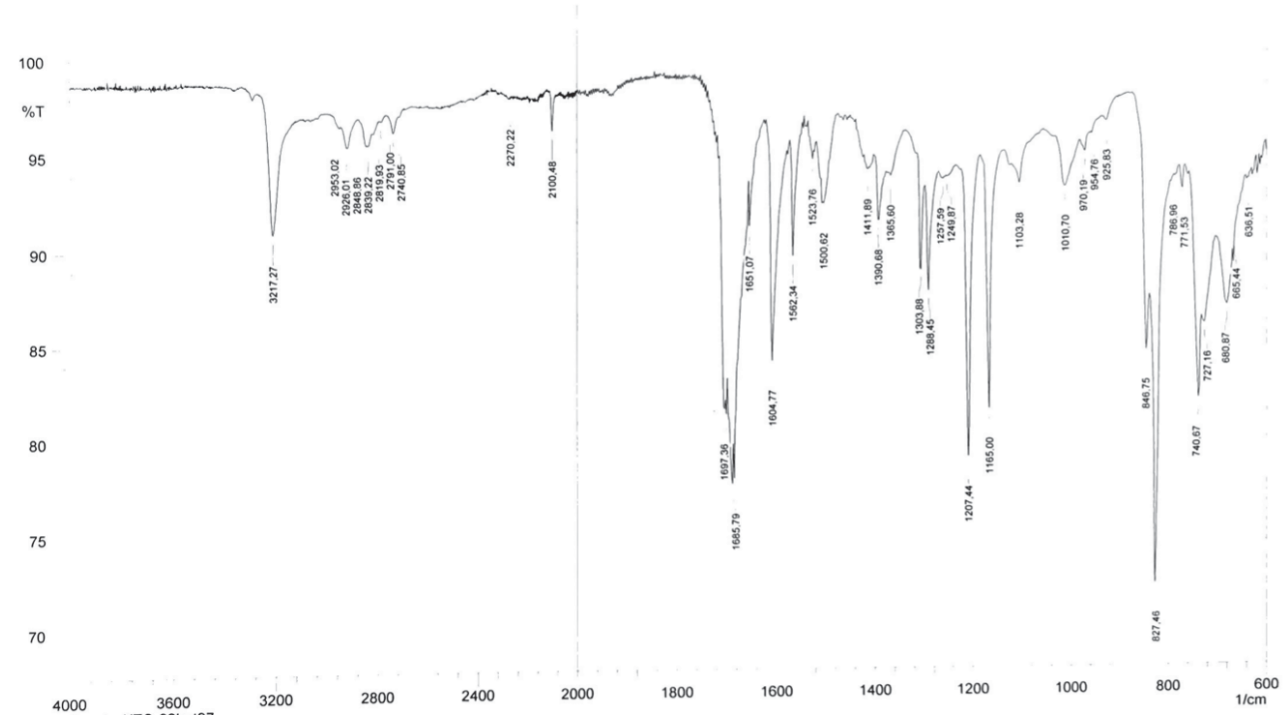

Figure S174: AT-IR spectrum of aldehyde **22**.

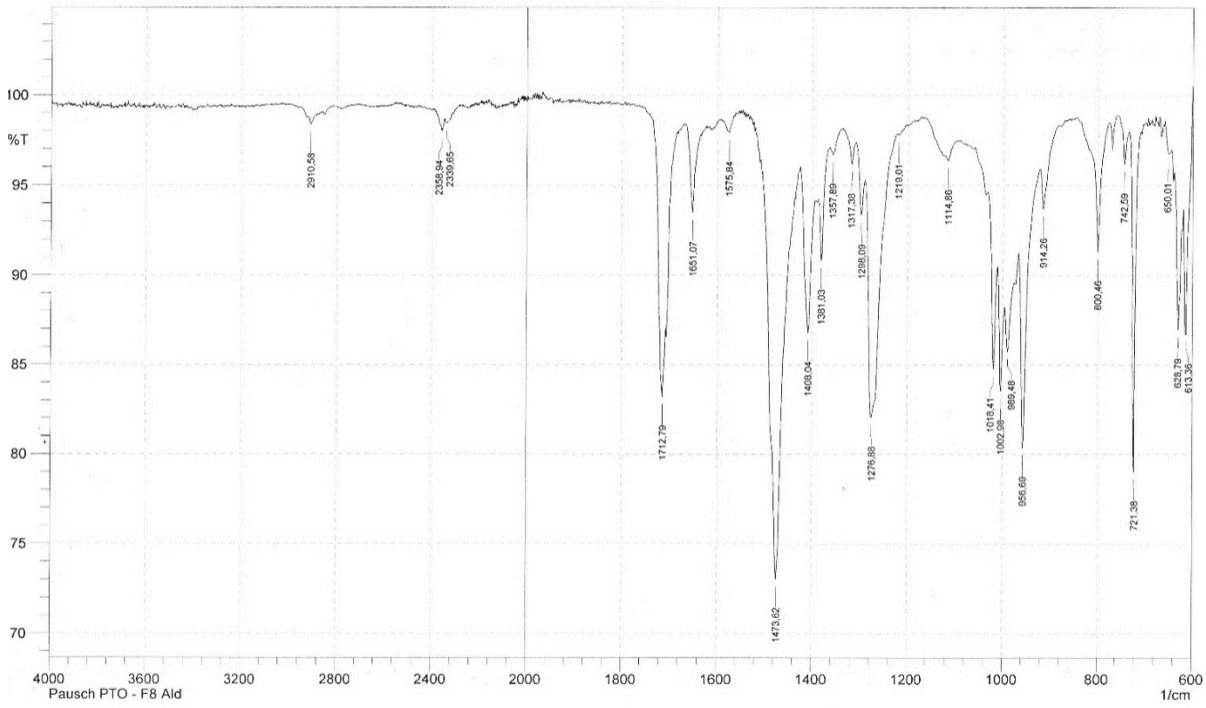

Figure S175: AT-IR spectrum of aldehyde **23**.

MS spectra

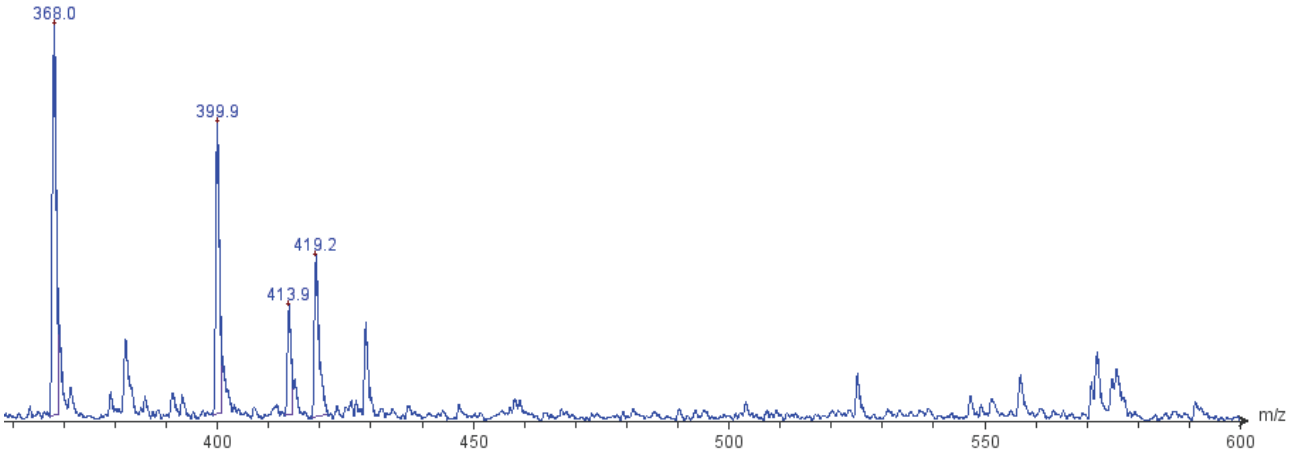

Figure S176: CI-MS spectrum of aldehyde **22;** the found ion mass of 368.0 m/z corresponds very well with the calculated mass of 368.0 m/z for [**22**+H]$^+$.

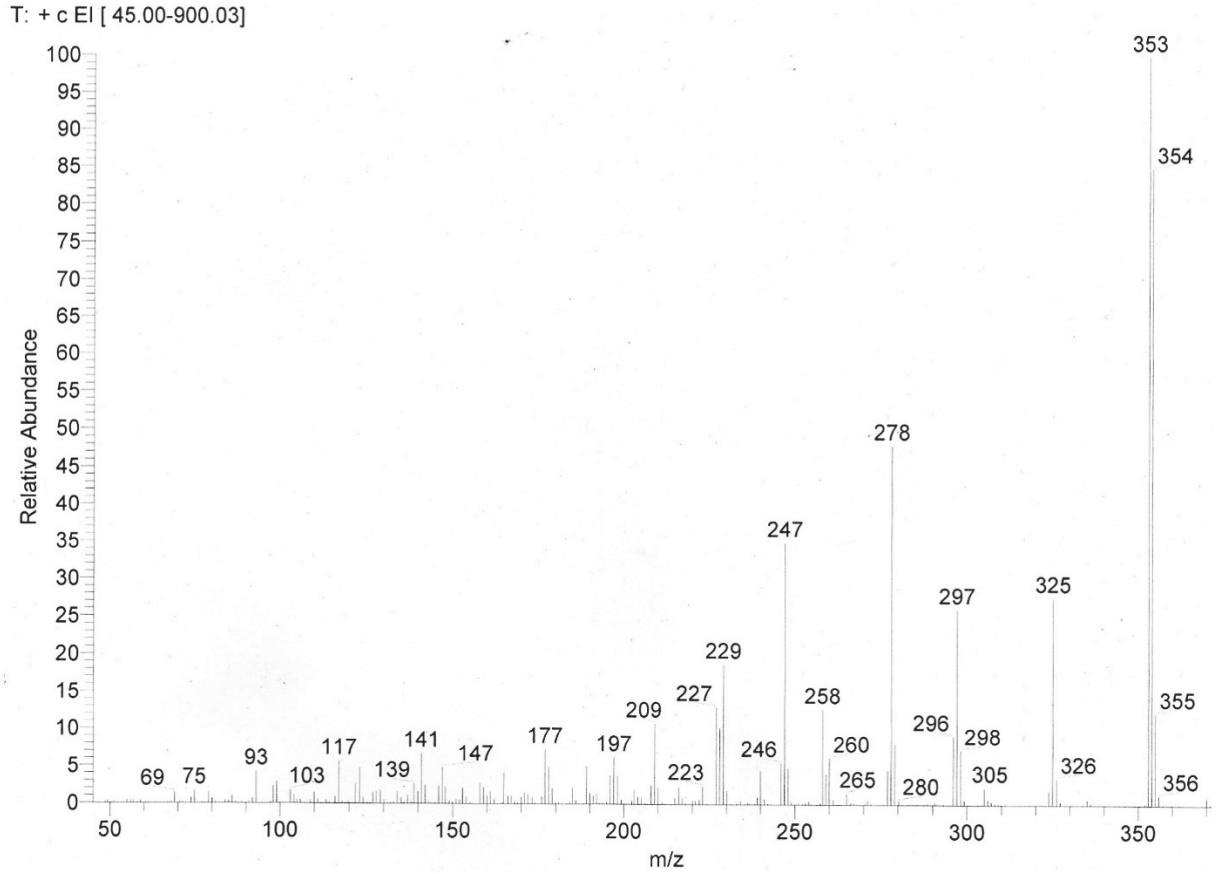

Figure S177: EI-MS spectrum of aldehyde **23**.

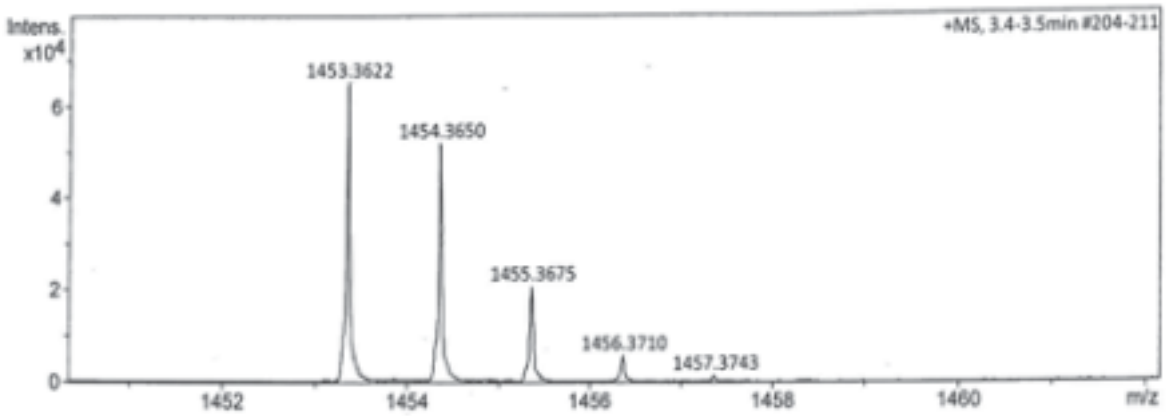

Figure S178: ESI-HRMS spectrum of **FPOC9**, the found: 1453.3622 m/z signal for [**FPOC9**+H]$^+$ corresponds very well with the calculated: 1453.3630 m/z.

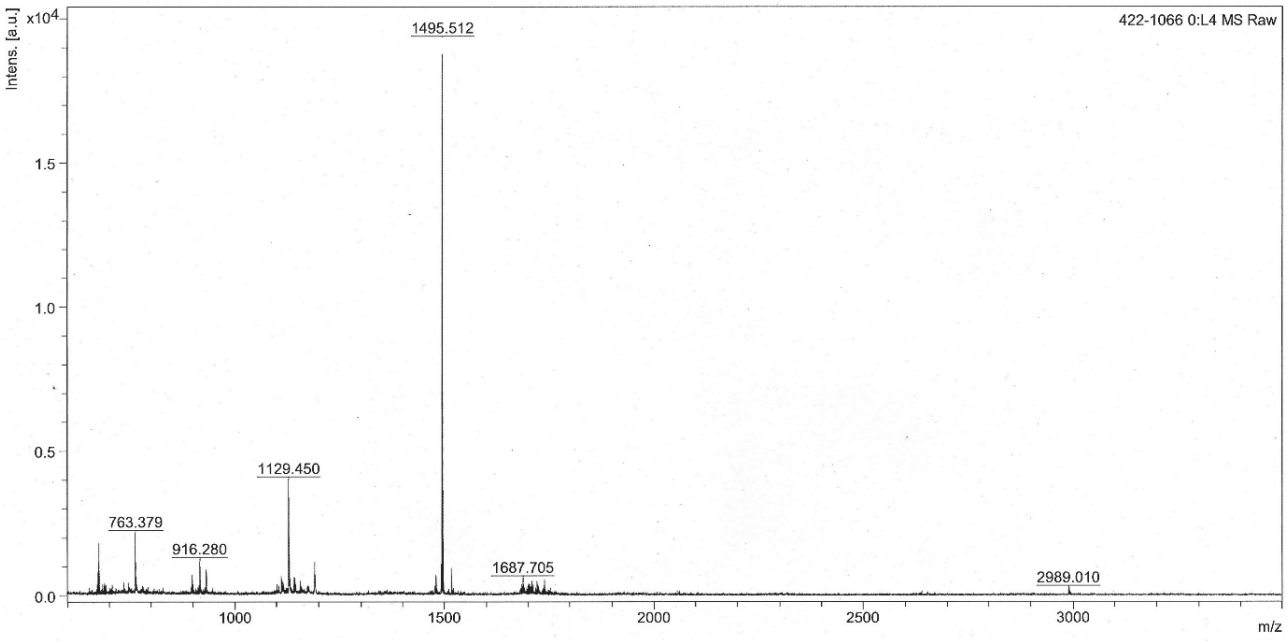

Figure S179: MALDI MS spectrum of **FPOC7**, the found: 1495.512 m/z signal for [**FPOC7**+H]$^+$ corresponds very well with the calculated: 1495.510 m/z.

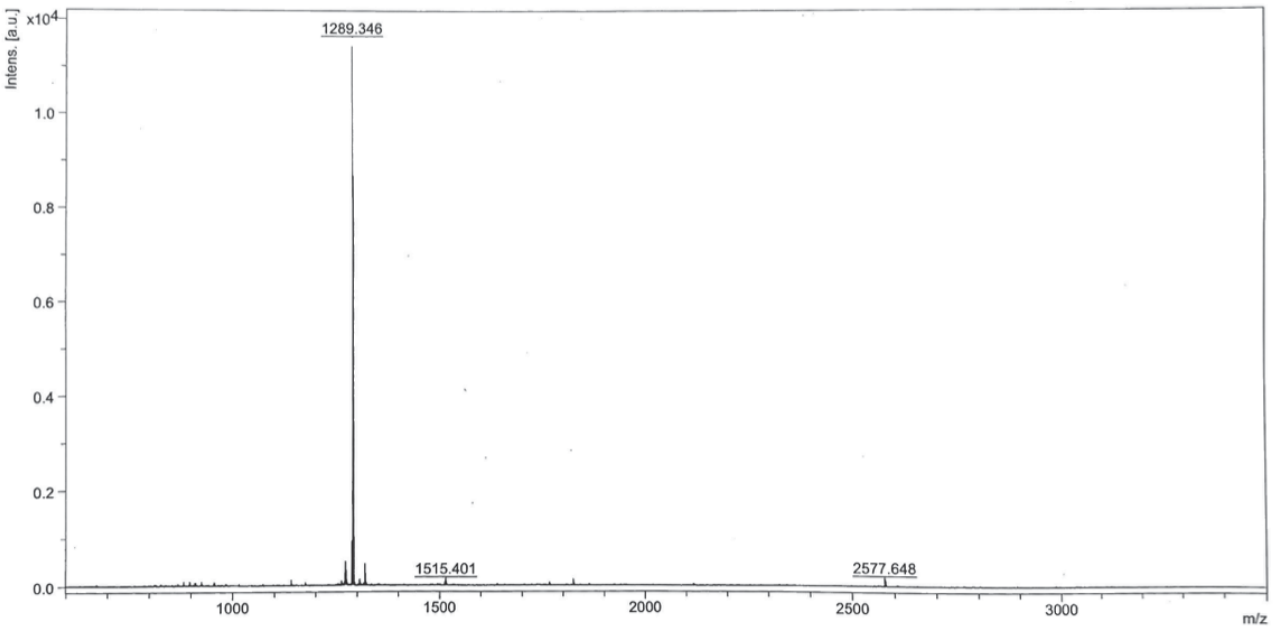

Figure S180: MALDI MS spectrum of **FPOC8**, the found: 1289.346 m/z signal for [**FPOC7**+H]$^+$ corresponds very well with the calculated: 1289.275 m/z.

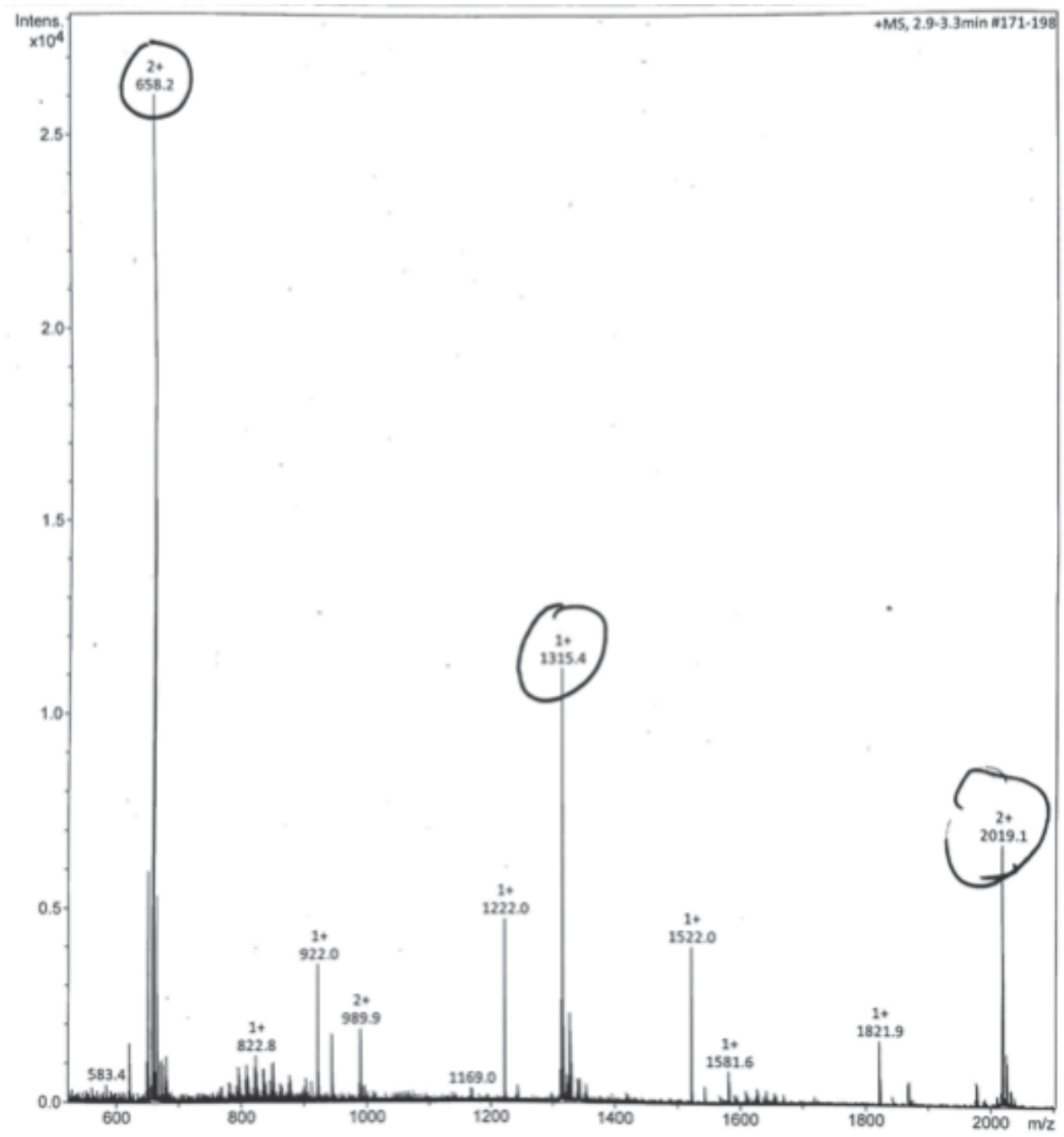

Figure S181: MALDI MS spectrum of **RFPOC8**, the found: 1315.4 m/z signal for [**FPOC7**+H]$^+$ corresponds very well with the calculated: 1315.5 m/z.

6.3. Spectra for Section 3.3

NMR spectra

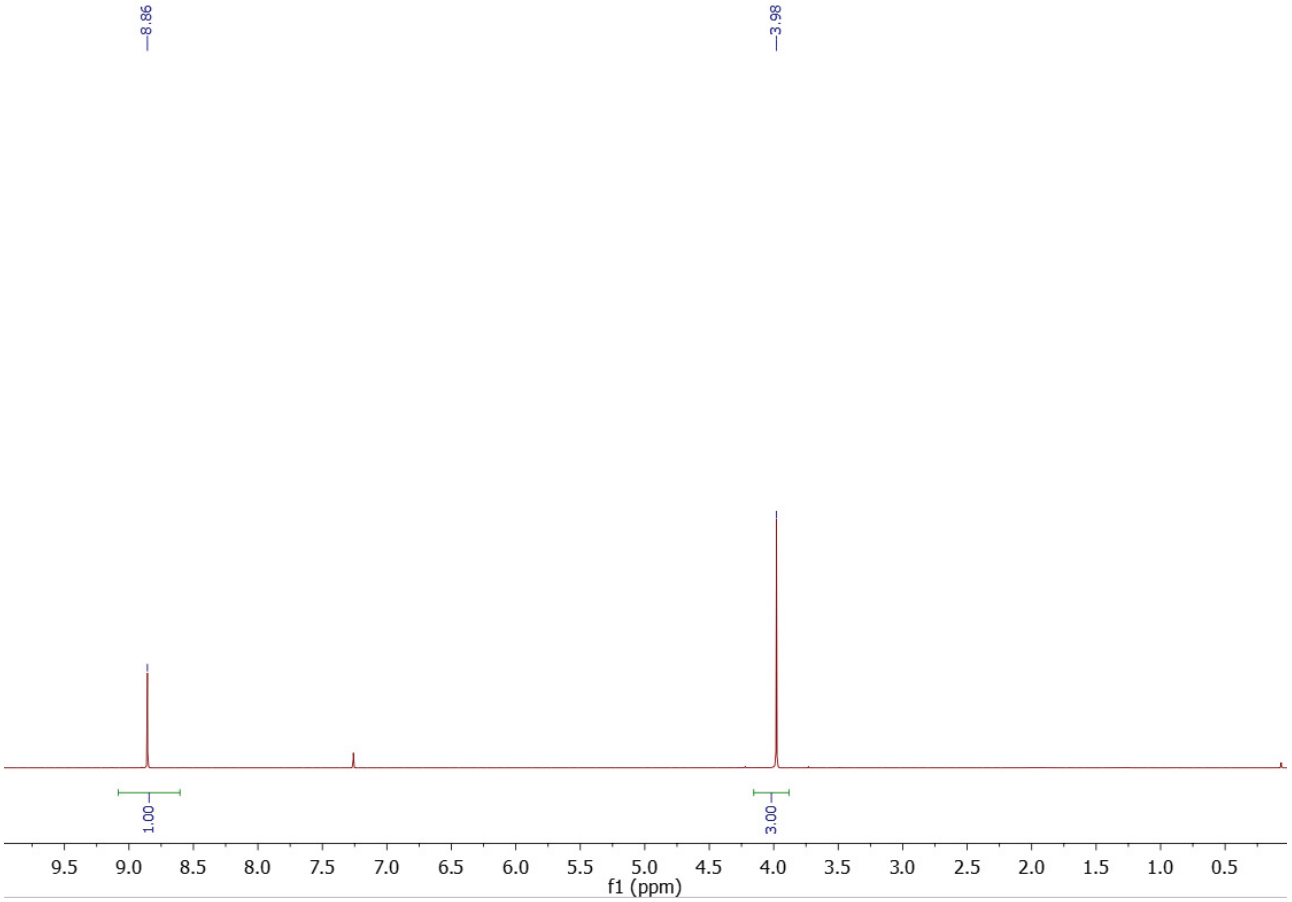

Figure S182: ^{1}H NMR spectrum (300 MHz, $CDCl_3$) of **26**.

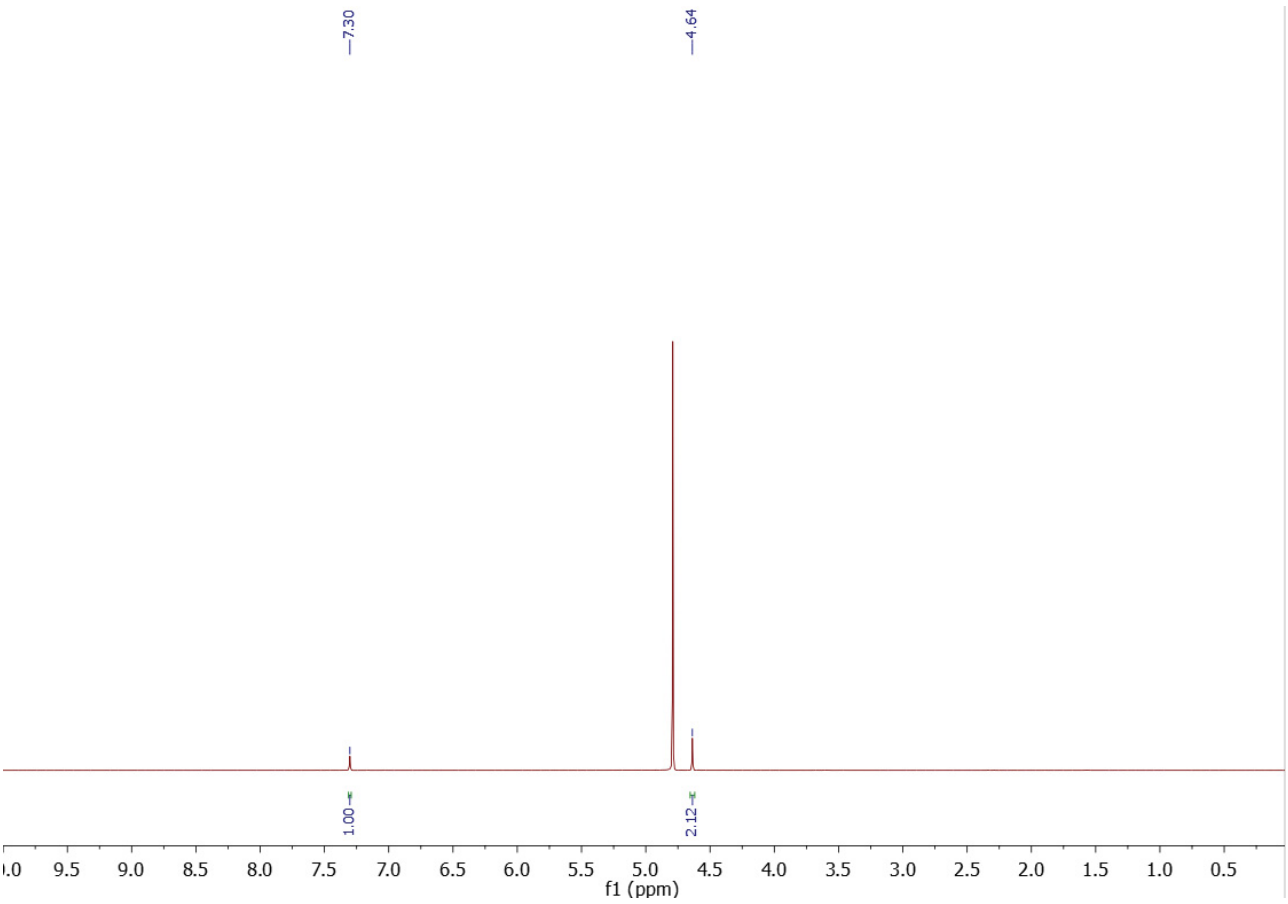

Figure S183: ^{1}H NMR spectrum (300 MHz, $CDCl_3$) of **27**.

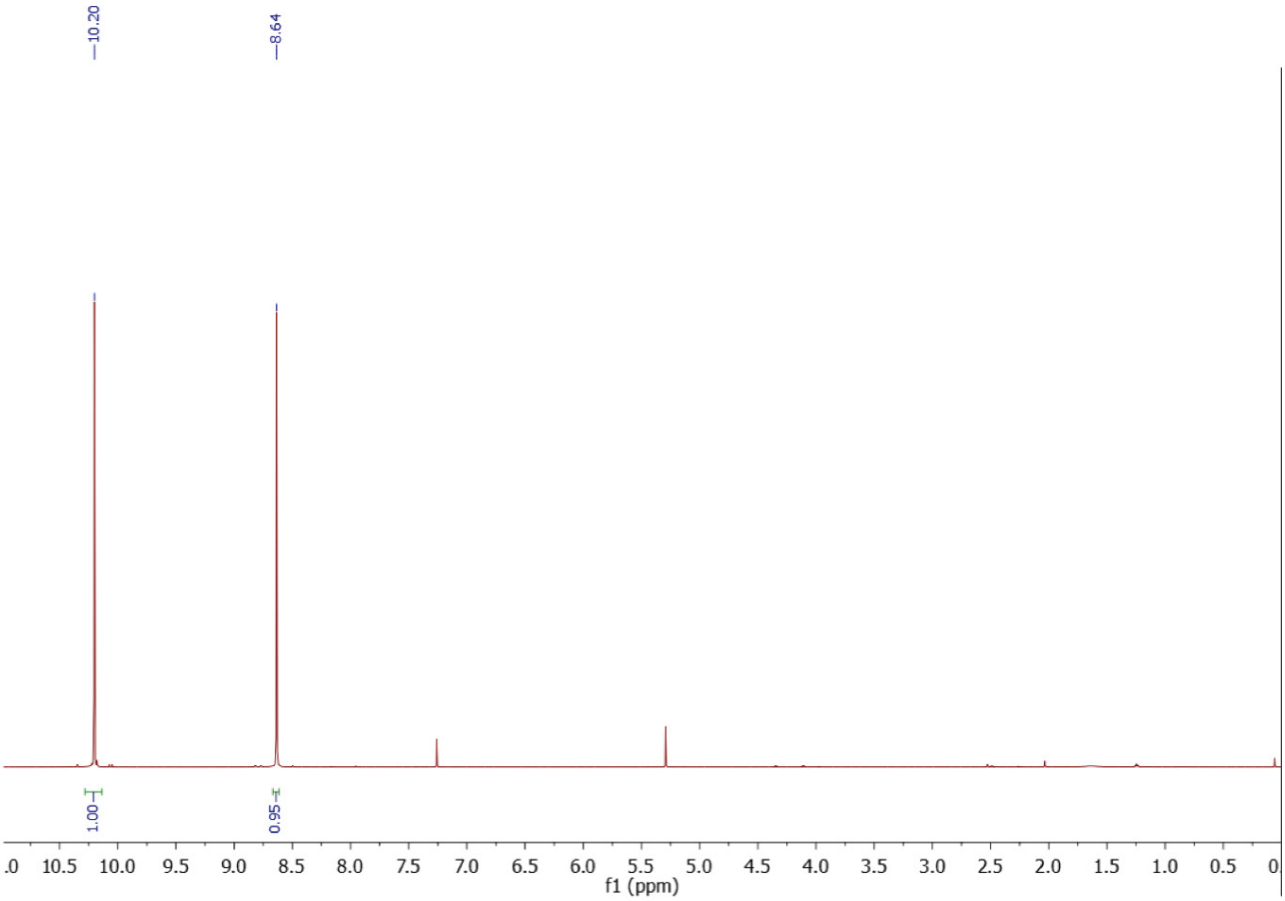

Figure S184: ^{1}H NMR spectrum (300 MHz, $CDCl_3$) of **TFB**.

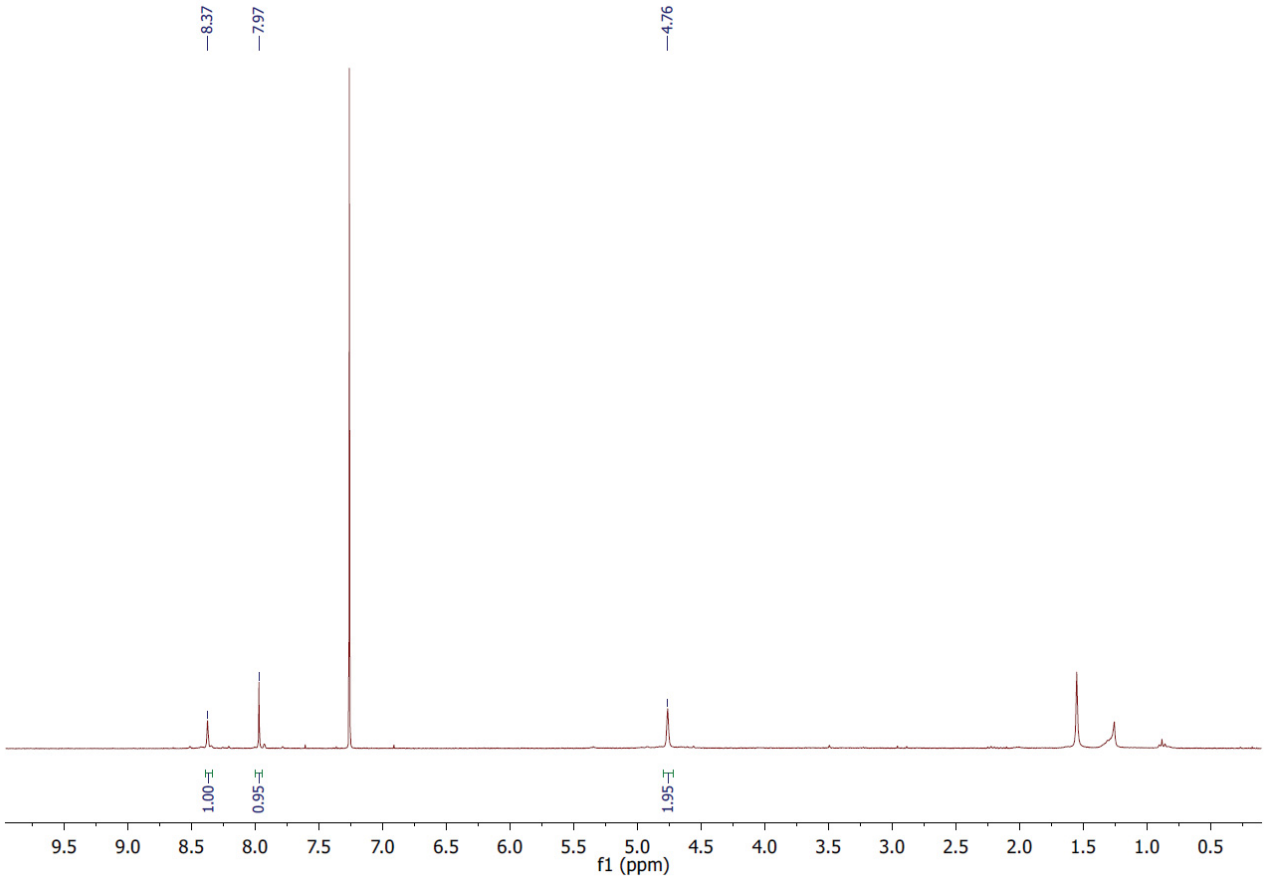

Figure S185: ^{1}H NMR spectrum (300 MHz, $CDCl_3$) of **FC1**.

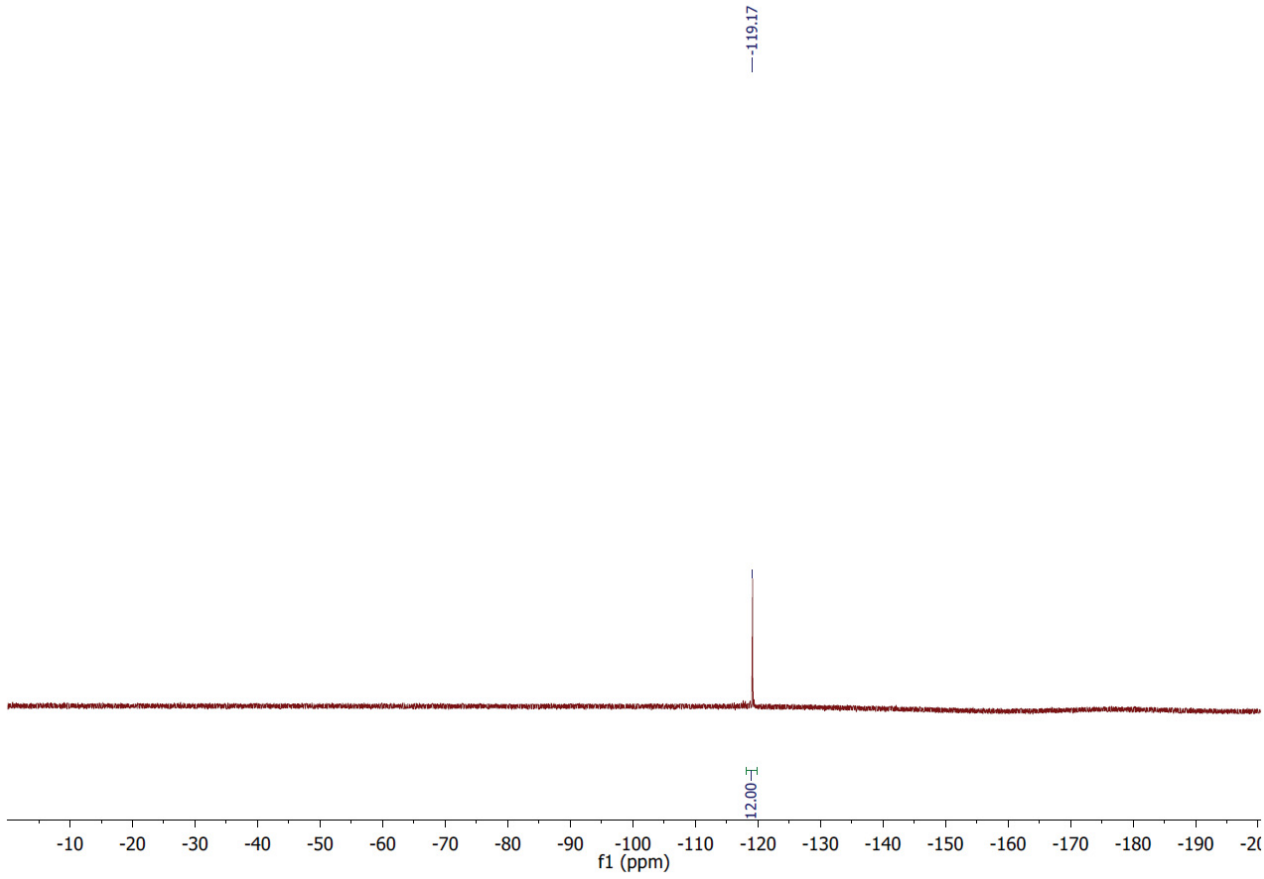

Figure S186: ^{19}F NMR spectrum (282 MHz, $CDCl_3$) of **FC1**.

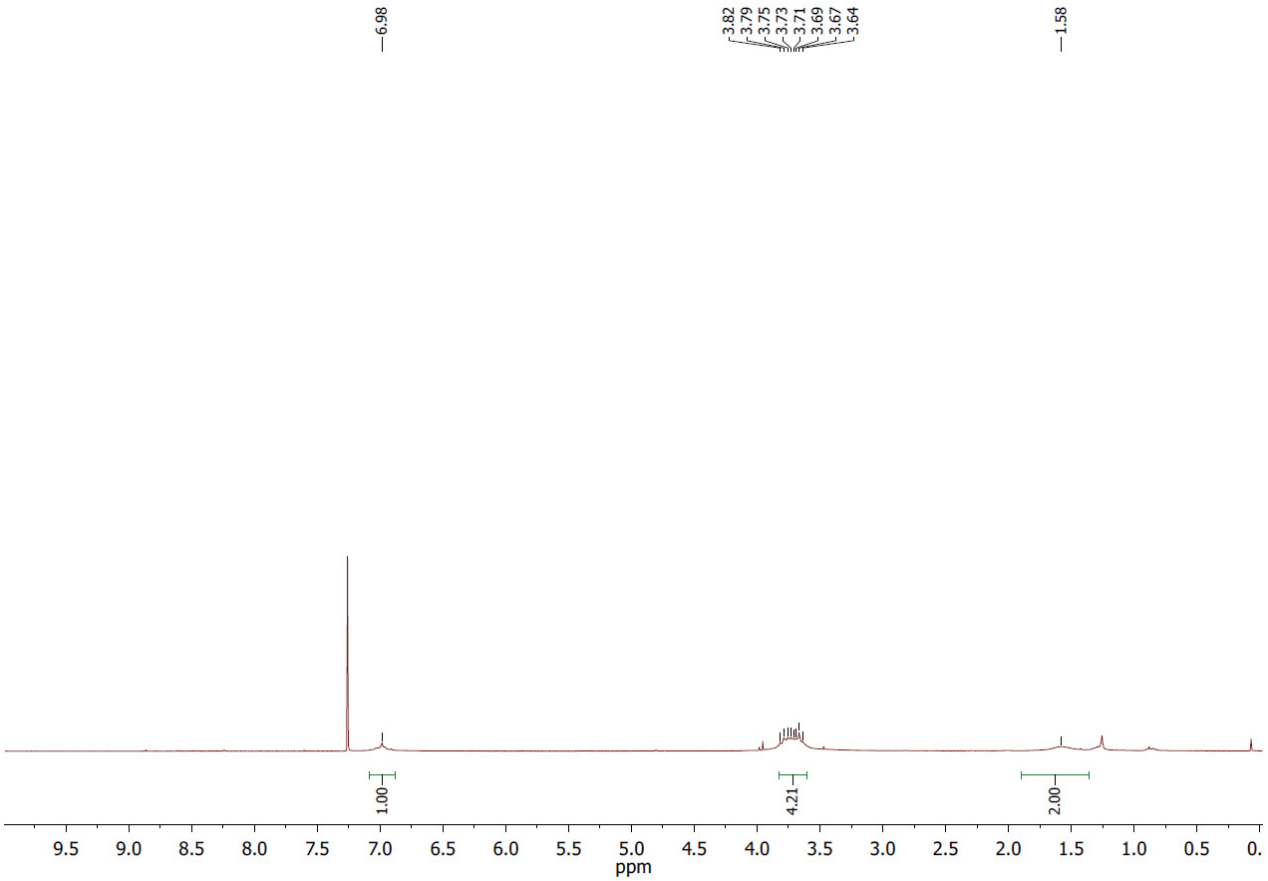

Figure S187: ^{1}H NMR spectrum (300 MHz, $CDCl_3$) of **FC1L**.

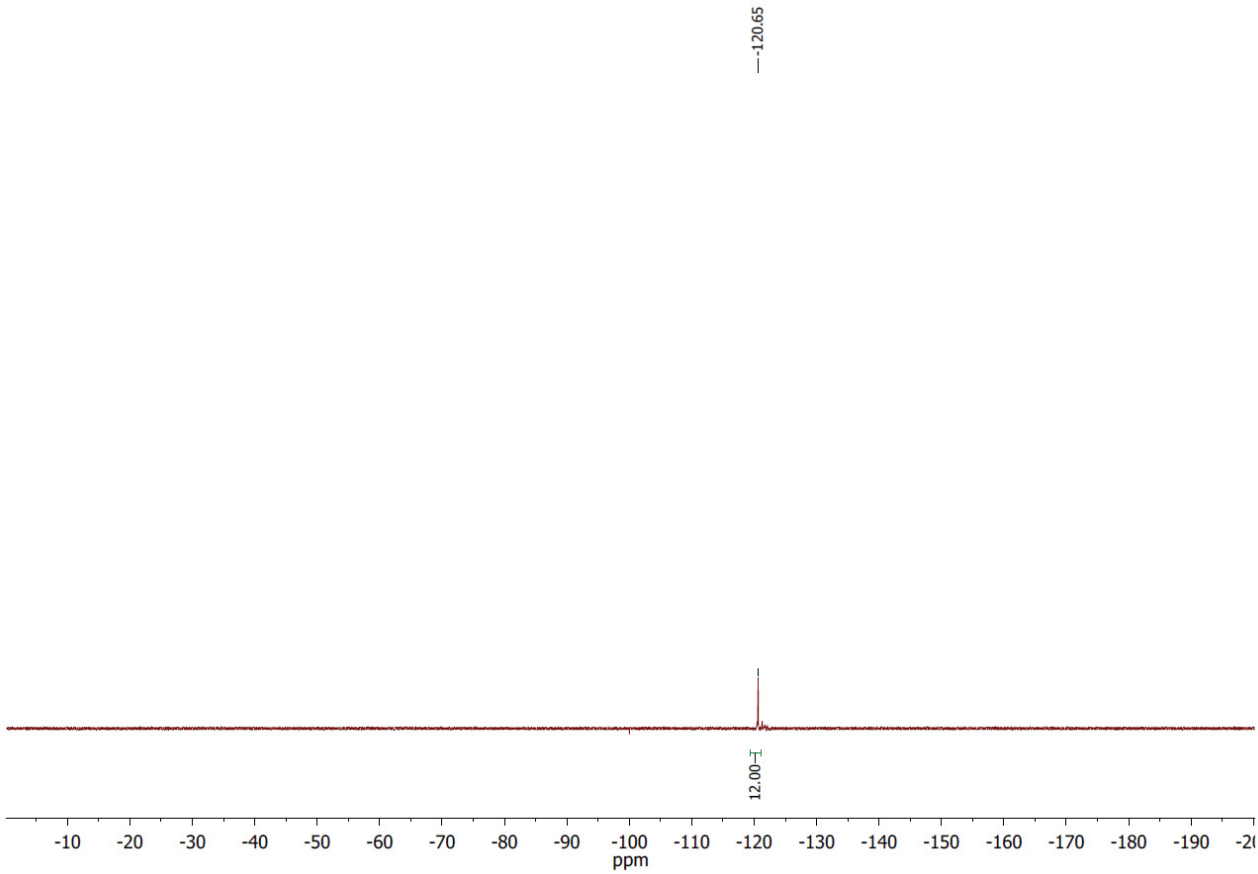

Figure S188: ^{19}F NMR spectrum (282 MHz, $CDCl_3$) of **FC1L**.

IR spectra

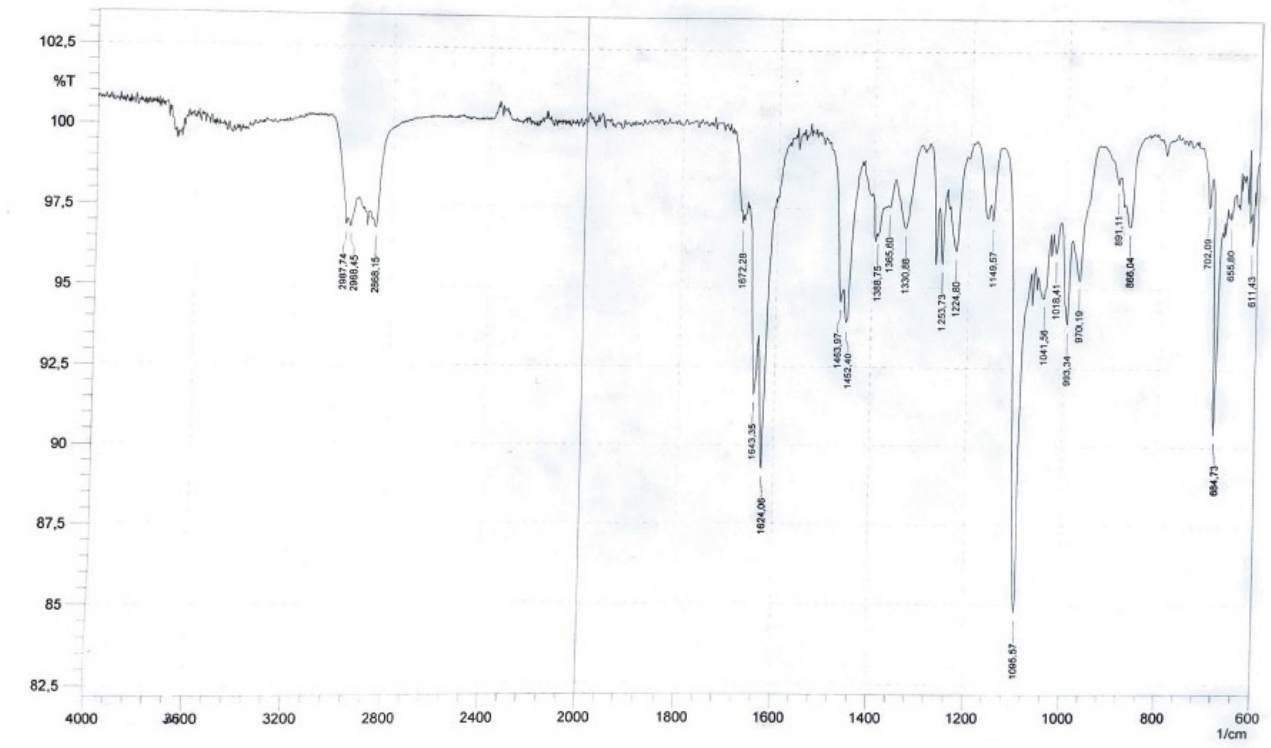

Figure S189: AT-IR spectrum of **FC1** in crystalline form.

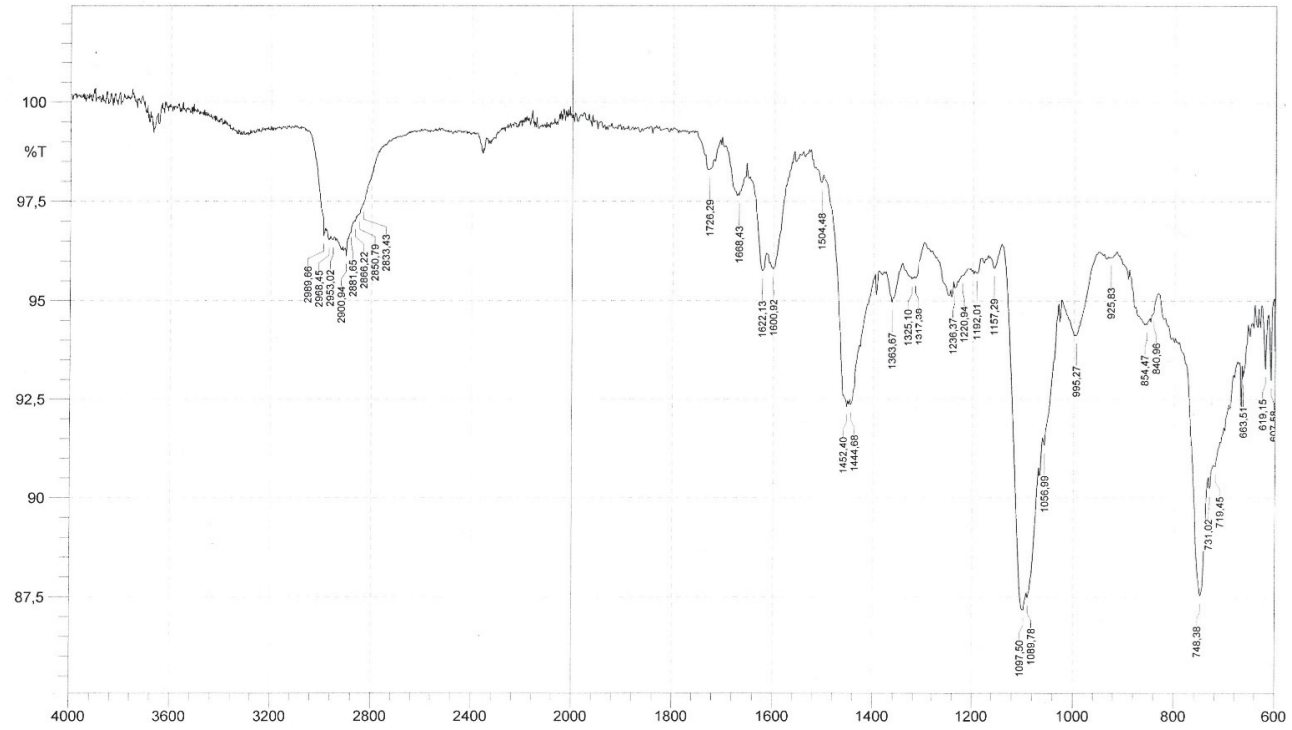

Figure S190: AT-IR spectrum of amine cage **FC1L**.

MS spectra

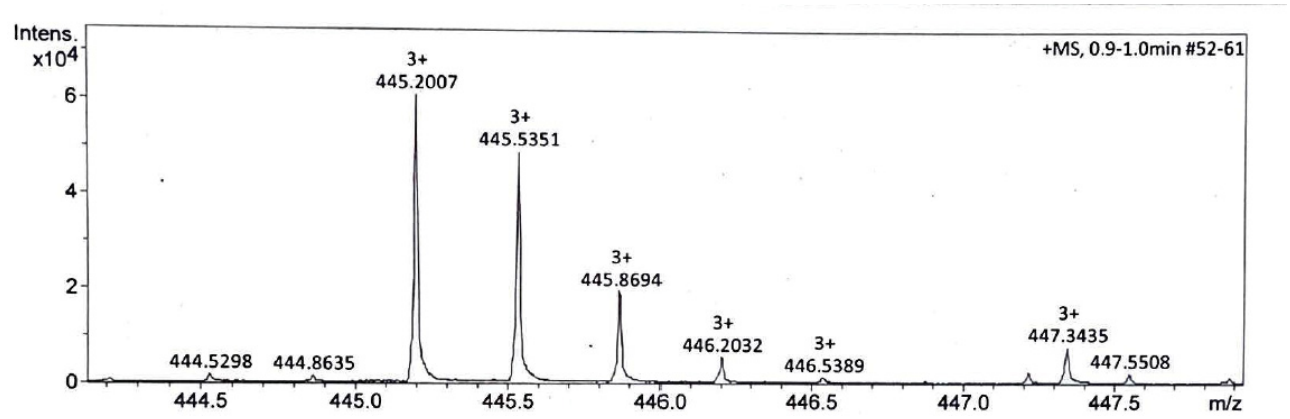

Figure S191: ESI-HRMS spectrum of **FC1L**. The found $[M+3H]^{3+}$ ion mass: 445.2007 m/z corresponds very well to the calculated triply charged m/z = 445.2010.

6.4. Spectra for Section 3.4

NMR spectra

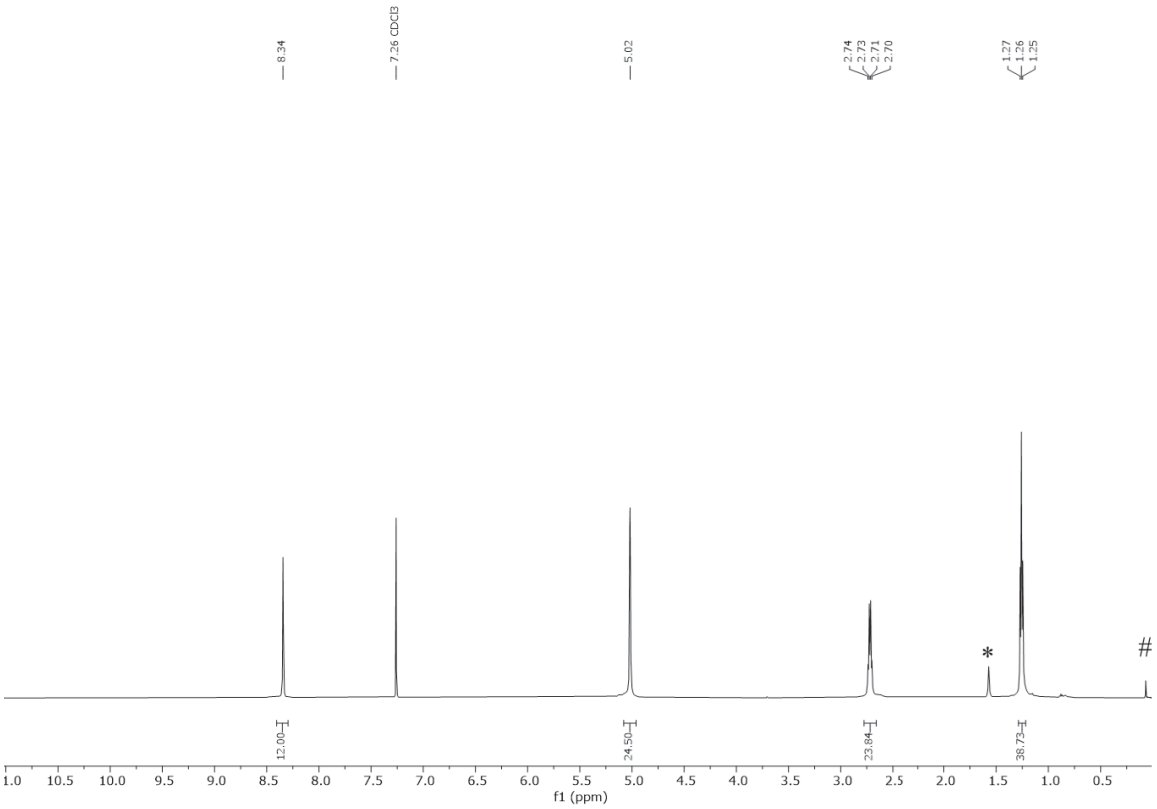

Figure S192: ^{1}H NMR spectrum (600 MHz, $CDCl_3$) of cage compound $\mathbf{A_4F_6}$. *water #H-grease

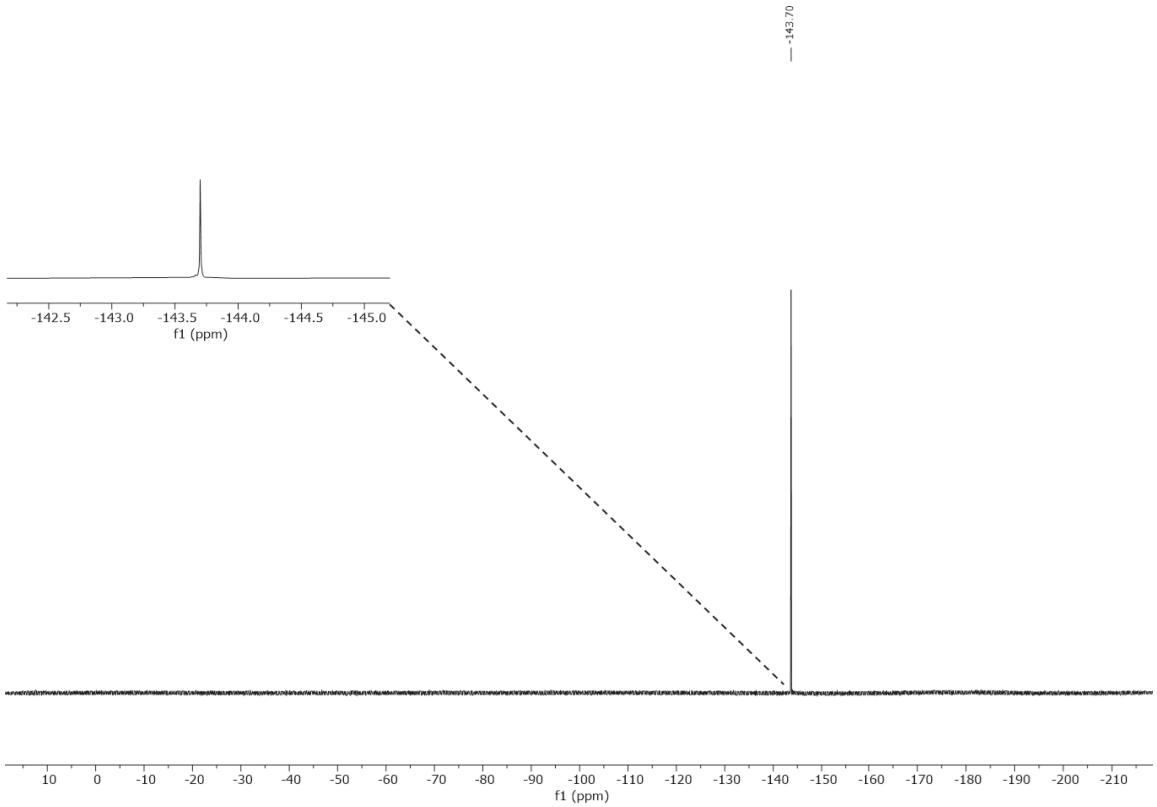

Figure S193: ^{19}F NMR spectrum (565 MHz, $CDCl_3$) of cage compound $\mathbf{A_4F_6}$.

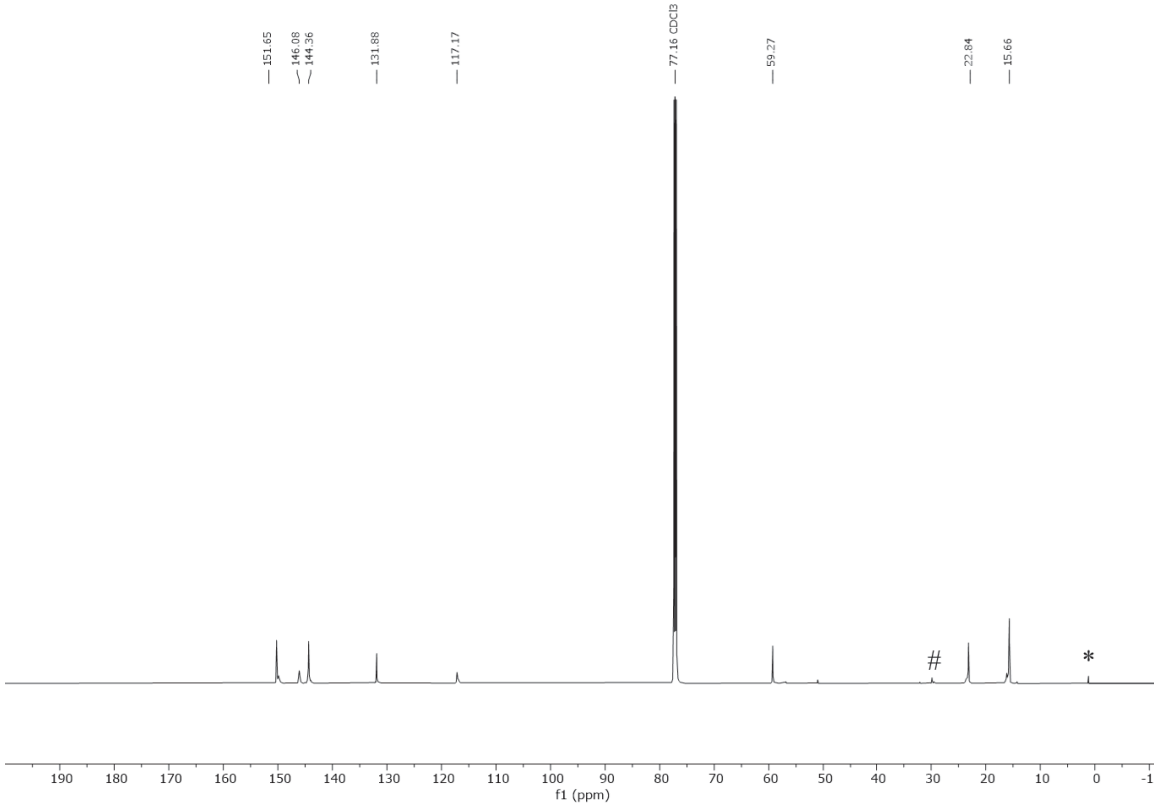

Figure S194: $^{13}C\{^1H\}$ NMR (151 MHz, $CDCl_3$) spectrum of cage compound $\mathbf{A_4F_6}$. *silicone grease #H-grease

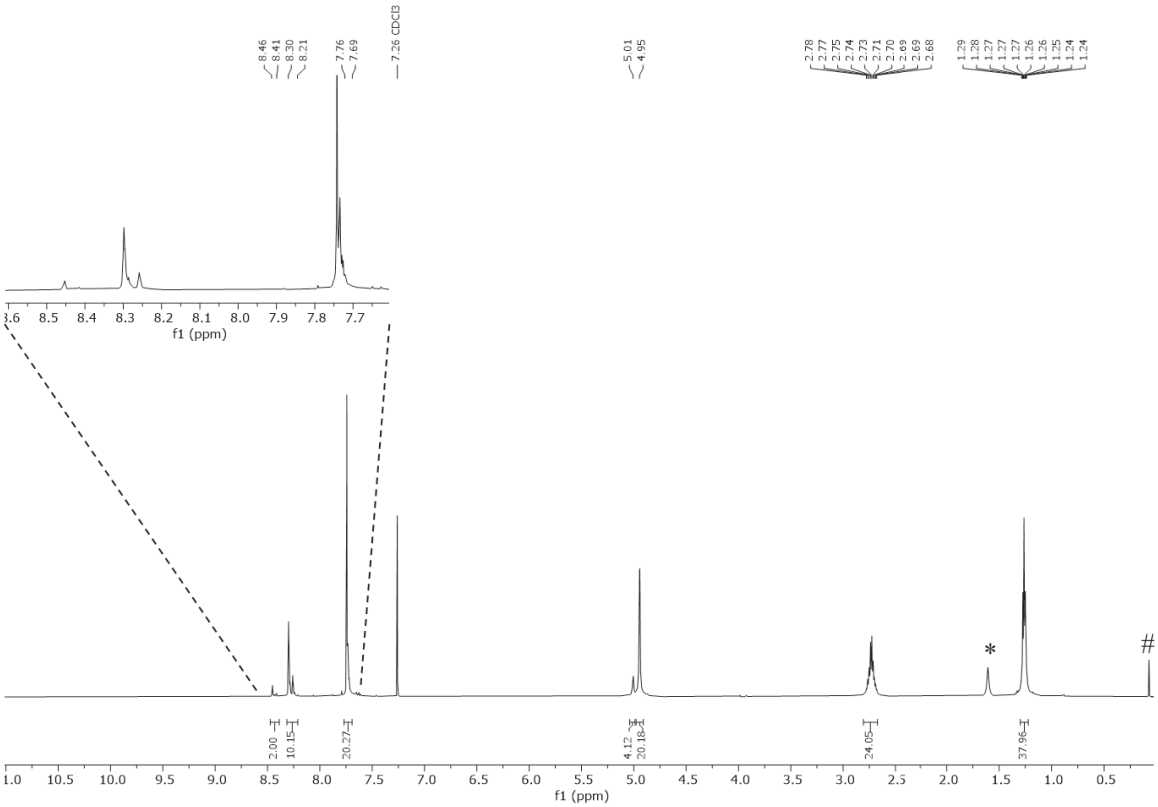

Figure S195: ^{1}H NMR spectrum (600 MHz, $CDCl_3$) of cage mixture $\mathbf{A_4H_5F_1}$. *water, #H-grease

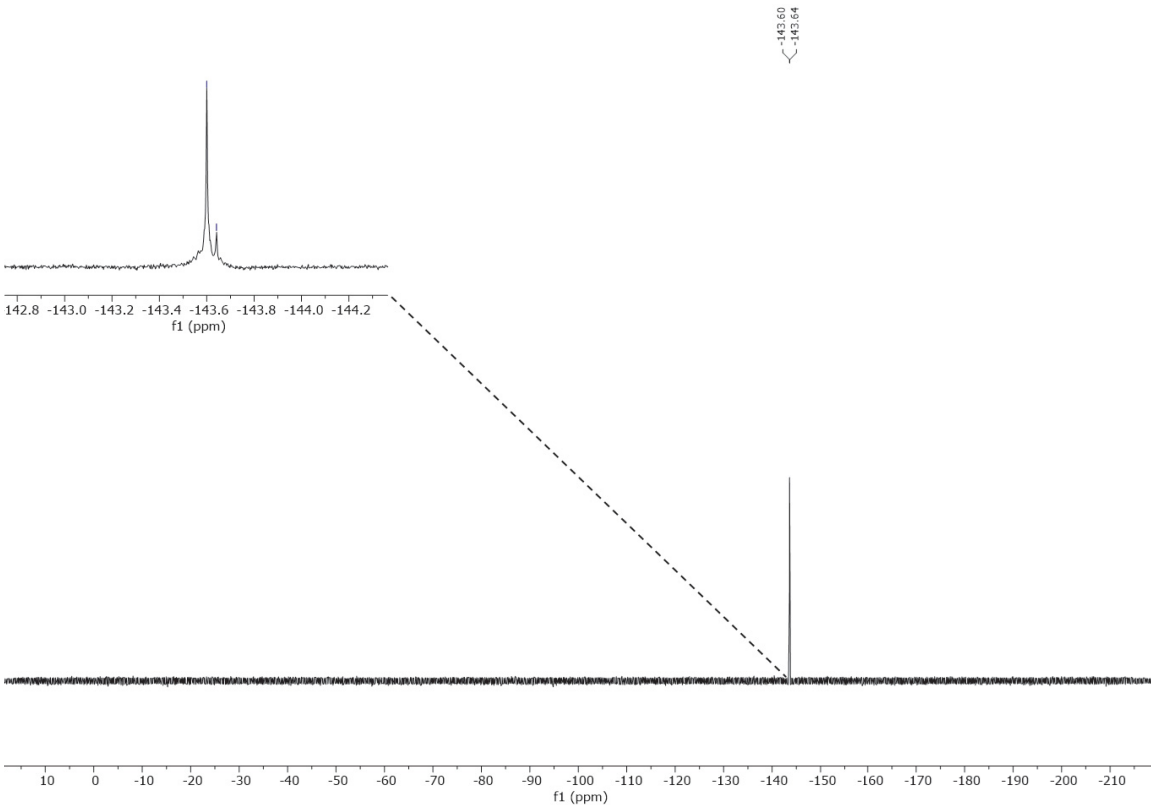

Figure S196: ^{19}F NMR spectrum (565 MHz, $CDCl_3$) of cage mixture $\mathbf{A_4H_5F_1}$.

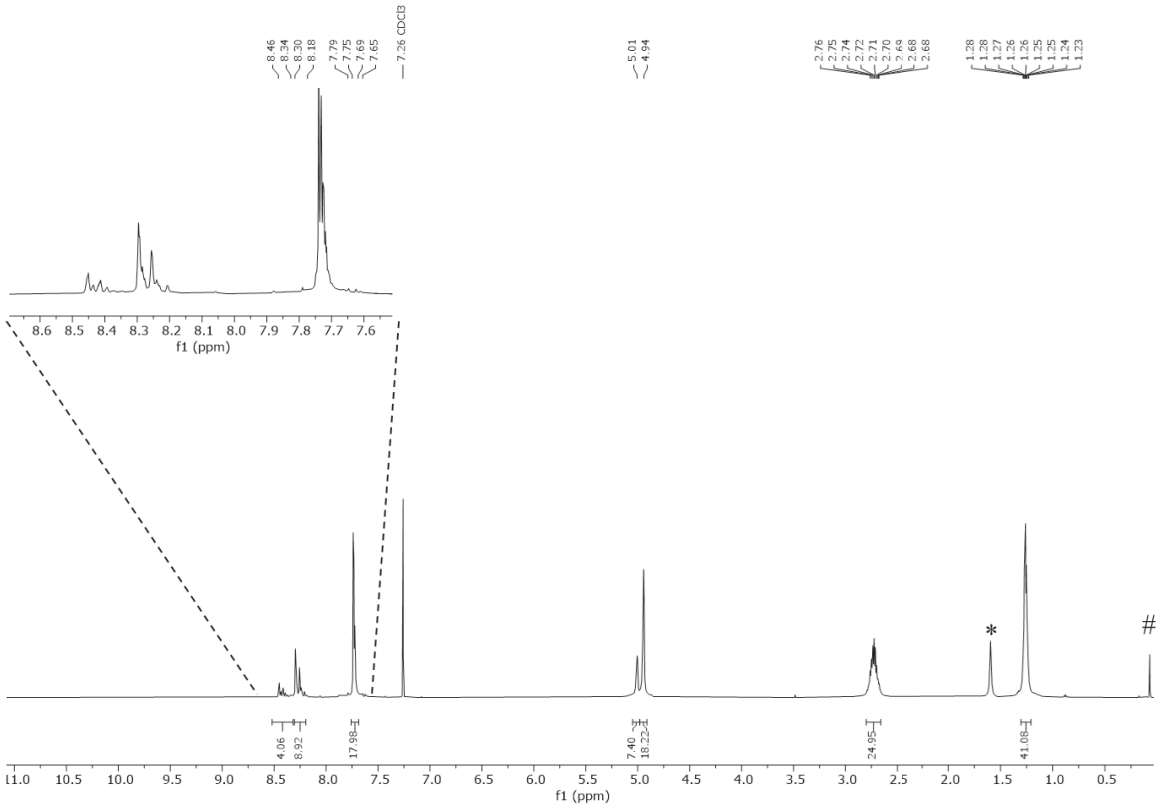

Figure S197: ^{1}H NMR spectrum (600 MHz, $CDCl_3$) of cage mixture $\mathbf{A_4H_4F_2}$. *water, #H-grease

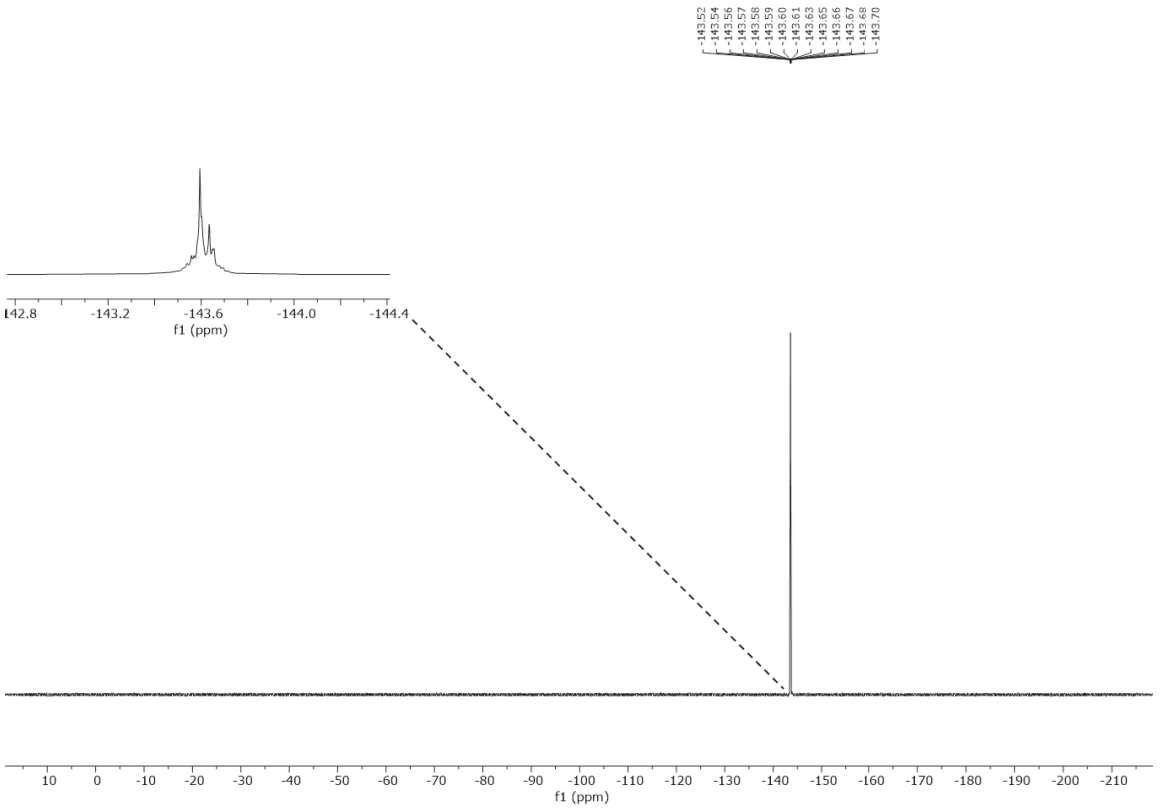

Figure S198: ^{19}F NMR spectrum (565 MHz, $CDCl_3$) of cage mixture $\mathbf{A_4H_4F_2}$.

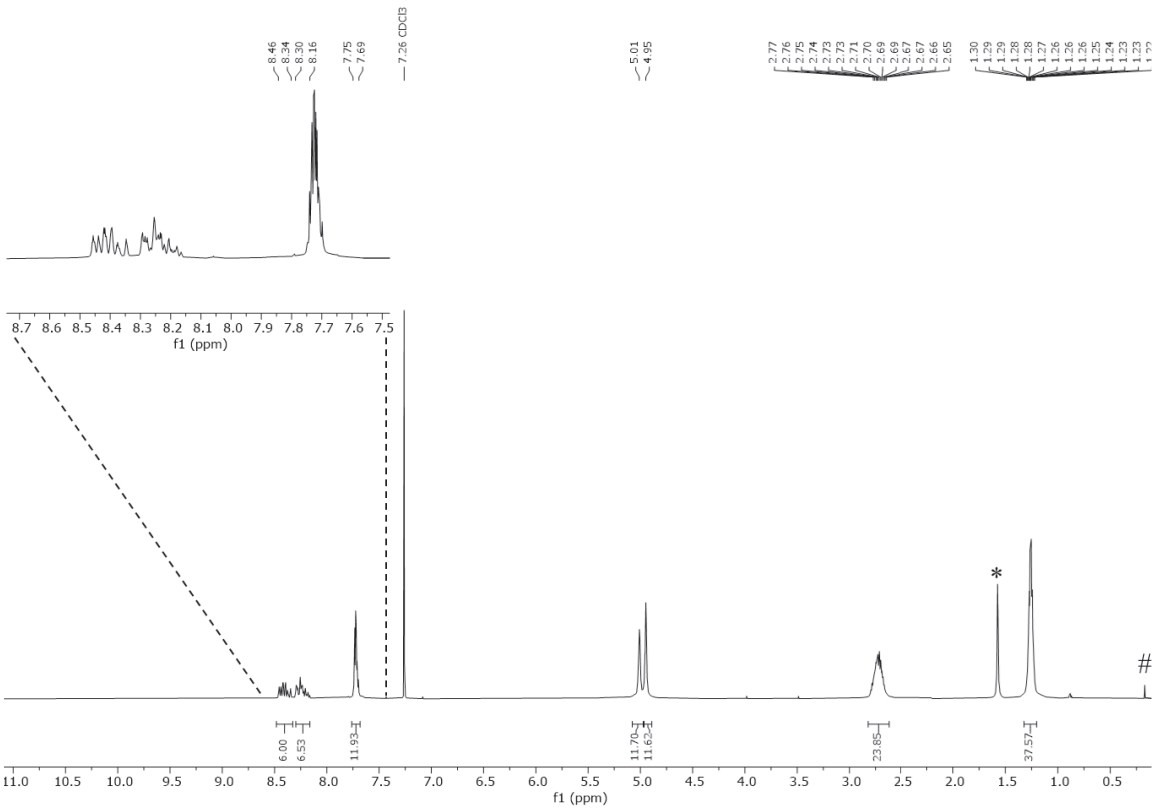

Figure S199: ^{1}H NMR spectrum (600 MHz, $CDCl_3$) of cage mixture $\mathbf{A_4H_3F_3}$. *water, #H-grease

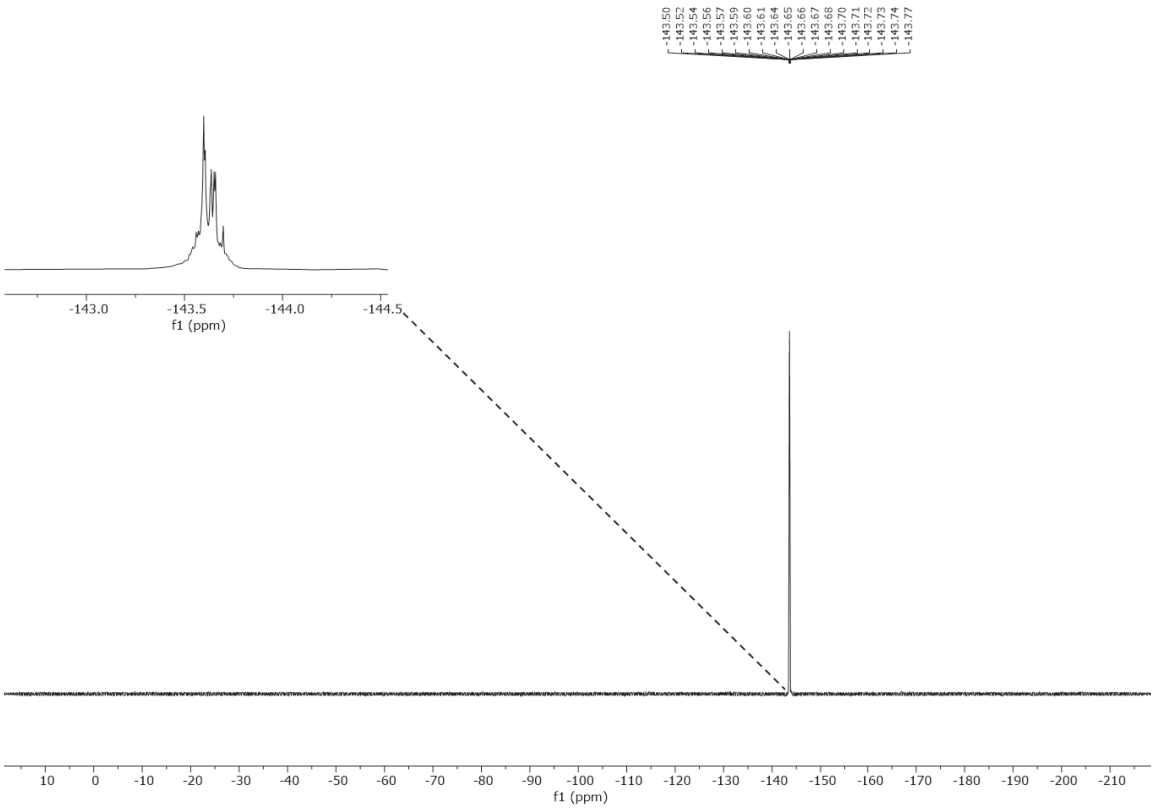

Figure S200: ^{19}F NMR spectrum (565 MHz, $CDCl_3$) of cage mixture $\mathbf{A_4H_3F_3}$.

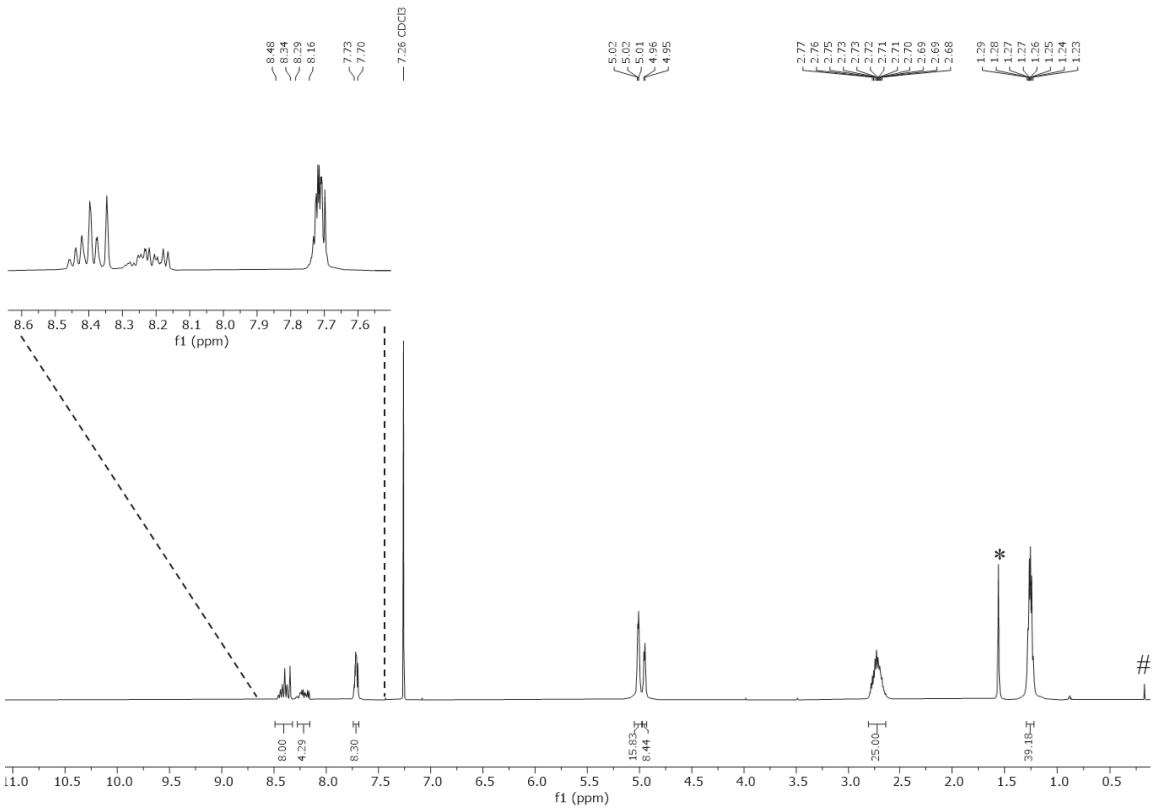

Figure S201: ^{1}H NMR spectrum (600 MHz, $CDCl_3$) of cage mixture $\mathbf{A_4H_2F_4}$. *water, #H-grease

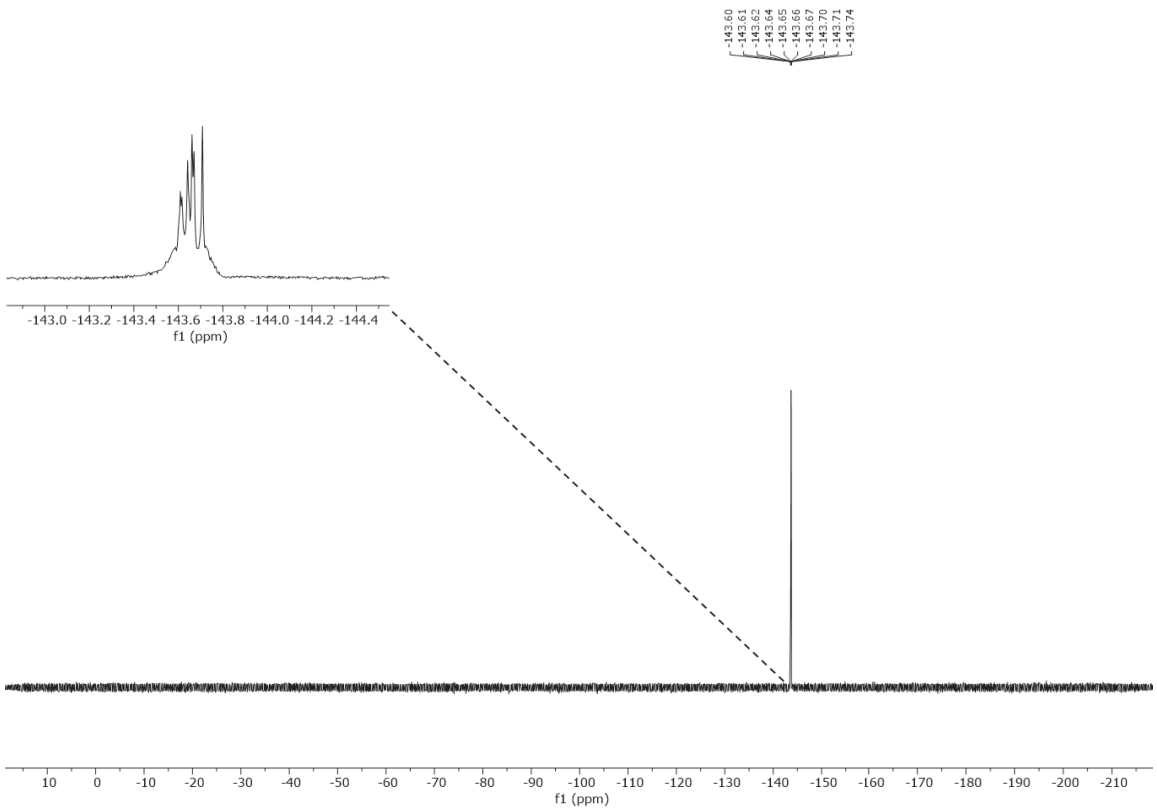

Figure S202: ^{19}F NMR spectrum (565 MHz, $CDCl_3$) of cage mixture $\mathbf{A_4H_2F_4}$.

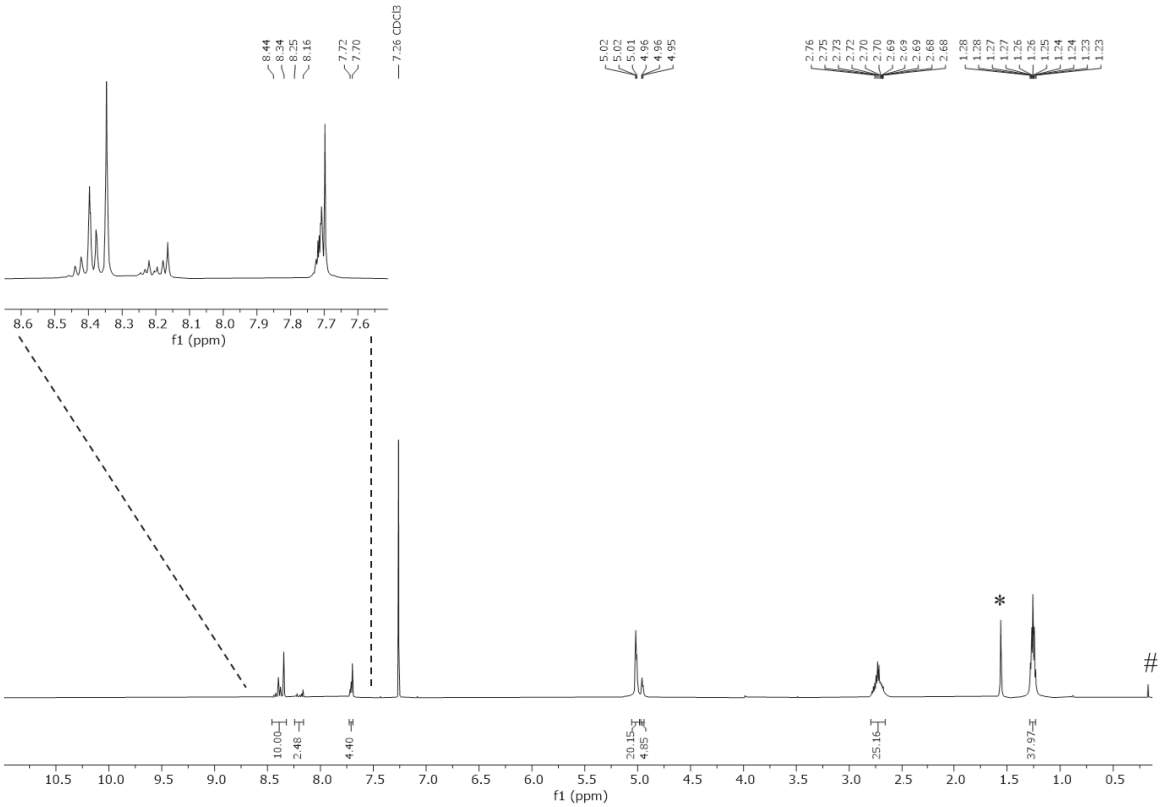

Figure S203: ^{1}H NMR spectrum (600 MHz, $CDCl_3$) of cage mixture $\mathbf{A_4H_1F_5}$. *water, #H-grease

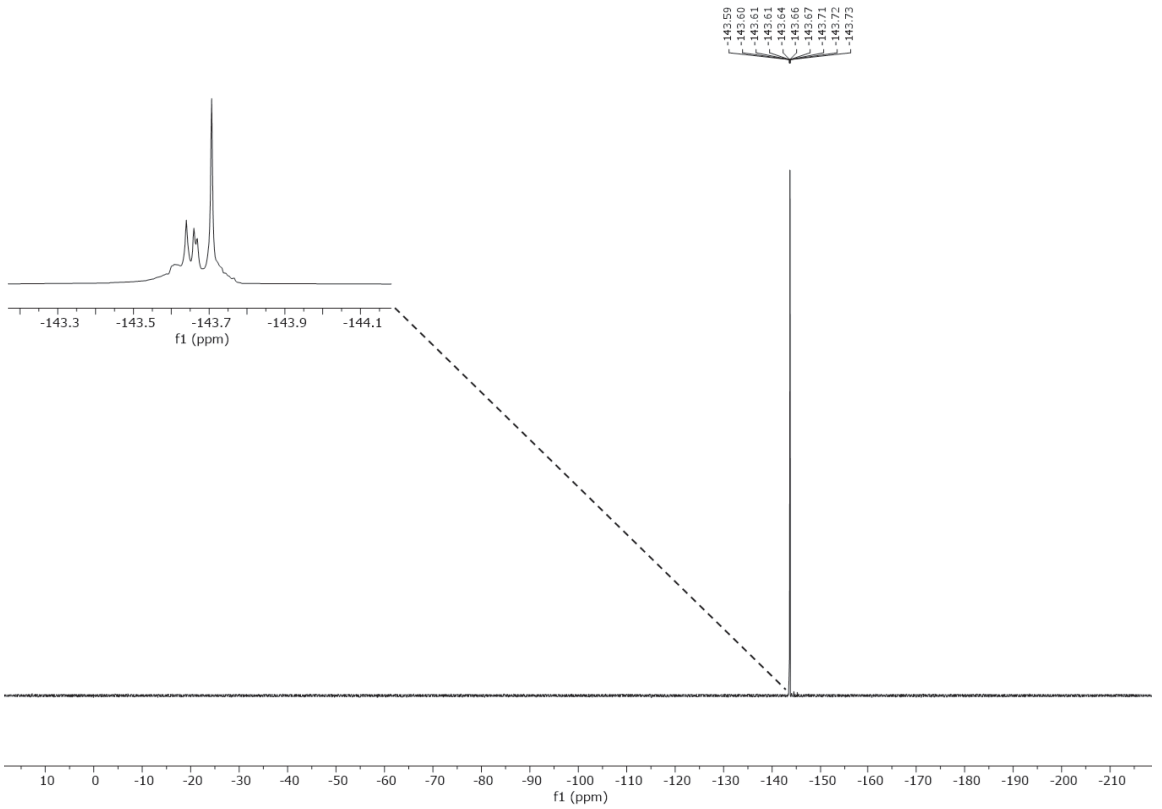

Figure S204: ^{19}F NMR spectrum (565 MHz, $CDCl_3$) of cage mixture $\mathbf{A_4H_1F_5}$.

IR spectra

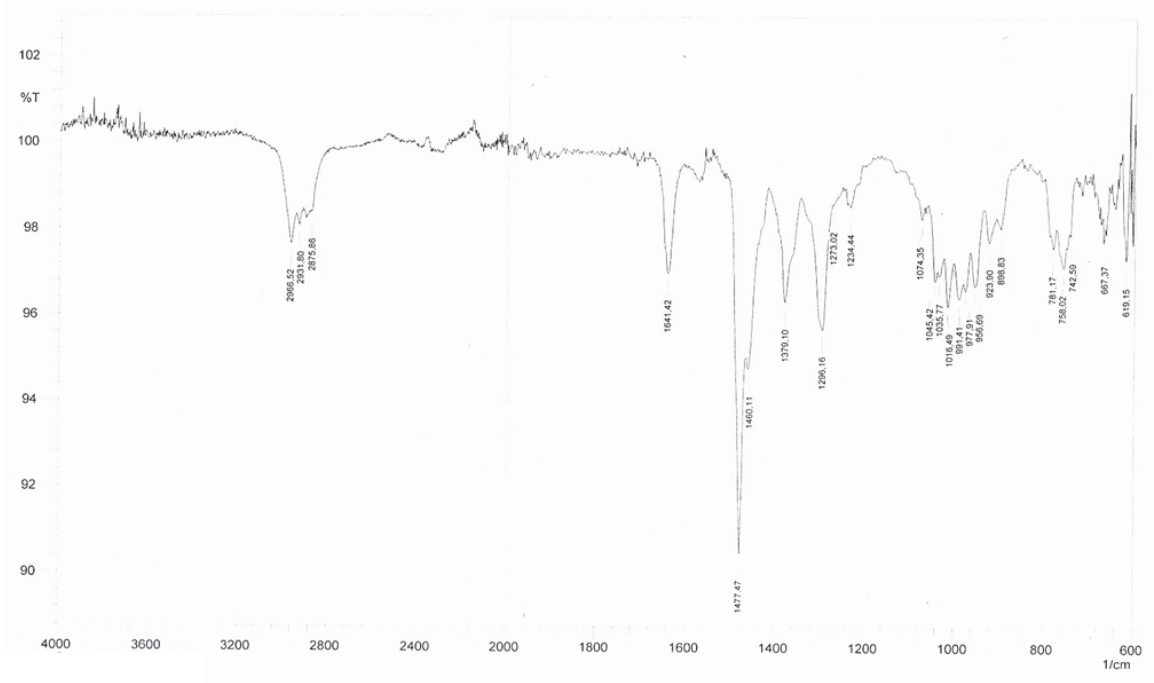

Figure S205: AT-IR spectrum of cage compound $\mathbf{A_4F_6}$.

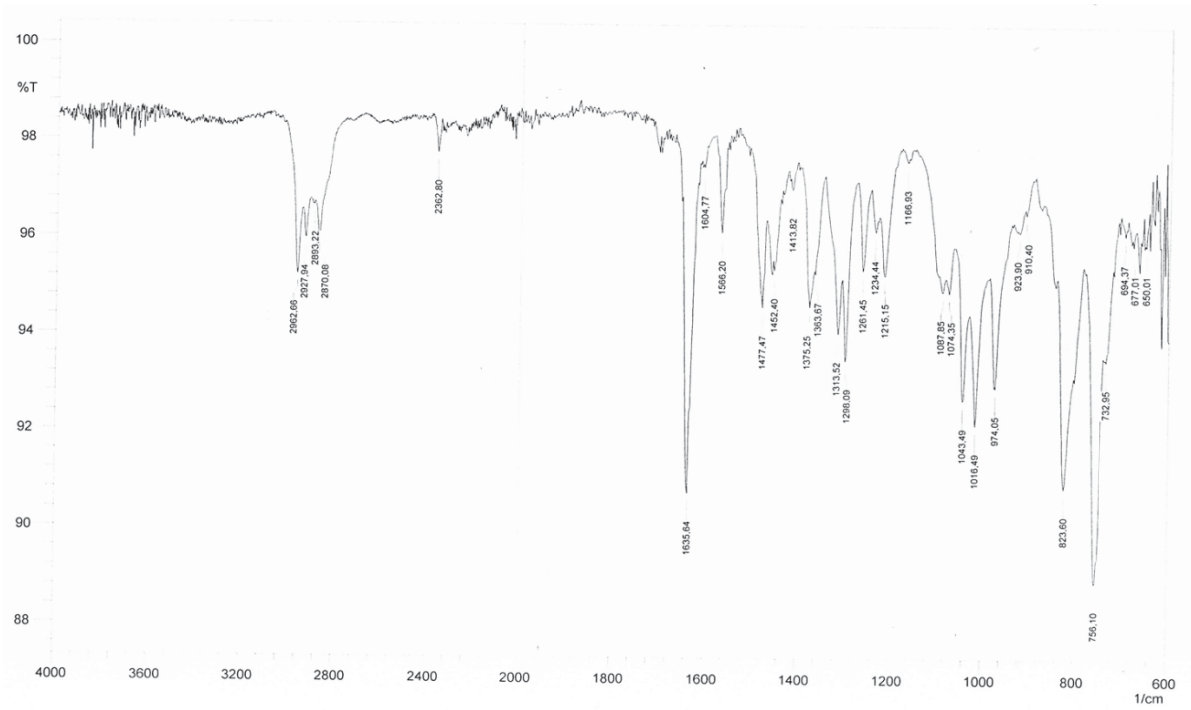

Figure S206: AT-IR spectrum of hybrid cage mixture $\mathbf{A_4H_5F_1}$.

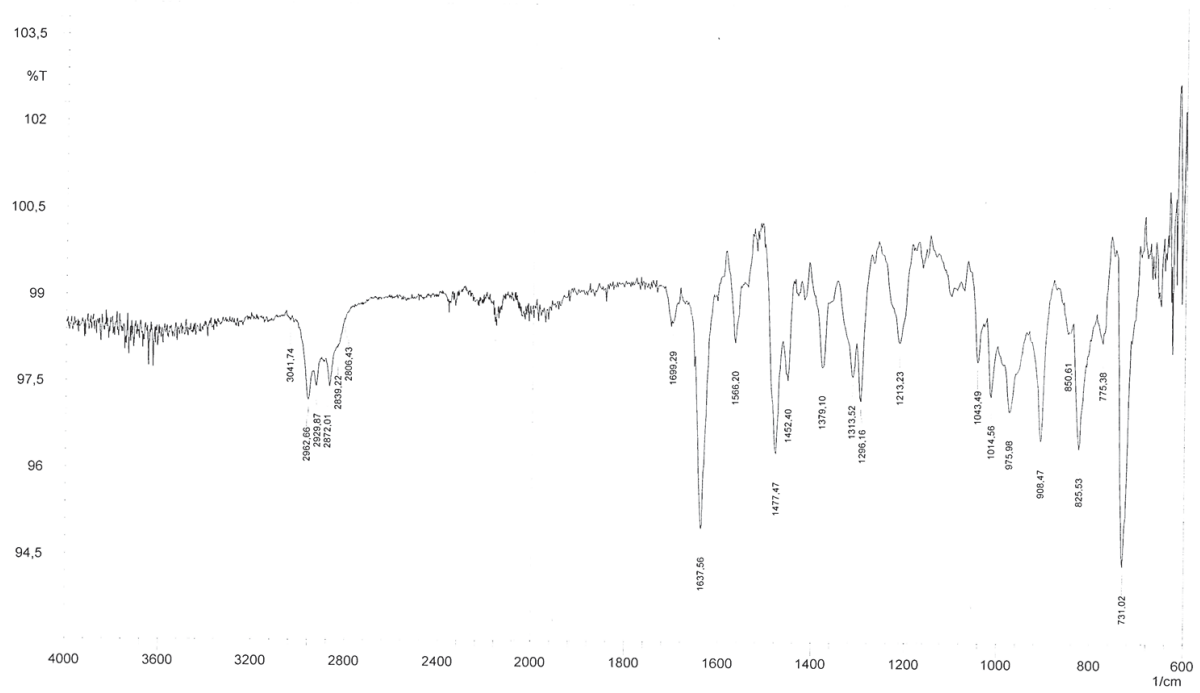

Figure S207: AT-IR spectrum of hybrid cage mixture $\mathbf{A_4H_4F_2}$.

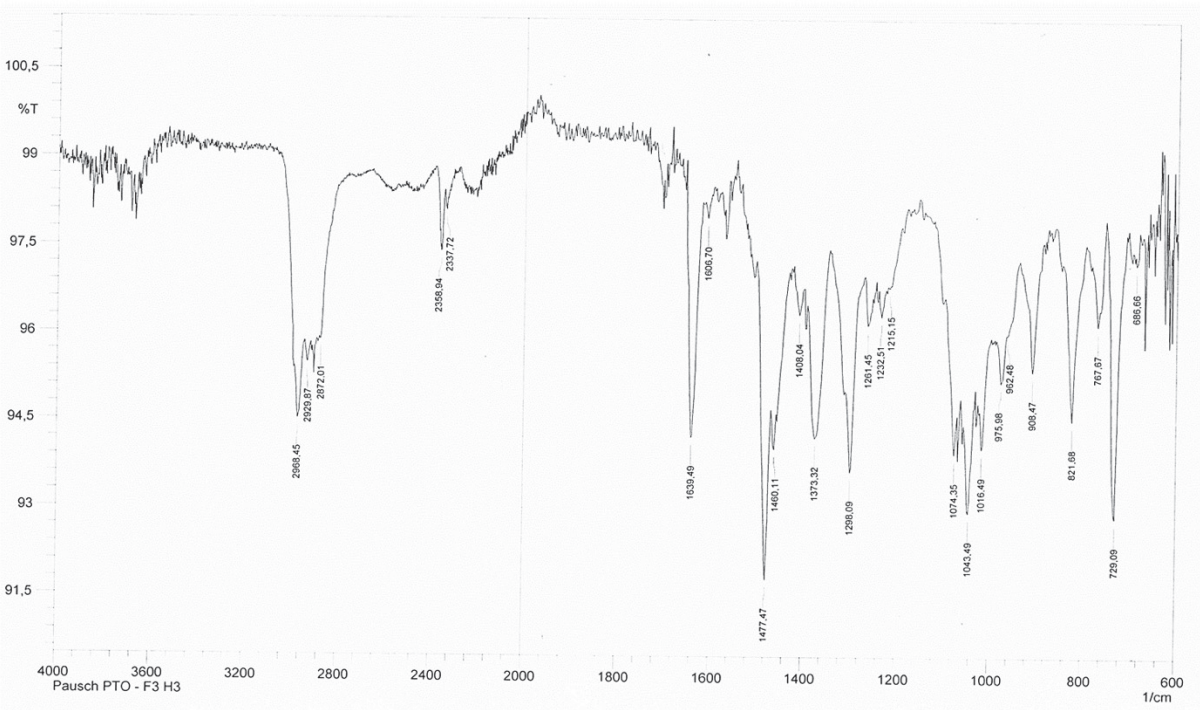

Figure S208: AT-IR spectrum of hybrid cage mixture $\mathbf{A_4H_3F_3}$.

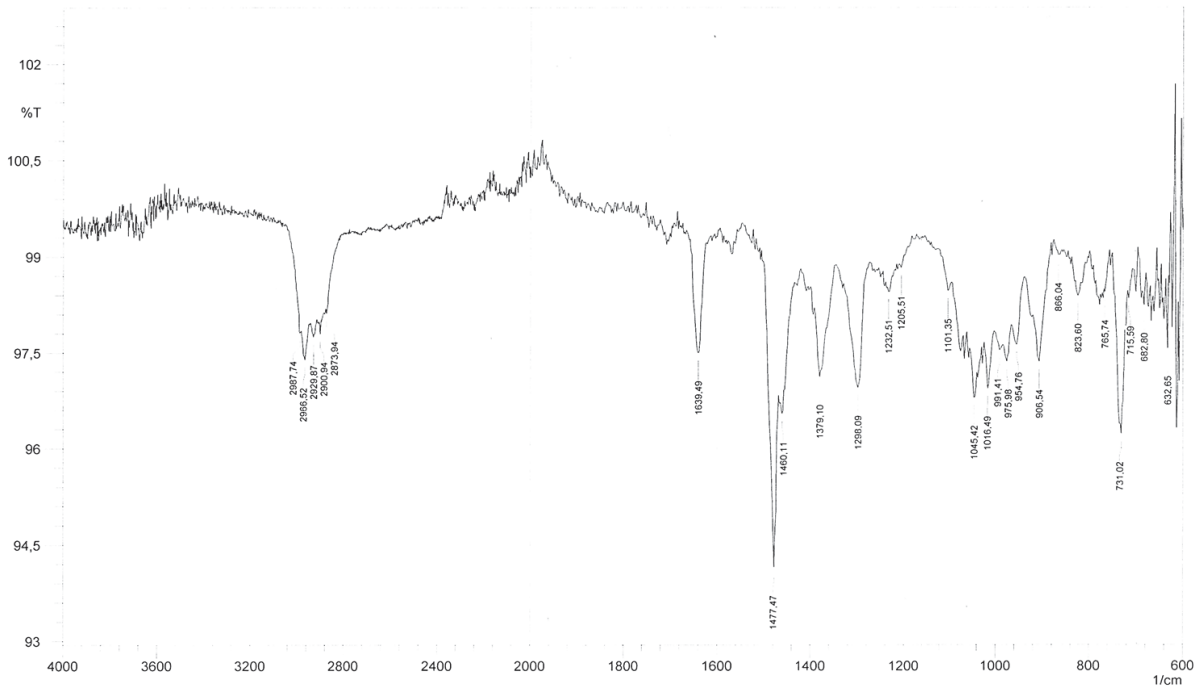

Figure S209: AT-IR spectrum of hybrid cage mixture $\mathbf{A_4H_2F_4}$.

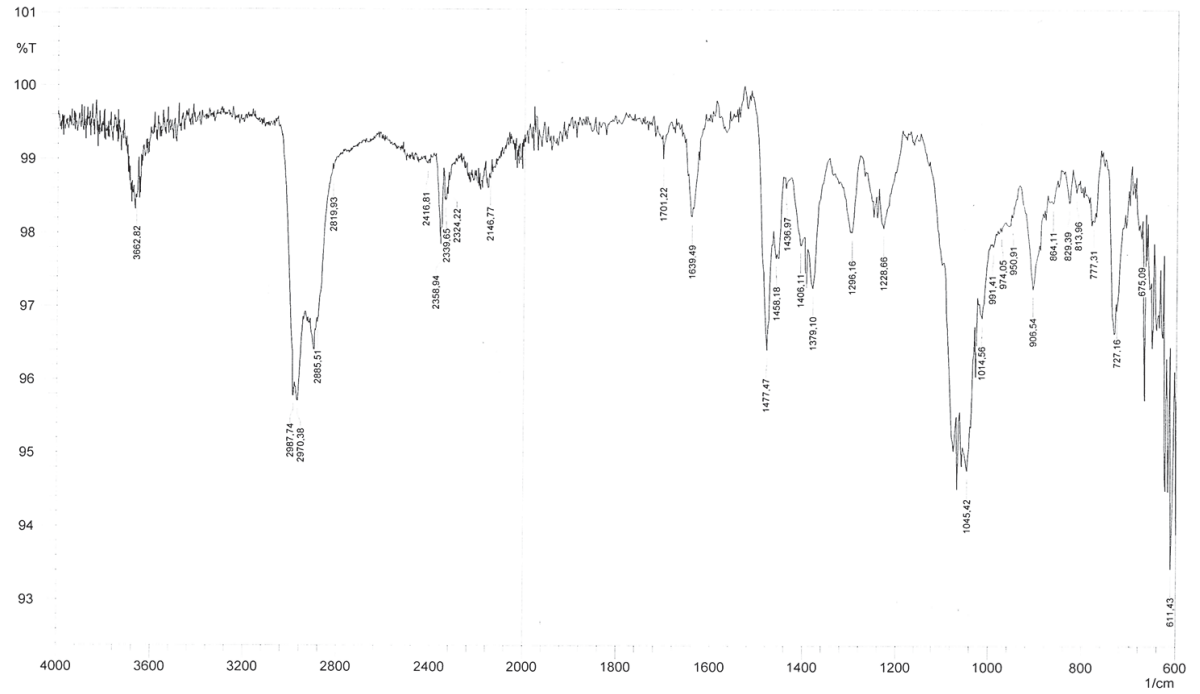

Figure S210: AT-IR spectrum of hybrid cage mixture $\mathbf{A_4H_1F_5}$.

MS spectra

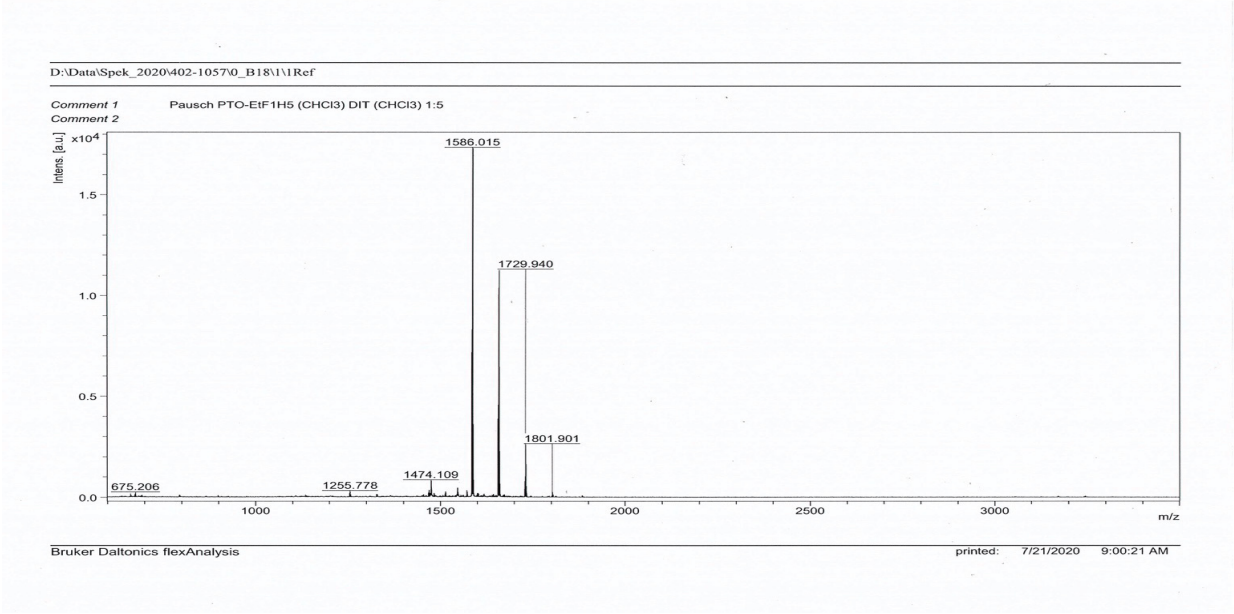

Figure S211: MALDI-MS spectrum of an amorphous sample isolated from the reaction with a feed ratio of **TFTA:TA** corresponding to the formation of cage mixture $\mathbf{A_4H_5F_1}$.

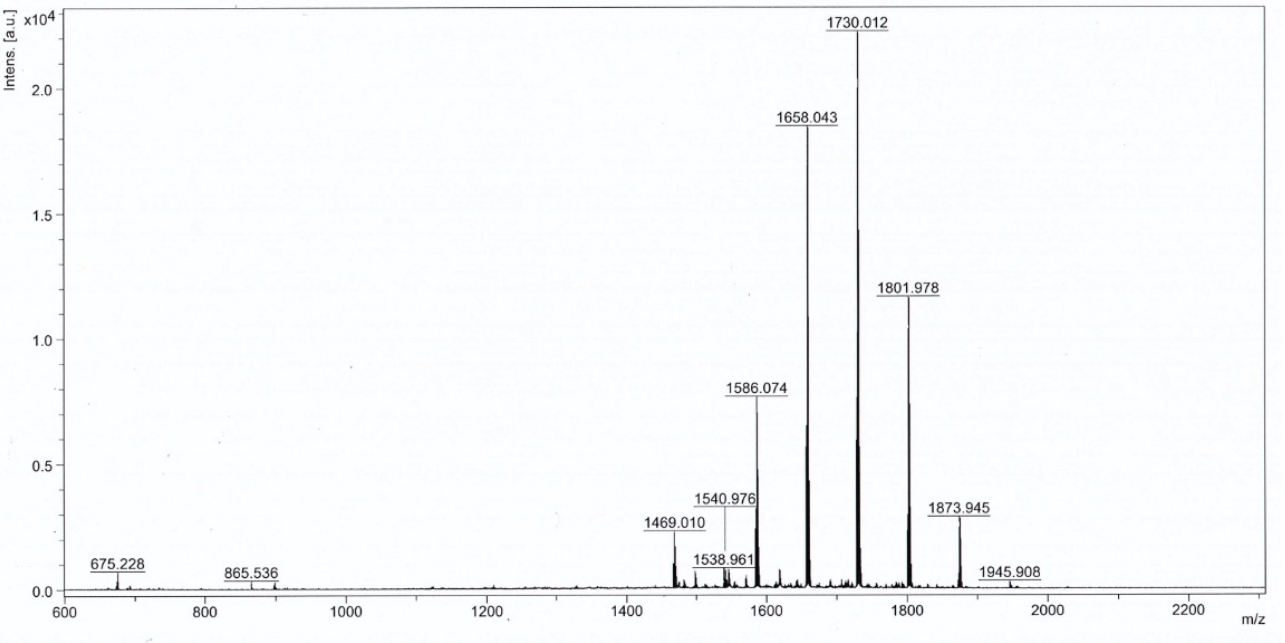

Figure S212: MALDI-MS spectrum of an amorphous sample isolated from the reaction with a feed ratio of **TFTA:TA** corresponding to the formation of cage mixture $\mathbf{A_4H_4F_2}$.

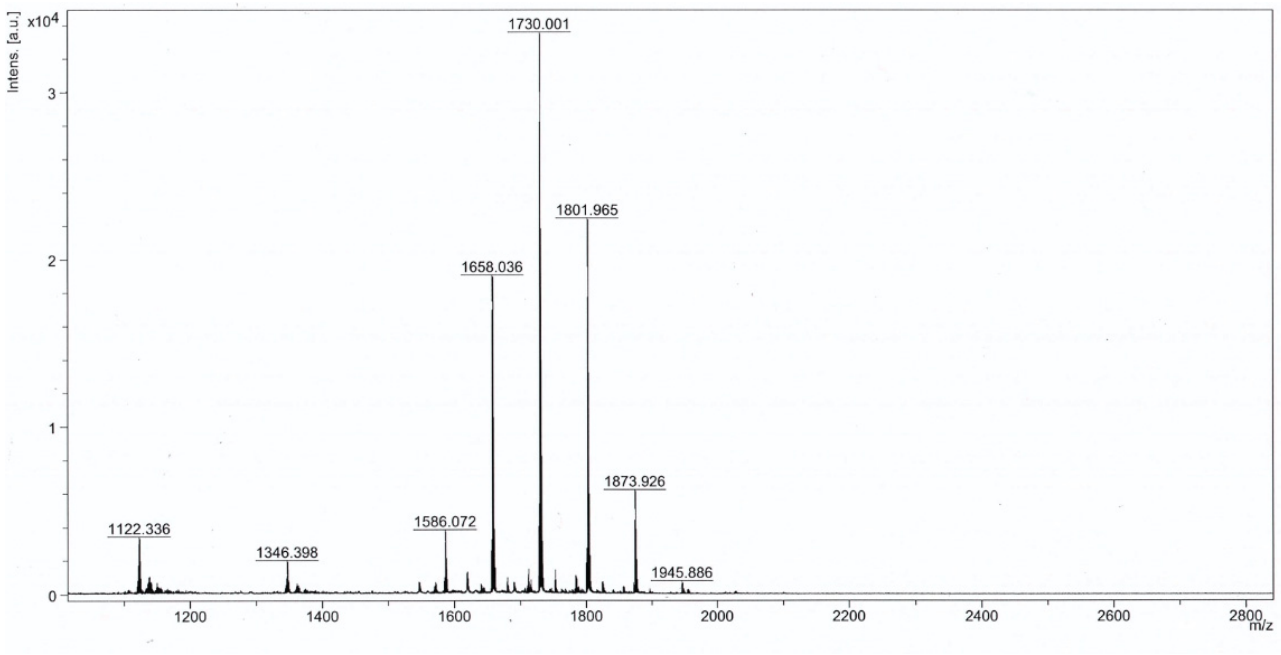

Figure S213: MALDI-MS spectrum of a crystal isolated by recrystallization of cage mixture $\mathbf{A_4H_4F_2}$ from $CHCl_3$/acetonitrile.

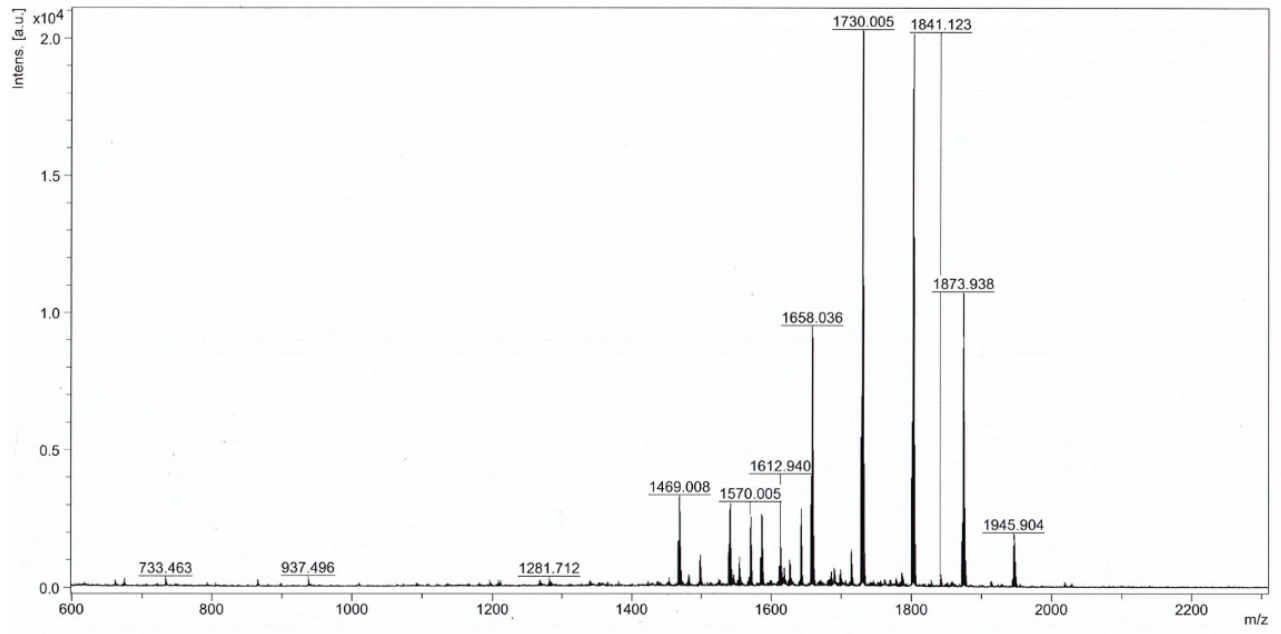

Figure S214: MALDI-MS spectrum of an amorphous sample isolated from the reaction with a feed ratio of **TFTA:TA** corresponding to the formation of cage mixture $\mathbf{A_4H_3F_3}$.

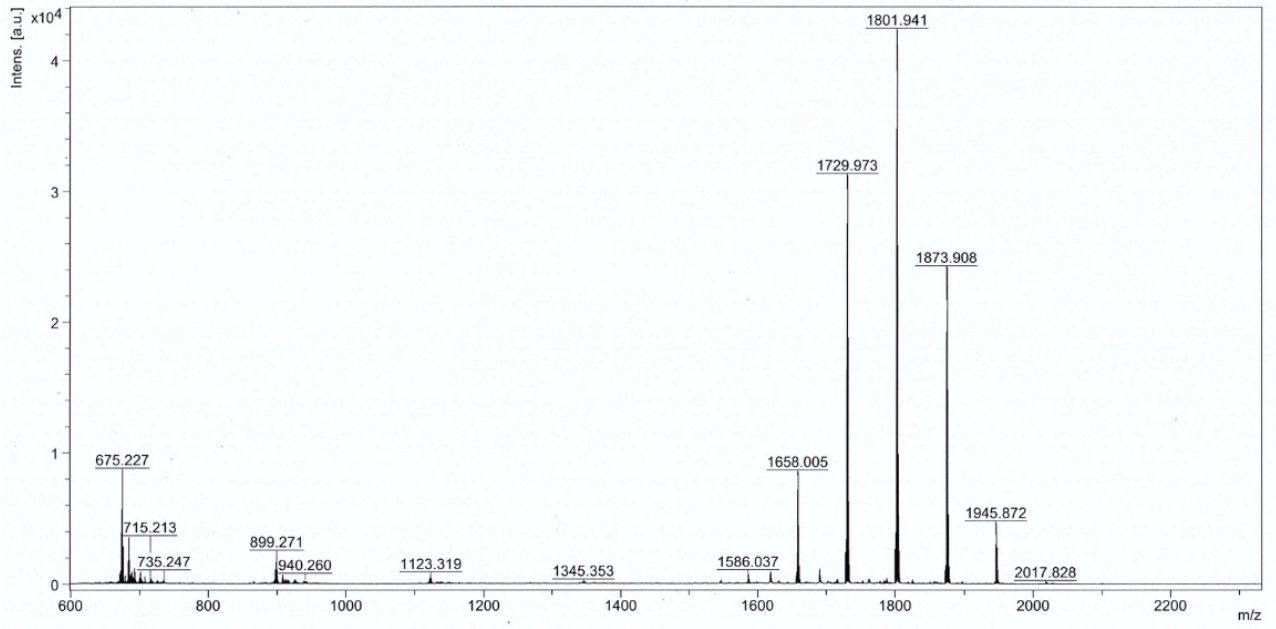

Figure S215: MALDI-MS spectrum of a crystal isolated by recrystallization of cage mixture $\mathbf{A_4H_3F_3}$ from $CHCl_3$/acetonitrile.

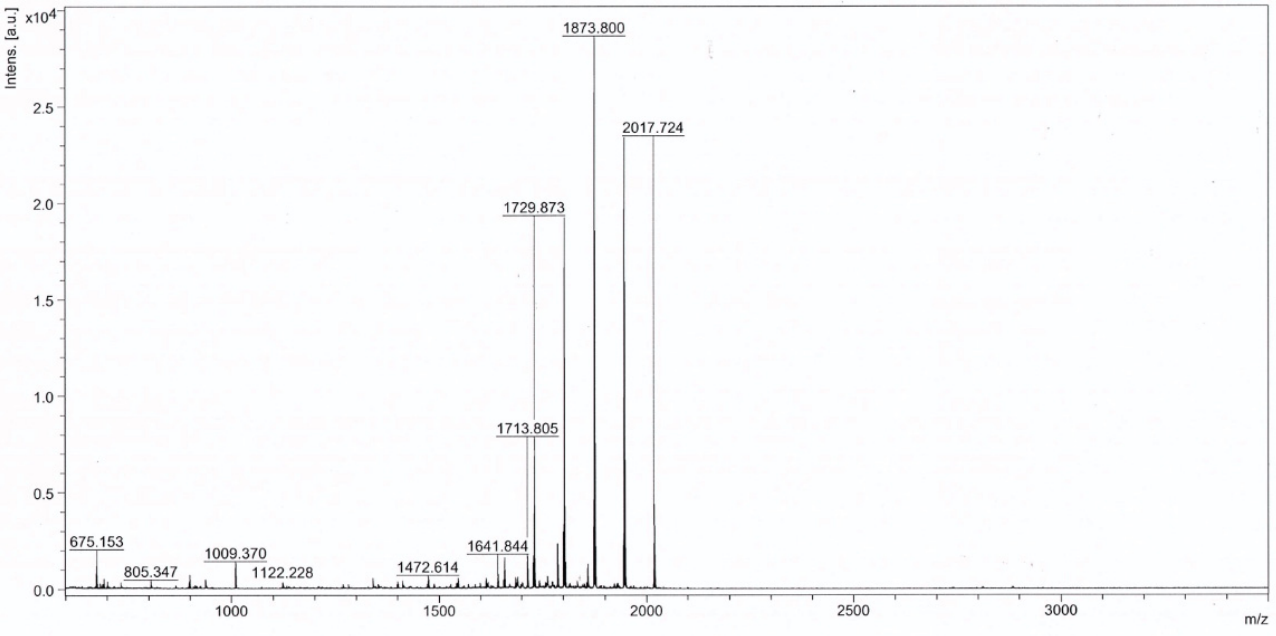

Figure S214: MALDI-MS spectrum of an amorphous sample isolated from the reaction with a feed ratio of **TFTA:TA** corresponding to the formation of cage mixture $\mathbf{A_4H_2F_4}$.

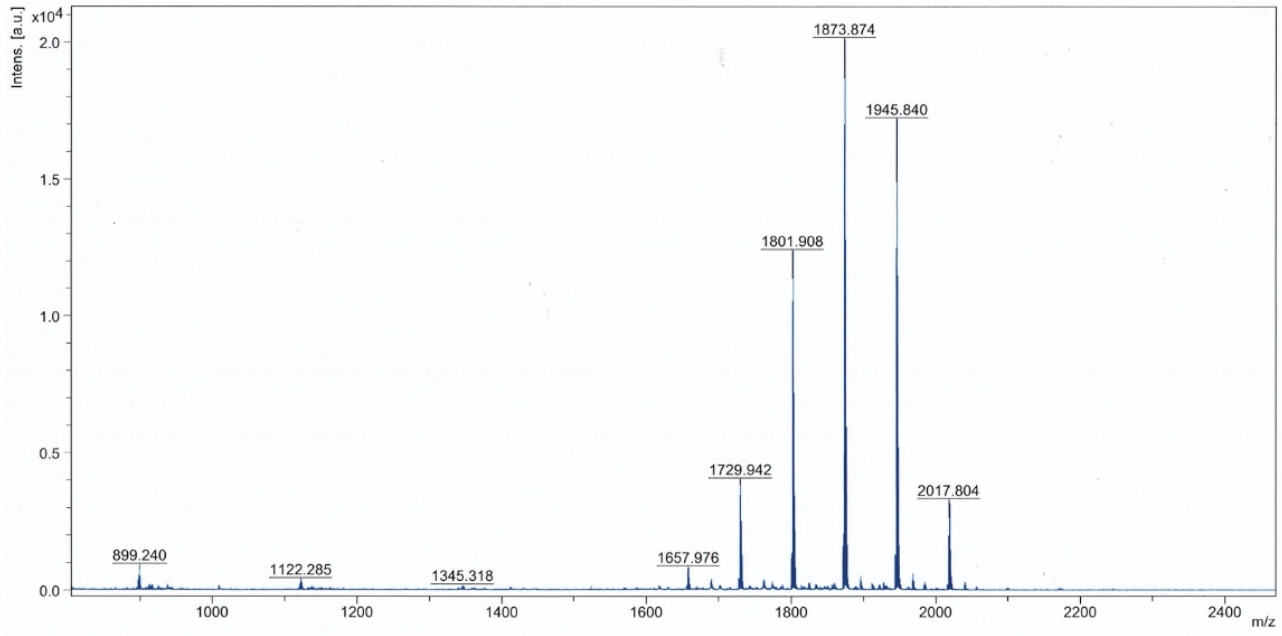

Figure S216: MALDI-MS spectrum of a crystal isolated by recrystallization of cage mixture $\mathbf{A_4H_2F_4}$ from $CHCl_3$/acetonitrile.

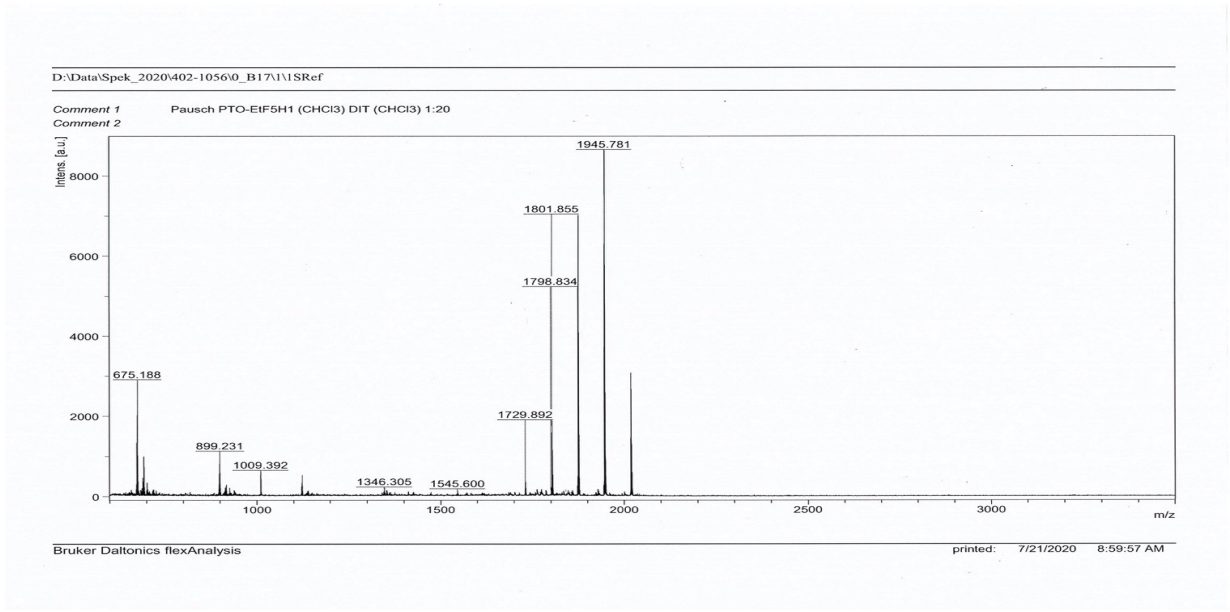

Figure S217: MALDI-MS spectrum of an amorphous sample isolated from the reaction with a feed ratio of **TFTA:TA** corresponding to the formation of cage mixture $\mathbf{A_4H_1F_5}$.

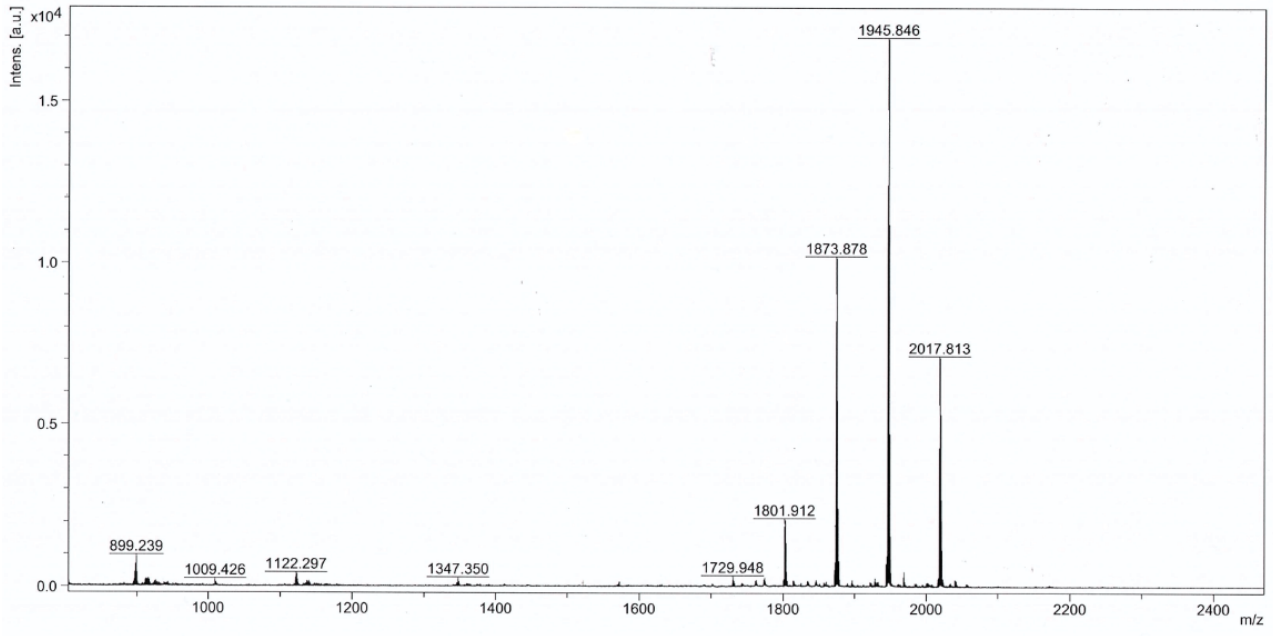

Figure S218: MALDI-MS spectrum of a crystal isolated by recrystallization of cage mixture $\mathbf{A_4H_1F_5}$ from $CHCl_3$/acetonitrile.

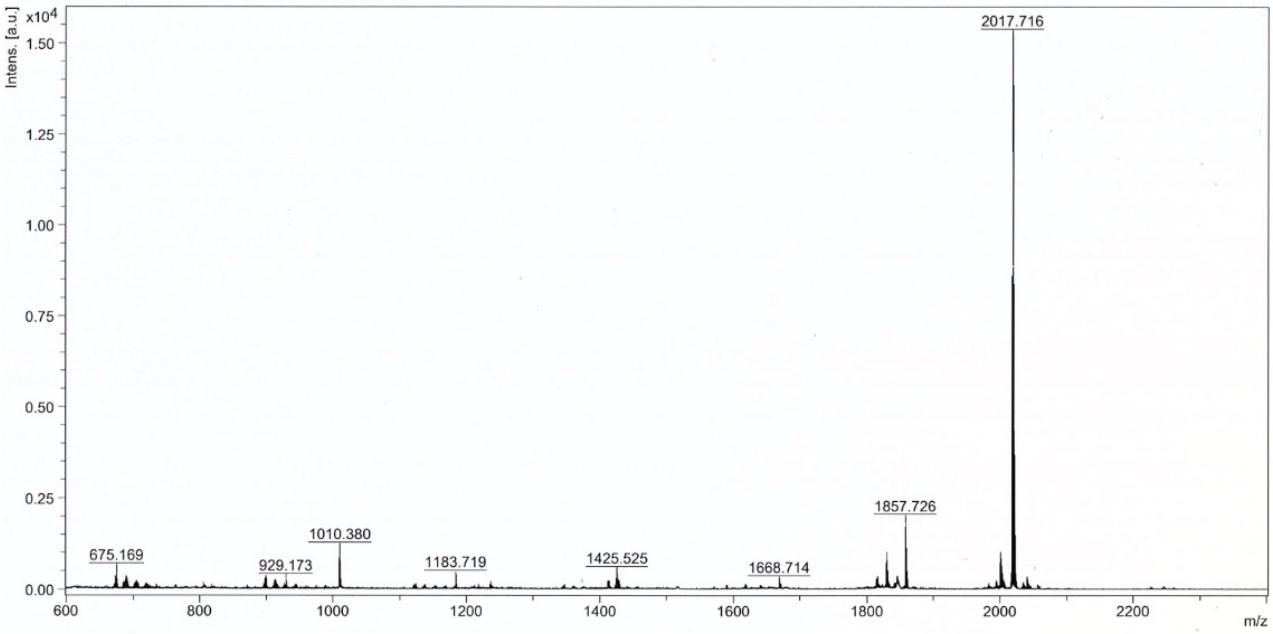

Figure S219: MALDI-MS spectrum of a semicrystalline sample isolated from the reaction with a feed ratio of **TFTA:TA** corresponding to the formation of $\mathbf{A_4F_6}$.

6.5. Spectra for Section 3.5

NMR spectra

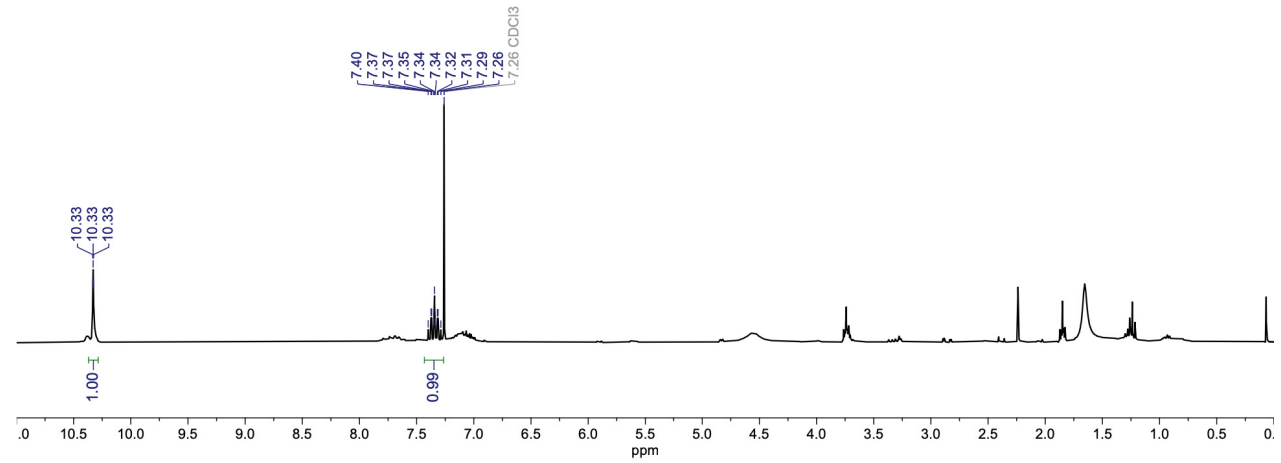

Figure S220: ^{1}H NMR spectrum (300 MHz, $CDCl_3$) of aldehyde **28**.

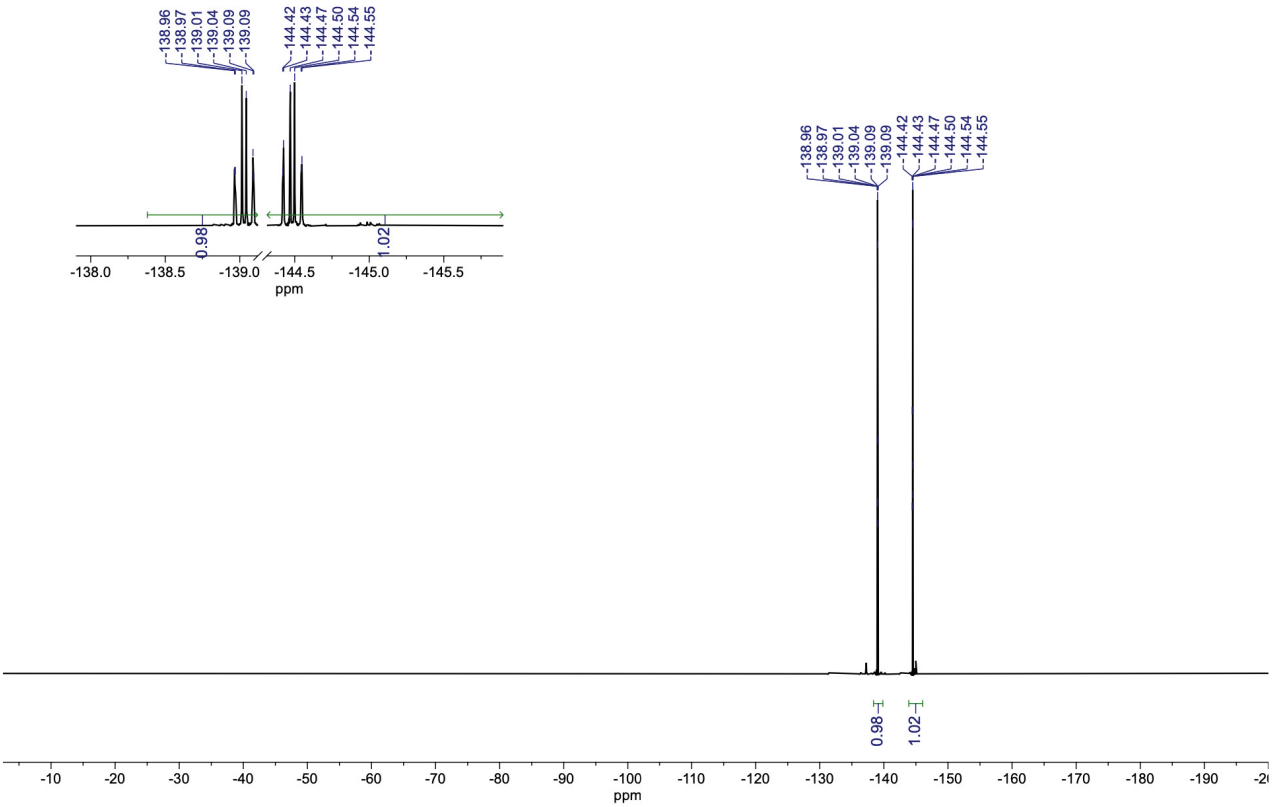

Figure S221: ^{19}F NMR spectrum (282 MHz, $CDCl_3$) of aldehyde **28**.

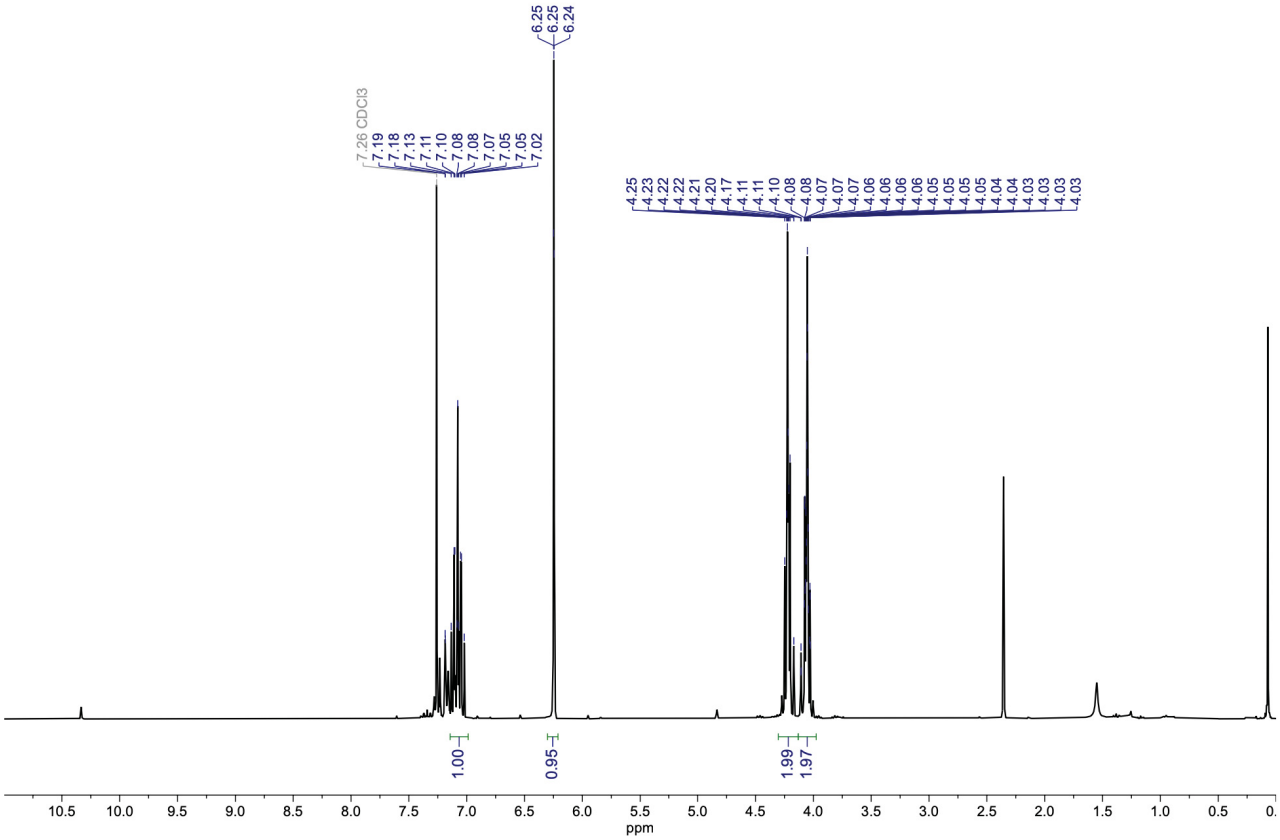

Figure S222: ^{1}H NMR spectrum (300 MHz, $CDCl_3$) of acetal **29**.

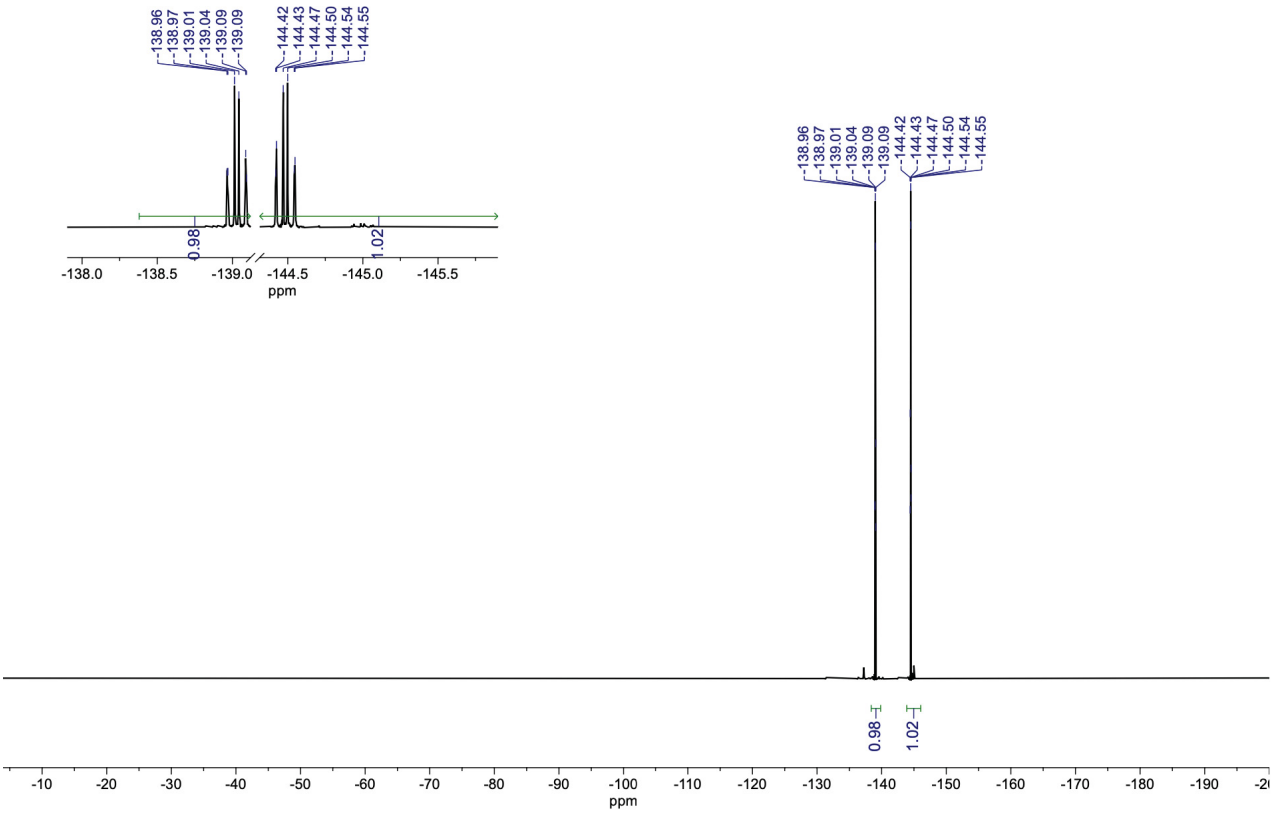

Figure S223: ^{19}F NMR spectrum (282 MHz, $CDCl_3$) of acetal **29**.

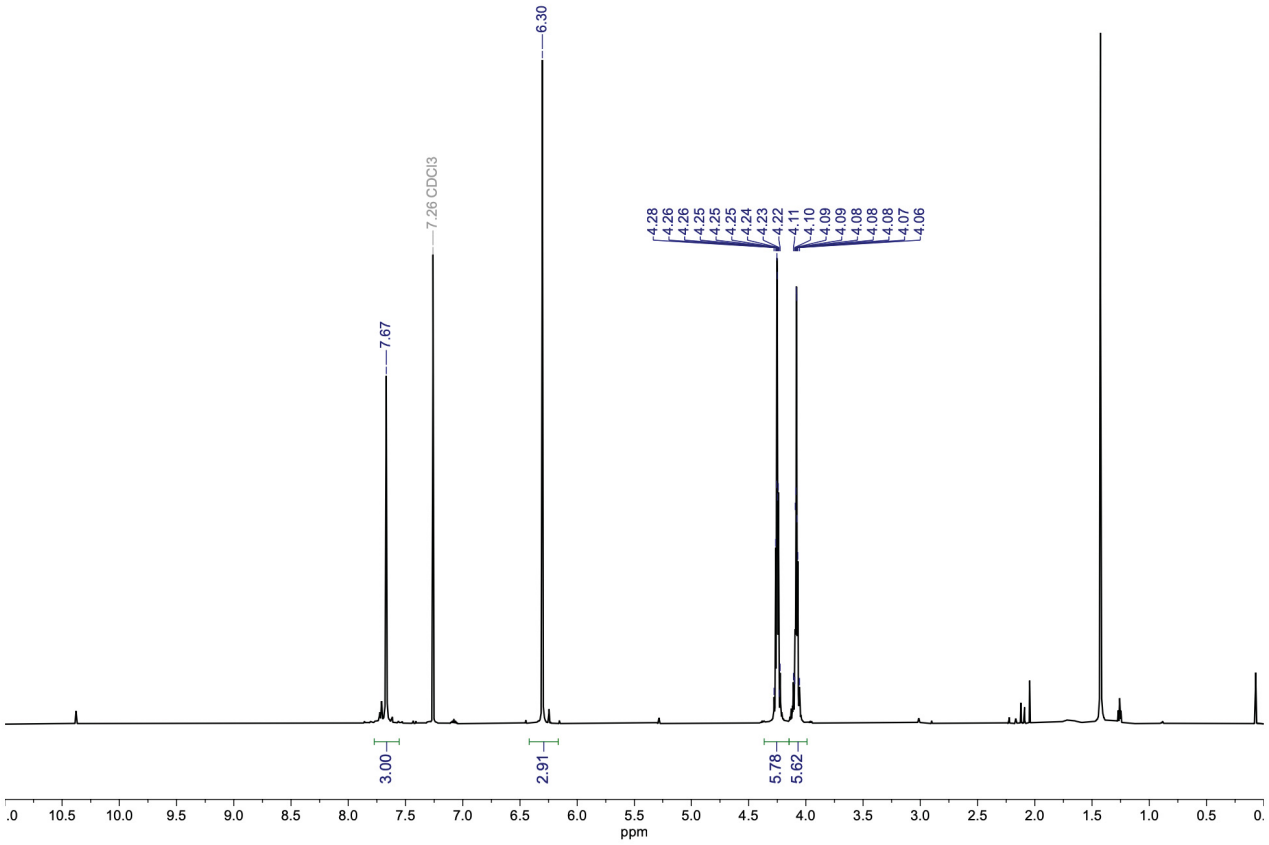

Figure S224: ^{1}H NMR spectrum (300 MHz, $CDCl_3$) of triacetal **30**.

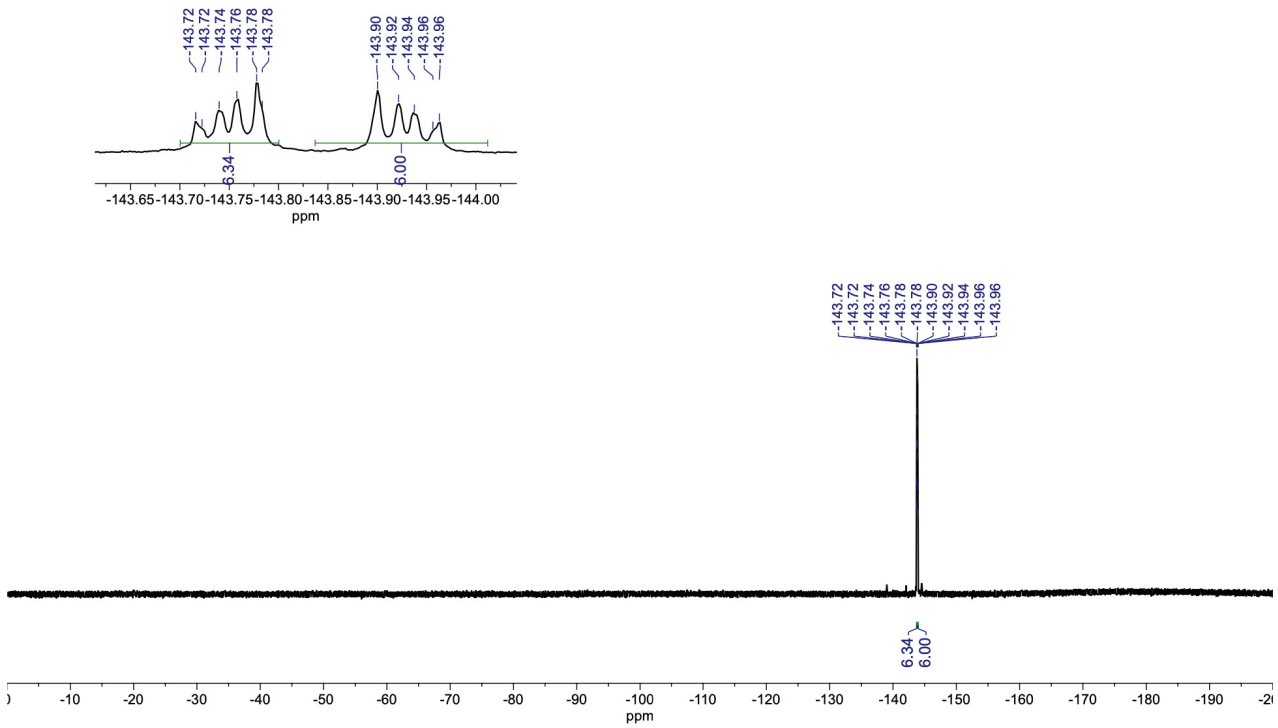

Figure S225: ^{19}F NMR spectrum (282 MHz, $CDCl_3$) of triacetal **30**.

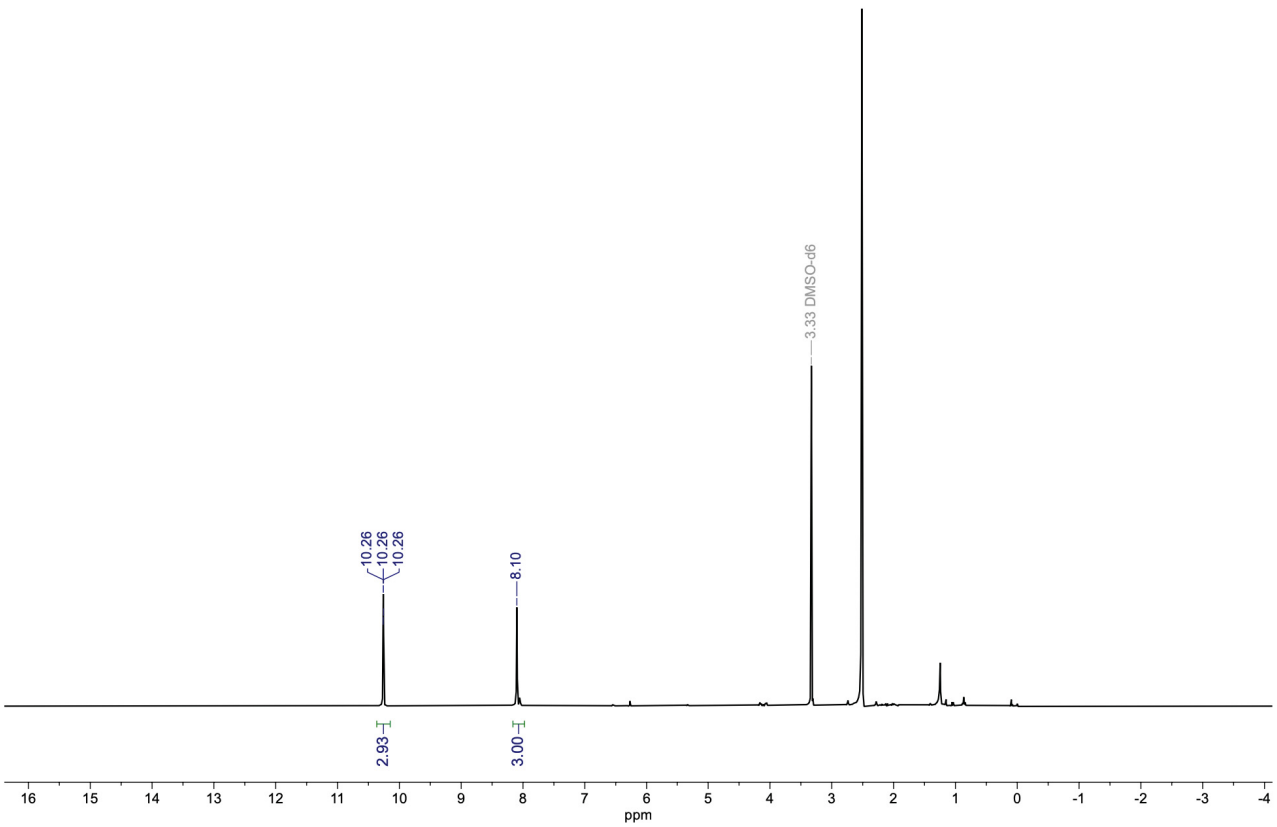

Figure S226: ^{1}H NMR spectrum (300 MHz, $CDCl_3$) of trialdehyde **31**.

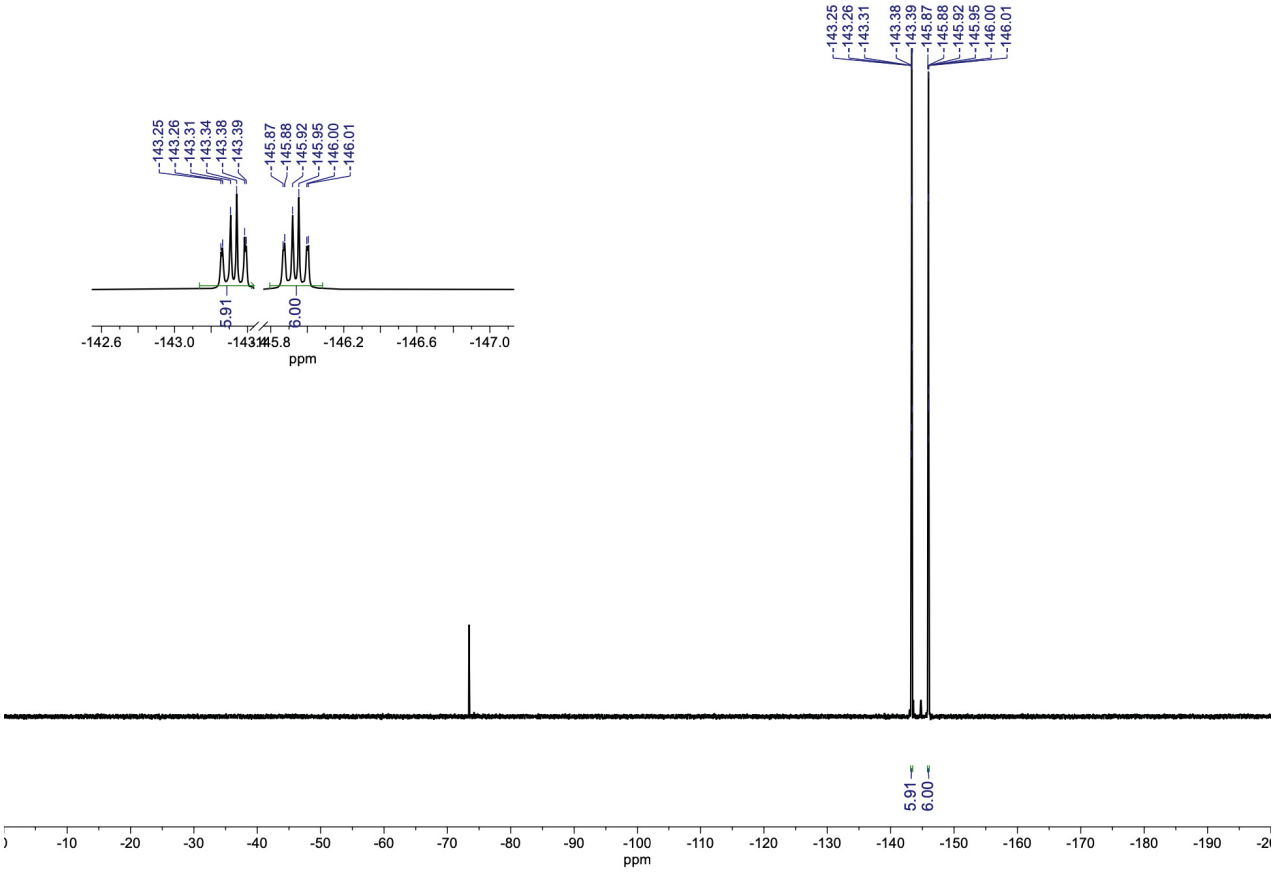

Figure S227: ^{19}F NMR spectrum (282 MHz, $CDCl_3$) of trialdehyde **31**. The signal at -73 ppm can be assigned to residual trifluoroacetic acid.

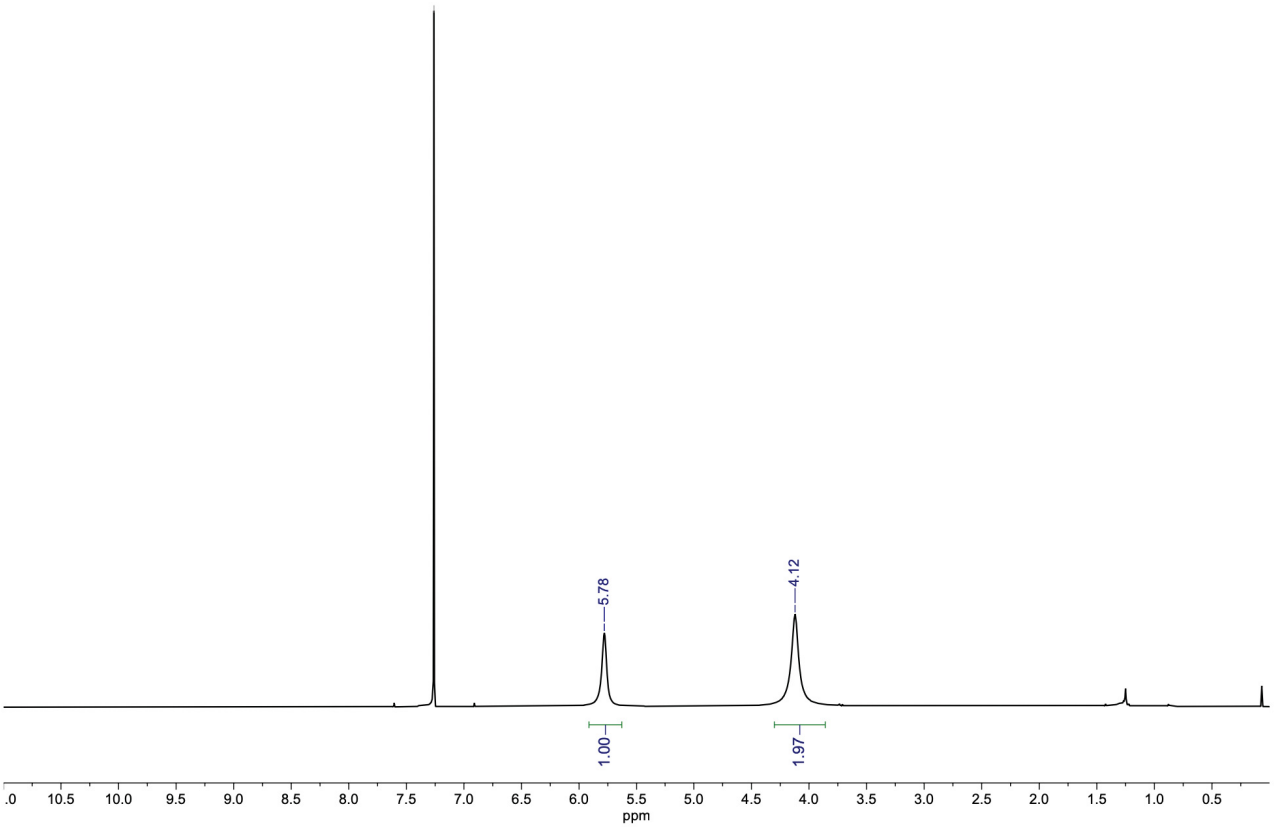

Figure S228: ^{1}H NMR spectrum (300 MHz, $CDCl_3$) of hydrazine compound **32**.

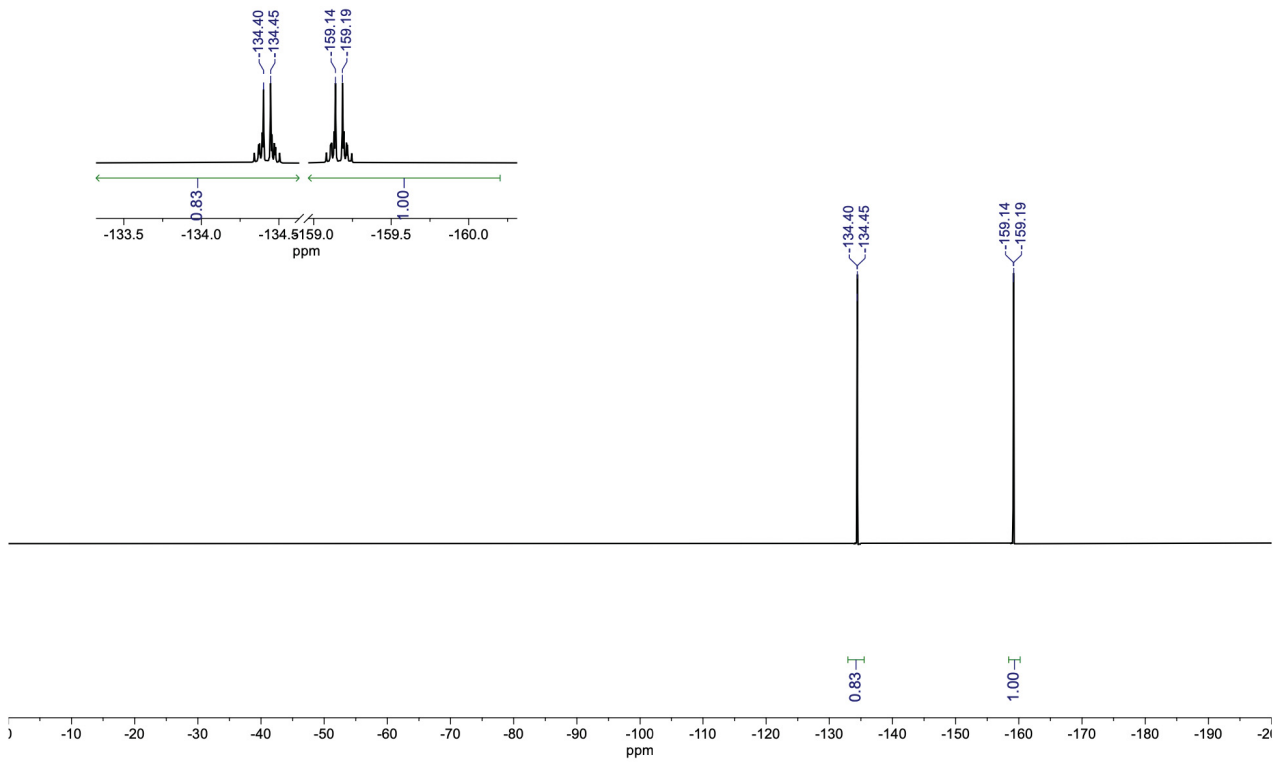

Figure S229: ^{19}F NMR spectrum (282 MHz, $CDCl_3$) of hydrazine compound **32**.

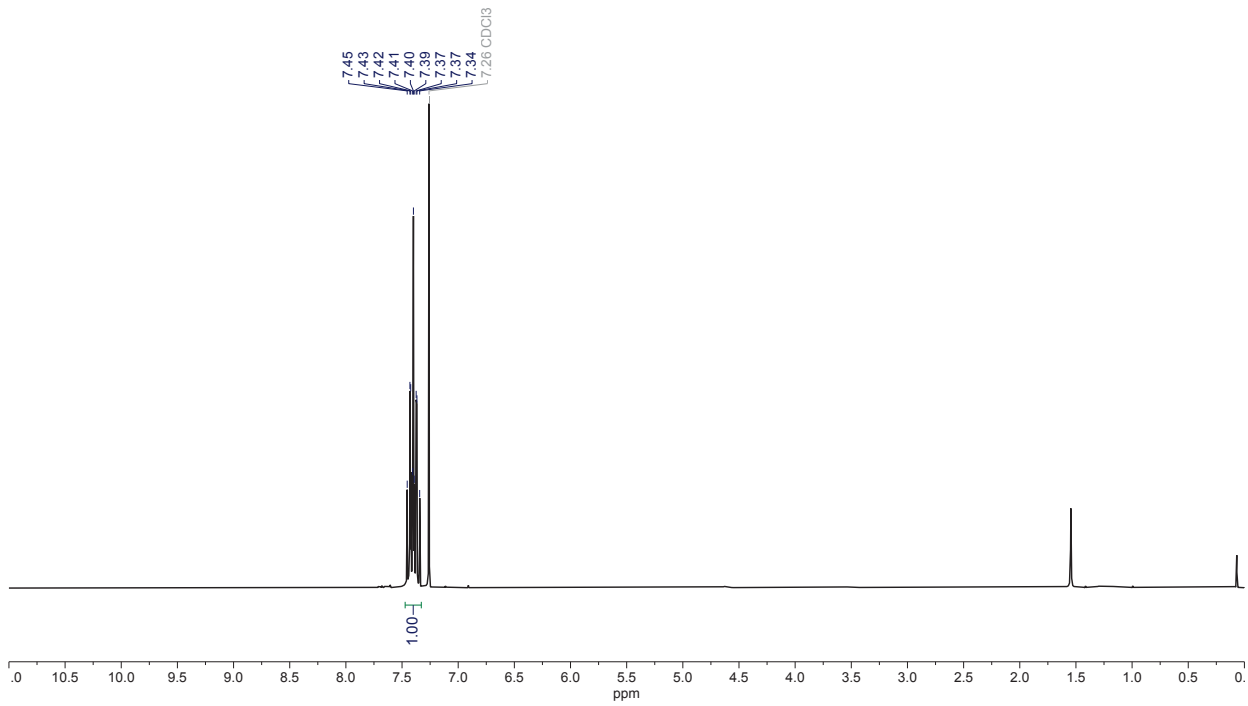

Figure S230: ^{1}H NMR spectrum (300 MHz, $CDCl_3$) of tetrafluorobenzonitrile **33**.

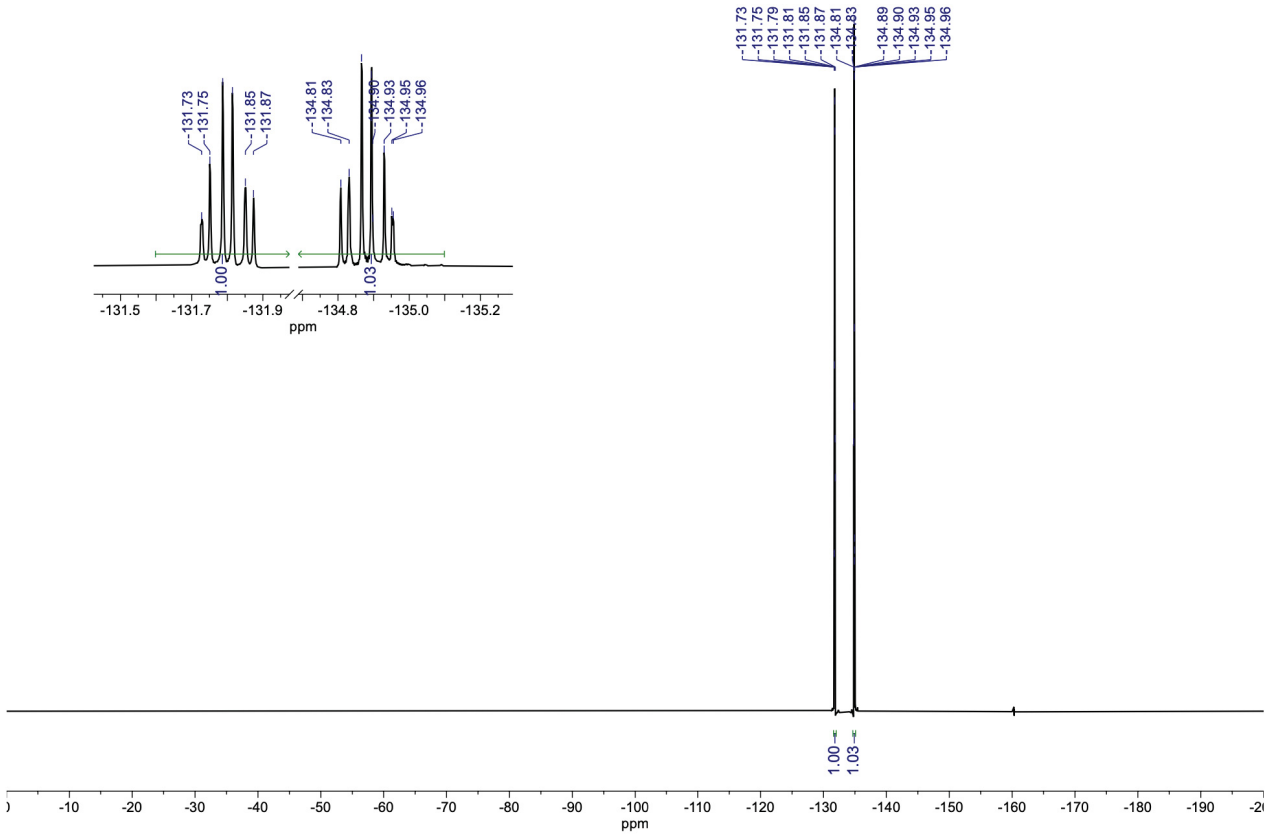

Figure S231: ^{19}F NMR spectrum (282 MHz, $CDCl_3$) of tetrafluorobenzonitrile **33**.

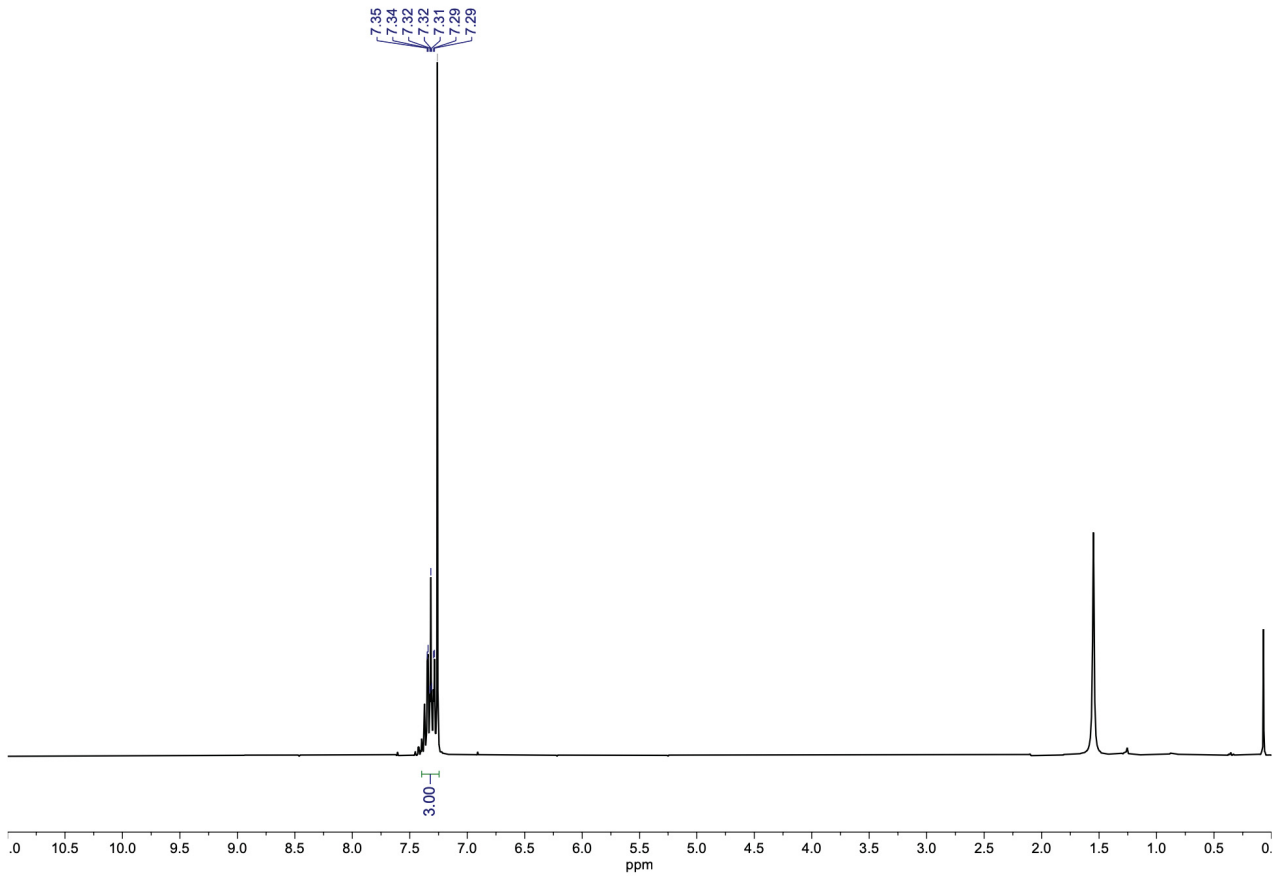

Figure S232: ^{1}H NMR spectrum (300 MHz, $CDCl_3$) of triazine compound **34**.

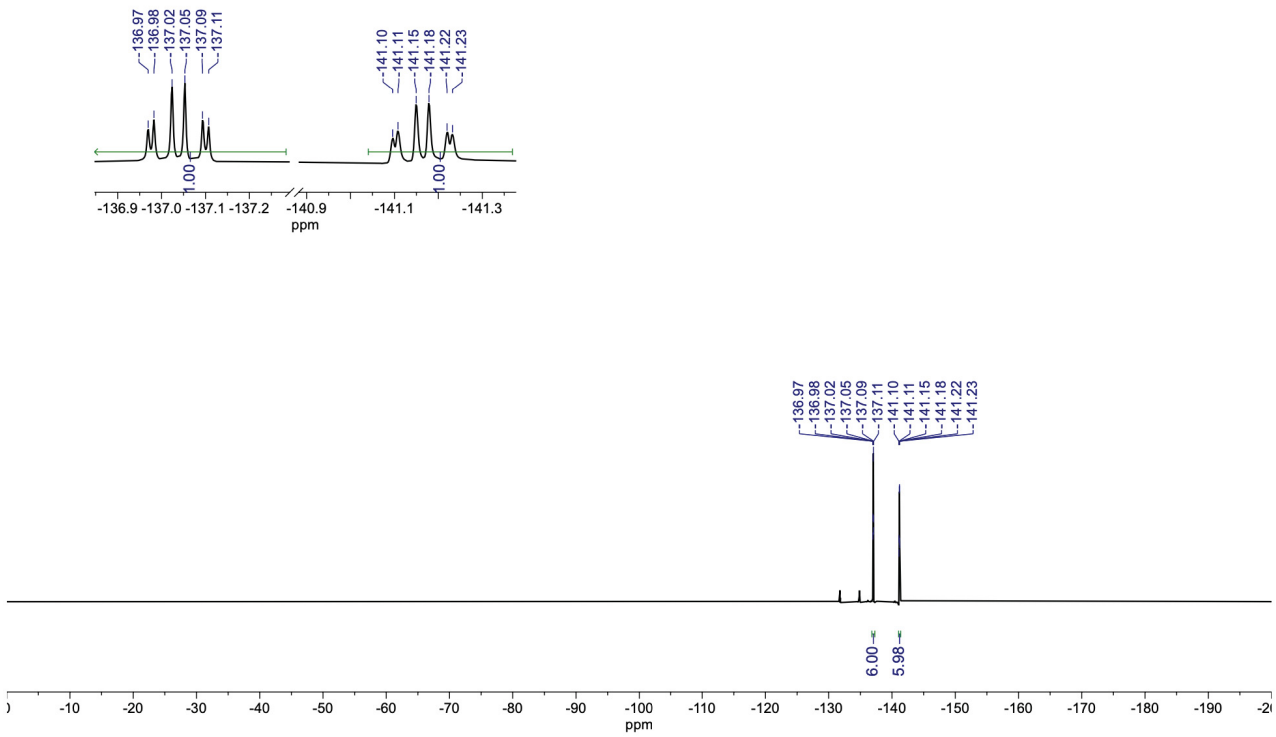

Figure S233: ^{19}F NMR spectrum (282 MHz, $CDCl_3$) of triazine compound **34**.

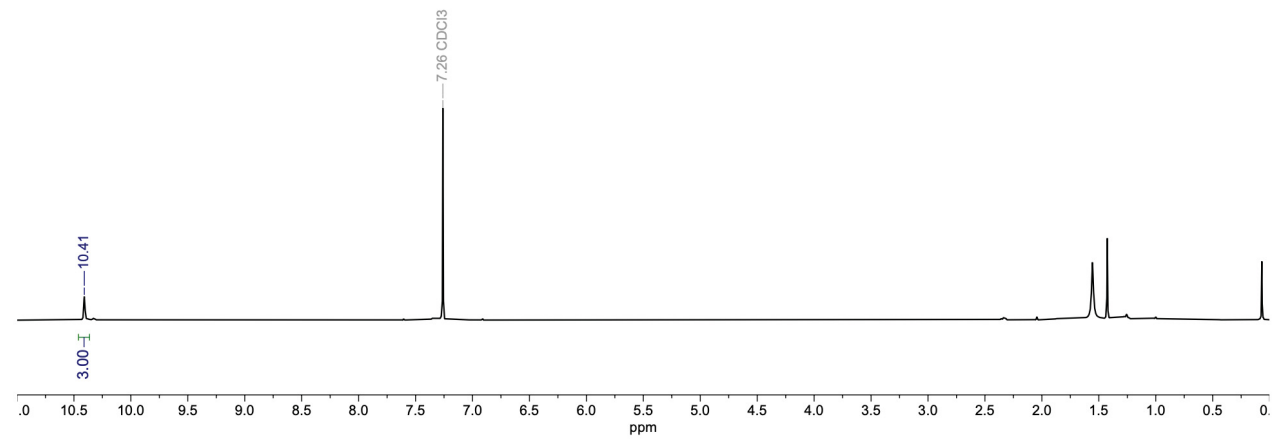

Figure S234: ^{1}H NMR spectrum (300 MHz, $CDCl_3$) of triazine aldehyde **35**.

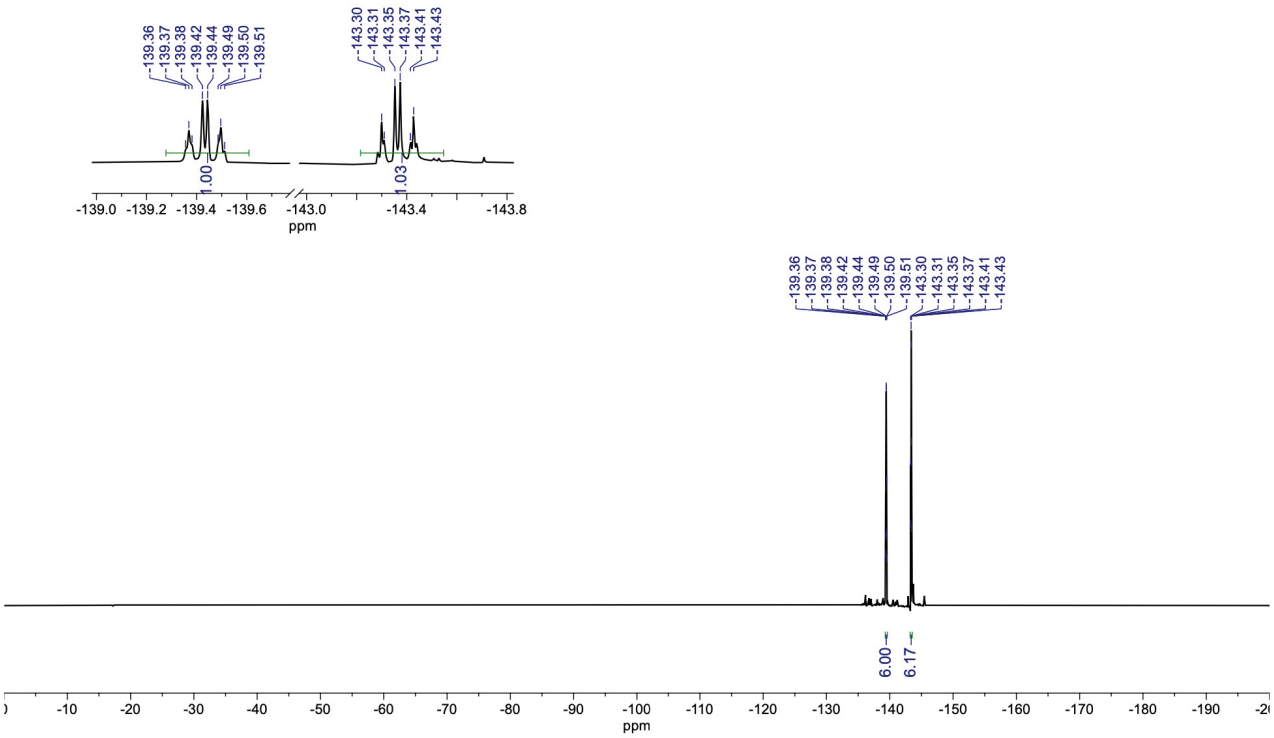

Figure S235: ^{19}F NMR spectrum (282 MHz, $CDCl_3$) of triazine aldehyde **35**.

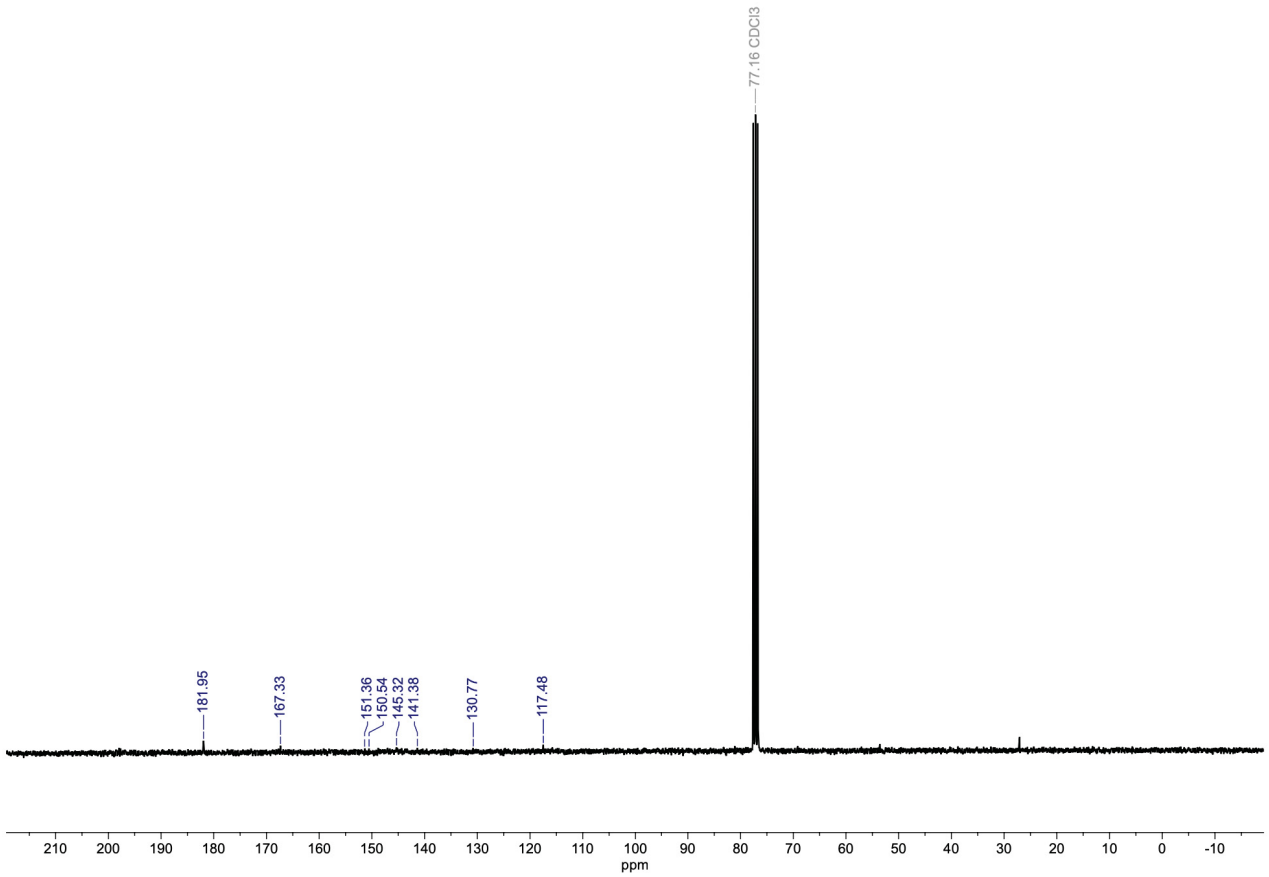

Figure S236: ^{13}C NMR spectrum (75 MHz, $CDCl_3$) of triazine aldehyde **35**.

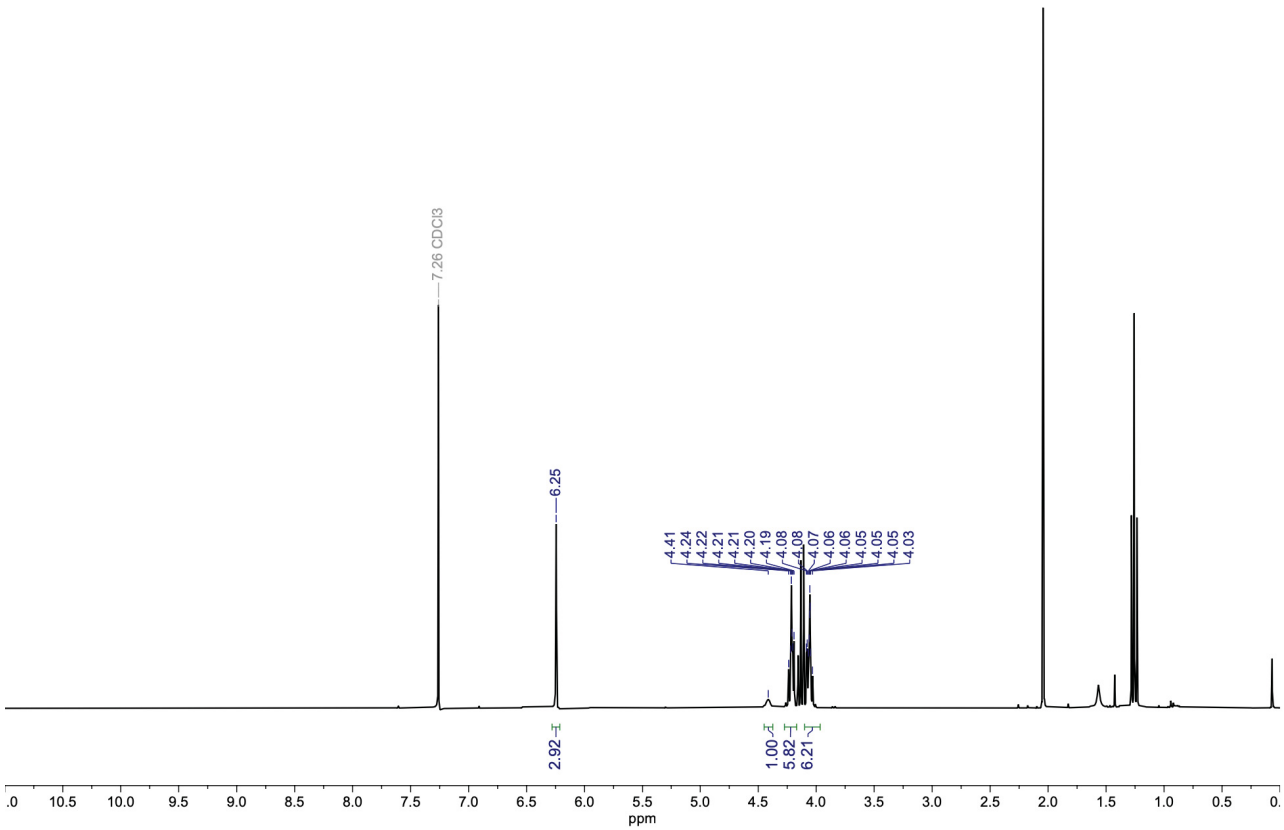

Figure S237: ^{1}H NMR spectrum (300 MHz, $CDCl_3$) of triacetal **36**.

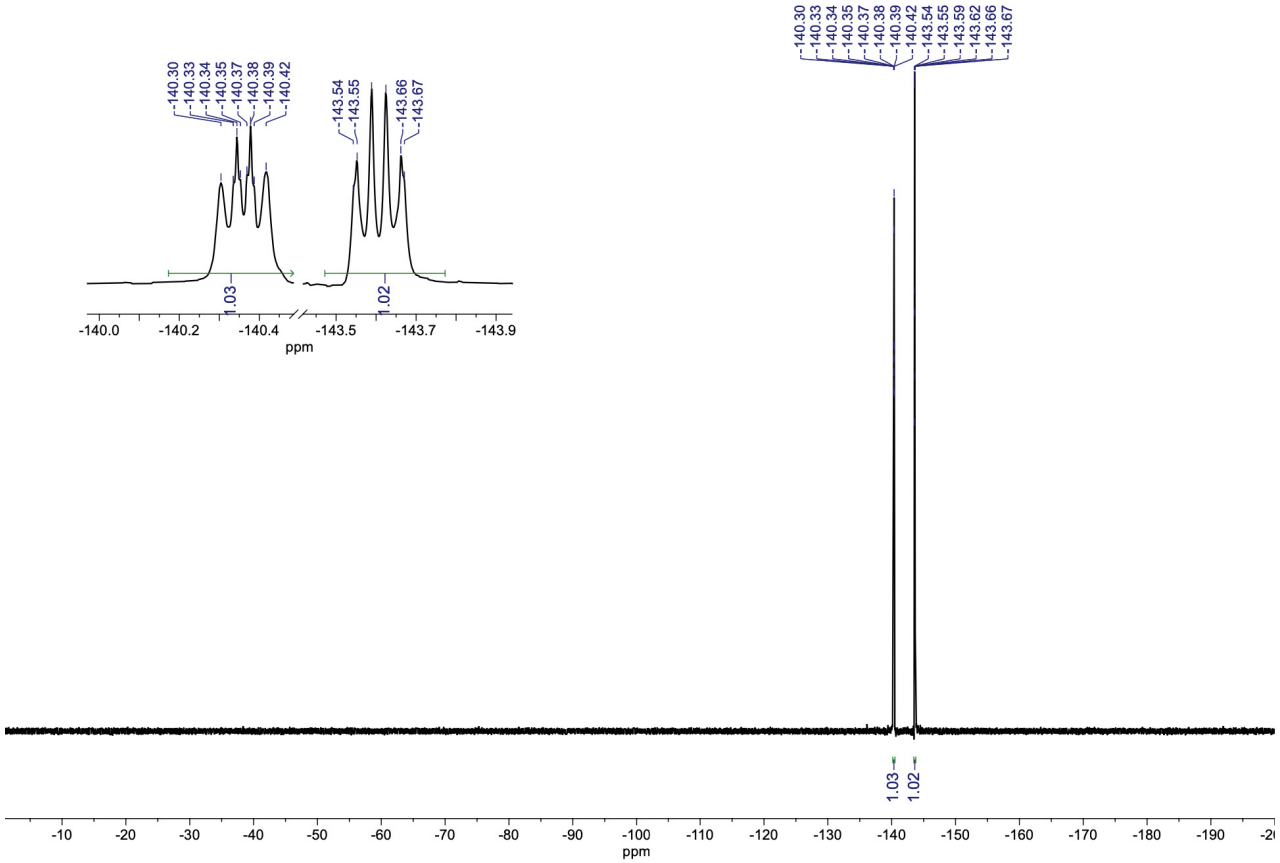

Figure S238: ^{19}F NMR spectrum (282 MHz, $CDCl_3$) of triacetal **36**.

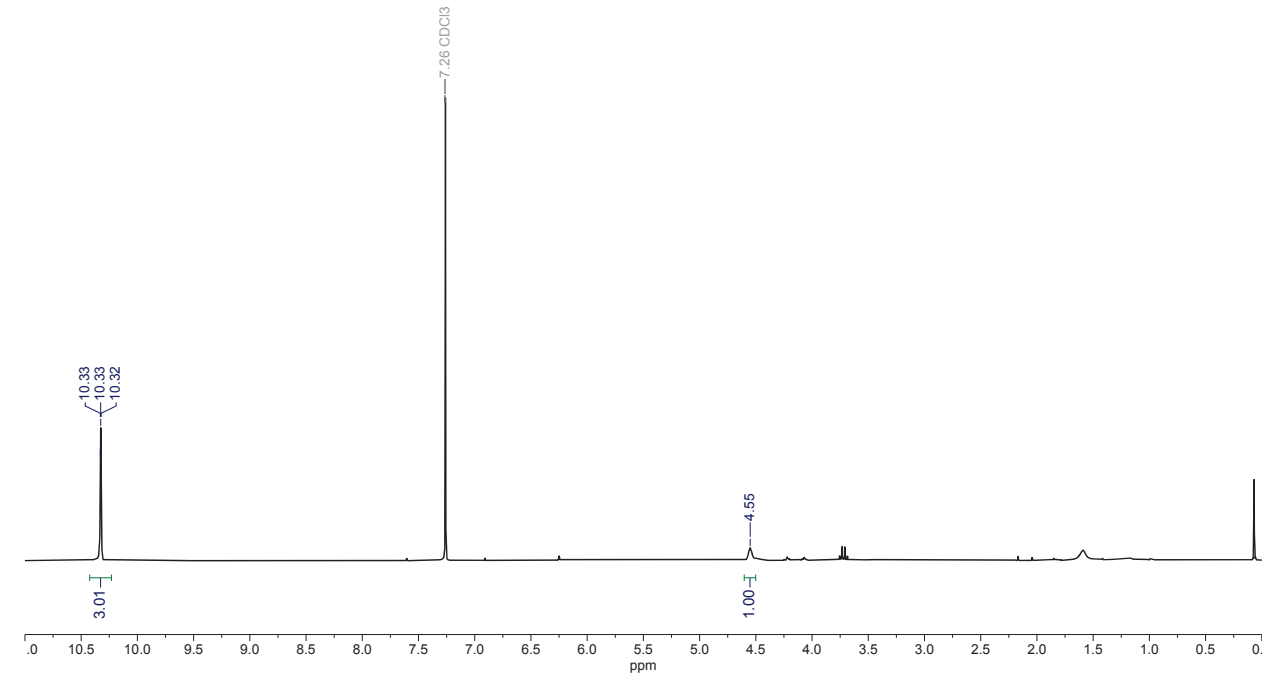

Figure S239: ^{1}H NMR spectrum (300 MHz, $CDCl_3$) of trialdehyde **37**.

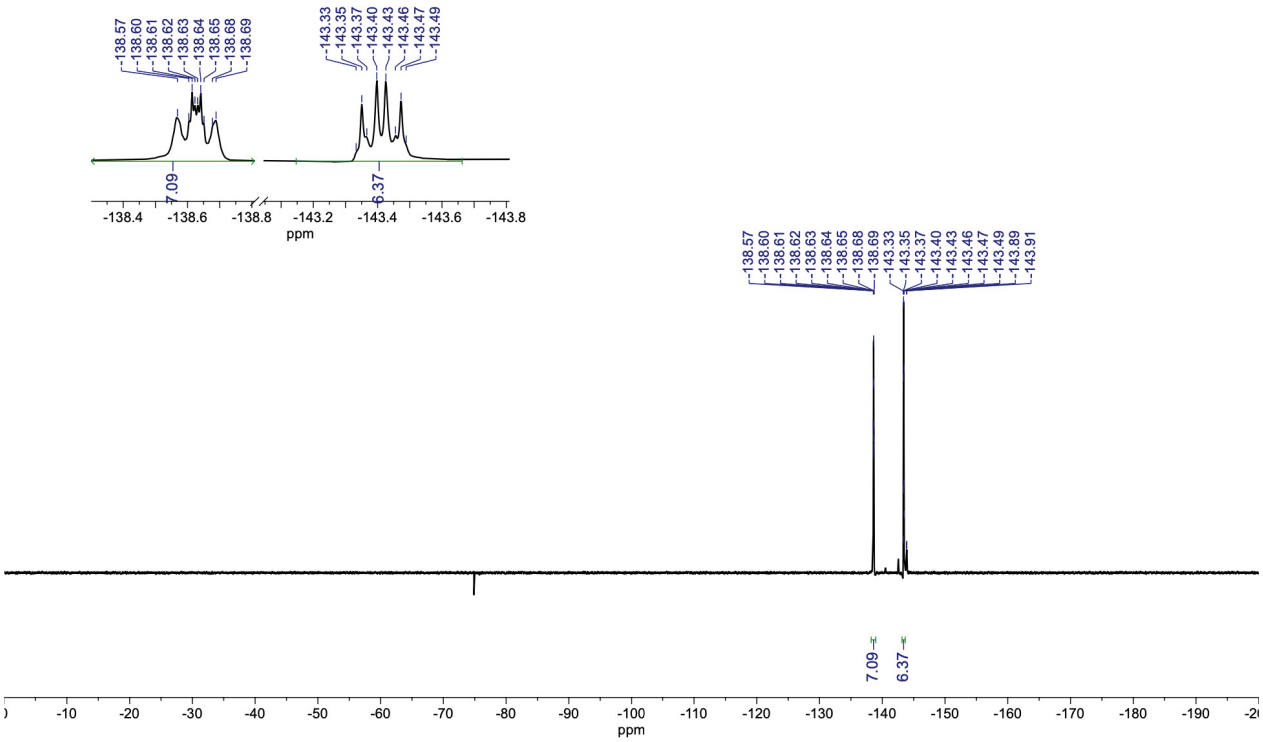

Figure S240: ^{19}F NMR spectrum (282 MHz, $CDCl_3$) of trialdehyde **37**.

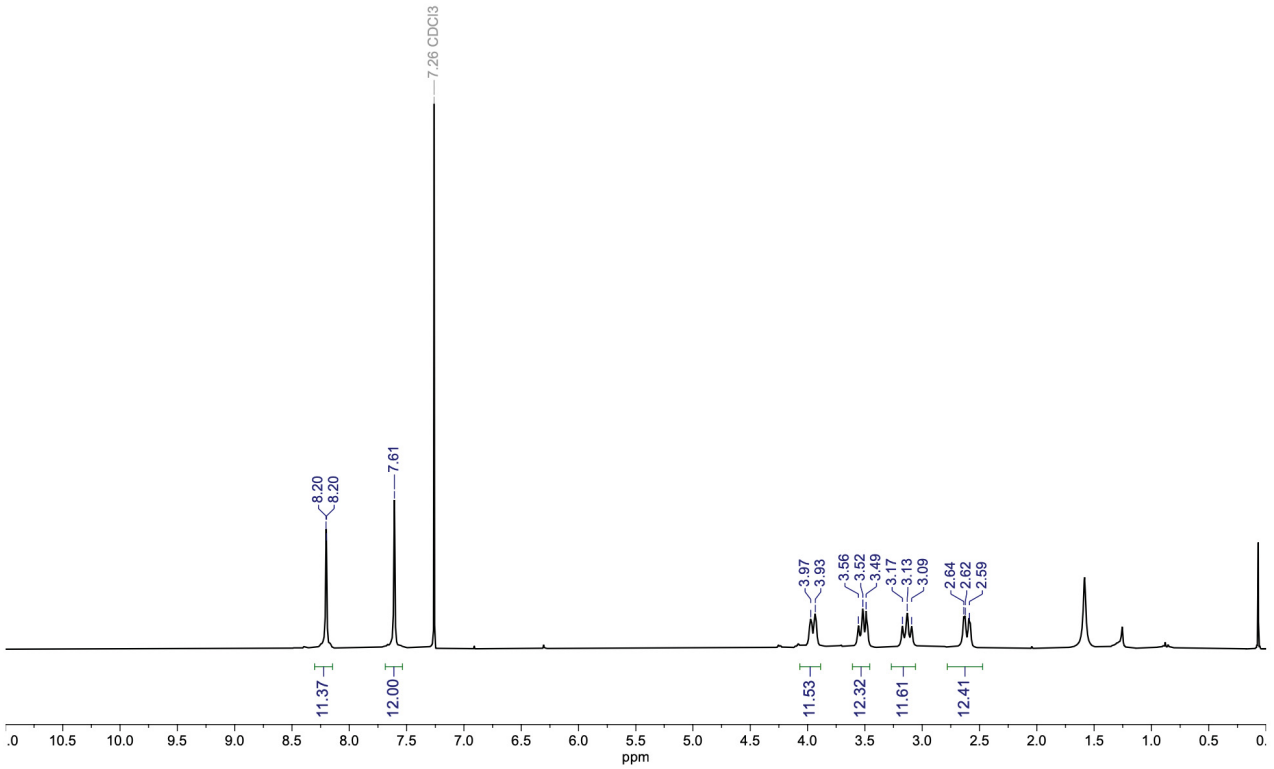

Figure S241: ^{1}H NMR spectrum (300 MHz, $CDCl_3$) of cage compound **FPOC10**.

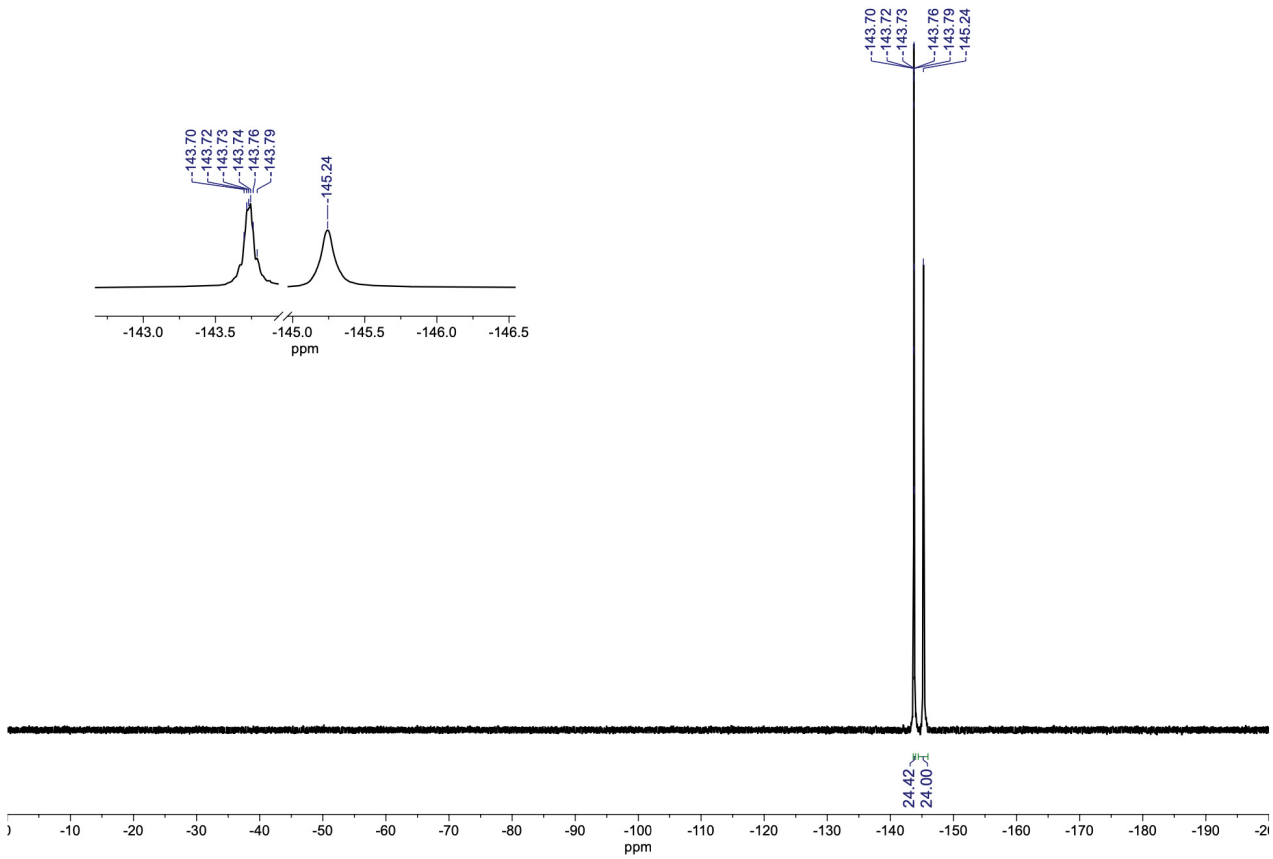

Figure S242: ^{19}F NMR spectrum (282 MHz, $CDCl_3$) of cage compound **FPOC10**.

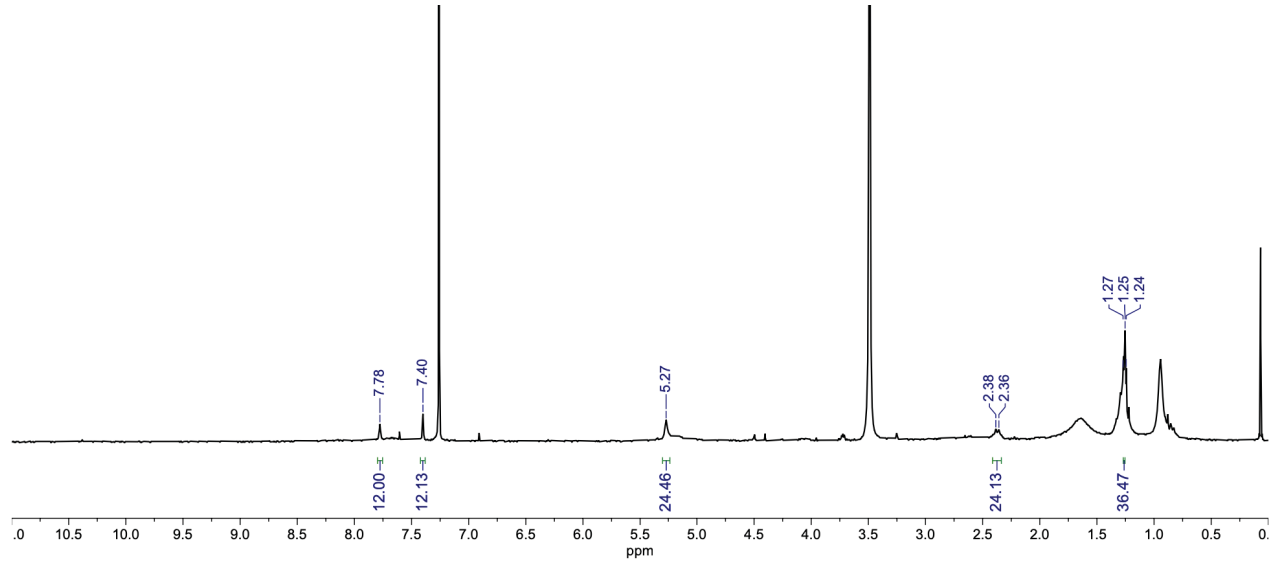

Figure S243: ^{1}H NMR spectrum (300 MHz, $CDCl_3$) of cage compound **FPOC13**.

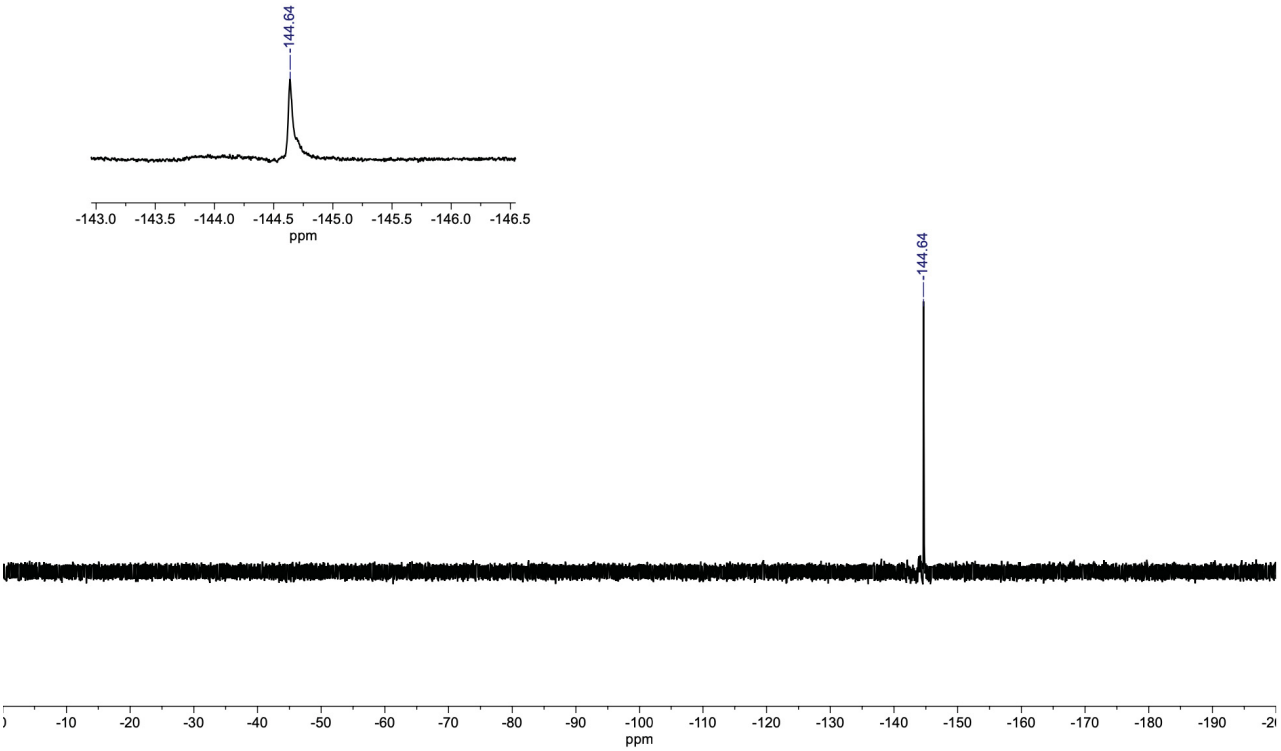

Figure S244: ^{19}F NMR spectrum (282 MHz, $CDCl_3$) of cage compound **FPOC13**.

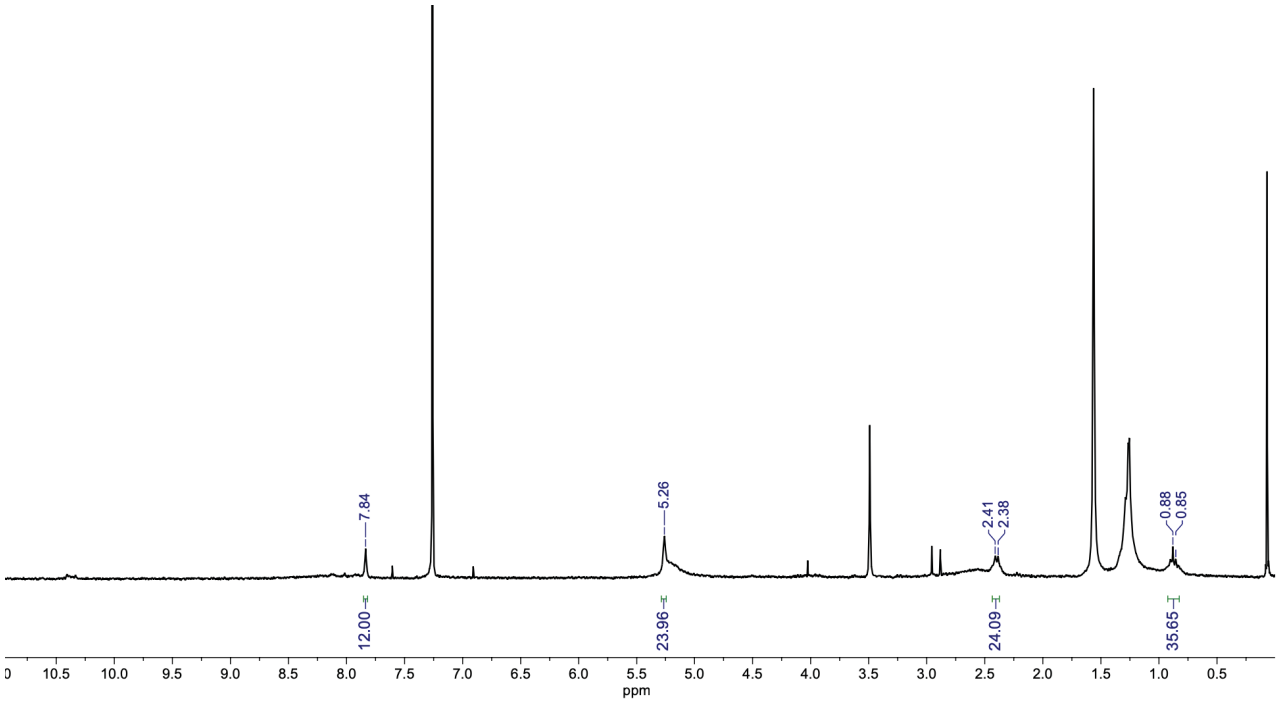

Figure S245: ^{1}H NMR spectrum (300 MHz, $CDCl_3$) of cage compound **FPOC14**.

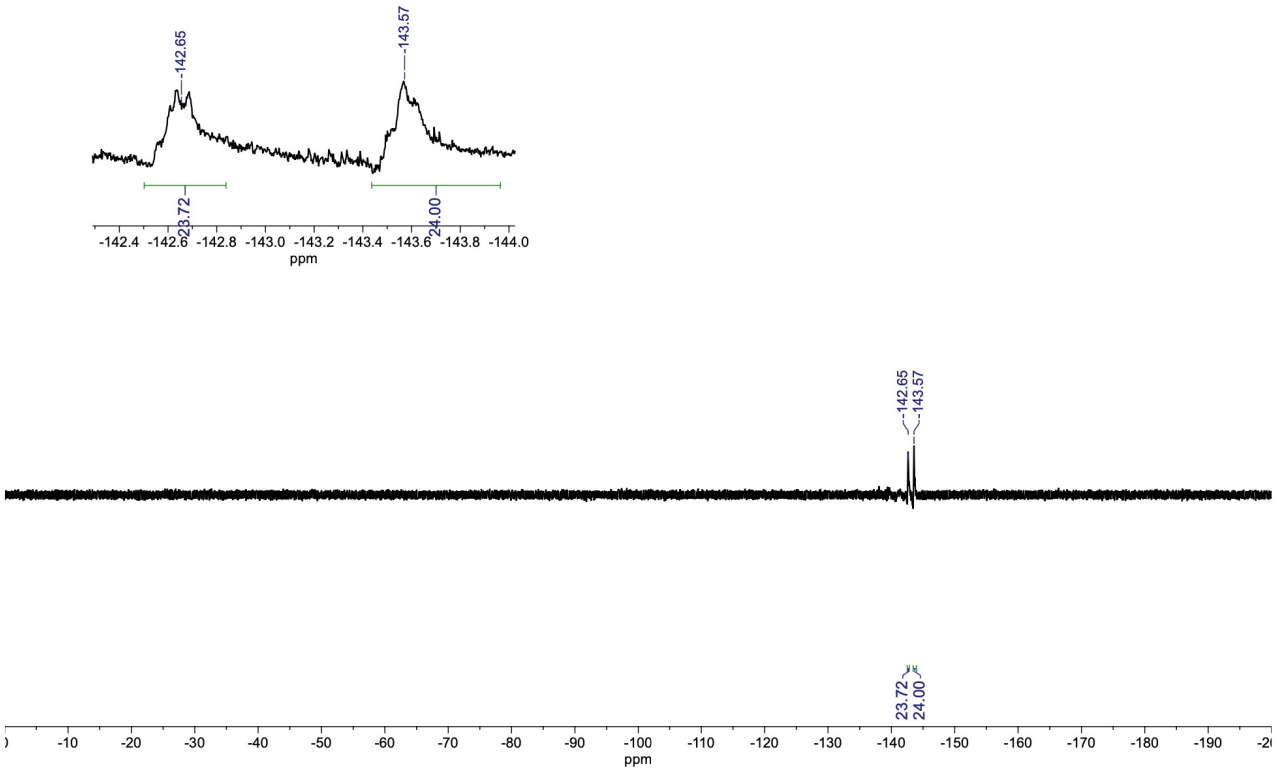

Figure S246: ^{19}F NMR spectrum (282 MHz, $CDCl_3$) of cage compound **FPOC14**.

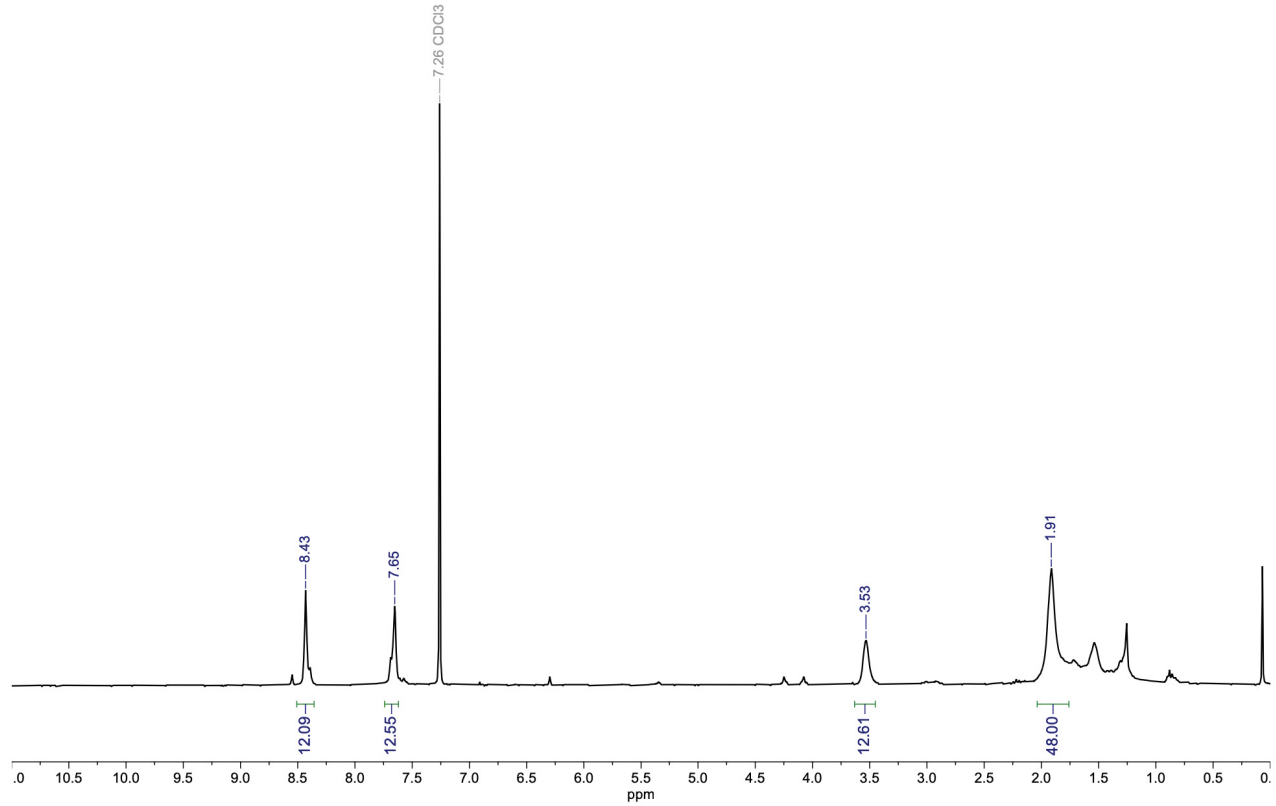

Figure S247: ^{1}H NMR spectrum (300 MHz, $CDCl_3$) of cage compound **FPOC16**.

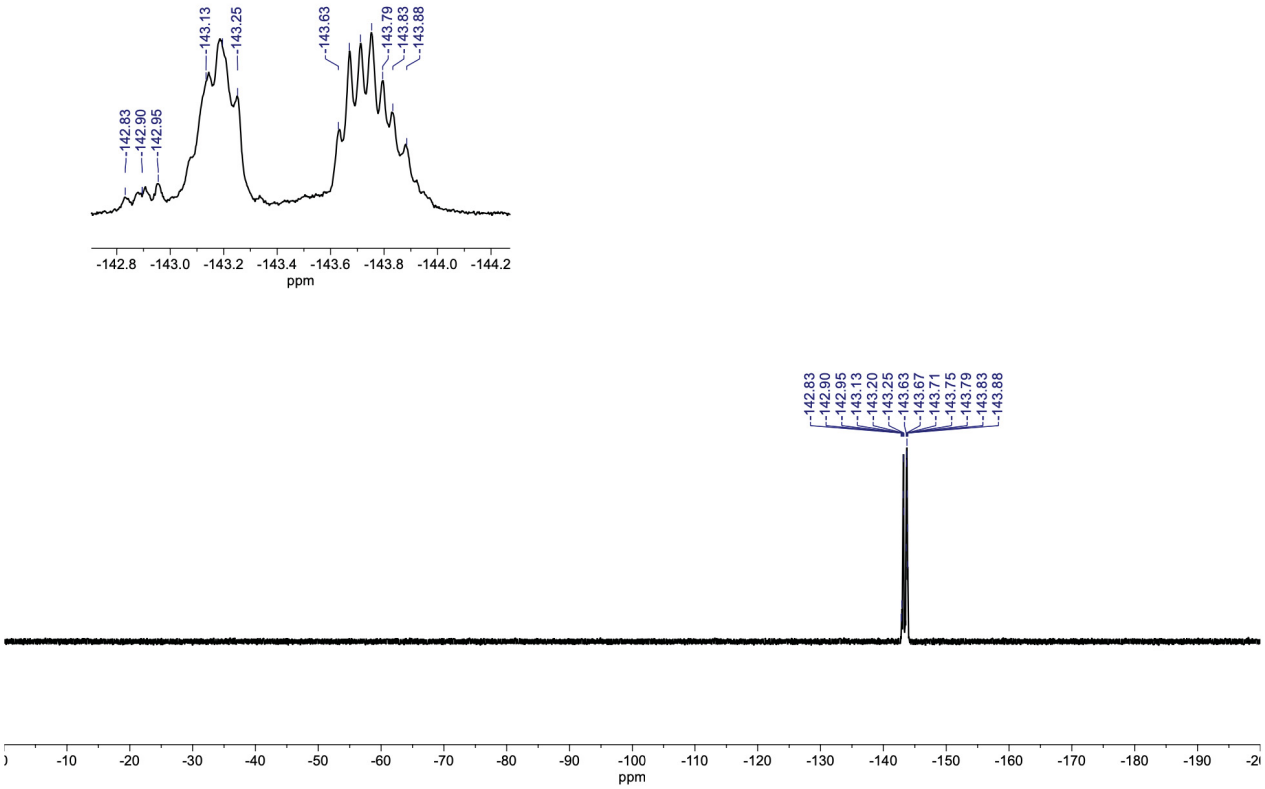

Figure S248: ^{19}F NMR spectrum (282 MHz, $CDCl_3$) of cage compound **FPOC16**.

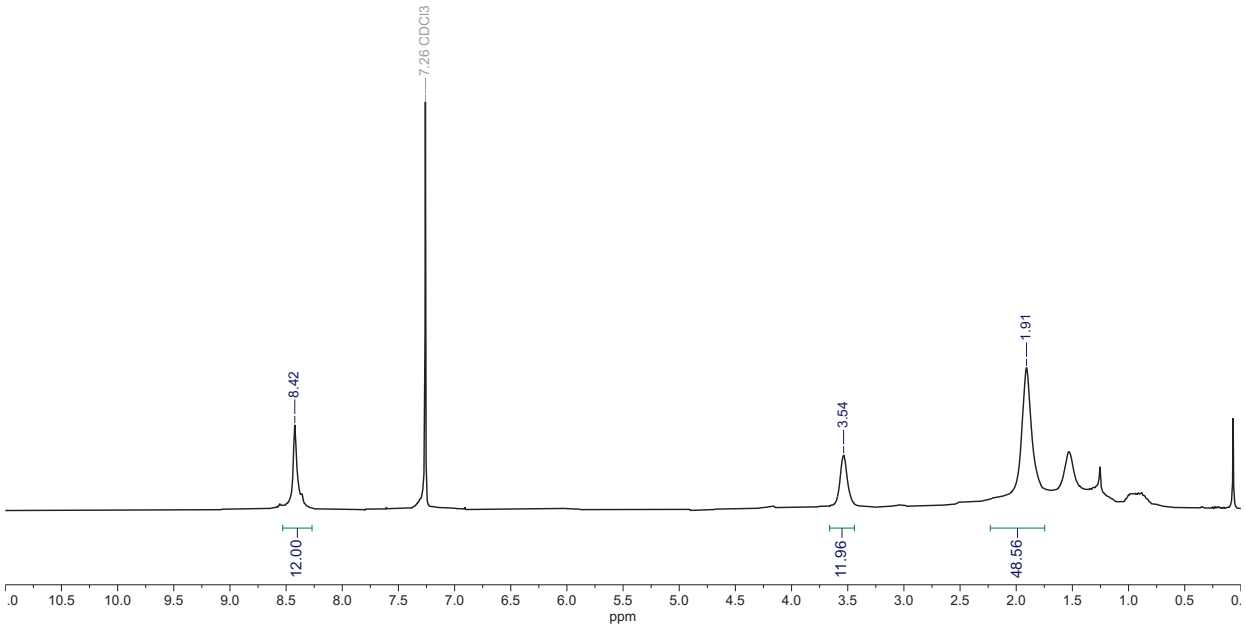

Figure S249: ^{1}H NMR spectrum (300 MHz, $CDCl_3$) of cage compound **FPOC17**.

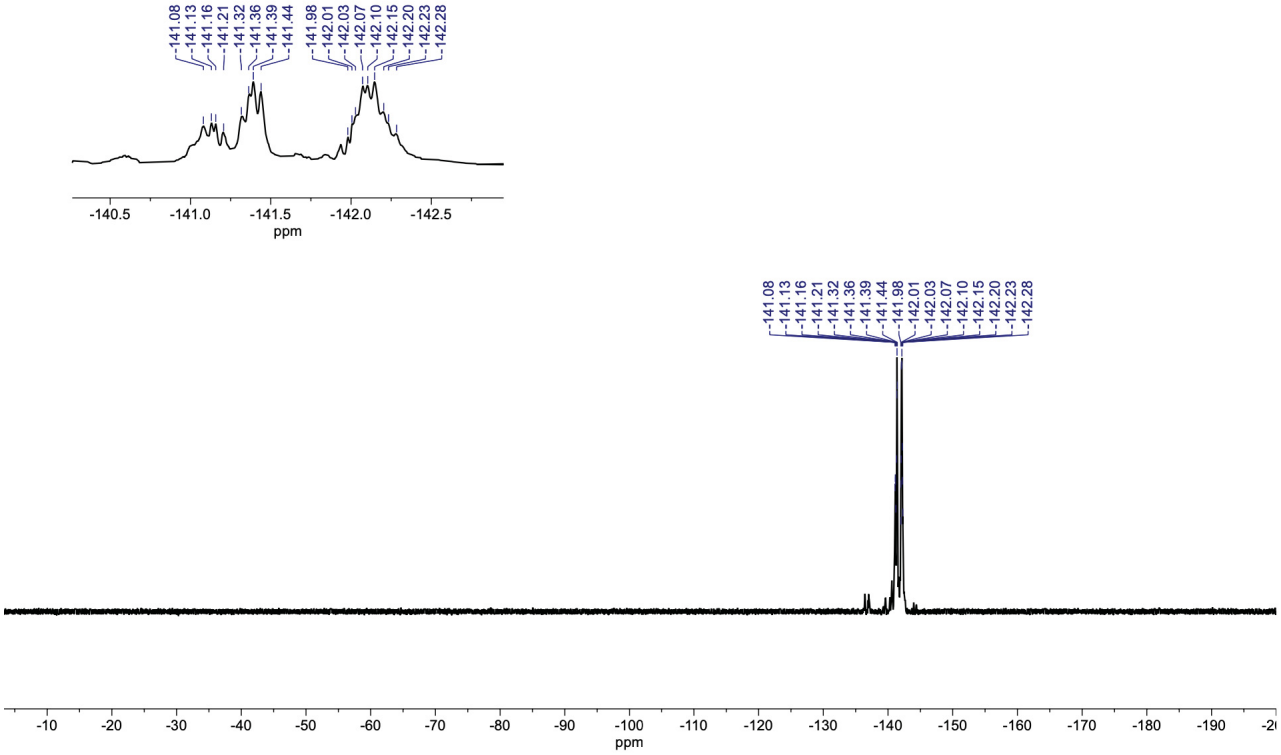

Figure S250: ^{19}F NMR spectrum (282 MHz, $CDCl_3$) of cage compound **FPOC17.**

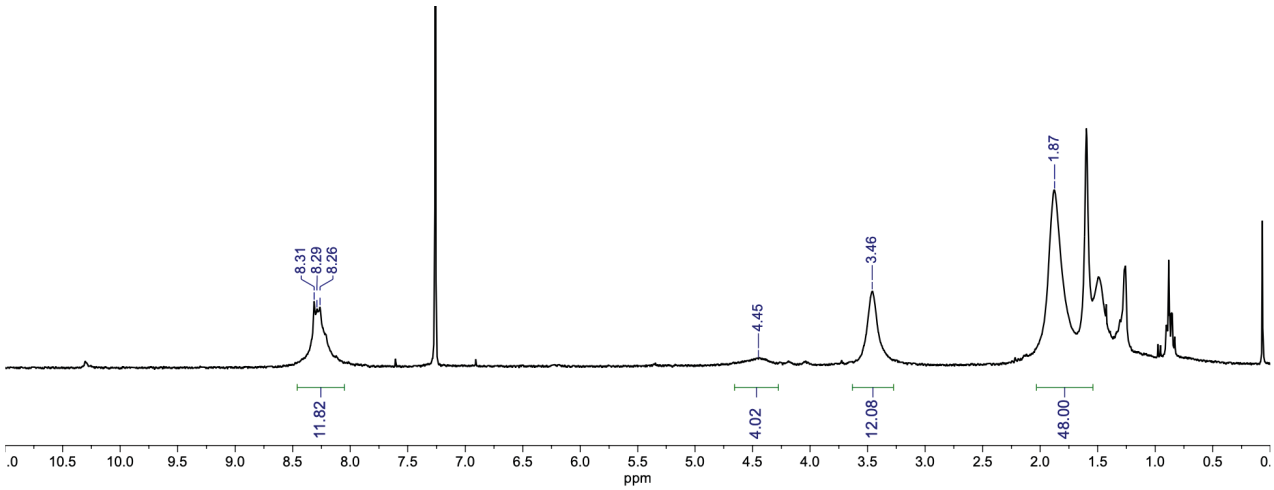

Figure S251: ^{1}H NMR spectrum (300 MHz, $CDCl_3$) of cage compound **FPOC18**.

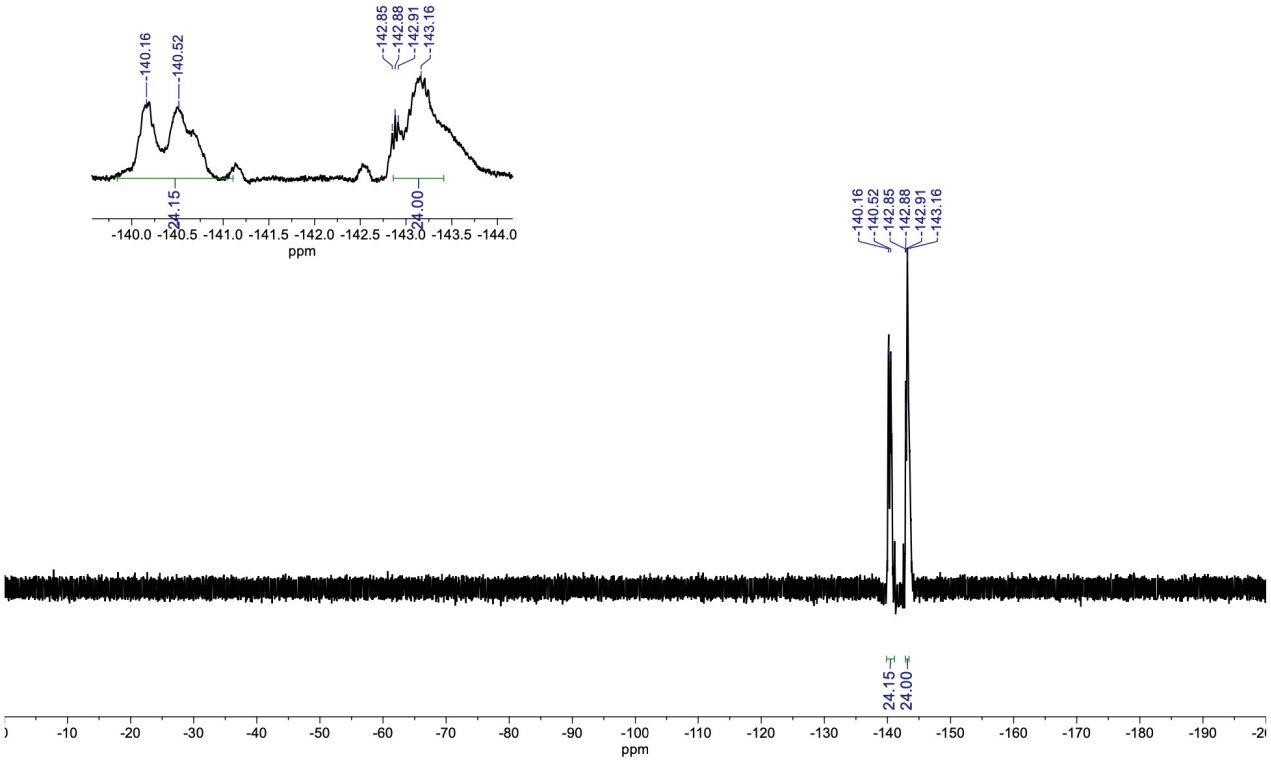

Figure S252: ^{19}F NMR spectrum (282 MHz, $CDCl_3$) of cage compound **FPOC18.**

IR spectra

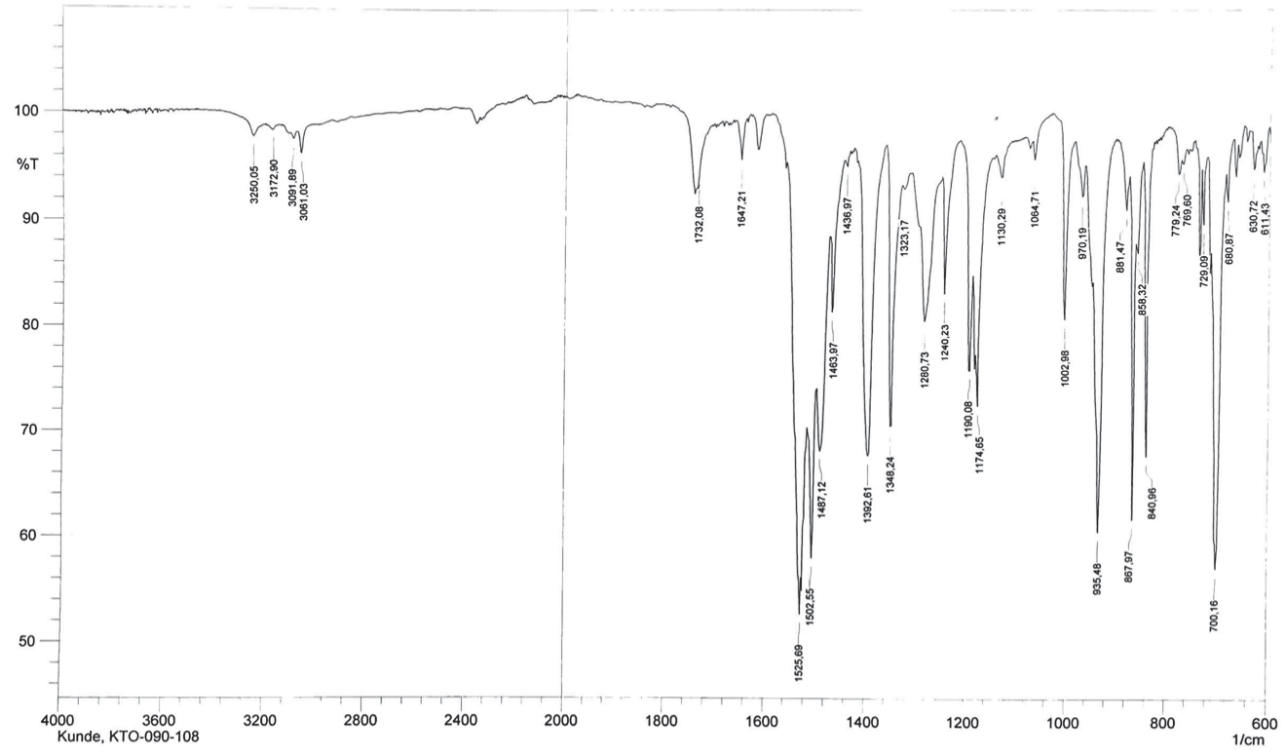

Figure S253: AT-IR spectrum of triazine compound **34**.

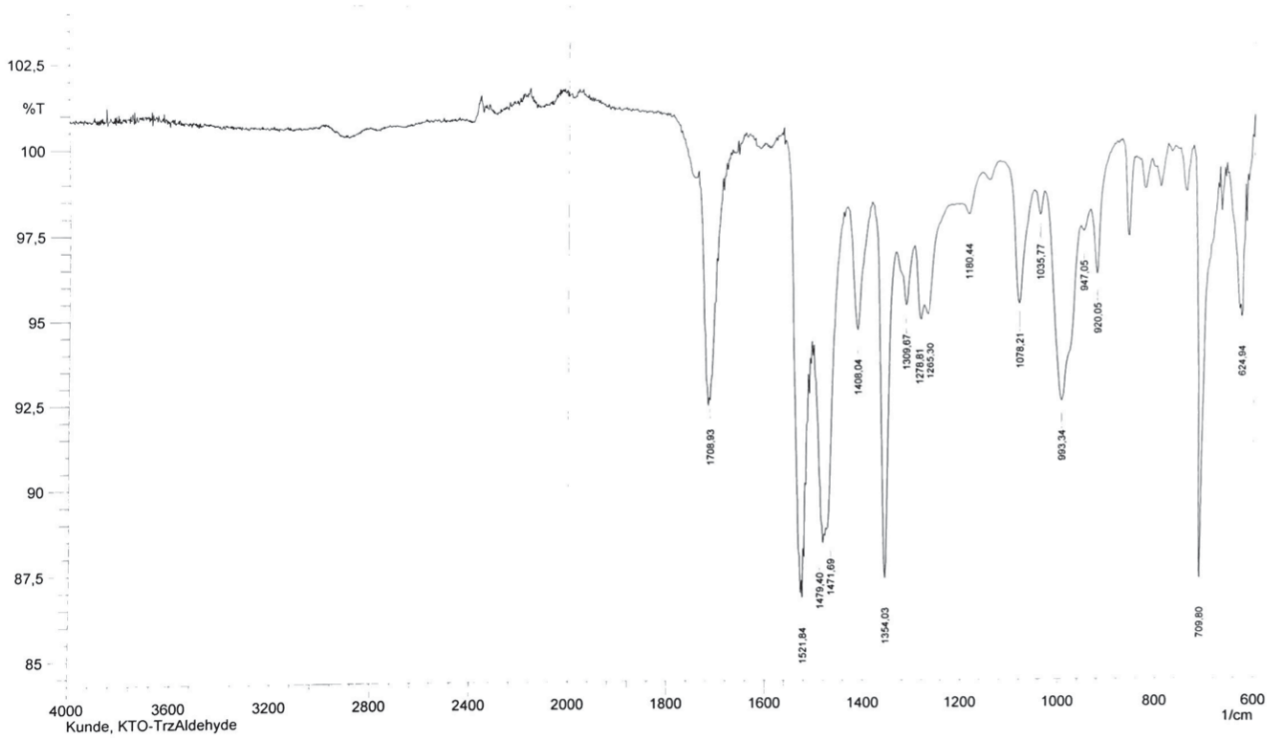

Figure S254: AT-IR spectrum of triazine aldehyde **35**.

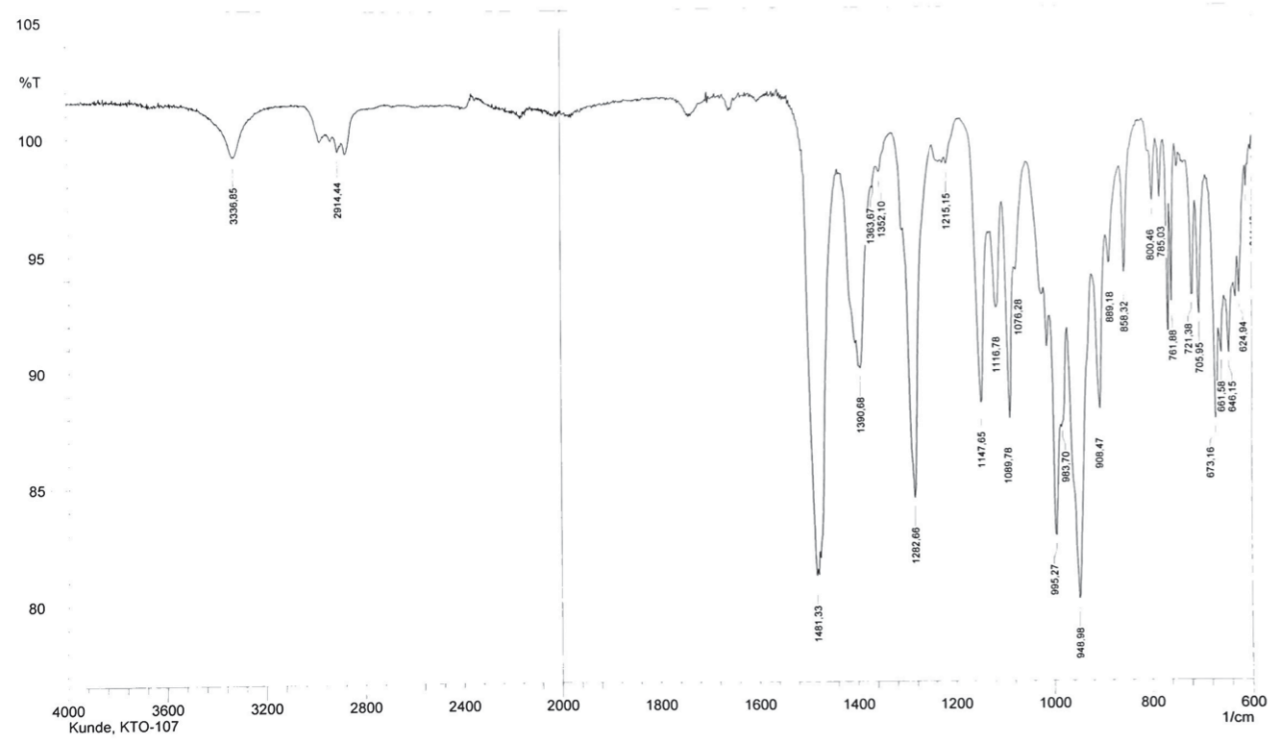

Figure S255: AT-IR spectrum of triacetal **36**.

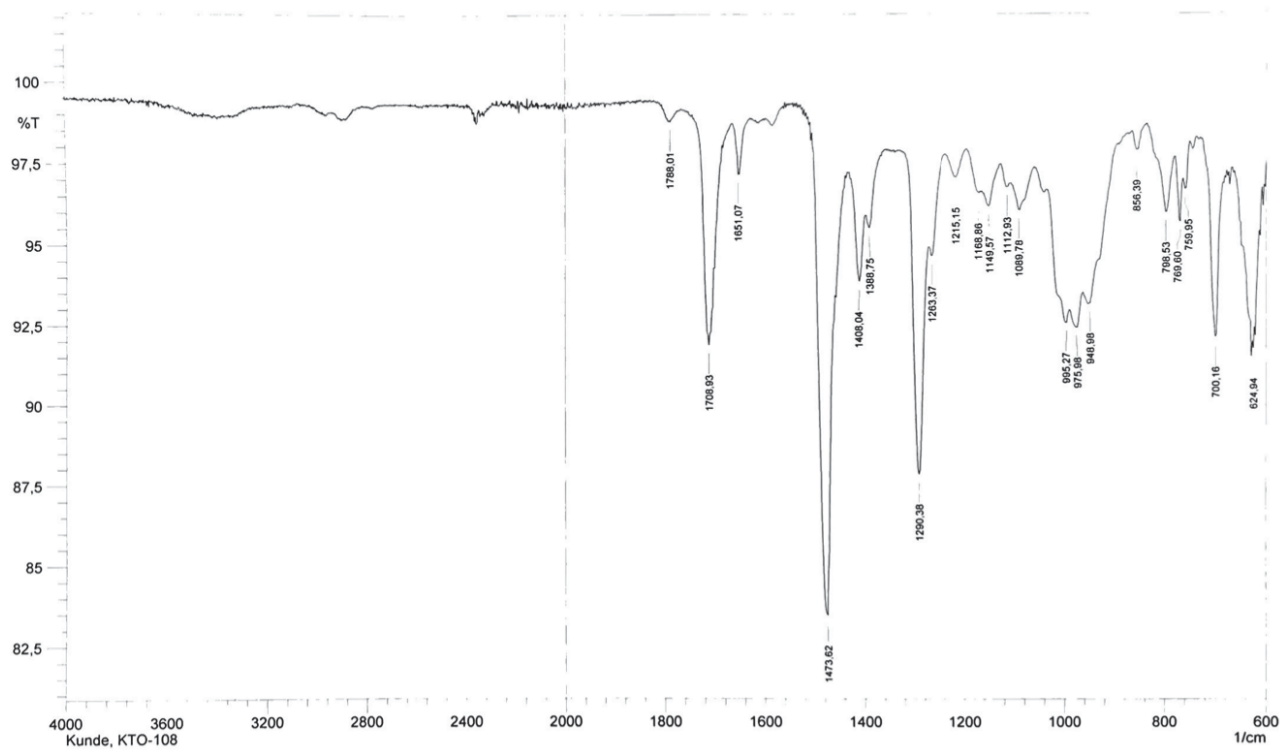

Figure S256: AT-IR spectrum of trialdehyde **37**.

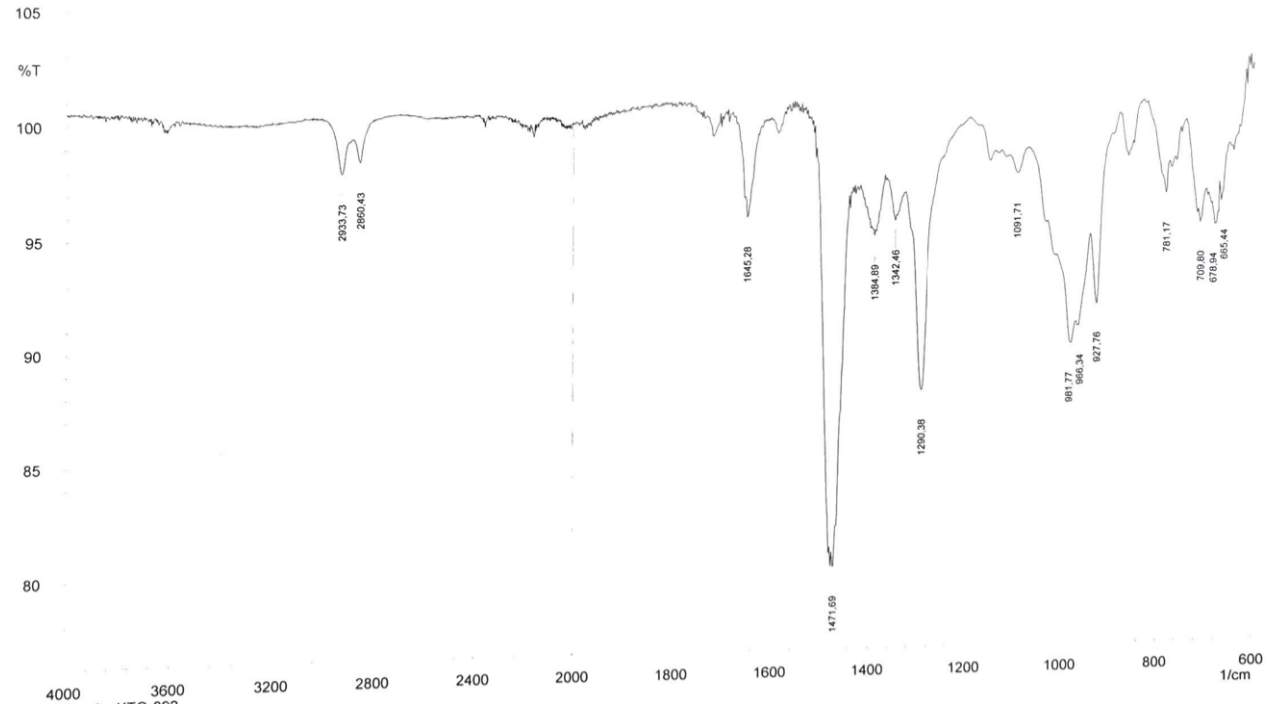

Figure S257: AT-IR spectrum of **FPOC13**.

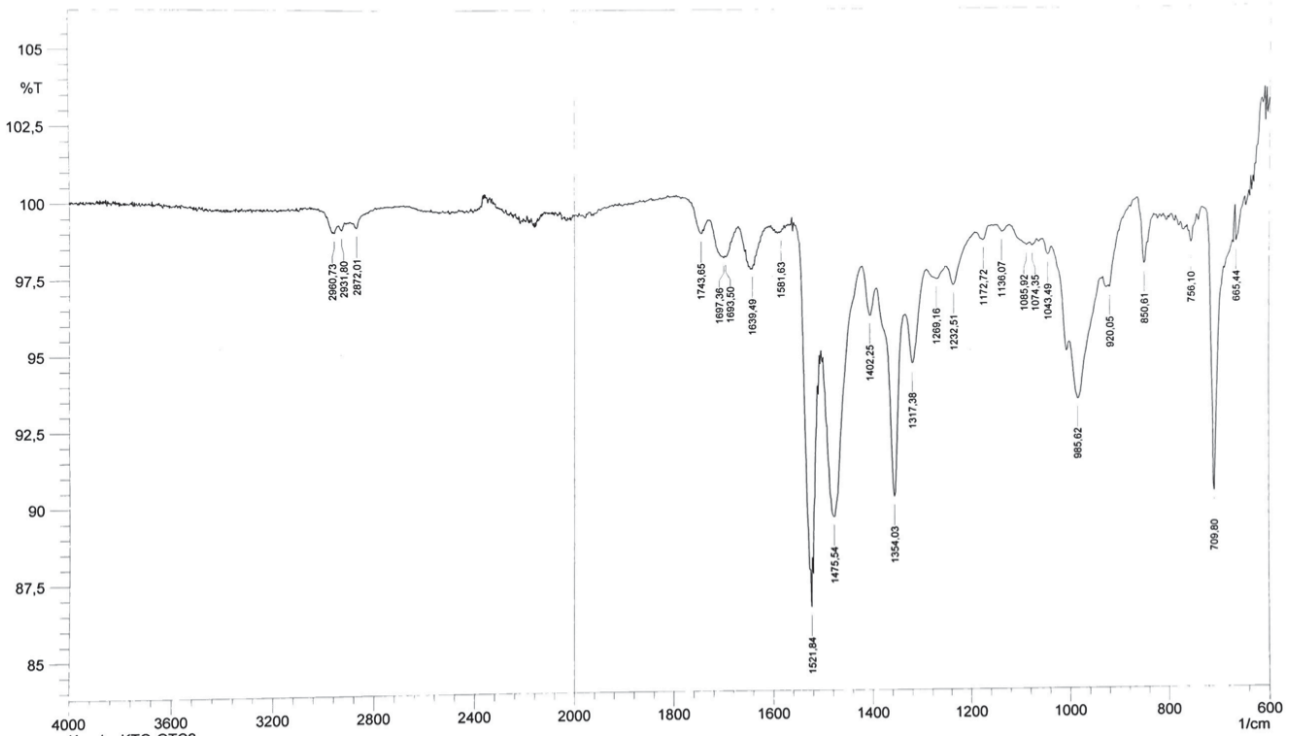

Figure S258: AT-IR spectrum of **FPOC14**.

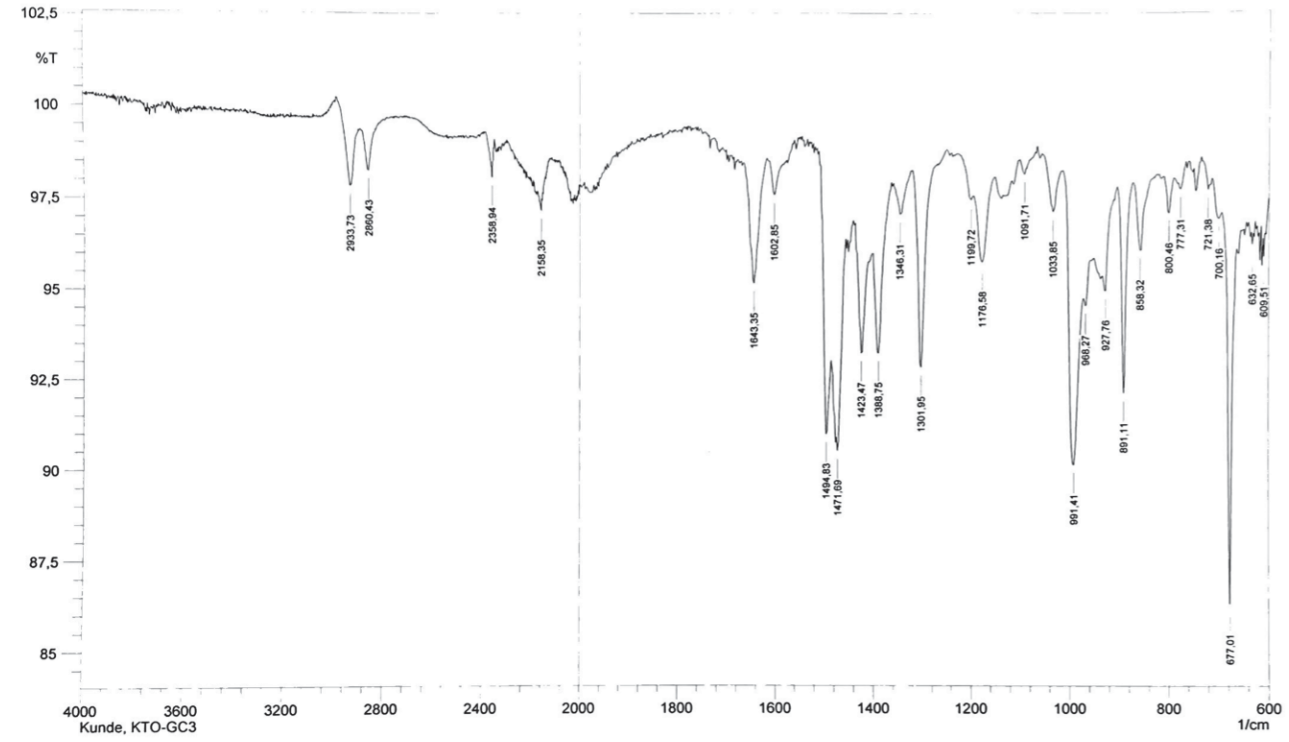

Figure S259: AT-IR spectrum of **FPOC16**.

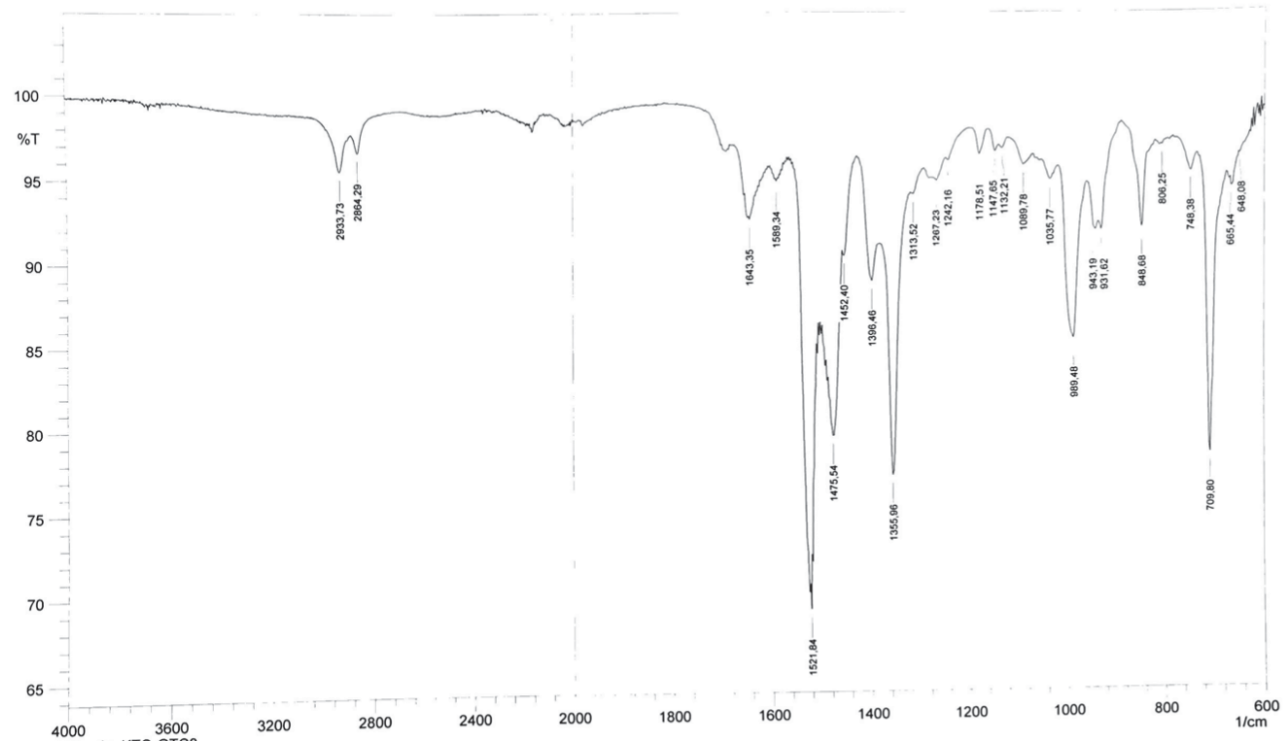

Figure S260: AT-IR spectrum of **FPOC17**.

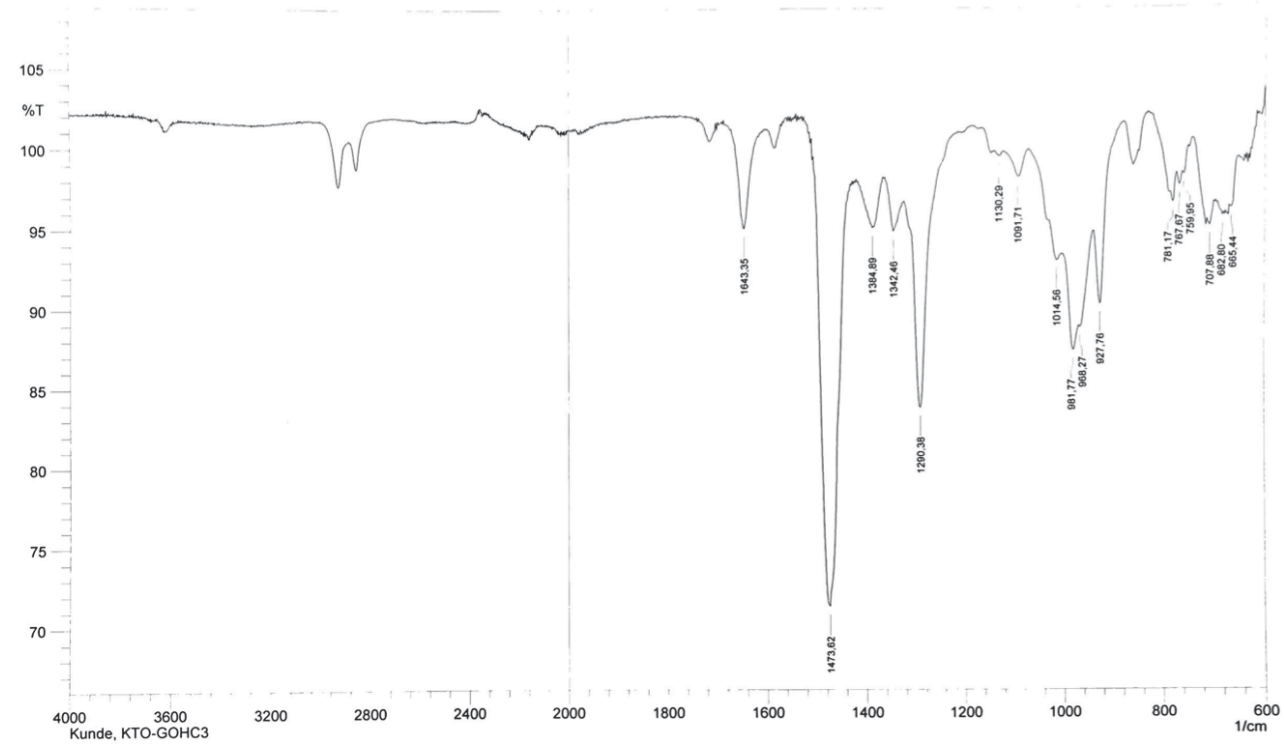

Figure S261: AT-IR spectrum of **FPOC18**.

MS spectra

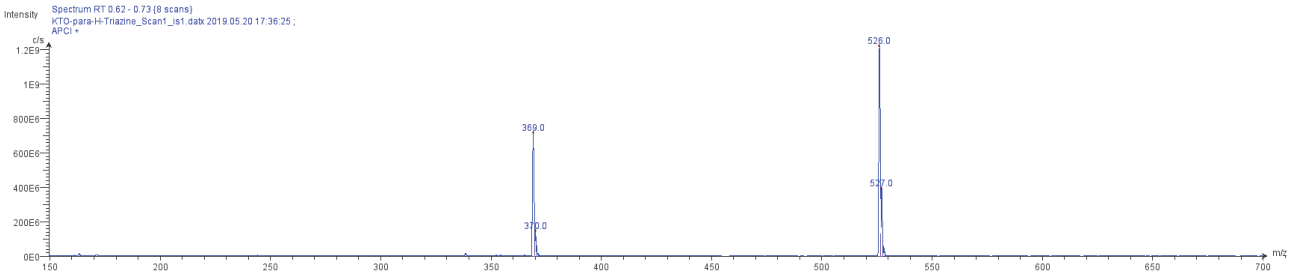

Figure S262: CI-MS spectrum of triazine compound **34.**

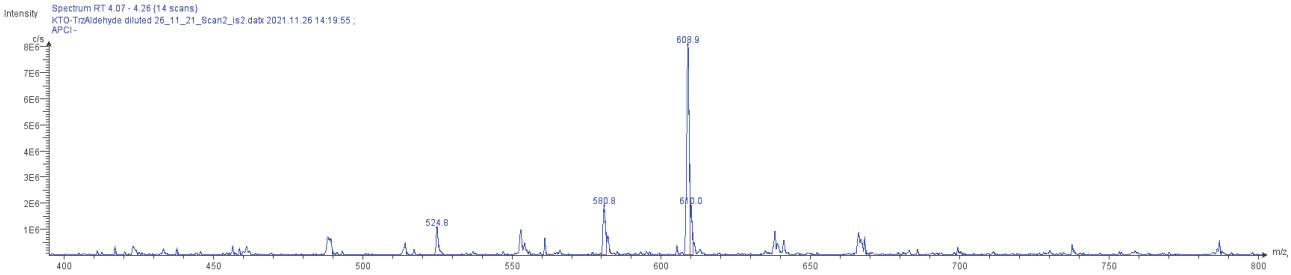

Figure S263: CI-MS spectrum of triazine aldehyde **35.**

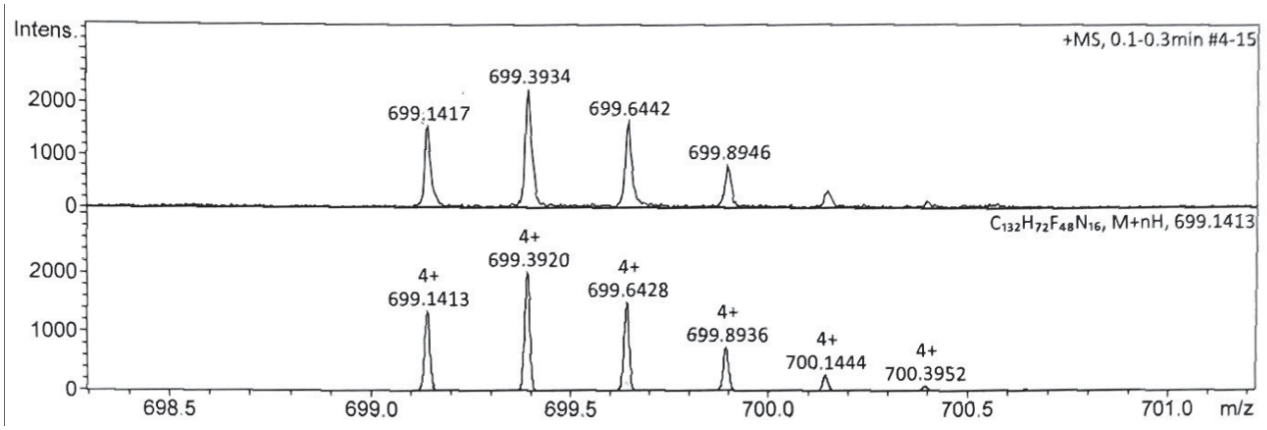

Figure S264: ESI-HRMS spectrum of cage compound **FPOC10** (top) and calculated mass ion distribution (bottom); the found ion: 699.3934 m/z corresponds very well with the calculated [**FPOC10**+4H]$^{4+}$ species of 699.3920 m/z**.**

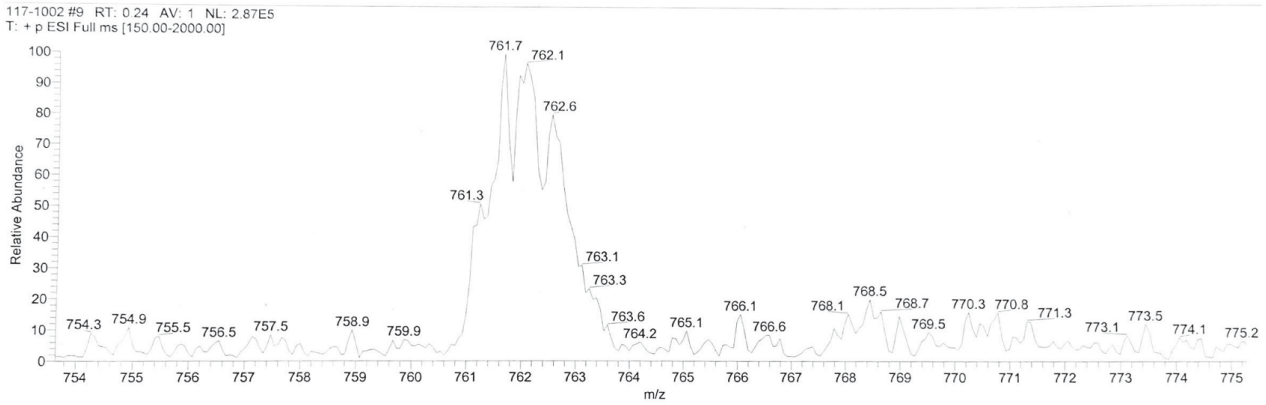

Figure S265: ESI-MS spectrum of cage complex **CuFPOC10** (top); the found ion: 762.1 m/z corresponds very well with the calculated [**CuFPOC10**+4H]$^{4+}$ species of 762.1 m/z species**.**

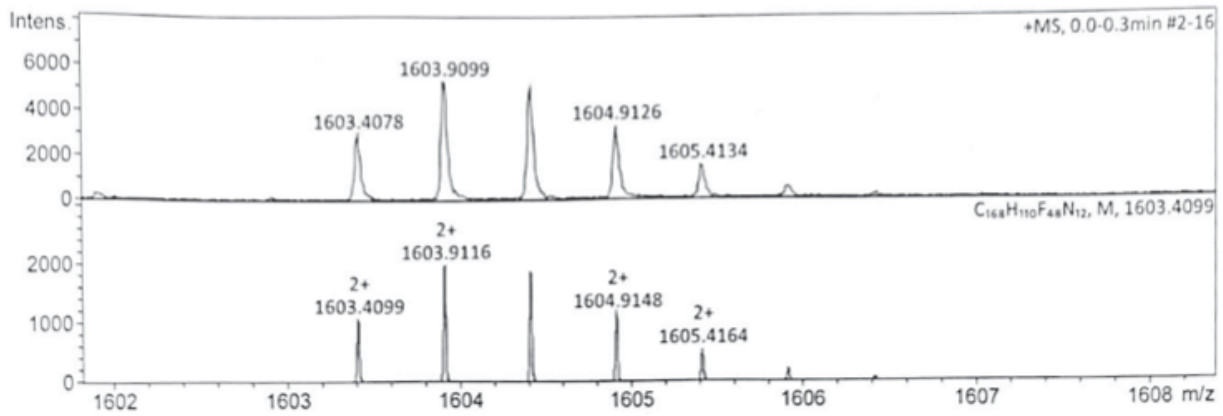

Figure S266: ESI-HRMS spectrum of cage compound **FPOC13** (top) and calculated mass ion distribution (bottom); the found ion: 1603.9099 m/z corresponds very well with the calculated [**FPOC13**+2H]$^{2+}$ species of 1603.9116 m/z**.**

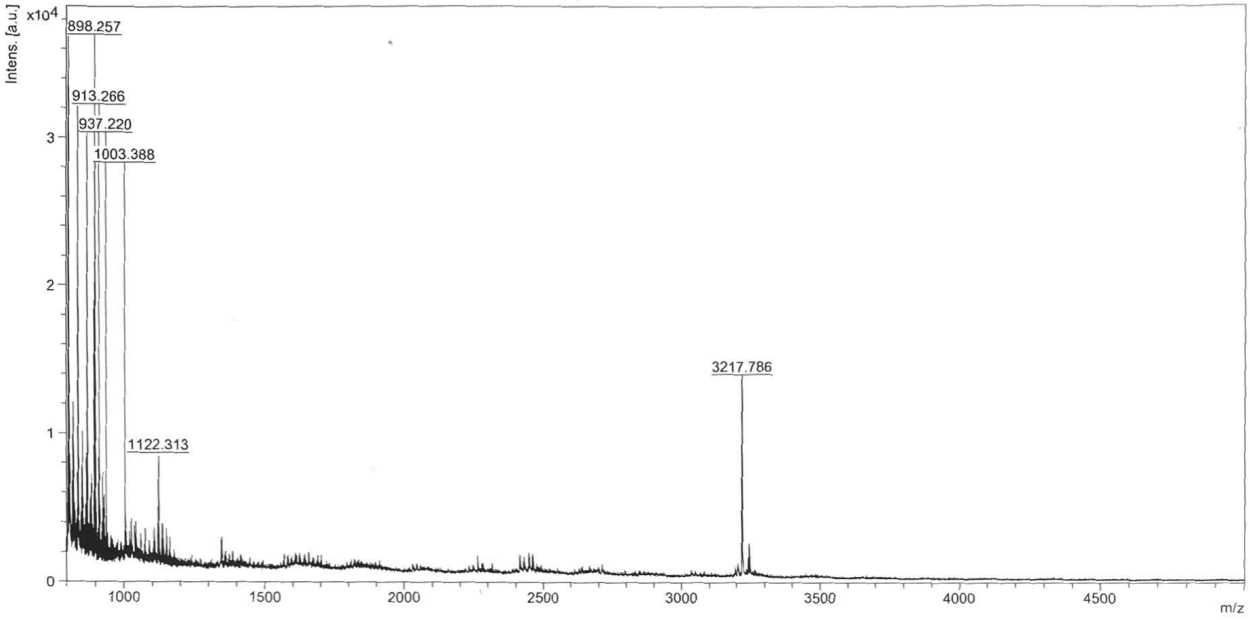

Figure S267: MALDI-MS spectrum of cage compound **FPOC14** the found ion: 3217.786 m/z corresponds very well with the calculated [**FPOC14**+H]$^{+}$ species of 3217.756 m/z.

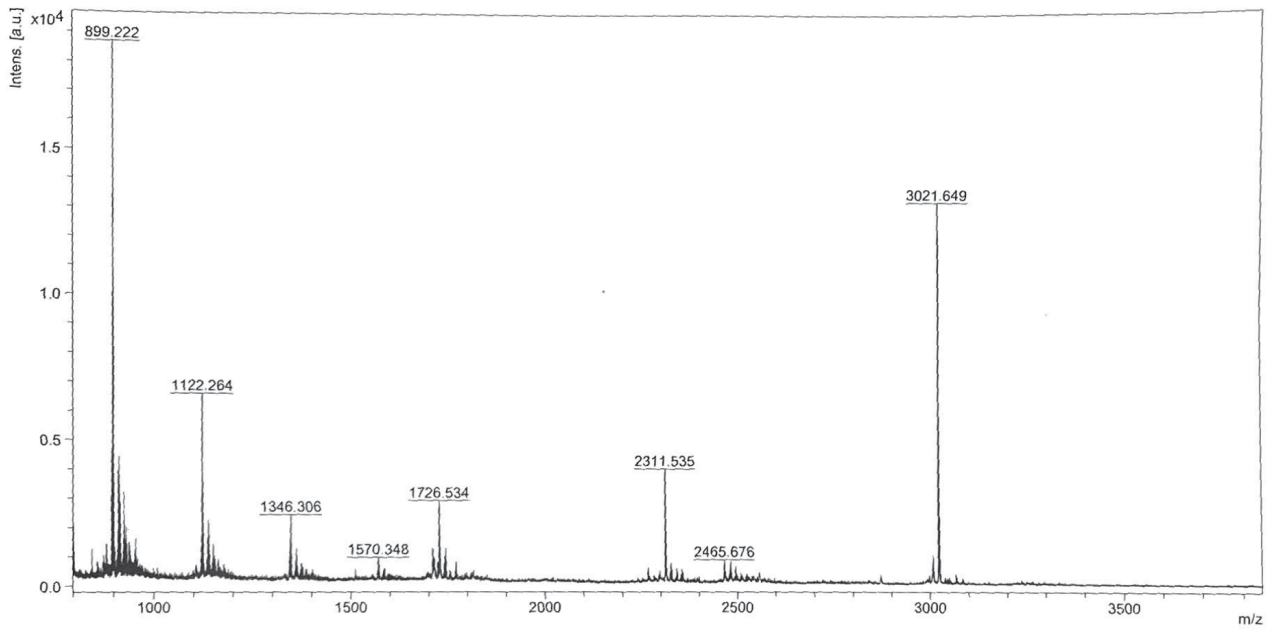

Figure S268: MALDI-MS spectrum of cage compound **FPOC15** the found ion: 3021.649 m/z corresponds very well with the calculated [**FPOC15**+H]$^+$ species of 3021.730 m/z.

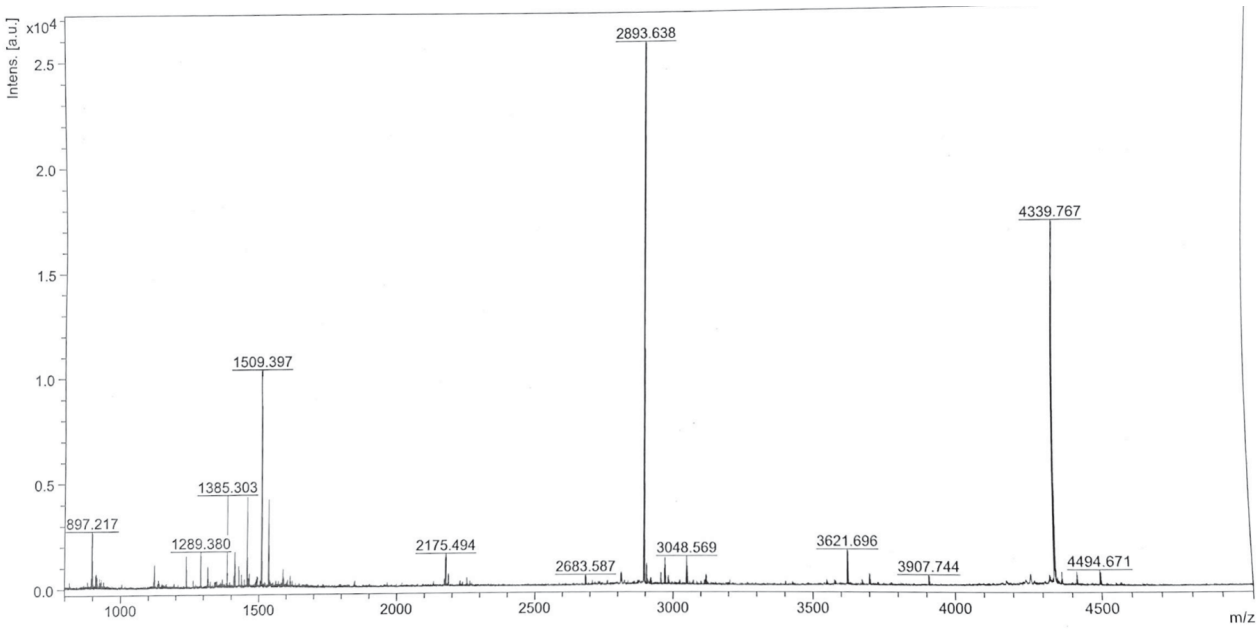

Figure S269: MALDI-MS spectrum of cage compound **FPOC16** and the corresponding **Tri^{6}Di^9** cage; the found ions: 2893.660 m/z and 4339.788 m/z correspond very well with the calculated [**FPOC16**+H]$^+$ species of 2893.625 m/z species and of [**Tri^{6}Di^9** + H]$^+$ with 4339.940 m/z.

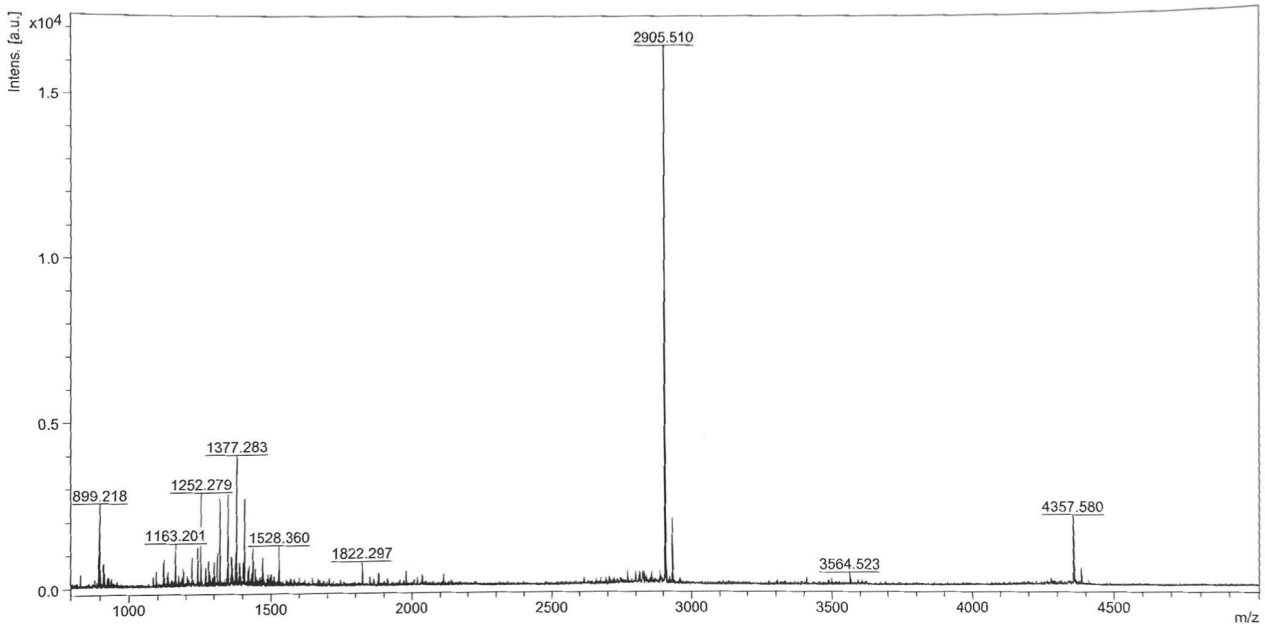

Figure S270: MALDI-MS spectrum of cage compound **FPOC17**; the found ion: 2905.510 m/z corresponda very well with the calculated [**FPOC17**+H]$^+$ species of 2905.568 m/z.

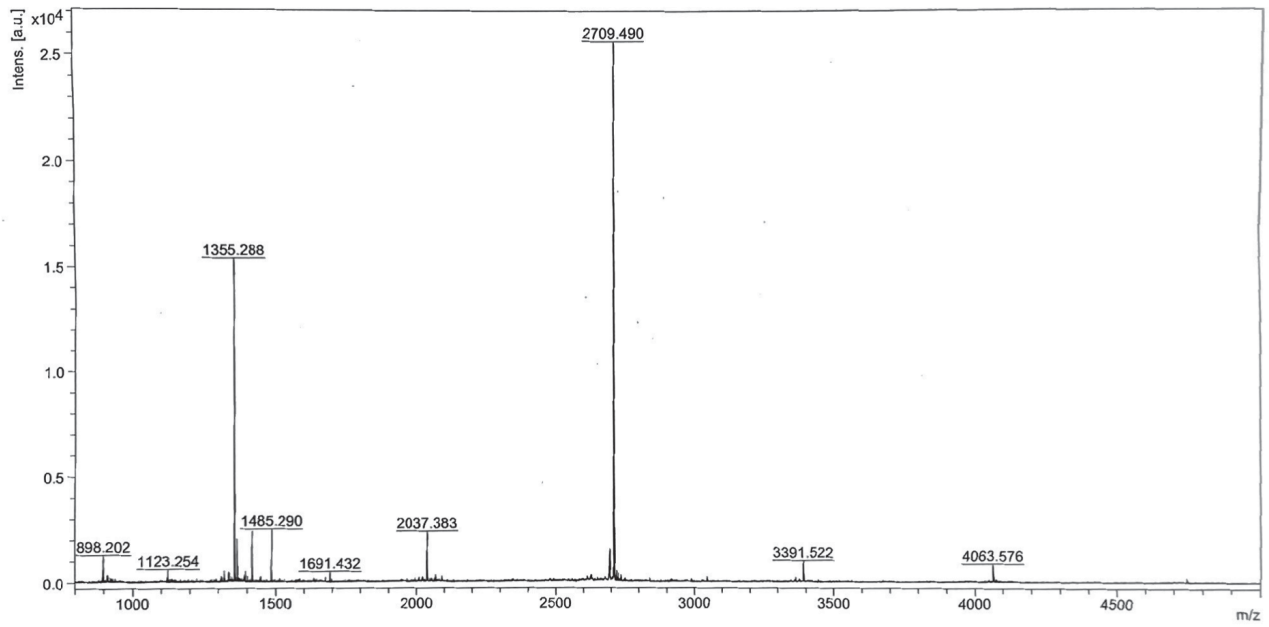

Figure S271: MALDI-MS spectrum of cage compound **FPOC18**; the found ion: 2709.490 m/z corresponds very well with the calculated [**FPOC18**+H]$^+$ species of 2709.542 m/z.

6.6. Spectra for Section 3.6

NMR spectra

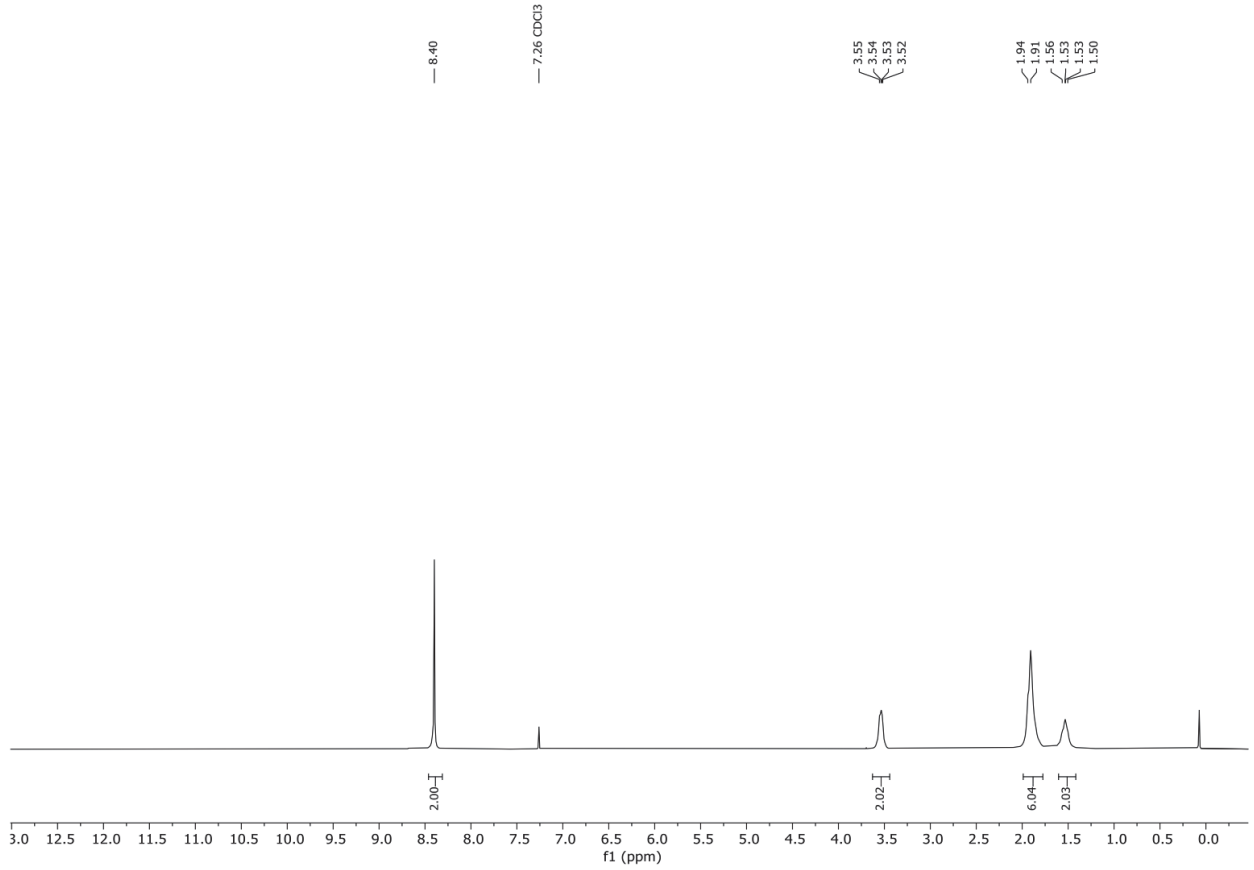

Figure S272: ^{1}H NMR (300 MHz, $CDCl_3$) spectrum of highly fluorinated macrocycle **RRF$_{24}$**.

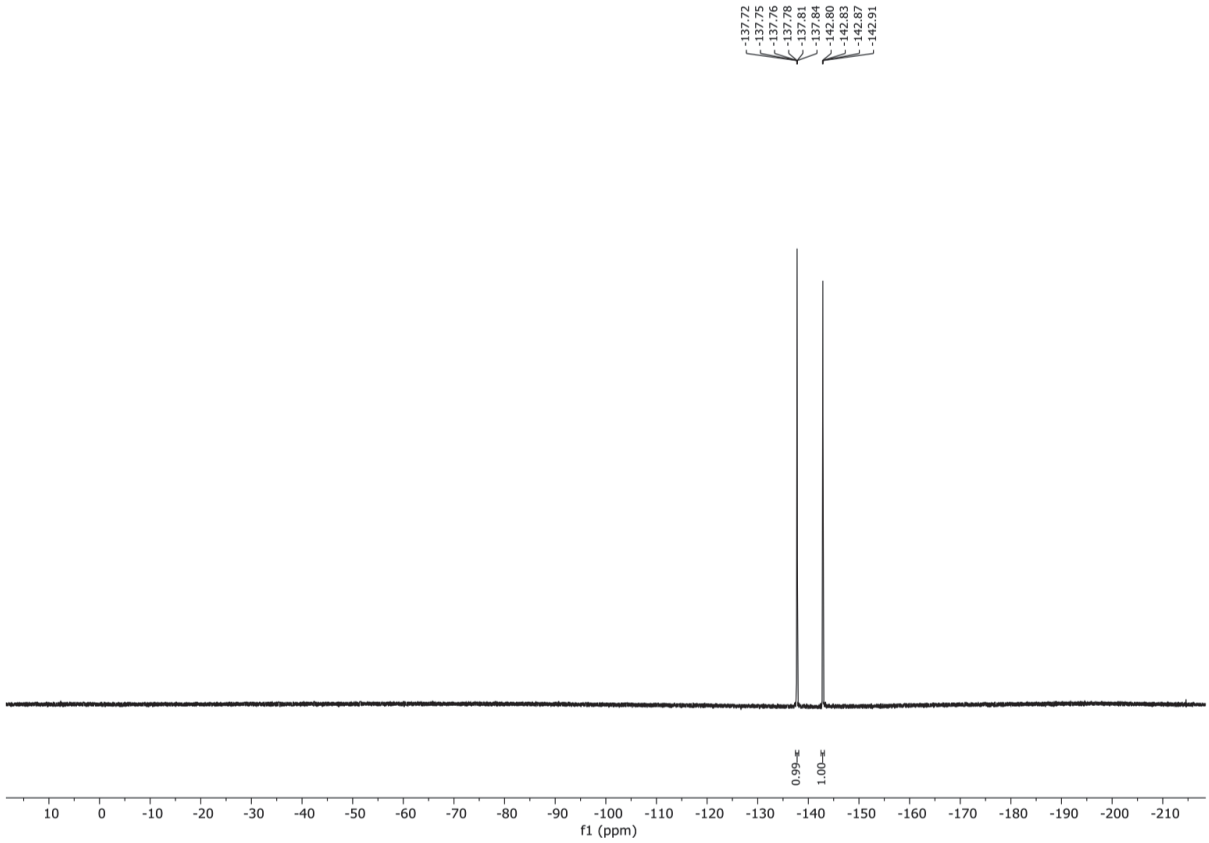

Figure S273: ^{19}F NMR (282 MHz, $CDCl_3$) spectrum of highly fluorinated macrocycle **RRF24**.

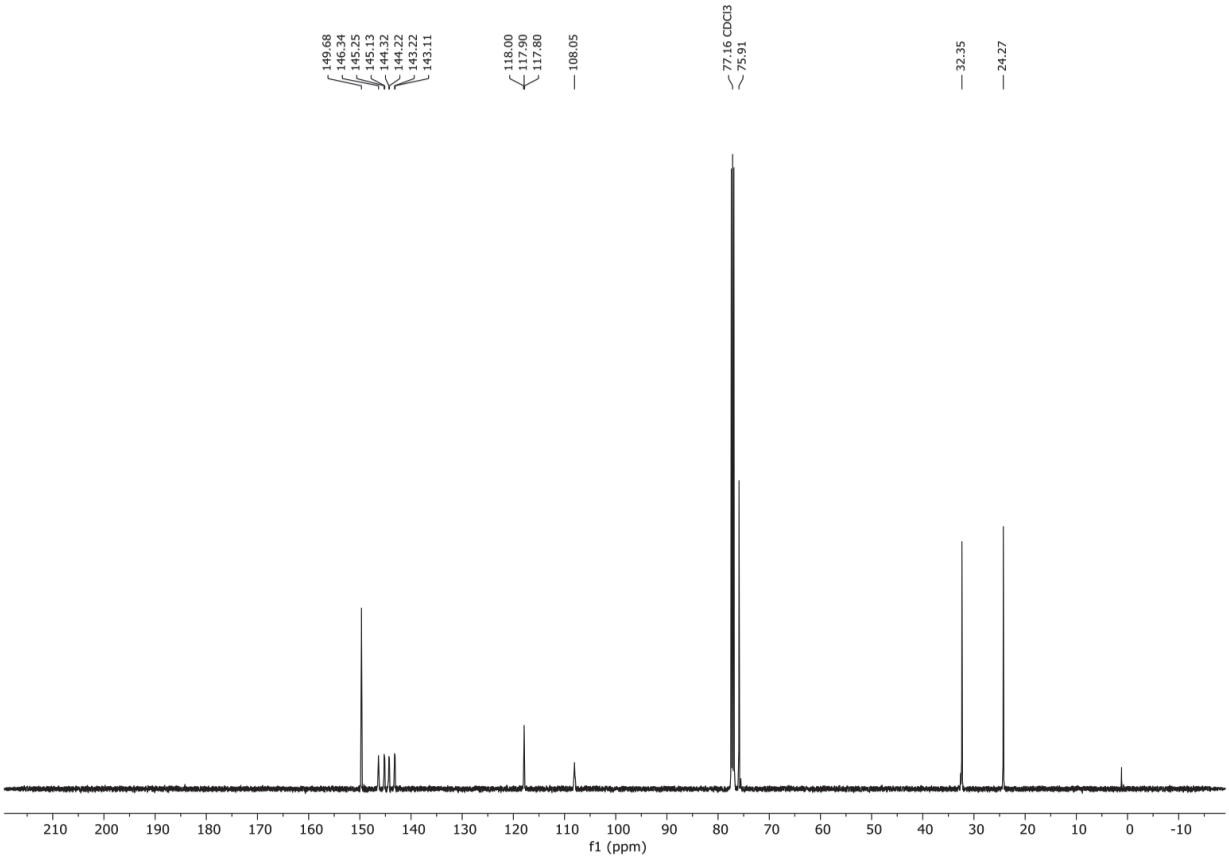

Figure S274: $^{13}C\{^1H\}$ NMR (75 MHz, $CDCl_3$) spectrum of highly fluorinated macrocycle **RRF24**.

MS spectra

Acquisition Parameter

Source Type	ESI	Ion Polarity	Positive	Set Nebulizer	0.3 Bar
Focus	Active	Set Capillary	4000 V	Set Dry Heater	180 °C
Scan Begin	300 m/z	Set End Plate Offset	-500 V	Set Dry Gas	4.0 l/min
Scan End	2800 m/z	Set Collision Cell RF	2500.0 Vpp	Set Divert Valve	Source

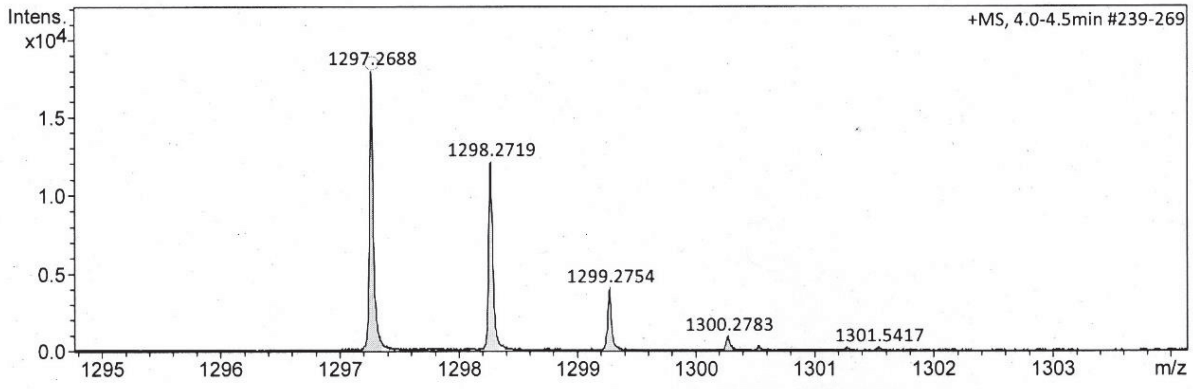

Meas. m/z	#	Ion Formula	m/z	err [ppm]	mSigma	# mSigma	Score	rdb	e⁻ Conf	N-Rule
1297.2688	1	C60H37F24N6	1297.2691	0.2	2.2	1	100.00	33.5	even	ok
	2	C59H41F24N2O4	1297.2678	-0.8	10.6	2	70.30	28.5	even	ok

Figure S275: ESI-HRMS spectrum of highly fluorinated macrocycle **RRF24**; the found mass ion of 1297.2688 m/z corresponds very well to the calculated mass of 1297.2688 m/z.

IR spectra

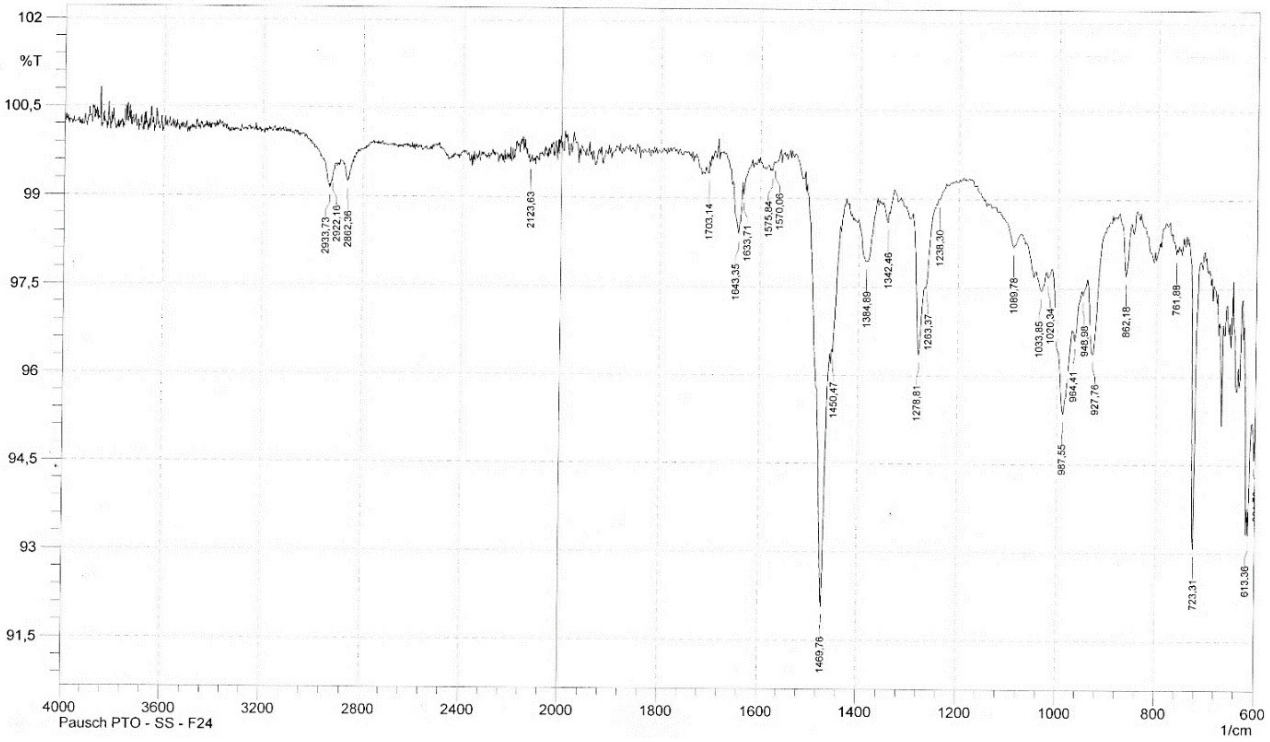

Figure S276: AT-IR spectrum of highly fluorinated macrocycle **RRF24**.

7. References

[1] J. M. Lehn, *Science*, 2002, **295**, 2400–2403.

[2] a) J.-B. Lin, T. T. T. Nguyen, R. Vaidhyanathan, J. Burner, J. M. Taylor, H. Durekova, F. Akhtar, R. K. Mah, O. Ghaffari-Nik, S. Marx, N. Fylstra, S. S. Iremonger, K. W. Dawson, P. Sarkar, P. Hovington, A. Rajendran, T. K. Woo and G. K. H. Shimizu, *Science*, 2021, **374**, 1464–1469; b) A. Ahmed, S. Seth, J. Purewal, A. G. Wong-Foy, M. Veenstra, A. J. Matzger and D. J. Siegel, *Nat. Commun.,* 2019, **10**, 1–9.

[3] P. M. Budd, B. S. Ghanem, S. Makhseed, N. B. McKeown, K. J. Msayib and C. E. Tattershall, *Chem. Commun.*, 2004, **2**, 230–231.

[4] J. Weber, N. Du and M. D. Guiver, *Macromolecules*, 2011, **44**, 1763–1767.

[5] a) A. P. Katsoulidis, D. Antypov, G. F. S. Whitehead, E. J. Carrington, D. J. Adams, N. G. Berry, G. R. Darling, M. S. Dyer and M. J. Rosseinsky, *Nature*, 2019, **565**, 213–217; b) A. G. Slater and A. I. Cooper, *Science*, 2015, **348**, aaa8075.

[6] a) J. Huang, X. Han, S. Yang, Y. Cao, C. Yuan, Y. Liu, J. Wang and Y. Cui, *J. Am. Chem. Soc.*, 2019, **141**, 8996–9003; b) L. Zhiqiang, L. Luojia, N. Jiaxin, L. Kaixiang, L. Yong, L. Fujun, C. Jun, Z. Luo, L. Liu, J. Ning, K. Lei, Y. Lu, F. Li and J. Chen, *Angew. Chem. Int. Ed.*, 2018, **57**, 9443–9446; c) H.-L. Qian, C.-X. Yang and X.-P. Yan, *Nat. Commun.*, 2016, **7**, 12104; for excellent summaries on the field see: Review 1: S.-Y. Ding, W. Wang, D. San-Yuan and W. Wei, *Chem. Soc. Rev.*, 2013, **42**, 548–568; Review 2: A. P. Côté, A. I. Benin, N. W. Ockwig, M. O'Keeffe, A. J. Matzger and O. M. Yaghi, *Science*, 2005, **310**, 1166–1170.

[7] a) N. Hanikel, X. Pei, S. Chheda, H. Lyu, W. S. Jeong, J. Sauer, L. Gagliardi and O. M. Yaghi, *Science*, 2021, **374**, 454–459; b) J. H. Dou, M. Q. Arguilla, Y. Luo, J. Li, W. Zhang, L. Sun, J. L. Mancuso, L. Yang, T. Chen, L. R. Parent, G. Skorupskii, N. J. Libretto, C. Sun, M. C. Yang, P. V. Dip, E. J. Brignole, J. T. Miller, J. Kong, C. H. Hendon, J. Sun and M. Dincă, *Nat. Mater.*, 2020, **20**, 222–228; c) C. Liu, Q. Sun, L. Lin, J. Wang, C. Zhang, C. Xia, T. Bao, J. Wan, R. Huang, J. Zou and C. Yu, *Nat. Commun.*, 2020, **11**, 4971; d) H. Furukawa, N. Ko, Y. B. Go, N. Aratani, S. B. Choi, E. Choi, A. Ö. Yazaydin, R. Q. Snurr, M. O'Keeffe and J. Kim, *Science*, 2010, **329**, 424–428; for comprehensive reviews regarding this field of research please see - Review 1: S. Yuan, L. Feng, K. Wang, J. Pang, M. Bosch, C. Lollar, Y. Sun, J. Qin, X. Yang, P. Zhang, Q. Wang, L. Zou, Y. Zhang, L. Zhang, Y. Fang, J. Li and H.-C. Zhou, *Adv. Mater.*, 2018, **30**, 1704303; Review2: N. L. Rosi, J. Eckert, M. Eddaoudi, D. T. Vodak, J. Kim, M. O'Keeffe and O. M. Yaghi, *Science*, 2003, **300**, 1127–1129.

[8] a) T. D. Bennett, F. X. Coudert, S. L. James and A. I. Cooper, *Nat. Mater.*, 2021, **20**, 1179–1187; b) M. Mastalerz, *Acc. Chem. Res.*, 2018, **51**, 2411–2422; c) T. Hasell and A. I. Cooper, *Nat. Rev. Mater.*, 2016, **1**, 16053; d) T. Tozawa, J. T. A. Jones, S. I. Swamy, S. Jiang, D. J. Adams, S. Shakespeare, R. Clowes, D. Bradshaw, T. Hasell, S. Y. Chong, C. Tang, S. Thompson, J. Parker, A. Trewin, J. Bacsa, A. M. Z. Slawin, A. Steiner and A. I. Cooper, *Nat. Mater.*, 2009, **8**, 973–978.

[9] T. Kunde, T. Pausch and B. M. Schmidt, *Eur. J. Org. Chem.*, 2021, **43**, 5844–5856.

[10] a) Z. Zhang, O. Š. Miljanić, Z. Zhenglin and M. Š Ognjen, *Org. Mater.*, 2019, **1**, 19–29; b) A. Cadiau, Y. Belmabkhout, K. Adil, P. M. Bhatt, R. S. Pillai, A. Shkurenko, C. Martineau-Corcos, G. Maurin and M. Eddaoudi, *Science*, 2017, **356**, 731–735; c) T.-H. Chen, W. Kaveevivitchai, A. J. Jacobson and O. Š. Miljanić, *Chem. Commun.*, 2015, **51**, 14096–14098; d) N. Shin-ichiro, N. Takayoshi, S. Noro and T. Nakamura, *NPG Asia Mater.*, 2017, **9**, e433–e433; f) T.-H. Chen, I. Popov, O. Zenasni, O. Daugulis and O. Š. Miljanić, *Chem. Commun.*, 2013, **49**, 6846–6848

[11] a) E. M Sven, R. I Nicolas, S. Dorothee, Z. Wen-Shan, R. Frank, S. R Rasmus, M. Michael, S. M. Elbert, N. I. Regenauer, D. Schindler, W.-S. Zhang, F. Rominger, R. R. Schröder and M. Mastalerz, *Chem. Eur. J.*, 2018, **24**, 11438–11443; b) M. J. Bojdys, M. E. Briggs, J. T. A. Jones, D. J. Adams, S. Y. Chong, M. Schmidtmann and A. I. Cooper, *J. Am. Chem. Soc.*, 2011, **133**, 16566–16571.

[12] W. Kiggen and F. Vögtle, *Angew. Chem. Int. Ed. English*, 1984, **23**, 714–715, for a summary of the concept of high-dilution techniques see: L. Rossa and F. Vögtle, Top. Curr. Chem., 1983, 1–86.

[13] M. L. C. Quan and D. J. Cram, *J. Am. Chem. Soc.,* 1991, **113**, 7, 2754–2755.

[14] A. P. Davis, R. S. Wareham, W. Ellis, T. K. Hollis, W. Odenkirk, J. Whelan, R. Ostrander, A. L. Rheingold, B. Bosnich, M. E. Huttenloch, J. Diebold, U. Rief, H. H. Brintzinger, A. M. Gilbert, T. J. Katz, H. Wiesenfeldt, A. Reinmuth, E. Barsties, K. Evertz and H. H. Brint, *Angew. Chem. Int. Ed. Engl.*, 1998, **37**, 4045.

[15] H. Masu, K. Katagiri, T. Kato, H. Kagechika, M. Tominaga and I. Azumaya, *J. Org. Chem.*, 2008, **73**, 5143–5146.

[16] F. Vögtle, J. Gross, C. Seel and M. Nieger, *Angew. Chem. Int. Ed. English*, 1992, **31**, 1069–1071.

[17] T. J. Mcmurry, S. J. Rodgers and K. N. Raymond, *J. Am. Chem. Soc.*, 2002, **109**, 3451–3453.

[18] R. Lavendomme, T. K. Ronson and J. R. Nitschke, *J. Am. Chem. Soc.*, 2019, **141**, 12147–12158.

[19] A. R. Stefankiewicz, M. R. Sambrook and J. K. M. Sanders, *Chem. Sci.*, 2012, **3**, 2326–2329.

[20] J. M. Lehn, *Chem. Eur. J*, 1999, **5**, 2455-2463.

[21] a) R. L. Greenaway, V. Santolini, F. T. Szczypiński, M. J. Bennison, M. A. Little, A. Marsh, K. E. Jelfs and A. I. Cooper, *Chem. Eur. J.*, 2020, **26**, 3718–3722; b) S. Klotzbach and F. Beuerle, *Angew. Chem. Int. Ed.*, 2015, **54**, 10356–10360.

[22] a) A. I. Kosińska, M. K. Nisiewicz, A. M. Nowicka and A. Kasprzak, *Chempluschem*, 2021, **86**, 820–826; b) D. Beaudoin, F. Rominger and M. Mastalerz, *Angew. Chem. Int. Ed.*, 2017, **56**, 1244–1248; for a review discussing the equilibrium between cages, macrocycles and polymers please see: Y. Jin, Q. Wang, P. Taynton and W. Zhang, *Acc. Chem. Res.*, 2014, **47**, 1575–1586.

[23] a) H. H. Huang, K. S. Song, A. Prescimone, A. Aster, G. Cohen, R. Mannancherry, E. Vauthey, A. Coskun and T. Šolomek, *Chem. Sci.*, 2021, **12**, 5275–5285; b) M. Hähsler and M. Mastalerz, *Chem. Eur. J.*, 2021, **27**, 233–237; c) H. Kudo, R. Hayashi, K. Mitani, T. Yokozawa, N. C. Kasuga and T. Nishikubo, *Angew. Chem. Int. Ed.*, 2006, **45**, 7948–7952.

[24] a) G. F. Feng, J. Geng, F. Da Feng and W. Huang, *Sci. Reports*, 2020, **10**, 1–5; b) B. Teng, M. A. Little, T. Hasell, S. Y. Chong, K. E. Jelfs, R. Clowes, M. E. Briggs and A. I. Cooper, *Cryst. Growth Des.*, 2019, **19**, 3647–3651; c) D. P. McMahon, A. Stephenson, S. Y. Chong, M. A. Little, J. T. A. Jones, A. I. Cooper and G. M. Day, *Faraday Discuss.*, 2018, **211**, 383–399.

[25] P. Wagner, F. Rominger, W. S. Zhang, J. H. Gross, S. M. Elbert, R. R. Schröder and M. Mastalerz, *Angew. Chem. Int. Ed.*, 2021, **60**, 8896–8904.

[26] a) M. Fujita, D. Oguro, M. Miyazawa, H. Oka, K. Yamaguchi and K. Ogura, *Nat.*, 1995, **378**, 469–471; b) T. Kusukawa and M. Fujita, *J. Am. Chem. Soc.*, 2002, **124**, 13576–13582.

[27] H. Ding, Y. Yang, B. Li, F. Pan, G. Zhu, M. Zeller, D. Yuan and C. Wang, *Chem. Commun.*, 2015, **51**, 1976–1979.

[28] a) R. L. Greenaway, V. Santolini, M. J. Bennison, B. M. Alston, C. J. Pugh, M. A. Little, M. Miklitz, E. G. B. Eden-Rump, R. Clowes, A. Shakil, H. J. Cuthbertson, H. Armstrong, M. E. Briggs, K. E. Jelfs and A. I. Cooper, *Nat. Commun.,* 2018, **9**, 1–11; b) T. P. Moneypenny, A. Yang, N. P. Walter, T. J. Woods, D. L. Gray, Y. Zhang and J. S. Moore, *J. Am. Chem. Soc.*, 2018, **140**, 5825–5833; c) W. M. Bloch, J. J. Holstein, W. Hiller and G. H. Clever, *Angew. Chem. Int. Ed.*, 2017, **56**, 8285–8289; for a comprehensive review on different geometries and building blocks see: F. Beuerle and B. Gole, *Angew. Chem. Int. Ed.*, 2018, **57**, 4850–4878.

[29] a) J. C. Lauer, Z. Pang, P. Janßen, F. Rominger, T. Kirschbaum, M. Elstner and M. Mastalerz, *ChemistryOpen*, 2020, **9**, 183–190; b) J. C. Lauer, W.-S. Zhang, F. Rominger, R. R. Schröder and M. Mastalerz, *Chem. Eur. J.*, 2018, **24**, 1816–1820.

[30] V. Santolini, M. Miklitz, E. Berardo and K. E. Jelfs, *Nanoscale*, 2017, **9**, 5280–5298.

[31] M. Mastalerz, *Angew. Chem. Int. Ed.*, 2010, **49**, 5042–5053.

[32] Y. Lei, Q. Chen, P. Liu, L. Wang, H. Wang, B. Li, X. Lu, Z. Chen, Y. Pan, F. Huang and H. Li, *Angew. Chem. Int. Ed.*, 2021, **60**, 4705–4711.

[33] a) D. Zarzeczańska, A. Adamczyk-Woźniak, A. Kulpa, T. Ossowski and A. Sporzyński, *Eur. J. Inorg. Chem.*, 2017, **2017**, 4493–4498; b) D. G. Hall, *Boronic acids: preparation, applications in organic synthesis and medicine*, John Wiley & Sons, 2006.

[34] S. Ivanova, E. Köster, J. J. Holstein, N. Keller, G. H. Clever, T. Bein and F. Beuerle, *Angew. Chem. Int. Ed.*, 2021, **60**, 17455–17463.

[35] a) M. S. Collins, M. E. Carnes, B. P. Nell, L. N. Zakharov and D. W. Johnson, *Nat. Commun. 2016 71*, 2016, **7**, 1–7.

[36] a) T. P. Moneypenny, H. Liu, A. Yang, I. D. Robertson and J. S. Moore, *J. Polym. Sci. Part A Polym. Chem.*, 2017, **55**, 2935–2948; b) H. Wettach, S. Höger, D. Chaudhuri, J. M. Lupton, F. Liu, E. M. Lupton, S. Tretiak, G. Wang, M. Li, S. De Feyter, S. Fischer and S. Förster, *J. Mater. Chem.*, 2011, **21**, 1404–1415; c) L. Shu and M. Mayor, *Chem. Commun.*, 2006, **39**, 4134–4136.

[37] S. Hiraoka, Y. Yamauchi, R. Arakane and M. Shionoya, *J. Am. Chem. Soc.*, 2009, **131**, 11646–11647.

[38] S. Lee, A. Yang, T. P. Moneypenny and J. S. Moore, *J. Am. Chem. Soc.*, 2016, **138**, 2182–2185.

[39] a) A. Kai, B. D. Egleston, A. Tarzia, R. Clowes, M. E. Briggs, K. E. Jelfs, A. I. Cooper, R. L. Greenaway, *Adv. Funct. Mater.*, 2021, **31**, 2106116; b) K. Jie, N. Onishi, J. A. Schott, I. Popovs, D. Jiang, S. Mahurin and S. Dai, *Angew. Chem. Int. Ed. ,* 2020, **59**, 2268–2272; c) N. Giri, M. G. Del Pópolo, G. Melaugh, R. L. Greenaway, K. Rätzke, T. Koschine, L. Pison, M. F. C. Gomes, A. I. Cooper and S. L. James, *Nature,* 2015, **527**, 216–220.

[40] Q. Song, S. Jiang, T. Hasell, M. Liu, S. Sun, A. K. Cheetham, E. Sivaniah, A. I. Cooper, *Adv. Mater.*, 2016, **28**, 2629–2637.

[41] a) M. Brutschy, M. W. Schneider, M. Mastalerz and S. R. Waldvogel, *Chem. Commun.*, 2013, **49**, 8398–8400; b) M. Brutschy, M. W. Schneider, M. Mastalerz and S. R. Waldvogel, *Adv. Mater.*, 2012, **24**, 6049–6052.

[42] a) J. L. Atwood, L. J. Barbour, A. Jerga and B. L. Schottel, *Science (80-.).*, 2002, **298**, 1000–1002; b) J. L. Atwood, L. J. Barbour and A. Jerga, *Science (80-.).*, 2002, **296**, 2367–2369.

[43] A. G. Slater, M. A. Little, A. Pulido, S. Y. Chong, D. Holden, L. Chen, C. Morgan, X. Wu, G. Cheng, R. Clowes, M. E. Briggs, T. Hasell, K. E. Jelfs, G. M. Day and A. I. Cooper, *Nat. Chem.*, 2017, **9**, 17–25.

[44] S. Jiang, Q. Song, A. Massey, S. Y. Chong, L. Chen, S. Sun, T. Hasell, R. Raval, E. Sivaniah, A. K. Cheetham and A. I. Cooper, *Angew. Chem. Int. Ed.*, 2017, **56**, 9391 – 9395

[45] a) T. Mitra, X. Wu, R. Clowes, J. T. A. Jones, K. E. Jelfs, D. J. Adams, A. Trewin, J. Bacsa, A. Steiner and A. I. Cooper, *Chem. Eur. J.*, 2011, **17**, 10235–10240; b) T. Tozawa, J. T. A. Jones, S. I. Swamy, S. Jiang, D. J. Adams, S. Shakespeare, R. Clowes, D. Bradshaw, T. Hasell, S. Y. Chong, C. Tang, S. Thompson, J. Parker, A. Trewin, J. Bacsa, A. M. Z. Slawin, A. Steiner and A. I. Cooper, *Nat. Mater. 2009*, **8**, 973–978.

[46] T. Hasell, J. L. Culshaw, S. Y. Chong, M. Schmidtmann, M. A. Little, K. E. Jelfs, E. O. Pyzer-Knapp, H. Shepherd, D. J. Adams, G. M. Day and A. I. Cooper, *J. Am. Chem. Soc.*, 2014, **136**, 1438–1448.

[47] S. Spicher, M. Bursch and S. Grimme, *J. Phys. Chem. C*, 2020, **124**, 27529–27541.

[48] J. T. A. Jones, D. Holden, T. Mitra, T. Hasell, D. J. Adams, K. E. Jelfs, A. Trewin, D. J. Willock, G. M. Day, J. Bacsa, A. Steiner and A. I. Cooper, *Angew. Chem. Int. Ed.*, 2011, **50**, 749–753.

[49] a) L. Turcani, R. L. Greenaway and K. E. Jelfs, *Chem. Mater.*, 2019, **31**, 714–727; b) V. Santolini, G. A. Tribello and K. E. Jelfs, *Chem. Commun.*, 2015, **51**, 15542–15545; c) M. A. Little, M. E. Briggs, J. T. A. Jones, M. Schmidtmann, T. Hasell, S. Y. Chong, K. E. Jelfs, L. Chen and A. I. Cooper, *Nat. Chem.*, 2015, **7**, 153–159; for a comprehensive review see: J. D. Evans, K. E. Jelfs, G. M. Day and C. J. Doonan, *Chem. Soc. Rev.*, 2017, **46**, 3286–3301.

[50] R. L. Greenaway, V. Santolini, M. J. Bennison, B. M. Alston, C. J. Pugh, M. A. Little, M. Miklitz, E. G. B. Eden-Rump, R. Clowes, A. Shakil, H. J. Cuthbertson, H. Armstrong, M. E. Briggs, K. E. Jelfs and A. I. Cooper, *Nat. Commun.*, 2018, **9**, 1–11.

[51] M. W. Schneider, I. M. Oppel, H. Ott, L. G. Lechner, H. J. S. Hauswald, R. Stoll and M. Mastalerz, *Chem. Eur. J.*, 2012, **18**, 836–847.

[52] a) K. E. Jelfs, X. Wu, M. Schmidtmann, J. T. A Jones, J. E. Warren, D. J. Adams, A. I. Cooper, *Angew. Chem. Int. Ed.*, 2011, **50**, 10653–10656; b) Y. Jin, B. A. Voss, A. Jin, H. Long, R. D. Noble and W. Zhang, *J. Am. Chem. Soc.*, 2011, **133**, 6650–6658; c) M. Mastalerz, M. W. Schneider, I. M. Oppel and O. Presly, *Angew. Chem. Int. Ed.*, 2011, **50**, 1046–1051.

[53] M. Liu, M. A. Little, K. E. Jelfs, J. T. A. Jones, M. Schmidtmann, S. Y. Chong, T. Hasell and A. I. Cooper, *J. Am. Chem. Soc.*, 2014, **136**, 7583–7586.

[54] a) P. E. Alexandre, W. S. Zhang, F. Rominger, S. M. Elbert, R. R. Schröder and M. Mastalerz, *Angew. Chem. Int. Ed.*, 2020, **59**, 19675–19679; b) A. S. Bhat, S. M. Elbert, W. Zhang, F. Rominger, M. Dieckmann, R. R. Schröder and M. Mastalerz, *Angew. Chem. Int. Ed.*, 2019, **58**, 8819–8823.

[55] M. E. Briggs and A. I. Cooper, *Chem. Mater.*, 2016, **29**, 149–157.

[56] I. Langmuir, *J. Am. Chem. Soc.*, 1918, **40**, 1361–1403.

[57] S. Brunauer, P. H. Emmett and E. Teller, *J. Am. Chem. Soc.*, 1938, **60**, 309–319.

[58] M. M. Deegan, M. R. Dworzak, A. J. Gosselin, K. J. Korman and E. D. Bloch, *Chem. Eur. J.*, 2021, **27**, 4531–4547.

[59] Y. Xia, Z. Yang and Y. Zhu, *J. Mater. Chem. A*, 2013, **1**, 9365–9381.

[60] a) Y. Belmabkhout, P. M. Bhatt, K. Adil, R. S. Pillai, A. Cadiau, A. Shkurenko, G. Maurin, G. Liu, W. J. Koros and M. Eddaoudi, *Nat. Energy*, 2018, **3**, 1059–1066; b) T. Chen, I. Popov, W. Kaveevivitchai, Y. Chuang, Y. Chen, A. J. Jacobson and O. Š. Miljanić, *Angew. Chen. Int. Ed.*, 2015, **54**, 13902–13906; c) P. Pachfule, Y. Chen, J. Jiang and R. Banerjee, *Chem. Eur. J.*, 2012, **18**, 688–694; d) C. Yang, X. Wang and M. A. Omary, *J. Am. Chem. Soc.*, 2007, **129**, 15454–15455.

[61] a) C. Gao, J. Li, S. Yin, G. Lin, T. Ma, Y. Meng, J. Sun and C. Wang, *Angew. Chem. Int. Ed*., 2019, **58**, 9770–9775; b) Z. Yang, S. Wang, Z. Zhang, W. Guo, K. Jie, M. I. Hashim, O. Miljanić, D. E. Jiang, I. Popovs and S. Dai, *J. Mater. Chem. A*, 2019, **7**, 17277–17282; c) S. B. Alahakoon, G. Occhialini, G. T. McCandless, A. A. K. Karunathilake, S. O. Nielsen and R. A. Smaldone, *CrystEngComm*, 2017, **19**, 4882–4885: d) S. B. Alahakoon, G. T. McCandless, A. A. K. Karunathilake, C. M. Thompson and R. A. Smaldone, *Chem. Eur. J.*, 2017, **23**, 4255–4259; e) X. Chen, M. Addicoat, S. Irle, A. Nagai and D. Jiang, *J. Am. Chem. Soc.*, 2013, **135**, 546–549.

[62] M. I. Hashim, H. T. M. Le, T. H. Chen, Y. S. Chen, O. Daugulis, C. W. Hsu, A. J. Jacobson, W. Kaveevivitchai, X. Liang, T. Makarenko, O. Miljanić, I. Popovs, H. V. Tran, X. Wang, C. H. Wu and J. I. Wu, *J. Am. Chem. Soc.*, 2018, **140**, 6014–6026.

[63] a) P. Mateus, R. Delgado, P. Brandão, S. Carvalho and V. Félix, *Org. Biomol. Chem.*, 2009, **7**, 4661–4673; b) O. Francesconi, C. Nativi, S. Roelens, A. Ienco and G. Moneti, *Angew. Chem. Int. Ed.*, 2006, **45**, 6693–6696.

[64] T. H. G. Schick, F. Rominger and M. Mastalerz, *J. Org. Chem.*, 2020, **85**, 13757–13771.

[65] T. Jiao, G. Wu, L. Chen, C. Y. Wang and H. Li, *J. Org. Chem.*, 2018, **83**, 12404–12410.

[66] K. J. Wallace, R. Hanes, E. Anslyn, J. Morey, K. V. Kilway and J. Siegel, *Synthesis*, 2005, **2005**, 2080–2083.

[67] M. Mayor and J. M. Lehn, *J. Am. Chem. Soc.*, 1999, **121**, 11231–11232.

[68] Y. Cohen, L. Avram and L. Frish, *Angew. Chem. Int. Ed. Engl.*, 2005, **44**, 520–554.

[69] M. Mastalerz, *Chem. Commun.*, 2008, 4756–4758.

[70] a) J. Yoo, M. S. Kim, S. J. Hong, J. L. Sessler and C. H. Lee, *J. Org. Chem.*, 2009, **74**, 1065–1069; b) P. Gamez, T. J. Mooibroek, S. J. Teat and J. A. N. Reedijk, *Acc. Chem. Res.*, 2007, **40**, 435–444; c) H. Miyaji and J. L. Sessler, *Angew. Chem. Int. Ed*., *2001*, **40**, 154-157; for a comprehensive review see: P. A. Gale and C. Caltagirone, *Chem. Soc. Rev.*, 2015, **44**, 4212–4227.

[71] a) B. W. Tresca, L. N. Zakharov, C. N. Carroll, D. W. Johnson and M. M. Haley, *Chem. Commun.*, 2013, **49**, 7240–7242; b) J. M. Engle, C. N. Carroll, D. W. Johnson and M. M. Haley, *Chem. Sci.*, 2012, **3**, 1105–1110.

[72] W. J. Ong and T. M. Swager, *Nat. Chem. 2018*, **10**, 1023–1030.

[73] S. Rohrbach, A. J. Smith, J. H. Pang, D. L. Poole, T. Tuttle, S. Chiba and J. A. Murphy, *Angew. Chem. Int. Ed.*, 2019, **58**, 16368–16388.

[74] T. Mizuhara, S. Oishi, N. Fujii and H. Ohno, *J. Org. Chem.*, 2010, **75**, 265–268.

[75] K. Acharyya, S. Mukherjee and P. S. Mukherjee, *J. Am. Chem. Soc.*, 2013, **135**, 554–557.

[76] L. A. Hartmann, J. F. Stephen and W. Chester, *US4783547A*, 1986.

[77] T. Kaneko, *JP2006273766A*, 2006.

[78] a) V. Amendola, E. Bastianello, L. Fabbrizzi, C. Mangano, P. Pallavicini, A. Perotti, A. M. Lanfredi, F. Ugozzoli, P. Pallavicini, A. Perotti, A. M. Lanfredi and F. Ugozzoli, *Angew. Chem. Int. Ed*, 2000, **39**, No.16, 2917-2920; b) R. J. Motekaitis, A. E. Martell, B. Dietrich and J. M. Lehn, *Inorg. Chem.*, 1984, **23**, 1588–1591; for an excellent review see: G. Alibrandi, V. Amendola, G. Bergamaschi, L. Fabbrizzi and M. Licchelli, *Org. Biomol. Chem.*, 2015, **13**, 3510–3524.

[79] T. Kunde, E. Nieland, H. V Schröder, C. A. Schalley and B. M. Schmidt, *Chem. Commun.*, 2020, **56**, 4761–4764.

[80] M. Miklitz and K. E. Jelfs, *J. Chem. Inf. Model.*, 2018, **58**, 2387–2391.

[81] a) G. Zhang, O. Presly, F. White, I. M. Oppel and M. Mastalerz, *Angew. Chem. Int. Ed.,* 2014, **53**, 5126; b) T. Hasell, X. Wu, J. T. Jones, J. Bacsa, A. Steiner, T. Mitra, A. Trewin, D. J. Adams and A. I. Cooper, *Nat. Chem.,* 2010, **2**, 750.

[82] a) A. Kruve, K. Caprice, R. Lavendomme, J. M. Wollschläger, S. Schoder, H. V. Schröder, J. R. Nitschke, F. B. L. Cougnon and C. A. Schalley, *Angew. Chem. Int. Ed.*, 2019, **58**, 11324; b) K. Caprice, M. Pupier, A. Kruve, C. A. Schalley and F. B. L. Cougnon, *Chem. Sci.*, 2018, **9**, 1317; c) U. Warzok, M. Marianski, W. Hoffmann, L. Turunen, K. Rissanen, K. Pagel and C. A. Schalley, *Chem. Sci.*, 2018, **9**, 8343.

[83] T. Kunde, T. Pausch and B. M. Schmidt, *Chem. - A Eur. J.*, 2021, **27**, 8457–8460.

[84] T. H. G. Schick, J. C. Lauer, F. Rominger and M. Mastalerz, *Angew. Chem. Int. Ed.*, 2019, **58**, 1768–1773.

[85] T. Jiao, L. Chen, D. Yang, X. Li, G. Wu, P. Zeng, A. Zhou, Q. Yin, Y. Pan, B. Wu, X. Hong, X. Kong, V. M. Lynch, J. L. Sessler and H. Li, *Angew. Chemie*, 2017, **129**, 14737–14742.

[86] a) S. Ren, M. J. Bojdys, R. Dawson, A. Laybourn, Y. Z. Khimyak, D. J. Adams, A. I. Cooper and Y. Z. Khimyak, *Adv. Mater.*, 2012, **24**, 2357–2361; b) P. Kuhn, A. Forget, D. Su, A. Thomas and M. Antonietti, *J. Am. Chem. Soc.*, 2008, **130**, 13333–13337.

[87] a) Z. Yang, H. Chen, B. Li, W. Guo, K. Jie, Y. Sun, D. Jiang, I. Popovs and S. Dai, *Angew. Chemie*, 2019, **131**, 13901–13905; b) W. A. Braunecker, K. E. Hurst, K. G. Ray, Z. R. Owczarczyk, M. B. Martinez, N. Leick, A. Keuhlen, A. Sellinger and J. C. Johnson, *Cryst. Growth Des.*, 2018, **18**, 4160–4166.

[88] T. Kunde, T. Pausch, G. J. Reiss and B. M. Schmidt, *Synlett*, 2022, **33**, 161–165.

[89] a) J. Gawronski, K. Gawronska, J. Grajewski, M. Kwit, A. Plutecka and U. Rychlewska, *Chem. – A Eur. J.*, 2006, **12**, 1807–1817; b) J. Gawroński, H. Kołbon, M. Kwit and A. Katrusiak, *J. Org. Chem.*, 2000, **65**, 5768–5773.

[90] a) H. F. Nour, M. F. Matei, B. S. Bassil, U. Kortz and N. Kuhnert, *Org. Biomol. Chem.*, 2011, **9**, 3258–3271; b) N. Kuhnert, C. Patel and F. Jami, *Tetrahedron Lett.*, 2005, **46**, 7575–7579; c) N. Kuhnert, N. Burzlaff, C. Patel and A. Lopez-Periago, *Org. Biomol. Chem.*, 2005, **3**, 1911–1921; d) N. Kuhnert, G. M. Rossignolo and A. Lopez-Periago, *Org. Biomol. Chem.*, 2003, **1**, 1157–1170; e) N. Kuhnert and A. M. Lopez-Periago, *Tetrahedron Lett.*, 2002, **43**, 3329–3332.

[91] N. Kuhnert, D. Göbel, C. Thiele, B. Renault and B. Tang, *Tetrahedron Lett.*, 2006, **47**, 6915–6918.

[92] A. Janiak, M. Bardziński, J. Gawroński and U. Rychlewska, *Cryst. Growth Des.*, 2016, **16**, 2779–2788.

[93] a) A. Dey, S. Chand, B. Maity, P. M. Bhatt, M. Ghosh, L. Cavallo, M. Eddaoudi and N. M. Khashab, *J. Am. Chem. Soc.*, 2021, **143**, 4090–4094; b) B. Hua, Y. Ding, L. O. Alimi, B. Moosa, G. Zhang, W. S. Baslyman, J. Sessler and N. M. Khashab, *Chem. Sci.*, 2021, **12**, 12286–12291; c) A. Dey, S. Chand, M. Ghosh, M. Altamimy, B. Maity, P. M. Bhatt, I. A. Bhat, L. Cavallo, M. Eddaoudi and N. M. Khashab, *Chem. Commun.*, 2021, **57**, 9124–9127; d) A. Chaix, G. Mouchaham, A. Shkurenko, P. Hoang, B. Moosa, P. M. Bhatt, K. Adil, K. N. Salama, M. Eddaoudi and N. M. Khashab, *J. Am. Chem. Soc.*, 2018, **140**, 14571–14575.

[94] T. Huang, B. A. Moosa, P. Hoang, J. Liu, S. Chisca, G. Zhang, M. AlYami, N. M. Khashab and S. P. Nunes, *Nat. Commun.*, 2020, **11**, 1–10.

[95] D. He, R. Clowes, M. A. Little, M. Liu and A. I. Cooper, *Chem. Commun.*, 2021, **57**, 6141–6144.

[96] S. Viel, F. Ziarelli, G. Pages, C. Carrara, S. Caldarelli, *J. Magn. Reson.*, 2008, **190**, 113.

[97] Y. H. Zhao, M. H. Abraham and A. M. Zissimos, *J. Org. Chem.*, 2003, **68**, 7368.

[98] Frisch, M. J. *et al*.; Gaussian16 Revision B.01. (**2016**).

[99] A. Burkhardt et al., Status of the crystallography beamlines at PETRA III, *Eur. Phys. J. Plus*, 131:56 (*2016*)

[100] A. Meents et al., Development of an in-vacuum x-ray microscope with cryogenic sample cooling for beamline P11 at PETRA III, *Proceedings of SPIE* 8851, 88510K (**2013**).

[101] G. M. Sheldrick, SADABS, program for empirical absorption correction of area detector data, University of Göttingen, Göttingen, **1996.**

[102] G. M. Sheldrick, SHELXT-2013, Program for Crystal Structure Solution, University of Göttingen, Göttingen, **2013**.

[103] G. M. Sheldrick, SHELXL-2014, Program for Crystal Structure Refinement, University of Göttingen, Göttingen, **2014.**

8. Abbreviations

ACN	Acetonitrile
AIE	Aggregation Induced Emission
Ar	Aryl
AT-IR	Attenuated Transmission Infrared Spectroscopy
BET	Brunauer-Emmett-Teller
CCDC	Cambridge Crystallographic Data Center
CFC	Chlorofluorocarbons
CID	Collision Induced Dissociation
COF	Covalent Organic Framework
CTF	Covalent Triazine Framework
DACH	1,2-Diaminocyclohexane
DBU	1,8-Diazabicyclo(5.4.0)undec-7-ene
DCM	Dichloromethane
DESY	Deutsches Elektronen-Synchrotron
DIBAL-H	Diisobutyl Aluminum Hydride
DFT	Density functional theory
DMF	Dimethylformamide
DMSO	Dimethylsulfoxide
DOSY	Diffusion Ordered Spectroscopy
ESI	Electron Spray Ionization
FPOC	Fluorinated Porous Organic Cage
GPC	Gel Permeation Chromatography
HRMS	High Resolution Mass Spectroscopy
IAST	Ideal Adsorption Solution Theory
IR	Infrared Spectroscopy
I-PrOH	*iso*-Propanol
MALDI	Matrix Assisted Laser Desorption Ionization
MOF	Metal Organic Framework
MS	Mass Spectroscopy
NMR	Nuclear Magnetic Resonance
ORTEP	Oak Ridge Thermal Ellipsoid Plot
PFOA	Perfluorooctanoic Acid
PIM	Polymers with Intrinsic Microporosity
POC	Porous Organic Cage

POP	Porous Organic Polymer
PTFE	Polytetrafluoroethylene
PXRD	Powder X-ray diffraction
r.t.	room temperature
SA	Surface Area
SC-XRD	Single Crystal X-ray diffraction
SEM	Scanning Electron Microscopy
SOF	Supramolecular Organic Framework
TA	Terephthalaldehyde
TFA	Trifluoroacetic Acid
TFTA	Tetrafluoroterephthalaldehyde
TGA	Thermogravimetrical Analysis
THF	Tetrahydrofurane
TLC	Thin Layer Chromatography
TOF	Time Of Flight
TREN	Tris(2-aminoethyl)amine
UFF	Universal Force Field

9. Selbstständigkeitserklärung

Ich versichere an Eides Statt, dass die Dissertation von mir selbständig und ohne unzulässige fremde Hilfe unter Beachtung der „Grundsätze zur Sicherung guter wissenschaftlicher Praxis an der Heinrich-Heine-Universität Düsseldorf“ erstellt worden ist.

Düsseldorf, den 17.02.2022

Tom Kunde